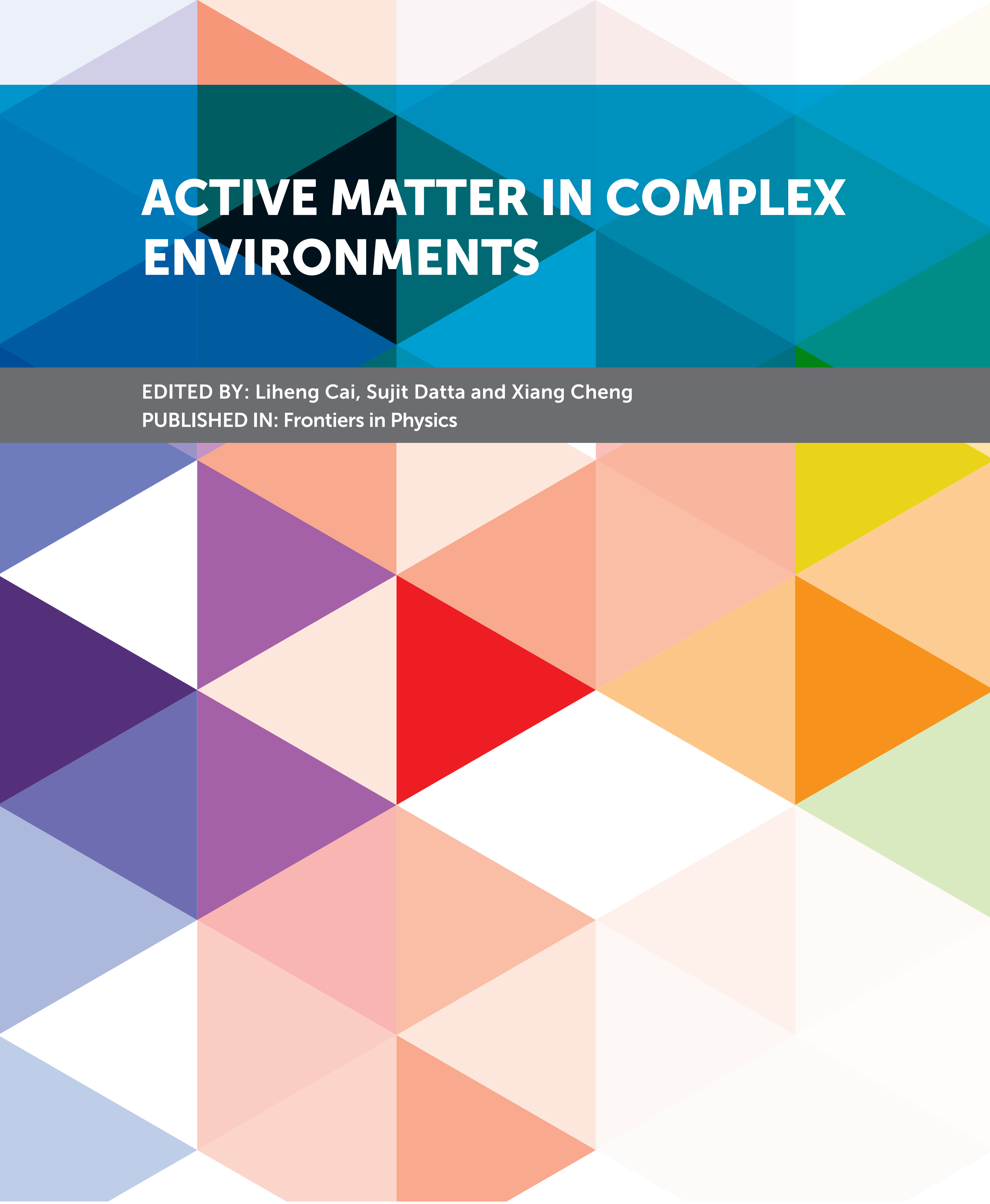

ACTIVE MATTER IN COMPLEX ENVIRONMENTS

EDITED BY: Liheng Cai, Sujit Datta and Xiang Cheng
PUBLISHED IN: Frontiers in Physics

frontiers Research Topics

ISSN 1664-8714
ISBN 978-2-83250-219-8
DOI 10.3389/978-2-83250-219-8

About Frontiers

Frontiers is more than just an open-access publisher of scholarly articles: it is a pioneering approach to the world of academia, radically improving the way scholarly research is managed. The grand vision of Frontiers is a world where all people have an equal opportunity to seek, share and generate knowledge. Frontiers provides immediate and permanent online open access to all its publications, but this alone is not enough to realize our grand goals.

Frontiers Journal Series

The Frontiers Journal Series is a multi-tier and interdisciplinary set of open-access, online journals, promising a paradigm shift from the current review, selection and dissemination processes in academic publishing. All Frontiers journals are driven by researchers for researchers; therefore, they constitute a service to the scholarly community. At the same time, the Frontiers Journal Series operates on a revolutionary invention, the tiered publishing system, initially addressing specific communities of scholars, and gradually climbing up to broader public understanding, thus serving the interests of the lay society, too.

Dedication to Quality

Each Frontiers article is a landmark of the highest quality, thanks to genuinely collaborative interactions between authors and review editors, who include some of the world's best academicians. Research must be certified by peers before entering a stream of knowledge that may eventually reach the public - and shape society; therefore, Frontiers only applies the most rigorous and unbiased reviews.
Frontiers revolutionizes research publishing by freely delivering the most outstanding research, evaluated with no bias from both the academic and social point of view. By applying the most advanced information technologies, Frontiers is catapulting scholarly publishing into a new generation.

What are Frontiers Research Topics?

Frontiers Research Topics are very popular trademarks of the Frontiers Journals Series: they are collections of at least ten articles, all centered on a particular subject. With their unique mix of varied contributions from Original Research to Review Articles, Frontiers Research Topics unify the most influential researchers, the latest key findings and historical advances in a hot research area! Find out more on how to host your own Frontiers Research Topic or contribute to one as an author by contacting the Frontiers Editorial Office: frontiersin.org/about/contact

ACTIVE MATTER IN COMPLEX ENVIRONMENTS

Topic Editors:
Liheng Cai, University of Virginia, United States
Sujit Datta, Princeton University, United States
Xiang Cheng, University of Minnesota Twin Cities, United States

Citation: Cai, L., Datta, S., Cheng, X., eds. (2022). Active Matter in Complex Environments. Lausanne: Frontiers Media. doi: 10.3389/978-2-83250-219-8

Table of Contents

frontiers | Frontiers in Physics

TYPE Editorial
PUBLISHED 01 September 2022
DOI 10.3389/fphy.2022.1005146

EDITED AND REVIEWED BY
Jasper Van Der Gucht,
Wageningen University and Research,
Netherlands

*CORRESPONDENCE
Li-Heng Cai,
liheng.cai@virginia.edu
Sujit S. Datta,
ssdatta@princeton.edu
Xiang Cheng,
xcheng@umn.edu

SPECIALTY SECTION
This article was submitted to Soft Matter Physics,
a section of the journal
Frontiers in Physics

RECEIVED 28 July 2022
ACCEPTED 15 August 2022
PUBLISHED 01 September 2022

CITATION
Cai L-H, Datta SS and Cheng X (2022),
Editorial: Active matter in
complex environments.
Front. Phys. 10:1005146.
doi: 10.3389/fphy.2022.1005146

Editorial: Active matter in complex environments

Li-Heng Cai [1]*, Sujit S. Datta [2]* and Xiang Cheng [3]*

[1]Soft Biomatter Laboratory, Department of Materials Science and Engineering, Department of Chemical Engineering, and Department of Biomedical Engineering, University of Virginia, Charlottesville, VA, United States, [2]Department of Chemical and Biological Engineering, Princeton University, Princeton, NJ, United States, [3]Department of Chemical Engineering and Materials Science, University of Minnesota, Minneapolis, MN, United States

KEYWORDS

active matter, soft matter physics, complex fluids, porous media, responsive materials

Editorial on the Research Topic
Active matter in complex environments

Unlike inert materials in equilibrium, active matter is intrinsically out of equilibrium. Whether as individual or a collective of many self-propelled objects, active matter is often surrounded by physically, chemically, and/or biologically complex environments. Articles of this issue described how such complexities change the behavior of active matter in fascinating and often unexpected ways.

At the level of individuals, theoretical and numerical models are providing new insights into the fundamental physics of motility. For example, Barriuso-Gutierrez et al. developed a numerical algorithm based on dissipative particle hydrodynamics, which properly accounts for hydrodynamic interactions and thermal fluctuations. This approach allowed them to investigate active particles of different swimming mechanisms and shapes in bulk fluids and under confinement. They showed that geometric confinement could substantially vary the translational and orientational dynamics of active spherical colloids and modify the morphology of active polymers. In a related work, Faúndez et al. used simulations to investigate how adhesive active Brownian particles interact with a cylindrical obstacle under an imposed fluid flow. When the flow is strong, particles encounter and adhere to the entire obstacle surface, leading to the formation of multi-layered deposits. Conversely, when the flow is weak, particles directly intercept and adhere to the obstacle in a single-layered deposit. The crossover of these two regimes then defines an optimal flow velocity at which the number of deposited particles is maximized, which provides a useful guide for applications seeking to e.g., filter and retain microswimmers.

Fluid flow also plays an important role in influencing the transport of biological swimmers, such as bacteria. As an example, Savorana et al. experimentally explored how the shear rate and the rheological behavior of polymer solutions affect the motility of *Pseudomonas aeruginosa* in a Poiseuille flow. They found that in the flow of Newtonian fluids, the bacteria are more concentrated towards the center of the microchannel where the shear rate is minimum. By contrast, in the flow of a shear-thinning fluid, the concentration profile of bacteria is not much different from that in the low-viscosity, Newtonian buffer, despite the zero-shear viscosity of the shear-thinning fluid being two orders of magnitude higher than that of the buffer. Intrigued by the oscillatory motion of cilia and flagella, Tamayo et al. used numerical simulations to study the instabilities and dynamics of a minimal filament-motor system in model viscoelastic fluids. Their model successfully captures some very interesting features. In a Newtonian fluid, the oscillation frequency is determined by motor kinetics and decreases with the increase of fluid viscosity. In viscoelastic fluids that have the same viscosity as the Newtonian fluid, the filament can exhibit stable oscillatory states with larger amplitudes and higher frequencies than in the Newtonian case.

Unlike bacteria, mammalian cells constantly reorganize their cytoskeleton to generate contractility and migrate. Bergeron-Sandoval et al. explored the biological mechanisms of shear stress-mediated cell contractility. They discovered that only cells with dynamic Filamin A (FLNa), a protein critical to cell structure and mechanosensation, and FilGAP, a specific GTPase activating protein (GAP), convert shear stress into GTPase activity to result downstream contractile changes. Yet, in the absence of intact FLNa-FilGAP mechanosensing, the contractile activity of cells can be rescued using pharmaceuticals to manipulate Rho and Rac activity, which are known to mediate cellular migration by directing the formation and organization of actin filaments. These studies clarify a precise mechanomolecular pathway used for cellular force sensing that may play critical roles in e.g., cancer metastasis and cardiovascular disease.

Moving to even more complex environments, Modica et al. used experiments with self-propelled Janus particles, Brownian dynamics simulations, and theory to investigate how active particles navigate through arrays of *multiple* obstacles, which act as a model of more complex porous media. In this case, accumulation at the obstacle surfaces hinders the long-time effective diffusion of the particles. Remarkably, this hindrance is much larger than the hindrance experienced by passive Brownian particles—highlighting the importance of the coupling between active forces and boundary interactions on the transport properties of active matter.

Two articles of the issue investigated the collective dynamics of active matter and examined their behaviors under geometric confinement. Inspired by the inter-cell interaction mediated by deformed elastic substrates, Bose et al. explored the emergent collective states of active particles with elastic dipolar interactions in simulations. They showed the formation of polar particle clusters and used confinement to modify the collision dynamics of the motile chains. Gulati et al. addressed the important question on how boundary conditions affect the collective dynamics of active liquid crystals. Combining simulations with stability analysis, they showed a series of transitions between different collective states and revealed the interplay between symmetry and geometry in dictating the collective dynamics of active matter. Both works illustrated the great potential of using confinement to tune the dynamics of active systems.

Active materials can also respond to and alter the environments they interact with. As a fascinating example of this point, Pönisch and Zaburdaev computationally studied how bacteria that use surface appendages ("pili") to self-propel can power the persistent rotation of a micron-sized turbine. Their work is motivated by the observation that many bacteria use pili protrusion and retraction to bind to and crawl along surfaces, and that the molecular motors involved are among the strongest motors known in nature. Indeed, Pönisch and Zaburdaev found that when groups of cells attach to and pull on the turbine, it can rotate persistently, depending on specific changes in pili binding and adhesion. Not only does this work further elucidate active matter-boundary interactions at a fundamental level, but it also suggests a way to put active matter to work!

Going beyond studies in the lab, the mathematical modeling of Vachier and Wettlaufer provided insights into bacterial locomotion in ice under temperature and chemical gradients. The authors considered the interplay between bio-enhanced interfacial premelting, thermal regelation, particle motility and chemotaxis and analyzed its consequence on particle dynamics and nutrient distributions in ice. Their work reveals interesting aspects of life in extreme environments and may be useful for understanding the covariation of life and climate and potential biosignatures in extraterrestrial life.

Finally, moving beyond natural and synthetic microswimmers, Tepermeister et al. reviewed the use of soft responsive materials to make functional devices—highlighting how activity, encoded by material properties, can be exploited for applications. The researchers outlined the physical principles for soft ionic materials and devices, discussed the progress for each of the potential device components, and pointed out opportunities for future research.

Author contributions

All authors contributed equally to the conceptualization and writing of this editorial.

Conflict of interest

The authors declare that the research was conducted in the absence of any commercial or financial relationships that could be construed as a potential conflict of interest.

Publisher's note

Frontiers in Physics

ORIGINAL RESEARCH
published: 08 April 2022
doi: 10.3389/fphy.2022.869175

Porous Media Microstructure Determines the Diffusion of Active Matter: Experiments and Simulations

Kevin J. Modica, Yuchen Xi and Sho C. Takatori*

Department of Chemical Engineering, University of California, Santa Barbara, Santa Barbara, CA, United States

Active swimmers are known to accumulate along external boundaries owing to their persistent self-motion, resulting in a significant reduction in their effective mobility through heterogeneous and tortuous materials. The dynamic interplay between the slowdown experienced by the active constituents near boundaries and their long-time diffusivity is critical for understanding and predicting active transport in porous media. In this work, we study the impact of boundary layer accumulation on the effective diffusivity of active matter by analyzing the motion of active Brownian particles in an array of fixed obstacles. We combine Janus particle experiments, Brownian dynamics simulations, and a theoretical analysis based on the Smoluchowski equation. We find that the shape, curvature, and microstructure of the obstacles play a critical role in governing the effective diffusivity of active particles. Indeed, even at dilute packing fractions of obstacles, ϕ = 12%, we observed a 25% reduction in the effective diffusivity of active particles, which is much larger than the hindrance experienced by passive Brownian particles. Our combined experimental and computational results demonstrate a strong coupling between the active force and the porous media microstructure. This work provides a framework to predict and control the transport of active matter in heterogeneous materials.

Keywords: active matter, colloidal transport, porous media, brownian motion, active suspensions, janus particles

Edited by:
Sujit Datta,
Princeton University, United States

Reviewed by:
Tapomoy Bhattacharjee,
National Centre for Biological Sciences, India
Christina Kurzthaler,
Princeton University, United States

***Correspondence:**
Sho C. Takatori
stakatori@ucsb.edu

Specialty section:
This article was submitted to Soft Matter Physics, a section of the journal Frontiers in Physics

Received: *04 February 2022*
Accepted: *04 March 2022*
Published: *08 April 2022*

Citation:
Modica KJ, Xi Y and Takatori SC (2022) Porous Media Microstructure Determines the Diffusion of Active Matter: Experiments and Simulations. Front. Phys. 10:869175. doi: 10.3389/fphy.2022.869175

INTRODUCTION

The transport of living, colloidal-sized species through crowded environments plays a crucial function in many natural and synthetic processes. For example, the transport of bacteria through soil plays a beneficial role in bioremediation [1, 2], and novel drug delivery mechanisms seek to utilize the proliferation of *S. typhimurium* to access tumor tissues that have been conventionally out of reach [3, 4]. In contrast, the transport of pathogens into wounds sites and mucosa can lead to life-threatening infections without proper treatment [5–7]. The effective transport properties of bacteria in crowded environments depend on the interplay between the swimmer motility and the boundaries that make up the porous material [8]. Many forms of microscopic life enhance their transport via directed self-propulsion, including *E. coli* bacteria, spermatozoa cells, and *C. reinhardtii* algae [9–11]. Recent advancements in micro/nanoscale synthesis have also led to the creation of artificial swimmers that are excellent tools in the study of autonomous self-propulsion [12–19]. Understanding the motion of these living and synthetic "active matter" constituents embedded within heterogeneous materials is a challenging problem because of the complex interactions between the swimmer and the material boundaries. For porous materials composed of polymer networks, particle transport may be affected by steric hindrance, nonspecific interactions (hydrophobicity, electrostatics), and specific

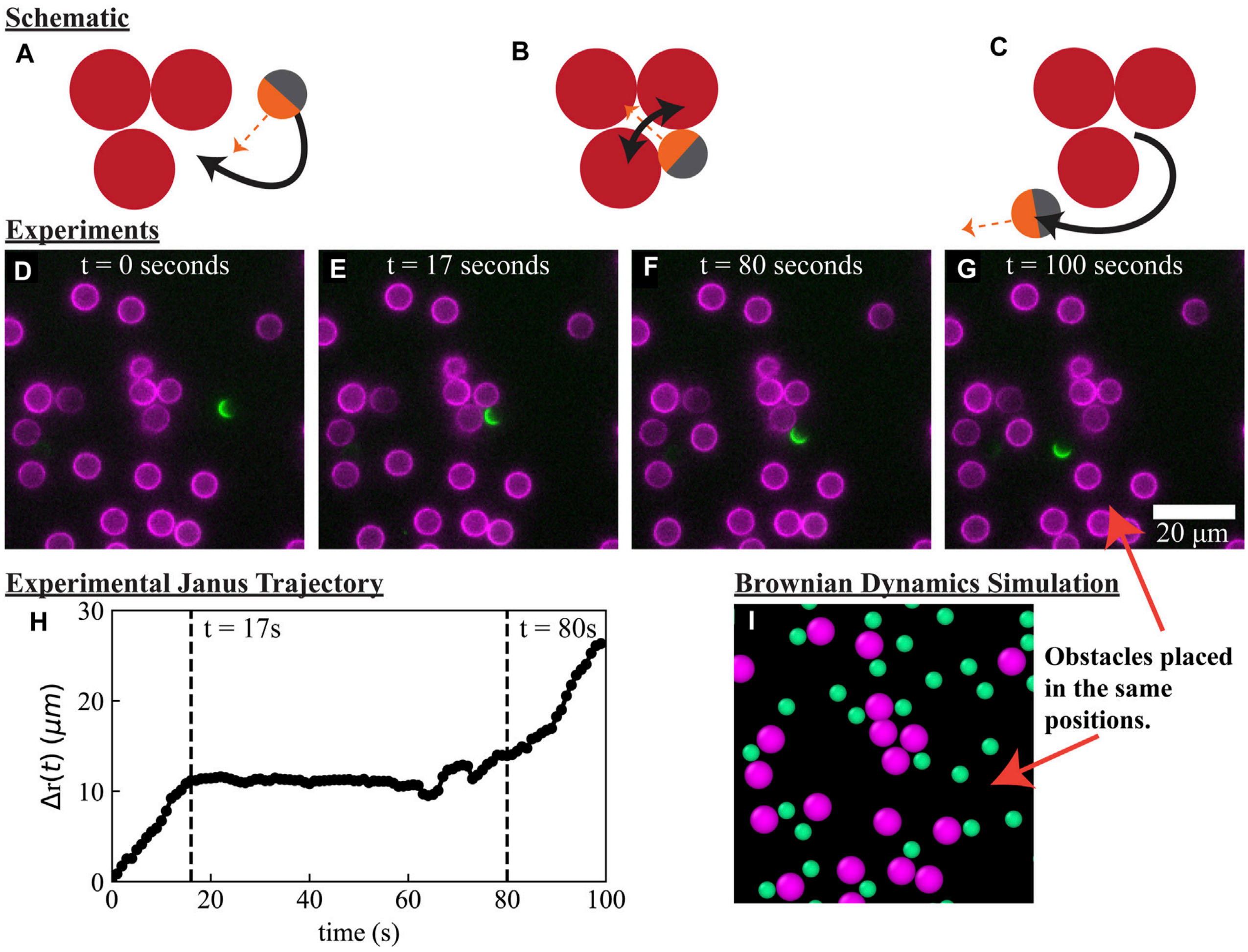

FIGURE 1 | Active particles experience a significant slowdown near obstacle boundaries and a reduction in effective diffusivity in a random array of fixed obstacles. **(A–C)**: Schematic demonstrating the obstructed motion of an active particle near a grouping of three obstacles. **(D–G)**: Experimental images of a 4 *µm* Janus particle (green semicircle) moving through 6.5 *µm* obstacle particles (magenta). **(H)** Displacement of the active Janus particle (green semicircle) tracked for 100 s. **(I)** Brownian Dynamics (BD) simulation snapshot of active Brownian particles moving through a recreated copy of the same porous media as in the experiments. More individual particle trajectories are available in the **Supplementary Information** (**Supplementary Figure S1**).

interactions (ligand-receptor binding) [20, 21]. This behavior is not unique to polymer networks; introducing even a dilute concentration of immobile obstacles with purely excluded-volume interactions provides a substantial slowdown to diffusive flux [22–24].

In addition to the interactions experienced by non-motile Brownian particles, active particles accumulate at physical boundaries due to their persistent self-motion, characterized by a boundary layer near the surface. This accumulation occurs even in the absence of attractive interactions; the active particles propel freely until hitting a surface and continue to propel themselves toward the surface until they reorient and escape into the bulk fluid. This behavior has been observed experimentally and in simulations of rods and spheres, both with and without hydrodynamic interactions [25–40]. A mechanistic understanding of how the local accumulation near physical boundaries affects the macroscopic mobility of active matter through heterogeneous and tortuous materials is lacking. In this work, we study the impact of boundary accumulation on the effective diffusivity of active matter by analyzing the motion of active Brownian particles (ABPs) in a system of rigid 2D obstacles. The presence of boundaries in active systems reduces the effective long-time self diffusivity by an amount that depends on the average swimming speed (U_0) and the average reorientation time (τ_R). This is in sharp contrast to passive Brownian particles, which do not accumulate along boundaries, and whose effective diffusivity depends primarily on the packing fraction of the obstacles [23, 41].

Many studies on active matter transport focus on the effect of alignment along surfaces due to steric or hydrodynamic torques aligning the swimmer parallel or perpendicular to boundaries [27, 36, 38, 40, 42–46]. However, a connection between transport and surface accumulation of active matter [28, 32–34, 37, 47, 48] without any imposed torques has not been fully explored. For

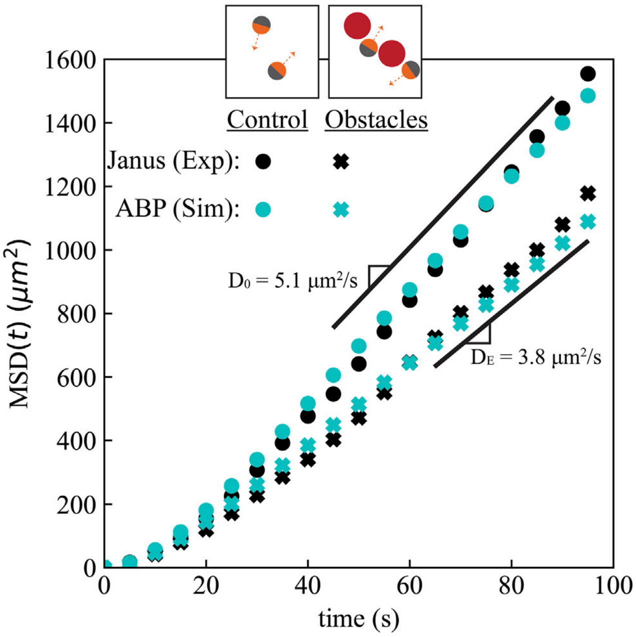

FIGURE 2 | The effective diffusivity of active particles decreased by 25% in a random array of fixed obstacles at ϕ ≈12% area fraction. The mean squared displacement (MSD) of 4 μm active Janus colloids in experiments (black symbols) agrees with that in our BD simulation of the equivalent system using the active Brownian particle (ABP) model (cyan symbols), for both the control case without obstacles (circles) and with a random distribution of 6.5 μm obstacles (cross marks). Labelled diffusivities correspond to the fit to the slope at times past 50 s in the experiments. Standard error of the mean for the MSDs is available in the **Supplementary Figure S2**. Additional MSD simulation data for different ABP activities is available in **Supplementary Figure S3**.

active systems, the precise shape and curvature of the boundary can have a strong effect on motility induced accumulation [33, 34, 49]. This increased accumulation corresponds to more time spent "trapped" in the boundary layer, which inhibits the transport of active matter in tight pores. Therefore, we hypothesize that active swimmers experience a strong reduction in the relative diffusivity in porous media due to the synergistic effects of active boundary accumulation and boundary shape.

While many existing theories predict the diffusive transport of passive Brownian particles through porous media [20, 22, 50–54], the unique accumulation of active matter along boundaries—especially at regions of large curvature—leads to unexpected diffusive slowdowns that are not captured in traditional theories. In this work, we combine Janus particle experiments, Brownian dynamics simulations, and theory to demonstrate that the transport of active matter in heterogeneous materials is a strong function of the obstacle shape, curvature, and microstructure. Experimentally, we rely upon optical tracking of active particle trajectories, which has been a powerful tool to study both living and artificial swimmers in porous environments [49, 55–62], and allows for direct comparisons to particle based simulations [63–71]. In addition to advancing our basic understanding of active matter transport, our work provides a mechanism to control the transport of active matter in heterogeneous materials.

RESULTS

To obtain a mechanistic understanding of boundary layer accumulation and slowdown of active matter in heterogeneous materials, we combined Janus particle experiments, Brownian dynamics (BD) simulations, and analytical theory. In our experiments, we immobilized 6.5 μm lipid bilayer-coated silica particles in a random distribution at the bottom of an imaging chamber at $\phi \approx 12\%$ area fraction. We added a dilute concentration of 4 μm silica Janus particles, coated on one side with a thin layer of platinum and the other side with a lipid bilayer containing fluorescently-labeled lipids (see Materials and Methods). The silica beads sedimented to the bottom of the imaging chamber, so our experiments are conducted in 2D. The lipid bilayers on the obstacles and Janus half-coating contain different fluorescent dyes, which enabled us to track both types of particles simultaneously in different fluorescence channels. Upon adding 2% hydrogen peroxide in Milli-Q water, the Janus particles self-propelled [72–74] with speed $U_0 = 0.84 \pm 0.01\ \mu m/s$ and reorientation time $\tau_R = 14 \pm 2$ s. The self-propulsive speed and the reorientation time were determined via the mean instantaneous velocity and a fit to the known mean squared displacement (see in Materials and Methods). We conducted time lapse imaging and tracked the positions of the obstacles and the Janus particles using a tracking algorithm [75]. In **Figure 1**, we show the motion of a single Janus particle moving through a random array of obstacles, punctuated by an obstructed motion of over 1 min in a local grouping of obstacles creating a concave boundary. Eventually, the Janus particle reoriented, propelled away from the concave boundary, and resumed an active random walk (**Figure 1H**).

To corroborate our experiments, we developed BD simulations in which the motion of ABPs are evolved following the overdamped Langevin equation (see Materials and Methods). We compare the experimental mean squared displacement (MSD) with simulated active Brownian particle MSD to determine if this simple model quantitatively captures the transport behavior observed in the Janus particle experiments in **Figure 2**. Comparing the two MSDs also allowed us to determine that the entropic effect of immobile obstacles was the cause of the diffusivity reduction, and not some unaccounted for mechanism (e.g. hydrodynamic forces or interparticle attractions). To simulate a dilute system, the active Brownian particles interact with obstacle particles via a purely repulsive potential, but do not interact with each other ("ideal gas" particles). We chose the active particle swimming speed and reorientation time to match our Janus particles, and we placed obstacles of the same size in the same positions as the experiments. By using the experimental obstacle particle positions as inputs into our simulations, we recapitulated our precise experimental system in the simulations (**Figure 1I**). Consistent with our experimental observations, we also observed a similar accumulation of particles in local groupings of obstacles that form a concave boundary.

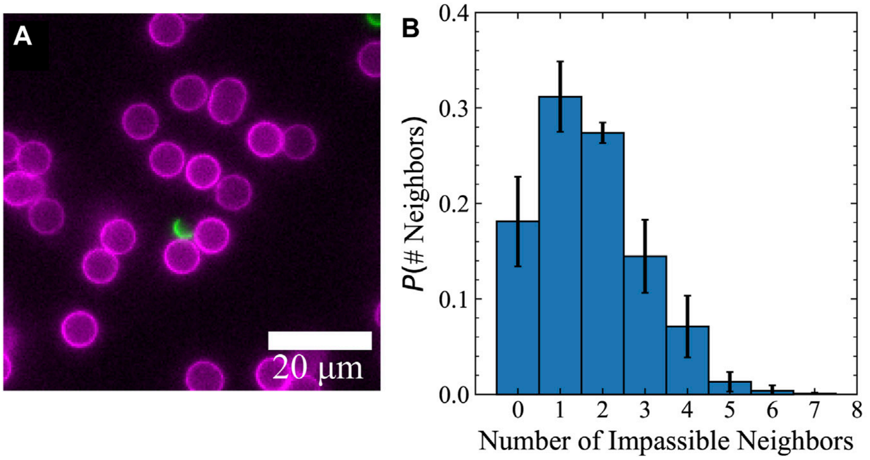

FIGURE 3 | Active Janus particles spent a significant amount of time near obstacle clusters that formed curved boundaries with narrow constriction sites. **(A)** Image of an active Janus particle interacting with a grouping of obstacles that forms a curved boundary with concavity. **(B)** Histogram quantifying obstacle particle grouping. Number of impassible neighbors is found by counting all the obstacle neighbors within distance 4 μm from a reference obstacle's surface. Groups of obstacles within this distance are impassible by a Janus swimmer with diameter 4 μm. Error bars are the standard deviation from six independent experiments. **(C)** Schematic demonstrating the concave shape formed by the packing of obstacles.

To quantify the effect of active particle accumulation and slowdown near boundaries, we computed the mean squared displacement (MSD) of the active particles in our experiments and BD simulations, $\mathrm{MSD}(t) = \langle |\mathbf{r}(t) - \mathbf{r}\ (0)|^2 \rangle$, where $\mathbf{r}(t)$ is the position of the active particle at time t. We obtained the slope of the MSD at large times to find the long-time self diffusivity of the active particles in the experiments and simulations, $D = \lim_{t\to\infty} (1/4)\,(\mathrm{dMSD}/\mathrm{d}t)$. As shown in **Figure 2**, we found that the effective diffusivity of active Janus particles decreases by 25% in the presence of fixed obstacles, from $D_0 = 5.1 \pm 0.2\ \mu m^2/s$ (without obstacles) to $D_E = 3.8 \pm 0.2\ \mu m^2/s$ (with obstacles). An ABP in a dilute suspension in two dimensions has a self diffusivity of $D_0 = D_T + U_0^2 \tau_R/2$ without any obstacles present, where D_T is the thermal Brownian diffusivity of an isolated particle. Our BD simulations agreed quantitatively with the experimental values when we used identical activity parameters with obstacles placed in the same positions, confirming that our active Brownian particle simulations are a proficient model of the experiments. For passive Brownian particles in a dilute packing of rigid obstacles, the effective diffusivity reduces to $D_T\ (1 - \phi)$ [22]. Therefore, our 25% reduction in the effective diffusivity for active particles is about twice as large as the relative reduction experienced by passive Brownian particles at the same obstacle packing fraction, $\phi \approx 12\%$.

In our experiments, we noticed that several 6.5 μm obstacle particles formed local groupings with narrow constrictions (**Figure 3A**), even at semi-dilute packing fractions ($\phi \approx 12\%$). Indeed, we quantified the crowding by finding the number of other obstacle neighbors located within a surface-to-surface distance of 4 μm (**Figure 3B**). We observed that the Janus particles spent significantly more time in the concave region of these emergent shapes as opposed to the convex side (**Figure 3C**). We therefore hypothesized that the presence of these structures with curved geometries plays an important role in reducing the effective transport properties of active particles beyond the $1 - \phi$ correction observed in passive particles. Furthermore, we anticipated that the role of obstacle geometry on the effective diffusivity is much larger for active particles undergoing persistent self-propulsion compared to passive particles translating due to thermal Brownian motion.

To test our hypothesis and to develop a micromechanical understanding of the role of obstacle geometry on active particle diffusion, we analyzed the distribution of active particles near obstacle boundaries, $P\ (x, y, \theta, t)$, which satisfies the Smoluchowski equation

$$\frac{\partial P}{\partial t} + \nabla \cdot (U_0 \mathbf{q} P - D_T \nabla P) - D_R \frac{\partial^2 P}{\partial \theta^2} = 0, \qquad (1)$$

where U_0 is the self-propulsive speed of the active particles, $\mathbf{q} = [\cos(\theta), \sin(\theta)]$ is the unit orientation vector indicating the direction of self-propulsion, and D_T and $D_R = 1/\tau_R$ are the translational and rotational diffusivity, respectively. **Eq. 1** is subject to the no-flux boundary condition along the obstacle surface, $\hat{\mathbf{n}} \cdot [U_0 \mathbf{q} P - D_T \nabla P] = 0$, and periodic boundary conditions across the unit cell. The probability distribution is normalized, $\iiint P\ dx dy d\theta = 1$. We computed the density and polar order fields of active particles at steady state ($\partial P/\partial t = 0$) by solving **Eq. 1** using the finite element method via the software *Freefem++* [76].

We obtained steady-state density and polarization fields by taking orientational integrals over the full probability distribution,

$$n(x, y) = \int_0^{2\pi} P(x, y, \theta)\ \mathrm{d}\theta, \qquad (2a)$$

$$\mathbf{m}(x, y) = \int_0^{2\pi} P(x, y, \theta) \mathbf{q}(\theta)\ \mathrm{d}\theta, \qquad (2b)$$

We numerically solved the full Smoluchowski equation for a point-sized active particle around fixed obstacles with different shapes. For a circular obstacle, we observed a small accumulation of active particles near the surface, as shown in **Figure 4A**. In contrast, for a curved obstacle, we

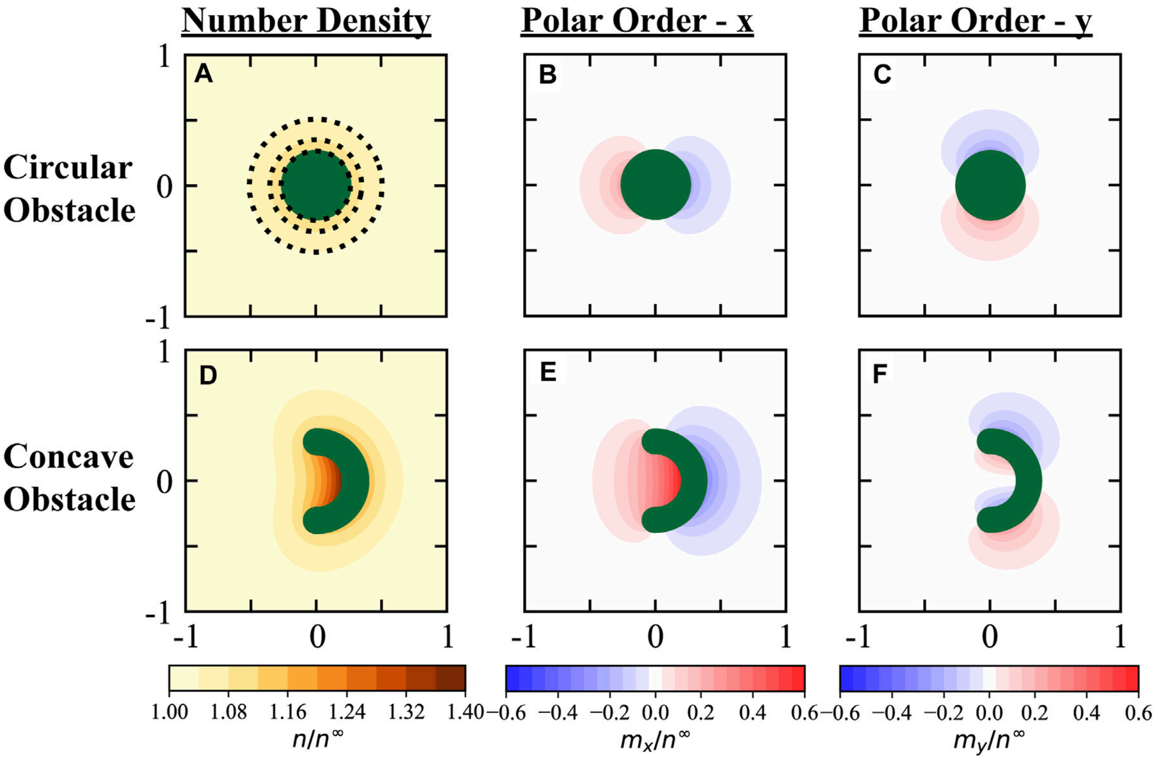

FIGURE 4 | Active constituents accumulate along boundaries due to their persistent self-motion, with a significant increase in density and polar order along curved boundaries with large concavity. **(A–C)**: Density and polarization fields around a circular obstacle (radius over run length $R/(U_0\tau_R) = \sqrt{7}/4$) with dashed lines to guide the eye around the faint increase in contours. The fields are normalized by n^∞, the bulk concentration of active particles far away from the boundary. **(D–F)**: the concentration and polarization fields around a curved obstacle with large concavity ($R_{\text{inner}}/(U_0\tau_R)$=1/2, $R_{\text{outer}}/(U_0\tau_R)$=1). A convex, circular obstacle experiences a 12% increase in active particle accumulation, while a concave shape in the same active bath experiences a 40% increase in active particle accumulation at the inner side, indicating that the specific arrangement and shape of obstacles play a key role in the effective diffusivity of active particles. We used the same obstacle area fraction of $\sigma \approx 5.5\%$ and activity $U_0\tau_R/\delta$ =1 in both cases, where $\delta = \sqrt{D_T\tau_R}$ is the microscopic length.

observed a significant increase in the number density $n\ (x, y)$ and polar order vector $\mathbf{m}\ (x, y)$ near the obstacle surface, especially at regions of large concavity (**Figures 4D–F**). Our results in **Figure 4** are presented for a mild activity of $U_0\tau_R/\delta = 1$, where $\delta = \sqrt{D_T\tau_R}$ is the microscopic length describing how far the active particle thermally diffuses before it reorients. Even for mild activity, we observed a 40% increase in density accumulation along the inner surface compared to only 12% near the circular obstacle. The active Janus particles in our experiments have an activity of $U_0\tau_R/\delta = 100$, which would cause an even larger increase in the density and polar order enhancement at concave boundaries. Our Smoluchowski analysis suggests that the obstacle arrangement and shape play a critical role in governing local trapping of active particles in porous media.

Motivated by our micromechanical understanding of active particles near curved obstacles (**Figure 4**), we hypothesized that the effective diffusivity of active particles in an array of obstacles should depend on the specific shape of the obstacles. To these ends, we conducted BD simulations of active Brownian particles moving through a square lattice of obstacles, carefully varying the curvature while preserving the packing fraction to keep the excluded volume constant within a unit cell. As a model obstacle shape with smoothly-varying curvature, we utilized the "Cassini Oval" (**Figures 5B–D**), which is described by the equation

$$\left[(x+a)^2+y^2\right]\left[(x-a)^2+y^2\right]=b^4, \tag{3a}$$

$$A = 2b^2 E\left(\frac{a^4}{b^4}\right), \tag{3b}$$

$$\kappa^* = \frac{1}{b}\left(\frac{2a^2/b^2-1}{\sqrt{1-a^2/b^2}}\right) \tag{3c}$$

where a and b are two shape parameters ($a < b$), κ^* is the maximum curvature in the shape, A is the shape area, and $E(x)$ is the complete elliptic integral of the second kind. The Cassini Oval is a modification of the traditional ellipse with the product of the distance to two foci (located at $x = \pm a$) kept constant at b^2. The shape extends laterally and shrinks vertically as it is deformed at constant area, which would generate anisotropies and slowdowns in the effective diffusivity for even passive Brownian particles. Since we wish to isolate the effects of curvature, and not the artifacts from lateral elongation of the shape, we performed BD simulations on both passive and active Brownian particles to quantify the effects of curvature and shape elongation. Passive Brownian particles with purely excluded-volume interactions do not accumulate along boundaries, so any change in their

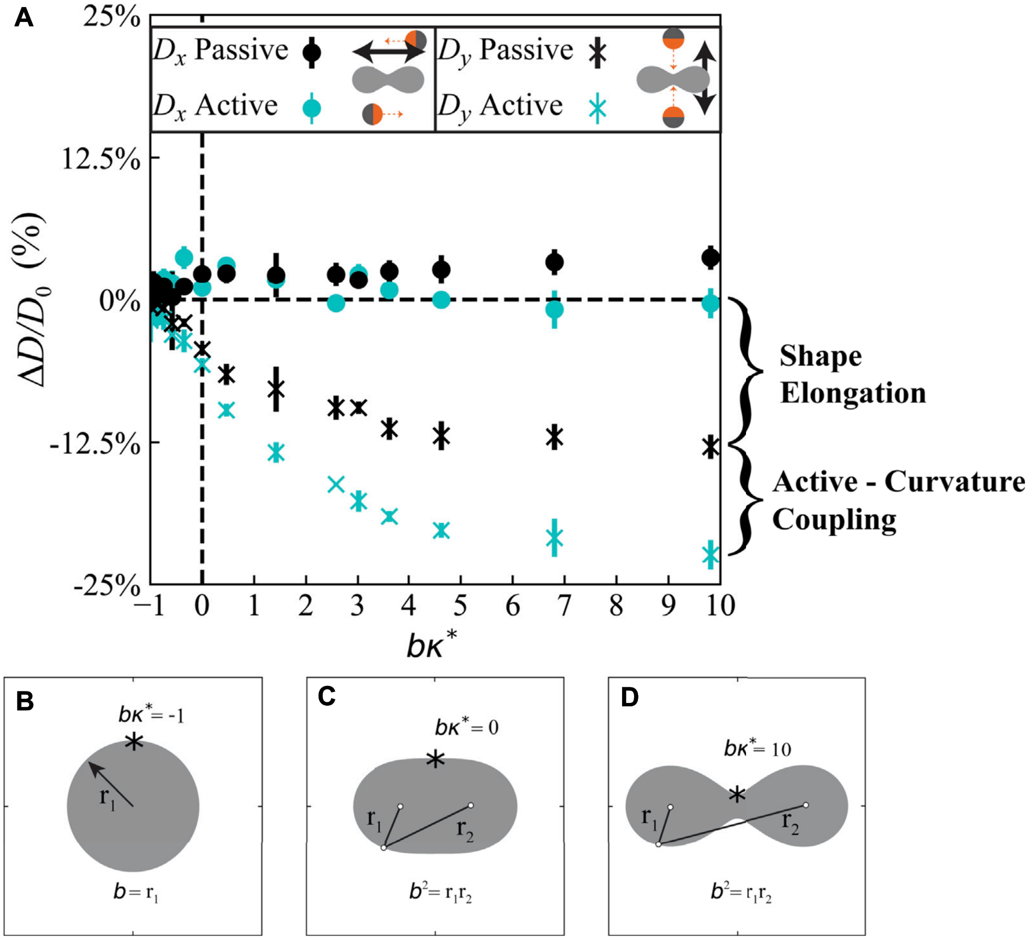

FIGURE 5 | Curved obstacles with a large concavity generate a significant slowdown in diffusive transport of active particles compared to purely convex shapes at the same packing fraction. **(A)** Scaled diffusivity deviation as a function of shape concavity for the Cassini Oval shape described by **Eq. 3**, where $b\kappa^*$ is the non-dimensional curvature at the top of the inclusion. The diffusivity along the direction facing the concavity, D_y, decreases by 24% for the active particles for highly concave obstacles compared to 12.5% for the passive Brownian particles, indicating that the coupling between the active force and curvature plays a key role. Total packing fraction is fixed at $\phi \approx 5.5\%$, and error bars are the standard deviation of three independent trials. **(B–D)**: Schematics of area preserving Cassini Ovals for three different parameter sets. The two foci are separated a distance of 2a. Beyond a critical distance, $a = b/\sqrt{2}$, the shape becomes concave.

diffusivity is due to shape elongation within the unit cell. We have conducted BD simulations at different activities and obstacle packing fractions, and found that the effective diffusivity is well-approximated by the expression $D_0(1-\phi)$ for dilute packing fractions, where D_0 is the bulk diffusivity in 2D in the absence of any obstacles. This is a proficient analytical expression for all activities at dilute obstacle densities (See **Supplementary Figures S4, S5**). However, at larger packing fractions of obstacles greater than $\phi \approx 5\%$, we observe deviations in this expression as a function of varying activity parameters. For example, as $(U_0\tau_R)\kappa^* > 1$, the scaled diffusivity decreases compared to the passive case, due to the reduced swim diffusivity in the boundary layer.

To isolate the diffusivity reduction due to obstacle shape, we computed a scaled diffusivity deviation given by

$$\frac{\Delta D}{D_0} = \frac{D_E - \tilde{D}}{D_0}, \tag{4}$$

where D_E is the effective diffusivity measured from the MSD, $D_0 = D_T + U_0^2\tau_R/2$ is the diffusivity without any obstacles, and $\tilde{D} = D_0(1-\phi)$ is a first correction to the diffusion constant due to excluded volume effects of circles in a square lattice [22]. In **Figure 5**, we show our BD simulation results for an obstacle packing of $\phi = 5.5\%$. Using active particles of diameter σ, we set the activity as $U_0\tau_R/\sigma = 100$, $\delta/\sigma = 5\sqrt{2}$, and the shape area as $A/\sigma^2 = 400\pi$. As the concave curvature of the obstacle increased, we found a large reduction in the effective diffusivity along the direction facing the concavity (D_y) whereas the diffusivity along the other direction (D_x) remained approximately constant. As the local curvature of the shape increased, the conserved area moves off to the sides, slightly thinning its vertical projection and expanding its horizontal projection. The effect of obstacle shape elongation on the effective diffusivity is measured by the deviation in the passive case (black circles and crosses in **Figure 5A**). In the active case, there is an additional contribution that we designate as the active-curvature coupling.

As shown in our data for D_y in **Figure 5A**, the active-curvature coupling contribution to the effective diffusivity is equally as large as the diffusivity reduction due to obstacle shape elongation. Due to their persistent self-propulsion, the active particles experience a large accumulation of density and polar order fields near boundaries with large concavity, consistent with our Smoluchowski analysis in **Figure 4**. The magnitude of this boundary layer accumulation is a strong function of curvature and activity, and we have observed that the effect becomes more important at high activity and semi-dilute obstacle packing (see **Supplementary Figures S4, S5**). Our results validate our hypothesis that the shape and curvature of the obstacles play a critical role in governing the effective mobility of active particles in porous materials. The physical mechanism behind this phenomenon is that active matter accumulates along boundaries, especially along curved and concave surfaces, where active particles are trapped. Therefore, the specific shape and arrangement of obstacles within a porous material modulate the effective diffusivity of the active particles in a manner that is more significant compared to passive Brownian particles.

DISCUSSION

In this work, we discovered that the obstacle packing fraction alone is insufficient to provide an accurate prediction of effective active particle diffusivity. The specific shape and distribution of physical obstacles plays a critical role in determining active transport. The *microscopic* details of the external boundary strongly influences the *macroscopic* observables like the long-time self diffusivity. Both in our experiments and simulations, a random packing of obstacles led to concave structures with narrow constriction sites that gave rise to a significant accumulation of active particles. We showed that the local slowdown of active particles within the boundary layers has a direct effect on their overall mobility across the porous material. We focused on obstacle curvature and microstructure as metrics for predicting the effective diffusivity, which is complementary to other porosity metrics, like chord-length distributions [77] or tortuosity measurements [52].

Our scientific basis for focusing on the obstacle shape and curvature was inspired by the strong connection between active matter accumulation and its force generation along boundaries [32, 74, 78, 79]. For example, Burkholder and Brady derived a macrotransport based model to connect fluctuations in surface accumulation and the enhancement in diffusivity of passive spherical tracers [80]. Furthermore, the surface accumulation is highly dependent on surface curvature [28, 31, 33, 34]; the accumulation on certain parts of an asymmetric shape can lead to a pressure imbalance and net translation of anisotropic colloidal tracers [11, 81]. These studies showed that active matter can impart forces on its environment; however, in our work, we focused on how the micromechanical details of the environment, like curved boundaries, can alter the dynamical properties of the active particles. We validated that a strong coupling between surface curvature and active matter accumulation decreases the diffusivity of active particles by a much larger relative degree than the slowdown expected for equivalent passive Brownian particles.

The surface accumulation of active particles around a single obstacle with small curvature ($(U_0\tau_R)$, $\delta \ll 1/\kappa$) is shown by Yan and Brady [33]:

$$\frac{n_{\mathrm{surf}}}{n^{\infty}} = 1 + \frac{\ell^2}{2\delta^2} + \kappa\ell^2\lambda' + \mathcal{O}\left(\kappa\ell^2\lambda'\right)^2, \tag{5}$$

where n^{∞} is the bulk concentration of active particles, κ is the curvature in units of inverse obstacle length, $\ell = U_0\tau_R$ is the run length, and $\lambda' = \sqrt{(1 + \frac{1}{2}(\ell/\delta)^2/\delta}$ is the inverse screening length of the boundary layer. As the curvature goes from $\kappa = 0$ (e.g. a flat wall) to a convex curvature $\kappa < 0$ (e.g. the outside of a circle), the surface accumulation decreases proportionally. However, if regions of the shape have a concave curvature $\kappa > 1$ (e.g. the inside of a circle), the accumulation increases. To first order in curvature, the accumulation described in **Eq. 5** predicts no net force on an asymmetric surface [33], and higher order curvature expansions are needed to get a nonzero force. The need for large curvatures is consistent with our simulations (**Figure 5**), where we found that the active-curvature coupling effect on the diffusivity is small until the nondimensional curvature is large, $\kappa\ell \gg 1$, (see **Supplementary Figure S4**). For our most curved obstacle in **Figure 5D**, our analysis from **Eq. 5** leads us to define our grouping of $\kappa\ell^2\lambda' \approx 7 \times 10^3$. The effect of active-curvature coupling is expected to increase dramatically in dense, tortuous media, leading to the mechanism of hopping and trapping transport. Other mechanisms of motility, such as the run-reverse mechanism seen in bacteria and archaea [82, 83], can enable swimmers to avoid the slowdown resulting from boundary accumulation and enhance transport between highly curved pores [64].

We focused on the effects of immobile obstacles with purely excluded volume interactions. However, soft porous materials present a rich opportunity for future study. Boundary fluctuations of soft surfaces are important for particle transport in mucus, hydrogels, and other polymeric networks [20, 84, 85]. Active particles have been shown to induce large deformations on soft membranes [86, 87], changing the curvature and transport drastically. Hydrogel networks and sediments in 3D provide an additional degree of freedom for a swimmer to avoid obstacles. In 2D, close packing of disks precludes transport; however, a close packing of spheres in 3D allows for bicontinous percolation, resulting in a reduced but nonzero diffusivity.

Our work opens up opportunities for future experimental work to control active matter diffusion *via* the design of obstacle shape and arrangement. Convex, nonspherical inclusions can be used to control transport and create anisotropic spreading of bacteria along a predefined axis. Novel sorting mechanisms have already been developed using asymmetric blockers [37], and the method could be extended to sort mixtures of swimmers with different types of motility [88]. Precise consideration of the activity-curvature coupling on transport serves as a promising route to increase the efficacy of these sorting methods, and may lead to more accurate predictions of bacterial transport coefficients.

MATERIALS AND METHODS

Experiment Preparation

Lipid-coated silica beads were created by coating silica microbeads with a supported lipid bilayer (SLB). Small unilamellar vesicles (SUVs) were prepared by rehydrating a lipid sheet composed of a mixture of phospholipids with pure deionized water to a concentration of 0.2 mg/ml. For the Janus particles, we used 1,2-dioleoyl-sn-glycero-3-phos-phocholine (DOPC) with 5% of 1,2-dioleoyl-sn-glycero-3-phospho-L-serine (DOPS) and 0.3% of Atto 488-1,2-dioleoyl-sn-glycero-3-phosphoethanolamine (DOPE-Atto 488) fluorescent dye. For the obstacle particles, we used DOPC with 5% of 1,2-dioleoyl-3-trimethylammonium-propane (DOTAP) and 0.3% of Atto 647-DOPE (DOPE-Atto 647). After rehydrating the lipids for 30 min, the solution was vigorously vortexed, sonicated at low-power (20% power) using a tip sonicator (Branson SFX250 Sonifier). The resulting SUV solution was buffered with a MOPS buffer (50 mM MOPS, 100 mM sodium chloride, pH 7.5). DOPC (catalog number: 850375), DOPS (catalog number: 840035), and DOTAP (catalog number: 890890) were purchased from Avanti polar lipids. DOPE-Atto 488 and DOPE-Atto 647 were purchased from ATTO-TEC GmbH. Silica microspheres ($4.0\mu m$; catalog code: SS05002 and $6.5\mu m$; catalog code: SS06N) were purchased from Bangs Laboratories.

Silica microspheres with diameters 4 and 6.5 μm were cleaned using a 3:2 mixture of sulfuric acid:hydrogen peroxide (Piranha) for 30 min in a bath sonicator, and were spun down at 1000g and washed 3 times before being resuspended in pure water. We fabricated Janus particles from the cleaned 4 μm particles by depositing a monolayer on a glass slide, and coating half of the particle surface with a 2 nm-thick layer of chromium and 8 nm-thick layer of platinum using an E-beam evaporator at a deposition rate of 0.1 $\mathring{A}/s$. To form SLBs on the Janus particles and the beads, 50 μL of SUV solution was mixed gently with 10 μL of clean bead suspension. The bead/SUV mixture was incubated for 15 min at room temperature while allowing the beads to sediment to the bottom of the tube. Beads were washed 5 times with pure deionized water by gently adding/removing the liquid without resuspending the beads into solution. We verified the fluidity of the SLB by imaging beads on a glass coverslip at high laser intensity, where the diffusion of labeled lipids was visible after photo-bleaching a small region.

For the 4 μm Janus particles, the SLBs coated only half of the particle surface exposed to clean silica. The side with the platinum did not get coated with an SLB. When these SLB half-coated Janus particles were deposited in a 2% solution of hydrogen peroxide, the particles self-propelled pointing away from their platinum half-coating *via* self-diffusiophoresis. Since silica is more dense than water, the Janus particles moved in 2D along the bottom of the imaging chamber. Within the time frame of our experimental measurements, we did not observe any significant degradation of the SLB from hydrogen peroxide.

For the 6.5 μm obstacle particles, we obtained a uniform SLB across the entire surface of the silica bead. We added a positively-charged DOTAP lipid to the SLB to facilitate a strong electrostatic attraction between the obstacle particles and the borosilicate coverslip substrate. We found that most obstacle particles remained fixed along the bottom substrate with no observable Brownian motion. We did not observe any adhesion or fusion of the SLBs between the obstacles and the Janus particles.

The SLB-coated obstacle particles were added into the imaging chamber at a desired density, followed by the SLB half-coated Janus particles. We added 2% hydrogen peroxide into the chamber and conducted time lapse imaging. All imaging was carried out on an inverted Nikon Ti2-Eclipse microscope (Nikon Instruments) using an oil-immersion objective (Apo ×60, numerical aperture (NA) 1.4, oil). Lumencor SpectraX Multi-Line LED Light Source was used for excitation (Lumencor, Inc.). Fluorescent light was spectrally filtered with emission filters (515/30 and 680/42, Semrock, IDEX Health and Science) and imaged on a Photometrics Prime 95 CMOS Camera (Teledyne Photometrics). Experimental results presented in this work are an average over six independent replicates of systems with obstacles and three independent replicates of systems without obstacles as a control.

Particle Tracking in Experiments

To determine the effect of the porous media on transport, we measured the Janus particle trajectories with and without the presence of the fixed obstacles. We used a modified MATLAB script based on IDL code by Crocker and Grier [75] to track the individual Janus particles by identifying each particle center and tracking its trajectory over time using an image stack with one frame taken every second. We removed any macroscopic drifts by enforcing that the mean displacement over all particles was zero at any time. We filtered out any Janus particles that were immobile due to defects of the particle (defined as moving less than 30 μm over 100 s or if it moved in only one direction via macroscopic drifts). In all experimental results, we tracked the particles for times $t > 7\tau_R$. We obtained the Janus particle mean swim speed, U_0, and reorientation time, τ_R, using the control experiments in the absence of obstacles. We obtained the mean swim speed by averaging all tracked particles' velocity over time,

$$U_0 = \langle \frac{\Delta r}{\Delta t} \rangle. \tag{6}$$

The mean swim speed was determined to be $U_0 = 0.84 \pm 0.01\ \mu m/s$ with the reported error as the standard error of the mean. We obtained the reorientation time by measuring the bulk diffusivity for the control experiment in the absence of obstacles,

$$D_0 = D_T + \frac{U_0^2 \tau_R}{2}, \tag{7}$$

where $D_T \approx 0.1\ \mu m^2/s$ is the thermal Brownian diffusivity for 4 μm diameter spheres using the Stokes-Einstein-Sutherland relation [89–91]. We note that the thermal Brownian diffusivity is negligible compared to the self-propulsive component. Using the experimental measurement of the bulk diffusivity,

$D_0 = 5.1\ \mu m^2/s$, we obtained the reorientation time and standard deviation $\tau_R = 14 \pm 2$ s using **Eq. 7**. As a separate measurement, we computed τ_R using the Janus particle orientation autocorrelation in 2D,

$$\langle \mathbf{q}(t) \cdot \mathbf{q}(0) \rangle = e^{-t/\tau_R}. \tag{8}$$

We obtained the Janus particle orientations directly from particle tracking, and we obtained a reorientation time $\tau_R \approx 10$ s using **Eq. 8**. This measurement is similar to the value we obtained using **Eq. 7**, especially considering the difficulty in finding the orientation using the velocity vector. We concluded that the particles are behaving as active Brownian particles in 2D. In principle, the Janus particles are located along a 2D plane but can reorient in 3D. However, the platinum coating makes the catalytic half-surface more heavy and causes the Janus particles to tilt downwards, making the particle move effectively in 2D. We note that the direction of self-propulsion points away from the platinum half-surface, so the configuration of the platinum half-surface pointing vertically down appears to be an unstable state.

Brownian Dynamics Simulations

The parameters (U_0, τ_R) obtained from the control experiment are then used as inputs into our Brownian dynamics simulations in **Figure 2**. In **Figure 5**, the parameters were chosen as described in the caption. We implemented our simulations using HOOMD-blue, a molecular dynamics (MD) simulation package in *Python* [92]. We focused on the dilute limit of a single active Brownian particle (ABP) in 2D interacting with fixed hard-sphere obstacles. Hydrodynamic interactions are ignored in these simulations. The ABP model describes a swimmer with constant propulsion force but white noise torques [11, 93–96]. Hard-sphere like interactions between the obstacles and the ABPs were implemented using the Weeks-Chandler-Andersen (WCA) [97] potential (**Eq. 10**). For the nonspherical Cassini Oval, the structure was formed using overlapping rigid surface particles offset so that the surfaces of the particles formed the boundaries of the Cassini Oval.

The ABPs were initialized and integrated according to the overdamped Langevin equations of motion:

$$\frac{d\mathbf{x}_i}{dt} = \sqrt{2D_T}\boldsymbol{\eta}_i(t) + \frac{\mathbf{F}_{wca}\left(x_i, x_j\right)}{\zeta} + U_0\mathbf{q} \tag{9a}$$

$$\frac{d\theta_i}{dt} = \sqrt{2D_R}\xi_i(t) \tag{9b}$$

where $\mathbf{F}_{wca}$ is the force on the particle from all potentials and constraints, ζ is the drag coefficient, $\mathbf{q} = [\cos\theta, \sin\theta]$ is the unit vector describing particle orientation in 2D, $D_R = 1/\tau_R$ is the rotational diffusion coefficient, and ($\boldsymbol{\eta}_i$, ξ_i) are random variables obeying the zero mean and variance consistent with the fluctuation-dissipation theorem. We used a timestep of $\Delta t = 0.001$ s, and set the thermal diffusivity to match our experiments at $D_T = 0.1\ \mu m^2/s$. The drag coefficient and the energy scale of the potential were chosen such that force induced velocity at contact is $\frac{24\varepsilon}{\zeta\sigma_{avg}} = 0.6\ \mu m/s$, which is similar in magnitude as the self-propelled velocity U_0. The WCA force is given by

$$\mathbf{F}_{wca} = -\nabla V_{wca} \tag{10a}$$

$$V_{wca}\left(r_{ij}\right) = 4\varepsilon\left[\left(\frac{\sigma}{r_{ij}}\right)^{12} - \left(\frac{\sigma}{r_{ij}}\right)^{6}\right] + \varepsilon,\ r \le 2^{1/6}\sigma. \tag{10b}$$

The particle diameters σ_{ABP} and σ_{obs} were preset to 4 and 6.5 μm for **Figure 2**, and for **Figure 5** they were chosen to be small compared to the radius of the disk shown in **Figure 5B**, $\sigma/R = 1/20$. We used periodic boundary conditions to simulate a continuous domain. Simulations are visualized using OVITO [98].

DATA AVAILABILITY STATEMENT

The original contributions presented in the study are included in the article/**Supplementary Material**, further inquiries can be directed to the corresponding author.

AUTHOR CONTRIBUTIONS

KM and ST conceived of the study; KM and ST designed research; KM performed finite element calculations; KM and YX performed simulations and analyzed data; ST performed experiments; ST supervised the study; and KM, YX, and ST wrote the paper.

FUNDING

This material is based upon work supported by the Air Force Office of Scientific Research under award number FA9550-21-1-0287. KM is supported by the National Science Foundation Graduate Research Fellowship under Grant No. 1650114. Use was made of computational facilities purchased with funds from the National Science Foundation (OAC-1925717) and administered by the Center for Scientific Computing (CSC). The CSC is supported by the California NanoSystems Institute and the Materials Research Science and Engineering Center (MRSEC; NSF DMR 1720256) at UC Santa Barbara.

ACKNOWLEDGMENTS

The authors would like to thank Parth Shah for help in Janus particle synthesis, Dr. Joseph Barakat for a careful reading of this manuscript, and Prof. Ahmad K. Omar for enlightening conversations and insights that helped to conceive of this project.

SUPPLEMENTARY MATERIAL

The Supplementary Material for this article can be found online at: https://www.frontiersin.org/articles/10.3389/fphy.2022.869175/full#supplementary-material

REFERENCES

1. Gannon JT, Mingelgrin U, Alexander M, Wagenet RJ. Bacterial Transport through Homogeneous Soil. *Soil Biol Biochem* (1991) 23:1155–60. doi:10.1016/0038-0717(91)90028-I
2. Adadevoh JST, Triolo S, Ramsburg CA, Ford RM. Chemotaxis Increases the Residence Time of Bacteria in Granular Media Containing Distributed Contaminant Sources. *Environ Sci Technol* (2016) 50:181–7. doi:10.1021/acs.est.5b03956
3. Toley BJ, Forbes NS. Motility Is Critical for Effective Distribution and Accumulation of Bacteria in Tumor Tissue. *Integr Biol* (2012) 4:165–76. doi:10.1039/c2ib00091a
4. Kasinskas RW, Forbes NS. *Salmonella typhimurium* Specifically Chemotax and Proliferate in Heterogeneous Tumor Tissue *In Vitro*. *Biotechnol Bioeng* (2006) 94:710–21. doi:10.1002/bit.20883
5. Ribet D, Cossart P. How Bacterial Pathogens Colonize Their Hosts and Invade Deeper Tissues. *Microbes Infect* (2015) 17:173–83. doi:10.1016/j.micinf.2015.01.004
6. Gu SX, Lentz SR. Fibrin Films: Overlooked Hemostatic Barriers against Microbial Infiltration. *J Clin Invest* (2018) 128:3243–5. doi:10.1172/JCI121858
7. Kao CY, Lin WH, Tseng CC, Wu AB, Wang MC, Wu JJ. The Complex Interplay Among Bacterial Motility and Virulence Factors in Different *Escherichia coli* Infections. *Eur J Clin Microbiol Infect Dis* (2014) 33:2157–62. doi:10.1007/s10096-014-2171-2
8. Martínez-Calvo A, Trenado-Yuste C, Datta SS. *Active Transport in Complex Environments (Preprint)*. arXiv:2108.07011v2 (2021).
9. Chaban B, Hughes HV, Beeby M. The Flagellum in Bacterial Pathogens: For Motility and a Whole Lot More. *Semin Cel Developmental BiologyBiomineralisation Motorisation Pathog* (2015) 46:91–103. doi:10.1016/j.semcdb.2015.10.032
10. Woolley D. Motility of Spermatozoa at Surfaces. *Reproduction* (2003) 126:259–70. doi:10.1530/rep.0.1260259
11. Bechinger C, Di Leonardo R, Löwen H, Reichhardt C, Volpe G, Volpe G. Active Particles in Complex and Crowded Environments. *Rev Mod Phys* (2016) 88:045006. doi:10.1103/RevModPhys.88.045006
12. Golestanian R, Liverpool TB, Ajdari A. Propulsion of a Molecular Machine by Asymmetric Distribution of Reaction Products. *Phys Rev Lett* (2005) 94:220801. doi:10.1103/PhysRevLett.94.220801
13. Howse JR, Jones RAL, Ryan AJ, Gough T, Vafabakhsh R, Golestanian R. Self-Motile Colloidal Particles: From Directed Propulsion to Random Walk. *Phys Rev Lett* (2007) 99:048102. doi:10.1103/PhysRevLett.99.048102
14. Sanchez S, Ananth AN, Fomin VM, Viehrig M, Schmidt OG. Superfast Motion of Catalytic Microjet Engines at Physiological Temperature. *J Am Chem Soc* (2011) 133:14860–3. doi:10.1021/ja205012j
15. Soto R, Golestanian R. Self-Assembly of Catalytically Active Colloidal Molecules: Tailoring Activity through Surface Chemistry. *Phys Rev Lett* (2014) 112:068301. doi:10.1103/PhysRevLett.112.068301
16. Ma X, Jannasch A, Albrecht U-R, Hahn K, Miguel-López A, Schäffer E, et al. Enzyme-Powered Hollow Mesoporous Janus Nanomotors. *Nano Lett* (2015) 15:7043–50. doi:10.1021/acs.nanolett.5b03100
17. Ma X, Hahn K, Sanchez S. Catalytic Mesoporous Janus Nanomotors for Active Cargo Delivery. *J Am Chem Soc* (2015) 137:4976–9. doi:10.1021/jacs.5b02700
18. Dreyfus R, Baudry J, Roper ML, Fermigier M, Stone HA, Bibette J. Microscopic Artificial Swimmers. *Nature* (2005) 437:862–5. doi:10.1038/nature04090
19. Bricard A, Caussin JB, Das D, Savoie C, Chikkadi V, Shitara K, et al. Emergent Vortices in Populations of Colloidal Rollers. *Nat Commun* (2015) 6:7470. doi:10.1038/ncomms8470
20. Cai LH, Panyukov S, Rubinstein M. Hopping Diffusion of Nanoparticles in Polymer Matrices. *Macromolecules* (2015) 48:847–62. doi:10.1021/ma501608x
21. Witten J, Ribbeck K. The Particle in the Spider's Web: Transport through Biological Hydrogels. *Nanoscale* (2017) 9:8080–95. doi:10.1039/C6NR09736G
22. Mangeat M, Guérin T, Dean DS. Effective Diffusivity of Brownian Particles in a Two Dimensional Square Lattice of Hard Disks. *J Chem Phys* (2020) 152:234109. doi:10.1063/5.0009095
23. Saxton M. Anomalous Diffusion Due to Obstacles: a Monte Carlo Study. *Biophysical J* (1994) 66:394–401. doi:10.1016/S0006-3495(94)80789-1
24. Alonso-Matilla R, Chakrabarti B, Saintillan D. Transport and Dispersion of Active Particles in Periodic Porous media. *Phys Rev Fluids* (2019) 4:043101. doi:10.1103/PhysRevFluids.4.043101
25. Volpe G, Gigan S, Volpe G. Simulation of the Active Brownian Motion of a Microswimmer. *Am J Phys* (2014) 82:659–64. doi:10.1119/1.4870398
26. Wysocki A, Elgeti J, Gompper G. Giant Adsorption of Microswimmers: Duality of Shape Asymmetry and wall Curvature. *Phys Rev E* (2015) 91:050302. doi:10.1103/PhysRevE.91.050302
27. Elgeti J, Gompper G. Self-propelled Rods Near Surfaces. *EPL (Europhysics Letters)* (2009) 85:38002. doi:10.1209/0295-5075/85/38002
28. Elgeti J, Gompper G. Wall Accumulation of Self-Propelled Spheres. *EPL (Europhysics Letters)* (2013) 101:48003. doi:10.1209/0295-5075/101/48003
29. Elgeti J, Winkler RG, Gompper G. Physics of Microswimmers—Single Particle Motion and Collective Behavior: a Review. *Rep Prog Phys* (2015) 78:056601. doi:10.1088/0034-4885/78/5/056601
30. Wensink HH, Löwen H. Aggregation of Self-Propelled Colloidal Rods Near Confining walls. *Phys Rev E* (2008) 78:031409. doi:10.1103/PhysRevE.78.031409
31. Wang M. Effect of Boundaries on Noninteracting Weakly Active Particles in Different Geometries. *Phys Rev E* (2021) 103:042609. doi:10.1103/PhysRevE.103.042609
32. Yan W, Brady JF. The Force on a Boundary in Active Matter. *J Fluid Mech* (2015) 785:R1. doi:10.1017/jfm.2015.621
33. Yan W, Brady JF. The Curved Kinetic Boundary Layer of Active Matter. *Soft Matter* (2018) 14:279–90. doi:10.1039/c7sm01643c
34. Smallenburg F, Löwen H. Swim Pressure on walls with Curves and Corners. *Phys Rev E* (2015) 92:032304. doi:10.1103/PhysRevE.92.032304
35. Takatori SC, Yan W, Brady JF. Swim Pressure: Stress Generation in Active Matter. *Phys Rev Lett* (2014) 113:028103. doi:10.1103/PhysRevLett.113.028103
36. Berke AP, Turner L, Berg HC, Lauga E. Hydrodynamic Attraction of Swimming Microorganisms by Surfaces. *Phys Rev Lett* (2008) 101:038102. doi:10.1103/PhysRevLett.101.038102
37. Martinez R, Alarcon F, Aragones JL, Valeriani C. Trapping Flocking Particles with Asymmetric Obstacles. *Soft Matter* (2020) 16:4739–45. doi:10.1039/C9SM02427A
38. Giacché D, Ishikawa T, Yamaguchi T. Hydrodynamic Entrapment of Bacteria Swimming Near a Solid Surface. *Phys Rev E* (2010) 82:056309. doi:10.1103/PhysRevE.82.056309
39. Galajda P, Keymer J, Chaikin P, Austin R. A Wall of Funnels Concentrates Swimming Bacteria. *J Bacteriol* (2007) 189:8704–7. doi:10.1128/JB.01033-07
40. Molaei M, Barry M, Stocker R, Sheng J. Failed Escape: Solid Surfaces Prevent Tumbling of escherichia Coli. *Phys Rev Lett* (2014) 113:068103. doi:10.1103/PhysRevLett.113.068103
41. Kalnin J, Kotomin E, Maier J. Calculations of the Effective Diffusion Coefficient for Inhomogeneous media. *J Phys Chem Sol* (2002) 63:449–56. doi:10.1016/S0022-3697(01)00159-7
42. Li G, Tang JX. Accumulation of Microswimmers Near a Surface Mediated by Collision and Rotational Brownian Motion. *Phys Rev Lett* (2009) 103:078101. doi:10.1103/PhysRevLett.103.078101
43. Sipos O, Nagy K, Di Leonardo R, Galajda P. Hydrodynamic Trapping of Swimming Bacteria by Convex walls. *Phys Rev Lett* (2015) 114:258104. doi:10.1103/PhysRevLett.114.258104
44. Das S, Garg A, Campbell AI, Howse J, Sen A, Velegol D, et al. Boundaries Can Steer Active Janus Spheres. *Nat Commun* (2015) 6:8999. doi:10.1038/ncomms9999
45. Takagi D, Palacci J, Braunschweig AB, Shelley MJ, Zhang J. Hydrodynamic Capture of Microswimmers into Sphere-Bound Orbits. *Soft Matter* (2014) 10:1784–9. doi:10.1039/C3SM52815D
46. Morin A, Lopes Cardozo D, Chikkadi V, Bartolo D. Diffusion, Subdiffusion, and Localization of Active Colloids in Random post Lattices. *Phys Rev E* (2017) 96:042611. doi:10.1103/PhysRevE.96.042611
47. Das S, Gompper G, Winkler RG. Confined Active Brownian Particles: Theoretical Description of Propulsion-Induced Accumulation. *New J Phys* (2018) 20:015001. doi:10.1088/1367-2630/aa9d4b
48. Kjeldbjerg CM, Brady JF. Theory for the Casimir Effect and the Partitioning of Active Matter. *Soft Matter* (2021) 17:523–30. doi:10.1039/D0SM01797C

49. Volpe G, Buttinoni I, Vogt D, Kümmerer HJ, Bechinger C. Microswimmers in Patterned Environments. *Soft Matter* (2011) 7:8810–5. doi:10.1039/C1SM05960B
50. Reguera D, Rubí JM. Kinetic Equations for Diffusion in the Presence of Entropic Barriers. *Phys Rev E* (2001) 64:061106. doi:10.1103/PhysRevE.64.061106
51. Brenner H, Edwards DA. *Macrotransport Processes*. Elsevier (1993). doi:10.1016/C2009-0-25915-0
52. Shen L, Chen Z. Critical Review of the Impact of Tortuosity on Diffusion. *Chem Eng Sci* (2007) 62:3748–55. doi:10.1016/j.ces.2007.03.041
53. Burada PS, Hänggi P, Marchesoni F, Schmid G, Talkner P. Diffusion in Confined Geometries. *ChemPhysChem* (2009) 10:45–54. doi:10.1002/cphc.200800526
54. Ning L, Liu P, Ye F, Yang M, Chen K. Diffusion of Colloidal Particles in Model Porous media. *Phys Rev E* (2021) 103:022608. doi:10.1103/PhysRevE.103.022608
55. Perez LJ, Bhattacharjee T, Datta SS, Parashar R, Sund NL. Impact of Confined Geometries on Hopping and Trapping of Motile Bacteria in Porous media. *Phys Rev E* (2021) 103:012611. doi:10.1103/PhysRevE.103.012611
56. Bhattacharjee T, Datta SS. Bacterial Hopping and Trapping in Porous media. *Nat Commun* (2019) 10:2075. doi:10.1038/s41467-019-10115-1
57. Figueroa-Morales N, Dominguez-Rubio L, Ott TL, Aranson IS. Mechanical Shear Controls Bacterial Penetration in Mucus. *Scientific Rep* (2019) 9:9713. doi:10.1038/s41598-019-46085-z
58. Truong VK, Mainwaring DE, Murugaraj P, Nguyen DHK, Ivanova EP. Impact of Confining 3-D Polymer Networks on Dynamics of Bacterial Ingress and Self-Organisation. *J Mater Chem B* (2015) 3:8704–10. doi:10.1039/c5tb01880c
59. Bansil R, Celli JP, Hardcastle JM, Turner BS. The Influence of Mucus Microstructure and Rheology in *Helicobacter pylori* Infection. *Front Immunol* (2013) 4. doi:10.3389/fimmu.2013.00310
60. Wu H, Greydanus B, Schwartz DK. Mechanisms of Transport Enhancement for Self-Propelled Nanoswimmers in a Porous Matrix. *Proc Natl Acad Sci* (2021) 118. doi:10.1073/pnas.2101807118
61. Licata NA, Mohari B, Fuqua C, Setayeshgar S. Diffusion of Bacterial Cells in Porous Media. *Biophysical J* (2016) 110:247–57. doi:10.1016/j.bpj.2015.09.035
62. Brun-Cosme-Bruny M, Bertin E, Coasne B, Peyla P, Rafaï S. Effective Diffusivity of Microswimmers in a Crowded Environment. *J Chem Phys* (2019) 150:104901. doi:10.1063/1.5081507
63. Sandoval M, Dagdug L. Effective Diffusion of Confined Active Brownian Swimmers. *Phys Rev E - Stat Nonlinear, Soft Matter Phys* (2014) 90:062711. doi:10.1103/PhysRevE.90.062711
64. Kurzthaler C, Mandal S, Bhattacharjee T, Löwen H, Datta SS, Stone HA. A Geometric Criterion for the Optimal Spreading of Active Polymers in Porous media. *Nat Commun* (2021) 12:7088. doi:10.1038/s41467-021-26942-0
65. Chepizhko O, Peruani F. Diffusion, Subdiffusion, and Trapping of Active Particles in Heterogeneous Media. *Phys Rev Lett* (2013) 111:160604. doi:10.1103/PhysRevLett.111.160604
66. Reichhardt C, Olson Reichhardt CJ. Active Matter Transport and Jamming on Disordered Landscapes. *Phys Rev E* (2014) 90:012701. doi:10.1103/PhysRevE.90.012701
67. Reichhardt CJO, Reichhardt C. Avalanche Dynamics for Active Matter in Heterogeneous media. *New J Phys* (2018) 20:025002. doi:10.1088/1367-2630/aaa392
68. Jakuszeit T, Croze OA, Bell S. Diffusion of Active Particles in a Complex Environment: Role of Surface Scattering. *Phys Rev E* (2019) 99:012610. doi:10.1103/PhysRevE.99.012610
69. Chamolly A, Ishikawa T, Lauga E. Active Particles in Periodic Lattices. *New J Phys* (2017) 19:115001. doi:10.1088/1367-2630/aa8d5e
70. Volpe G, Volpe G. The Topography of the Environment Alters the Optimal Search Strategy for Active Particles. *Proc Natl Acad Sci* (2017) 114:11350–5. doi:10.1073/pnas.1711371114
71. Yuan C, Chen A, Zhang B, Zhao N. Activity–crowding Coupling Effect on the Diffusion Dynamics of a Self-Propelled Particle in Polymer Solutions. *Phys Chem Chem Phys* (2019) 21:24112–25. doi:10.1039/C9CP04498A
72. Paxton WF, Kistler KC, Olmeda CC, Sen A, St Angelo SK, Cao Y, et al. Catalytic Nanomotors: Autonomous Movement of Striped Nanorods. *J Am Chem Soc* (2004) 126:13424–31. doi:10.1021/ja047697z
73. Howse JR, Jones RAL, Ryan AJ, Gough T, Vafabakhsh R, Golestanian R. Self-motile Colloidal Particles: From Directed Propulsion to Random Walk. *Phys Rev Lett* (2007) 99:048102. doi:10.1103/PhysRevLett.99.048102
74. Takatori SC, De Dier R, Vermant J, Brady JF. Acoustic Trapping of Active Matter. *Nat Commun* (2016) 7:1–7. doi:10.1038/ncomms10694
75. Crocker JC, Grier DG. Methods of Digital Video Microscopy for Colloidal Studies. *J Colloid Interf Sci* (1996) 179:298–310. doi:10.1006/jcis.1996.0217
76. Hecht F. New Development in Freefem++. *J Numer Mathematics* (2012) 20. doi:10.1515/jnum-2012-0013
77. Torquato S, Lu B. Chord-length Distribution Function for Two-phase Random media. *Phys Rev E* (1993) 47:2950–3. doi:10.1103/PhysRevE.47.2950
78. Takatori SC, Brady JF. Swim Stress, Motion, and Deformation of Active Matter: Effect of an External Field. *Soft Matter* (2014) 10:9433–45. doi:10.1039/C4SM01409J
79. Omar AK, Wang ZG, Brady JF. Microscopic Origins of the Swim Pressure and the Anomalous Surface Tension of Active Matter. *Phys Rev E* (2020) 101:012604. doi:10.1103/PhysRevE.101.012604
80. Burkholder EW, Brady JF. Tracer Diffusion in Active Suspensions. *Phys Rev E* (2017) 95:052605. doi:10.1103/PhysRevE.95.052605
81. Kaiser A, Peshkov A, Sokolov A, ten Hagen B, Löwen H, Aranson IS. Transport Powered by Bacterial Turbulence. *Phys Rev Lett* (2014) 112:158101. doi:10.1103/PhysRevLett.112.158101
82. Son K, Guasto JS, Stocker R. Bacteria Can Exploit a Flagellar Buckling Instability to Change Direction. *Nat Phys* (2013) 9:494–8. doi:10.1038/nphys2676
83. Thornton KL, Butler JK, Davis SJ, Baxter BK, Wilson LG. Haloarchaea Swim Slowly for Optimal Chemotactic Efficiency in Low Nutrient Environments. *Nat Commun* (2020) 11:4453. doi:10.1038/s41467-020-18253-7
84. Bodrenko IV, Salis S, Acosta-Gutierrez S, Ceccarelli M. Diffusion of Large Particles through Small Pores: From Entropic to Enthalpic Transport. *J Chem Phys* (2019) 150:211102. doi:10.1063/1.5098868
85. Ledesma-Aguilar R, Yeomans JM. Enhanced Motility of a Microswimmer in Rigid and Elastic Confinement. *Phys Rev Lett* (2013) 111:138101. doi:10.1103/PhysRevLett.111.138101
86. Takatori SC, Sahu A. Active Contact Forces Drive Nonequilibrium Fluctuations in Membrane Vesicles. *Phys Rev Lett* (2020) 124:158102. doi:10.1103/PhysRevLett.124.158102
87. Vutukuri HR, Hoore M, Abaurrea-Velasco C, van Buren L, Dutto A, Auth T, et al. Active Particles Induce Large Shape Deformations in Giant Lipid Vesicles. *Nature* (2020) 586:52–6. doi:10.1038/s41586-020-2730-x
88. Khatami M, Wolff K, Pohl O, Ejtehadi MR, Stark H. Active Brownian Particles and Run-And-Tumble Particles Separate inside a Maze. *Scientific Rep* (2016) 6:37670. doi:10.1038/srep37670
89. Sutherland W. Lxxv. A Dynamical Theory of Diffusion for Non-electrolytes and the Molecular Mass of Albumin. *Lond Edinb Dublin Philosophical Mag J Sci* (1905) 9:781–5. doi:10.1080/14786440509463331
90. von Smoluchowski M. Zur kinetischen theorie der brownschen molekularbewegung und der suspensionen. *Annalen der Physik* (1906) 326:756–80. doi:10.1002/andp.19063261405
91. Einstein A. Eine neue bestimmung der moleküldimensionen. *Annalen der Physik* (1906) 324:289–306. doi:10.1002/andp.19063240204
92. Anderson JA, Glaser J, Glotzer SC. HOOMD-Blue: A Python Package for High-Performance Molecular Dynamics and Hard Particle Monte Carlo Simulations. *Comput Mater Sci* (2020) 173:109363. doi:10.1016/j.commatsci.2019.109363
93. Takatori SC, Brady JF. Forces, Stresses and the (Thermo?) Dynamics of Active Matter. *Curr Opin Colloid Interf Sci* (2016) 21:24–33. doi:10.1016/j.cocis.2015.12.003
94. Shaebani MR, Wysocki A, Winkler RG, Gompper G, Rieger H. Computational Models for Active Matter. *Nat Rev Phys* (2020) 2:181–99. doi:10.1038/s42254-020-0152-1
95. Marchetti MC, Joanny JF, Ramaswamy S, Liverpool TB, Prost J, Rao M, et al. Hydrodynamics of Soft Active Matter. *Rev Mod Phys* (2013) 85:1143–89. doi:10.1103/RevModPhys.85.1143

96. Solon AP, Cates ME, Tailleur J. Active Brownian Particles and Run-And-Tumble Particles: A Comparative Study. *Eur Phys J Spec Top* (2015) 224: 1231–62. doi:10.1140/epjst/e2015-02457-0
97. Weeks JD, Chandler D, Andersen HC. Role of Repulsive Forces in Determining the Equilibrium Structure of Simple Liquids. *J Chem Phys* (1971) 54:5237–47. doi:10.1063/1.1674820
98. Stukowski A. Visualization and Analysis of Atomistic Simulation Data with OVITO–The Open Visualization Tool. *Model Simulation Mater Sci Eng* (2009) 18:015012. doi:10.1088/0965-0393/18/1/015012

Conflict of Interest: The authors declare that the research was conducted in the absence of any commercial or financial relationships that could be construed as a potential conflict of interest.

frontiers | Frontiers in Physics

ORIGINAL RESEARCH
published: 03 May 2022
doi: 10.3389/fphy.2022.876126

Collective States of Active Particles With Elastic Dipolar Interactions

Subhaya Bose[1†], *Patrick S. Noerr*[1†], *Ajay Gopinathan*[1], *Arvind Gopinath*[2] *and*
Kinjal Dasbiswas[1]*

[1]*Department of Physics, School of Natural Sciences, University of California, Merced, Merced, CA, United States,* [2]*Department of Bioengineering, University of California, Merced, Merced, CA, United States*

Many types of animal cells exert active, contractile forces and mechanically deform their elastic substrate, to accomplish biological functions such as migration. These substrate deformations provide a mechanism in principle by which cells may sense other cells, leading to long-range mechanical inter–cell interactions and possible self-organization. Here, inspired by cell mechanobiology, we propose an active matter model comprising self-propelling particles that interact at a distance through their mutual deformations of an elastic substrate. By combining a minimal model for the motility of individual particles with a linear elastic model that accounts for substrate-mediated, inter–particle interactions, we examine emergent collective states that result from the interplay of motility and long-range elastic dipolar interactions. In particular, we show that particles self-assemble into flexible, motile chains which can cluster to form diverse larger-scale compact structures with polar order. By computing key structural and dynamical metrics, we distinguish between the collective states at weak and strong elastic interaction strength, as well as at low and high motility. We also show how these states are affected by confinement within a channel geometry–an important characteristic of the complex mechanical micro-environment inhabited by cells. Our model predictions may be generally applicable to active matter with dipolar interactions ranging from biological cells to synthetic colloids endowed with electric or magnetic dipole moments.

Keywords: mechanobiology, cell motility, active brownian particle, active polymer, elastic dipole interactions, self-organisation, brownian dynamics, confinement

Edited by:
Xiang Cheng,
University of Minnesota Twin Cities,
United States

Reviewed by:
Ehssan Nazockdast,
University of North Carolina at Chapel Hill, United States
Abdul Malmi Kakkada,
Augusta University, United States

Correspondence:
Kinjal Dasbiswas
kdasbiswas@ucmerced.edu

†*These authors have contributed equally to this work*

Specialty section:
This article was submitted to
Soft Matter Physics,
a section of the journal
Frontiers in Physics

Received: *15 February 2022*
Accepted: *12 April 2022*
Published: *03 May 2022*

Citation:
Bose S, Noerr PS, Gopinathan A,
Gopinath A and Dasbiswas K (2022)
Collective States of Active Particles
With Elastic Dipolar Interactions.
Front. Phys. 10:876126.
doi: 10.3389/fphy.2022.876126

1 INTRODUCTION

Active matter typically comprises autonomous agents, biological or synthetic in origin, that harness internal energy sources to move [1, 2]. These agents often undergo complex interactions with each other and their surrounding media that influence their collective behavior [3]. Mammalian cells that move by crawling on elastic substrates such as tissue and constitute a canonical example of biological active matter in complex media, can cluster into persistently moving or rotating flocks [4]. These cells locomote by adhering to and exerting mechanical forces on their elastic extracellular substrate which they actively deform [5, 6]. The overall motility is guided by the cell's interactions with its substrate as well as with other cells [7]. Cell-cell interactions can include mechanical interactions mediated by their mutual deformations of the surrounding elastic substrate [8, 9]. This is particularly the case in dilute cell cultures where cells are not in direct contact. On the other hand, in dense active matter systems such as in confluent epithelial cell monolayers, direct cell-cell interactions including steric interactions can dominate [10]. Mechanical interactions through a material medium are by their nature long-range and are expected to govern the collective states of active particles [11], and enrich the large–scale phenomena such as phase separation that arise purely from motility [12, 13].

Mechanobiology experiments with adherent cells cultured on elastic hydrogel substrates [14, 15], suggest that substrate elasticity may provide a robust route to long lived and long ranged cell-cell interactions. Indeed, cell culture experiments indicate that cells exert measurable forces on their neighbors, either through direct cell-cell contacts, or indirectly through mutual deformations of a compliant, extracellular substrate [16, 17]. The substrate-mediated elastic interactions between such cells has important implications for biological processes such as self-organization during blood vessel morphogenesis [18] and synchronization of beating cardiac muscle cells [19–22]. The overall motility of spatially separated cells is expected to depend on cell-cell mechanical interactions. This is revealed by experimental observations of substrate stiffness-dependent interactions of pairs of motile cells [23, 24].

In general, active particles endowed with a dipole moment are expected to interact at long range with each other while also propelling themselves. Passive dipolar particles such as ferromagnetic colloids at equilibrium will align end-to-end into linear structures such as chains or rings [25, 26]. At higher densities, the chains intersect to form gel-like network structures [27]. Topological defects in the networks such as junctions and rings are expected to affect the phases of passive dipolar fluids [28, 29]. When powered by chemical activity, dipolar colloidal systems exhibit self-assembly that depends on both the long-range, anisotropic interactions, as well as active motion, as revealed in recent experiments [30]. Such structures have also been studied in simulation in the context of active dipolar particles representing auto-phoretic colloids [31, 32], as well as swimming microorganisms [33] such as magnetotactic bacteria [34]. In related theoretical studies, constrained or bundled chains of self-propelling colloidal particles [35–38] have also been shown to exhibit collective instabilities. Elasticity mediated interactions are seen to play critical roles, with the competition between mechanical interactions, steric interactions and activity determining the eventual dynamical behavior.

Here we build a minimal model of interacting elastic dipoles that is inspired by the mechanobiology of animal cells that actively deform their elastic substrate, while also exhibiting persistent motility. The starting point is the observation and deduction that contractile deformations of the underlying substrate originate from the elastic dipolar nature of stresses exerted by the cell on the substrate [39]. We show that incorporation of these substrate-mediated interactions offers a robust way to the formation of compact, and relatively stable collective states. Our model combining active self-propulsion of the particles with their long-range dipolar interactions applies to a general class of experimentally realizable systems, including synthetic colloids endowed with permanent or induced magnetic or electric dipole moments [40]. By performing Brownian dynamics simulations on a collection of such dipolar active particles, we demonstrate the rich array of collective states that they can self-organize into. In particular, strong dipolar interactions promote end-to-end alignment of active particles, leading to self-assembled, motile chains. These chains can then further self-assemble into a hierarchy of larger-scale structures.

2 MODEL

Our model system consists of soft, repulsive, active Brownian particles (ABPs) [41, 42] in two dimensions (2D), that interact at long range through elastic dipolar interactions and strongly repel when they overlap. We have previously studied a simple isotropic interaction model valid in the limit where the propulsion direction was decoupled from the magnitude of cell-cell interactions [43]. Here, we analyze a more general model that accounts for the anisotropy of cell interactions, expected for the elongated shapes characteristic of migrating cells.

The basis of elastic interactions between model cells is illustrated in **Figure 1**. The schematic **Figure 1A** shows the typical scenario of an adherent cell on top of an elastic substrate. The internal cytoskeletal machinery of the cell comprising actin stress fibers and myosin II molecular motors generates contractile mechanical forces, that are communicated to the external substrate through cell-substrate focal adhesions [44]. In a minimal, coarse-grained description, the traction force distribution of an elongated cell with a long axis $\mathbf{a}$ and exerting a typical force $\mathbf{F}$ at the adhesion sites, can be modeled as a force dipole with dipole moment $P_{ij} = F_i a_j$. The theory of continuous elastic media then determines that the distribution of forces from multiple cells will lead to a restoring stress $\boldsymbol{\sigma}$ in the medium, that satisfies a force balance [45], $\partial_j \sigma_{ij} = -\partial_j p_{ij}$, where the net dipole density, $p_{ij}(\mathbf{x}) = \Sigma_\alpha P^\alpha_{ij} \delta(\mathbf{x} - \mathbf{x}^\alpha)$ is the sum of traction forces exerted by each point-like cell dipole, here labeled by an index α. In modeling cells as point-like dipoles, we ignore their finite size, an assumption that is valid only at "far field", i.e., at distances large compared to cell length. While this is not strictly the case in our simulations, a more general model accounting for finite separation of the cell forces is expected to lead to qualitatively similar interactions [22].

By considering two dipoles $\mathbf{P}^\alpha$ and $\mathbf{P}^\beta$, we can show that the work done by a dipole β in deforming the elastic medium in the presence of the strain created by the other dipole α, is given by [46]: $W^{\alpha\beta} = P^\beta_{ij} u^\alpha_{ij}(\mathbf{x}^\beta)$. This minimal coupling between dipolar stress and medium strain represents the mechanical interaction energy between dipoles. The strain in the elastic medium created by dipole α at the position of the dipole β is given by the gradient of the displacement, $u_{ij}(x) = \frac{1}{2}\left(\frac{\partial u_i}{\partial x_j} + \frac{\partial u_j}{\partial x_i}\right)$ and can be calculated using standard methods in linear elastic theory [45]. This is detailed in the Methods section, where we follow the treatment introduced in Ref. [46]. The mechanical interaction between a pair of force dipoles is illustrated by the schematic in **Figure 1B** in the form of a 1D series of springs representing the effect of the elastic substrate. While the springs underlying the contractile dipoles are compressed, the springs between them are stretched. By moving to different positions in the medium for a given position of dipole α, the dipole β can reduce the net substrate deformation energy by compressing regions stretched by dipole α. This leads to a substrate deformation-mediated elastic force on the dipole β,

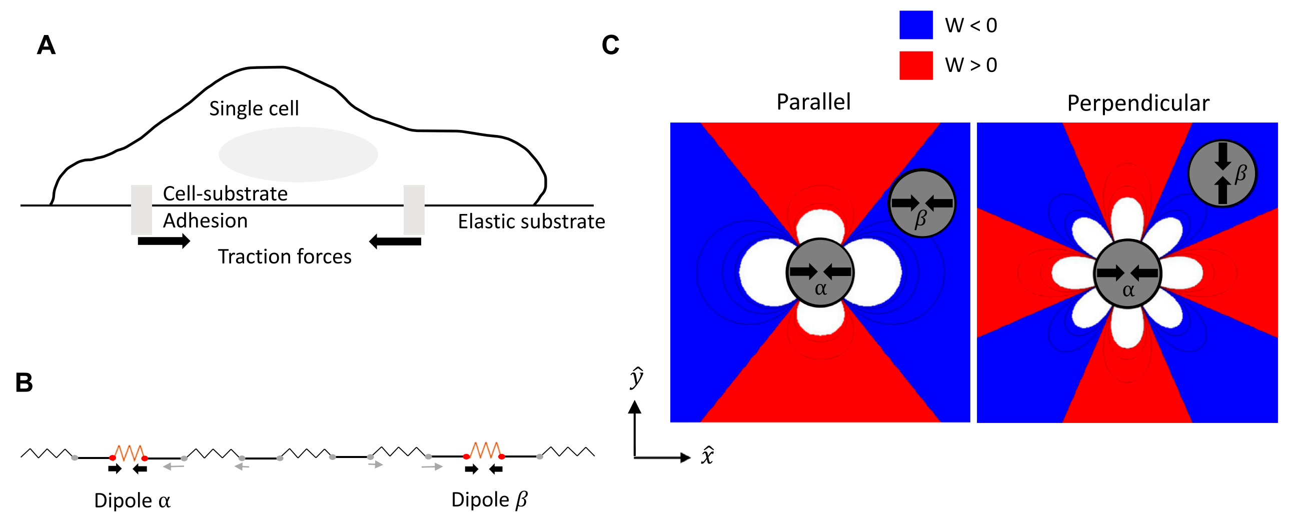

FIGURE 1 | Elastic interactions between model cells on a substrate. **(A)** Schematic of adherent cell on an elastic substrate. **(B)** 1D spring model illustrating origin of elastic interaction potential between two contractile dipoles. The elastic energy stored in the medium corresponding to the deformation of springs depends on the relative placement of the dipoles. In particular, placing a contractile dipole in a region where the medium is already expanded by the other dipole can help to reduce the overall deformation of the medium. This leads to a strain-dependent interaction potential between the two dipoles. **(C)** Representative spatial maps of the interaction potential $W^{\alpha\beta}$ between two dipoles, from the solution of the strain field for the full linear elastic problem of forces exerted on the surface of a semi-infinite medium are shown. The interaction potential corresponds to the work done by a point-like dipole in deforming the substrate in the presence of the strain created by the other. The potential maps shown here are for a pair of contractile force dipoles of fixed orientation. The second dipole is free to translate but held parallel (left) or perpendicular (right) to the central dipole which is placed at the origin and aligned along the x-axis. The contour lines show how the potential decays in space, whereas blue and red regions correspond to attractive ($W^{\alpha\beta} < 0$) and repulsive ($W^{\alpha\beta} > 0$) interactions, respectively.

$$f^{\beta}_{el} = -\frac{\partial W^{\alpha\beta}}{\partial \mathbf{x}^{\beta}} = -P^{\beta}_{ij}\frac{\partial u^{\alpha}_{ij}\left(\mathbf{x}_{\beta}\right)}{\partial \mathbf{x}^{\beta}_{j}}, \tag{1}$$

given by the gradient of the strain induced by the other dipole, where the strain therefore acts as a potential. While the expressions vary in detail, this physical interaction between elastic dipoles considered here is analogous to the interaction of an electric dipole with the electric field induced by another dipole. A similar reciprocal force results on dipole α, since the interactions are based on an elastic free energy. The physical origin of this force is the tendency of the passive elastic medium to minimize its deformations in response to the active, contractile forces generated by the cells. This generic mechanical interaction between dipoles is not limited to cells [46], but also occurs for passive inclusions in an elastic medium [47]. Experimentally, hydrogen atoms in metals were shown to diffuse and distribute themselves according to configurations dictated by these elastic interactions [48].

Pairwise dipolar interactions are anisotropic and depend on both the distance between and relative orientations of the two particles with respect to their separation axis. Insights into the nature of the elastic interaction potential between a pair of force dipoles, may be obtained from **Figure 1C** where we plot spatial maps of the interaction potential $W^{\alpha\beta}$ for 2 cells with fixed orientation. To plot these functions, we choose a reference contractile force dipole α that is fixed at the origin with its axis along the $-x$ direction, i.e., whose dipole moment has purely the P_{xx} component. A second dipole β interacts with the reference dipole according to its position and orientation. The red (blue) regions in the potential maps in **Figure 1C** represent repulsion (attraction) which arises from the substrate strain. Here, we use the convention that stretched (compressed) regions have positive (negative) strain, while compressive dipole moment is negative. While the map on the left corresponds to parallel alignment, that on the right maps the interaction potential for perpendicular alignment of the two dipoles. In this example, we fix the orientation of the second dipole to be either parallel or perpendicular, and therefore it couples to either the u_{xx} or the u_{yy} component of the strain according to **Eq. 1**. In general, the dipoles can also rotate and change their relative orientations. In particular, while the favorable parallel configuration shown here leads to end-to-end alignment of the dipoles, the unfavorable perpendicular configuration will lead to mutual torques that tend to orient them in the favorable parallel configuration. The elastic material comprising the substrate is treated as homogeneous and isotropic with shear and compression Moduli proportional to the Young's modulus E, and a Poisson ratio ν that provides a measure of its compressibility [49]. While the Poisson's ratio can in principle have the full range $-1 < \nu < 1/2$ in linear elasticity theory, the figures plotted here correspond to $\nu = 0.1$[1].

---

[1] This choice ensures end-to-end alignment of dipoles and provides interactions seen not just in cells but also in other types of active matter that feature particles with magnetic or electric dipole moments. The interactions at $\nu > 0.3$ have a different symmetry and can result in more complex structures such as short rings without any electric or magnetic analogs [50].

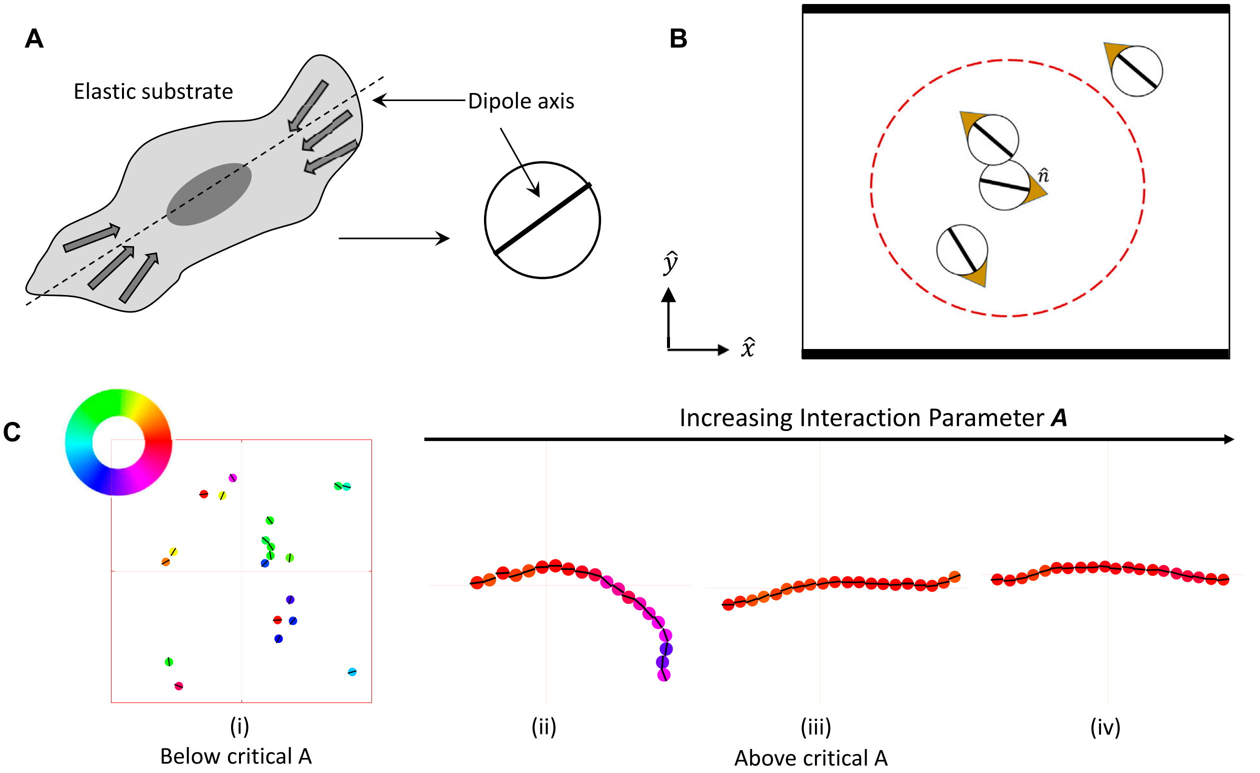

FIGURE 2 | Overview of agent based simulations of active Brownian particles (ABPs) moving in the x-y plane and interacting mechanically *via* elastic deformations induced by contractile, active force dipoles. **(A)** An elongated cell with traction forces distributed around its long axis is modeled as a disk-like particle endowed with a dipole moment. **(B)** Each ABP has a dipole axis represented by the bold black line and an in-plane self-propulsion direction represented by the gold arrow. These particles move on a linearly elastic, thick, flat substrate, on which they exert contractile dipolar stresses. Substrate deformation due to one particle is sensed by neighboring particles. These dipole-dipole elastic interactions are confined to particles within a cutoff distance $r_{\text{cut}} = 7\sigma$ (shown as the dashed red circle). Particle overlap is penalized by a short range steric repulsion. They are confined by steric repulsions along the top and bottom walls shown by the thick lines, while being free to move through periodic boundaries shown by the thin lines. **(C)** for figure (i) Simulation snapshot shows that weakly interacting particles do not stick to each other and move as independent entities. As the elastic dipolar interaction parameter A increases, the particles self-assemble into long chains ((ii)-(iv), zoomed view shown). The flexibility of the chains and fluctuations in the mean curvature both decrease with increasing values of the interaction parameter. The colors represent the self-propulsion direction of each particle, as indicated by the color wheel.

The interaction potential and model dynamics are detailed in the Methods **Section 4** in **Eqs 4–7**. As shown in **Figure 2A**, the ABPs–here termed particles–are modeled as circular disks of diameter σ, each particle being endowed with a dipole moment and a self-propulsion direction $\hat{\mathbf{n}}$. The orientation of $\hat{\mathbf{n}}$ is aligned with the dipole axis (shown as the bold black line). This assumption is reasonable for motile cells with elongated shape, but is not necessarily satisfied for all cell types, where higher force multipoles may be relevant [24]. Particles are assumed to self-propel with a speed v_0. This phenomenologically models the movement of cells which require internal cell forces arising from actomyosin activity as well as the remodeling dynamics of the cell-substrate adhesions, not explicitly modeled here. Additionally, the motion of each particle is subject to forces and torques arising from dipolar interactions with other particles, as well as a random stochastic force. The latter mimics the effect of the thermal environment surrounding the particles, and leads to diffusive effects in both orientation and spatial position of the ABPs.

Since we are motivated by adherent cells on elastic substrates whose contractile traction forces act as elastic dipoles, a cutoff distance of $r_{\text{cut}} = 7\sigma$ (red dashed circle in **Figures 2B**) is imposed on the long-range dipolar interactions. The choice of a cut-off length for interactions is consistent with experimental observations that cells can interact with one another *via* mechanical signalling at distances that are up to a few cell lengths away [8, 19]. In addition to the “long-range” interactions mediated by the elastic substrate, cells may also interact *via* “short-range” interactions. Here we introduce short-range steric repulsion using a mechanical model using compressive springs that discourage overlap between neighboring particles. Specifically, two particles in close-contact exert a repulsive elastic force on each other when the center-to-center distance is less than the rest length σ of these springs.

The ensuing dipolar interactions, when strong enough relative to the stochastic noise, cause end-to-end chaining of the particles along their dipole axis. Examples of this chaining process are seen to occur in our simulations and representative snapshots are shown in **Figure 2C**. As expected intuitively, increasing interaction gives rise to stronger alignment resulting in chains that are progressively less flexible. The effective elastic bending modulus of these chains that determines the fluctuations of the backbone contour of the chained ABPs is thus higher with increasing interaction strength.

To illustrate the bulk behavior of interacting ABPs as well as the effect of confinement on emergent collective patterns, we simulate a few hundred of these particles in a box confined in the y – direction, and periodic in the x – direction. The confining boundary is lined by repulsive springs of the same type used to penalize particle overlap, and keeps the ABPs from escaping the simulation box. This setup mimics a channel geometry typically used in cell motility experiments [51] and is used in other works on simulations of ABPs under confinement [52–54]. We focus on the physical barriers to cell motility and not interfaces in the elastic medium. In principle, such elastic interfaces can lead to additional elastic torques and forces on dipoles by inducing “image forces” [46], but this is outside the scope of the present work. One way to realize this type of confining boundary that does not induce stresses in the elastic medium is to culture cells on a large and thick slab of hydrogel with uniform elastic properties, but micropattern a specific region of the substrate with ligands to which the cells can adhere–a common technique in mechanobiological cell culture studies [14].

The important nondimensional control parameters in the model are the effective elastic interaction strength A, the active self-propulsion velocity characterized by a Péclet number, Pe, and the packing fraction, ϕ. The packing fraction used in simulations below is typically either $\phi = 0.08$ or 0.25 corresponding to relatively dilute regimes, except in a narrow channel geometry where we go up to $\phi = 0.75$. Definitions and physical interpretations of these parameters are provided in **Section 4**.

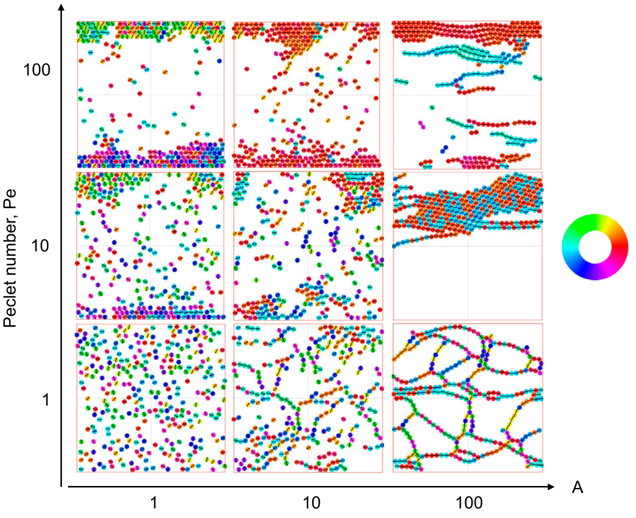

FIGURE 3 | Simulation snapshots of active particles with short range steric repulsions and long-range elastic dipole-dipole interactions as a function of effective elastic interaction $A \equiv P^2/E\sigma^3 k_B T_{\text{eff}}$ and Péclet number $Pe \equiv \sigma v_0/D_T$. Particles are confined in the y-direction, while they experience periodic boundary conditions in the x-direction. They are colored according to their self-propulsion direction $\hat{\mathbf{n}}$, and coded based on the color wheel. Motile particles at low effective elastic interaction collect into clusters at the boundaries. Strong elastic interactions promote network formation at low activity. Strong elastic interactions paired with high activity gives rise to active polymers and polar bands. The full movies corresponding to ABPs, networks, traveling cluster, and active polymers can be seen in **Supplementary movies S1–S4**, respectively.

3 RESULTS

3.1 Characteristic States of Active Dipolar Particles: Chains, Polar Bands, Clusters and Networks

We first explore the possible collective structures that result from the combination of active self-propulsion with dipolar attraction and alignment. We explore the parameter space of activity (given by the Péclet number, Pe) and strength of dipolar interactions (given by the effective elastic interaction parameter, A) for two representative systems: one dilute and the other semi-dilute. We show representative snapshots of the steady states of the simulations by coloring the particles according their orientation. Collections of these snapshots as well as the color wheel corresponding to particle orientations are shown in **Figure 3**, where the packing fraction $\phi \approx 0.25$, and **Figure 4**, where the packing fraction $\phi \approx 0.08$.

We see from **Figure 3** that at both low motility and weak elastic interactions ($A = 1$), particles do not form any ordered structures but are distributed uniformly in space, over the utilized simulation time. As motility is increased ($Pe \geq 10$), particles are seen to clump up at the boundary with their orientation vectors facing the wall at which they are localized. This is a familiar result of confined active Brownian particles (ABPs) wherein these tend to point towards the wall until their orientation is sufficiently randomized by the rotational diffusion [55]. As elastic interactions are dialed up such that the motions resulting from the dipolar interactions are much stronger than the stochastic diffusion of the system, structures characteristic of dipolar interactions emerge. In the case of low particle motility ($Pe = 1$), and high elastic interactions, we see a branched network form. In the case of intermediate motility ($Pe = 10$), networks are broken down into a single traveling cluster. In the former case, the particles comprising any given chain can either be oriented parallel (0) or anti-parallel (π) with respect to one another as the dipolar interaction is head-tail symmetric. In the latter case, networks form at short time scales and are compressed into one motile cluster at long time scales. This motile cluster contains numerous defects (shown by their different color)–particles oriented anti-parallel to the direction of cluster motion–caused by the earlier stage of network formation. Lastly, in the case of high particle motility ($Pe = 100$), particles assemble into traveling flexible chains which predominantly move parallel to the confining boundary and undergo inter-chain collisions in the bulk. Much of our forthcoming analysis is focused on these highly ordered, yet highly dynamic, structures.

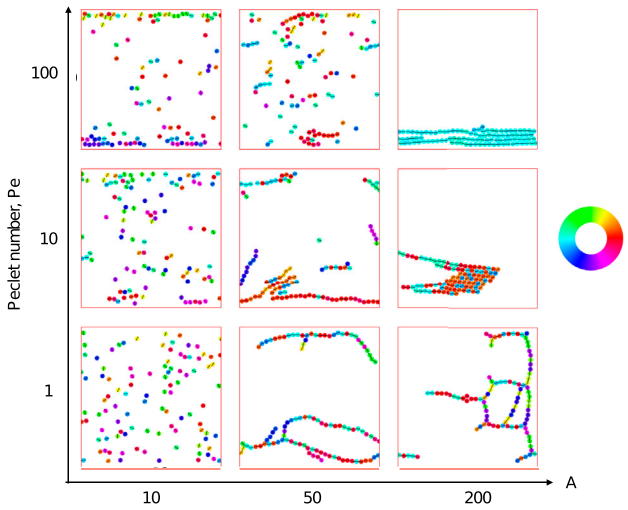

FIGURE 4 | Simulation snapshots of active particles at low packing fraction. The interaction parameter $A \equiv P^2/E\sigma^3 k_B T_{\text{eff}}$ and Péclet number $Pe \equiv \sigma v_0/D_T$ define the collective behavior of the particles. Particles are confined in the *y*-direction, while they experience periodic boundary conditions in the *x*-direction. They are colored based on the direction of $\hat{\mathbf{n}}$, as indicated by the color wheel. At low interaction parameter A = 10, the particles remain isolated and diffuse (**Supplementary Movie S6**). At high *Pe*, more particles get collected at the confining boundary. At higher values of the interaction parameter, *A*, particles form chains. The typical length of the chains is seen to decrease with increasing *Pe*. At very high interaction parameter, A = 200, networks with multiple branches form at low *Pe*, while chains aggregate into polar clusters at Pe = 10 (**Supplementary Movie S7**). Although the particles in the cluster are oriented in opposite directions, the cluster is stable and moves in the direction given by its overall polarity. Again at very high Péclet, Pe = 100, the particles in the chains are oriented in the same direction.

At low packing fraction (**Figure 4**), for A = 10 the elastic interaction between the particles is low and they diffuse around in the simulation space which is in contrast to what we see for higher packing fraction (**Figure 3**) where particles show alignment with weak attraction. Accumulation of the particles can be seen at the confining boundaries which is attributed to the activity of the particles. Upon increasing the elastic strength to A = 50, formation of chains is observed. At Pe = 1, long and branched chains of particles are formed. Increasing motility leads to a decrease in length of the chains and an increased polarity. At even higher elastic strength of A = 200, long chains with multiple branches are seen for Pe = 1. At increased activity, the chains stick to each other and form an ordered cluster that moves coherently in the direction determined by the net polarity of the constituent particles.

3.2 Pair Correlations Reveal Spatial Organization of Active Chains

To quantify the spatial distribution of particles around their neighbors, we calculate the pair correlation function, $g(r, \theta)$, the probability of finding a neighboring particle at a distance r in a direction θ from the central agent's orientation axis. We calculate this quantity by averaging over the positions of all agents over time, and binning every other agent according to its separation vector (both distance and angle) from the current central agent. Finally the distribution is normalized such that $g(r, \theta)$ approaches 1 for distance r going to infinity. We then analyze the peaks in (r, θ) space. **Figure 5** shows four such distance and angle dependent maps in the space of motility and elastic interaction. Elastic interactions localize the peaks of the pair correlation function. When motility is low, particles form branched networks and the primary configuration of particles is in straight chains. In this case, there exists two prominent peaks in the pair correlation function at $(\sigma, 0)$ and (σ, π). When both motility and elastic interactions are high, particles form into flexible traveling chains that have a tendency to join one another in a parallel fashion with an offset - a configuration that is energetically favorable to the elastic interaction and can be seen prominently in the simulation snapshot corresponding to A = 100 and Pe = 100 in **Figure 3**. In this case, the primary peaks still occur at $(\sigma, 0)$ and (σ, π), but secondary peaks are present at $(\sigma, \frac{\pi}{3} \bmod \pi)$ and $(\sigma, \frac{2\pi}{3} \bmod \pi)$, indicating the offset parallel band structure. Low elastic interactions constitute the more familiar case of collections of repulsive ABPs. In this regime, the head-tail symmetry characteristic of the elastic interactions is broken as particles are more likely to encounter other particles along their direction of propulsion [56]. There exists a single prominent peak at the head of the dipole that monotonically decreases on either side of the head axis. Increasing motility in the ABP system adds layers to the single peak function in integer multiples of particle size σ as collision frequency increases.

3.3 Activity and Elastic Interactions Promote Orientational Order

At higher interaction strength, A, and higher motility, Pe, we see chains that move parallel to each other forming polar bands at high density (top right of **Figure 3**). Since chains are elongated objects, a collection of them can give rise to orientational order, similar to active nematic and polar states that result from active, anisotropic particles [1]. This type of order is commonly seen in active matter comprising suspensions of cytoskeletal filaments and motors [57]. To quantify the orientational order in these cases and to distinguish from the individual ABPs under confinement, we measure the nematic and polar order for these states. The magnitude of the nematic order parameter is defined as an average over the orientation of all particles, $S \equiv 2\langle \cos^2\theta \rangle - 1$, where θ is the angle between a particle's orientation and the average director. In this case, the global alignment direction is parallel to the confining boundaries given by the $x-$axis. The nematic order tells us how well the dipoles are aligned, without distinguishing between the head and tail and contains no information about the motility direction. To quantify the oriented motion, we calculate the polar order, whose magnitude is given by, $|p| \equiv \sqrt{\langle n_x \rangle^2 + \langle n_y \rangle^2}$, where n_x and n_y are the x and y components of the orientation vector, $\hat{\mathbf{n}}$, respectively. This quantity is higher if the particles are oriented in the same direction, in addition to being aligned. While nematic alignment is encouraged by the passive dipolar interactions, active motility induces polar order.

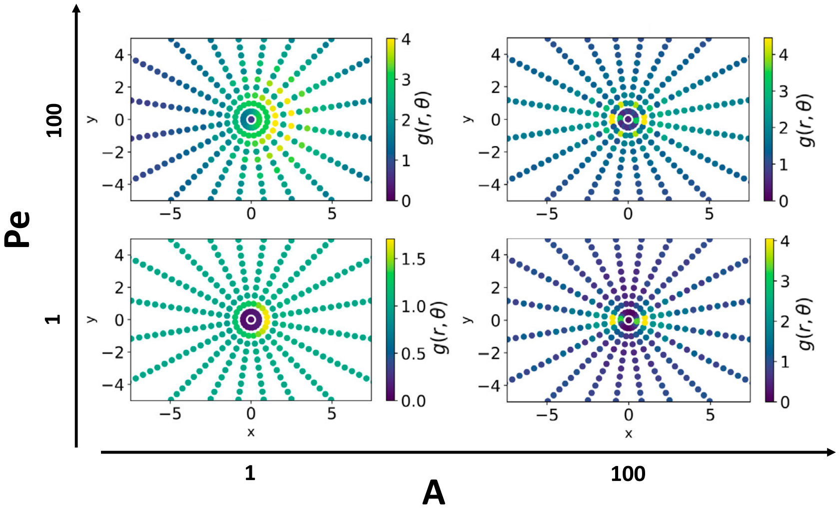

FIGURE 5 | Angular dependent pair correlation function is affected by both motility and elastic interactions. Strong elastic interactions promote pair correlation peaks at $(r, \theta) = (\sigma, 0)$, (σ, π). At $Pe = 1$, these are the only prominent peaks in the pair correlation function. Motile activity gives rise to secondary peaks at roughly $(r, \theta) = (\sigma, \frac{\pi}{3} \bmod \pi)$, $(\sigma, \frac{2\pi}{3} \bmod \pi)$ as the preeminent structures are bundles of offset traveling chains. Weak elastic interactions broaden the pair correlation distribution. In this case, motility breaks head-tail symmetry and peaks can be seen at multiple integers of particle diameter at the head ($\theta = 0$ axis).

Figures 6A,C shows the global nematic order in time and **Figures 6B,D** shows the time averaged spatial map of the polar order parameter, calculated by subdividing the simulation box into regions of dimension $3.75\sigma \times 3.75\sigma$, for both ABPs and traveling flexible chains. In the ABP system, the global nematic order is small due to the tendency of particles at the walls to be oriented orthogonal to the wall and those in the bulk to be oriented parallel to the wall, as well as the presence of orientational fluctuations from rotational diffusion. Traveling flexible chains of dipolar particles exhibit a global nematic order close to unity as all particles in this system tend to point along a director parallel to the confined boundary. Spatially resolving the average of the magnitude of the polar order parameter gives us a picture of particle alignment at a smaller length scale. ABPs exhibit polar alignment at the boundary. This alignment quickly diminishes and no polar order is seen in the bulk. Traveling chains form bands at the boundary such that $|\mathrm{p}| > 0.7$ up to 6σ away from the wall. The polar order of these flexible chains drops off far less drastically in the bulk than the ABP system.

3.4 Transport Properties of Active Chains Are Distinct From Single Particles

The mean-squared displacement, or MSD, is a typical metric that quantifies how motile entities cover space in time. In **Figure 7**, we report the MSD for simulations with a packing fraction $\phi \approx 0.08$ in a square box of size 30σ, corresponding to the structures shown in **Figure 4**. Given the confinement along one direction, we calculate the MSD separately for the confined (y-) and unconfined (x-) directions. The unconfined MSD, $\langle x^2 \rangle$, for particles with low elastic interaction e.g., at $A = 10$, shows similar trends to individual active Brownian particles [58]. At short time intervals, individual ABPs propel persistently in the direction of their orientation, leading to ballistic behavior. In **Figure 7A**, we see such behavior at very short time scales which gave way to super-diffusive behavior at intermediate time scales, where particles are slowed down by collisions with other particles. At sufficiently long time scales, the particles are diffusive as the rotational diffusion randomizes their orientation. Increasing Péclet number increases the time scale for superdiffusive behavior as the persistence time is longer.

We see qualitatively different regimes in the MSD for particles with stronger interaction in **Figure 7B**. At interaction strength $A \geq 100$, which leads to formation of long, stable chains, we observe larger-scale structures such as branches, clusters and networks in the simulation snapshots shown in **Figure 4**. In this case, the particles show sub-diffusive behavior at shorter time scales when they are still moving individually in an uncorrelated manner and beginning to form these structures. On the other hand, at longer time scales, they cluster into larger scale structures that move coherently in a specific direction like polar flocks, giving rise to a ballistic behavior. The crossover from subdiffusive to nearly ballistic behavior occurs earlier for higher Péclet numbers. At higher particle motility, we obtain ballistic behavior for all time scales. The resulting behavior is thus qualitatively different from single ABP behavior, which shows a crossover from persistent to diffusive motion at time scales longer than the persistence time ($\sim Pe$). Here, on the other hand, the long time behavior is dictated by large-scale, polar structures that self-assemble irreversibly and move persistently at long times.

The MSD in the confined direction, $\langle y^2 \rangle$, plateaus at long times, both for the individual ABPs (**Figure 7C**) and the larger scale structures (**Figure 7D**). The time scale to reach a plateau in the MSD corresponds to the time it takes an entity to reach the confining walls from the bulk of the simulation box. Thus, $\langle y^2 \rangle$ reaches a plateau at a shorter time scale for highly motile particles,

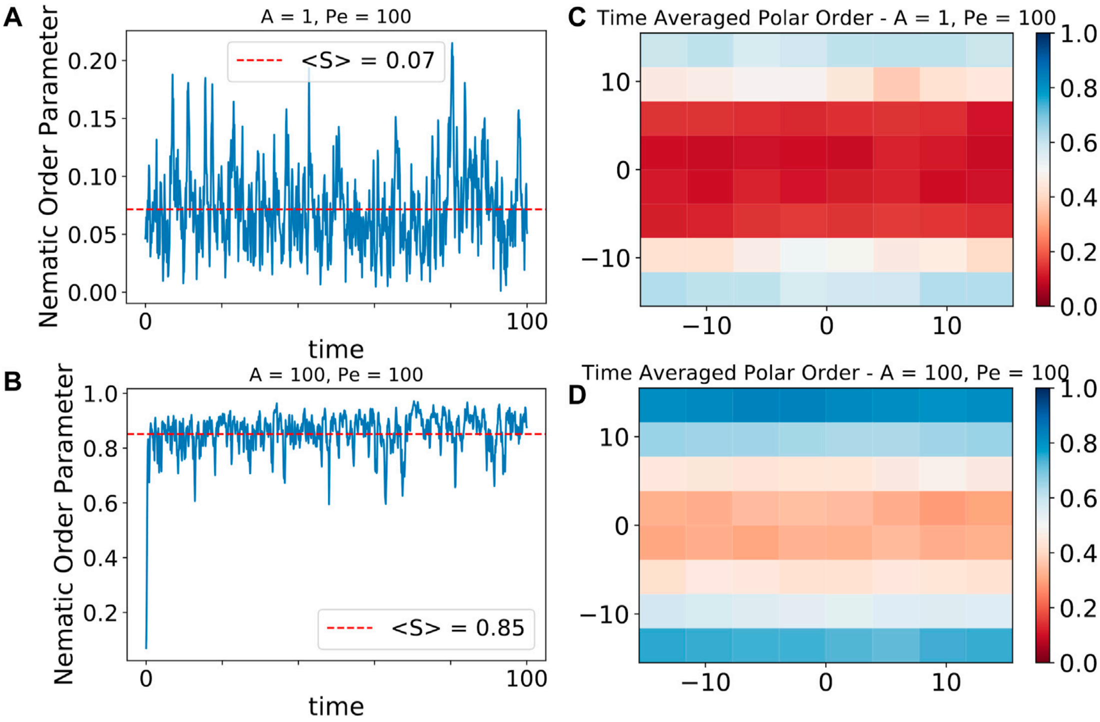

FIGURE 6 | Elastic interactions promote global nematic order and local polar order. **(A)** Global nematic order, measuring the overall alignment of the particles' dipole axes, *vs*. time for low effective elastic interaction and high activity. Average global nematic order is negligible for these parameters. **(B)** Global nematic order *vs*. time for high effective elastic interaction and high activity. The system quickly gains a persistent global nematic order parameter near unity because the chains align parallel to each other. **(C)** Spatial distribution of time averaged polar order, where grid size is $3.75\sigma \times 3.75\sigma$, measuring the overall orientation of motility for the particles, for a characteristic run at low effective elastic interaction and high activity. Particles accumulate at the boundary and exhibit polar order along that boundary. This order rapidly decays away from the boundary and there is virtually no polar order observed in the bulk. **(D)** Spatial distribution of time averaged polar order, where grid size is $3.75\sigma \times 3.75\sigma$, for a characteristic run at high effective elastic interaction and high activity. A polar order near unity is observed at the boundary and persists into the bulk where near the middle of the channel $|p| \approx 0.3$.

as compared to the less motile ones. Due to the confining wall in the y-direction and strong alignment with neighboring particles at $A = 100$, the particles line up into chains that orient and move parallel to the confining walls, and not as much in the y-direction. Thus, $\langle y^2 \rangle$ for $A = 100$ reaches the plateau later than for the $A = 10$ case, for corresponding values of Pe.

3.5 Collisions of Active Chains Reveal Stable, Mobile Structures

We observe from simulations at low packing fraction (**Figure 4**) that once particles self-assemble into chains, they can intersect to form junctions and get organized into larger-scale polar structures. We now explore in more detail the inter-chain interactions responsible for this self-organization. To do this, particles were initialized in an ordered chain and oriented in the same direction. Two such chains were oriented initially at different angles to control their approach direction, as shown in the insets in **Figure 8**.

At $A = 200$ the junctions formed by chains depended on the Péclet number and the angle and position of approach. The "Y" junction was the most observed for all Péclet number, which is formed from when the second chain attaches itself at the middle of the first chain (**Figure 8**, top left). An "eye" (**Figure 8**, top right) is formed from two closely spaced "Y"s, which is observed for higher Péclet number, $Pe = 5$ and 10, and when the chains are oriented in the same direction. Again, at low particle motility ($Pe = 1$), the chains, upon colliding head on, form a longer and more rigid chain (**Figure 8**, bottom left). On the other hand, at $Pe = 5$, chains show buckling upon undergoing head on collision which leads to a propelling "necklace" (**Figure 8**, bottom right). At even higher Péclet number, the force between the particles is overpowered causing particles to detach from a chain and thereby creating defects. All these cases have been observed for $A = 200$. These junctions are also observed at lower elastic strength $A = 50$ and 100, but were unstable giving rise to many defects. Chains may interact with each other in a head-tail fashion which results in a stable longer chain. Chains with multiple defects have also been observed to form these "Y" and "eye" structures at $A = 200$ and $Pe = 1$ (**Figure 4**).

3.6 Stronger Confinement in Narrow Channels Reveals Polar Clustering Dynamics

In our system of traveling flexible chains comprised of strongly interacting and highly motile dipolar particles ($A = 100$, $Pe =$

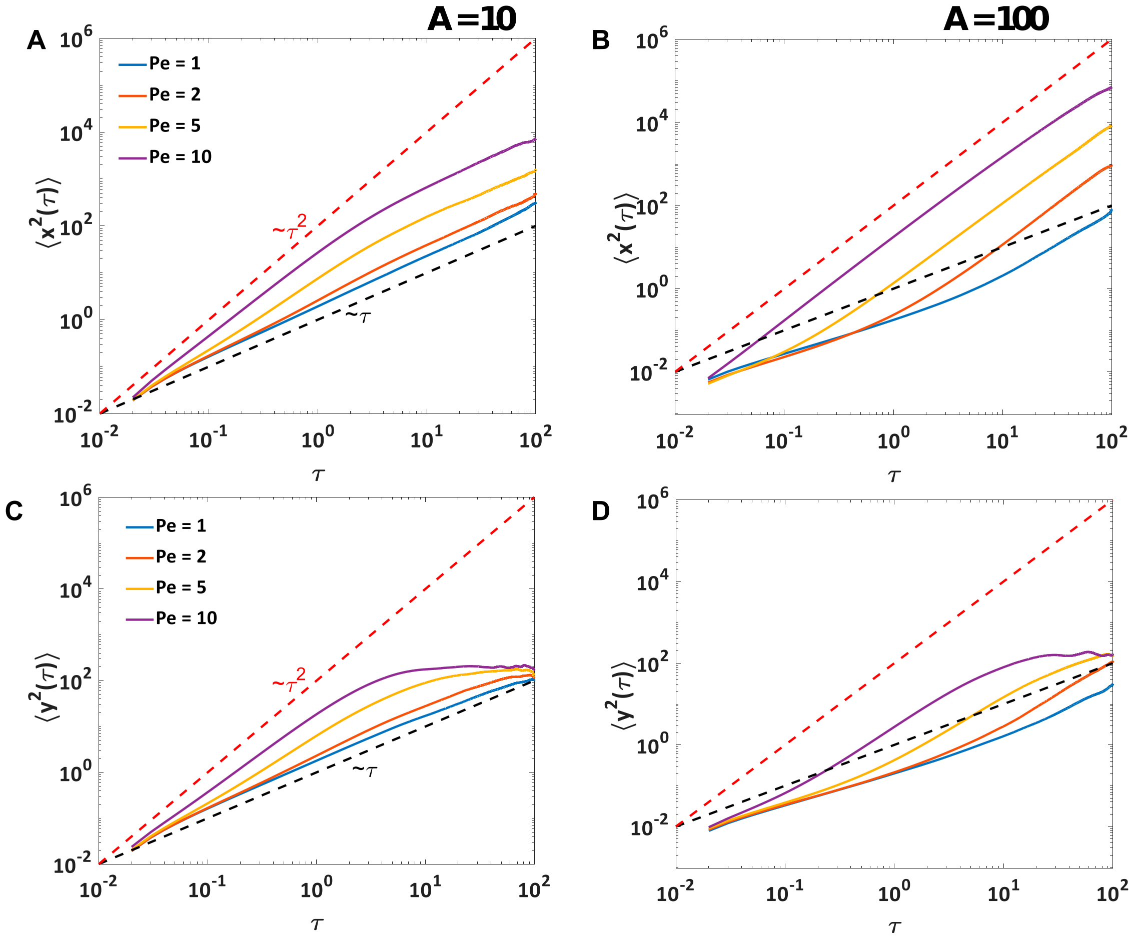

FIGURE 7 | Mean-Squared Displacement, or MSD, *vs*. time interval, for 100 particles in a square simulation box of 30σ. Due to confinement of particles in y-direction, MSD is plotted separately for x and y components of displacement. **(A)**, **(B)** MSD along unconfined direction: for $A = 10$, particles are super-diffusive at short time scale and diffusive at longer time scale, where the crossover time scale is determined by the Péclet number (*Pe*) of the particles. At $A = 100$, particles align themselves to form chains or clusters. At low *Pe*, the particles show sub-diffusive behavior at shorter times and ballistic behavior at longer times. At higher *Pe*, the ballistic behavior of particles is observed at all time scales. **(C)**, **(D)** MSD along confined direction: particles reach the confining boundary at shorter times for high *Pe* number, and also at low elastic interactions *A*. At higher *A*, particles chain up and move predominantly parallel to the confining boundary.

100), bands that form along the confining boundary are relatively stable compared to those that form in the bulk. The latter are subject to more frequent collisions with other traveling chains. In order to gain understanding of these chain collision dynamics, we confine the same number of particles into a channel of width $L_y = \frac{L}{3}$, where L is the box size of our original simulation space, in order to induce more frequent and global chain-chain collisions. In this system we find a cyclic tripartite state dynamic. As shown in **Figure 9A**, at some point, the particles with orientations $+x$ become well mixed with particles with orientations $-x$. The particles will then separate into lanes according to their polarity so that they can move unimpeded. These lanes will then collide which initializes another well mixed system and the cycle repeats.

This effect of colliding lanes can be seen quantitatively by tracking the magnitude of the polar order parameter averaged over boxes of width 3σ and height 2.5σ in time shown in **Figure 9B**. The well mixed system has an average polar order parameter of $|p| \approx 0.2$. The system then phase separates into lanes with average polar order parameter ≈ 0.6. The $+x$ and $-x$ lanes collide and the resultant combination has an average polar order parameter ≈ 0.4. When the channel is sufficiently wide, collisions between opposite lanes is less common, and the average polar order is bolstered by persistent polar chains at the confining boundary as seen in **Figure 9C**. This time dependent formation and disbanding of polar structures is consistent with bead spring simulations of semiflexible filaments in the high activity regime [59].

4 METHODS

Here, we present the equations governing the motion of the active motile particles discussed earlier and their interaction *via* the elastic substrate on which they move. In our model, we treat the particles as circular active Brownian particles (ABPs) that interact with other particles *via* long-range substrate modulated

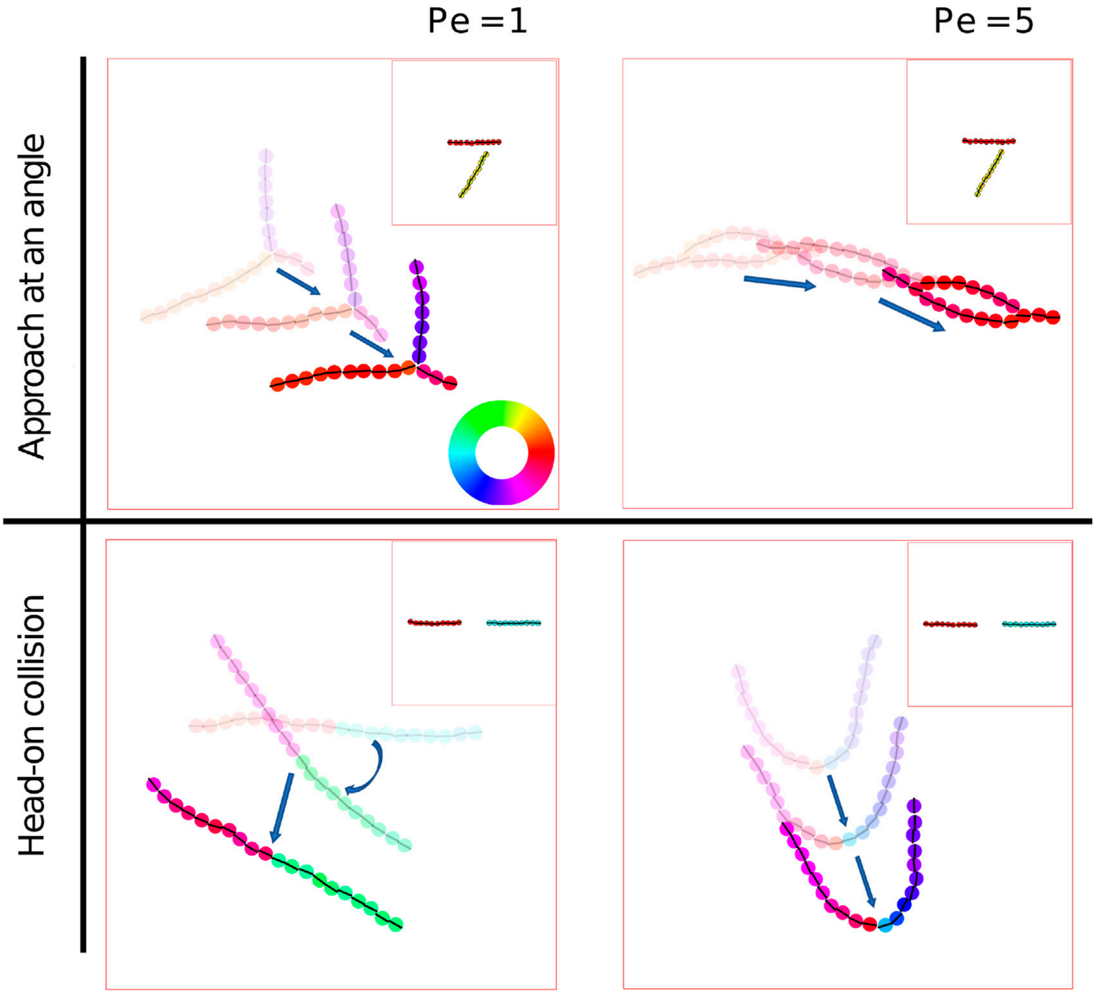

FIGURE 8 | Interaction of two motile chains (Supplementary Movie (**Supplementary Movie S8**). Two straight chains of 10 particles each are initialized to approach each other at an angle of $\frac{\pi}{3}$ and also π ("head-on") at $Pe = 1$ and 5. At $Pe = 1$, a "Y" junction forms for an approach angle of $\frac{\pi}{3}$ whereas at $Pe = 5$, an "eye" (two junctions) occurs. Upon head-on collision, a longer fluctuating chain with negligible net motility results at $Pe = 1$, and a propelling, buckled shape is observed at $Pe = 5$. Insets at the top corners represent the approach of the chains. Color represents angle of orientation of particles. The arrows indicate progression in time and suggest that the configurations are both stable and motile.

interactions and direct short-range particle-particle steric contact interactions. Long range interactions arise as each ABP exerts a contractile stress dipole $\mathbf{P}$ on the flat, semi-infinite, linearly elastic, isotropic substrate, thereby inducing strain fields which induce an effective force on nearby particles. For simplicity, we assume that the dipole axis is coincident with the direction of motion of the particle. For instance in an elongated cell, the force dipole axis coincides with the orientational axis of the cell, that is also the direction of self-propulsion.

In the derivation that follows we use Einstein summation convention over the Latin indices, while Greek indices are used to label the particles. Consider a particle α that deforms the substrate. The work done by the associated dipole, $\mathbf{P}^{\alpha}$ in deforming the substrate in the presence of the strain created by a second dipole $\mathbf{P}^{\beta}$ (generated by a second particle β) is given by [46],

$$W_{\alpha\beta} = P^{\beta}_{ij}\partial_j\partial_l G^{\alpha\beta}_{ik}\left(\mathbf{r}_{\alpha\beta}\right)P^{\alpha}_{kl}, \tag{2}$$

where $\mathbf{r}_{\alpha\beta} = \mathbf{r}_{\beta} - \mathbf{r}_{\alpha}$ is the separation vector connecting the centers of particles α and β (**Figure 10**) (c.f [39, 49]). The elastic half space or Boussinesq Green's function that gives the displacement field in the linearly elastic medium at the location of one particle caused by the application of a point force at the location of the other is given by [45],

$$G^{\alpha\beta}_{ik}\left(\mathbf{r}_{\alpha\beta}\right) = \frac{1+\nu}{\pi E}\left[(1-\nu)\frac{\delta_{ik}}{r_{\alpha\beta}} + \nu\frac{r_{\alpha\beta,i}r_{\alpha\beta,k}}{r^3_{\alpha\beta}}\right], \tag{3}$$

where E is the stiffness (Young's modulus) and ν is Poisson's ratio of the substrate. Given the linearity of the problem, superposition of strain fields, each of which is obtained by using the Green's function (1), appropriately provides the net displacement at a test position due to particles around it.

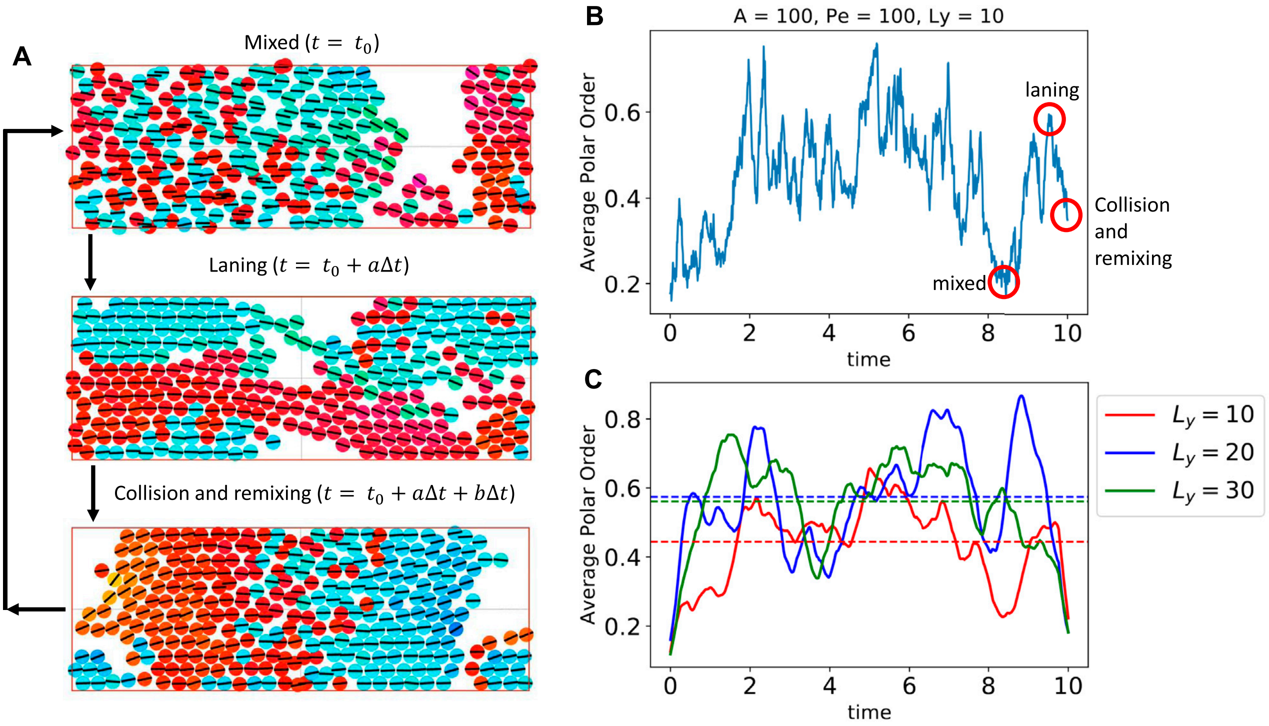

FIGURE 9 | Traveling chains in a narrow channel exhibit cycles of mixing, laning, and collision and remixing. **(A)** Snapshots of a simulation where channel width has been decreased by a factor of 3. Dynamics of the system are encompassed by three cyclic states: A mixed state shown at an arbitrary initial time t_0, a phase separated laning state shown a short time after t_0, and a collision and remixing state shown a short time after the laning state. **(B)** Polar order averaged over boxes of width 3σ and height 2.5σ versus time is shown to elucidate the three states described in **(A)**. The polar order for a mixed–laning–collision and remixing cycle are shown in the red circles. When the system is well mixed, the average polar order is small ($p \approx 0.2$). When the particles separate into lanes, the polar order increases rapidly ($p \approx 0.6$). When the lanes then collide and begin remixing, the remnants of the bulk of the lanes provide polar order while mixed particles and the interface between lanes decreases polar order ($p \approx 0.4$). **(C)** Polar order averaged over boxes of width 3σ and height 2.5σ versus time for three channel widths. Time averaged polar order, shown in dashed horizontal lines, is similar for the $L_y = 20$ and $L_y = 30$ cases when collision dynamics occur in the bulk, but non-interacting traveling chains line the boundaries. Time averaged polar order is smaller for the $L_y = 10$ case as collision dynamics are global phenomena. The full movie corresponding to the narrow channel can be seen in **Supplementary Movie S5**.

Two particles in our model interact *via* a combination of pairwise long-range and short-range interactions. The long-range interaction forces originate from the substrate-mediated, elastic dipole-dipole interaction potential, $W^{\alpha\beta}$. The short-range interactions are steric in nature and prevent ABPs from overlapping. This functionality is achieved in the framework of our model by linear springs that only resist compression. Taken together, the total interaction potential between particles α and β can be written as,

$$\begin{aligned} W^{\alpha\beta} &= \frac{1}{2}k\left(\sigma - r_{\alpha\beta}\right)^2, \quad \text{when} \quad 0 \le r_{\alpha\beta} < \sigma \\ &= \frac{P^2}{E}\frac{f\left(\nu, \theta_\alpha, \theta_\beta\right)}{r_{\alpha\beta}^3}, \quad \text{when} \quad \sigma \le r_{\alpha\beta} < r_{\text{cut}} \\ &= 0, \quad \text{when} \quad r_{\alpha\beta} \ge r_{\text{cut}}, \end{aligned} \tag{4}$$

where k is the spring constant of the linear (repulsive) spring preventing overlap, σ is the particle diameter (kept constant in our simulations), and r_{cut} is a cutoff distance beyond which the dipolar interactions are neglected. The magnitude of each force dipole is taken to be the same value denoted by P. The dependence of the pairwise dipolar interactions on the orientations of the two dipoles with respect to their separation vectors, and on the Poisson ratio of the medium, ν, is expressed compactly in the expression [49],

$$\begin{aligned} f\left(\nu, \theta_\alpha, \theta_\beta\right) = \frac{\nu(\nu+1)}{2\pi}\Big(&3\Big(\cos^2\theta_\alpha + \cos^2\theta_\beta - 5\cos^2\theta_\alpha\cos^2\theta_\beta - \frac{1}{3}\Big) \\ &-\left(2-\nu^{-1}\right)\cos^2\left(\theta_\alpha - \theta_\beta\right) - 3\left(\nu^{-1}-4\right)\cos\theta_\alpha\cos\theta_\beta\cos\left(\theta_\alpha - \theta_\beta\right)\Big). \end{aligned} \tag{5}$$

where $\cos\theta_\alpha = \hat{\boldsymbol{n}}_\alpha \cdot \vec{\boldsymbol{r}}_{\alpha\beta}$ and $\cos\theta_\beta = \hat{\boldsymbol{n}}_\beta \cdot \vec{\boldsymbol{r}}_{\alpha\beta}$ are the orientations of particles, α and β, with respect to their separation vector, respectively (**Figure 10**).

Motivated by natural and synthetic systems to which our model is applicable, we assume that the particles are in an over-damped viscous environment, and the inertia of the ABPs can be ignored. We can then write the equations of motion governing the translation and rotation, respectively, of particle α as,

$$\frac{d\mathbf{r}_\alpha}{dt} = v_0\hat{\mathbf{n}}_\alpha - \mu_T\sum_\beta \frac{\partial W^{\alpha\beta}}{\partial \mathbf{r}_\alpha} + \sqrt{2D_{\text{T}}}\ \boldsymbol{\eta}_{\text{T},\alpha}(t) \tag{6}$$

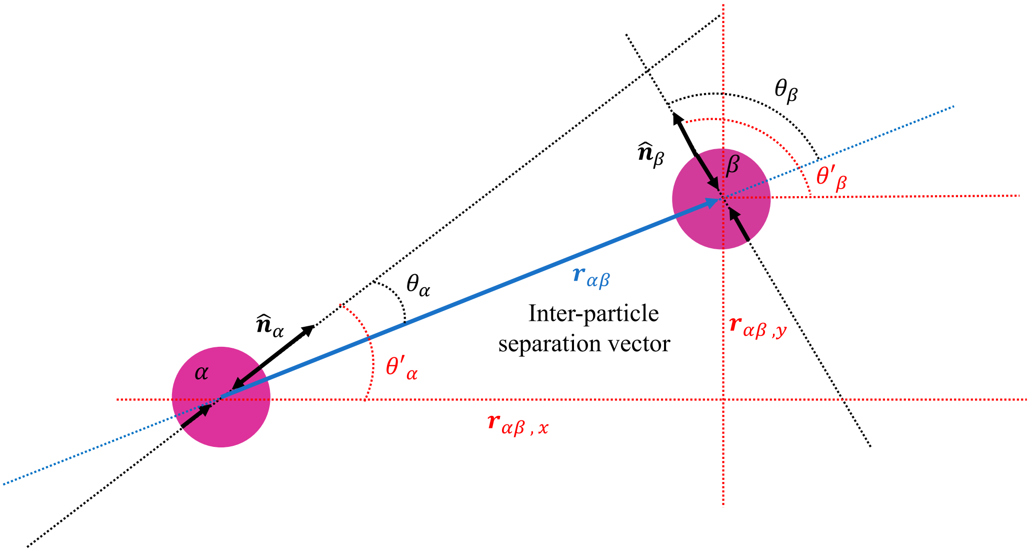

FIGURE 10 | Schematic of two interacting particles with all relevant angles and vectors labeled. $\hat{\mathbf{n}}_i$ are unit vectors of force dipoles. θ'_i are angles of force dipoles with respect to the lab frame x-axis. θ_α and θ_β are angles of force dipoles with respect to their separation vector $\mathbf{r}_{\alpha\beta}$ which has components $\mathbf{r}_{\alpha\beta,x}$ and $\mathbf{r}_{\alpha\beta,y}$.

and

$$\frac{d\hat{\mathbf{n}}_\alpha}{dt} = -\mu_R \sum_\beta \hat{\mathbf{n}}_\alpha \times \frac{\partial W^{\alpha\beta}}{\partial \hat{\mathbf{n}}_\alpha} + \sqrt{2D_R}\ \boldsymbol{\eta}_{R,\alpha}(t), \tag{7}$$

where $\mathbf{r}_\alpha$ and $\hat{\mathbf{n}}_\alpha$ are the position and orientation of particle α, respectively. In the equations above D_T and D_R are the translational and rotational diffusivity quantifying the random motion of a single particle, respectively. The viscous environment results in the translational and rotational mobilities, μ_T and μ_R respectively. Random white noise terms $\boldsymbol{\eta_T}$ and $\boldsymbol{\eta_R}$ have components that satisfy $\langle \eta_{T,i}(t)\eta_{T,j}(t')\rangle = \delta(t - t')\delta_{ij}$ and $\langle \eta_{R,i}(t)\eta_{R,j}(t')\rangle = \delta(t - t')\delta_{ij}$. Since the fluctuation dissipation theorem is not necessarily satisfied for a nonequilibrium system, the translational and rotational diffusivity are independent of each other. However, to reduce the number of free parameters and in the interest of simplicity, we assume that $D_T = \sigma^2 D_R$ and $\mu_T = \sigma^2\mu_R$. This allows the definition of an effective temperature, $k_B T_{\text{eff}} = D_T/\mu_T$. Finally we emphasize that each particle is endowed with the same dipole strength, P, and self-propulsion velocity, v_0, both of which are constant.

We now choose the cell diameter σ, the diffusion time, σ^2/D_T, and the effective thermal energy that quantifies the strength of stochastic fluctuations, D_T/μ_T, as physically relevant length, time, and energy scales in our model. Solutions to the scaled dynamical model are then dependent on three non-dimensional numbers,

$$Pe = \frac{v_0\sigma}{D_T},\ A = \frac{\mu_T P^2}{E\sigma^3 D_T},\ k^* = \frac{\mu_T k\sigma^2}{D_T} \tag{8}$$

where Pe is the Péclet number that is a measure of the self-propulsion in terms of the diffusion of motile particles, A is an effective elastic dipole-dipole interaction parameter, and k^* is the nondimensional steric spring constant.

Nondimensional forms of the dynamical equations **Eqs 6, 7** are discretized and numerically solved using the explicit half-order Euler-Maruyama method [60]. We use a time step of $\Delta t = 10^{-4}$ for a total of $10^5 - 10^6$ timesteps corresponding to a total simulation time of $10 - 100$. Each particle was initialized with a random position and orientation in our simulation box of size $L_x = 30\sigma$ and $10\sigma \le L_y \le 30\sigma$ with periodic boundary conditions in x and confinement modeled by repulsive springs identical to those used for particle-particle steric repulsions, with a fixed spring constant, $k^* = 10^4$, placed along the top and bottom walls. In our simulations, we want particles near each other to interact *via* the elastic potential at every time step, and to ensure that the overlap of particles is minimized. Furthermore, to ensure that the particles are not subject to unphysical repulsive forces, we choose k^* such that $k^*\Delta t = 1$. We show in the **Supplementary Figure S1** that the higher order structures formed by the particles at different k^* are qualitatively similar when the timestep is appropriately rescaled. A and Pe are varied and analyzed in the Results section of the text.

5 DISCUSSION

We have shown the typical collective behavior that emerges when active particles interact with each other as dipoles, using Brownian dynamics simulations. This minimal model is inspired by collective cell motility on elastic substrates where the cell-cell interaction is mediated by their mutual deformations of the passive substrate. While some of the emergent collective structures have analogs in cell culture experiments, such as the network organization of endothelial cells [61], our model is not intended to capture any specific biological behavior. We expect the first tests of our model to happen in dilute cell culture experiments that measure both pairwise cell interactions and substrate traction forces as in Ref. [23, 24].

The passive dipolar interactions lead to the end-to-end alignment of the particles into motile chains, which can be mutually aligned into polar bands and clusters because of their active motion. Polar chains that travel in opposite directions would be sorted into bands that get out of each others' way. These basic implications of our model, while specifically demonstrated here for elastic dipoles, belong to a broader class of active particles with dipolar interactions [31, 32, 62], and may therefore also be experimentally realized in active colloids endowed with permanent or induced dipole moments [30, 63]. We note that the symmetry of the elastic dipolar interactions is modified at higher Poisson's ratio [49], which is expected to result in structures such as active rings with rotational motion. This richer behavior with elastic interactions is a direct consequence of the tensorial, as opposed to vectorial nature of the elastic dipoles, in contrast with magnetic or electric dipoles, and will be the subject of future study. We further note that the mechanical interactions between cells in elastic media is in reality expected to include effects not considered here including from the nonlinear elastic properties of the substrate and nonlinear effects arising from the cells actively maintaining mechanical homeostasis at their boundaries, such as by regulating their shape [64]. We also ignore the elastic response of the cells themselves, which can give rise to additional interactions similar to that between rigid inclusions in soft media [65].

We focused on the strong elastic interaction cases in the dilute regime, where the self-assembly and dynamics of single chains can be studied. Since the chains are stable in this regime, they resemble other active polymer systems [57], that typically arise in gliding assays of biological filaments [66] or with synthetic colloids [26]. Polar bands are also seen at a higher density of active polymers [59]. However, in our system where these chains are self-assembled by dipolar interactions, multiple chains can stick to each other at higher interaction strength, while they can also fall apart, when colliding at high motility. By showing how a pair of chains interact with each other, we show the stable higher order structures that form and contribute to the polar clusters seen at higher density. Although not investigated in detail here, it will also be interesting to explore the bending dynamics of a single active polymer [67, 68] and characterize how the bending rigidity increases with dipolar interaction strength or decreases with particle motility.

To conclude, we note that our cell mechanobiology-inspired model also realizes a new class of active matter with long-range dipolar interactions. The emergent self-organization behavior distinct from the two typically studied pathways to the clustering of active particles: motility-induced phase separation [12], and Vicsek-style models [69]. In the latter, particle alignment is imposed in an agent-based manner, whereas here alignment emerges as a natural consequence of physical interactions.

DATA AVAILABILITY STATEMENT

The raw data supporting the conclusions of this article will be made available by the authors, without undue reservation.

AUTHOR CONTRIBUTIONS

ArG, AjG, and KD conceived the study and the models. SB and PN performed the numeric simulations and analyses. All authors wrote the manuscript.

FUNDING

PN was supported by a graduate fellowship funding from the National Science Foundation: NSF-CREST: Center for Cellular and Biomolecular Machines (CCBM) at the University of California, Merced: NSF-HRD-1547848. ArG acknowledges funding from the National Science Foundation *via* the CAREER award NSF-CBET-2047210. AjG would like to acknowledge support from the National Science Foundation (NSF-DMS-1616926), NSF-CREST: Center for Cellular and Biomolecular Machines at UC Merced (NSF-HRD-1547848) and the NSF Center for Engineering Mechanobiology grant (CMMI-154857).

ACKNOWLEDGMENTS

PN and SB acknowledge computing time on the Multi-Environment Computer for Exploration and Discovery (MERCED) cluster at UC Merced (NSF-ACI-1429783). SB and PN acknowledge useful discussions with Farnaz Golnaraghi and Jimmy Gonzalez Nunez.

SUPPLEMENTARY MATERIAL

The Supplementary Material for this article can be found online at: https://www.frontiersin.org/articles/10.3389/fphy.2022.876126/full#supplementary-material

REFERENCES

1. Marchetti MC, Joanny JF, Ramaswamy S, Liverpool TB, Prost J, Rao M, et al. Hydrodynamics of Soft Active Matter. *Rev Mod Phys* (2013) 85:1143–89. doi:10.1103/RevModPhys.85.1143
2. Gompper G, Winkler RG, Speck T, Solon A, Nardini C, Peruani F, et al. The 2020 Motile Active Matter Roadmap. *J Phys Condensed Matter* (2020) 32: 193001. doi:10.1088/1361-648x/ab6348
3. Bechinger C, Di Leonardo R, Löwen H, Reichhardt C, Volpe G, Volpe G. Active Particles in Complex and Crowded Environments. *Rev Mod Phys* (2016) 88:045006. doi:10.1103/revmodphys.88.045006

4. Copenhagen K, Malet-Engra G, Yu W, Scita G, Gov N, Gopinathan A. Frustration-Induced Phases in Migrating Cell Clusters. *Sci Adv* (2018) 4: eaar8483. doi:10.1126/sciadv.aar8483
5. Ladoux B, Mège R-M. Mechanobiology of Collective Cell Behaviours. *Nat Rev Mol Cel Biol* (2017) 18:743–57. doi:10.1038/nrm.2017.98
6. Alert R, Trepat X. Physical Models of Collective Cell Migration. *Annu Rev Condens Matter Phys* (2020) 11:77–101. doi:10.1146/annurev-conmatphys-031218-013516
7. Angelini TE, Hannezo E, Trepat X, Fredberg JJ, Weitz DA. Cell Migration Driven by Cooperative Substrate Deformation Patterns. *Phys Rev Lett* (2010) 104:168104. doi:10.1103/PhysRevLett.104.168104
8. Reinhart-King CA, Dembo M, Hammer DA. Cell-Cell Mechanical Communication through Compliant Substrates. *Biophysical J* (2008) 95: 6044–51. doi:10.1529/biophysj.107.127662
9. Schwarz US, Safran SA. Physics of Adherent Cells. *Rev Mod Phys* (2013) 85: 1327–81. doi:10.1103/revmodphys.85.1327
10. Henkes S, Kostanjevec K, Collinson JM, Sknepnek R, Bertin E. Dense Active Matter Model of Motion Patterns in Confluent Cell Monolayers. *Nat Commun* (2020) 11:1405. doi:10.1038/s41467-020-15164-5
11. Chaté H, Ginelli F, Grégoire G, Peruani F, Raynaud F. Modeling Collective Motion: Variations on the Vicsek Model. *Eur Phys J B* (2008) 64:451–6. doi:10.1140/epjb/e2008-00275-9
12. Cates ME, Tailleur J. Motility-Induced Phase Separation. *Annu Rev Condens Matter Phys* (2015) 6:219–44. doi:10.1146/annurev-conmatphys-031214-014710
13. Digregorio P, Levis D, Suma A, Cugliandolo LF, Gonnella G, Pagonabarraga I. Full Phase Diagram of Active Brownian Disks: From Melting to Motility-Induced Phase Separation. *Phys Rev Lett* (2018) 121:098003. doi:10.1103/PhysRevLett.121.098003
14. Balaban NQ, Schwarz US, Riveline D, Goichberg P, Tzur G, Sabanay I, et al. Force and Focal Adhesion Assembly: A Close Relationship Studied Using Elastic Micropatterned Substrates. *Nat Cel Biol* (2001) 3:466–72. doi:10.1038/35074532
15. Mandal K, Wang I, Vitiello E, Orellana LAC, Balland M. Cell Dipole Behaviour Revealed by Ecm Sub-Cellular Geometry. *Nat Commun* (2014) 5:5749. doi:10.1038/ncomms6749
16. Pelham RJ, Wang Y-L. Cell Locomotion and Focal Adhesions are Regulated by Substrate Flexibility. *Proc Natl Acad Sci U.S.A* (1997) 94:13661–5. doi:10.1073/pnas.94.25.13661
17. Dembo M, Wang Y-L. Stresses at the Cell-To-Substrate Interface during Locomotion of Fibroblasts. *Biophysical J* (1999) 76:2307–16. doi:10.1016/S0006-3495(99)77386-8
18. van Oers RFM, Rens EG, LaValley DJ, Reinhart-King CA, Merks RMH. Mechanical Cell-Matrix Feedback Explains Pairwise and Collective Endothelial Cell Behavior *In Vitro*. *PLoS Comput Biol* (2014) 10:e1003774. doi:10.1371/journal.pcbi.1003774
19. Tang X, Bajaj P, Bashir R, Saif TA. How Far Cardiac Cells Can See Each Other Mechanically. *Soft Matter* (2011) 7:6151–8. doi:10.1039/C0SM01453B
20. Dasbiswas K, Majkut S, Discher DE, Safran SA. Substrate Stiffness-Modulated Registry Phase Correlations in Cardiomyocytes Map Structural Order to Coherent Beating. *Nat Commun* (2015) 6:6085. doi:10.1038/ncomms7085
21. Nitsan I, Drori S, Lewis YE, Cohen S, Tzlil S. Mechanical Communication in Cardiac Cell Synchronized Beating. *Nat Phys* (2016) 12:472–7. doi:10.1038/nphys3619
22. Cohen O, Safran SA. Elastic Interactions Synchronize Beating in Cardiomyocytes. *Soft matter* (2016) 12:6088–95. doi:10.1039/c6sm00351f
23. Reinhart-King CA, Dembo M, Hammer DA. Endothelial Cell Traction Forces on Rgd-Derivatized Polyacrylamide Substrata. *Langmuir* (2003) 19:1573–9. doi:10.1021/la026142j
24. Palmieri B, Scanlon C, Worroll D, III, Grant M, Lee J. Substrate Mediated Interaction between Pairs of Keratocytes: Multipole Traction Force Models Describe Their Migratory Behavior. *PLoS One* (2019) 14:e0212162. doi:10.1371/journal.pone.0212162
25. Gennes PG, Pincus PA. Pair Correlations in a Ferromagnetic Colloid. *Phys Kondens Materie* (1970) 11:189–98. doi:10.1007/BF02422637
26. Nishiguchi D, Iwasawa J, Jiang H-R, Sano M. Flagellar Dynamics of Chains of Active Janus Particles Fueled by an AC Electric Field. *New J Phys* (2018) 20: 015002. doi:10.1088/1367-2630/aa9b48
27. Ilg P, Del Gado E. Non-Linear Response of Dipolar Colloidal Gels to External Fields. *Soft Matter* (2011) 7:163–71. doi:10.1039/C0SM00592D
28. Tlusty T, Safran SA. Defect-Induced Phase Separation in Dipolar Fluids. *Science* (2000) 290:1328–31. doi:10.1126/science.290.5495.1328
29. Rovigatti L, Russo J, Sciortino F. No Evidence of Gas-Liquid Coexistence in Dipolar Hard Spheres. *Phys Rev Lett* (2011) 107:237801. doi:10.1103/physrevlett.107.237801
30. Sakaï N, Royall CP. Active Dipolar Colloids in Three Dimensions: Strings, Sheets, Labyrinthine Textures and Crystals. arXiv preprint arXiv:2010.03925 (2020).
31. Kaiser A, Popowa K, Löwen H. Active Dipole Clusters: From Helical Motion to Fission. *Phys Rev E* (2015) 92:012301. doi:10.1103/PhysRevE.92.012301
32. Liao G-J, Hall CK, Klapp SHL. Dynamical Self-Assembly of Dipolar Active Brownian Particles in Two Dimensions. *Soft Matter* (2020) 16:2208–23. doi:10.1039/c9sm01539f
33. Guzmán-Lastra F, Kaiser A, Löwen H. Fission and Fusion Scenarios for Magnetic Microswimmer Clusters. *Nat Commun* (2016) 7:13519. doi:10.1038/ncomms13519
34. Telezki V, Klumpp S. Simulations of Structure Formation by Confined Dipolar Active Particles. *Soft Matter* (2020) 16:10537–47. doi:10.1039/D0SM00926A
35. Fatehiboroujeni S, Gopinath A, Goyal S. Nonlinear Oscillations Induced by Follower Forces in Prestressed Clamped Rods Subjected to Drag. *J Comput Nonlinear Dyn* (2018) 13:121005. doi:10.1115/1.4041681
36. Sangani AS, Gopinath A. Elastohydrodynamical Instabilities of Active Filaments, Arrays, and Carpets Analyzed Using Slender-Body Theory. *Phys Rev Fluids* (2020) 5:083101. doi:10.1103/physrevfluids.5.083101
37. Fily Y, Subramanian P, Schneider TM, Chelakkot R, Gopinath A. Buckling Instabilities and Spatio-Temporal Dynamics of Active Elastic Filaments. *J R Soc Interf* (2020) 17:20190794. doi:10.1098/rsif.2019.0794
38. Chelakkot R, Hagan MF, Gopinath A. Synchronized Oscillations, Traveling Waves, and Jammed Clusters Induced by Steric Interactions in Active Filament Arrays. *Soft Matter* (2021) 17:1091–104. doi:10.1039/d0sm01162b
39. Schwarz US, Safran SA. Elastic Interactions of Cells. *Phys Rev Lett* (2002) 88: 048102. doi:10.1103/PhysRevLett.88.048102
40. Yan J, Han M, Zhang J, Xu C, Luijten E, Granick S. Reconfiguring Active Particles by Electrostatic Imbalance. *Nat Mater* (2016) 15:1095–9. doi:10.1038/nmat4696
41. Romanczuk P, Bär M, Ebeling W, Lindner B, Schimansky-Geier L. Active Brownian Particles. *Eur Phys J Spec Top* (2012) 202:1–162. doi:10.1140/epjst/e2012-01529-y
42. Marchetti MC, Fily Y, Henkes S, Patch A, Yllanes D. Minimal Model of Active Colloids Highlights the Role of Mechanical Interactions in Controlling the Emergent Behavior of Active Matter. *Curr Opin Colloid Interf Sci* (2016) 21: 34–43. doi:10.1016/j.cocis.2016.01.003
43. Bose S, Dasbiswas K, Gopinath A. Matrix Stiffness Modulates Mechanical Interactions and Promotes Contact between Motile Cells. *Biomedicines* (2021) 9:428. doi:10.3390/biomedicines9040428
44. Boal D. *Mechanics of the Cell*. 2 edn.. Cambridge: Cambridge University Press (2012). doi:10.1017/CBO9781139022217
45. Landau LD, Lifshitz EM. *Theory of Elasticity, Course of Theoretical Physics*, 7. London: Pergamon Press (1959).
46. Bischofs IB, Safran SA, Schwarz US. Elastic Interactions of Active Cells with Soft Materials. *Phys Rev E Stat Nonlin Soft Matter Phys* (2004) 69:021911. doi:10.1103/PhysRevE.69.021911
47. Wagner H, Horner H. Elastic Interaction and the Phase Transition in Coherent Metal-Hydrogen Systems. *Adv Phys* (1974) 23:587–637. doi:10.1080/00018737400101401
48. Zabel H, Peisl H. Sample-Shape-Dependent Phase Transition of Hydrogen in Niobium. *Phys Rev Lett* (1979) 42:511–4. doi:10.1103/physrevlett.42.511
49. Bischofs IB, Schwarz US. Cell Organization in Soft media Due to Active Mechanosensing. *Proc Natl Acad Sci U.S.A* (2003) 100:9274–9. doi:10.1073/pnas.1233544100
50. Bischofs I, Schwarz U. Collective Effects in Cellular Structure Formation Mediated by Compliant Environments: A Monte Carlo Study. *Acta Biomater* (2006) 2:253–65. doi:10.1016/j.actbio.2006.01.002
51. Marel A-K, Zorn M, Klingner C, Wedlich-Söldner R, Frey E, Rädler JO. Flow and Diffusion in Channel-Guided Cell Migration. *Biophysical J* (2014) 107: 1054–64. doi:10.1016/j.bpj.2014.07.017

52. Ezhilan B, Alonso-Matilla R, Saintillan D. On the Distribution and Swim Pressure of Run-And-Tumble Particles in Confinement. *J Fluid Mech* (2015) 781, R4. doi:10.1017/jfm.2015.520
53. Elgeti J, Gompper G. Run-And-Tumble Dynamics of Self-Propelled Particles in Confinement. *EPL (Europhysics Letters)* (2015) 109:58003. doi:10.1209/0295-5075/109/58003
54. Yan W, Brady JF. The Force on a Boundary in Active Matter. *J Fluid Mech* (2015) 785, R1. doi:10.1017/jfm.2015.621
55. Wagner CG, Hagan MF, Baskaran A. Steady-State Distributions of Ideal Active Brownian Particles under Confinement and Forcing. *J Stat Mech* (2017) 2017: 043203. doi:10.1088/1742-5468/aa60a8
56. Poncet A, Bénichou O, Démery V, Nishiguchi D. Pair Correlation of Dilute Active Brownian Particles: From Low-Activity Dipolar Correction to High-Activity Algebraic Depletion Wings. *Phys Rev E* (2021) 103, 012605. doi:10.1103/physreve.103.012605
57. Winkler RG, Gompper G. The Physics of Active Polymers and Filaments. *J Chem Phys* (2020) 153:040901. doi:10.1063/5.0011466
58. Volpe G, Gigan S, Volpe G. Simulation of the Active Brownian Motion of a Microswimmer. *Am J Phys* (2014) 82:659–64. doi:10.1119/1.4870398
59. Vliegenthart GA, Ravichandran A, Ripoll M, Auth T, Gompper G. Filamentous Active Matter: Band Formation, Bending, Buckling, and Defects. *Sci Adv* (2020) 6:eaaw9975. doi:10.1126/sciadv.aaw9975
60. Allen MP, Tildesley DJ. *Computer Simulation of Liquids*. Oxford: Oxford University Press (2017).
61. Califano JP, Reinhart-King CA. A Balance of Substrate Mechanics and Matrix Chemistry Regulates Endothelial Cell Network Assembly. *Cel Mol Bioeng* (2008) 1:122–32. doi:10.1007/s12195-008-0022-x
62. Vutukuri HR, Lisicki M, Lauga E, Vermant J. Light-Switchable Propulsion of Active Particles with Reversible Interactions. *Nat Commun* (2020) 11:2628. doi:10.1038/s41467-020-15764-1
63. Vutukuri HR, Bet B, Van Roij R, Dijkstra M, Huck WTS. Rational Design and Dynamics of Self-Propelled Colloidal Bead Chains: from Rotators to Flagella. *Sci Rep* (2017) 7:16758. doi:10.1038/s41598-017-16731-5
64. Golkov R, Shokef Y. Shape Regulation Generates Elastic Interaction between Living Cells. *New J Phys* (2017) 19:063011. doi:10.1088/1367-2630/aa70ef
65. Puljiz M, Huang S, Auernhammer GK, Menzel AM. Forces on Rigid Inclusions in Elastic Media and Resulting Matrix-Mediated Interactions. *Phys Rev Lett* (2016) 117:238003. doi:10.1103/PhysRevLett.117.238003
66. Phillips R, Kondev J, Theriot J. *Physical Biology of the Cell*. New York: Garland Science, Taylor & Francis Group (2008).
67. Eisenstecken T, Gompper G, Winkler R. Conformational Properties of Active Semiflexible Polymers. *Polymers* (2016) 8:304. doi:10.3390/polym8080304
68. Liao X, Purohit PK, Gopinath A. Extensions of the Worm-Like-Chain Model to Tethered Active Filaments under Tension. *J Chem Phys* (2020) 153:194901. doi:10.1063/5.0025200
69. Vicsek T, Czirók A, Ben-Jacob E, Cohen I, Shochet O. Novel Type of Phase Transition in a System of Self-Driven Particles. *Phys Rev Lett* (1995) 75:1226–9. doi:10.1103/physrevlett.75.1226

Conflict of Interest: The authors declare that the research was conducted in the absence of any commercial or financial relationships that could be construed as a potential conflict of interest.

ORIGINAL RESEARCH
published: 03 May 2022
doi: 10.3389/fphy.2022.890865

GTPase-Dependent Mechanointegration of Shear-Mediated Cell Contractility Through Dynamic Binding of FLNa and FilGAP

L. P. Bergeron-Sandoval[1], *Alex Cai*[1,2], *Anna Clouvel*[1], *Cynthia Hitti*[1] *and Allen Ehrlicher*[1,2,3,4,5]*

[1]*Department of Bioengineering, McGill University, Montreal, Canada,* [2]*Department of Anatomy and Cell Biology, McGill University, Montreal, Canada,* [3]*Rosalind and Morris Goodman Cancer Research Institute, McGill University, Montreal, Canada,* [4]*Department of Biomedical Engineering, McGill University, Montreal, Canada,* [5]*Department of Mechanical Engineering, McGill University, Montreal, Canada*

Edited by:
Liheng Cai,
University of Virginia, United States

Reviewed by:
Yinan Shen,
Harvard University, United States
Jing Xia,
Princeton University, United States

***Correspondence:**
Allen Ehrlicher
allen.ehrlicher@mcgill.ca

Specialty section:
This article was submitted to Biophysics, a section of the journal Frontiers in Physics

Received: 06 March 2022
Accepted: 04 April 2022
Published: 03 May 2022

Citation:
Bergeron-Sandoval LP, Cai A, Clouvel A, Hitti C and Ehrlicher A (2022) GTPase-Dependent Mechanointegration of Shear-Mediated Cell Contractility Through Dynamic Binding of FLNa and FilGAP. Front. Phys. 10:890865. doi: 10.3389/fphy.2022.890865

Cellular mechanotransduction is a common mechanism by which cells convert mechanical cues (or stimuli) from their environment into biochemical and cellular responses. In the case of shearing forces, such as when individual cells encounter interstitial shear stress and blood shear stress, mechanotransduction involves mechanical stretching and spatial reconfiguration of Filamin A (FLNa) binding sites and subsequent release of FilGAP molecules normally bound to FLNa. However, the connection and importance of downstream molecular effectors and cellular metrics involved in response to shear stress are not understood. Here we reveal mechano-sensitive GTPase-mediated changes in cell contractility. By varying expression of FilGAP, and expression of FLNa, we show that microfluidic shear stress results in cell contractile changes only when FilGAP and FLNa dynamically bind and dissociate. By using FRET sensors that quantify the Rho or Rac charge state, we demonstrate that only cells with dynamic FLNa and FilGAP convert shear stress into GTPase activity, and the resulting downstream contractile changes. Finally, we show that manipulation of Rho and Rac through pharmacological means rescues the contractile activity, in the absence of intact FLNa-FilGAP mechanosensing. This research clarifies a precise mechanomolecular pathway used for cellular force sensing and may play critical roles in human health challenges from cancer metastasis to cardiovascular disease.

Keywords: mechanointegration, mechanotransduction, mechanocomplexes, shear stress, filamin A, FilGAP, GTPases

INTRODUCTION

Cells *in vivo* are subjected to diverse shear stresses depending on their anatomical location [1]. In the vascular system, shear stress on the order of 1Pa caused by blood and lymph flow has been shown to regulate vasodilation and blood pressure, modulate the development and adaptation of vascular beds, and contribute to the remodeling of blood vessels [2–4]. A majority of cells are also exposed to interstitial fluid flow up to 0.1 Pa due to plasma that leaks out of capillaries to drain into the lymphatic system [1]. Shear stress has been shown to cause cytoskeletal filament reorganization and stiffening of the cytoskeleton [3]. The ability of cells to actively respond to these mechanical forces is essential for cell homeostasis and fitness, with aberrant behavior contributing to pathology. For example, mechanical sensors and their downstream signaling factors are implicated in the regulation of cardiac contractile dysfunction and diastolic heart disease [5]. Shear stress in particular has also been shown to promote migration of breast cancer cells [1].

While mechanosensing has clear roles in physiology and pathology, the precise sensing mechanisms at the cellular level that regulate responses have remained unclear. In general, physical forces deform diverse intracellular structures, converting these mechanical stimuli into biochemical signals through a process broadly known as mechanotransduction [6]. The ability of cells to continuously detect and actively respond to these mechanical forces is mediated by an emerging group of specialized molecules called mechanosensors [7, 8].

In addition to specific structures such as stretch activated channels, the cytoskeleton itself is ideally poised to be a mechanosensor, as it is the principal generator of cellular forces, and the mechanical conductor of stress and strain [9]. One molecular mechanotransduction mechanism for shear stress involves the actin-binding protein Filamin A (FLNa). FLNa is a homodimer protein that plays important roles in cell structure and mechanosensation. FLNa is made up of an actin binding domain (ABD) and 24 repeat immunoglobulin-like domains (IGD). It can be classified into three sections, rod 1 (IGD 1–15), rod 2 (IGD 15–23), and a dimerization domain in IGD24 [10]. *Via* its ABD, FLNa crosslinks and anchors actin filaments to stabilize the plasma membrane, provide cellular cortical rigidity, and contribute to the mechanical stability of the cell [10]. FLNa also directs the formation of dynamic actin stress fibers to contribute to the shape and movement of the cell [11, 12]. Beyond its role in regulating cell structure, FLNa also forms diverse interactions with other proteins to serve as a versatile signaling scaffold. As such, FLNa may integrate external physical forces such as shear to elicit specific cellular responses. Prior work has shown that FLNa is recruited to the cell cortex in response to shear stress exposure [1]. The properties of the F-actin network are also dependent on the concentrations of FLNa [8, 13]. In response to shear force, it has been observed that F-actin networks soften at low FLNa concentrations and strain-harden at high FLNa concentrations [13]. FLNa has also been shown to play a role in tumorigenesis: in cancer cells, researchers have observed abnormal expression and subcellular localization of FLNa, suggesting it influences cytoskeleton rearrangement, migration, proliferation, and signal transduction in tumor cells [11]. For example, Filamin A-deficient human melanoma M2 cells have adhesion, motility and migration related defects and are softer than other melanoma cell lines that express FLNa [14–16]. Critically, M2 cells are insensitive to mechanical stimuli, strongly implicating FLNa as an essential mechanosensor, however, the details of this interaction have remained unclear.

Shear stress subjects the intracellular actin network to strain and deformations at the molecular level of actin associated proteins, including FLNa. It is hypothesized that as forces deform the actin cytoskeleton, FLNa's rod2 domain undergoes conformational changes to expose cryptic binding sites for signaling proteins. This changes FLNa's binding affinity for other proteins to regulate many cellular functions including motility, maintenance of cell shape, and differentiation [10]. Filamin's mechanism of mechanotransduction regulation may be linked to the more than 100 unique binding partners including integrins, kinases, and GTPases [12, 17]. One specific GTPase activating protein (GAP), FilGAP, appears to play a key role in mediating FLNa's ability to respond to shear stress.

Like other GTPases, Rac and Rho are regulated by GEFs and GAPs, which directly modulate the charge state of Rac and Rho [18–20]. FilGAP is a GAP that binds FLNa [21]. Nakamura and collaborators [22] have previously identified the binding sites that facilitate the FLNa-FilGAP interaction. Using biochemical assays, they identified that residues 723–726 in the coiled coil domain of FilGAP bind to the 23rd immunoglobulin like domain of FLNa (IGD23). Inducing a point mutation (M2474E) into IGD23 of FLNa is sufficient to abolish the FilGAP-FLNa interaction, thus FLNa M2474E does not form complexes with FilGAP. The conformation of FLNa's rod2 domain also modulates the FLNa-FilGAP interaction. Upon force generation, the rod2 domain of FLNa is deformed, reducing FLNa's binding affinity for FilGAP, and allowing the recruitment of FilGAP to the sites of membrane protrusion and force transfer where it interacts with Rac [12, 23]. At these sites, FilGAP antagonizes Rac activity to inhibit cell spreading and lamellae formation, and disruptions in the FLNa-FilGAP interaction can lead to increased force-induced apoptosis [13]. This suggests that the force-induced recruitment of FLNa and FilGAP to the cell periphery contributes to mechanoprotection [12, 24]. Several key studies from McCulloch have identified the mechanoprotective nature of FilGAP and FLNa in force mediated apoptosis, demonstrating broad importance of this mechanotransduction interaction [24–26].

FilGAP has also been shown to regulate tumor progression in glioblastoma, astrocytoma, carcinoma, and breast cancers [21, 27–29]. FilGAP promotes the mesenchymal to amoeboid transition in tumorigenesis and regulates the front-rear polarity of migrating tumor cells [28, 29]. FilGAP is thus poised to be an effective mechanosensor by regulating the relative levels of Rho and Rac activity. FilGAP directly deactivates Rac as a GAP which indirectly leads to Rho activation [21, 29, 30].

While novel upstream mechanosensors are being discovered in diverse contexts, the downstream balance of Rac and Rho activities appears to be a commonly employed biochemical switch that changes cytoskeletal activity, and in turn determines cell morphology and behavior [20]. Rac and Rho belong to the family of GTPases that regulate numerous cellular processes including actin polymerization and cell signalling [31]. The spatiotemporal coordination of Rac and Rho activity mediates cellular migration by directing the formation and organization of actin filaments. In studies using GTPase biosensors, Rho activation was observed at the leading edge of migrating cells whereas Rac activation occurred afterwards and further away from the edge, suggesting that Rho may initiate membrane protrusion whereas Rac could promote the reinforcement and stabilization of newly formed protrusions [32]. In contradiction, another study using GTPase biosensors found that in neutrophils Rho is absent from protrusions [33].

Rac and Rho signaling also regulate the cell cycle by promoting progression through the G1 checkpoint and the formation of the mitotic spindle [31]. As Rho and Rac regulate cellular migration and proliferation, the dysregulation of their signaling may promote tumorigenesis and metastasis [34]. Although FilGAP's biochemical properties and role in cancer pathogenesis have been examined, the acute responses of FilGAP activity on biophysical activity of the cell, such as contractility under mechanical stimuli, have remained unclear. Specifically, the environmental factors that modulate cellular responses to shear stress and the characterization of Rho and Rac GTPase in contractile response to shear stress have yet to be examined. Resolving the contractile response to mechanical stimuli would thus offer a closed loop understanding of how cells physically react to changes in their environment and tune their behavior accordingly.

Here we used traction force microscopy (TFM) and Förster resonance energy transfer (FRET) to reveal that FLNa expression and dynamic FLNa-FilGAP interaction are essential for cellular response to shear stress. Using FLNa deficient cells, FLNa M2474E mutants (lacking the FilGAP binding domain), and siRNA FilGAP gene knockdown, we show that dynamic FLNa-FilGAP interactions are required to detect shear, and regulate the spatiotemporal modulation of GTPase activity, which in turn induces changes in cell contractility. By confining cells to fibronectin micropatterns, we modulated the effective shear impinging on cells, and demonstrated that cell profile and cell orientation to flow determine the timing of the cellular response. Lastly, we demonstrate the Rho pathway conservation by rescuing cell contractility through pharmacological Rho activation in cells with inhibited FLNa-FilGAP interactions. Our results cumulatively suggest that the amount of cell strain modulates the amount of FilGAP released by FLNa into the cytosol. This unbound FilGAP regulates the activity levels of RhoGTPases, and the resulting contractile response, with diverse physiological and pathological consequences.

RESULTS

We fabricated laminar flow microfluidic shear in combination with a deformable compliant lower cell substrate, allowing us to apply precisely controlled shear stress, while quantifying cell contractility using Traction Force Microscopy [35], and GTPase activity with quantitative FRET (see methods). Using this microfluidic device (**Suppplementary Figure S1A**), we imposed a 5 min flow of shear stress onto cells. We observed that FLNa expressing A7 cells display a reversible increase in contractile work (strain energy) in response to shear (**Figure 1B**). A characteristic time delay is observed for this contractile response, and cell strain energy comes back to original levels after the peak response. In FLNa-deficient M2 cells, no contractile response to shear stress is observed (**Figure 1B**).

Dynamic FLNa-FilGAP Interaction is Required for Shear Mechanosensing

To understand FLNa-dependent mechanosensing, we explored the physical and molecular underpinnings of this response within a population of Filamin A-complemented melanoma cells. We first explored the importance of the FLNa-FilGAP interaction in the cell response to shear force and assessed the impact of FLNa expression levels on shear mechanotransduction. While FLNa-deficient M2 cells displayed no mechanostimulation, transient FLNa complementation in M2 cells showed a partial recovery by demonstrating cell contractile work under shear (**Figure 1C** and **Supplementary Figure S2**). We next introduced a FLNa variant (M2474E mutation) into the M2 cells (**Supplementary Figure S2**) which has been shown to functionally crosslink actin and interact with other FLNa binding partners but lacks the binding site for FilGAP on Ig repeat 23 [22]. We observed that M2474E M2 cells are unresponsive to the applied shear stress compared to the FLNa rescue (**Figure 1C**), suggesting that FLNa's binding with FilGAP is essential for mechanotransduction. To examine if this disruption is only sensitive to changes in FLNa, we then suppressed FilGAP expression using siRNA in A7 cells (**Supplementary Figure S2**), which stably express FLNa. Cells expressing WT FLNa with downregulated FilGAP were unresponsive to external shear stress similar to cells which do not express FLNa (**Figures 1C,D**). Together these results demonstrate that both FLNa and FilGAP expression are necessary but not sufficient for mechanosensing, and that dynamic binary binding interactions are required for mechanosensing of shear stress.

Cell Contractile Response is Modulated by Cell Prestress and Shear Flow Magnitude

On the basis that cell mechanoresponse also depends on environmental factors, we next set out to determine how shear stress magnitude and substrate stiffness influence contractile response. We exposed single cells to a range of shear stress from 0.5 to 1.5 Pa; as before, no response in FLNa deficient M2 cells was observed, however, in the FLNa expressing A7 cell we observed an increase in contractile work as a function of applied shear stress (**Figures 2A,B**). To determine whether substrate material properties can impact the timing of cell response to shear, we first measured cell strain energy in response to a burst of shear in A7 cells in the main text KPa is used, in the **Figure 2C** kPa grown on PDMS substrates with a stiffness of either 10 KPa or 25 KPa. We observed that on average, cells grown on a stiffer substrate have a higher pre-shear strain energy and see a linear relationship between the prestress in the cell and the peak contractile strain energy after application of shear stress (**Figure 2C**). Since stiffer cells will deform less under an applied shear, our data suggests that cell strain is a more determinant factor than physical stress (i.e., force per area) in the cell contractile response.

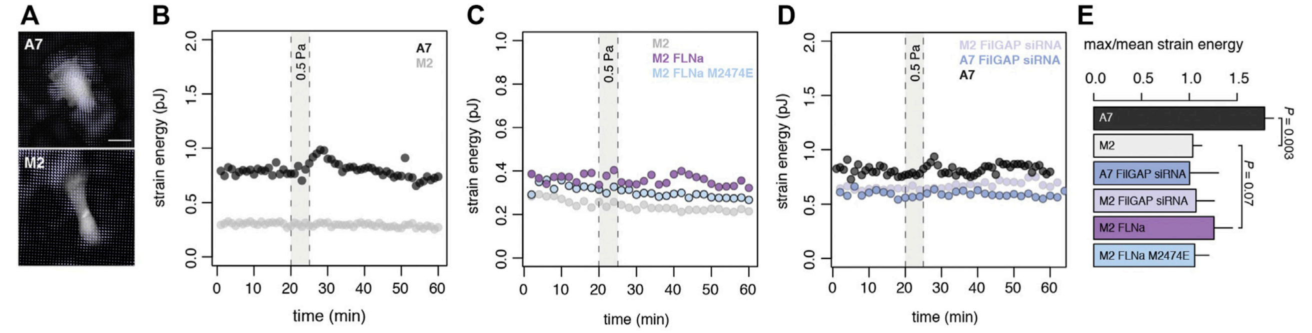

FIGURE 1 | FLNa-FilGAP interaction is necessary for mechanosensing shear **(A)** Traction stress map of A7 cells (top panel) and FLNa-null M2 cells (bottom panel) in absence of shear on time 0. Scale bar, 25 μm **(B)** Representative time series of strain energy in A7 cell (black) and M2 cell (grey). Under shear stress (5 min at 0.5 Pa) A7 cells undergo a reversible traction increase while FLNa-null M2s cell do not respond. See Panel E **(C)** Representative time series of strain energy in M2 cell (light grey) or M2 cell complemented with either mEmerald-FLNa (purple) or mEmerald-FLNa M2474E (light blue). Rescue of the contractile work is observed only in M2 mEmerald-FLNa cells when exposed to shear stress (5 min at 0.5 Pa) **(D)** Representative time series of strain energy in M2 FilGAP siRNA cell (light purple) or A7 cell (black) or A7 FilGAP siRNA cell (blue). Contractile work of A7 cells under shear is abrogated with loss of FilGAP **(E)** Maximum strain energy divided by mean strain energy for cell lines in B-D (A7 *n* = 10 cells; M2 *n* = 10 cells; A7 FilGAP siRNA *n* = 3 cells; M2 FilGAP siRNA *n* = 3 cells; M2 FLNa *n* = 3 cells; M2 FLNa M2474E *n* = 3 cells; two-sided *t*-test).

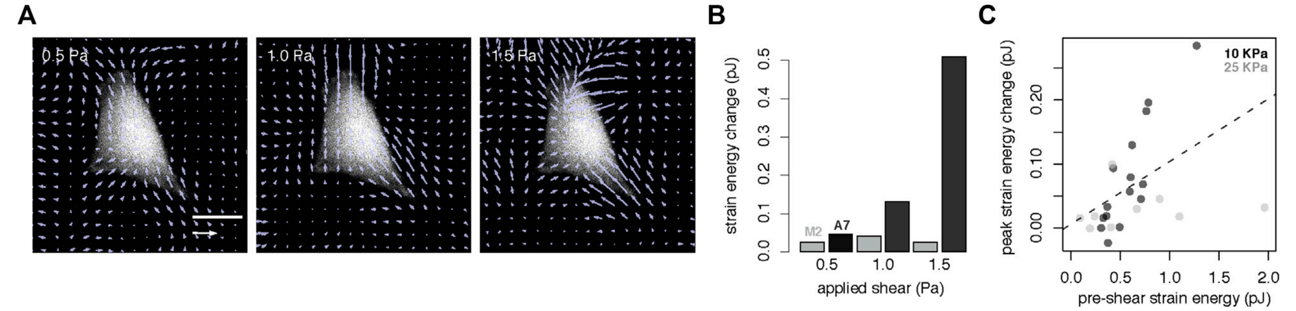

FIGURE 2 | Cell contractile response is modulated by shear flow magnitude and cell prestress **(A)** Traction stress map of example A7 cell under applied shear from 0.5 to 1.5 Pa. Scale bar, 25 μm **(B)** Change in strain energy as a function of shear for an individual A7 (black) and M2 (grey) cell **(C)** Peak strain energy change under shear (5 min at 0.5 Pa) as a function of pre-shear strain energy suggests that cells with higher prestress also display larger changes in contractility (black, 10 KPa substrate, *n* = 15 cells; grey, 25 KPa substrate, *n* = 11 cells; dashed line, linear least squares fit).

Contractile Response Timing is Driven by Total Shear Force

The challenges of imposing varied flow rates within a single device prompted us to approach the question of varied shear force using other means, and we thus considered the varied cross-sections of cells exposed to the same shear flow to determine their individual shear forces. Using substrates of low and high stiffness, we observed similar heterogeneity for A7 cells to reach peak contractile response to shear (**Figure 3A**). Time lapse traction force microscopy at the population level also reveals an unexpected heterogeneity in peak response lag of A7 cells exposed to shear stress (**Figure 3A** and **Supplementary Figure S3**), suggesting that additional factors beyond substrate stiffness and applied stress determine response delay. We used this heterogeneity to probe the cell response to shear under constant shear regimes.

Since the effective shear force is a function of cell surface exposed to flow, we next determined if cell shape and geometry influence the timing of cell response to shear in a force dependent manner. We first quantified the profile and aspect ratio of cells exposed to shear and measured the cell contractile work. We observed that cells with lower aspect ratios respond faster than cells with higher aspect ratios (**Figure 3B**). As prior work has demonstrated that increased cell spreading flattens cells [36], our result suggests that A7 cells with low aspect ratio have a round and high profile. A high profile increases the cell cross-section exposed to the shear flow, resulting in a higher effective total shear force. Cells with high aspect ratio are also generally flatter and stiffer [36], and thus would be deformed less under the same applied stress.

Another factor that may influence the amount of cell surface exposed to shear flow is cellular orientation. We also calculated the impact of the cell major axis orientation to the shear flow on the effective shear force (**Figure 3C**). Using this approach, we noticed that randomly seeded cells exposed to a higher effective shear force have a shorter response lag than cells subject to low effective shear force (**Figure 3D**). We find an inverse linear relationship between contractile response lag and magnitude of shear stress.

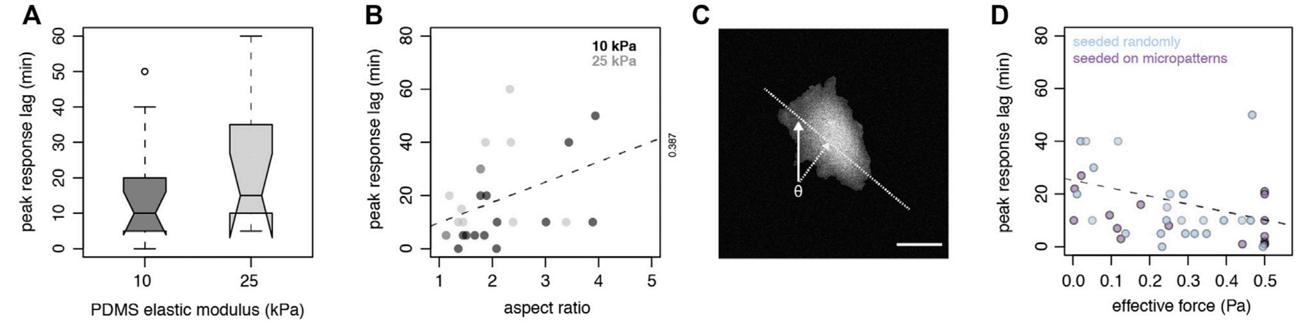

FIGURE 3 | Cell geometry, material properties and orientation to shear flow contribute to the timing of cell contractile response to shear flow **(A)** Boxplot (center line, median; box, upper and lower quartiles; whiskers, 1.5x IQR; crosses, outliers; two-sided *t*-test $p = 0.215$) of peak contractile response lag (min) to shear (5 min, 0.5 Pa) in A7 cells cultured on 10 KPa ($n = 15$ cells) or 25 KPa ($n = 11$ cells) PDMS substrates **(B)** Peak contractile response lag (min) to shear (5 min at 0.5 Pa) in randomly seeded A7 cells as a function of cell aspect ratio on 10 KPa ($n = 15$ cells) or 25 KPa ($n = 11$ cells; dashed line, linear least squares fit) **(C)** Incident angle (θ) of shear flow to cell major axis determines the *effective force* = sin(θ) *x applied shear*. Scale bar, 25 μm **(D)** Peak contractile response lag (min) to shear (5 min at 0.5 Pa) in A7 cells as a function of effective force (Pa) of randomly seeded cells on TFM substrates (blue, $n = 26$ cells) or cells seeded on micropatterned TFM substrates (purple, $n = 21$ cells; dashed line, linear least squares fit).

Strain Heterogeneity is Regulated by Prestress and Cell Orientation

To examine more closely how cell geometry and cell orientation influence the cellular response to shear, we used fibronectin-coated micropatterns on PDMS substrates to confine cells into fixed aspect ratios and orientations to shear flow, where each pattern dictates the cell spreading (**Supplementary Figure S4**). We also determined that cell height is inversely proportional to the aspect ratio determined by cell adhesion on the fibronectin micropatterns (**Supplementary Figure S4D**).

Our TFM results on micropatterns show that the contractile response delay is also inversely proportional to the effective shear determined by the cell aspect ratio and orientation to flow (**Figure 3D**). This suggests that larger cell strains initiate faster contractile responses. Our data reinforces the idea that as forces deform the actin cytoskeleton, FLNa undergoes conformational changes to expose cryptic binding sites for signaling proteins implicated in mechanotransduction. Since dynamic binary binding interactions are required for mechanosensing, our results suggest that mechanical release of FilGAP under strain is a key step in FLNa-dependent mechanotransduction.

Strain Heterogeneity Triggers GTPase Rate Heterogeneity

Based on these observations, we next quantified FLNa-dependent mechanotransduction by probing the activity of intracellular Rac or Rho sensors. FilGAP is released from its FLNa-bound state when the cell actin network is under shear strain, making FilGAP then available to interact with and inhibit Rac [21]. The reduction in Rac activity under shear could increase the activity of the Rho pathway that stimulates actomyosin contraction [37]. To test this, we complemented cell contractility measurements with intracellular FRET-based sensors that report the charge state of Rac or Rho.

We used FRET sensors that specifically detect either Rac (Raichu-Rac1), RhoA or RhoB activity throughout the cell [38, 39]. Using a custom parallel-plate shear stress device (**Supplementary Figures S1B–C**) and the RhoA2G FRET sensor [40], we observed increased RhoA activity at the cell leading edge when cells that express FLNa are exposed to shear stress, while RhoA activity in FLNa-null cells remains unaffected by shear (**Supplementary Figure S5**). Modulation of Rho activity in time after cells are exposed to shear in a microfluidic device (**Supplementary Figure S1A**) reveals a peak of activity compared to prestress or recovery levels (**Figure 4A**).

We next performed simultaneous time-lapse analysis of traction forces, pattern deformation and Rho (DORA-RhoB sensor) activity in single cells grown on micropatterns. When cells are exposed to shear stress, we measured an increase in both cell contractility and Rho activity in FLNa complemented A7 cells (**Figure 4B**). In contrast, we observed no changes in cell contractility nor DORA-RhoB sensor activity in A7 cells in the absence of shear. FLNa deficient M2 cells show no contractile response nor RhoB activation under shear regardless of cell height or orientation to flow (**Supplementary Figure S6A**).

We also see that Rho activation speed is correlated with the magnitude of Rho signal change (**Figure 4C**). This trend is more noticeable under a high shear regime and suggests that Rho activity is strain dependent. We indeed observed that the DORA-RhoB sensor YFP/CFP ratio is significantly higher in cells exposed to an applied shear of 2.5 Pa compared to 0.5 Pa (**Figure 4D**). A proportional relationship between YFP/CFP ratio and shear is observed when we converted the applied shear into effective force (**Figure 4E**) as determined by the incident angle of flow to the cell major axis and the cell aspect ratio. These results show that Rho activation is correlated with applied shear and effective shear force, and that Rho activity is modulated by strain.

GTPase-dependent Mechanointegration of Shear-Mediated Cell Contractility

We next probed the landscape of cell contractility as a function of Rho activity to better understand how the magnitude of GTPase

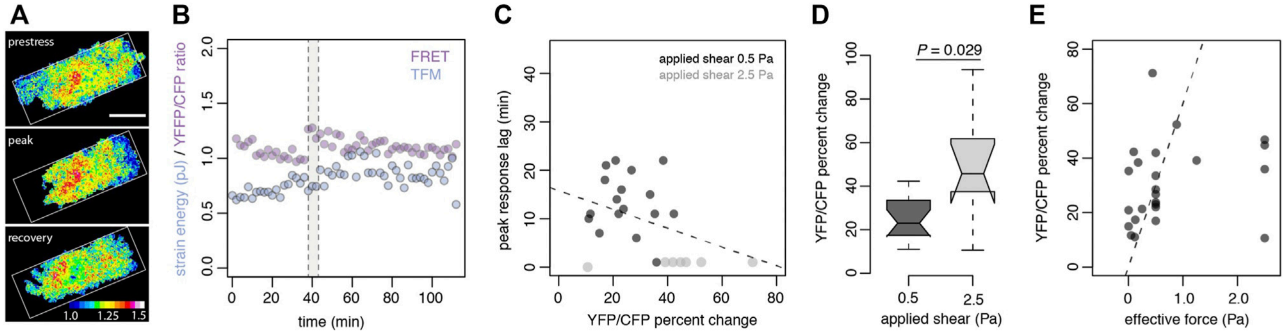

FIGURE 4 | Rho response is faster and of higher magnitude under high strain **(A)** An A7 cell stably expressing DORA-RhoB sensor on a fibronectin micropattern (white outlines; 2:1 aspect ratio rectangle, 1,000 micron^2) was exposed to shear flow to quantify prestress (top), peak (middle) and recovery (bottom) levels of DORA-RhoB activity (left panels). Scale bar, 22 μm **(B)** Representative quantification of cell contractility probed by TFM (blue) or DORA-RhoB sensor YFP/CFP ratio (purple) in A7 (*n* = 1 cell) exposed to shear (5 min at 0.5Pa; grey bar). No changes are observed in absence of shear or in FLNa-depleted M2 cells. **Supplementary Figure S6** **(C)** Scatterplot of peak response lag time of Dora RhoB sensor under applied shear of 0.5 Pa (black) or 2.5 Pa (grey) as a function of Dora RhoB sensor YFP/CFP ratio change. A7 cells display a faster and higher magnitude response under high strain (dashed line, linear least squares fit) **(D)** Boxplot (center line, median; box, upper, and lower quartiles; whiskers, ×1.5 IQR; crosses, outliers; two-sided *t*-test) of Dora RhoB sensor YFP/CFP ratio change as a function of applied shear (n = 30 cells) **(E)** Scatterplot of Dora RhoB sensor YFP/CFP ratio change as a function of controlled (cell orientation and aspect ratio) effective force (Pa) (*n* = 30 cells). Higher magnitude of Dora RhoB sensor YFP/CFP ratio change is observed in cells exposed to higher values of effective shear (dashed line, linear least squares fit).

signaling is coupled to actomyosin contraction. We used the time-dependent contractile response and GTPase biosensor ratios as readouts of population states. We observed that strain energy increase in A7 cells depends on Rho activation whereas Rho magnitude fluctuations are independent of the cell contractile work (**Figure 5A**). Our data suggests that while Rho is required to drive contractility it can also be decoupled from the cell contractile response. Rho is thus necessary but not sufficient for mechanoresponse. When we compared the integration of Rho sensor activity in A7 cells that respond to shear, we also observed that a characteristic threshold of total Rho activity is required for the cell to contract (**Figure 5B**). Together these results suggest that while cells need to integrate Rho activity up to a certain threshold for cell contraction, Rho activation is not a reliable predictor of a contractile response to shear. This is expected as Rho signaling regulates a number of different intracellular processes, but it also suggests that other molecular players are involved in regulating Rho-dependent shear mechanotransduction. Our observations further support the existence of contractile checkpoints that participate in the integration of external mechanical stimuli and to the overall contractile response heterogeneity.

Based on our molecular, traction and FRET data, we propose a contractile mechanism that hinges on the release and activation of FilGAP for direct inactivation of Rac and indirect activation of Rho. We next designed a pharmacological assay to confirm this idea and to control Rho and Rac activity with specific inhibitors to circumvent the absence of FLNa and trigger a contractile response in M2 cells. We successfully simulated contraction in FLNa-deficient M2 cells by combining the Rac inhibitor Ehop-16 (20 uM) [41] and the Rho agonist nocodazole (10 uM) [42] to stimulate the GTPase response and cell contraction (**Figures 5C–F**). We also reversed the GTPase and contractile responses with ROCK-inhibitor Y-27632 (10 uM) treatment (**Figures 5C,D**). These results suggest that reversible contractile work is driven by modulations in the respective Rho and Rac activity levels. To confirm that decrease of Rac activity coupled with increase of Rho activity leads to contraction, we used the same pharmacological treatment to recreate the impact of FilGAP release and activation that we observe in A7 cells under strain (**Figure 5D**). As expected, we observed an initial increase in cell traction after treatment with the combined Rac inhibitor Ehop-16 (20 uM) and the Rho agonist nocodazole (10 uM) (**Figure 5F**). We also quantified a subsequent decrease in traction after the same cell was treated with the ROCK-inhibitor Y-27632 (10 uM) (**Figure 5F**). These observations show that other drug-induced mechanoeffectors remain functional in this M2 cell in absence of FLNa. Together our results confirm that shear mechanotransduction in melanoma cells is mediated by dynamic binding of FLNa and FilGAP (**Figures 1**, **2**), the cell strain (**Figures 3**, **4**) and the modulation of Rac and Rho activities (**Figures 4**, **5**).

DISCUSSION

Mechanosensing must integrate a broad range of stimuli and draws upon diverse mechanisms. Depending on cellular and environmental context, various mechanocomplexes act as direct shear force sensors such as the Plexin D1-neuropilin 1-VEGFR system in endothelial cells [43] or the FLNa-FilGAP system [24] we studied here in melanoma cells. Mechanotransduction through the FLNa-FilGAP sensor depends on common molecular players including integrins and small GTPase. Force-dependent activation of integrins and GTPase is also a feature shared with the PECAM-1 system in endothelial cells [44].

As a mechanointegrator, the FLNa-FilGAP system convolves a broad range of stimuli and produces a breadth of responses. We

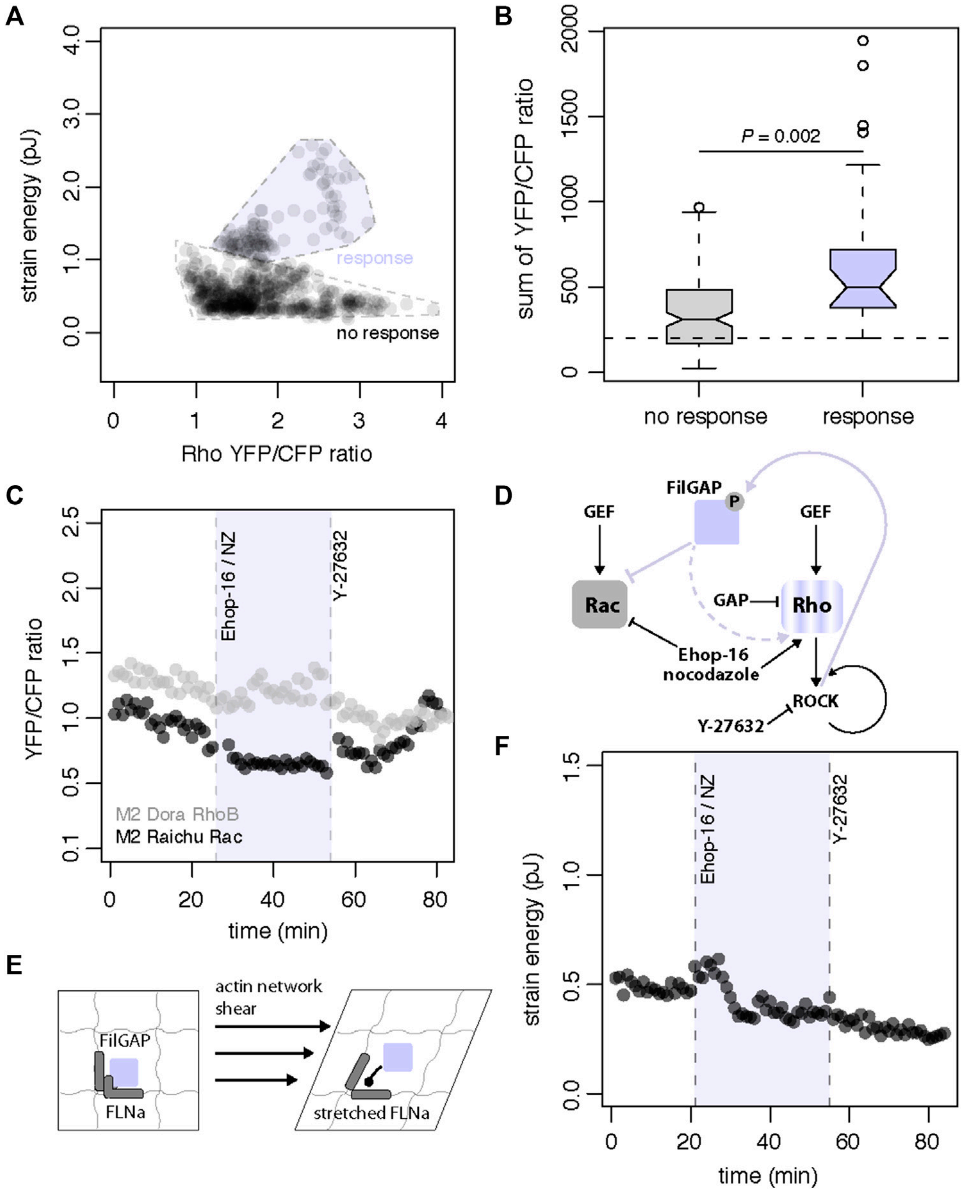

FIGURE 5 | Model of shear stress mechanosensing through FLNa-FiLGAP interaction **(A)** Landscape of strain energy in A7 cells as a function of DORA-RhoB sensor YFP/CFP ratio. High strain energy depends on DORA-RhoB sensor YFP/CFP ratio increase whereas magnitude fluctuations in DORA-RhoB sensor YFP/CFP ratio can be independent of strain energy (*n* = 371 cells) **(B)** Boxplot (center line, median; box, upper, and lower quartiles; whiskers, 1.5x IQR; crosses, outliers; two-sided *t*-test) of sum of DORA-RhoB sensor YFP/CFP ratio as a function of cell contractile response (*n* = 129 cells total). A7 cells that display a contractile response have significantly higher values for the sum of DORA-RhoB YFP/CFP ratio (*p* = 0.002) and integrate DORA RhoB sensor levels up to a characteristic threshold of YFP/CFP ratio **(C)** Time series of DORA-RhoB (grey, *n* = 1 cell) and Raichu-Rac (black, *n* = 1 cell) YFP/CFP ratios in pharmacological treatment of M2 cells with combined 20 uM Ehop-16 and 10 uM nocodazole (NZ) at 26 min and subsequent treatment with 10uM Y-27632 at 54 min **(D)** FLNa-unbound FilGAP can directly inhibit Rac and indirectly leads to cell contraction through the Rho branch. Conversely, Rac inhibitor Ehop-16 and the Rho agonist nocodazole can stimulate the GTPases response and cell contraction. The GTPases and contractile responses with ROCK-inhibitor Y-27632 treatment (arrowheads represent stimulatory modifications, flatheads represent inhibitory modifications, lines are direct modifications and dotted lines represent tentative modifications) **(E)** A molecular model of FLNa-dependent mechanotransduction. Shear stress mechanotransduction is proposed to begin through mechanical stretching and spatial reconfiguration of Filamin A (FLNa). When FLNa is stretched, it reduces the binding affinity for FilGAP and releases FilGAP in the cytosol **(F)** Time series of strain energy in pharmacological treatment of M2 cell with combined 20 μM Ehop-16 and 10 μM nocodazole at 26 min and subsequent treatment with 10 μM Y-27632 at 54 min.

observed that the delay of contractile response to shear could be predicted by the effective shear force applied to cells. Effective shear force is the deformation of cells due to shear force and is determined by cellular orientation to fluid flow and height of cell profile. This may represent a "bet-hedging" strategy used by cells to optimize the timing and magnitude of their shear response. Cells integrate many different frequencies and amplitudes of mechanical deformation from the environment; FLNa mediated mechanosensing may use this strategy to tune their response to fluctuations in shear stress in order to maintain fitness. Indeed, we have shown that identical shear stress elicits diverse magnitudes and timing of the response; we attribute this to the varied actual resulting strain based on cell stiffness, and effective shear force. Thus, this sensitivity variation based on cell to cell geometry and alignment differences allows a collection of cells to process a broader dynamic range of stimuli than possible for a single cell's random orientation of FLNa networks [45].

Evidence for a smaller dynamic range of contractility in FLNa-complemented M2 cells reflect the importance of protein expression levels and amount of sequestered FilGAP through dynamic binding in response heterogeneity. Surprisingly, no difference in baseline Raichu-Rac activity was observed between A7 and M2 cells whereas DORA-RhoB signal is higher in M2 cells compared to A7 cells (**Supplementary Figure S7**) suggesting the existence of a feedback mechanism to control GTPases levels when the FLNa-FilGAP dynamic interaction is broken and only unbound FilGAP is present in M2 cells. FilGAP is inactive in the bound state and active in unbound state; as a result, the change in GTPase activity and contractile shear response is dampened in absence of FLNa.

FilGAP's mechanosensory role likely has broad relevance in cancer metastasis. Small GTPases have been shown to play extensive roles in regulating apical & basal polarity of individual cells, but are also crucial to regulate collective multicellular migration and fragmentation [46]. In metastatic tumor invasion FilGAP regulates polarity of breast cancer cells leading to increased migration penetration [28]. Future work will continue to resolve the extent of FilGAP mechanotransduction in diverse physiology and pathology.

MATERIALS AND METHODS

Fabrication of Soft Silicone Substrates

Compliant polydimethylsiloxane (PDMS) substrates were prepared as described by Yoshie and colleagues [47]. We obtained substrates of different modulus by mixing an equal weight ratio of PDMS components A and B (NuSil® 8100, NuSil Silicone Technologies) with respective concentrations of dimethyl siloxane-methyl hydrogen siloxane copolymer (Sylgard 184, NuSil Silicone Technologies) that effectively crosslink the PDMS. We measured with a parallel plate rheometer (Anton Paar MCR302) that PDMS substrates with weight percentage concentrations of Sylgard 184 of 0.20, 0.36 and 0.50 have Young's moduli of 5.0 ± 0.04, 12.0 ± 0.71, and 23.4 ± 1.86 kPa respectively. We laminated two layers of PDMS on 1.0 mm thick glass slides (75 × 25 mm, VWR) to obtain a uniform thickness of ~150 microns. For each layer, 0.75 ml of PDMS solution were spin coated (WS-650, Laurell Technologies) at 500 rpm for 1 min and cured at 100°C for 1 h. An additional PDMS layer with fiduciary beads was added at 2000 rpm for 1 min and cured 1 h for our traction force microscopy experiments. Substrate surfaces were functionalized with sulfo-sanpah exposed to under UV for 2 min, washed with phosphate buffered saline and incubated with fibronectin for 1 h.

Printing of Fibronectin Micropatterns for Controlled Cell Attachment

PDMS substrates were micropatterned with a UV-patterning system as described by Ghagre and collaborators [48]. PDMS substrates were incubated with 5 mg/ml poly-L-lysine (Sigma) for 30 min, washed with miliQ water and treated with 10 mg/ml polyethylene glycol valeric acid (Laysan Bio) in 0.1 M HEPES pH8.5 for 30 min. Substrates were then washed with phosphate buffered saline, covered with UV sensitive photo initiator solution (Alveole Lab) and exposed for 30 s to a patterned 29 mW/mm^2 375 nm UV laser with a Primo unit (Alveole Lab) mounted on a Ti2 eclipse microscope (Nikon) equipped with a 20x/0.45NA objective (Nikon). After the UV-based micropatterning step, the substrates were washed with phosphate buffered saline and incubated with 40 μg/ml fibronectin 5 μg/ml Alexa-555-labelled bovine serum albumin solution for 1 h. Substrates were finally washed with phosphate buffered saline and stored at 4°C prior to cell seeding.

Plasmid Preparation

mEmerald-FilaminA-N-9 plasmid (Addgene) was used to generate mEmerald-FilaminA M2474E using the GeneArt site-directed mutagenesis system (Thermo). Plasmid stocks were prepared by transforming One Shot™ TOP10 (Thermo) chemically competent *E. coli* cells, with a transformation efficiency of ~10^9 cfu/μg plasmid DNA and performing an overnight bacterial culture on kanamycin (50 μg/ml) LB Petri plates. Colonies were selected on the petri plates, and inoculation of liquid bacterial culture was done overnight in shaking incubator at 37°C. DNA was purified with QIAprep® Spin Miniprep Kit (Qiagen) and DNA was quantified with a NanoDrop spectrophotometer (Thermo).

Cell Culture, Seeding and Transfection

The human melanoma cell lines M2 and A7 cell lines were maintained in DMEM with 10% fetal bovine serum and 1% penicillin streptomycin antibiotics. Media for A7 cell lines complemented for filaminA expression also contained G418. Cell lines in filtered flasks were incubated at 37°C with 5% CO_2. Cells were seeded and incubated on fibronectin coated substrates or micropatterns for 1 h and washed with phosphate buffered saline to avoid nonspecific adhesion. Cell lines were otherwise plated onto a 6-well plate for transfection purposes. M2 cells were transfected with FLNa and FLNa M2474E using the GenJet™ DNA *In Vitro* Tranfection Reagent (SignaGen Laboratories). Cell lines with no fluorescent labels were dyed with CellTracker Green CMFDA (Invitrogen) for confocal microscopy purposes. Stable cell lines that respectively express the FRET sensors DORA-RhoB [38] and Raichu-Rac [39, 49] were generated using lentiviral transduction followed by Blasticidin selection, with codon-optimized fluorophores that prevent unwanted recombination during lentiviral gene transfer.

RNA Interference Experiments

Cells were transfected with control siRNA or siRNA oligonucleotide duplexes targeting human ARHGAP24 (siRNA ID 148940, Thermo) using Lipofectamine® RNAiMAX Transfection Reagent (Thermo) and cultured on plastic plates for 48 h. Alternatively, cells were stably transfected with a short hairpin RNA (shRNA) against FLNa and grown in the presence of 1 g/ml puromycin.

Protein Extraction and Western Blot

Protein extraction was performed 48 h after transfection by cell lysis with ice-cold cell lysis RIPA Buffer and protein extraction protocol. Extracted proteins were stored in microcentrifuge tubes at -20°C. SDS-PAGE was performed using 4–15% Mini-PROTEAN® TGX™ precast gels (Bio-Rad) and the Mini-PROTEAN Tetra cell system (Bio-Rad) gel electrophoresis apparatus. 4X Laemmli sample buffer (Bio-Rad) was used as loading buffer. Blotting was done using the Trans-Blot® Turbo system and cassettes (Bio-Rad). Membranes were blocked with 5% bovine serum albumin (BSA) solution and primary antibody staining was performed with either 1:1,000 Filamin A monoclonal antibody (FLMN01 (PM6/317), Thermo) or 1:1,000 polyclonal mouse anti-human ARHGAP24 antibody (LS-C306327, LSBio) or 1:5,000 actin monoclonal antibody (mAbGEa, Thermo) in 1% BSA. Secondary antibody staining was done with 1:1,000 goat anti-mouse IgG (H + L)-HRP conjugate (1,706,516, Bio-Rad) in 1% BSA and imaging is done using the ChemiDoc Imaging System (Thermo). Results are processed using Image Lab Software (Bio-Rad) and ImageJ (NIH).

Confocal Microscopy

Cells on PDMS substrates were imaged on a TCS SP8 confocal microscope (Leica) equipped with a 10X/0.4NA objective (Leica) in a controlled culture environment at 37°C perfused with a 5% CO_2. We used a live cell imaging solution (Molecular Probes) for acquisition of all the fluorescence images.

Pharmalogical Treatments

For the FRET experiments we stimulated Rho activity with 5uM Nocodazole (Sigma Aldrich). We also used 10 μM Y-27632 (Sigma Aldrich) ROCK inhibitor to reduce RhoB activity. We inhibited Rac activity with 20 μM Ehop-16 (Sigma Aldrich).

Microfluidics Setup

Shear flow was applied with a μ-Slide microfluidic system (Ibidi) perfused with a syringe pump (Harvard Apparatus). μ-Slides with a channel height of 600 μm were glued over cells mounted on PDMS substrates before confocal imaging on a TCS SP8 confocal microscope and mechanical stimulation of cells unless mentioned otherwise.

Rheoconfocal Setup

We developed a customized rheometer-confocal platform to investigate the mechanical interplay between cells and shear stress. We combined a parallel plate rheometer (Anton Paar MCR302) over a TCS SP8 confocal microscope equipped with a 10X/0.4NA objective (Leica) to image cells transfected with pTriExRhoA2G (Addgene). Used for **Supplementary Figure S5** only. Sample fluorescence and interference reflection microscopy imaging was performed through a customized metal cup with a heating element and infused with 5% CO_2 (**Supplementary Figure S1**).

Live-Cell FRET Measurements

Cells mounted on PDMS substrates were stimulated and/or exposed to shear when indicated. Live-cell FRET imaging was performed on a TCS SP8 confocal microscope (Leica) equipped with a 10X/0.4NA objective (Leica). CFP was excited with a continuous wave 448 nm laser and excitation filter. Simultaneous detection of CFP (455–505 nm) and YFP (520–600 nm) channels was performed with two respective photomultiplier tubes. Images were acquired with the Leica application suite X software (Leica) and YFP/CFP ratio analysis was performed in ImageJ (NIH).

Traction Force Microscopy

Cell contractile work was measured with fiduciary beads as described previously [50]. Images of fiduciary particles in the top PDMS layer were acquired with a TCS SP8 confocal microscope (Leica) equipped with a 10X/0.4NA objective (Leica). Once the individual regions of interest with cells had been recorded, a 2% TritonX-100, 50 mM sodium azide, 500 mM potassium hydroxide solution was added prior to acquisition of the force-free reference images of the fiduciary particles. Cell strain energy were calculated with the available pyTFM script (https://github.com/fabrylab/pyTFM) based on traction force and force-free images of the fiduciary particles [35].

Pattern-Based Quantification of Cell Contractile Work

Cells' contractile work was measured with a pattern-based method as described previously [49]. The deformed and undeformed pattern areas were segmented based on fluorescent intensity threshold with ImageJ (NIH). Cell strain energies were calculated with the available MATLAB script (https://github.com/ajinkyaghagre/PaCS_156matlabcode) based on the PDMS substrate modulus and the initial pattern area.

DATA AVAILABILITY STATEMENT

The original contributions presented in the study are included in the article/**Supplementary Material**, further inquiries can be directed to the corresponding author.

AUTHOR CONTRIBUTIONS

LPB-S and AE designed the research; LPB-S and ACa performed biological research; ACl and CH performed the western blot experiments; LPB-S, ACa, and AE analyzed the biological data; LPB-S, ACa, and AE wrote the paper.

FUNDING

AE acknowledges support from NSERC (RGPIN/05843–2014, EQPEQ/472339–2015 and RTI/00348–2018), CIHR # 143,327, and Canadian Foundation for Innovation Project #32749. LPB-S was supported by an FRQNT fellowship.

ACKNOWLEDGMENTS

The authors thank Dr Arnold Hayer for contributing four stably transfected FRET construct cell lines and his comments on the manuscript, as well as A. Ghagre and B. Guerin for technical assistance.

SUPPLEMENTARY MATERIAL

The Supplementary Material for this article can be found online at: https://www.frontiersin.org/articles/10.3389/fphy.2022.890865/full#supplementary-material

REFERENCES

1. Cole A, Buckler S, Marcucci J, Artemenko Y. Differential Roles of Actin Crosslinking Proteins Filamin and α-Actinin in Shear Flow-Induced Migration of *Dictyostelium discoideum*. *Front Cel Develop Biol* (2021) 9: 743011. doi:10.3389/fcell.2021.743011
2. Davies PF, Spaan JA, Krams R. Shear Stress Biology of the Endothelium. *Ann Biomed Eng* (2005) 33(12):1714–8. doi:10.1007/s10439-005-8774-0
3. Fletcher DA, Mullins RD. Cell Mechanics and the Cytoskeleton. *Nature* (2010) 463(7280):485–92. doi:10.1038/nature08908
4. Alonso JL, Goldmann WH. Cellular Mechanotransduction. *AIMS Biophys* (2016) 1(7):50. doi:10.3934/biophy.2016.1.50
5. Dostal DE, Feng H, Nizamutdinov D, Golden HB, Afroze SH, Dostal JD, et al. Mechanosensing and Regulation of Cardiac Function. *J Clin Exp Cardiolog* (2014) 5(6):314. doi:10.4172/2155-9880.1000314
6. Martino F, Perestrelo AR, Vinarský V, Pagliari S, Forte G. Cellular Mechanotransduction: From Tension to Function. *Front Physiol* (2018) 9: 824. doi:10.3389/fphys.2018.00824
7. Swaminathan V, Gloerich M. Decoding Mechanical Cues by Molecular Mechanotransduction. *Curr Opin Cel Biol* (2021) 72:72–80. doi:10.1016/j.ceb.2021.05.006
8. Lamsoul I, Dupré L, Lutz PG. Molecular Tuning of Filamin A Activities in the Context of Adhesion and Migration. *Front Cel Develop Biol* (2020) 8:1432. doi:10.3389/fcell.2020.591323
9. Harris AR, Jreij P, Fletcher DA. Mechanotransduction by the Actin Cytoskeleton: Converting Mechanical Stimuli into Biochemical Signals. *Annu Rev Biophys* (2018) 47(1):617–31. doi:10.1146/annurev-biophys-070816-033547
10. Razinia Z, Mäkelä T, Ylänne J, Calderwood DA. Filamins in Mechanosensing and Signaling. *Annu Rev Biophys* (2012) 41:227–46. doi:10.1146/annurev-biophys-050511-102252
11. Zhou J, Kang X, An H, Lv Y, Liu X. The Function and Pathogenic Mechanism of Filamin A. *Gene* (2021) 784:145575. doi:10.1016/j.gene.2021.145575
12. Hu J, Lu J, Goyal A, Wong T, Lian G, Zhang J, et al. Opposing FlnA and FlnB Interactions Regulate RhoA Activation in Guiding Dynamic Actin Stress Fiber Formation and Cell Spreading. *Hum Mol Genet* (2017) 26(7):1294–304. doi:10.1093/hmg/ddx047
13. Chen H, Zhu X, Cong P, Sheetz MP, Nakamura F, Yan J. Differential Mechanical Stability of Filamin A Rod Segments. *Biophysical J* (2011) 101(5):1231–7. doi:10.1016/j.bpj.2011.07.028
14. Cunningham CC, Gorlin JB, Kwiatkowski DJ, Hartwig JH, Janmey PA, Byers HR, et al. Actin-binding Protein Requirement for Cortical Stability and Efficient Locomotion. *Science* (1992) 255(5042):325–7. doi:10.1126/science.1549777
15. Flanagan LA, Chou J, Falet H, Neujahr R, Hartwig JH, Stossel TP. Filamin A, the Arp2/3 Complex, and the Morphology and Function of Cortical Actin Filaments in Human Melanoma Cells. *J Cel Biol* (2001) 155(4):511–8. doi:10.1083/jcb.200105148
16. Kim H, McCulloch CA. Filamin A Mediates Interactions between Cytoskeletal Proteins that Control Cell Adhesion. *FEBS Lett* (2011) 585(1):18–22. doi:10.1016/j.febslet.2010.11.033
17. Ithychanda SS, Qin J. Evidence for Multisite Ligand Binding and Stretching of Filamin by Integrin and Migfilin. *Biochemistry* (2011) 50(20):4229–31. doi:10.1021/bi2003229
18. Spiering D, Hodgson L. Dynamics of the Rho-Family Small GTPases in Actin Regulation and Motility. *Cell Adhes Migration* (2011) 5(2):170–80. doi:10.4161/cam.5.2.14403
19. Parri M, Chiarugi P. Rac and Rho GTPases in Cancer Cell Motility Control. *Cell Commun Signal* (2010) 8:23. doi:10.1186/1478-811x-8-23
20. Ohashi K, Fujiwara S, Mizuno K. Roles of the Cytoskeleton, Cell Adhesion and Rho Signalling in Mechanosensing and Mechanotransduction. *J Biochem* (2017) 161(3):245–54. doi:10.1093/jb/mvw082
21. Ohta Y, Hartwig JH, Stossel TP. FilGAP, a Rho- and ROCK-Regulated GAP for Rac Binds Filamin A to Control Actin Remodelling. *Nat Cel Biol* (2006) 8(8): 803–14. doi:10.1038/ncb1437
22. Nakamura F, Heikkinen O, Pentikäinen OT, Osborn TM, Kasza KE, Weitz DA, et al. Molecular Basis of Filamin A-FilGAP Interaction and its Impairment in Congenital Disorders Associated with Filamin A Mutations. *PLoS One* (2009) 4(3):e4928. doi:10.1371/journal.pone.0004928
23. Ehrlicher AJ, Nakamura F, Hartwig JH, Weitz DA, Stossel TP. Mechanical Strain in Actin Networks Regulates FilGAP and Integrin Binding to Filamin A. *Nature* (2011) 478(7368):260–3. doi:10.1038/nature10430
24. Shifrin Y, Arora PD, Ohta Y, Calderwood DA, McCulloch CA. The Role of FilGAP-Filamin A Interactions in Mechanoprotection. *MBoC* (2009) 20(5): 1269–79. doi:10.1091/mbc.e08-08-0872
25. Pinto VI, Senini VW, Wang Y, Kazembe MP, McCulloch CA. Filamin A Protects Cells against Force-induced Apoptosis by Stabilizing Talin- and Vinculin-containing Cell Adhesions. *FASEB j.* (2014) 28(1):453–63. doi:10.1096/fj.13-233759
26. Shifrin Y, Pinto VI, Hassanali A, Arora PD, McCulloch CA. Force-induced Apoptosis Mediated by the Rac/Pak/p38 Signalling Pathway Is Regulated by Filamin A. *Biochem J* (2012) 445(1):57–67. doi:10.1042/bj20112119
27. Hara A, Hashimura M, Tsutsumi K, Akiya M, Inukai M, Ohta Y, et al. The Role of FilGAP, a Rac-specific Rho-GTPase-Activating Protein, in Tumor Progression and Behavior of Astrocytomas. *Cancer Med* (2016) 5(12): 3412–25. doi:10.1002/cam4.937
28. Saito K, Mori M, Kambara N, Ohta Y. FilGAP, a GAP Protein for Rac, Regulates Front-Rear Polarity and Tumor Cell Migration through the ECM. *FASEB J* (2021) 35(4):e21508. doi:10.1096/fj.202002155R
29. Saito K, Ozawa Y, Hibino K, Ohta Y. FilGAP, a Rho/Rho-Associated Protein Kinase-Regulated GTPase-Activating Protein for Rac, Controls Tumor Cell Migration. *MBoC* (2012) 23(24):4739–50. doi:10.1091/mbc.e12-04-0310
30. Nakamura F. FilGAP and its Close Relatives: a Mediator of Rho-Rac Antagonism that Regulates Cell Morphology and Migration. *Biochem J* (2013) 453(1):17–25. doi:10.1042/bj20130290
31. Jaffe AB, Hall A. Rho GTPases: Biochemistry and Biology. *Annu Rev Cel Dev. Biol.* (2005) 21:247–69. doi:10.1146/annurev.cellbio.21.020604.150721
32. Machacek M, Hodgson L, Welch C, Elliott H, Pertz O, Nalbant P, et al. Coordination of Rho GTPase Activities during Cell Protrusion. *Nature* (2009) 461(7260):99–103. doi:10.1038/nature08242
33. Yang HW, Collins SR, Meyer T. Locally Excitable Cdc42 Signals Steer Cells during Chemotaxis. *Nat Cel Biol* (2016) 18(2):191–201. doi:10.1038/ncb3292
34. Sanz-Moreno V, Marshall CJ. Rho-GTPase Signaling Drives Melanoma Cell Plasticity. *Cell Cycle* (2009) 8(10):1484–7. doi:10.4161/cc.8.10.8490
35. Bauer A, Prechová M, Fischer L, Thievessen I, Gregor M, Fabry B. pyTFM: A Tool for Traction Force and Monolayer Stress Microscopy. *Plos Comput Biol* (2021) 17(6):e1008364. doi:10.1371/journal.pcbi.1008364

36. Guo M, Pegoraro AF, Mao A, Zhou EH, Arany PR, Han Y, et al. Cell Volume Change through Water Efflux Impacts Cell Stiffness and Stem Cell Fate. *Proc Natl Acad Sci U S A* (2017) 114(41):E8618–E27. doi:10.1073/pnas.1705179114
37. Wozniak MA, Desai R, Solski PA, Der CJ, Keely PJ. ROCK-generated Contractility Regulates Breast Epithelial Cell Differentiation in Response to the Physical Properties of a Three-Dimensional Collagen Matrix. *J Cel Biol* (2003) 163(3):583–95. doi:10.1083/jcb.200305010
38. Reinhard NR, van Helden SF, Anthony EC, Yin T, Wu YI, Goedhart J, et al. Spatiotemporal Analysis of RhoA/B/C Activation in Primary Human Endothelial Cells. *Sci Rep* (2016) 6:25502. doi:10.1038/srep25502
39. Komatsu N, Aoki K, Yamada M, Yukinaga H, Fujita Y, Kamioka Y, et al. Development of an Optimized Backbone of FRET Biosensors for Kinases and GTPases. *MBoC* (2011) 22(23):4647–56. doi:10.1091/mbc.e11-01-0072
40. Fritz RD, Letzelter M, Reimann A, Martin K, Fusco L, Ritsma L, et al. A Versatile Toolkit to Produce Sensitive FRET Biosensors to Visualize Signaling in Time and Space. *Sci Signal* (2013) 6(285):rs12. doi:10.1126/scisignal.2004135
41. Autenrieth TJ, Frank SC, Greiner AM, Klumpp D, Richter B, Hauser M, et al. Actomyosin Contractility and RhoGTPases Affect Cell-Polarity and Directional Migration during Haptotaxis. *Integr Biol (Camb)* (2016) 8(10):1067–78. doi:10.1039/c6ib00152a
42. Chang Y-C, Nalbant P, Birkenfeld J, Chang Z-F, Bokoch GM. GEF-H1 Couples Nocodazole-Induced Microtubule Disassembly to Cell Contractility via RhoA. *MBoC* (2008) 19(5):2147–53. doi:10.1091/mbc.e07-12-1269
43. Mehta V, Pang K-L, Rozbesky D, Nather K, Keen A, Lachowski D, et al. The Guidance Receptor Plexin D1 Is a Mechanosensor in Endothelial Cells. *Nature* (2020) 578(7794):290–5. doi:10.1038/s41586-020-1979-4
44. Collins C, Guilluy C, Welch C, O'Brien ET, Hahn K, Superfine R, et al. Localized Tensional Forces on PECAM-1 Elicit a Global Mechanotransduction Response via the Integrin-RhoA Pathway. *Curr Biol* (2012) 22(22):2087–94. doi:10.1016/j.cub.2012.08.051
45. Kang J, Puskar KM, Ehrlicher AJ, LeDuc PR, Schwartz RS. Structurally Governed Cell Mechanotransduction through Multiscale Modeling. *Sci Rep* (2015) 5(1):8622. doi:10.1038/srep08622
46. Zegers MM, Friedl P. Rho GTPases in Collective Cell Migration. *Small GTPases* (2014) 5:e28997. doi:10.4161/sgtp.28997
47. Yoshie H, Koushki N, Kaviani R, Tabatabaei M, Rajendran K, Dang Q, et al. Traction Force Screening Enabled by Compliant PDMS Elastomers. *Biophysical J* (2018) 114(9):2194–9. doi:10.1016/j.bpj.2018.02.045
48. Ghagre A, Amini A, Srivastava LK, Tirgar P, Khavari A, Koushki N, et al. Pattern-Based Contractility Screening, a Reference-free Alternative to Traction Force Microscopy Methodology. *ACS Appl Mater Inter* (2021) 13(17):19726–35. doi:10.1021/acsami.1c02987
49. Bisaria A, Hayer A, Garbett D, Cohen D, Meyer T. Membrane-proximal F-Actin Restricts Local Membrane Protrusions and Directs Cell Migration. *Science* (2020) 368(6496):1205–10. doi:10.1126/science.aay7794
50. Yoshie H, Koushki N, Molter C, Siegel PM, Krishnan R, Ehrlicher AJ. High Throughput Traction Force Microscopy Using PDMS Reveals Dose-dependent Effects of Transforming Growth Factor-β on the Epithelial-To-Mesenchymal Transition. *J Vis Exp* (2019) 148:59364. doi:10.3791/59364

Conflict of Interest: The authors declare that the research was conducted in the absence of any commercial or financial relationships that could be construed as a potential conflict of interest.

frontiers | Frontiers in Physics

ORIGINAL RESEARCH
published: 18 May 2022
doi: 10.3389/fphy.2022.875687

A Pili-Driven Bacterial Turbine

Wolfram Pönisch[1]* and Vasily Zaburdaev[2,3]*

[1]Department of Physiology, Development and Neuroscience, University of Cambridge, Cambridge, United Kingdom, [2]Department of Biology, Friedrich-Alexander-Universität Erlangen-Nürnberg, Erlangen, Germany, [3]Max Planck Zentrum für Physik und Medizin, Erlangen, Germany

Work generated by self-propelled bacteria can be harnessed with the help of microdevices. Such nanofabricated microdevices, immersed in a bacterial bath, may exhibit unidirectional rotational or translational motion. Swimming bacteria that propel with the help of actively rotating flagella are a prototypical example of active agents that can power such microdevices. In this work, we propose a computational model of a micron-sized turbine powered by bacteria that rely on active type IV pili appendages for surface-associated motility. We find that the turbine can rotate persistently over a time scale that significantly exceeds the characteristic times of the single cell motility. The persistent rotation is explained by the collective dynamics of multiple pili of groups of cells attaching to and pulling on turbine. Furthermore, we show that the turbine can rotate permanently in the same direction by altering the pili binding to the turbine surface in an asymmetric fashion. We thus can show that by changing the adhesive properties of the turbine while keeping its symmetric geometry, we can still break the symmetry of its rotation. Altogether, this study widely expands the range of bacteria that can be used to power nanofabricated microdevices, and, due to high pili forces generated by pili retraction, promises to push the harnessed work by several orders of magnitude.

Keywords: bacterial turbine, bacterial motility, microdevice, type IV pili, active motion

Edited by:
Sujit Datta,
Princeton University, United States

Reviewed by:
Stefan Klumpp,
University of Göttingen, Germany
Hepeng Zhang,
Shanghai Jiao Tong University, China

***Correspondence:**
Wolfram Pönisch
wp269@cam.ac.uk
Vasily Zaburdaev
vasily.zaburdaev@fau.de

Specialty section:
This article was submitted to
Biophysics,
a section of the journal
Frontiers in Physics

Received: 14 February 2022
Accepted: 16 March 2022
Published: 18 May 2022

Citation:
Pönisch W and Zaburdaev V (2022) A
Pili-Driven Bacterial Turbine.
Front. Phys. 10:875687.
doi: 10.3389/fphy.2022.875687

1 INTRODUCTION

The last years have seen significant advances in nanofabrication, permitting the invention of a wide range of micron-sized artificial devices. A fascinating question is how such devices can be powered by actively moving biological matter, typically consisting of bacteria. Examples are beads that move due to collision or attachment of cells to its surface [1, 2], swimming devices due to individual swimming cells and bacterial carpets attached to their surface [3] or confined in the microdevice structure [4, 5], and geometrically asymmetric devices immersed in a bath of actively moving cells that rotate due to random collisions with the cells [6–10]. Usually, bacteria that swim with the help of rotating flagella were employed. In this study, we propose to consider twitching bacteria that exhibit surface-associated locomotion mediated by type IV pili [11, 12]. Pili are microns long active polymeric appendages protruding from the cell membrane. They undergo cycles of protrusion and retraction and can bind to a substrate and the pili of other cells. The combination of these two processes leads to aggregation of cells [13–15] and twitching motility on a substrate [16–19] by a mechanism reminiscent of a grappling hook (see **Figure 1A**).

Here, we investigate how bacteria that can attach type IV pili to a micron-sized turbine can drive its rotation. This system is especially interesting since multiple pili belonging to an individual bacterium can generate total forces in the range of nano-Newtons [20]. In contrast to that, bacteria that swim with the help of flagella typically have thrust forces in the order of 1–10 pN [21]. The molecular motor involved in the disassembly an hence, in the retraction of an individual pilus, called

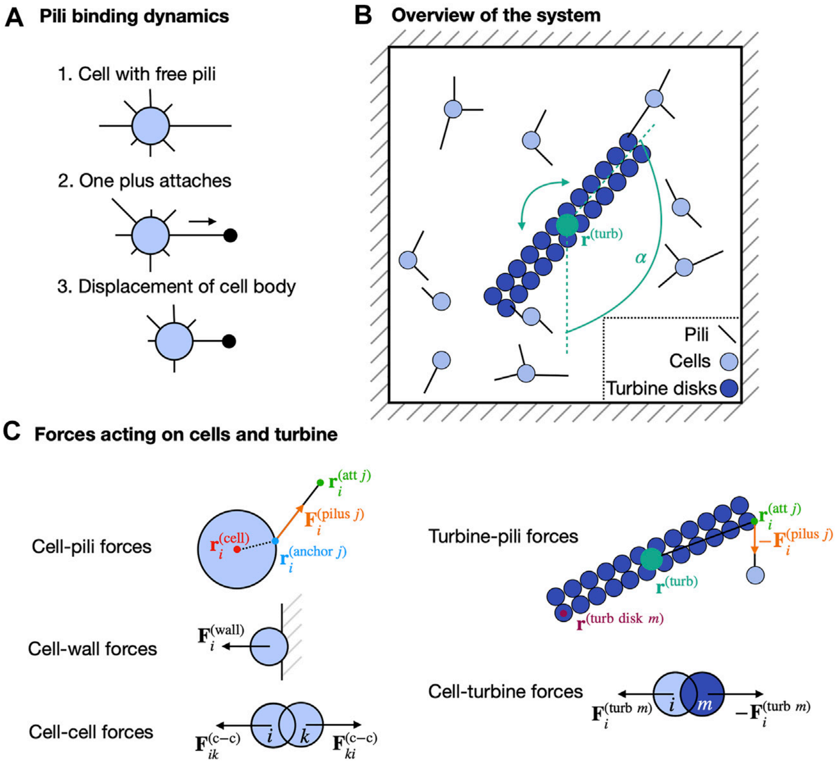

FIGURE 1 | Overview of the computational model of bacteria driving a rotatable turbine by attachment of type IV pili. **(A)** Sketch of how pili binding and retraction can lead to a force acting on a cell, a process reminiscent of a grappling hook. **(B)** Overview of the system. Cells are located in a box together with the rotatable turbine. The cells possess pili which they use for the motility on the substrate and for attachment to the turbine. The turbine center is located at $\mathbf{r}^{(\mathrm{turb})}$ and has an orientation defined by the angle α. **(C)** Summary of all forces acting on the cells and turbine. Friction forces with the environment (surrounding liquid and substrate) are not shown.

pilT, can generate forces in the range of 100 - 180 pN [22]. This makes pilT the strongest molecular motor known in nature, with forces up to 20 times larger than those generated by kinesins or polymerases [20]. Hence, we are asking if cells with type IV pili that can create so large forces might be more attractive candidates to power microdevices.

In this work, by means of a computational model, we study the dynamics of a rotatable turbine immersed in a bath of twitching bacteria. We investigate how the turbine rotation is affected by the binding and unbinding of the bacterial pili. We find that, due to the adhesion of multiple pili to the turbine over time scales that can strongly exceed the characteristic time scales of the individual pili attachment, the turbine can persistently rotate in one direction over extensive durations. While these persistent rotations have a limited lifetime, one can engineer a system where they become permanently unidirectional by introducing asymmetric binding of the pili to the turbine.

2 MATERIALS AND METHODS

First, we introduce the computational model of twitching bacteria and their interactions with a turbine. A related version of this computational model was considered previously to describe bacterial surface motility [19] and bacterial aggregates [23–25]. While we consider the bacterium *Neisseria gonorrhoeae* as the primary biological example, the computational model can be easily adapted to account for other bacteria that use type IV pili, e.g., *Neisseria meningitidis* [14] or *Pseudomonas aeruginosa* [26]. In the following, we focus on the regime of low cell density. This allows us not to consider cell-cell interactions and the formation of bacterial aggregates mediated by the binding of the pili of different cells. As a result, we do not expect three dimensional aggregates to form [23, 24]. This also enables us to only consider a simpler two-dimensional system.

2.1 Geometry of the Cells, Pili and Turbine

The experimental system we are mimicking are bacterial cells confined in a box with the turbine at its center (see **Figure 1B**). The cells can move over the substrate via pili binding and unbinding and additionally interact with the turbine by pili attachment and excluded volume effects.

While *Neisseria gonorrhoeae* cells typically have a diplococcus shape [27], we simplify the *in silico* cell shape of bacteria as two-dimensional circular disks with a radius R. Please note, however, that a diplococcus shape can be also considered [19, 23–25]. Each cell possesses exactly N_p pili that are homogeneously distributed on the cell outline (see **Figure 1A**). We approximate pili as straight lines connecting two points: their start point (also called anchor point), located at the circular cell surface, and their end point. The distance between these two points is called the contour length l_c of the pilus.

The turbine is described by $N_{\text{turb}} \times 2$ disks (with radius R) arranged in a double row array (see **Figure 1B**). Since the only way how the turbine can move is by rotation, the relative locations of the turbine disks towards each other are fixed. The orientation of the turbine is described by the angle α with respect to the y-axis and the turbine center is located at the position $\mathbf{r}^{(\text{turb})}$ (see **Figure 1B**).

2.2 Pili Dynamics and Binding Properties

Initially, a pilus protrudes with the velocity v_p in a direction perpendicular to the cell surface. When a pilus reaches a specific length, drawn from an exponential length distribution with mean length l_p [17, 18], it starts to retract with a velocity $v_r^{(0)}$. This retraction continues until the pilus has a contour length $l_c = 0$. In that case, the pilus is removed and immediately, a new pilus protrudes from the cell from the same position.

A pilus binds stochastically to the substrate or the turbine disks, independently whether it is protruding or retracting. In both cases, a pilus can only bind with its tip and it can bind only to either the substrate or the turbine disks. After binding, a pilus immediately starts to retract [28]. The binding is modeled as a Poisson process with the binding rate $\kappa_{\text{att}}^{(\text{sub})}$ to the substrate and $\kappa_{\text{att}}^{(\text{turb})}$ to any of the turbine disks. Since the model is two-dimensional, we ignore that, for pili to bind to a substrate, they first need to be long enough to reach the substrate with their tips. In 3D, this leads to a delay in the initial binding event of a newly protruding pilus, but is less relevant for following attachments of pili. Hence, initially, the binding rate might be smaller to allow a pilus to protrude to reach the substrate. To account for this process, pili that bind to the substrate the first time do so with a rate $\kappa_{\text{att}}^{(\text{sub},0)} = v_p/l_p$. Again, the binding is modelled as a Poisson process. The rate $\kappa_{\text{att}}^{(\text{sub},0)}$ corresponds to the binding of a pilus that protrude with the velocity v_p until it reaches a length determined by an exponential distribution with mean length l_p, in which case it binds. On average, this takes the time $1/\kappa_{\text{att}}^{(\text{sub},0)}$.

An attached pilus will generate a pulling force that acts on the cell and, if attached to a turbine disk, also on the turbine. Each pilus is modeled as a Hookean spring with the spring constant k_p. After attachment, a pilus is stretched due to its retraction and hence, mediates a pulling force. This force is proportional to the difference between the contour length l_c and the length of the pilus that it would have if it was not attached, here called the free length l_f. Here, we consider the case where a pilus can only generate a pulling force and no pushing force, thus the force is zero if $l_c \leq l_f$.

Experimentally, it has been shown that the pilus force affects the retraction velocity by

$$v_r = \max\left[0, v_r^{(0)}\left(1 - \frac{F}{F_s}\right)\right], \tag{1}$$

with the stalling force F_s [22]. The force of a pilus also affects the unbinding from the substrate. Pilus detachment is modelled by a Poisson process with the rate

$$\kappa_{\text{det}}^{(\text{sub})}(F) = \frac{1}{\tau_{\text{det}}^{(\text{sub},1)} \exp\left(-\frac{F}{F_{\text{det}}^{(\text{sub},1)}}\right) + \tau_{\text{det}}^{(\text{sub},2)} \exp\left(-\frac{F}{F_{\text{det}}^{(\text{sub},2)}}\right)}, \tag{2}$$

for detachment from the substrate, as motivated by [18]. Here, we introduce the detachment times $\tau_{\text{det}}^{(\text{sub},1)}$ and $\tau_{\text{det}}^{(\text{sub},2)}$ and the detachment forces $F_{\text{det}}^{(\text{sub},1)}$ and $F_{\text{det}}^{(\text{sub},2)}$. For detachment from a turbine disk, we describe the rate by a simpler relation

$$\kappa_{\text{det}}^{(\text{turb})} = \frac{1}{\tau_{\text{det}}^{(\text{turb})}} \exp\left(\frac{F}{F_{\text{det}}^{(\text{turb})}}\right), \tag{3}$$

with the detachment time $\tau_{\text{det}}^{(\text{turb})}$ and detachment force $F_{\text{det}}^{(\text{turb})}$. We picked a different expression for the pili-turbine detachment (in comparison to the pili-substrate detachment) because in general, the turbine does not necessarily have to consist of the same material as the substrate, which determines pili binding properties [16, 17]. Below, we will explore turbine rotation in dependence on pili-turbine interactions, thus favouring a simpler single exponential form.

2.3 Cell Forces and Motility

We model pili as Hookean springs with the spring constant k_p. For a cell i at location $\mathbf{r}_i^{(\text{cell})}$, an attached pilus j causes a force $\mathbf{F}_i^{(\text{pilus j})}$ at the pilus anchor point $\mathbf{r}_i^{(\text{anchor j})}$ on the surface of the cell in the direction of the point $\mathbf{r}_i^{(\text{att j})}$ where the pilus tip is attached (see **Figure 1C**).

Next to the active pili force, passive excluded volume forces are acting on the cells. Cells are located in a two-dimensional box with size $L \times L$ and a cell i that overlaps with the boundary wall is exposed to a repulsive force $\mathbf{F}_i^{(\text{wall})}$ (see **Figure 1C**). This force is modelled as a harmonic interaction with spring constant $k^{(\text{wall})}$ and acts on the cell center in the normal direction of the boundary wall if the overlap is smaller than the cell radius R. Additionally, intersections of 2 cells i and k lead to a repulsive force $\mathbf{F}_{ik}^{(\text{c-c})}$ of the centers of both cells with the spring constant $k^{(\text{c-c})}$ (see **Figure 1C**). A similar type of repulsive force $\mathbf{F}_i^{(\text{turb m})}$ is acting between the cells and the turbine disks m with the spring constant $k^{(\text{turb})}$ (see **Figure 1C**).

The total force of the cell i is given by

$$\mathbf{F}_i^{(\text{tot})} = \sum_{\text{attached pili } j} \mathbf{F}_i^{(\text{pilus j})} + \mathbf{F}_i^{(\text{wall})} + \sum_{\text{cells } k} \mathbf{F}_{ik}^{(\text{c-c})} + \sum_{\text{turbine disks } m} \mathbf{F}_i^{(\text{turb m})}. \tag{4}$$

Additionally, the total torque acting on a cell is

$$\mathbf{T}_i^{(\text{tot})} = \sum_{\text{attached pili } j} \left(\mathbf{r}_i^{(\text{anchor j})} - \mathbf{r}_i^{(\text{cell})}\right) \times \mathbf{F}_i^{(\text{pilus j})} \tag{5}$$

In the overdamped limit [29], a force mediates a translational motion of the cell with the velocity

$$\frac{d\mathbf{r}_i^{(\text{cell})}}{dt} = \mu_t \mathbf{F}_i^{(\text{tot})} \tag{6}$$

and the torque leads to a rotation with the angular velocity vector

$$\boldsymbol{\omega}_i^{(\text{cell})} = \mu_r \mathbf{T}_i^{(\text{tot})} \tag{7}$$

TABLE 1 | List of parameters used in this study.

Name		Value	References
Cell and turbine disk radius	R	0.5 μm	[17]
Cell number	N	40	
Cell density	ρ	0.1 μm^{-2}	
Pili number per cell	N_{p}	15	[16, 17]
Number of turbine disk pairs	N_{turb}	12	
Pili protrusion velocity	v_{p}	2 μm/s	[22]
Pili mean length	l_{p}	1.5 μm	[18, 17]
Pili retraction velocity	$v_{\mathrm{r}}^{(0)}$	2 μm/s	[22]
Pili-substrate attachment rate	$\kappa_{\mathrm{att}}^{(\mathrm{sub},0)}$	1.33333 Hz	[22]
	$\kappa_{\mathrm{att}}^{(\mathrm{sub})}$	10 Hz	[18]
Pili-turbine attachment rate	$\kappa_{\mathrm{att}}^{(\mathrm{turb})}$	2 Hz	
Pili spring constant	k_{p}	2000 pN/μm	[31]
Stalling force	F_{s}	180 pN	[22]
Pili detachment times	$\tau_{\mathrm{det}}^{(\mathrm{sub},1)}$	0.85 s	[18]
	$\tau_{\mathrm{det}}^{(\mathrm{sub},2)}$	0.04 s	[18]
	$\tau_{\mathrm{det}}^{(\mathrm{turb})}$	50 s	
Pili detachment forces	$F_{\mathrm{det}}^{(\mathrm{sub},1)}$	1.24 pN	[18]
	$F_{\mathrm{det}}^{(\mathrm{sub},2)}$	33.8 pN	[18]
	$F_{\mathrm{det}}^{(\mathrm{turb})}$	180 pN	
Box size	L	20 μm	
Wall spring constant	$k^{(\mathrm{wall})}$	5,000 pN/μm	
Cell-cell spring constant	$k^{(\mathrm{c-c})}$	5,000 pN/μm	
Cell-turbine spring constant	$k^{(\mathrm{turb})}$	5,000 pN/μm	
Cell translational mobility	μ_{t}	2 μm/(s pN)	[23]
Cell rotational mobility	μ_{r}	720/π °/(μm *pN s*)	[23]
Turbine rotational mobility	μ_{turb}	0.9/π °/(μm *pN s*)	
Time step	δt	10^{-5} s	
Simulation time	T	10^4–10^5 s	
Simulation No. per parameter set	N_{sim}	80–100	

Here, we introduce the translational mobility μ_{t} and the rotational mobility μ_{r}. The same forces and torques cause an equivalent displacement of the pili anchor points $\mathbf{r}_i^{(\mathrm{anchor}\ j)}$ and attachment points $\mathbf{r}_i^{(\mathrm{att}\ j)}$ in case of attachment to a turbine disk. The mobilities introduced here are a result of friction with the viscous solvent and the substrate on which the cells are moving.

2.4 Turbine Torque and Rotation

The turbine is only able to undergo rotational motion. The total torque acting on the turbine is given by

$$\mathbf{T}^{(\mathrm{turb})} = \sum_{\text{attached pili } j} \left(\mathbf{r}_i^{(\mathrm{att}\ j)} - \mathbf{r}^{(\mathrm{turb})}\right) \times \mathbf{F}_i^{(\mathrm{pilus}\ j)} + \sum_{\text{cells } i} \sum_{\text{turbine disks } m} \left(\mathbf{r}_i^{(\mathrm{cell})} - \mathbf{r}^{(\mathrm{turb})}\right) \times \left(-\mathbf{F}_i^{(\mathrm{turb}\ m)}\right). \tag{8}$$

The rotation of the turbine is modelled in the overdamped limit with a mobility μ_{turb}. In that case, the turbine angular velocity vector is

$$\boldsymbol{\omega}^{(\mathrm{turb})} = \mu_{\mathrm{turb}} \mathbf{T}^{(\mathrm{turb})}. \tag{9}$$

2.5 Parameters and Details of Numerical Solution

The simulations were performed on the local computing cluster of the Max Planck Institute for the Physics of Complex Systems (Dresden, Germany), consisting of x86-64 GNU/Linux systems. The code was written in C++. We use an Euler algorithm to solve the equations of motion with a time step δt. While this is one of the most simple numerical schemes to solve the equations of our computational model, it often leads to numerical errors and instabilities when modelling molecular dynamics systems for long times [30]. We do not expect that this is a problem in our system due to the stochastic nature of the pili binding and unbinding, which basically represents our system as a series of many short time events, continuously interrupted by rearrangements in the pili network. Hence, we do not expect any differences in the qualitative outcome of the simulations.

If not stated otherwise, we use the parameters provided in **Table 1**. Most parameters we use are based on previous studies. The excluded volume spring constants $k^{(\mathrm{c-c})}$, $k^{(\mathrm{turb})}$ and $k^{(\mathrm{wall})}$ have no effect on the simulation outcome as long as they are chosen large enough to be able to compete with the pili forces. For the remaining parameters, e.g., the turbine mobility, we do not expect a qualitative difference in the results of the simulation.

We initialize the simulation by randomly distributing the cells in the box and only analyse the turbine rotation after an initialization period of 1,000 s. To calculate the angular velocity of the turbine rotation, we compute

$$\omega_\alpha(t) = \frac{\alpha(t + \Delta t) - \alpha(t)}{\Delta t}, \tag{10}$$

with $\Delta t = 0.5$ s and the turbine orientation α (see **Figure 1B**).

3 RESULTS

In the following, we first demonstrate that bacteria binding to the turbine with the help of pili can cause a persistent turbine rotation over time scales that exceed the pili detachment times significantly. Next, we study how the persistent turbine rotation depends on the binding properties of the pili to the turbine and the number of cells in the system. This allows us to unravel the underlying mechanism that causes the persistent rotation of the turbine. Finally, we propose a system where an asymmetric binding of the pili to the turbine causes a permanent unidirectional rotation of the turbine.

3.1 Adhesion of Motile Bacteria Drives Turbine Rotation

To investigate how the adhesion of cells to a turbine affects the turbine rotation, we first simulate the computational model for three different cases: 1) pili detach with detachment times of $\tau_{\mathrm{det}}^{(\mathrm{turb})} = 50$ s (see **Figure 2A** and **Supplementary Movie S1**), motivated by binding times in the order of a few minutes inferred from cell trajectories on plastic surfaces [17], 2) pili detach with $\tau_{\mathrm{det}}^{(\mathrm{turb})} = 2$ s (see **Supplementary Movie S2**), motivated by considerably smaller binding times experimentally measured for BSA coated beads [18] and 3) pili not bind to the turbine at all (see **Supplementary Movie S3**)

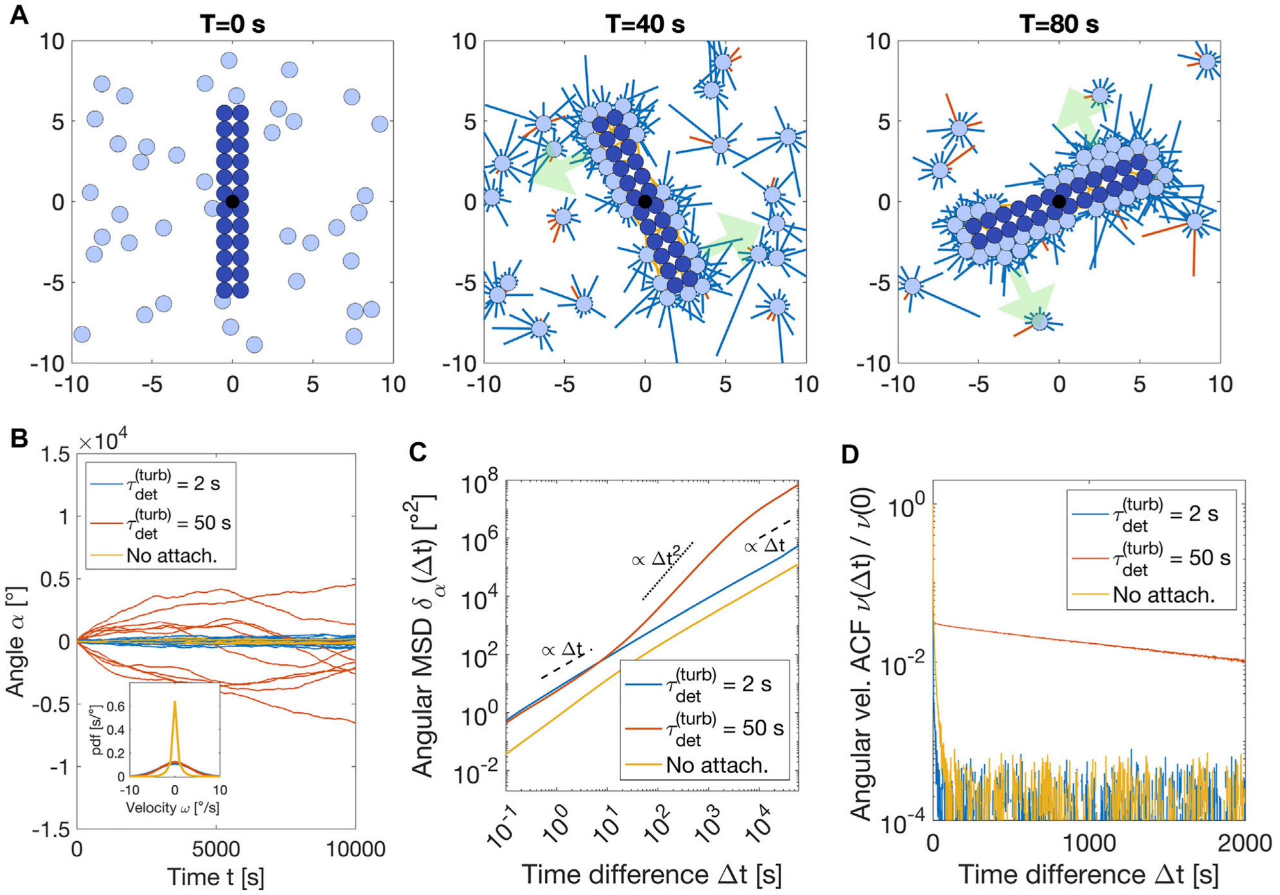

FIGURE 2 | Analysis of rotary motion of a turbine in a bath of twitching bacteria. **(A)** Snapshots of the initial phase of the simulations of a turbine in a bath of bacteria with pili detachment rate $\tau_{\mathrm{det}}^{(\mathrm{turb})} = 50$ s. Blue pili are not attached, orange pili are attached to the turbine and red pili are attached to the substrate. The green arrow indicates the direction of the turbine rotation. **(B)** Turbine angle α as a function of the time t (see **Figure 1B**.). The inset figure shows the probability density function of the turbine angular velocity ω. **(C)** Angular mean squared displacement (angular MSD) of the turbine angle, see **Eq. 11**. **(D)** Normalised angular velocity autocorrelation function of the turbine angle, see **Eq. 12**.

and the only way how cells interact with the turbine is by excluded volume forces. Here, we only vary the turbine detachment time $\tau_{\mathrm{det}}^{(\mathrm{turb})}$ and not the detachment force $F_{\mathrm{det}}^{(\mathrm{turb})}$. We expect that there will be no qualitative difference in the turbine rotation for both cases, an increase (decrease) of $\tau_{\mathrm{det}}^{(\mathrm{turb})}$ and a increase (decrease) of $F_{\mathrm{det}}^{(\mathrm{turb})}$, pili will bind more (less) strongly to the turbine. For simplicity, we assume that $F_{\mathrm{det}}^{(\mathrm{turb})} := F_s$ with the pilus stalling force F_s, see **Eq. 1**. In **Figure 2B**, we show the dynamics of the turbine angle α for the three cases. We find that for the largest detachment time, $\tau_{\mathrm{det}}^{(\mathrm{turb})} = 50$ s, the rotation is the strongest. If pili are not permitted to attach to the turbine, the rotation appears to be the weakest. Additionally, the distribution of velocities shows that if pili cannot bind to the turbine, the turbine will move with smaller angular velocities ω, while the distributions seem to not depend on the detachment rate $\tau_{\mathrm{det}}^{(\mathrm{turb})}$, as long as pili are capable of binding to the turbine. We also find that the turbine does not undergo extended phases in which it is not moving, but instead seems to be continuously rotating (see **Supplementary Figure S1**).

To quantify how strong the rotation is, we compute the angular mean squared displacement (angular MSD), given by

$$\delta_\alpha(\Delta t) = \langle [\alpha(t+\Delta t) - \alpha(t)]^2 \rangle_t, \tag{11}$$

(see **Figure 2C**). Indeed, the angular MSD is the highest for $\tau_{\mathrm{det}}^{(\mathrm{turb})} = 50$ s and the lowest for the case where pili do not attach to turbine disks. For $\tau_{\mathrm{det}}^{(\mathrm{turb})} = 2$ s, the angular MSD is identical to the case $\tau_{\mathrm{det}}^{(\mathrm{turb})} = 50$ s for small time differences (Δt). In both cases, $\tau_{\mathrm{det}}^{(\mathrm{turb})} = 2$ s and non-attaching pili, the angular MSD follows a linear scaling, $\delta_\alpha \propto \Delta t$, corresponding to a diffusive regime. For $\tau_{\mathrm{det}}^{(\mathrm{turb})} = 50$ s, we find a superdiffusive regime for intermediate time differences $\Delta t \approx 10, -,10^3$ s. For particles undergoing translational motion, such superdiffusive regimes usually emerge from ballistic motion. For the rotatable turbine, this corresponds to a regime where the turbine moves persistently in a random direction. Indeed, such a behaviour is observed in **Figure 2B**, where trajectories of the angle α move persistently in one direction over periods of hundreds to thousands of seconds before the rotation turns towards the opposite direction. For larger

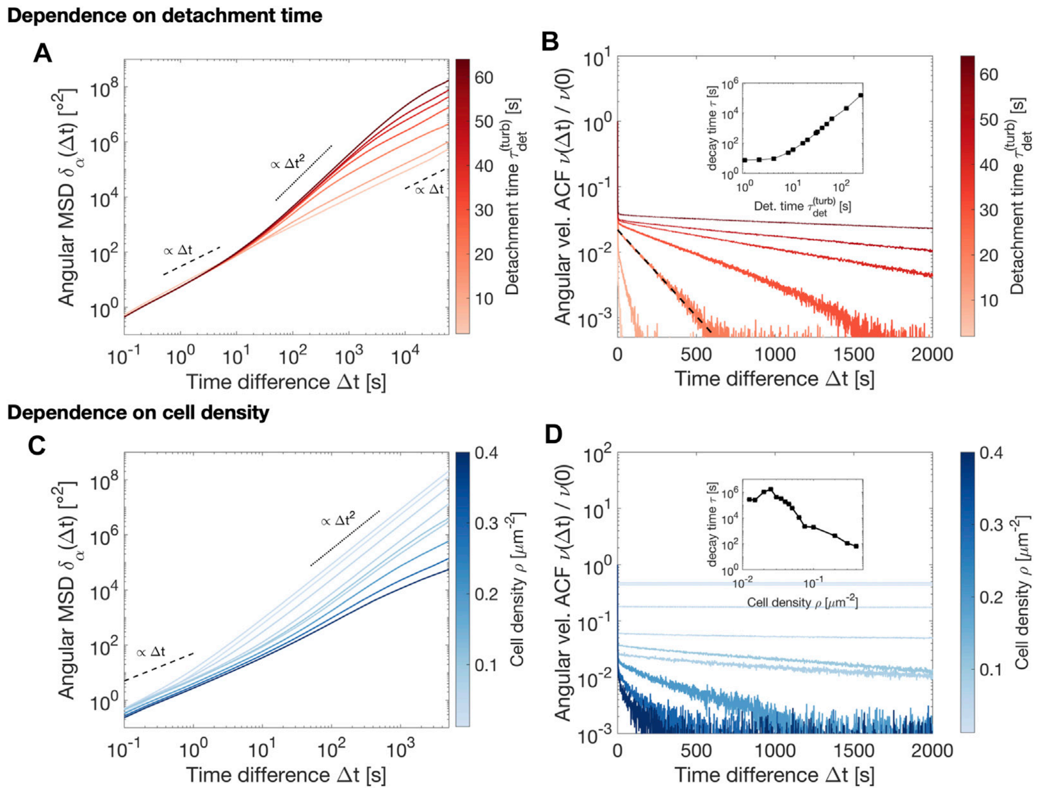

FIGURE 3 | Dependence of the turbine rotation on pili detachment time $\tau_{det}^{(turb)}$ and cell density ρ. **(A,C)** Angular mean squared displacement (angular MSD) $\delta_\alpha(\Delta t)$ of the turbine angle α as a function of the pili-turbine detachment time $\tau_{det}^{(turb)}$ (with the cell density at ρ =0.1 μm^2) or cell density ρ (with the detachment time $\tau_{det}^{(turb)}$ = 50 s). **(B,D)** Normalised angular velocity autocorrelation function (angular velocity ACF) $\nu(\Delta t)/\nu(0)$ of the turbine angle α as a function of the pili-turbine detachment time $\tau_{det}^{(turb)}$ or cell density ρ. The inset figure shows the characteristic time scale of $\nu(\Delta t)$, resulting from a fit $\nu(\Delta t) \propto \exp(-\Delta t/\tau)$. To account for the initial drop of the angular velocity ACF, we only do the fitting for Δt >2s. An example fit is shown in **(B)** (black dashed line). Please note that for the investigation of the cell density dependence of the turbine rotation, we only consider a smaller range of Δt to avoid too high numerical cost. As a result, we do not show the diffusive regime in the MSD for large values of Δt since the angular velocity ACF is decaying with increasing Δt.

time differences, the angular MSD becomes again diffusive, implying that while the rotation is persistent over a certain time scale, for larger time intervals it becomes random again.

To learn more about how persistent the turbine rotation is, we compute the angular velocity autocorrelation function (angular velocity ACF), given by

$$\nu(\Delta t) = \langle \omega_\alpha(t+\Delta t)\omega_\alpha(t)\rangle_t. \tag{12}$$

Independently of whether pili can bind to the turbine or not, we find that the correlation function $\nu(\Delta t)$ is decaying with time (see **Figure 2D**). This confirms our previous observation for the angular MSD where we found that for very large time differences the turbine rotation is diffusive and no longer shows signs of persistence. We also find that for $\tau_{det}^{(turb)}$ = 50 s, the normalised angular velocity ACF $\nu(\Delta t)/\nu(0)$ has the slowest decay. This behaviour correlates with the persistent rotation for time differences between $\Delta t \approx 10$, $-,10^3$. Surprisingly, we find that the decay of the angular velocity ACF is faster for $\tau_{det}^{(turb)}$ = 2 s than for the case where pili do not bind to the turbine. We will provide an explanation for this behaviour in **Section 3.3**. Before doing that, we will have a closer look at how the turbine rotation depends on the cell adhesion to the turbine disks and the number of cells in the system.

3.2 Turbine Rotation Is Controlled by Bacterial Adhesion Strength and Cell Number

We begin with a systematic analysis of how the angular MSD $\delta_\alpha(\Delta t)$ depends on the detachment time of pili from the turbine disks $\tau_{det}^{(turb)}$, shown in **Figure 3A**. For small time differences $\Delta t <$ 10 s, we find that δ_α is independent of $\tau_{det}^{(turb)}$ and exhibits a linear scaling, $\delta_\alpha \propto \Delta t$, corresponding to a diffusive regime. For high enough values of the detachment time $\tau_{det}^{(turb)}$ and $\Delta t >$ 10 s, the angular MSD becomes superdiffusive, $\delta_\alpha \propto \Delta t^2$. The duration of this superdiffusive regime increases with increasing $\tau_{det}^{(turb)}$ and is barely observable for detachment times $\tau_{det}^{(turb)} <$ 10 s. For even longer time differences Δt, the MSD becomes diffusive again, $\delta_\alpha \propto \Delta t$.

Next, we investigate the normalised angular velocity ACF $\nu(\Delta t)/\nu(0)$ (see **Figure 3B**) and find that for $\Delta t <$ 2 s, it rapidly decreases. For $\Delta t \geq$ 2 s, it exponentially decreases with the Δt. By fitting a function of the form $\nu(\Delta t) \propto \exp(-\Delta t/\tau)$ to this

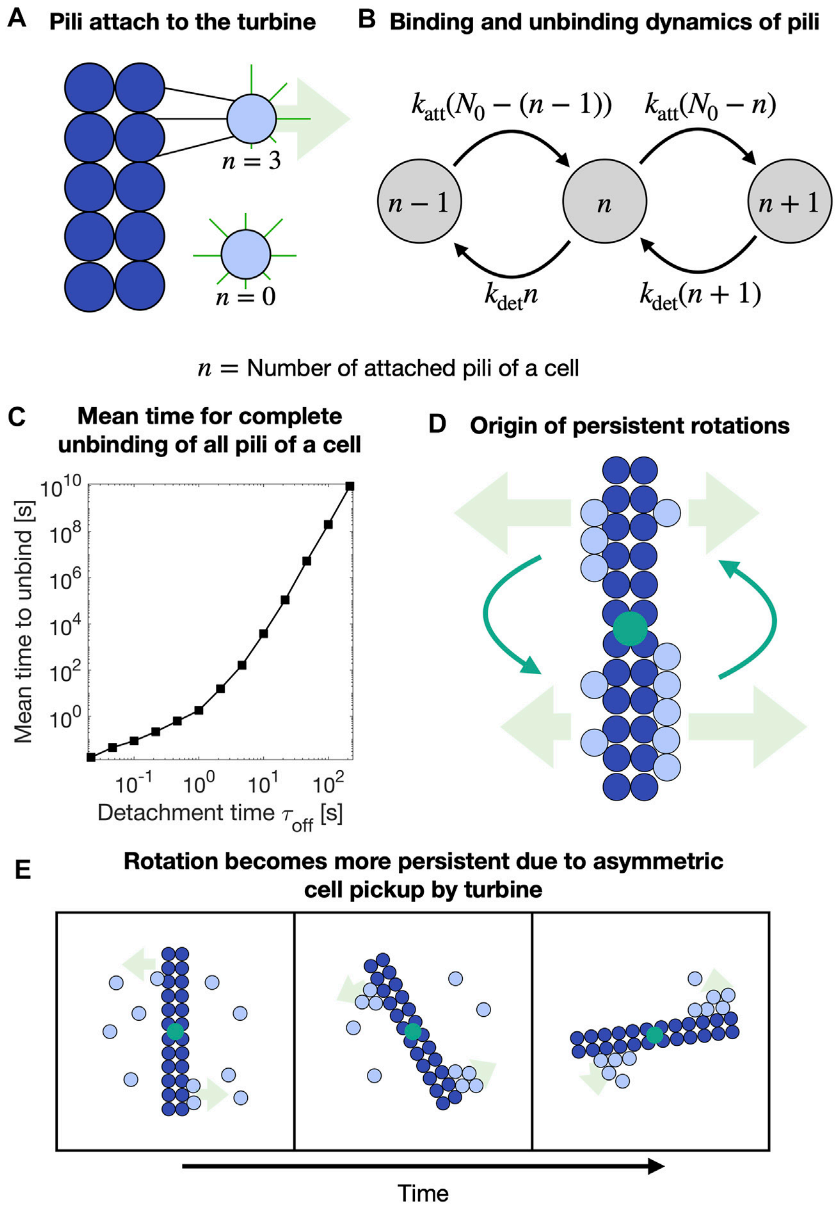

FIGURE 4 | Overview of the mechanism driving the persistent rotation of the turbine. **(A)** A cell (light blue circle) with $n = 3$ or $n = 0$ pili attached to a turbine (dark blue circles). **(B)** Stochastic model of n pili attached to a turbine with pili binding (with constant rate k_{att}) and unbinding (with constant rate k_{det}). **(C)** Mean unbinding time to reach for the first time the state $n = 0$ in the stochastic model. Here, we chose $N_0 = 5$, $n(t = 0) = 5$, $k_{\mathrm{att}} = 2$ Hz, $k_{\mathrm{det}} = (\exp 1)/\tau_{\mathrm{off}}$. **(D)** Sketch of how turbine rotation is affected by multiple cells binding to the turbine surface. The turbine rotates in the direction in which more cells are attached to its surface (turbine is pulled by cells). **(E)** Sketch of how turbine rotation leads to a pickup and binding of cells on the turbine surface.

later regime, we identify the characteristic time τ of the exponential decay of $\nu(\Delta t)$ and can investigate its dependence on $\tau_{\mathrm{det}}^{(\mathrm{turb})}$. We find that it is increasing with increasing detachment times $\tau_{\mathrm{det}}^{(\mathrm{turb})}$. This is in accordance with the increasing duration of the superdiffusive regime of the angular MSD. The stronger pili of a cell bind to the turbine, the more persistently the turbine rotates in one direction before it inverts its direction.

Additionally, we investigated how the rotation of the turbine is affected by the density ρ of cells in the system. We find that with increasing density, the angular MSD δ_α becomes smaller (see **Figure 3C**). While we observe the diffusive regime of $\delta_\alpha(\Delta t)$ for $\Delta t < 10$ s, a pronounced superdiffusive regime for larger Δt vanishes if the cell density becomes too large. For the normalised angular velocity ACF $\nu(\Delta t)/\nu(0)$ (see **Figure 3D**), the characteristic decay time τ is initially increasing with cell density ρ and then decreases when ρ increases further.

In the following section, we provide qualitative arguments that explain the observed behaviours.

3.3 Unbinding Dynamics of Attached Bacteria Explains Characteristic Time of Turbine Rotation

To understand how the persistent rotation of the turbine in an otherwise symmetric system can emerge, we first consider how strongly cells bind to the turbine disks with the help of their pili and how pili binding affects substrate attachment of the remaining pili. Our hypothesis is the following: if cells stay attached to the same position on the turbine surface for an extended time, which is considerably larger than average attachment times of individual pili, the cells will continuously pull the turbine in the same direction. This mechanism is dramatically different to the previously reported rotary microdevices driven by swimming bacteria [6, 7], where cells collide with the microdevice and hence, push it. Instead, in our simulations, cells pull on the turbine. In **Figure 4A**, we show sketch of a cell which is attached to the turbine disk with some of its pili, while the other pili bind or unbind from the substrate. Only pili that protrude towards the turbine disks can attach, while pili protruding away from the turbine can only attach to the substrate. Thus, cells preferentially bind to the substrate in the direction away from the turbine. Since the cell is also attached with some of its pili to the turbine disks, it is pulling the turbine along the direction pointing from the turbine towards the cell. Thus, the cell pulls on the turbine, leading to a rotation of the turbine in the direction of the attached cell. This process is enhanced by the cooperation of multiple pili of a cell. To clarify this, we investigate the durations of cells attaching to the turbine disk before they detach again. To this aim, we solve a stochastic model of pili binding and unbinding, where a cell, possessing in total N_0 pili that are all growing in the direction of the turbine, has n pili attached to the turbine. With a rate $k_{\mathrm{att}}\,(N_0 - n)$ a non-attached pilus attaches to the turbine, while with the rate $k_{\mathrm{det}}n$ a pilus detaches from the turbine (see **Figure 4B**). By describing the attachment and detachment as Poisson processes, we can numerically solve this system with the help of a Gillespie algorithm and investigate the mean time for a complete unbinding of all pili of a cell from the turbine (see **Figure 4C**). We find that the mean unbinding time is increasing rapidly with the pili detachment time $\tau_{\mathrm{off}} = \exp\left(F_{\mathrm{s}}/F_{\mathrm{det}}^{(\mathrm{turb})}\right)/k_{\mathrm{det}}$, reaching around 10 s for $\tau_{\mathrm{off}} = 2$ s and 10^7 s for $\tau_{\mathrm{off}} = 50$ s. For simplicity, we assume that all pili pull with their stalling force and that the detachment force is identical to the stalling force, $F_{\mathrm{s}} = F_{\mathrm{det}}^{(\mathrm{turb})}$. The duration of how long cells bind to the turbine corresponds to the duration of superdiffusive behaviour in **Figure 3A** and also exhibits the same qualitative behaviour as the decay time of the angular velocity autocorrelation (see **Figure 3B**). We do not expect a perfect quantitative agreement between the two time scales (**Figure 3B** and **Figure 4C**) as the simplified model of pili binding and unbinding of a cell to the turbine provided here ignores that cells can indeed move even if its pili are bound to the turbine, e.g., parallel to the turbine surface. Additionally, when multiple cells bind to the same region of the turbine, they will interact *via* excluded volume effects. This will lead to additional forces acting on the involved pili and thus, might enhance their detachment.

We can now provide an explanation of the three time regimes observed in the angular MSD in **Figure 2C** and angular velocity ACF in **Figure 2D**. For short times, $\Delta t < 10$ s, individual pili stochastically bind and unbind to the substrate, pulling on the turbine, and additionally, cells randomly collide with the turbine. This causes small displacements of the turbine angle α in one direction, also explaining the very sudden drop of the angular velocity ACF for short times since the life time of such displacements is very small. This leads to random fluctuations of the turbine, and as a result, to a diffusive scaling. For larger times, $10\ \mathrm{s} < \Delta t < 10^3$ s, asymmetries in the distribution of cells on the surface of the turbine lead to a unidirectional rotation of the turbine and as a result, to a superdiffusive regime. The persistence in the turbine rotation also explains the positive angular velocity ACF. The duration of this regime depends on how strong pili bind to the turbine disk (see **Figure 4C**). Finally, for $\Delta t > 10^3$ s, the distribution of cells on the turbine surface is re-arranged up to such a degree that the turbine can change its direction of motion. This will then lead to a diffusive regime again. This time also corresponds to the characteristic time of the angular velocity ACF decay, confirming that for large enough times, the turbine forgets its initial direction of motion.

For cases where pili bind stronger to the turbine, we expect to not only have more pili to bind to the turbine, but also more cells to be bound to the turbine with its pili. To this aim, we check the number of cells and pili bound to the turbine as a function of time (see **Supplementary Figure S2**). We find that after an initial phase of pili attachment, for larger pili-turbine detachment times $\tau_{\mathrm{det}}^{(\mathrm{turb})}$ more cells and more pili are bound to the turbine on average. This is in agreement with our previously introduced hypothesis that the turbine exhibits persistent rotational motion due to cells that are bound to the turbine surface.

Next, we consider the origin of the cell density dependent rotation of the turbine, see **Figure 3C** and **Figure 3D**. If the cell density is very small, often no cell will bind to the turbine most of the time and thus, the angular MSD is initially increasing with cell density. For moderate cell densities the difference between cells attaching to different sides of the turbine (see **Figure 4D**) will be significant and due to the random asymmetry, the turbine will rotate persistently in one direction until cells randomly unbind from the turbine. If the cell density gets too large, more and more cells are pulling in the opposite direction of the turbine rotation, reducing its persistence.

There are additional processes that can have a significant impact on the turbine rotation: 1) Due to the rotation of the turbine, it will constantly "pick up" cells it collides with. For the traditional rotary microdevices that are driven by swimming bacteria that collide with the device and push it [6–8], this would lead to a torque that acts in the opposite direction of the original rotation. When cells pull on the turbine instead, the persistent rotation is being enhanced since asymmetric distribution of cells bound to the turbine disks is getting even stronger (see **Figure 4E**). 2) In **Section 3.1**, we found that the angular velocity ACF seems to decay faster for the case with pili attachment and $\tau_{\mathrm{det}}^{(\mathrm{turb})} = 2$ s, than for the case without pili attachment (see **Figure 2D**). A possible explanation for this is that even without pili-turbine attachment, cells can still rotate the turbine due to collisions and resulting excluded volume forces. That

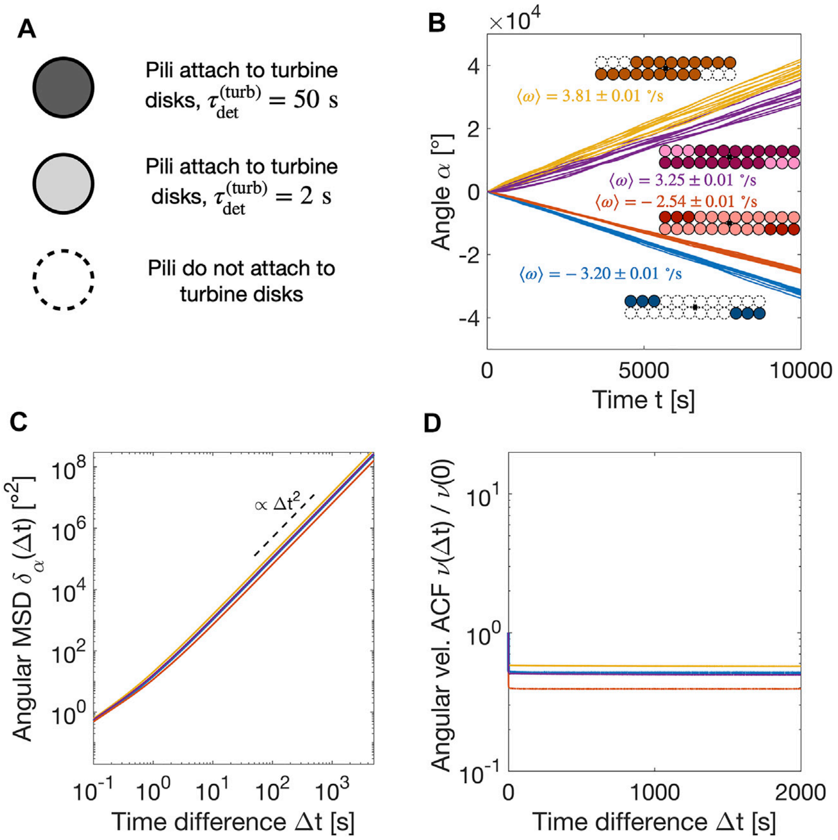

FIGURE 5 | Unidirectional persistent turbine rotation is caused by asymmetric pili binding to the turbine. **(A)** Overview of the different types of turbine disks considered here. **(B)** Angle α of the turbine as a function of time t for different combinations of the manipulated turbine disks. We also provide the average angular velocity $\langle\omega\rangle$ and its standard error for each condition. **(C)** The angular mean squared displacement exhibits superdiffusive (ballistic) scaling, $\delta_\alpha \propto \Delta t^2$. **(D)** The normalised angular velocity auto correlation function is no longer decaying with increasing time differences Δt, corresponding to the unidirectional rotation.

way, we reproduce a system where cells push the turbine, instead of pulling on it. This process possesses its own characteristic time scales that are linked to the substrate motility of the cells.

To summarise, the persistent rotation of the turbine originates from persistent attachment of cells to the turbine over times scales much longer than the characteristic detachment times of individual pili. While the resulting rotation is indeed persistent and, depending on the binding properties, can go on over multiple revolutions, it is not permanently unidirectional. There is no asymmetry in the initial rotational direction of the turbine and even though the turbine can move in one direction over an extended time, this rotation will at some point reverse direction. Next, we will provide an example of how cells using type IV pili can drive a permanent unidirectional rotation of a turbine.

3.4 Permanent Unidirectional Rotation due to Asymmetric Cell-Turbine Attachment

In order to produce a permanent unidirectional rotation of the turbine, an asymmetry of the turbine is required. Typically, such assymetries are created by altering the turbine geometry [7, 8, 12], but here we have a chance to exploit asymmetries in the adhesion of cells to the turbine instead. In **Figure 5A**, **Figure 5B** and **Supplementary Movie S4**, we provide an example of how altered pili binding properties on one side of the turbine wings can lead to a unidirectional rotation. Here, we consider different cases: 1) pili bind stronger to the manipulated turbine disks, corresponding to a larger detachment time $\tau_{\rm det}^{\rm (turb)}$ or 2) pili bind weaker to the manipulated turbine disks, with a lower value of $\tau_{\rm det}^{\rm (turb)}$. Depending on how pili bind to these regions, the direction of the turbine is affected as, on average, cells are more or less strongly adhered to the manipulated region and thus, more or less cells are bound to these sides of the turbine and mediate the turbine rotation. In case (i), the turbine rotates in the direction of manipulated region because more cells are attached there, for 2) less cells are attached in the manipulated region and the turbine rotates in the opposite direction.

We also estimate the average angular velocity ω of the turbine and find values around 2–4°/s. For the used rotational mobility of the turbine $\mu_{\rm turb}$ (see **Table 1**), this corresponds to a turbine torque around $10\,pN\,\mu m$, comparable to previously published values for rotary devices in bacterial baths of hundreds of swimming cells [7]. Here, however, the system consists of 40 cells only. Note that this is only the lower limit of the turbine torque and the same turbine might be able to generate larger torques if it experiences an opposing torque. In the absence of a counteracting torque, the rotation speed of the turbine is limited by the retraction velocity of pili, around $2\,\mu$m/s [22].

We see evidence that the rotation is permanently unidirectional in the angular MSD (see **Figure 5C**) which is superdiffusive (ballistic) for arbitrary time differences Δt, equivalent to a rotation in one direction. Additionally, the normalised angular velocity ACF (see **Figure 5D**) is no longer decaying with time Δt, suggesting a constant rotation in the same direction.

In experiments, such manipulated regions on the surface of the turbine could be generated by coating it with a chemical such as BSA, which has been shown to alter the detachment time of the pili [17, 18, 32].

4 DISCUSSION

In this study, we investigated how bacteria that use type IV pili for surface motility may drive the rotation of a micron-sized turbine. We found that due to spatial asymmetries in the amount of cells that are bound to the turbine, a persistent rotation is observed over time scales that can strongly exceed the characteristic time scales of the pili. The persistent rotation is enhanced when pili bind more strongly to the turbine and weaker when the density of cells becomes larger. The observed persistent rotation of a symmetric turbine has a characteristic time scale. For larger times, the rotation direction is reversed stochastically and there is no preferred direction of rotation. A persistent and unidirectional rotation can be generated by altering the binding properties of the type IV pili on parts of the turbine in an asymmetric manner.

To build a rotatable micron-sized device, typically microfabrication technologies are used [5, 6, 8]. Established technologies make it easy to construct the turbine body, but normally the microdevices are not attached to the substrate [9]. In that case, a geometrically symmetric turbine becomes comparable to a passive rod or polymer in a bath of active particles [33, 34], with two major differences: forces are exerted by pulling instead of pushing, and the attachment of a pulling cell to the microdevice can last longer compared to the single pilus retraction time. In this case, we may expect to see rotational and translational diffusion but also some more complex trajectories, e.g., where the turbine rotates itself and its center of mass is on a circular track. Interestingly, if the rod is not straight, but has a concave shape, it can lead to trapping of particles and persistent motion of the turbine [33, 35, 36] Harnessing the power of the turbine is considerably harder if the turbine exhibits translational motion. Hence, it is required to immobilise the center of rotation of the turbine to only allow for rotation. One way to do that would be to plug the turbine onto a immobile column. The column must have been microfabricated such that it is tightly connected to the substrate and can withstand the forces generated by the cells. An alternative solution could be to trap the turbine in a circular depression [6] that has the same radius as the turbine, so that the only degree of freedom is the turbine rotation.

Here, we have shown that microdevices immersed in a bath of bacteria that use pili, such as *Neisseria gonorrhoeae* or *Pseudomonas aeruginosa*, can efficiently harness the power of the type IV pilus machinery. This system is particularly superior to previously reported microdevices driven by swimming bacteria [6–8], since the involved molecular motor pilT is the strongest known molecular motor [22] and a single cell is capable of generating forces in the nano-Newton range.

In the future, it will be interesting to investigate the interplay of asymmetries in the geometrical and adhesive properties of the turbine. Additionally, we expect that the binding of pili with the substrate will also have an effect on the turbine rotation. Higher values of the pili-substrate detachment times $\tau_{\mathrm{det}}^{(\mathrm{sub},1)}$ and $\tau_{\mathrm{det}}^{(\mathrm{sub},2)}$ will lead to an increase in the torque exerted by attached cells on the turbine and will likely exceed the observed lower limit of the torque of around $10\,pN\,\mu m$. This will enable the turbine to more efficiently harness the work generated by type IV pili. Importantly, one needs to consider that if pili bind too strongly to the substrate, their substrate mobility will be weakened [19] and hence, it will be less likely that cells will be in the vicinity of the turbine. Furthermore, cells pulling in the direction opposite to the turbine rotation will exert larger forces opposing the rotation. In the future, it will be interesting to investigate the optimal substrate binding properties to maximize the turbine torque. Additionally, bacteria use type IV pili to form aggregates consisting of hundreds to thousands of cells [15, 23, 24, 37, 38]. The impact of this aggregation process on the turbine rotation remains unclear.

DATA AVAILABILITY STATEMENT

The source code of the computational model can be accessed via https://github.com/wolframponisch/Pili-Driven-Bacterial-Turbine. The Matlab scripts used to analyse the data and generate the figures are available upon request.

AUTHOR CONTRIBUTIONS

WP and VZ designed the research. WP carried out all numerical solutions. WP carried out analytical calculations. WP analyzed the data. WP and VZ wrote the article.

FUNDING

WP kindly acknowledges support from the Herchel Smith Fund (Herchel Smith Postdoctoral Fellowship).

ACKNOWLEDGMENTS

WP and VZ would like to thank the MPI-PKS IT department for access and help with the computer cluster.

SUPPLEMENTARY MATERIAL

The Supplementary Material for this article can be found online at: https://www.frontiersin.org/articles/10.3389/fphy.2022.875687/full#supplementary-material

Supplementary Figure S1 | Turbine angle α as a function of time t > 50000 s after the simulations started for three cases: Small Pili-turbine detachment rate τ (turb) det = 2 s, larger τ (turb) det = 50 s and no attachment of pili to the turbine. The turbine seems to be constantly rotating and does not exhibit extended periods without motion.

Supplemental Figure S2 | Number of cells that are attached to the turbine via its pili, number of pili attached to the turbine and number of pili per cell attached to the turbine as a function of time for two different cases: pili-turbine detachment rate τ (turb) det = 2 s and τ (turb) det = 50 s. We find that for τ (turb) det = 50 s the highest number of pili and cell are bound to the turbine. Additionally, we observe an intitial phase where the number of attached cells and pili increases before reaching a plateau. This corresponds to the phase where randomly distributed cells move into the vicinity of the turbine and binding to it randomly.

Supplementary Movie S1 | Movie of turbine in a bath of twitching bacteria with pili-turbine detachment time τ (turb) 378 ret = 50 s

Supplementary Movie S2 | Movie of turbine in a bath of twitching bacteria with pili-turbine detachment time τ (turb) 380 ret = 2 s.

Supplementary Movie S3 | Movie of turbine in a bath of twitching bacteria that do not bind to the turbine with their pili.

Supplementary Movie S4 | Movie of turbines with binding properties specified in **Figure 5**.

REFERENCES

1. Martel S, Tremblay CC, Ngakeng S, Langlois G. Controlled Manipulation and Actuation of Micro-objects with Magnetotactic Bacteria. *Appl Phys Lett* (2006) 89:233904. doi:10.1063/1.2402221
2. Behkam B, Sitti M. Effect of Quantity and Configuration of Attached Bacteria on Bacterial Propulsion of Microbeads. *Appl Phys Lett* (2008) 93:223901. doi:10.1063/1.3040318
3. Darnton N, Turner L, Breuer K, Berg HC. Moving Fluid with Bacterial Carpets. *Biophysical J* (2004) 86:1863–70. doi:10.1016/s0006-3495(04)74253-8
4. Gao Z, Li H, Chen X, Zhang HP. Using Confined Bacteria as Building Blocks to Generate Fluid Flow. *Lab Chip* (2015) 15:4555–62. doi:10.1039/c5lc01093d
5. Vizsnyiczai G, Frangipane G, Maggi C, Saglimbeni F, Bianchi S, Di Leonardo R. Light Controlled 3d Micromotors Powered by Bacteria. *Nat Commun* (2017) 8:15974–7. doi:10.1038/ncomms15974
6. Hiratsuka Y, Miyata M, Tada T, Uyeda TQP. A Microrotary Motor Powered by Bacteria. *Proc Natl Acad Sci U.S.A* (2006) 103:13618–23. doi:10.1073/pnas.0604122103
7. Angelani L, Di Leonardo R, Ruocco G. Self-starting Micromotors in a Bacterial bath. *Phys Rev Lett* (2009) 102:048104. doi:10.1103/PhysRevLett.102.048104
8. Di Leonardo R, Angelani L, Dell'Arciprete D, Ruocco G, Iebba V, Schippa S, et al. Bacterial Ratchet Motors. *Proc Natl Acad Sci U.S.A* (2010) 107:9541–5. doi:10.1073/pnas.0910426107
9. Sokolov A, Apodaca MM, Grzybowski BA, Aranson IS. Swimming Bacteria Power Microscopic Gears. *Proc Natl Acad Sci U.S.A* (2010) 107:969–74. doi:10.1073/pnas.0913015107
10. Pietzonka P, Fodor É, Lohrmann C, Cates ME, Seifert U. Autonomous Engines Driven by Active Matter: Energetics and Design Principles. *Phys Rev X* (2019) 9:041032. doi:10.1103/physrevx.9.041032
11. Wall D, Kaiser D. Type Iv Pili and Cell Motility. *Mol Microbiol* (1999) 32:01–10. doi:10.1046/j.1365-2958.1999.01339.x
12. Harshey RM. Bacterial Motility on a Surface: many Ways to a Common Goal. *Annu Rev Microbiol* (2003) 57:249–73. doi:10.1146/annurev.micro.57.030502.091014
13. Klausen M, Heydorn A, Ragas P, Lambertsen L, Aaes-Jørgensen A, Molin S, et al. Biofilm Formation by pseudomonas Aeruginosa Wild Type, Flagella and Type Iv Pili Mutants. *Mol Microbiol* (2003) 48:1511–24. doi:10.1046/j.1365-2958.2003.03525.x
14. Imhaus AF, Duménil G. The Number of neisseria Meningitidis Type Iv Pili Determines Host Cell Interaction. *Embo J* (2014) 33:1767–83. doi:10.15252/embj.201488031
15. Taktikos J, Lin YT, Stark H, Biais N, Zaburdaev V. Pili-induced Clustering of N. Gonorrhoeae Bacteria. *PLoS One* (2015) 10:e0137661. doi:10.1371/journal.pone.0137661
16. Holz C, Opitz D, Greune L, Kurre R, Koomey M, Schmidt MA, et al. Multiple Pilus Motors Cooperate for Persistent Bacterial Movement in Two Dimensions. *Phys Rev Lett* (2010) 104:178104. doi:10.1103/physrevlett.104.178104
17. Zaburdaev V, Biais N, Schmiedeberg M, Eriksson J, Jonsson A-B, Sheetz MP, et al. Uncovering the Mechanism of Trapping and Cell Orientation during neisseria Gonorrhoeae Twitching Motility. *Biophysical J* (2014) 107:1523–31. doi:10.1016/j.bpj.2014.07.061
18. Marathe R, Meel C, Schmidt NC, Dewenter L, Kurre R, Greune L, et al. Bacterial Twitching Motility Is Coordinated by a Two-Dimensional Tug-Of-War with Directional Memory. *Nat Commun* (2014) 5:3759–10. doi:10.1038/ncomms4759
19. Pönisch W, Weber CA, Zaburdaev V. How Bacterial Cells and Colonies Move on Solid Substrates. *Phys Rev E* (2019) 99:042419.
20. Maier B, Potter L, So M, Seifert HS, Sheetz MP. Single Pilus Motor Forces Exceed 100 Pn. *Proc Natl Acad Sci U.S.A* (2002) 99:16012–7. doi:10.1073/pnas.242523299
21. Chattopadhyay S, Moldovan R, Yeung C, Wu XL. Swimming Efficiency of Bacterium *Escherichia coli*. *Proc Natl Acad Sci U.S.A* (2006) 103:13712–7. doi:10.1073/pnas.0602043103
22. Maier B. The Bacterial Type IV Pilus System - a Tunable Molecular Motor. *Soft Matter* (2013) 9:5667–71. doi:10.1039/c3sm50546d
23. Pönisch W, Weber CA, Juckeland G, Biais N, Zaburdaev V. Multiscale Modeling of Bacterial Colonies: How Pili Mediate the Dynamics of Single Cells and Cellular Aggregates. *New J Phys* (2017) 19:015003. doi:10.1088/1367-2630/aa5483
24. Pönisch W, Eckenrode KB, Alzurqa K, Nasrollahi H, Weber C, Zaburdaev V, et al. Pili Mediated Intercellular Forces Shape Heterogeneous Bacterial Microcolonies Prior to Multicellular Differentiation. *Sci Rep* (2018) 8:16567–10. doi:10.1038/s41598-018-34754-4
25. Zhou K, Hennes M, Maier B, Gompper G, Sabass B. *Non-equilibrium Dynamics of Growing Bacterial Colonies* (2021). arXiv. doi:10.48550/ARXIV.2106.06729
26. Jin F, Conrad JC, Gibiansky ML, Wong GCL. Bacteria Use Type-Iv Pili to Slingshot on Surfaces. *Proc Natl Acad Sci U.S.A* (2011) 108:12617–22. doi:10.1073/pnas.1105073108
27. Westling-Häggström B, Elmros T, Normark S, Winblad B. Growth Pattern and Cell Division in neisseria Gonorrhoeae. *J Bacteriol* (1977) 129:333–42. doi:10.1128/JB.129.1.333-342.1977
28. Chang YW, Rettberg LA, Treuner-Lange A, Iwasa J, Søgaard-Andersen L, Jensen GJ. Architecture of the Type iva Pilus Machine. *Science* (2016) 351:aad2001. doi:10.1126/science.aad2001
29. Purcell EM. Life at Low reynolds Number. *Am J Phys* (1977) 45:3–11. doi:10.1119/1.10903
30. Bou-Rabee N. Time Integrators for Molecular Dynamics. *Entropy* (2014) 16:138–62.
31. Biais N, Higashi DL, Brujić J, So M, Sheetz MP. Force-dependent Polymorphism in Type Iv Pili Reveals Hidden Epitopes. *Proc Natl Acad Sci U.S.A* (2010) 107:11358–63. doi:10.1073/pnas.0911328107
32. Whitchurch CB. Biogenesis and Function of Type Iv Pili in pseudomonas Species. In: *Pseudomonas*. Springer (2006). p. 139–88.
33. Kaiser A, Sokolov A, Aranson IS, Löwen H. Motion of Two Micro-wedges in a Turbulent Bacterial bath. *Eur Phys J Spec Top* (2015) 224:1275–86. doi:10.1140/epjst/e2015-02459-x
34. Xu R-k., Jiang H-j., Hou Z-h. Simulation Study of Passive Rod Diffusion in Active bath: Nonmonotonic Length Dependence and Abnormal Translation-

Rotation Coupling. *Chin J Chem Phys* (2021) 34:157–64. doi:10.1063/1674-0068/cjcp2006091

35. Bechinger C, Di Leonardo R, Löwen H, Reichhardt C, Volpe G, Volpe G. Active Particles in Complex and Crowded Environments. *Rev Mod Phys* (2016) 88:045006. doi:10.1103/revmodphys.88.045006
36. Shin J, Cherstvy AG, Kim WK, Zaburdaev V. Elasticity-based Polymer Sorting in Active Fluids: A Brownian Dynamics Study. *Phys Chem Chem Phys* (2017) 19:18338–47. doi:10.1039/c7cp02947k
37. Bonazzi D, Lo Schiavo V, Machata S, Djafer-Cherif I, Nivoit P, Manriquez V, et al. Intermittent Pili-Mediated Forces Fluidize neisseria Meningitidis Aggregates Promoting Vascular Colonization. *Cell* (2018) 174:143–55. doi:10.1016/j.cell.2018.04.010
38. Alston H, Parry AO, Voituriez R, Bertrand T. *Intermittent Attractive Interactions lead to Microphase Separation in Non-motile Active Matter* (2022). arXiv. doi:10.48550/ARXIV.2201.04091

Conflict of Interest: The authors declare that the research was conducted in the absence of any commercial or financial relationships that could be construed as a potential conflict of interest.

frontiers | Frontiers in Physics

ORIGINAL RESEARCH
published: 09 June 2022
doi: 10.3389/fphy.2022.865937

Microbial Adhesion on Circular Obstacles: An Optimization Study

Tamara Faúndez[1], Bastián Espinoza[2], Rodrigo Soto[1] and Francisca Guzmán-Lastra[3]*

[1]Departamento de Física, FCFM Universidad de Chile, Santiago, Chile, [2]CMM, FCFM Universidad de Chile, Santiago, Chile, [3]Escuela de Data Science, Facultad de Estudios Interdisciplinarios, Universidad Mayor, Santiago, Chile

Microbial filtration is an important process with applications in environmental, mining, and sanitary engineering. Here, we study the interplay between the motility of microswimmers and the imposed flow to determine the adhesion of bacteria at the surface of the solid obstacle. For that, we perform numerical simulations of active Brownian particles interacting with a single cylindrical obstacle when an imposed laminar flow is present. Highly and weakly persistent swimmers are studied, representing extreme cases of bacteria used in experiments and we vary the swimmers' velocity u_0, the imposed flow velocity U_∞, and the obstacle radius R. Starting with no swimmers close to the cylinder, we inject them steadily until a constant number of swimmers are adhered to the obstacle surface. The deposition/erosion process is characterized by the number of bacteria in contact with the obstacle, quantified by the average coverage of the cylinder surface λ_{trap}, and the relaxation time to reach the steady state τ_{trap}. Two regimes are found. The Brownian deposition is attained when swimmer velocities are smaller than the imposed flow. In this case, the particles can diffuse across the streamlines and settle around the obstacle covering the whole perimeter, forming multiple layers. The direct interception is obtained when the particle's velocities are larger, reaching the obstacle by direct swimming, in which case they form approximately one layer on the obstacle surface. It is found that λ_{trap} decreases with u_0 and R, but the dependence with the imposed flow U_∞ is non-monotonic, with and optimum coverage for intermediate flows, given by the crossover of the two regimes. The relaxation rate τ_{trap} decreases with u_0 and increases with R. The dependence of τ_{trap} with U_∞ is more complex, depending on the persistence of the swimmers. The existence of an optimum value of the flow velocity to reach maximum values of the number of deposited swimmers is an important design information for different applications that use microbial filtration. Finally, in general, it is found that optimal adhesion that has larger values of λ_{trap} and smaller values of τ_{trap} is obtained for more-persistent swimmers moving at small velocities interacting with small obstacles.

Keywords: ABP, biofilm, filtration, motility, bacterial accumulation, microswimmers

Edited by:
Sujit Datta,
Princeton University, United States

Reviewed by:
Jian Sheng,
Texas A&M University Corpus Christi,
United States
Harold Auradou,
Automatique et Systèmes Thermiques
(FAST), France

Correspondence:
Francisca Guzmán-Lastra
franciscaglastra@gmail.com

Specialty section:
This article was submitted to
Interdisciplinary Physics,
a section of the journal
Frontiers in Physics

Received: *30 January 2022*
Accepted: *06 April 2022*
Published: *09 June 2022*

Citation:
Faúndez T, Espinoza B, Soto R and
Guzmán-Lastra F (2022) Microbial
Adhesion on Circular Obstacles: An
Optimization Study.
Front. Phys. 10:865937.
doi: 10.3389/fphy.2022.865937

1 INTRODUCTION

The interaction of microorganisms with surfaces has been extensively studied in the last years [1–5], showing that active particles, in general, spend long times exploring surfaces, enhancing microbes' first adhesion or attachment to them [6–9]. This seed or precursor of biofilm formation might be optimized if, for instance, bacteria self-organize forming stains or clusters in the space producing density gradients or, in very dense systems, orientation gradients [10, 11]. In this last case, the bacteria produce attractive fluxes on the fluid that can replenish nutrients or oxygen to the biofilm.

On the other hand, one of the principle benefits of active particle's attraction to surfaces is microbes filtration [12]. This has been studied theoretically in the first works of Rubenstein *et al.* [13] and later with the work of Shimeta *et al.* [14]. In both cases, they analyzed the problem of microbes passing through a circular obstacle moving in a Stokes flow. By performing a dimensional analysis among different filtration parameters such as microbes activity, relative size, and relative density, they could give glances of how microbes filtration, depending on this parameters, experience different regimes where microbes' adhesion to the surface is mediated by different physical mechanisms.

In Nature and industry, motile and non-motile microorganisms are often constrict to move on micro-channels or through porous media in the presence of external flows such as sperm in the female reproductive tract, microbes on the urine tract, soil bacteria through roots, bacteria on phytoremediation treatment, plants and bacteria on mining bioflotations [7, 15–17]. Microorganisms in all these cases are constricted to move through a series of obstacles that, recently, has been reproduced under novel laboratory conditions. It has been observed that the transport and particle's dispersion across obstacles are strongly dependent on the external flow, obstacle radius, and bacterial strains or motility [18–21]. In this aspect, Alonso-Matilla *et al.* [22] studied theoretically the transport of active agents through an array of obstacles of different shapes, showing that the external flow might span different dispersion mechanisms. Recently, Secchi *et al.* [20] performed experiments using different strains of bacteria, whereby measuring the capture efficiency, they found that depending on their motility, the external flow, and obstacle size, the bacteria attachment was located at specific regions of the collecting surface. In recent works, the role of hydrodynamic interactions (HI) and activity, in microbe adhesion on complex surfaces, has been studied either numerically [23–27], theoretically [28–31], and experimentally [19, 20, 32–35], showing that motility define a sharp difference in particle adhesion with non-motile particles. In the case of flagellated microswimmers, their hydrodynamic interactions with the surface are crucial to understand the contact angle for particle-obstacle interactions, and therefore determine the contact time with the surface, which is a key to prop the first adhesion [6]. HI are also important to enhance predation opportunity by microbe's entrainment on convex surfaces [28, 33] and relevant in the accumulation of active particles in the rear of an obstacle, under the effect of an external flow and due to the effect of upstream swimming for elongated microswimmers [23]. Surprisingly, the artificial microswimmers such as active colloids also explore pillar's surfaces for long time, revealing that varying microswimmer's activity effectively changes microswimmer's accumulation on surfaces [32]. Sipos *et al.* [35] explored the role of obstacle curvature on bacterial adhesion finding that there is a characteristic radius of 140 μm, where entrapment is reduced.

Here, we present a simple model for active Brownian particles [36] to study microbe's adhesion on convex surfaces under the effect of an external flow. The particle-obstacle hydrodynamic interactions are modeled with a short-range attractive interaction to the obstacle's surface. Two types of active particles are studied, with different swimming persistences (low and large persistence). By adding a short-range repulsive interaction between microswimmers, we can reproduce bacterial attachment over circular obstacles of different radii [35] and the bacterial attachment on specific regions of the obstacle, depending on the relation between microswimmer's activity and external flow [20]. Furthermore, by varying the microbe's activity, we found a narrow velocity screen where microswimmer's adhesion strongly changes and might determine microbes first adhesion to the surface by changing the contact time with the surface. We find that more-persistent microswimmers with low activity moving close to small obstacles, rather than big ones, in the presence of intermediate external flows optimize microbe's adhesion on the surfaces, where the number of microswimmers attached to the surface increases and the system reaches faster the steady state. We expect that this detail study might help to improve *in vitro* fertilization, bio-inspired chemical treatments in industry to optimize biofilm formation, and other processes where the accumulation in surfaces is relevant.

1.1 Numerical Model

To describe the microbe's motion, we model microswimmers as active Brownian particles (ABP) in two dimensions [37]. Here, each swimmer moves at constant speed u_0 with a persistent orientation $\hat{e}(t)$ that undergoes rotational diffusion. That is, the orientation changes smoothly on time as compared to run-and-tumble particles (RTP), for which the director changes abruptly at discrete events. Although different, it has been shown that at large times, both models present similar dynamics and there is a direct mapping of the tumbling rate to rotational diffusion coefficient D_R [38]. The microswimmers are circular particles with diameter $2a$ that interact between them by excluded volume only, and no mutual alignment takes place. The ABP model, despite its simplicity, is known to reproduce many of the observed properties of microswimmers, in particular the accumulation near walls, regime where it has also been shown that the key features are equivalent to other models of active particles [39]. On the other hand, the simplicity of the ABP model, characterized by a few parameters, allows for systematic analysis and to unveil the key features of relevant phenomena for a wide range of microswimmers, without needing to model specific details of each microswimmer under study. Finally, we restrict to spherical swimmers as it has been shown that considering the ellipticity only changes quantitatively the results, with the same phenomenology as for spherical particles for the study of accumulation in surfaces [23]. The use of this model here shows how different accumulation regimes appear as a function of the self-propulsion speed compared to the imposed flow.

There is a single circular obstacle of radius R, which is impenetrable by the swimmers. At short distances, due to hydrodynamic interactions, pusher swimmers, like bacteria, are attracted to solid surfaces and they are aligned to swim parallel to them [2]. To correctly describe this interaction, for example, to get finite-induced velocities, near field hydrodynamics should be considered [40, 41], which are specific for each microbe. Instead, to mimic this effect in a more general way, without introducing hydrodynamic interactions, which are also computationally expensive, we introduce a short-range attractive force that exerts the obstacle on the swimmers and a torque that aligns them. The whole system is subject to an imposed external flow. We assume that the swimmer concentration is low enough such that the induced flow generated by them can be neglected. Hence, the form of this velocity profile is simply the one that results from the interaction of the external flow with the obstacle. Finally, the modeling is done in two spatial dimensions; the extension to three dimensions is direct.

The swimmers' motion is completely described by the low Reynolds dynamics, i.e., inertia can be completely neglected. Hence, instead of forces and torques, it is more convenient to describe interactions by the induced linear and angular velocities they generate. Thus, the equations of motion for the position $\vec{r}_i$ of swimmer i are

$$\frac{d\vec{r}_i}{dt} = u_0\hat{e}_i + u\left(\vec{r}_i\right) + \vec{u}_O\left(\vec{r}_i\right) + \sum_{i\neq j}\vec{u}_S\left(|\vec{r}_i - \vec{r}_j|\right), \qquad (1)$$

where the first term is the self-propulsion along the director, the second term is the drift produced by the external flow, and the last two terms are the induced velocities produced by the interaction with the obstacle and other swimmers, respectively. Similarly, for the director $\hat{e}_i$,

$$\frac{d\hat{e}_i}{dt} = \left[\frac{1}{2}\nabla\times\vec{u}\left(\vec{r}_i\right) + \vec{\Omega}_O\left(\vec{r}_i, \hat{e}_i\right) + \sqrt{2D_R}\,\vec{\xi}\right]\times\hat{e}_i, \qquad (2)$$

where the first term describes the rotation induced by the flow vorticity, that for a spherical swimmer adopts this simple form [42, 43], the second one accounts for the reorientation of the swimmer by the interaction with the obstacle, and the last one is a stochastic term, with ξ a white noise, that produces rotational diffusion with a diffusion coefficient D_R. The cross product with the director guarantees that remains unitary. No swimmer-swimmer torques are considered.

For an ambient fluid with density ρ, viscosity η, and a small imposed flow $U_\infty\hat{x}$ far from the obstacle, the presence of the obstacle centered at the origin of the coordinate system results in the velocity profile $\vec{u}(\vec{r}) = U_\infty[(1 + \frac{R^3}{2r^3} - \frac{3R}{2r})\cos\theta\,\hat{r} - (1 - \frac{R^3}{4r^3} - \frac{3R}{4r})\sin\theta\,\hat{\theta}]$. Here, $r = |\vec{r}|$ is the distance to the origin, θ is measured with respect to the $\hat{x}$ axis and $(\hat{r}, \hat{\theta})$ is the pair of polar unit vectors.

The obstacle has radius R and the interaction is modeled with a potential U_O, such that $\vec{u}_O(\vec{r}) = -\nabla U_O(\vec{r})$. The potential is attractive in the adhesion region, $R < r_i < \varepsilon_0 + R$, and is repulsive for $r < R$, describing the rigidity of the surface (see **Figure 1A**). This interaction mimics, in a simple way, electrostatic, hydrodynamic, or substrate effects on surfaces [16, 32, 33, 35], and allows for reversible adhesion to the surface. For simplicity, we use a Morse potential to have a simple expression valid for all distances:

$$U_O\left(\vec{r}_i\right) = U_O\left[e^{-2\beta_M(r_i - r_M)} - 2e^{-\beta_M(r_i - r_M)}\right]. \qquad (3)$$

When the microswimmer is close to the surface of the obstacle, there is also a torque that aligns the swimmer with the surface. For simplicity, we consider that the induced angular velocity is

$$\vec{\Omega}_O\left(\vec{r}_i, \hat{e}_i\right) = \begin{cases} \Omega_O\hat{r}_i\times\hat{e}_i & \text{, if } |\vec{r}_i| < R + \varepsilon_0 \\ 0 & \text{, otherwise} \end{cases}, \qquad (4)$$

with the same range as the interaction potential.

For the swimmer-swimmer interaction, we use a simple repulsive Yukawa potential

$$\vec{U}_S\left(\vec{r}\right) = U_S e^{-r/(2a)}\Big/ r, \qquad (5)$$

which gives the induced velocity $\vec{u}_S(\vec{r}) = -\nabla U_S(\vec{r})$.

The simulation is performed in a stripe of size $L_y = 4R$ in the vertical direction and unbounded in the x direction. Periodic boundary conditions are used in the y direction. To generate a continuous injection of microswimmers that approach the obstacle, particles are released periodically, every τ_{wave}, at a distance $d_0 = 3R$, randomly distributed along L_y. Each wave is composed of $N = 100$ microswimmers, uniformly distributed in the chamber all pointing initially in the positive $\hat{x}$ direction (see **Figure 1A**). The distance to the obstacle is sufficient for the swimmers to randomize and in the different observables that quantify the accumulation of swimmers in the obstacle, and there is no signature of the periodicity τ_{wave}.

1.2 Model Parameters and Numerical Implementation

The model has several parameters, characterizing the motion of the swimmers, their mutual interaction, and the interaction with the wall, as well as the properties of the imposed flow and obstacle size. In this study, we focus on varying the swimmer's speed u_0, the imposed flow U_∞, and the obstacle radius R. The rest of the parameters are fixed to represent typical experimental and natural conditions.

We set the microswimmer's diameter $2a = 1$ μm in the Yukawa potential, as the length scale of the problem. The time scale of the problem is set by the rate of particle injections $\tau_{\text{wave}} = 1$ s. Hence, in what follows, all lengths and times, and the derived units, are expressed as dimensionless quantities.

We define the obstacle adhesion region in $\varepsilon_0 = 7$, which accounts for the typical hydrodynamic effects in the vicinity of the obstacle [19, 20, 28]. The intensity of the interactions is rather arbitrary as it is only needed that excluded volume is accurately achieved. We use $U_S = 2$, $U_O = 3.2$, $\beta_M = 1.44$, and $\Omega_O = 0.28$, which are sufficient to enforce the excluded volume with the integration time step $\Delta t/\tau_{\text{wave}} = 1\times10^{-3}$ and a rapid

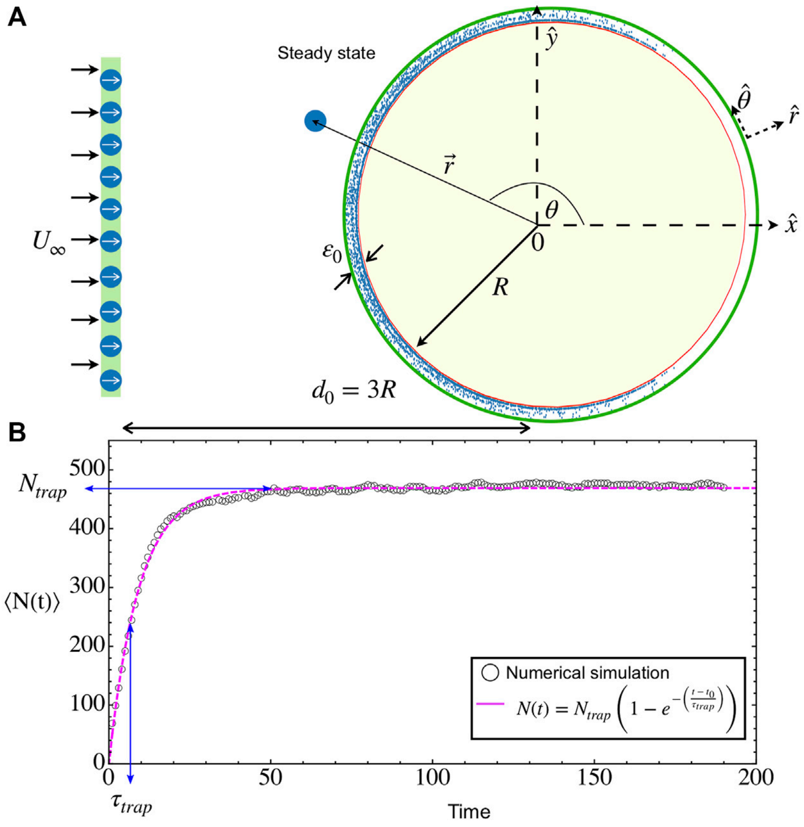

FIGURE 1 | Microbial adhesion on a circular obstacle. **(A)** Snapshot of a transient state (Brownian deposition): Microswimmers are released in waves at a fixed distance 3R from the obstacle center while they are immersed in a constant upstream flow $U_\infty \hat{x}$. When microswimmers (blue points) come into contact with the obstacle, they explore its surface forming different bacterial layers on the adhesion space, delimited by the outer green circle, at a distance ε_0 from the surface. **(B)** Characterization of the steady state: The average bacterial number on the adhesion space $\langle N(t)\rangle$ increases monotonically on time until it saturates. It is well fitted to the expression $\langle N(t)\rangle = N_{\mathrm{trap}}[1 - e^{-(t-t_0)/\tau_{\mathrm{trap}}}]$, which allows to compute two relevant observables: the steady state number of trapped particles N_{trap} and the growth time τ_{trap} which determines how fast the steady state is reached.

alignment with the obstacle. We consider two microswimmer types, with very different persistences, characterized by their rotational diffusion coefficient: *more-persistent* microswimmers with D_R = 0.16 [44, 45], and *less-persistent* ones with D_R = 0.6 [46]. This classification is related with different bacterial strains modified and used for medical or experimental tasks [17].

We solve the equations of motion (1) and (2) using molecular dynamics simulations with the Euler-Maruyama integration method, for a total time of 200 s. To improve the computational efficiency, we implemented *cell lists* for the particle-particle interactions and an effective *cut-off* for the particle-obstacle interaction in order to avoid unnecessary interactions when their distance is large [47].

To study how the activity u_0, obstacle radius R, and external flow U_∞ affect the first adhesion of microbes, we performed three different studies varying different parameters, for both microswimmer's types.

i. Microswimmer activity: in this case, we will fix the obstacle radius $R = 100$ and the external flow $U_\infty = 40$, unless otherwise indicated. We study bacterial activity in the range u_0 = 14, . . . , 65.
ii. Obstacle radius: in this case, we will fix $u_0 = 20$ and $U_\infty = 40$, while varying R in the range 10, . . . , 350.
iii. External flow: in this case, we fix the obstacle radius $R = 100$ and the microswimmer activity $u_0 = 20$, while varying U_∞ = 10, . . . , 200.

With these set of parameters, the concentration of swimmers in the bulk of the system is dilute. Yet, still accounts a considerable accumulation of microswimmers on the obstacle surface. We performed 24 different simulations for each studied parameter combination and, for all cases, we show the average results.

2 RESULTS

2.1 General Features and Observables

For all considered cases of velocities and obstacle radii, the temporal dynamics is rather similar. First, it takes a time t_0 ~

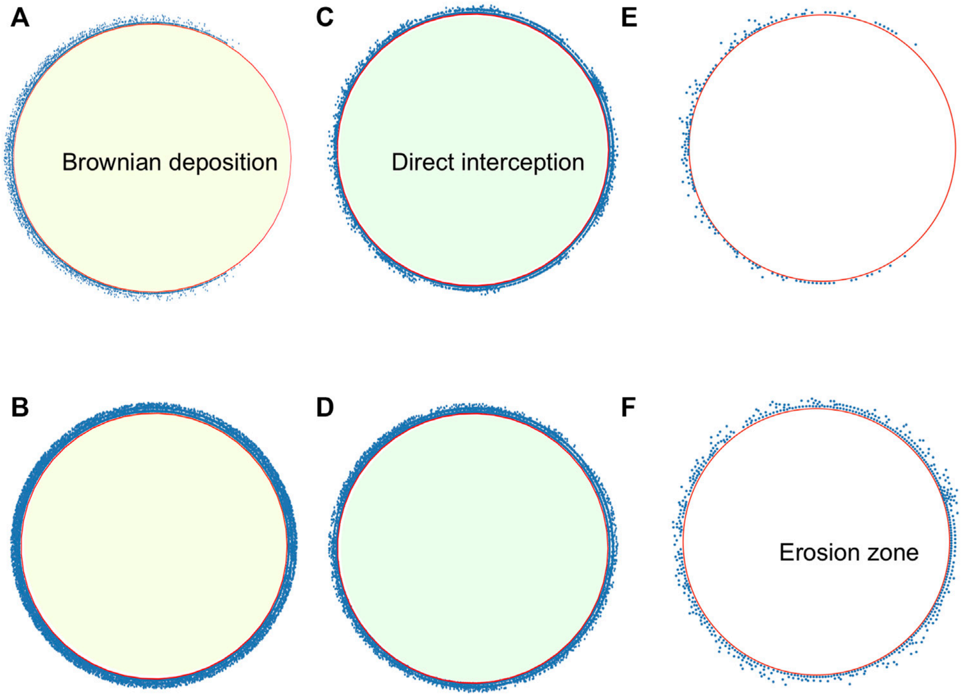

FIGURE 2 | Snapshots of microswimmers on the adhesion region at different regimes. Brownian deposition for more-persistent microswimmers for $u_0 = 14$, $U_\infty = 40$, $R = 100$ **(A)** at $t = \tau_{\text{trap}}$ **(B)** at $t = 200$. Direct interception for less-persistent microswimmers for $u_0 = 50$, $U_\infty = 40$, $R = 100$ **(C)** at $t = \tau_{\text{trap}}$, **(D)** at $t = 200$. Microswimmers, in the adhesion region, for $u_0 = 20$, $U_\infty = 150$, $R = 100$, **(E)** at $t = \tau_{\text{trap}}$ **(F)** at $t = 200$.

$3R/(u_0 + U_\infty)$ for the first swimmers that were injected into the system to reach the obstacle. After this time, there is a continuous income of swimmers to the obstacle. Some of them will reach the adhesion region and remain there while swimming and being advected by the flow. Interactions between swimmers create crowded environments that enhance the residence time in this zone but, also, it is possible to scatter bacteria from the surface after an encounter, helping their erosion by the external flow. As a whole, the total number of particles in the adhesion zone $N(t)$ starts to increase steadily after t_0 until it saturates to the steady value N_{trap} (see **Figure 1B** and the **Supplementary Video S1**). In all cases, the average growth curves can be well fitted to the model

$$\langle N(t)\rangle = N_{\text{trap}}\left[1 - e^{-(t-t_0)/\tau_{\text{trap}}}\right], \tag{6}$$

where τ_{trap} gives the relaxation time to reach the steady state, similar to the probability of successful interaction presented in Refs. [28, 48]. Considering that the incoming rate is constant, having **Eq. 6** as solution of the balance equation implies that the desorption rate is proportional to the actual number of particles in the adhesion layer. In the steady state, the obstacle is saturated and ready for microbes to form the first adhesion [6, 8]. From the simulations, we will obtain τ_{trap} and N_{trap}, which are important parameters to characterize and optimize the microbe's adhesion in convex surfaces.

Figure 2 presents snapshots of the system in the three regimes that are described in the text for the transient at $t = \tau_{\text{trap}}$ and in the steady state. In the transient, the distribution is not uniform with particles still being transported along the perimeter, except for the direct interception regime, where the distribution is uniform, although with less particles than in the steady state. In all cases, it is seen that the steady-state distribution in rather uniform in the circle, contrary to other studies where there is a larger accumulation in the back [20, 23]. The three regimes differ notably on the number of accumulated particles.

Another relevant observable is the contact time of microswimmers with obstacle's surface, τ_{contact}. This parameter gives the average residency time of microbes on the surface and therefore the time available to realize an irreversible adhesion to prompt a biofilm. It is measured, for each set of parameters, as the mode considering 24 realizations of the time that particles spend inside the adhesion region.

The number of trapped particles can be compared to the maximum occupation in a monolayer, $N_{\max} \equiv 2\pi R/(2a)$, which allows us to define the dimensionless average number of deposited layers $\lambda_{\text{trap}} = N_{\text{trap}}/N_{\max}$. Similarly, the relaxation time and the contact time can be compared to the time it takes a swimmer to travel the obstacle by its own, $\tau_s \equiv \pi R/u_0$.

Using dimensional analysis, we expect that the microbial behavior depends on the Péclet number which compares advective transport with diffusion $\text{Pe} = u_0/(RD_R)$. Then, in the limit of $\text{Pe} \to 0$, we expect that Brownian diffusivity dominates microswimmer's exploration of the medium, the phenomenon is known as "Brownian deposition." While in the other limit $\text{Pe} \to \infty$, the advection dominates and particles encounter the obstacle surface by "direct interception" [13, 14]. When varying the

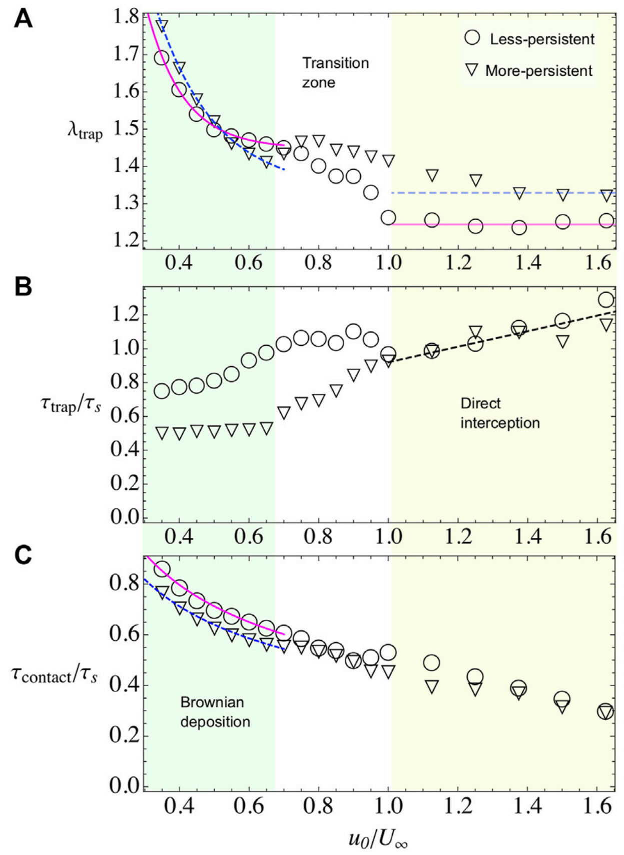

FIGURE 3 | Bacterial adhesion observables when varying the microswimmer's activity u_0 and when U_∞=40 and R =100. Different symbols represent different microswimmer's types. For less-persistent microswimmers, we use triangles and for more-persistent circles. Two regimes are identified throughout the observables, *Brownian deposition* and *direct interception*, which are indicated by shading color and separated by a white transition zone between them. **(A)** λ_{trap} for less- and more-persistent microswimmers, respectively. The solid and dashed lines, during Brownian deposition, are phenomenological fits with the law $\lambda_{trap} = A(1+ B\exp(-C(u_0/U_\infty)))$. The blurry lines represent a guide to the eye, for the tendency during the direct interception regime. **(B)** τ_{trap} for less- and more-persistent microswimmers, respectively. The dashed line in the direct interception regime is a phenomenological linear fit $\tau_{trap}/\tau_s = A(1+(u_0/U_\infty))$. **(C)** The contact time decreases monotonically with the microswimmer's activity. Less-persistent microswimmers spend slightly more time in contact with the surface during the Brownian deposition, while during the direct interception regime the residency time is the same for both microswimmer's types.

microswimmer's activity, in a biological range of velocities [8], we are changing the Péclet number in a narrow window for each microswimmer's type, and the two limiting cases are not always achieved. Furthermore, the external velocity allows to define new dimensionless parameters. Therefore, for simplicity, we present the results in terms of the control parameters, where the transition between both regimes can also be appreciated.

2.2 Varying Swimmer's Activity

Here we keep the obstacle radius constant to $R = 100$ and vary the swimmer's speed u_0. For the imposed flow, we consider three different values: $U_\infty = 20, 40$, and 60. We found that depending on the microswimmer's activity and external flow there are, basically, two different regimes. In one of them, the microswimmer's velocity is smaller compared with external flow, yet particles diffuse across the streamlines and settle around the obstacle covering the whole perimeter and forming multiple layers, this regime is known as *Brownian deposition* [13, 14]. In the second regime, when particle's activity is larger than the external flow, particles scatter faster forming approximately one layer on the obstacle surface. The particle's capture now depends only on the *direct interception* with the obstacle. In **Figure 3**, we show λ_{trap}, τ_{trap}, and the contact time $\tau_{contact}$ for the case $U_\infty = 40$, for both values of persistence. These three observables decrease with the parameter u_0/U_∞. Naturally, as the swim speed increases, the relaxation and contact times decrease accordingly. Also, the thickness of the deposited layer decreases as particles can escape more easily due to excluded volume interactions with other microswimmers.

2.2.1 First Regime: Brownian deposition

In this regime, microswimmers move slowly than the external flow. Nevertheless, the particles are not purely advected by the flow, on the contrary, they perform an exploration of the space crossing the streamlines and diffusing across the simulation area (see **Supplementary Video S1**). At contact with the obstacle, the flow velocity vanishes and it remains small in the adhesion region, defined as a ring of width $\varepsilon_0 = 7$ across the obstacle's surface. Hence, the attractive potential becomes a dominant factor, increasing the contact time between microswimmers and the obstacle (**Figure 3C**), and also increasing the number of microbes in the adhesion region λ_{trap} (**Figure 3A**, **Figure 4A,C**). Moreover, the microswimmers also present a transition zone (see **Figures 3,4**), at $u_0^* \sim 30$ for all external flow's values, where particle capture slightly increases before entering in the direct interception regime.

We find that λ_{trap} depends on the external flow. In general, when the external flow is slower than particle's velocity, the microswimmers can stay around the adhesion space increasing the number of trapped particles while, for stronger flows, the capture decreases. In the case of, less-persistent microswimmers (circles in **Figures 3,4**). For weak flows $U_\infty = 20, 40$ (**Figures 3A,4A**), respectively, the microswimmer's disperse more enhancing the adhesion [21] and exploring for longer times the obstacle's surface (**Figure 3C**), while for strong flows $U_\infty = 60$ (**Figure 4C**), since the particle trajectories are very noisy, it is highly probable to encounter another particle. As a result of the interaction, the particle can be easily kicked out from the adhesion area and dragged by the external flow, decreasing the fraction of microbes in the obstacle. We fit the fraction of microbes adhered to the obstacle, for all cases, with $\lambda_{trap}(u_0/U_\infty) = A + B\exp(-(u_0/U_\infty)C)$, finding that the rate of decay C for less-persistent microswimmers increases with U_∞ being $C(U_\infty = 20) = 3.68$, $C(U_\infty = 40) = 9.47$, and $C(U_\infty = 60) = 13.53$ with $A \approx 1.4$ and $B \approx 4$.

More-persistent microswimmers are less affected by the external flow, in this regime (inverted triangles in **Figures 3,4**), we found a less dramatic rate of decay C with $C(U_\infty =$

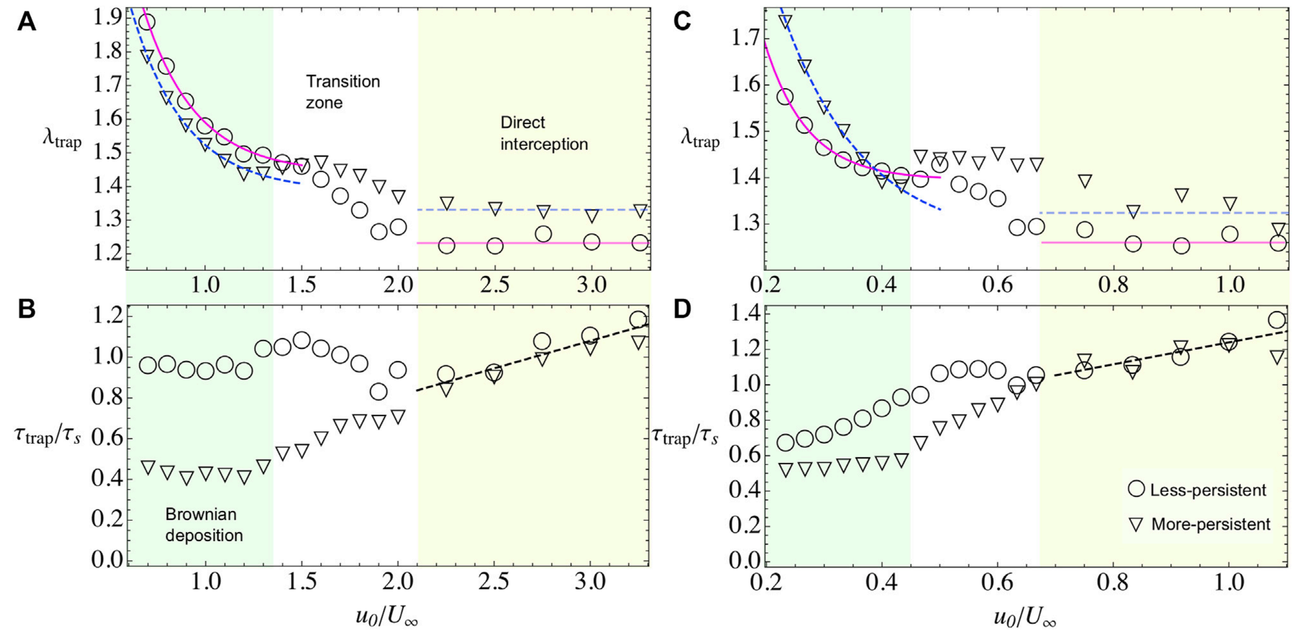

FIGURE 4 | Bacterial adhesion observables when varying the microswimmer's activity u_0 and when the external flow field is U_∞=20 **(A,B)** and when is U_∞=60 **(C,D)**. In both cases, we span the two regimes by shading the area and letting the transition zone in white. Less-persistent microswimmer's results are shown with triangles and more-persistent microswimmers in circles. **(A,C)** λ_{trap} for less- and more-persistent microswimmers, respectively. The solid and dashed lines, during Brownian deposition, are phenomenological fits with the law $\lambda_{\mathrm{trap}} = A(1+B\exp(-(u_0/U_\infty)C))$. The blurry lines represent a guide to the eye, for the tendency during the direct interception regime. **(B,D)** τ_{trap} for less- and more-persistent microswimmers, respectively. During the Brownian deposition, more-persistent microswimmers reach the steady state faster than the less-persistent microswimmers, being more dramatic the difference for the weak external flow case U_∞=20, where $\tau_{\mathrm{trap}}/\tau_s \sim 1$ showing that the steady state is reached when microswimmers travel half of the obstacle perimeter. Meanwhile, during the direct interception regime, both curves collapsed and are phenomenological described by a linear fit $\tau_{\mathrm{trap}}/\tau_s = A(1+(u_0/U_\infty))$.

20) = 3.57, $C(U_\infty = 40) = 5.91$, and $C(U_\infty = 60) = 7.15$, respectively, and $A \approx 1.3$, $B \approx 3$. Then, since the microswimmers perform less reorientations, microbe's capture is faster as we can observe in **Figure 3B**, **Figure 4B,D** for different external flows. The relaxation time τ_{trap} has a similar behavior for all U_∞. We found that during this regime, more-persistent microswimmers reach the steady state before a single microswimmer performs an exploration around the obstacle's perimeter with $\tau_{\mathrm{trap}}/\tau_s \sim 0.5$ in all cases, while less-persistent microswimmers take longer times depending on the external flow.

The contact time that in average microswimmers spent on the adhesion region decays as $\tau_{\mathrm{contact}} = (AU_\infty/u_0)^{1/2}$, with $A = 0.25$ and $A = 0.2$ for the less- and more-persistent microswimmers, respectively (**Figure 6A**), following a power law as [25]. According to Secchi *et al.* [20], non-motile particles distribute uniformly around the obstacle's surface while motile microswimmers accumulate on the back of the obstacle [19, 20]. Here, since microswimmers are slow, we observe something similar to the case of non-motile microswimmers since they spent more time close to the surface while they diffuse around the adhesion space.

2.2.2 Second Regime: Direct Interception

In this regime, the self-propulsion is higher than the external flow, thus microswimmers move freely around the obstacle's surface. They are scattered out from this region when they meet another microswimmer and, due to excluded volume interactions, they are deviated from their trajectory, or when they change their orientation due to rotation diffusion. Then, particle's capture decreases as they move faster and the steady state is also reached faster (see **Figure 3B**, **Figures 4B,D**). The number of captured particles is roughly independent of U_∞ for both the more- and less-persistent microswimmers, being the number of more-persistent microswimmers in the adhesion region higher than the less-persistent. The steady state is reached at the same time for all microswimmer's type, and varying slightly with the external flow. In **Figure 3B**, **Figure 4B,D**, the dashed line shows the best fit, which follows $\tau_{\mathrm{trap}}(u_0/U_\infty)/\tau_s = A(1 + u_0/U_\infty)$, with $A(U_\infty = 20) = 0.27$, $A(U_\infty = 40) = 0.46$, and $A(U_\infty = 60) = 0.62$. In average, the steady state is reached after one particle travels half of the obstacle's perimeter, that is, $\tau_{\mathrm{trap}} \approx \tau_s$ for both microswimmer's persistences and the same happens for the contact time (see **Figure 3C**). Thus, since microswimmers are fast, the steady state is reached after there is a constant number of microswimmers exploring the back of the obstacle's adhesion space [19, 20]. In this regime, the microbe's adhesion is optimized for the more-persistent microswimmers since the obstacle captures the same number of particles, and they spent the same amount of time on the surface, yet the steady state is reached faster.

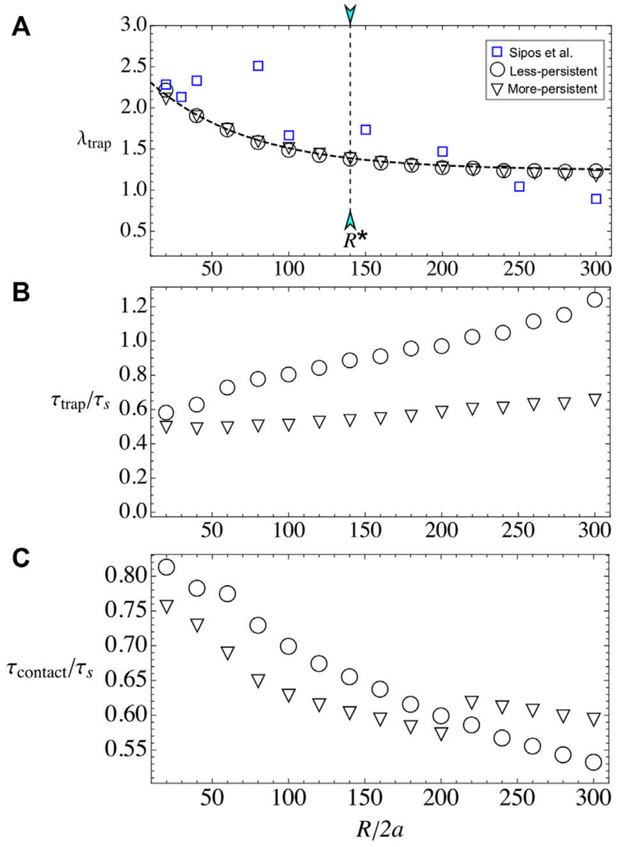

FIGURE 5 | Bacterial adhesion when varying obstacle radius *R*. **(A)** λ_{trap} for the less- and more-persistent microswimmers. In blue squares, the experimental data for **(E)** *E. coli* adhesion around pillar obstacles by Sipos *et al.* [35]. The dashed line corresponds to the best fit which is independent of bacterial strain with the law $\lambda_{trap}(R)=A[1+\exp(-R/R_0)]$. **(B)** τ_{trap} for the less- and more-persistent microswimmers. Less-persistent microswimmers (inverted triangles) steady state is reached at a constant time τ_{trap}/τ_s ~0.5, independent on the obstacle radius *R*. **(C)** The contact time increases monotonically with the obstacle radius *R* for u_0=20 and U_∞=40 fixed.

2.3 Varying the Obstacle Radius

Now, we vary the obstacle radius R, while keeping fixed the microswimmer's activity to $u_0 = 20$ and the external flow to $U_\infty = 40$, unless otherwise indicated. The number of layers λ_{trap} decreases with R (**Figure 5A**). Small pillars are capable to adhere more than two layers of microbes and for large radii, the number of layers saturates to a value slightly larger than one. The results are well fitted to the expression $\lambda_{trap}(R) = A[1 + \exp(-R/R_0)]$, with $A = 1.24$ and $R_0 = 65.2$, independent of microswimmer's type and external flow. With this, the total number of accumulated particles increases monotonically with R. Microbe's capture is in agreement with some experimental results in cylindrical pillars, either for biological microswimmers such as bacteria or algae [33, 34] or artificial microswimmers [35], where there is a critical radius for constant particle's capture located at $R^* \approx 140$.

Regarding the relaxation time, the more-persistent microswimmers reach the steady state faster than the less-persistent ones, and in both cases τ_{trap} grows with the radius. The results show that for more-persistent microswimmers follows $\tau_{trap}/\tau_s \sim 0.5$ for all R (see **Figure 5B**), while for less-persistent microswimmers the steady state increases linearly with the obstacle radius. The time that particles remain in contact with the surface $\tau_{contact}$ increases also with obstacle's radius, similar to Refs. [32, 35], but it does not follow the simple law $\tau_{contact}(R) \approx \tau_s$ (see **Figure 5C**). Instead, the contact time increases with R for both microswimmer's types, yet there is not linear dependence on its growth. Thus, the microbe's adhesion is enhanced with small pillar radius and less-persistent microswimmers.

2.4 Varying External Flow

Here, we vary the external flow U_∞, while we keep fixed the bacterial activity to $u_0 = 20$ and the obstacle radius to $R = 100$. The

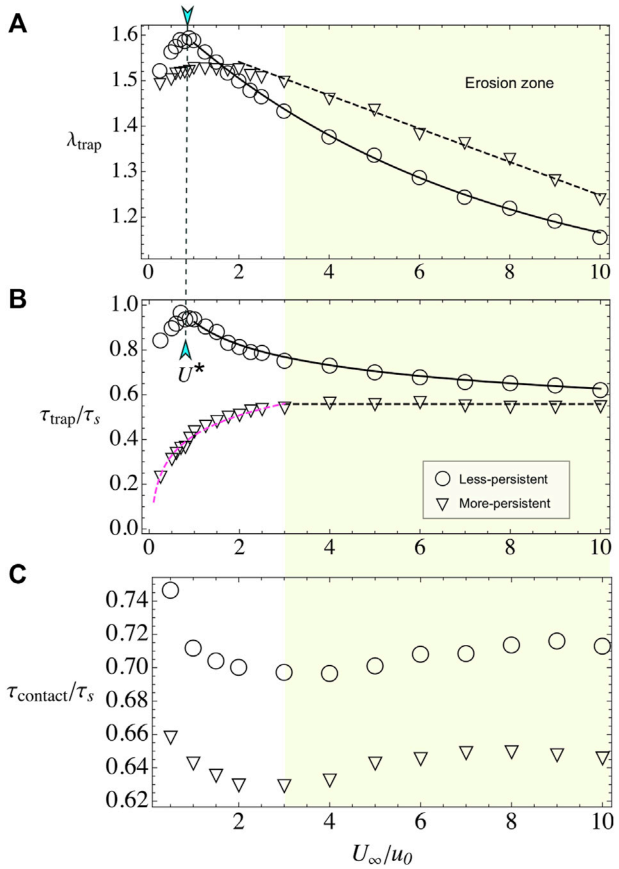

FIGURE 6 | Bacterial adhesion when varying external flow U_∞. **(A)** λ_{trap} for less- and more-persistent microswimmers. In both cases, the obstacle adheres an increasing number of microswimmers on the surface for weak flows, while for $U_\infty > U^*$ particles are rapidly eroded from the surface. **(B)** The time to reach the steady-state τ_{trap} has different behaviors depending on the microswimmer's persistence. **(C)** When varying external flow, U_∞, keeping R =100 and u_0=20 fixed, the contact time fluctuates around a constant value, with less-persistent microswimmers spending more time at the obstacle surface.

number of captured layers presents a non-monotonic behavior, with a pronounced maximum for the less-persistent swimmers at $U^* \approx 1$, where the microswimmer and the flow velocities are similar. For the more-persistent swimmers, the maximum is less pronounced and it is located at $U^* \approx 2$ (see **Figure 6A**). For larger external velocities, microbe's adhesion decreases due to erosion by the flow [19, 20, 49]. For the less-persistent swimmers, the erosion is well fitted to the expression $\lambda_{\text{trap}}(U_\infty/u_0) = 1 + 0.66\exp(-0.15U_\infty/u_0)$, according with microbe's erosion of the surface [20, 49]. For the more-persistent microswimmers, the decrease of λ_{trap} is slower and well fitted to $\lambda_{\text{trap}}(U_\infty/u_0) = 1.62\text{–}0.037(U_\infty/u_0)$, similar to the experimental limit for erosion observed by Miño *et al.* [19].

In the case of relaxation time, we observe a very different behavior for the two analyzed persistences. For the less-persistent microswimmers, τ_{trap} is non-monotonic, with a maximum at U^* and larger values than for the more-persistent swimmers (see **Figure 6B**). In the erosion phase, the time that takes to reach the steady state, for less-persistent microswimmers, decays as $\tau_{\text{trap}}(U_\infty/u_0)/\tau_s = 0.9\,(u_0/U_\infty)^{1/6}$. For more-persistent microswimmers, the τ_{trap} time increases following a law $\tau_{\text{trap}}(U_\infty/u_0)/\tau_s = 0.13\log(25.7U_\infty/u_0)$ in the first phase for $U_\infty/u_0 < 3$ and then, in the erosion zone, it is constant with $\tau_{\text{trap}}/\tau_s \approx 0.56$.

Surprisingly, the contact time is constant (see **Figure 6C**), even in the erosion zone, with small variations around $\tau_{\text{contact}}/\tau_s \approx 0.63$ for the more-persistent swimmers and $\tau_{\text{contact}}/\tau_s \approx 0.71$ for the less-persistent ones. We state that the existence of this almost constant value in the contact time is related with the accumulation of microswimmers in the front and in the back of the obstacle, where there are stagnation points. The particles are expelled from these regions then by their own activity but not on by the flow [20]. Consistent with this hypothesis, the less-persistent swimmers present larger contact times. Also, in the transport of the swimmers along the adhesion zone, the imposed flow almost vanishes there, resulting in that the contact time is dominated by the travel time τ_s.

3 DISCUSSION

We showed, with a simple ABP model, that optimizing microorganism attachment to surfaces is possible by using the right set of mechanical and biological parameters for a given problem. Our simple model proves to be in agreement with the previous quantitative and qualitative theoretical and experimental results for biological and artificial microswimmers [19, 20, 32, 35]. We found that particle's capture around the adhesion region of a circular obstacle diminishes with the particle's activity in all the regimes and for both studied microswimmer's types, namely less- and more-persistent ones. In the case of active Janus particles, Simmchen *et al.* [32] found that increasing hydrogen peroxide concentration or activity in their experiments results in a particle's fluorescence increase around the pillars. However, in that case, there was no external flow, and the same applies to the theoretical works for filters [13, 14]. In our model, we considered particle-particle interactions. Therefore, the scattering between particles is now very sensitive to the applied external flow showing that the limiting streamline around the obstacle determines particle's capture [24].

We also observed that the net accumulation is larger for the more-persistent swimmers. Also, although for both microswimmer's types the contact time increases with obstacle radius, more-persistent microswimmer's tend to reach the steady state faster, showing that again they are good candidates for the optimization in biofilm formation. Then, by choosing the right nutrient or fuel source for microswimmers and the right microswimmer strain (less or more noisy), it is possible to enhance the chances in bacterial encounter with the obstacle's surface. This might be also relevant for medical applications such as *in vitro* fertilization.

In the case of varying obstacle's radius, we found that small obstacles can capture more particle's layers. Larger obstacles, even though have more space to capture swimmers, are less efficient. We also found that for a limiting radius, particle's capture becomes constant in agreement to previous results by Sipos *et al.* [35]. Finally, we explored the case when we vary the external flow which in the lasts years has been one of the most revisited problems in microswimmer's filtration [21, 22, 27], particle hydrodynamic entrainment [28–30, 33, 34], and obstacle adhesion [19, 20]. We found a non-explored behavior for more-persistent microswimmers with a slower decay in particle's capture in the erosion region and lower times for the system to reach the steady state in this case. We also could predict the velocity for the external flow passing through a circular obstacle [19] at which the erosion of the surface starts.

Our model can be straightforward applied in 3D obstacles, dense systems, porous media, or in different external flow conditions. It is also possible to extend the simple ABP model to include aligning interactions for elongated microswimmers, far-field interactions to study complex microbes, tumbling, polydispersity, or other effects. Also, different experiments show that the microbe-wall interaction is more complex than the simple attraction and alignment that we incorporated in the model, including rheotaxis [50], upstream swim [51], circular motion [52], and changes in the tumbling rate [53]. The influence of these and other effects, as well as the extension to the ABP model, must be studied in detail for quantitative predictions for specific microbes. Finally, choosing the right set of mechanical parameters such as external flow and obstacle's radius could open new avenues in the control of bacterial deposition on roots in hydroponic crops or in mining bioflotations, opening new environmentally friendly alternatives in engineering and industrial applications.

DATA AVAILABILITY STATEMENT

All simulation codes and raw data used for this paper are available from the corresponding authors upon request.

AUTHOR CONTRIBUTIONS

FG-L and RS designed and planned research collaboratively and wrote the paper. BE and TF developed the theoretical model, and performed the numerical simulations.

FUNDING

This research is supported by Fondecyt Grant No. 1180791 (RS), Fondecyt Grant No. 11220683 (FG-L), and by the Millennium Science Initiative Program-NCN19 170 of ANID (Chile). Powered@NLHPC: This research was partially supported by the supercomputing infrastructure of the NLHPC (ECM-02).

ACKNOWLEDGMENTS

FG-L acknowledges Wolfram Alpha to support her with a free license for this research. We thankful to R. Di Leonardo and P. Galajda for the experimental data and the referees for their comments that improved our manuscript.

SUPPLEMENTARY MATERIAL

The Supplementary Material for this article can be found online at: https://www.frontiersin.org/articles/10.3389/fphy.2022.865937/full#supplementary-material

Supplementary Video S1 | Simulation for less-persistent microswimmers for an obstacle of radius $R = 100$, External flow $U_\infty = 40$ and microswimmer's activity $u_0 = 20$.

REFERENCES

1. Tuson HH, Weibel DB. Bacteria-Surface Interactions. *Soft Matter* (2013) 9: 4368–80. doi:10.1039/c3sm27705d
2. Berke AP, Turner L, Berg HC, Lauga E. Hydrodynamic Attraction of Swimming Microorganisms by Surfaces. *Phys Rev Lett* (2008) 101:038102. doi:10.1103/PhysRevLett.101.038102
3. Elgeti J, Kaupp UB, Gompper G. Hydrodynamics of Sperm Cells Near Surfaces. *Biophysical J* (2010) 99:1018–26. doi:10.1016/j.bpj.2010.05.015
4. Li G, Tang JX. Accumulation of Microswimmers Near a Surface Mediated by Collision and Rotational Brownian Motion. *Phys Rev Lett* (2009) 103:078101. doi:10.1103/PhysRevLett.103.078101
5. Smith DJ, Gaffney EA, Blake JR, Kirkman-Brown JC. Human Sperm Accumulation Near Surfaces: A Simulation Study. *J Fluid Mech* (2009) 621: 289–320. doi:10.1017/s0022112008004953
6. Dunne WM. Bacterial Adhesion: Seen Any Good Biofilms Lately? *Clin Microbiol Rev* (2002) 15:155–66. doi:10.1128/cmr.15.2.155-166.2002
7. Monteiro MP, Clerici JH, Sahoo PK, Cesar CL, de Souza AA, Cotta MA. Stiffness Signatures along Early Stages of Xylella Fastidiosa Biofilm Formation. *Colloids Surf B: Biointerfaces* (2017) 159:174–82. doi:10.1016/j.colsurfb.2017.07.075
8. Conrad JC, Poling-Skutvik R. Confined Flow: Consequences and Implications for Bacteria and Biofilms. *Annu Rev Chem Biomol Eng* (2018) 9:175–200. doi:10.1146/annurev-chembioeng-060817-084006
9. Sahoo PK, Janissen R, Monteiro MP, Cavalli A, Murillo DM, Merfa MV, et al. Nanowire Arrays as Cell Force Sensors to Investigate Adhesin-Enhanced Holdfast of Single Cell Bacteria and Biofilm Stability. *Nano Lett* (2016) 16: 4656–64. doi:10.1021/acs.nanolett.6b01998
10. Mathijssen AJTM, Guzmán-Lastra F, Kaiser A, Löwen H. Nutrient Transport Driven by Microbial Active Carpets. *Phys Rev Lett* (2018) 121:248101. doi:10.1103/physrevlett.121.248101
11. Martínez-García R, Nadell CD, Hartmann R, Drescher K, Bonachela JA. Cell Adhesion and Fluid Flow Jointly Initiate Genotype Spatial Distribution in Biofilms. *Plos Comput Biol* (2018) 14:e1006094. doi:10.1371/journal.pcbi.1006094
12. Humphries S. Filter Feeders and Plankton Increase Particle Encounter Rates through Flow Regime Control. *Proc Natl Acad Sci U.S.A* (2009) 106:7882–7. doi:10.1073/pnas.0809063106
13. Rubenstein DI, Koehl MAR. The Mechanisms of Filter Feeding: Some Theoretical Considerations. *The Am Naturalist* (1977) 111:981–94. doi:10.1086/283227
14. Shimeta J, Jumars PA. Physical Mechanisms and Rates of Particle Capture by Suspension Feeders. *Oceanogr Mar Biol Annu Rev* (1991) 29:191–257.
15. Kim G, Park K, Choi J, Gomez-Flores A, Han Y, Choi SQ, et al. Bioflotation of Malachite Using Different Growth Phases of Rhodococcus Opacus: Effect of Bacterial Shape on Detachment by Shear Flow. *Int J Mineral Process* (2015) 143:98–104. doi:10.1016/j.minpro.2015.09.012
16. Dwyer R, Bruckard WJ, Rea S, Holmes RJ. Bioflotation and Bioflocculation Review: Microorganisms Relevant for mineral Beneficiation. *Mineral Process. Extractive Metall* (2012) 121:65–71. doi:10.1179/1743285512y.0000000005
17. Costerton JW, Cheng KJ, Geesey GG, Ladd TI, Nickel JC, Dasgupta M, et al. Bacterial Biofilms in Nature and Disease. *Annu Rev Microbiol* (1987) 41: 435–64. doi:10.1146/annurev.mi.41.100187.002251
18. Figueroa-Morales N, Mino GL, Rivera A, Caballero R, Clément E, Altshuler E, et al. Living on the Edge: Transfer and traffic of e. coli in a confined flow. *Soft Matter* (2015) 11:6284–93. doi:10.1039/c5sm00939a
19. Miño GL, Baabour M, Chertcoff R, Gutkind G, Clément E, Auradou H, et al. E Coli Accumulation behind an Obstacle. *Adv Microbiol* (2018) 8:451–64. doi:10.4236/aim.2018.86030
20. Secchi E, Vitale A, Miño GL, Kantsler V, Eberl L, Rusconi R, et al. The Effect of Flow on Swimming Bacteria Controls the Initial Colonization of Curved Surfaces. *Nat Commun* (2020) 11:2851. doi:10.1038/s41467-020-16620-y
21. Creppy A, Clément E, Douarche C, d'Angelo MV, Auradou H. Effect of Motility on the Transport of Bacteria Populations through a Porous Medium. *Phys Rev Fluids* (2019) 4:013102. doi:10.1103/physrevfluids.4.013102
22. Alonso-Matilla R, Chakrabarti B, Saintillan D. Transport and Dispersion of Active Particles in Periodic Porous Media. *Phys Rev Fluids* (2019) 4:043101. doi:10.1103/physrevfluids.4.043101
23. Lee M, Lohrmann C, Szuttor K, Auradou H, Holm C. The Influence of Motility on Bacterial Accumulation in a Microporous Channel. *Soft Matter* (2021) 17: 893–902. doi:10.1039/d0sm01595d
24. Espinosa-Gayosso A, Ghisalberti M, Ivey GN, Jones NL. Particle Capture and Low-Reynolds-Number Flow Around a Circular Cylinder. *J Fluid Mech* (2012) 710:362–78. doi:10.1017/jfm.2012.367
25. Wysocki A, Elgeti J, Gompper G. Giant Adsorption of Microswimmers: Duality of Shape Asymmetry and wall Curvature. *Phys Rev E Stat Nonlin Soft Matter Phys* (2015) 91:050302. doi:10.1103/PhysRevE.91.050302
26. Takagi D, Palacci J, Braunschweig AB, Shelley MJ, Zhang J. Hydrodynamic Capture of Microswimmers into Sphere-Bound Orbits. *Soft Matter* (2014) 10: 1784–9. doi:10.1039/c3sm52815d
27. Sosa-Hernández JE, Santillán M, Santana-Solano J. Motility of Escherichia Coli in a Quasi-Two-Dimensional Porous Medium. *Phys Rev E* (2017) 95:032404. doi:10.1103/PhysRevE.95.032404
28. Mathijssen AJ, Jeanneret R, Polin M. Universal Entrainment Mechanism Controls Contact Times with Motile Cells. *Phys Rev Fluids* (2018) 3: 033103. doi:10.1103/physrevfluids.3.033103
29. Słomka J, Alcolombri U, Secchi E, Stocker R, Fernandez VI. Encounter Rates between Bacteria and Small Sinking Particles. *New J Phys* (2020) 22:043016. doi:10.1088/1367-2630/ab73c9
30. Desai N, Shaik VA, Ardekani AM. Hydrodynamic Interaction Enhances Colonization of Sinking Nutrient Sources by Motile Microorganisms. *Front Microbiol* (2019) 10:289. doi:10.3389/fmicb.2019.00289

31. Spagnolie SE, Moreno-Flores GR, Bartolo D, Lauga E. Geometric Capture and Escape of a Microswimmer Colliding with an Obstacle. *Soft Matter* (2015) 11: 3396–411. doi:10.1039/c4sm02785j
32. Simmchen J, Katuri J, Uspal WE, Popescu MN, Tasinkevych M, Sánchez S. Topographical Pathways Guide Chemical Microswimmers. *Nat Commun* (2016) 7:10598. doi:10.1038/ncomms10598
33. Jeanneret R, Pushkin DO, Kantsler V, Polin M. Entrainment Dominates the Interaction of Microalgae with Micron-Sized Objects. *Nat Commun* (2016) 7: 12518. doi:10.1038/ncomms12518
34. Contino M, Lushi E, Tuval I, Kantsler V, Polin M. Microalgae Scatter off Solid Surfaces by Hydrodynamic and Contact Forces. *Phys Rev Lett* (2015) 115: 258102. doi:10.1103/physrevlett.115.258102
35. Sipos O, Nagy K, Di Leonardo R, Galajda P. Hydrodynamic Trapping of Swimming Bacteria by Convex Walls. *Phys Rev Lett* (2015) 114:258104. doi:10.1103/physrevlett.114.258104
36. Volpe G, Gigan S, Volpe G. Simulation of the Active Brownian Motion of a Microswimmer. *Am J Phys* (2014) 82:659–64. doi:10.1119/1.4870398
37. Romanczuk P, Bär M, Ebeling W, Lindner B, Schimansky-Geier L. Active Brownian Particles-From Individual to Collective Stochastic Dynamics P. *Eur Phys J Spec Top* (2012) 202:1–162. doi:10.1140/epjst/e2012-01529-y
38. Cates ME, Tailleur J. Motility-Induced Phase Separation. *Annu Rev Condens Matter Phys* (2015) 6:219–44. doi:10.1146/annurev-conmatphys-031214-014710
39. Sepúlveda N, Soto R. Universality of Active Wetting Transitions. *Phys Rev E* (2018) 98:052141. doi:10.1103/PhysRevE.98.052141
40. Dunstan J, Miño G, Clement E, Soto R. A Two-Sphere Model for Bacteria Swimming Near Solid Surfaces. *Phys Fluids* (2012) 24:011901. doi:10.1063/1.3676245
41. Kantsler V, Dunkel J, Polin M, Goldstein RE. Ciliary Contact Interactions Dominate Surface Scattering of Swimming Eukaryotes. *Proc Natl Acad Sci U.S.A* (2013) 110:1187–92. doi:10.1073/pnas.1210548110
42. Jeffery GB. The Motion of Ellipsoidal Particles Immersed in a Viscous Fluid. *Proc R Soc Lond Ser A, Containing Pap a Math Phys character* (1922) 102: 161–79. doi:10.1098/rspa.1922.0078
43. Bretherton FP. The Motion of Rigid Particles in a Shear Flow at Low reynolds Number. *J Fluid Mech* (1962) 14:284–304. doi:10.1017/s002211206200124x
44. Miño GL, Dunstan J, Rousselet A, Clément E, Soto R. Induced Diffusion of Tracers in a Bacterial Suspension: Theory and Experiments. *J Fluid Mech* (2013) 729:423–44. doi:10.1017/jfm.2013.304
45. Mathijssen AJTM, Doostmohammadi A, Yeomans JM, Shendruk TN. Hotspots of Boundary Accumulation: Dynamics and Statistics of Micro-swimmers in Flowing Films. *J R Soc Interf* (2016) 13:20150936. doi:10.1098/rsif.2015.0936
46. Saragosti J, Silberzan P, Buguin A. Modeling E. coli tumbles by rotational diffusion. implications for chemotaxis. *PloS one* (2012) 7:e35412. doi:10.1371/journal.pone.0035412
47. Frenkel D, Smit B, Ratner MA. *Understanding Molecular Simulation: From Algorithms to Applications*, 2. San Diego: Academic Press (1996).
48. Gilpin W, Prakash VN, Prakash M. Vortex Arrays and Ciliary Tangles Underlie the Feeding-Swimming Trade-Off in Starfish Larvae. *Nat Phys* (2017) 13:380–6. doi:10.1038/nphys3981
49. Mathijssen AJTM, Doostmohammadi A, Yeomans JM, Shendruk TN. Hydrodynamics of Micro-Swimmers in Films. *J Fluid Mech* (2016) 806: 35–70. doi:10.1017/jfm.2016.479
50. Marcos FHC, Fu HC, Powers TR, Stocker R. Bacterial Rheotaxis. *Proc Natl Acad Sci U.S.A* (2012) 109:4780–5. doi:10.1073/pnas.1120955109
51. Figueroa-Morales N, Rivera A, Soto R, Lindner A, Altshuler E, Clément É. *E. coli* "Super-contaminates" Narrow Ducts Fostered by Broad Run-Time Distribution. *Sci Adv* (2020) 6:eaay0155. doi:10.1126/sciadv.aay0155
52. Lauga E, DiLuzio WR, Whitesides GM, Stone HA. Swimming in Circles: Motion of Bacteria Near Solid Boundaries. *Biophysical J* (2006) 90:400–12. doi:10.1529/biophysj.105.069401
53. Molaei M, Barry M, Stocker R, Sheng J. Failed Escape: Solid Surfaces Prevent Tumbling of Escherichia Coli. *Phys Rev Lett* (2014) 113:068103. doi:10.1103/PhysRevLett.113.068103

Conflict of Interest: The authors declare that the research was conducted in the absence of any commercial or financial relationships that could be construed as a potential conflict of interest.

frontiers | Frontiers in Physics

ORIGINAL RESEARCH
published: 21 June 2022
doi: 10.3389/fphy.2022.895536

Ambient Fluid Rheology Modulates Oscillatory Instabilities in Filament-Motor Systems

Joshua Tamayo[1†], *Anupam Mishra*[2†] and *Arvind Gopinath*[1]*

[1]Department of Bioengineering, University of California, Merced, Merced, CA, United States, [2]Department of Mechanical Engineering, University of California, Merced, Merced, CA, United States

Semi-flexible filaments interacting with molecular motors and immersed in rheologically complex and viscoelastic media constitute a common motif in biology. Synthetic mimics of filament-motor systems also feature active or field-activated filaments. A feature common to these active assemblies is the spontaneous emergence of stable oscillations as a collective dynamic response. In nature, the frequency of these emergent oscillations is seen to depend strongly on the viscoelastic characteristics of the ambient medium. Motivated by these observations, we study the instabilities and dynamics of a minimal filament-motor system immersed in model viscoelastic fluids. Using a combination of linear stability analysis and full non-linear numerical solutions, we identify steady states, test the linear stability of these states, derive analytical stability boundaries, and investigate emergent oscillatory solutions. We show that the interplay between motor activity, filament and motor elasticity, and fluid viscoelasticity allows for stable oscillations or limit cycles to bifurcate from steady states. When the ambient fluid is Newtonian, frequencies are controlled by motor kinetics at low viscosities, but decay monotonically with viscosity at high viscosities. In viscoelastic fluids that have the same viscosity as the Newtonian fluid, but additionally allow for elastic energy storage, emergent limit cycles are associated with higher frequencies. The increase in frequency depends on the competition between fluid relaxation time-scales and time-scales associated with motor binding and unbinding. Our results suggest that both the stability and oscillatory properties of active systems may be controlled by tailoring the rheological properties and relaxation times of ambient fluidic environments.

Keywords: spontaneous oscillations, active instabilities, rheology, motor assemblies, complex matter

Edited by:
Liheng Cai,
University of Virginia, United States

Reviewed by:
Xingbo Yang,
Harvard University, United States
Poornachandra Sekhar Burada,
Indian Institute of Technology
Kharagpur, India

***Correspondence:**
Arvind Gopinath
agopinath@ucmerced.edu

†These authors have contributed equally to this work

Specialty section:
This article was submitted to
Soft Matter Physics,
a section of the journal
Frontiers in Physics

Received: *14 March 2022*
Accepted: *06 May 2022*
Published: *21 June 2022*

Citation:
Tamayo J, Mishra A and Gopinath A (2022) Ambient Fluid Rheology Modulates Oscillatory Instabilities in Filament-Motor Systems.
Front. Phys. 10:895536.
doi: 10.3389/fphy.2022.895536

1 INTRODUCTION

Biology is replete with examples of rigid and semi-flexible filaments, that singly or as aggregate bundles, interact with molecular motors in intracellular or extracellular settings. For instance, actin-myosin systems are crucial for cell function, development and growth [1–5] and in the transport of DNA [2]. Structured filament-motor systems comprised of microtubules and axonemal dynein motor arrays drive sperm locomotion [6–8] and algal motility [9]. These also constitute crucial components of healthy respiratory and reproductive tracts [10–15]. In the synthetic realm, motor assays and reconstituted biofilament networks frequently feature molecular motors translating, deforming and bending filaments [16–18].

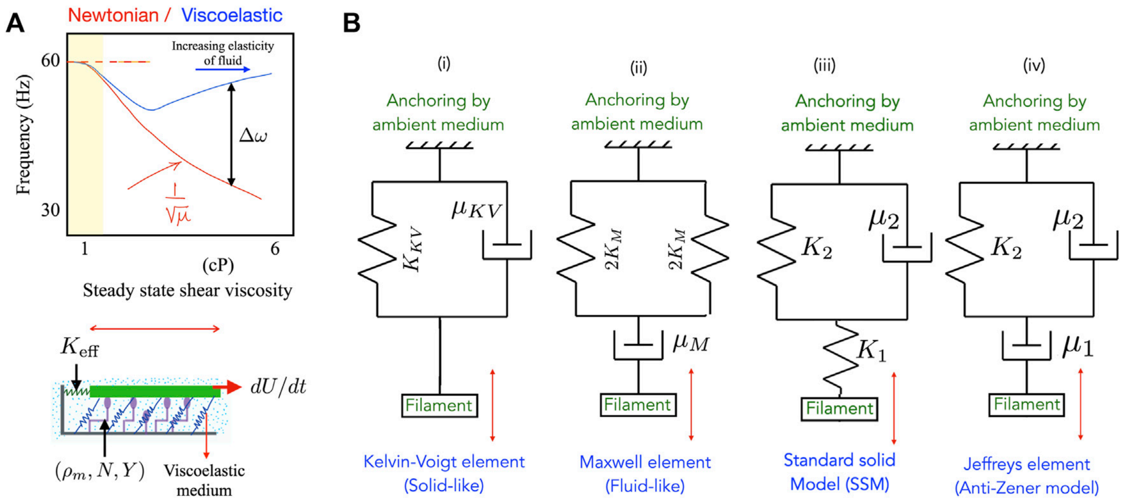

FIGURE 1 | (A) (Top) A schematic summarizing experimental observations of ciliary frequencies on bi-ciliated alga *Chlamydomonas reinhardtii* moving in model viscoelastic fluids [9] made by adding polymer to a Newtonian solvent. The observed ciliary beat frequency in polymeric fluids is much higher than in Newtonian fluids with the same viscosity. (Bottom) Schematic of the animated motor-filament segment that forms the basis of the minimal motor-filament system. Active motors (purple) may be in one of two states–attached to the segment (in green) or detached. Passive cross-linkers are shown in blue and are treated as linearly elastic springs. The resistance to motion of the test segment exerted by its neighbors are combined into an effective elastic resistance (spring constant $K_{\rm eff}$). The ambient medium in which the assembly is embedded is viscoelastic. In the minimal model this medium may be treated as a Maxwell medium or as a Kelvin-Voigt medium. **(B)** Representations of the viscoelastic ambient media considered in this article—here the spring stiffness K (if present) for each material is related to the elastic modulus of the material comprising the medium. (i) A Kelvin-Voigt material, (ii) a Maxwell fluid, and (iii) a generalized standard solid element. The anti-Zener Jeffrey element in (iv) results in a more complicated relationship involving second derivatives of the strain rather than first derivatives as in (i)-(iii).

A striking and well-studied feature of these filament-motor systems is the emergence of stable oscillations under favorable conditions. Examples include oscillatory instabilities in muscles and sarcomeres [19–21] and in microtubule assays involving NCD motors [22, 23], the periodic undulations of eukaryotic cilia [7, 8], and spontaneous oscillations during asymmetric cell division that involve microtubules interacting with cortical force generators [24–26]. These temporally varying patterns may follow complicated periodic functions, and are furthermore very tunable. Often, the onset of these oscillations may be controlled by quenching the system by depleting the molecular motors (the active agents driving these oscillations) of their energy source (ATP or Ca^{2+}). All these systems are open systems with continuous energy input, and highly non-linear. In all, these observations suggest that the onset of these oscillations may be interpreted as instabilities to a base state triggered by system changes.

Biological filaments and motors usually inhabit fluidic or gel-like media with non-Newtonian properties and viscoelastic properties. Such complex fluid environments can directly impact these active systems by exerting time-dependent stresses. For instance, a filament moving in a Newtonian fluid feels viscous drag stresses exerted by the ambient medium. A filament moving in viscoelastic environments will be subject to more complicated time dependent forces that include dissipative (viscous) and non-dissipative (elastic) components. Recent work on cilia in the green alga *Chlamydomonas reinhardtii* that enables whole-cell locomotion suggests a strong influence of the viscosity and complex rheology of the ambient fluidic medium [9, 27]. Sketched in **Figure 1A** is a schematic summarizing experiments from [9] that depicts the variation in ciliary beat frequency of an algal cell in Newtonian (red) and polymeric (blue) fluids. Frequencies are seen to be significantly higher in the viscoelastic polymeric fluid compared to a Newtonian fluid with the same viscosity. Similarly strong effects of viscoelasticity on ciliary beat frequency are seen in the human mucociliary tract. In diseased states or when there is ciliary dysfunction—as seen for instance in cystic fibrosis (CF), primary ciliary dyskinesia (PCD) or chronic obstructive pulmonary disease (COPD)—the mucus layer submerges cilia in an extremely viscoelastic environment that impacts their beating [10, 12–14].

Thus the effect of the rheology of the ambient fluid needs to be understood in order to predict the dynamical response in these biological filament-motor systems. There is however a significant gap in our understanding of these aspects since it is experimentally difficult to independently vary fluid viscosity and elasticity. Abstracting the ingredients crucial to the examples of actively driven motor-filament systems allows us to identify three main ingredients that may control system-level mesoscale and macroscale dynamics–1) passive elasticity, from intrinsic filament-motor elasticity, 2) rheological properties of the embedding medium, and 3) associated motor mechanochemistry and kinetics. Here, we will combine these elements to build a simple phenomenological model for a filament-motor aggregate interacting with model fluidic media. To enable analytical progress, we assume the ambient fluid to correspond to one of three canonical types–a Newtonian fluid, a Kelvin-Voigt gels or a Maxwell medium. Using our minimal model we investigate the onset, stability and control of oscillations and address associated questions: 1) how do variations in the fluid induced mechanical stresses affect the manner in which the internal biomechanical state of the molecular motors in the aggregate is modulated, 2) how do these modulations impact the onset of oscillations, and when may they stabilize an otherwise unstable system, and 3) how does fluid rheology affect the frequency of emergent oscillations and their amplitude? Biological filament-motor systems are of course much more complex than the minimal model analyzed here. Nonetheless, minimal models offer an essential tool for understanding basic biophysical mechanisms. In this sense, the simple minimal model analyzed here using model fluids represents an important step towards more complete computational models.

2 MINIMAL MODEL

Our model system is shown in **Figure 1A** (bottom pane). We model the filament bundle—referred to henceforth as (composite) filament—as a rigid sheet that is at a certain fixed height from an underlying flat substrate. In the reduced setting analyzed here, the sheet has length ℓ_A, thickness $b_A \ll \ell_A$ and lateral extent w_A satisfying $\ell_A \gg w_A \gg b_A$. The view shown in the figure is from the side, the axial dimension is the length and the lateral dimension into the paper (corresponding to the lateral extent, *b*) is treated as a neutral direction. The area of the segment that faces the underlying substrate is $\ell_A w_A$. Biofilaments and aggregates may have slender cylindrical geometries; the area $\ell_A w_A$ is thus to be interpreted as the projected area of the aggregate that faces the substrate.

The filament is held a fixed distance away from an underlying flat substrate by passive, permanently attached linear springs (blue springs) with areal density ρ_{p}, stiffness K_{p}, and equilibrium length ℓ_{p}. These passive springs resist shearing deformations and lateral translation of the filament. Additionally, the filament also interacts with a collection of model molecular motor proteins that are shown in purple in the figure. These motors are grafted to the lower plate with an areal density ρ_{m}. We treat these molecular motors as active linear elastic springs with spring constant k_{m} and equilibrium rest length ℓ_{m}. The tail of each motor is permanently attached to the substrate and thus we do not allow for diffusion of the motors. Motor heads meanwhile can periodically adhere to the filament and when attached generate forces displacing the filament laterally. We choose the inter-motor spacing to be small enough, and densities high enough that a continuum description of filament-motor interactions suffices. Finally, for ease of analysis without loss of generality, we set $\ell_{\mathrm{m}} = \ell_{\mathrm{p}} = 0$.

To aid in the analysis, we model motor-filament interactions using two-state cross-bridge models [8, 19, 21]. Each motor is either attached state or detached. Detached motors can attach to the filament in a forward-leaning position with specified attachment probabilities. They then quickly undergo a conformational change, which makes them strained. As the filament moves, so does the motor and this results in the extension of the motor and thus extension of the internal spring (with spring constant k_m). Attached motors can detach any time, and the statistics of this process is embodied via microscopic strain dependent detachment probabilities. The transitions between attached and detached states – the kinetics of the mechanochemical cycle – are thus determined by motor kinetics, and specifically the attachment and detachment probabilities (rates). Detailed microscale equations modeling the mechanochemistry and motor-filament interactions in systems such as these have been derived and used by others and by us (c.f [19, 28] and references therein). Briefly summarized, motor kinetics may be described by a set of population balances relating the attached and the detached probability densities to the attachment and detachment fluxes via microscopic transition rates. For simplicity we neglect motor diffusion, and consider the noiseless mean-field limit, where the number of motors (and the density) is large (high) enough that fluctuations in the time average of the density of attached motors are small compared to the mean value. When the distribution in extension of attached motors is sharply peaked about the typical (average) length, transients to this distribution occur over times very small compared to the averaged macroscopic time scale. The extension of attached motors is then peaked about the mean value with small deviations from the mean. We assume that detached motors relax to a delta function with the change occurring instantaneously. Coarse-graining the microscale dynamical equations provides a mean-field continuum description for the (mean) attached motor fraction, and the mean attached motor extension.

3 GOVERNING EQUATIONS FOR THE MINIMAL MODEL

Following the physical picture described in §2, we next derive equations governing the dynamics for our minimal system - an elastically constrained filament-motor assembly embedded in a viscoelastic fluid. To enable analytical progress, we assume that the rheology of the embedding fluidic medium behaves in one of three ways: as 1) a Newtonian fluid, as 2) a Kelvin-Voigt material, or as a 3) Maxwell medium. Based on these, filament-motor and filament-medium interactions may be modeled analytically.

Consider again the schematic in **Figure 1A**. As mentioned earlier, the (composite) filament interacts with motors via a projected area $\ell_A w_A$ where w_A is the width in the neutral direction. To model the effect of external elastic constraints on the filament, we choose to anchor the filament to a boundary with a linear elastic anchoring spring with stiffness K_{eff} and rest length L_o. We ignore edge effects and choose a reference frame with origin at the left attachment point where the spring is anchored. Due to the action of the motors, the rigid filament moves horizontally; with its motion resisted by the anchoring spring and the passive substrate attached springs. Filament motion is also resisted by fluid drag forces arising from the ambient viscoelastic medium. As a result of these restoring forces, when forced by attached molecular motors, the equilibrium stable state of the filament can either be one of rest or a time dependent state.

We define the displacement of material points on the plate relative to the rest state (where no motors are attached to the filament and the spring is not strained) by $U^* = L - L_o$; the speed of the plate is $\dot{U}^*$. In the absence of fluid and solid inertia, the sum of forces on the filament must vanish. If F_m^* is the effective active force density *per attached motor*, force balance on the filament provides the equation

$$F_{\rm d}^* + \ell_A w_A \rho_{\rm p} k_{\rm p} U^* + K_{\rm eff} U^* - \ell_A w_A \rho_m F_m^* = 0 \tag{1}$$

The active force F_m^* in **Eq. 1** is obtained from a knowledge of two variables describing the *state* and *quantity* of activity–the fraction of attached motors N and a mean motor extension Y^*. We follow a model that has been studied by others and by us previously [19, 28] that incorporates an experimentally motivated mean-field description of motor attachment and detachment kinetics. Motor kinetics is captured by the mean-field attachment rate $\omega_{\rm on}$, and the mean-field detachment rate $\omega_{\rm off}$. The overall motor density of motors that interacts with the filament is ρ_m, a fraction N of which is attached at any time. In the context of this simplified picture, the evolution of the fraction of attached motors, N follows

$$\dot{N} = \omega_{\rm on}^o (1-N) - \omega_{\rm off}(Y^*)N. \tag{2}$$

Here the mean attachment rate $\omega_{\rm on}^o$ is constant while the mean detachment rate $\omega_{\rm off} = \omega_{\rm off}^o \mathcal{F}$ incorporates the state dependent function $\mathcal{F}(Y^*)$ that depends on motor extension (stretch). This quantity—the stretch of attached motors, Y^*—follows

$$\dot{Y^*} = -\dot{U^*} + \omega_{\rm on}^o (\mathcal{A} - Y^*)\left(\frac{1-N}{N}\right) \tag{3}$$

Given N and Y^*, the effective active force per motor in **Eq. 1** is given by

$$F_m^* = k_m N Y^*. \tag{4}$$

We next model the fluid interaction term, F_d^*, in **Eq. 1** by specifying constitutive laws for the manner in which the fluid interacts with the filament.

1. Newtonian fluid: In the simplest case where the medium is a Newtonian fluid, the fluid drag per unit length acting on the plate depends just on the local shear rate at the plate surface. Since our intention is to capture qualitative aspects we proceed with scaling laws. Let us assume that the shear rate induced in the fluid at the filament surface is uniform along the filament and the velocity field penetrates to a distance ℓ_N so that an aerage measure of the local strain rate is $(1/\ell_N)dU^*/dt^*$. An approximate equation for the drag force is then

$$F_{\rm d,N}^* - (\ell_A w_A/\ell_N)\mu_{\rm N}\dot{U}^* = 0 \tag{5}$$

with $\mu_{\rm N}$ being the Newtonian viscosity. The reduction is consistent with an effective drag coefficient approximation used for motion of bodies at low Reynolds number (with drag force proportional to the instantaneous speed). Note that the segment length ℓ_A, segment width w_A and length ℓ_N are all assumed to be constants. This is a major simplification since this penetration depth can be time dependent.

2. Kelvin-Voigt fluid: When the embedding medium is a networked gel-like medium with both elastic and viscous features, the drag forces depend both on plate velocities as well as displacements. One may consider these displacement contributions to arise as a result of restoring forces as the plate moves relative to a fixed meshed elastic network. We choose a Kelvin-Voigt like model with a single retardation time scale and equilibrium mesh size $\ell_{\rm KV}$ represented by

$$\sigma_{\rm KV}^* = E^{\rm KV}\epsilon_{\rm KV}^* + \mu^{\rm KV}\dot{\epsilon}_{\rm KV}^*$$

relating the strain to the stress. Evaluating this at the surface of the plate and assuming no slip, we obtain (measuring strain in mesh lengths, and assuming a continuum formulation holds)

$$F_{d,KV}^* = \ell_A w_A \sigma_{\rm KV}^* = \ell_A w_A \left(E^{\rm KV}/\ell_{\rm KV}\right)U^* + \ell_A w_A \left(\mu^{\rm KV}/\ell_{\rm KV}\right)\dot{U}^* \tag{6}$$

3. MaxwelL gel: For a viscoelastic Maxwell-like with a single relaxation time scale and a mesh length $\ell^{\rm M}$, we have the relationship

$$E_M \mu_M \dot{\epsilon}_M^* = E_M \sigma_M^* + \mu_M \dot{\sigma}_M^*$$

or

$$\dot{\epsilon}_{\rm M}^* = \left(1/\mu^{\rm M}\right)\sigma_{\rm M}^* + \left(1/E^{\rm M}\right)\dot{\sigma}_{\rm M}^*.$$

Evaluating this at the surface of the plate and assuming no slip, we obtain (again measuring strain in units of mesh length and assuming a continuum formulation holds so that

$$\ell_{\rm A} w_{\rm A} \dot{U}^* = (\ell^{\rm M}/\mu^{\rm M})F_{\rm d,M}^* + (\ell^{\rm M}/E^{\rm M})\dot{F}_{\rm d,M}^* \tag{7}$$

Equations 1,**5**,**6**,**7** assume that the ambient medium is always quasi-statically coupled to motion of the upper plate. A similar analysis may be done for the Zener standard solid model of the type illustrated in **Figures 1B–iv**, but we do not pursue this in the current work.

We emphasize that **Equations 5–7** ignore transient stress fields induced as the viscous/viscoelastic boundary layer forms near the moving filament and associated time-dependent features. A more accurate description would necessitate solving the full Navier-Stokes equation with the appropriate constitutive equation relating the stress in the fluid to the strain and strain rate and is beyond the aim of this paper.

To obtain scaled equations that allow the identification of important non-dimensional parameters, we scale time with $1/\omega_{\rm on}^o$, and motor/filament extensions with $\mathcal{A}$. Defining $t^* = T(\omega_{\rm on}^o)^{-1}$, $Y^* \equiv \mathcal{A}Y$ and $U^* \equiv \mathcal{A}U$ allows us to recast (1), in dimensionless form. In this process, we find that re-scaling anchoring spring stiffness by defining $\bar{K}_{\rm eff} \equiv K_{\rm eff}/\ell_A w_A$ provides a further reduction. Since the fraction of attached motors $N \equiv \rho_a/\rho_m$ where ρ_a is the density of attached motors, the density of detached motors is $\rho_m - \rho_a$. **Tables 1** and **2** summarize the scaled parameters in our model. **Equations 8–10** constitute the final scaled nonlinear ODE's governing the evolution of the motor-filament system embedded in the viscoelastic medium.

$$\frac{dN}{dT} = (1-N) - \Psi\mathcal{F}(Y)N, \tag{8}$$

TABLE 1 | Motor-related parameters and scaled variables in the minimal model.

Symbol	Definition	Interpretation
$\mathcal{A}$	-	Typical dimensionless motor displacement and strain
$\mathcal{E}_s$	$k_m\mathcal{A}/k_BT$	Strain dependent force scale for motor detachment
β	$\rho_m k_m/(\rho_p k_p + \bar{K}_{\text{eff}})$	Scaled motor density and a measure of active elasticity
Ψ	$\omega_{\text{off}}^{o}/\omega_{\text{on}}^{o}$	Ratio of motor kinetic constants and related to motor duty ratio
$N(t)$	ρ_a/ρ_m	Ensemble averaged fraction of total motors attached
$Y(t)$	$Y^*/\mathcal{A}$	Ensemble averaged (mean) motor extension
$U(t)$	$U^*/\mathcal{A}$	Scaled filament extension (strain)

TABLE 2 | Dimensionless parameters quantifying the ambient medium stress on moving filament. Here, ℓ_A and w_A are the length and width of the filament aggregate interacting with motors and allow one to go from the stress to a force description. Displacements are scaled with $\mathcal{A}$. We assume a continuum description is valid and that strains in the fluid/medium network may be appropriately defined using elastic and viscous moduli. We consider three cases: (a) a Newtonian fluid, (b) Kelvin-Voigt liquid-like viscoelastic medium, and (c) Maxwell solid-like medium. Models (b) and (c) serve as limiting cases of the more general linear Jeffreys' model that belongs to the class of anti-Zener models and the standard solid model (SSM) of classical viscoelasticity. The ratio $\mathcal{B}_2/\mathcal{B}_1$ for the Kelvin-Voigt model is a ratio of rheological to motor kinetics time-scales. Parameter $\mathcal{B}_3$ has a similar interpretation for the Maxwell model. The anti-zener Jeffrey element results in a relationship involving the second derivative of the strain/displacement and results in the additional term with coefficient $\mathcal{B}_5$, and is not analyzed in this paper.

Symbol	Newtonian	Kelvin-Voigt	Maxwell
$\mathcal{B}_1$	0	$\frac{E^{\text{KV}}}{\ell_{\text{KV}}(\rho_{\text{p}}k_{\text{p}}+\bar{K}_{\text{eff}})}$	0
$\mathcal{B}_2$	$\frac{\mu_N\omega_{\text{on}}^0}{\ell_N(\rho_{\text{p}}k_{\text{p}}+\bar{K}_{\text{eff}})}$	$\frac{\mu^{\text{KV}}\omega_{\text{on}}^0}{\ell_{\text{KV}}(\rho_{\text{p}}k_{\text{p}}+\bar{K}_{\text{eff}})}$	$\frac{\mu^{\text{M}}\omega_{\text{on}}^0}{\ell_M(\rho_{\text{p}}k_{\text{p}}+\bar{K}_{\text{eff}})}$
$\mathcal{B}_3$	0	0	$\frac{\omega_{\text{on}}^0\mu^{\text{M}}}{E^{\text{M}}}$
$\mathcal{B}_4$	1	1	1
$\mathcal{B}_5$	0	0	0

$$\frac{dY}{dT} = -\frac{dU}{dT} + (1-Y)\left(\frac{1-N}{N}\right) \tag{9}$$

$$-F_{\text{d}} = U - \beta NY, \quad \text{where} \quad \mathcal{B}_1 U + \mathcal{B}_2\frac{dU}{dT} = \mathcal{B}_3\frac{dF_d}{dT} + \mathcal{B}_4 F_d \tag{10}$$

with dimensionless parameter β quantifying motor density while dimensionless parameters $\mathcal{B}_1$ to $\mathcal{B}_4$ quantifying the viscoelasticity of the fluid and fluid specific relaxation times. We would like to point out here that **Equation 10** is applicable to Newtonian, Maxwell, Kelvin-Voigt and the standard solid models (illustrated in **Figures 1B,I–1iii**. The anti-Zener Jeffrey element depicted in **Figures 1B–1iv** involves a more complicated relation with a second derivative of U as follows

$$\mathcal{B}_1 U + \mathcal{B}_2\frac{dU}{dT} + \mathcal{B}_3\frac{d^2U}{dT^2} = \mathcal{B}_3\frac{dF_d}{dT} + \mathcal{B}_4 F_d$$

In this article we will consider not consider models resulting in a second derivative of U. The linear stability analysis can however be extended to the Jeffrey element, albeit with slightly more involved algebra.

Following previous work, we model motor kinetics as responding to the deformation experienced by attached motors [1, 2, 19]. Attached motors behaving as slip bonds with a strain dependent detachment probability. This functionality is encoded in the detachment rate $\omega_{\text{off}}(Y) = \omega_{\text{off}}^0\mathcal{F}(Y)$ that modifies the bare detachment rate by a multiplicative factor $\mathcal{F}(Y)$. For the analytical investigations, we restrict $\mathcal{F}(Y)$ to functions that is at least twice differentiable but otherwise general. For plotting, we will use the following forms

$$\mathcal{F}(Y) = \cosh\left(\mathcal{E}_s Y^2\right), \quad \text{or} \quad \mathcal{F}(Y) = \cosh\left(\mathcal{E}_s Y\right). \tag{11}$$

Equations 8–11 admit a stationary state given by the set $(N, Y, U) = (N_0, Y_0, U_0)$ where these satisfy

$$Y_0 = 1, \quad N_0 = \left(\frac{1}{1+\Psi\mathcal{F}_0}\right), \quad U_0 = \left(\frac{\beta N_0}{1+\mathcal{B}_1/\mathcal{B}_4}\right). \tag{12}$$

In **Equation 11**, the dimensionless parameter $\mathcal{E}_s$ quantifies the characteristic force attached motors can withstand before detachment. Note that the ratio $\mathcal{B}_1/\mathcal{B}_2$ compares the motor time scale with the relaxation time scale of the Kelvin-Voigt medium. Dimensionless parameter $\mathcal{B}_3$ is similarly a ratio of motor time-scales to fluid relaxation times scales for the Maxwell fluid. Physical interpretations of variables (U, N, Y) and that of dimensionless parameters are summarized in **Tables 1** and **2**.

In our model, bending is ignored and the filament composite/aggregate is considered rigid and inextensible. While our model is not directly applicable to ciliary oscillations, using some numerical estimates relevant to filaments and motors in cilia provides understanding of the magnitudes of the parameters in the model. Our model also may allow us to interpret how oscillations may arise within and along an initially straight passive cilium. Localized elastically weak regions may result in cilia fragments driven by dynein arrays moving against their neighbors. In this scenario, we estimate $k_m \sim 10^{-3}$ N/m, the effective linear density $\rho_m w_A \sim O(10^8)$ m^{-1}, $w_A \sim 40$–60 nm, $k_{\text{N}} \sim 16$–100 pN μm^{-1} and $w_A\rho_{\text{N}} \sim 10^5$–$10^7$ m^{-1} [1, 29]. The value of K_{eff} depends on the material. Microtubules are relatively stiff with large persistent lengths and the Young's modulus $E \sim 1.2$ GPa providing the stiffness per length $K_{\text{eff}} \sim Gw_A$. For microtubules driven by dynein, previous studies report a persistence length ~ 5mm at room temperature, and for actin driven by myosin, ~ 16 μm at room temperature. These length scales provide an upper bound for ℓ_A. For polymeric fluids, relaxation times can vary significantly depending on the type of polymer and concentration, Carboxymethylcellulose (CMC) solutions for instance, with MW = 7×10^5 can have relaxation times ~ 20−50 ms as concentration is varied from 225 to 500 ppm [30]. At very high concentrations (4000 ppm), the relaxation time is as large as 0.2 s. Shear viscosity meanwhile for these can vary from ~ 1 mPa.s to ~ 18.8 mPa.s for concentrations ranging from 0–500 ppm. Polymeric solutions made using polyacrylamide also allows us to access a range of relaxation times. Specifically, in [9] viscoelastic fluids prepared by adding small amounts of high molecular weight polyacrylamide at concentration in solution ranging from 5 to 80 ppm resulted in fluid relaxation times that ranged from 6 ms to 0.12 s, respectively.

4 RESULTS AND DISCUSSION

4.1 Dynamics of the Unconstrained System

Before analyzing the dynamics of the constrained filament-motor system, we briefly address the dynamics of an unconstrained system. Accordingly, we set $\rho_p = 0$, $K_{\text{eff}} = 0$ and study the dynamics of the animated filaments on a rigid surface on which motors are grafted, as in motility assays. Short fragments in these assays are typically rigid enough that they move without bending. Long fragments on the other hand are susceptible to buckling instabilities as previous studied experimentally and analytically [18, 31–36] in these and similar systems involving driven active filaments.

Here, we invert the problem and study the dynamics of the motor variables (Y, N) as functions of the speed $Z = dU/dT$. In other words, we restrict ourselves to time scales where the dynamics of the motor kinetics is slaved to the speed of the filament. The speed Z may be envisioned as an independently controlled variable; we then enquire how steady values of N and Y depend on Z and if these solutions are linearly stable. **Eq. 10** is irrelevant in this limit, and **Equations 8**, **9** become.

$$\frac{dN}{dT} = (1 - N) - \Psi \mathcal{F}(\mathcal{E}_s, Y)N, \tag{13}$$

$$\frac{dY}{dT} = -Z + (1 - Y)\left(\frac{1 - N}{N}\right) \tag{14}$$

When $Z = 0$, **Equations 13**, **14** admit steady state solutions (N_s, Y_s) given by

$$N_s(Z = 0, \Psi, \mathcal{E}_s) = (1 + \Psi \mathcal{F}(1))^{-1}, \quad Y_s(Z = 0, \Psi, \mathcal{E}_s) = 1 \tag{15}$$

For each value of $Z \neq 0$, other steady solutions different from **Eq. 15** exist. To study both the steady solutions and their stability, we use an in-house numerical continuation implemented in Matlab@. Treating Z as the free variable, we plot steady solutions to **Equations 13**, **14** and investigate the stability of the solutions for various values of Ψ and $\mathcal{E}_s$ and for different functional forms of $\mathcal{F}$ the detachment function. **Figure 2** shows an example case where we keep $\mathcal{E}_s$ and Ψ the same while using two forms of $\mathcal{F}$. Solid curves (maroon and blue) represent stable solutions while dashed curves are unstable solution branches. Turning points, where these branches meet, are shown as circles.

Numerical investigation reveals that the existence and extent of the unstable region depends on the form of the detachment curve. When the detachment function is constant or a decreasing function of extension Y, no unstable regions exist. In these cases, typically each value of Z is associated with a unique value of N and Y. However when the detachment function is an increasing function of Y, some parts of the steady state solutions becomes unstable as seen in **Figure 2**. This is manifest clearly in bistability, evident for instance in the curves of N vs. Z with three possible values of Z (two stable, one unstable) corresponding to a single value of Z. A value of $N = 0.4$ in **Figure 2A**-(ii) and 2(b)-(ii) for instance is unstable and is susceptible to disturbances that can push the state to either the upper branch or the lower branch each with the same value of Z. The origin of this instability is the emergence of effective negative spring constants due to motor activity; such features have been studied previously [19].

4.2 Analytical Results: Oscillatory Instabilities and Emergent Frequencies

The question that arises naturally next is how $K_{\text{eff}} > 0$ impacts this response. To answer this question, we turn next to the stationary base state of the full **Equations 8–11** and the linear stability of the base state given by **Eq. 12**. We find that the base state exhibits linear instability for certain regions in parameter space. We derive analytical expressions for the locus of these critical points—the neutral stability curves. Classical linear stability analysis shows at these critical points, stable oscillatory solutions emerge via the Hopf-Andronov-Poincare bifurcation [37]. Limit cycles emanate at these points with fixed frequencies and small amplitude. We calculate the frequencies of these emergent solutions analytically and investigate their dependence on dimensionless parameters defined earlier. Predictions of our linear stability analysis are confirmed by full non-linear solutions of the equations.

To identify the stability of the stationary (base) state (**Eq. 12**), we analyze how small imposed perturbations to this state evolve in time. We introduce a small (amplitude) parameter $\epsilon \ll 1$ and write

$$(N, Y, U, F_d) = \left(N_0, 1, U_0, F_d^0\right) + \epsilon\left(\bar{N}, \bar{Y}, \bar{U}, \bar{F}_d\right). \tag{16}$$

Substituting (**Eq. 16**) in **Eqs 8-11**, expanding all terms, and retaining only terms that are $O(\epsilon)$, we get the three coupled linear ODE's:

$$\frac{d\bar{N}}{dT} = -(1 + \Psi \mathcal{F}_0)\,\bar{N} - \left(\Psi \mathcal{F}_0' N_0\right)\bar{Y} \tag{17}$$

$$\frac{d\bar{Y}}{dT} = -\frac{d\bar{U}}{dT} - (\Psi \mathcal{F}_0)\,\bar{Y} \tag{18}$$

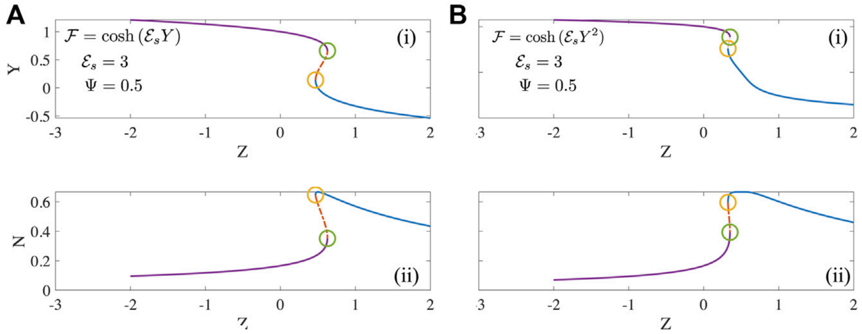

FIGURE 2 | The mean motor extension *Y* and fraction of motors that are attached *N* as a function of *Z* steady solutions to **Eqs 13**, **14** for two forms of the detachment function **(A)** $\mathcal{F} = \cosh(\mathcal{E}_s Y)$ and **(B)** $\mathcal{F} = \cosh(\mathcal{E}_s Y^2)$.

$$0 = -(\mathcal{B}_1 + \mathcal{B}_4)\bar{U} - (\mathcal{B}_2 + \mathcal{B}_3)\frac{d\bar{U}}{dT} + \beta\mathcal{B}_3\left(N_0\frac{d\bar{Y}}{dT} + \frac{d\bar{N}}{dT}\right) + \beta\mathcal{B}_4\left(N_0\bar{Y} + \bar{N}\right) \tag{19}$$

Substituting next

$$\left(\bar{N}, \bar{Y}, \bar{U}\right) = \exp(\sigma T)\left(\hat{N}, \hat{Y}, \hat{U}\right) \tag{20}$$

in **Eqs 17**-**19**, we obtain coupled algebraic equations for $(\hat{N}, \hat{Y})$ that determine the growth rate σ. Imposing solvability constraints, we get a cubic algebraic equation for σ:

$$a\sigma^3 + b\sigma^2 + c\sigma + d = 0 \tag{21}$$

where

$$\begin{aligned}
a &= (\beta N_0 + 1)\mathcal{B}_3 + \mathcal{B}_2, \quad d = (1 + \Psi\mathcal{F}_0)\Psi\mathcal{F}_0(\mathcal{B}_1 + \mathcal{B}_4)\\
b &= (\beta N_0 + 1)\mathcal{B}_4 + \mathcal{B}_1 + \beta N_0\mathcal{B}_3(1 + \Psi\mathcal{F}_0) + (\mathcal{B}_2 + \mathcal{B}_3)(1 + 2\Psi\mathcal{F}_0) - \Psi\mathcal{F}_0' N_0\beta\mathcal{B}_3\\
c &= \beta N_0\mathcal{B}_4(1 + \Psi\mathcal{F}_0) + (\mathcal{B}_1 + \mathcal{B}_4)(1 + 2\Psi\mathcal{F}_0) + (\mathcal{B}_2 + \mathcal{B}_3)\Psi\mathcal{F}_0(1 + \Psi\mathcal{F}_0) - \Psi\mathcal{F}_0' N_0\beta\mathcal{B}_4
\end{aligned}$$

The growth rates σ of **Eq. 21** depend crucially on the signs of b and c. We note that a and d are always positive. Since coefficients $a - d$ are real, **Equation 21** has—from the fundamental theorem of algebra—three roots. One of these is purely real and the other two may be complex conjugate. Since we set $\mathcal{B}_4 = 1$, and are more interested in varying the rheological parameters of the fluid, the dependence of b on $\mathcal{B}_3$ is the more important dependence. Here we will restrict our analysis to the physically relevant case where $b > 0$ and $c > 0$ (see **Supplementary Appendix A**).

Restricting ourselves to the subspace of solutions that comprise 1 real root and a complex conjugate pair, we write (σ_1), $\sigma_2 = \sigma + i\omega$ and $\sigma_3 = \sigma - i\omega$. When the base state is stable we have $\sigma_1 < 0$ and $\sigma < 0$. We seek incipient oscillatory instabilities such that emergent solutions may be stable and oscillating. At the onset of instability—that is *on the neutral stability curve*—this implies the condition $\sigma = 0$. The imaginary part ω may then be identified as the frequency of the emergent solutions.

4.2.1 Results From Stability Analysis

1. No drag from medium: Consider the simplest degenerate case where the medium does not exert any forces on the motor-filament system. In this case, we have $\mathcal{B}_1 = \mathcal{B}_2 = \mathcal{B}_3 = 0$ and $\mathcal{B}_4 = 1$. The equation for the growth rates is a quadratic equation for this degenerate case of the form $b\sigma^2 + c\sigma + d = 0$ where σ is the linear growth rate of infinitesimally small disturbances. For oscillatory instabilities, we require that $c < 0$ (so the growth rate, σ is non-negative); with this holding, $c = 0$ defines the locus of critical points. The neutral stability curve follows

$$\beta(\Psi, \mathcal{E}_s) = (1 + 2\Psi\mathcal{F}_0)\left[\left(\frac{\Psi\mathcal{F}_0'}{1 + \Psi\mathcal{F}_0}\right) - 1\right]^{-1}. \tag{22}$$

For constant Ψ and $\mathcal{E}_s$, **Equation 22** provides the critical value of β above which one can expect oscillatory limit cycles to bifurcate from the stationary steady state. Note that an essential condition here is $\mathcal{F}_0' > 0$ and that the magnitude be large enough for the equation to be satisfied. Formally, we require $\mathcal{F}$ to be a monotonically increasing function of Y consistent with previous work (see [2] for instance) in similar systems. The periodic solutions at onset have frequency

$$\omega^* = \sqrt{\frac{(1 + \Psi\mathcal{F}_0)\Psi\mathcal{F}_0}{\beta N_0 + 1}} \tag{23}$$

2. Newtonian fluid: For the simplest drag-producing medium - a Newtonian fluid - we have $\mathcal{B}_1 = \mathcal{B}_3 = 0$, $\mathcal{B}_2 > 0$ and $\mathcal{B}_4 = 1$ with specific forms listed in **Table 1**. The force balance reduces to

$$-\mathcal{B}_2\frac{dU}{dT} - U + \beta NY = 0$$

with first two left hand side terms being resisting (passive) forces and the third term the driving (active) force; the right hand is zero here due to the absence of inertia as explained earlier.The frequency of the bifurcating limit cycles at onset is given by

$$\omega_N = \sqrt{\frac{(1 + \Psi\mathcal{F}_0)\Psi\mathcal{F}_0}{(\beta N_0 + 1) + \mathcal{B}_2(1 + 2\Psi\mathcal{F}_0)}} = \sqrt{\frac{\beta + (1 + 2\Psi\mathcal{F}_0) + \mathcal{B}_2\Psi\mathcal{F}_0(1 + \Psi\mathcal{F}_0) - \Psi\mathcal{F}_0' N_0\beta}{\mathcal{B}_2}} \tag{24}$$

Combining (**Eqs 23**) and (**24**) yields

$$(\omega_N/\omega^*) = \sqrt{\frac{\beta N_0 + 1}{(\beta N_0 + 1) + \mathcal{B}_2 (1 + 2\Psi \mathcal{F}_0)}}$$

and so,

$$(\omega_N/\omega^*) \approx 1 - \frac{1}{2}\mathcal{B}_2 (1 + 2\Psi \mathcal{F}_0)(\beta N_0 + 1)^{-1} \quad \text{when} \quad \mathcal{B}_2 \ll 1$$

while

$$(\omega_N/\omega^*) = \sqrt{\frac{1}{\mathcal{B}_2}}\sqrt{\frac{\beta N_0 + 1}{1 + 2\Psi \mathcal{F}_0}} \quad \text{when} \quad \mathcal{B}_2 \gg (1 + \beta N_0).$$

Thus for very high viscosity μ_{N}, the frequency scales as $1/\sqrt{\mu_{\mathrm{N}}}$. The equation for the neutral stability curve simplifies to

$$\beta\left[\left(\frac{\Psi \mathcal{F}_0'}{1 + \Psi \mathcal{F}_0} - 1\right)\right] = (1 + 2\Psi \mathcal{F}_0) + \mathcal{B}_2 \Psi \mathcal{F}_0 (1 + \Psi \mathcal{F}_0) \left(\frac{\beta N_0 + \mathcal{B}_2 (1 + 2\Psi \mathcal{F}_0)}{\beta N_0 + 1 + \mathcal{B}_2 (1 + 2\Psi \mathcal{F}_0)}\right). \tag{25}$$

From the analytical expression for the neutral stability curve, we deduce that for oscillatory instabilities to exist we require that $\mathcal{F}_0' > 0$ and be a suitably large number. For large $\mathcal{B}_2$ such that $\mathcal{B}_2 \gg (\beta N_0 + 1)$, the critical value of β for onset of instability *is larger* than for the case of no drag and is consistent with expectation, since extra viscous drag implies higher dissipation rates. At constant motor properties—that is, at constant values of Ψ and $\mathcal{E}_s$ and with the form of $\mathcal{F}(Y)$ held fixed—the only way to enable this is by having a larger number (density) of active motors.

3. Kelvin-Voigt medium: Here, the drag force depends on the displacement and the rate of displacement. Thus we have $\mathcal{B}_4 = 1$, $\mathcal{B}_1 > 0$, $\mathcal{B}_2 > 0$ while $\mathcal{B}_3 = 0$. In this case again, oscillatory instabilities are possible at critical points provided $\mathcal{F}_0' > 0$. The frequency of the bifurcating limit cycles at onset is obtained as

$$\omega_{KV} = \sqrt{\frac{(1 + \Psi \mathcal{F}_0)\Psi \mathcal{F}_0 (\mathcal{B}_1 + 1)}{(\beta N_0 + 1) + \mathcal{B}_1 + \mathcal{B}_2 (1 + 2\Psi \mathcal{F}_0)}}. \tag{26}$$

For fixed motor parameters and fixed value of $\mathcal{B}_2$, the frequency in a KV medium is thus higher than the purely viscous medium (with the same viscosity/dissipative components, $\mathcal{B}_2$) consistent with experiment. The increment comes from the elastic component of rheology of the fluid but is augmented by the motor activity parameter Ψ and the strength of the detachment function but *not by its slope*. To compare with the two limiting cases analyzed earlier, we note that.

$$\frac{\omega_{KV}}{\omega^*} = \sqrt{\frac{(\beta N_0 + 1)(\mathcal{B}_1 + 1)}{(\beta N_0 + 1) + \mathcal{B}_1 + \mathcal{B}_2 (1 + 2\Psi \mathcal{F}_0)}} \tag{27}$$

$$\Delta\omega_{KV} = \left(\frac{\mathcal{B}_1}{\mathcal{B}_2}\right)\frac{(1 + 2\Psi \mathcal{F}_0)}{(\omega_{KV} + \omega_N)} \tag{28}$$

where we have defined the shift in frequency relative to a purely Newtonian fluid, $\Delta\omega_{KV} \equiv (\omega_{KV} - \omega_N)$. We can also derive the expression for the neutral stability curve

$$\beta\left[\left(\frac{\Psi \mathcal{F}_0'}{1 + \Psi \mathcal{F}_0} - 1\right)\right] = (1 + \mathcal{B}_1)(1 + 2\Psi \mathcal{F}_0) + \mathcal{B}_2 \Psi \mathcal{F}_0 (1 + \Psi \mathcal{F}_0) \left(\frac{\beta N_0 + \mathcal{B}_2 (1 + 2\Psi \mathcal{F}_0)}{\beta N_0 + 1 + \mathcal{B}_1 + \mathcal{B}_2 (1 + 2\Psi \mathcal{F}_0)}\right). \tag{29}$$

4. MaxwelL medium: For the Maxwell medium, the displacement rate is linearly coupled to the drag force and the rate of change of the drag force. We have for this case, $\mathcal{B}_1 = 0$, $\mathcal{B}_2 > 0$, $\mathcal{B}_3 > 0$ and $\mathcal{B}_4 = 1$.

From an estimation of constants $a - d$, we rule out the possibility of a fold-Hopf bifurcation, that is a fold bifurcation *coincident* with the Andronov-Hopf-Poincare bifurcation. However we can still satisfy conditions for the existence of an oscillatory instability. Further analysis (see **Supplementary Appendix A**) indicates a mathematical possibility for non-oscillatory instability for very high values of $\mathcal{B}_3$ for which b turns negative. We take this as evidence that the model is ill-posed for these high values of $\mathcal{B}_3$ and possibly inapplicable. We do not consider these unphysical solutions, and instead focus on the physically relevant oscillatory instabilities.

We therefore look for a subset of critical points for which exactly 1 real negative root (σ_1) and a complex conjugate pair ($\pm i\omega$) with zero real part ($\sigma = 0$) exists for the cubic. The neutral stability curve is defined by the locus of points that simultaneously satisfy $ad - bc = 0$. The frequency at onset is given by

$$\omega_M = \sqrt{\frac{(1 + \Psi \mathcal{F}_0)\Psi \mathcal{F}_0}{(\beta N_0 + 1) + \mathcal{B}_2 (1 + 2\Psi \mathcal{F}_0) + \mathcal{B}_3 (1 + \beta + 2\Psi \mathcal{F}_0 - \Psi \mathcal{F}_0' N_0 \beta)}} \tag{30}$$

Since $\mathcal{B}_3 > 0$, the overall sign of the term multiply B_3 depends on the magnitude of the term $\Psi \mathcal{F}_0' N_0 \beta$ that has a negative sign ahead of it. We have deduced earlier that for oscillations to exist we require that the detachment function be an increasing function of Y evaluated at the steady point Y_0. Combining these observations, we deduce that the frequency in a Maxwell medium can be higher than the Newtonian medium provided the term in red is negative. In fact the magnitude of this term (when negative in sign) can be readily modified two ways. First, for fixed $\mathcal{B}_3$, the magnitude can be adjusted by solely changing the form of the detachment function (through ω_{off}^0 and/or $\mathcal{E}_s$ and *independent* of the rheology parameters and the motor attachment rate. Second, for fixed motor mechanochemistry as long as the term in the parenthesis is negative, increasing $\mathcal{B}_3$ will increase the frequency of oscillations.

Before concluding this section, we address the biophysical origin of the oscillations. The simplest scenarios—the case of no fluid, and that of a Newtonian fluid—provide hints as to the destabilizing mechanism. Linearizing (**Eqs 8**)–(**11**) about the base

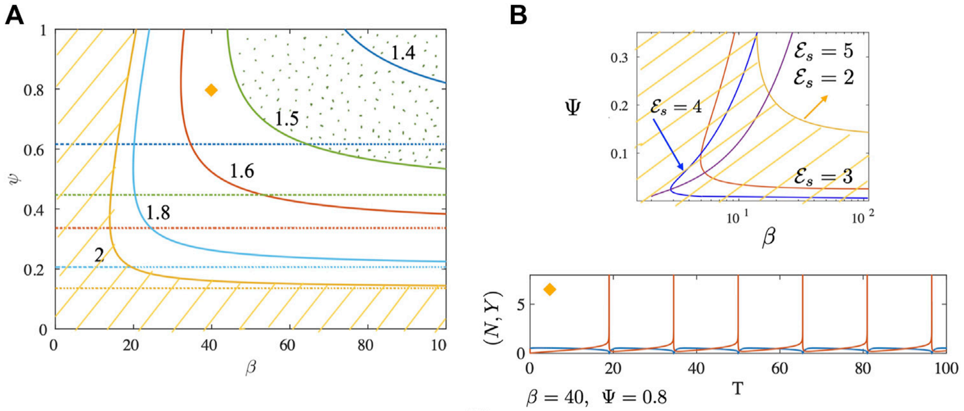

FIGURE 3 | (A) Neutral stability curves separating linearly stable from unstable regions are shown for the no drag case. Plotted as solid curves are results for different values of $\mathcal{E}_S$ (as indicated, from 1.4–2). The dash-dot lines are the limiting values of Ψ below which the base state is always stable. The shaded yellow region indicates the stable region for Ψ =2. The dotted green region indicates linearly unstable space susceptible to oscillatory instabilities for Ψ =1.5. The yellow rhombus point indicated in **(A)** is unstable for some parameter values, as demonstrated by full non-linear solutions when Ψ =2 (shown alongside). **(B)** For even larger values of $\mathcal{E}_S > 2$, the curves shift rightward as Ψ increases. In all these cases, $\mathcal{F}(\mathcal{E}_S, Y) = \cosh(\mathcal{E}_S Y)$.

state (**Eq. 12**) provides (in frequency space) a relationship between the displacement U and an effective compliance that includes contributions from the active motor-based interactions with the filament as well as the fluid response. When there is no drag/resistive force at all from the medium, we find that the instability arises when the active compliance has a negative effective elastic coefficient i. e, active motor induced elasticity overcomes the passive elastic resistances. This provides a mechanism by which *system-level* oscillations are initiated. Meanwhile the dissipative components of the system—i. e, viscous effects–limit the amplitude of the oscillations. Thus stable limit cycles can emerge. Interestingly no fluid or external medium is needed to initiate and sustain oscillations in this model system.

We have three independent parameters here that determine if oscillations exists–β, Ψ and $\mathcal{E}_s$. In general, we need the motors to detach so that the filament can slide back and forth. Very high motor attachment rates with no detachment also impedes oscillations by increasing the effective shear stiffness of the filament. Thus there is a lower limit for oscillations in terms of Ψ. For very high Ψ, the linear stable phase-space occupies larger extent. Similarly, there is a minimum value of $\mathcal{E}_s$ below which oscillations cannot be sustained—this is because motor detachment is not sufficient to sustain reversal of motion of the filament. Very high values of $\mathcal{E}_s$ on the other hand imply that motors detach almost as soon as they attach. Finally, there is also a minimum value of β, or equivalently a minimum density of active motors, needed to initiate oscillations.

4.3 Comparison to Non-linear Solutions

4.3.1 Amplitudes and Frequencies of Limit Cycles Vary Away From Critical Point

The linear stability analyses in **Section 4.1**, **Section 4.2** provide information on the stability boundaries for the stationary steady state (**Eq. 12**) and also on the emergent frequencies of the bifurcating limit cycles at critical points on these boundaries, the neutral stability curves. The frequency when parameters correspond to positions in phase space far away from the neutral stability curves will of course differ from the values at criticality. When all parameters are kept fixed, and just one parameter–say for example, β varies, the amplitude of the limit cycles is expected to scale ~ $\sqrt{\beta - \beta_c}$ where β_c is the critical value at which the instability manifests. While this scaling certainly holds close to criticality, actual amplitudes may deviate from this far from the critical point. Physically, oscillations and amplitudes are limited by a power balance. The active energy the motors generate and input into the system has to be dissipated viscously by fluid drag. Elasticity–from the anchoring spring, the underlying passive springs *and* from the fluid mediates oscillation amplitudes as well as provides a mechanism by which energy can be stored temporarily. Thus both the amplitude and the frequency of oscillations may vary significantly from linear stability predictions. Nonetheless, the emergent frequencies provide a good estimate and qualitative understanding of how the different biophysical parameters impact the frequency. Specifically, we are able to analytically calculate how motor density and elasticity (β), motor kinetics (Ψ and $\mathcal{E}_s$), and fluid rheology (parameters $\mathcal{B}_1$ to $\mathcal{B}_3$) impact the neutral stability curve and frequencies. The predicted trends are line with experimental observations of more complicated systems with both sliding and bending deformations such as that shown in **Figure 1A**. While a direct comparison is not possible, it is heartening to note that significantly higher frequencies (increase of up to a factor of 10) can be achieved by varying the rheological parameters of the model fluids, such as by keeping viscosity via $\mathcal{B}_2$ fixed while changing $\mathcal{B}_1$ in the Kelvin-Voigt model and $\mathcal{B}_3$ in the Maxwell model.

Our analysis also suggests that smooth modulation of the frequencies may be implemented once past the critical point but linear stability alone is insufficient to validate this. Furthermore the linear stability analysis does not show how the amplitude of the oscillations changes with parameters. The amplitude is

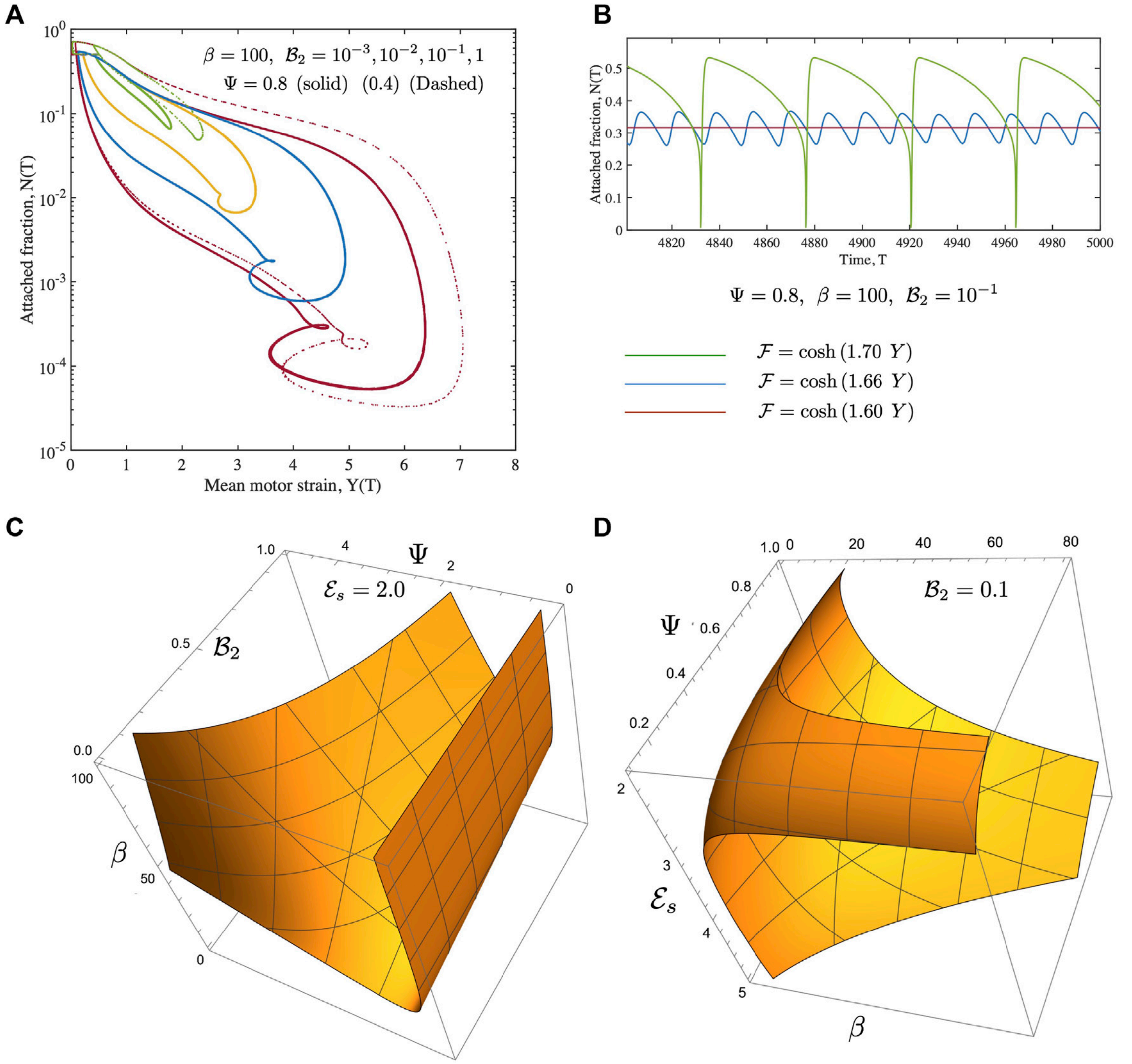

FIGURE 4 | (A) Phase-plots over complete cycles obtained from fully non-linear solutions for the Newtonian case are shown. The detachment function is cosh (2*Y*) and the motor activity parameter (density) β =100. We note that as $\mathcal{B}_2$ increases from 10^{-3} to 10^{-1}, the amplitude of oscillations decreases in sync with smaller variations in *N* and in *Y* over a cycle. **(B)** When motor density and kinetic parameters (β and Ψ) are kept constant, the value of $\mathcal{E}_s$ still controls if oscillations can ensure. Shown here are non-linear solutions—at $\mathcal{B}_2 = 10^1$—demonstrating the quenching of oscillations as $\mathcal{E}_s$ is reduced from 1.7 to 1.6 **(C,D)** Neutral stability curves shown here for the Newtonian case when $\mathcal{F} = \cosh(\mathcal{E}_s Y)$. Typically there are critical values of Ψ (for fixed β), or of β (for fixed Ψ) below which the base state is always stable.

dominated by non-linear terms. Thus to understand how non-linearity affects frequencies and amplitudes far from critical points, we solved **Equations 8–11** numerically using Matlab$^{@}$. **Equations 8–11** constitute a stiff set of equations especially in the limit of small $\mathcal{B}_2$ or large $\mathcal{B}_3$ and hence the suite ODE 15s that solves stiff equations using a variable order method was employed. Sample time-dependent solutions are shown as follows: no drag case - **Figure 3B**, for Newtonian fluid solutions are shown in **Figures 4A,B**. Features of the non-linear solution for the Kelvin-Voigt material is highlighted in **Figures 5E,F** that demonstrate important features of the full limit cycles. We also conducted systematic studies of how the amplitude and frequency varies for the fully non-linear solutions far from the critical point. Results are summarized in **Figures 6**, **7** for the Newtonian and Kelvin-Voigt model. Finally results for the Maxwell fluid are shown in **Figures 8–10**; here the focus was to study the characteristics and *shape* of these nonlinear solutions.

4.3.2 Supercritical Hopf Bifurcations and Fluid Limited Oscillation Amplitudes

Let us start with the two reference cases first. For the case of no fluid drag, the active energy input into the system by continuous motor activity is eventually dissipated away by internal motor friction with the anchoring spring as well as the passive links serving as intermediate storage agents. The motor activity derived internal friction is associated with the energy loss when motors detach and eventually go back to their rest length. We note that

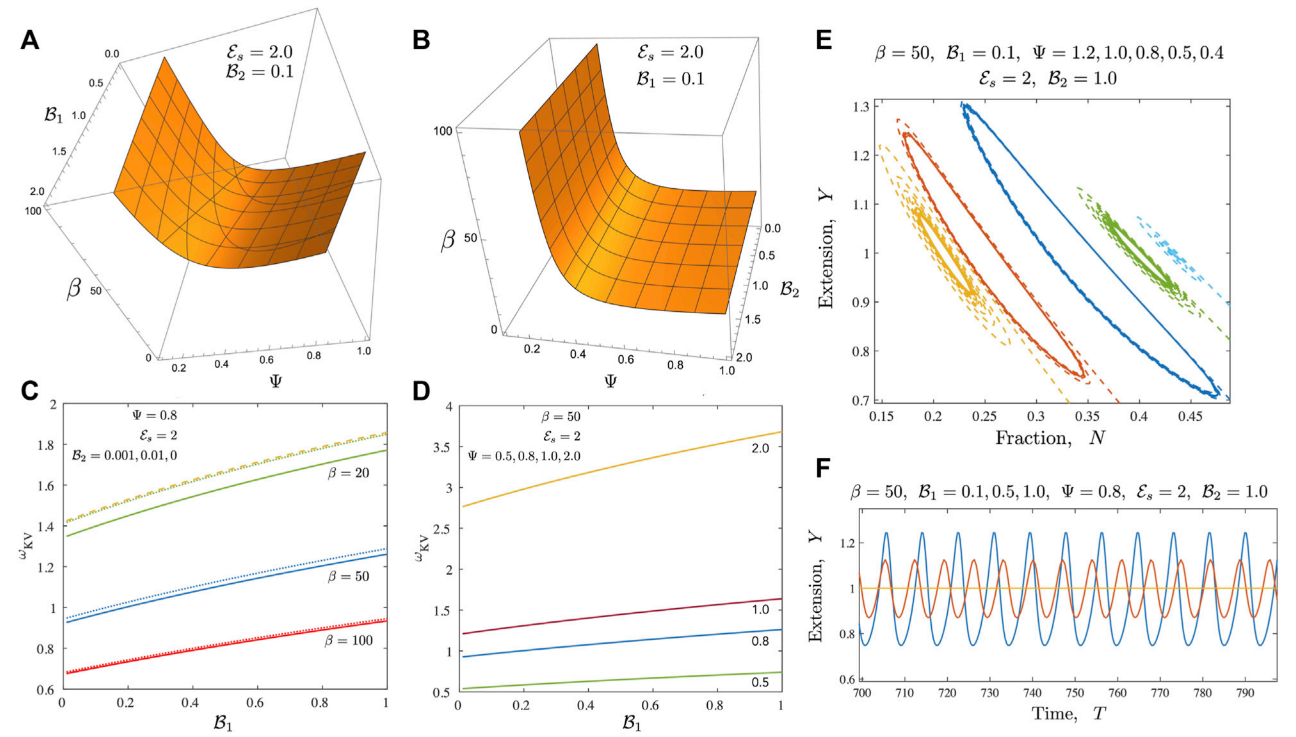

FIGURE 5 | Results for the case of a Kelvin-Voigt medium **(A,B)** Neutral stability curves from the linear stability analysis shown here for the Newtonian case when $\mathcal{F} = \cosh(\mathcal{E}_s Y)$. Typically there are critical values of Ψ (for fixed β), or of β (for fixed Ψ) below which the base state is always stable. As plotted, the region on the concave side of the surface is linearly unstable. **(C)** and **(D)** Plots of the emergent frequencies (at onset) corresponding to **Equation 26**, also obtained from the linear stability results. **(E)** and **(F)** Time-dependent long-time solutions obtained from a full non-linear solution to the ode system. In **(E)** we show phase-plots in $Y - N$ space that demonstrates how see oscillations exist only for a range of Ψ values (with other parameters fixed). Subplot **(F)** demonstrates how increasing $\mathcal{B}_1$ increases the frequency, and reduces the amplitude of the oscillations. Eventually at large values there is no instability.

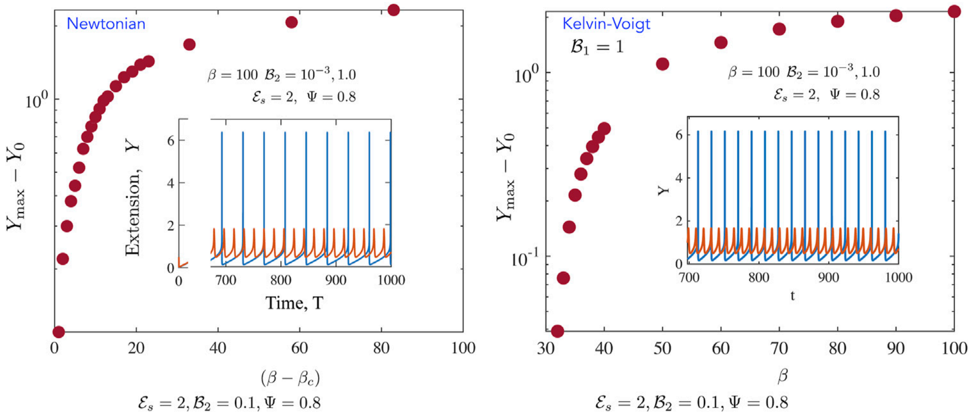

FIGURE 6 | Representative metrics for the fully non-linear periodic solutions for the (left) Newtonian, and (right) Kelvin-Voigt cases (Newtonian, left) We calculate the maximum value of $Y_{\max}$ over a cycle and plot $Y_{\max} - 1$ as a function of $\beta - \beta_c$ where the critical value of beta for these parameters ($\mathcal{E}_s = 2, \mathcal{B}_1 = 0.1, \Psi = 0.8$) is $\beta_c \approx 18.9$. That the bifurcating solutions arise via a *supercritical* Hopf-Poincare-Andronov bifurcation is deduced by the amplitude going to zero at criticality. For large deviations from the critical value of β. the amplitude decreases slowly. The inset shows sample steady periodic solutions at $\beta = 100 \gg 18.9$ (far from the critical point) for $\mathcal{B}_2 = 10^{-3}$ (blue) and 1.0 (red). We note that as one goes far from the critical point, oscillations become highly asymmetric and the maximum value of Y attained deviates significantly from the minimum value. (Kelvin-Voigt, right) Here we plot $Y_{\max} - 1$ as a function of β. Note that the amplitude of the oscillation tends to zero as one approaches the critical point. Comparison with the Newtonian case indicates a slower increase in the amplitude, as well as a lower magnitude of the amplitudes for large β. Examination of the time-series indicates that the frequencies (inset) are substantially higher than for the Newtonian case with the same value of $\mathcal{B}_2$ and β.

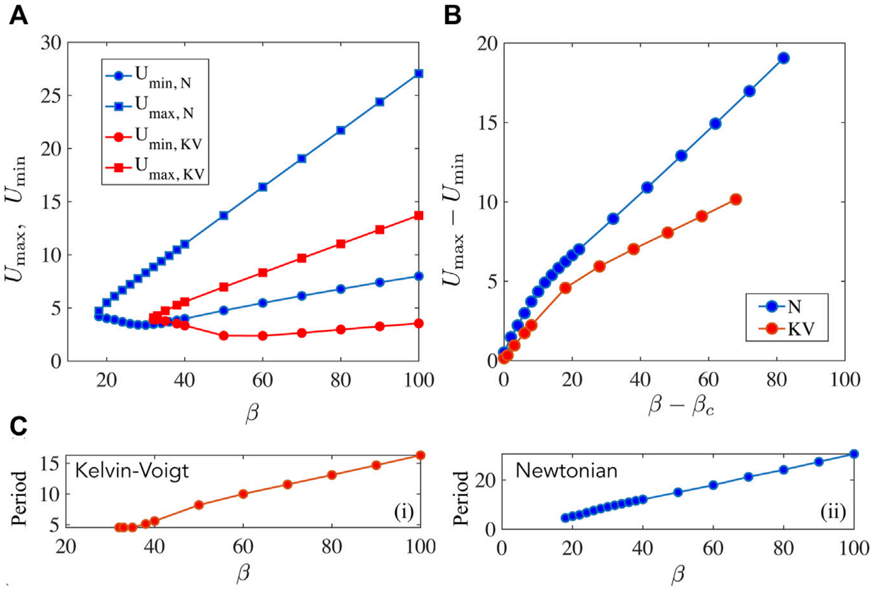

FIGURE 7 | Non-linear solutions for Newtonian and Kelvin-Voigt media compared with the focus on the filament displacements U and period of oscillations. **(A)** Here we plot $U_{\max}$ and $U_{\min}$, the maximum and minimum values attached by $U(t)$ over a cycle when the oscillations have stabilized, as a function of β. Parameters are $\mathcal{E}_s = 2$ and $\Psi = 0.8$. The Newtonian case (N) corresponds to $\mathcal{B}_2 = 0.1$ while the Kelvin-Voigt (KV) case corresponds to $\mathcal{B}_2 = 0.1$ and $\mathcal{B}_1 = 1$. **(B)** Amplitude of the *filament* oscillations $|U_{\max} - U_{\min}|$ here plotted as a function of the deviation from the critical point $\beta - \beta_c$. Here the critical values β_c are different for the N and KV cases and may be read off from **(A)**. In **(C)**, we plot the (dimensionless) oscillation period. Note that the period for the KV case shown in (i) is typically lower than that for the Newtonian case (ii) indicating higher frequencies.

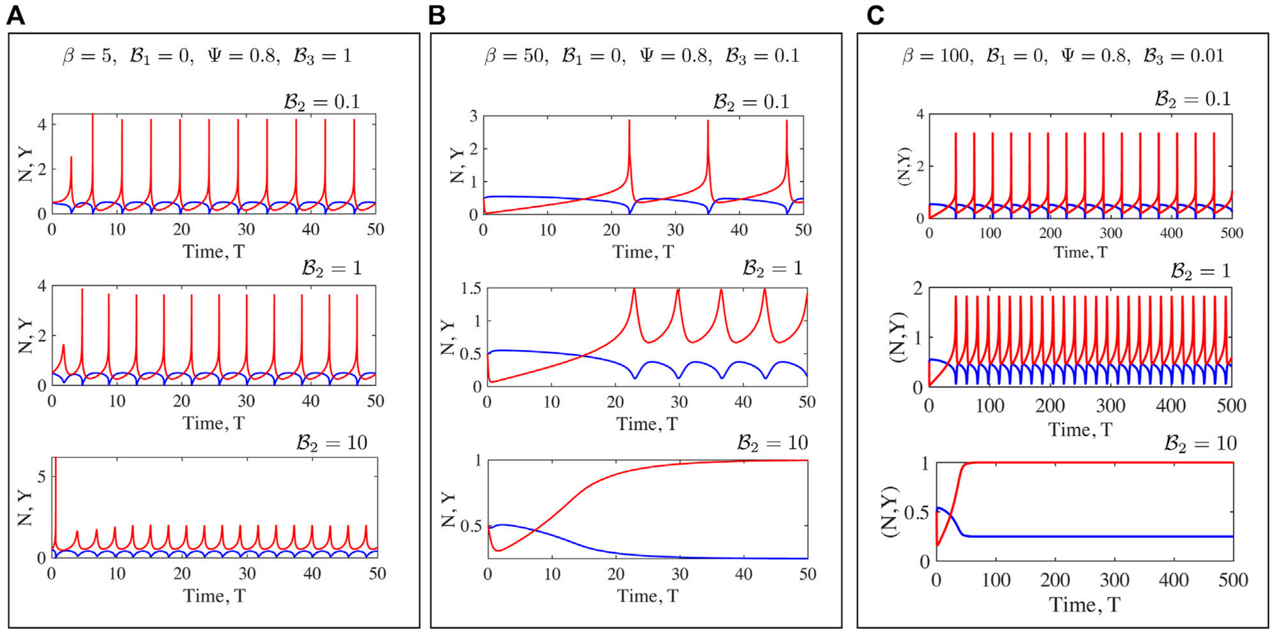

FIGURE 8 | Fully non-linear solutions for the Maxwell medium. Here to focus on the rheological parameters $\mathcal{B}_2$ and $\mathcal{B}_3$, we study solutions for constant Ψ (=0.8) with $\mathcal{F} = \cosh(\mathcal{E}_s Y)$ (here $\mathcal{E}_s = 2.0$ for all cases). Results are shown for increasing values of β (from left to right) **(A–C)** and increasing values of $\mathcal{B}_2$ (top to bottom).

oscillations can feature very sharp gradients in Y. Over a cycle, the attached motor fraction N can become very small reaching relative values of $O\,(10^{-4})$ as seen in **Figure 4A** (albeit for non-zero $\mathcal{B}_2 = 10^{-3}$). Also rather large values of Y are attained relative to the stationary state ($Y_0 = 1$). Increasing $\mathcal{E}_s$ enhances these features. When external viscosity starts to play a role and

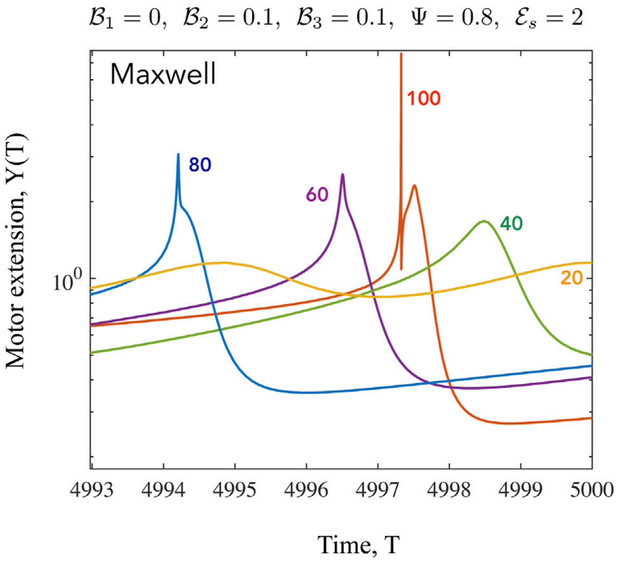

FIGURE 9 | Time series of the mean motor extension Y for the Maxwell case shown for β =20,40,60,80,100. Here we focus on the shape of the function close to the point where $Y = Y_{\max}$. When β to close to its critical value, the oscillations are harmonic as seen from the form of $Y(T)$ for β =20. As the value of β increases, the periodic profiles becomes highly asymmetric and also develop double maxima and double minima, especially evident for β =100. The high values of Y are associated with very low values of N when very few motors are attached, with these motors extended significantly.

becomes comparable to motor friction, the parameter range over which instability is exhibited becomes smaller. This is seen in **Figure 4C** where increasing $\mathcal{B}_2$ is seen to push the neutral stability envelope to the right. When at a point where oscillations are the stable state, increasing $\mathcal{B}_2$ is seen to reduce variations in (N, Y) (evident when plotted as a phase-plot, **Figure 4A**). For very large viscosity, oscillations become damped and then die out. Examination of the time-dependent behavior of N and Y just before and just after criticality confirms that the bifurcation is supercritical [37], with oscillations beginning with very small amplitudes. The farther the parameters are from their critical values, the larger the amplitude as is expected for a Hopf-Androvov-Poincare bifurcation. Thus external fluid viscosity, even in the purely Newtonian case, modulates the internal (mean-field) motor state captured by the two variables Y and N.

Introducing viscoelastic effects changes the dynamics in a variety of ways. When the ambient medium follows Kelvin-Voigt like response (a reasonable simple approximation to a gel), the ability to store energy increases for $\mathcal{B}_1 > 0$. When $0 < \mathcal{B}_2 \ll 1$, and with increasing $\mathcal{B}_1$ surprisingly increases the minimum value of Ψ (for fixed β) or the minimum value of β (for fixed Ψ) for the onset of oscillations. There is also a significant effect on the frequency on emergent solutions that we have analytically derived. Let us consider what happens when the motor parameters Ψ, $\mathcal{E}_s$ and β are held fixed, while $\mathcal{B}_1$ and $\mathcal{B}_2$ are allowed to vary (**Figure 5C**). We note modest increases in the frequency with *lower* values of β yielding larger increments with increasing $\mathcal{B}_1$ with $\mathcal{B}_1 = 0$ reducing to the case of a pure Newtonian fluid medium. More dramatic increases in the frequency are seen when the kinetic parameter Ψ is allowed to vary and attain values larger than 1. **Figure 5D** illustrates a case with fixed $\mathcal{B}_2$ where changing Ψ from 0.5 to 2.0 and simultaneously changing $\mathcal{B}_1$ from 0 to 1 results in the frequency increasing by nearly a factor of 7. The amplitude of the oscillations however decreases with increasing $\mathcal{B}_1$ with oscillations vanishing at sufficiently large values. Taken together, these results suggest that tuning the rheology of the fluid by adjusting $\mathcal{B}_1$ allows for modest increases in frequencies with reduced solution amplitudes.

We further probe the variation in amplitudes away from the critical point and present results in **Figures 6**, **7**. **Figure 6** focusses on the motor variables (or the motor state) for both the Newtonian model and the Kelvin Voigt model. In both cases, we confirm that limit cycles emerge via supercritical bifurcations [37]. **Figure 6A** illustrates this feature; plotted here is the quantity $|Y_{\max}(T) - Y_0|$ and we find that this tends to 0 as $\beta \rightarrow \beta_c$. Emergent oscillations also onset, as required for this class of bifurcations, with fixed non-zero frequency. When $\beta \gg \beta_c$, the amplitude saturates. This saturation is likely due to a combination of two features. First, even though the number of active motors increases with increasing β, attached motors generate passive resistance when pulled backwards and limit the amplitude of the oscillations. Secondly, increased amplitudes result in a zipper effect—almost all motors rapidly disengage and detach together.

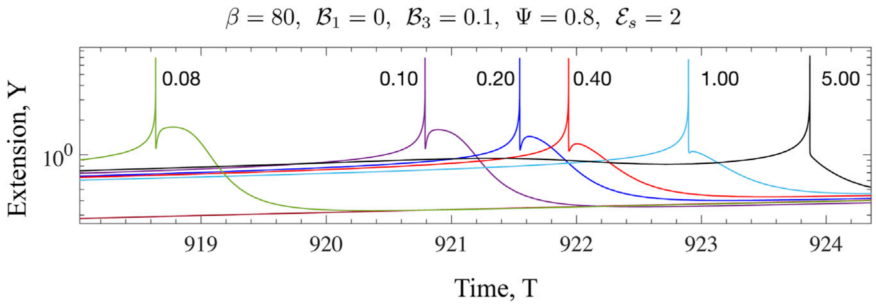

FIGURE 10 | The effect of increased dissipation (viscosity) on the form of $Y(T)$ for the Maxwell model is illustrated here. The value of β is much larger than the critical value for the onset of oscillations. Fixing $\mathcal{B}_3$ at 0.1, and Ψ at 0.8, we investigate how the profiles change as $\mathcal{B}_2$ increases from 0.08 to 5.0. Note that each time-series has a different frequency and we have shown just a part of the period for each.

Figure 6B illustrates that the emergent oscillations when the ambient medium is a Kelvin-Voigt medium also arise from supercritical bifurcations. We note increased frequencies as well as slightly larger amplitudes. **Figures 6A,B** suggest that in the absence of any energy constraints (an open system where energy limitations are not present), limit cycles can in viscoelastic media can exhibit larger amplitudes *and* higher frequencies than in the Newtonian case.

Until now we have focussed on how the motor variables Y and N are impacted by the fluid rheology dependent parameters. In experimental realizations of the filament motor system, one typically finds it easier to track filament related positions. For instance we may envision marking one end of the filament via florescent markers and tracking the position as a function of time. In **Figure 7**, we therefore illustrate how the filament displacement U varies over a period of a stable oscillation. For simplicity we treat all variables except β as constants and plot $U_{\max} \equiv \max\ [U(T)]$, $U_{\min} \equiv \min\ [U(T)]$, the characteristic amplitude $|U_{\max} - U_{\min}|$ and the period T_p defined implicitly via $U\ (T + T_p) = U(T)$ for stable oscillations. For the Newtonian case, we fix $\mathcal{B}_2 = 0.1$. For the Kelvin-Voigt case, we keep the viscous contribution the same but add an additional elastic component to the fluid response by setting $\mathcal{B}_1 = 1$. The following features can deduced from **Figures 7A,B**. Fluid elasticity as expected, shifts the critical point at which oscillations emerge via supercritical bifurcations. Very close to onset the amplitudes compare well with the expected square root scaling with significant deviations seen as one goes to larger values of β as the oscillations become highly non-sinusoidal. Interestingly, we note that $U_{\min}$ is non-monotonic in β demonstrating significant non-linear effects. As far as the oscillation periods are concerned, our numerical solutions reveal that, consistent with the linear stability results, oscillations in the Newtonian fluid have larger time periods than in the KV fluid and thus lower frequencies. At $\beta = 60$, the value for the VE case is ≈ 10 while for the Newtonian case is ≈ 17. For $\beta = 100$, the difference is more enhanced with a period of ≈ 17 for the KV case and ≈ 29 for the Newtonian case. We also see some evidence of a qualitative difference in the way the time period changes with β between the two cases. For the Kelvin-Voigt case; the slope of the curve is smaller initially than at higher values of β, a trend missing in the case of motion in a Newtonian fluid.

4.3.3 Differences Between the Maxwell and Kelvin-Voigt Models

Numerical solutions for oscillations in a Maxwell fluid indicate that the onset of oscillations and frequencies may be more readily tuned than for the Kelvin-Voigt case. Oscillations are enabled at even $O\,(1)$ values of β provided $\mathcal{B}_3 = O\,(1)$; with these oscillations persisting for even large values of the viscosity $\mathcal{B}_2$. For fixed motor kinetics, in general, the higher the value of β, the lower $\mathcal{B}_3$ needs to be to sustain oscillations. With Ψ, β and $\mathcal{B}_1$ fixed, oscillations decrease in amplitude but increase in. frequency as $\mathcal{B}_2$ increases. We hypothesize that the tuning of oscillations is made possible by changing the value of $\mathcal{B}_3$ which is the ratio of the relaxation time for the Maxwell fluid and the mean time a motor is attached to the filament and is able to animate the filament. The viscosity on the other hand controls the energy dissipate rate and limits the amplitude of the oscillations. **Figure 8** shows sample limit cycles seen for various parameter values. For $\mathcal{B}_3 = 1$ and keeping parameters $\Psi = 0.8$, $\mathcal{E}_s = 2$, $\mathcal{B}_1 = 0$ fixed and restricting $0 < \mathcal{B}_2 < 1$, oscillations are seen for $\beta = 5$ but not for $\beta = 50$. Decreasing $\mathcal{B}_3$ to 0.1 however moves the steady state to the linear stable phase space and thus oscillations are seen.

We have discussed the frequencies as well as the amplitudes (measured via suitable norms) of emergent oscillations until now. We conclude this section by focussing on the *shape* of the limit cycle and the asymmetries that may manifest. A motivation for looking at this in closer detail comes from the possibility of using synthetic versions of motor-filament systems as switching or triggering devices. One may imagine connecting this active viscoelastic unit in series to a dynamical system that uses the input dU/dT and/or U to provide downstream responses/signals. In **Figures 9**, **10** we examine the variation in the shape of the limit cycles for the specific case of the ambient fluid being a Maxwell fluid. In **Figure 9** close to onset, the variations in Y(T) are smooth, and in fact almost sinusoidal as one moves towards the critical point. Increasing β makes the profile asymmetric; the mean motor extension attains large extensions ($Y > 1$) and compressions but the profile develops three extrema with two maxima and 1 minimum as seen by comparing the curves for $\beta = 80$ and $\beta = 20$. **Figure 10** illustrates how the asymmetric double peaked shaped may be smoothened by increased viscosity (here by increasing the value of $\mathcal{B}_2$ from 0.08 to 5.00.

5 SUMMARY AND CONCLUSION

Here, we studied a minimal system comprised of an active bio-filament segment working against an elastic spring and immersed in model complex materials. A mean-field macroscale continuum description of filament-motor interactions was employed based on a cross-bridge model—however, other models can be readily used instead (see [28] for a general model that allows motors to undergo initial conformations as well as move relative to the filament). We used a combination of analytical and numerical methods to extract the conditions under which rheology of the fluid may be exploited to both shift the onset of instabilities, and modulate ensuing frequencies and amplitudes. We found that steady base states yield to stable oscillatory states or limit cycles. These solutions arise via supercritical Hopf-Andronov-Poincare' bifurcations with exponentially damped oscillation change to small limit cycle oscillation about the steady state. Linear stability results were validated and complemented with full time-dependent solutions that provide an indication of the manner in which the amplitude of these oscillations changes.

A shortcoming in our theoretical approach is that in the process of formulating analytically tractable equations, complex biochemical and biomechanical aspects are highly simplified. We have not considered noise and stochastic aspects of the problem that may be important for small to moderate values of β and/or low attachment rates [28]. While our model does not include motor driven filament bending which dominates in oscillatory dynamics of biological and synthetically devised ciliary structures, reduced dimensional and spatially dependent versions have been used to investigate oscillations of cilia in Newtonian fluids [8, 9, 29, 31, 36]. However, ciliary or flagellar motion in viscoelastic fluids remains an open challenge. Elastic and viscous responses of for a viscoelastic fluid made by adding polymers to a Newtonian solvent fluid may depend on concentration differently. Thus in a polymeric fluid the ratio $\mathcal{B}_1/\mathcal{B}_2$ may scale with concentration with different exponents. Furthermore, the rheological behavior of a real polymeric fluid is more complex than that we have modeled. Nonetheless, the results here provide a foundation for more comprehensive analysis using detailed computational techniques and more realistic models for polymeric viscoelastic fluids.

The governing equations we utilized employed simplifications that allow for analytical and independent exploration of fluid viscoelastic properties (both its effective viscosity and elasticity, measured appropriately and encapsulated in parameters $\mathcal{B}_1$ to $\mathcal{B}_4$), motor kinetics and specifically the ratio of detachment and attachment constants (via parameter Ψ), effective importance of elastic (restoring) and viscous (dissipative) forces that includes possible coupling between the filament and its neighbors or anchoring substrates (through ratios $\mathcal{B}_1$ and $\mathcal{B}_2$), the ratio of viscoelastic relaxation times and the motor kinetic time-scales, and the strain dependent motor detachment rate (parameter $\mathcal{S}_s$. A further advantage of the simple model we have proposed is highlighted by examining the steady state solutions given by **Eq. 5**. We note that the steady state motor extension Y_0 and the steady state fraction of attached motors N_0 are *independent* of the rheological characteristics of the bulk medium. Thus coupling between the fluid and the motor aggregate is purely dynamical in nature. In other words, the aggregate is pre-strained internally by motor activity; but this pre-strained state is independent of the ambient fluid. It is thus possible to identify clearly changes in the dynamical state of the aggregate induced purely due to viscoelastic contributions, and to compare these with the results from the Newtonian case.

Our results are also relevant to understanding the rheology and dynamical response of biological and synthetic muscles, and in devising actuators for soft-robots [38–41]. In general, active responses to imposed external stimuli or perturbations are analyzed using an effective frequency-dependent dynamic moduli in these systems. The minimal approach we have used here–modeling the ambient fluid in terms of minimal models with spring-like and dashpot-like elements—provide a clear means to evaluate these dynamic response functions (or transfer functions).

While direct comparison to ciliary experiments requires a spatially varying version of our model, there are experimental setups that can be used to check the theoretical predictions we have made. Motility assays offer an easy way to study the spatial dynamics of gliding microtubules or actin filaments. These filaments are animated by molecular motors that are grafted on the substrate and periodically attach to the filaments propelling them via tangential forces. Oscillations have been observed in filaments that are temporarily pinned in these systems with frequencies comparable to the values calculated in this paper for Newtonian fluids. In [18] we interpreted and analyzed bending oscillations for long filaments in Newtonian settings via a combination of linear stability analysis and non-linear computations. By using 1) very short rigid (non-bendable) filaments, 2) model viscoelastic fluids as the nutrient media in which the gliding takes place, and 2) additional polymeric binders that can attach to the filament and play the role of passive adhesive springs [42, 43], one can adapt current protocols and establish a setup that mimics closely the model analyzed in this paper. A natural next step would be the test of the model predictions from in these adapted gliding motility assays.

DATA AVAILABILITY STATEMENT

The original contributions presented in the study are included in the article/**Supplementary Material**, further inquiries can be directed to the corresponding author.

AUTHOR CONTRIBUTIONS

The project was conceived by AG. Theoretical calculations were done by AM and AG. Numerical analysis was conducted by AM and JT. All authors contributed to the final form of the manuscript.

FUNDING

AG acknowledges funding from the National Science Foundation via awards NSF-CBET-2047210 and NSF-MCB-2026782. JT was supported by funding from NSF-MCB-2026782.

SUPPLEMENTARY MATERIAL

The Supplementary Material for this article can be found online at: https://www.frontiersin.org/articles/10.3389/fphy.2022.895536/full#supplementary-material

REFERENCES

1. Howard J. *Mechanics of Motor Proteins and the Cytoskeleton*. Sunderland: Sinauer Associates (2001).
2. Grill SW, Kruse K, Jülicher F. Theory of Mitotic Spindle Oscillations. *Phys Rev Lett* (2005) 94(10):108104. doi:10.1103/physrevlett.94.108104
3. Bizzi E, Chapple W, Hogan N. Mechanical Properties of Muscles: Implications for Motor Control. *Trends Neurosciences* (1982) 5:395–8. doi:10.1016/0166-2236(82)90221-1

4. Hogan N. Adaptive Control of Mechanical Impedance by Coactivation of Antagonist Muscles. *IEEE Trans Automat Contr* (1984) 29:681–90. doi:10.1109/TAC.1984.1103644
5. Walcott S. Muscle Activation Described with a Differential Equation Model for Large Ensembles of Locally Coupled Molecular Motors. *Phys Rev E* (2014) 90:042717. doi:10.1103/PhysRevE.90.042717
6. Witman GB. Introduction to Cilia and Flagella. In: RA Bloodgood, editor. *Ciliary and Flagellar Membranes*. New York: Plenum (1990). p. 1–30. doi:10.1007/978-1-4613-0515-6_1
7. Machin KE. The Control and Synchronization of Flagellar Movement. *Proc Roy Soc B* (1963) 158(970):88–104.
8. Brokaw CJ. Molecular Mechanism for Oscillation in Flagella and Muscle. *Proc Natl Acad Sci U.S.A* (1975) 72(8):3102–6. doi:10.1073/pnas.72.8.3102
9. Qin B, Gopinath A, Yang J, Gollub JP, Arratia PE. Flagellar Kinematics and Swimming of Algal Cells in Viscoelastic Fluids. *Sci Rep* (2015) 5:9190. doi:10.1038/srep09190
10. Sears PR, Thompson K, Knowles MR, Davis CW. Human Airway Ciliary Dynamics. *Am J Physiology-Lung Cell Mol Physiol* (2013) 304:L170–L183. doi:10.1152/ajplung.00105.2012
11. Kempeneers C, Seaton C, Chilvers MA. Variation of Ciliary Beat Pattern in Three Different Beating Planes in Healthy Subjects. *Chest* (2017) 151:993–1001. doi:10.1016/j.chest.2016.09.015
12. Knowles MR, Leigh MW, Carson JL, Davis SD, Dell SD, Ferkol TW, et al. Mutations ofDNAH11in Patients with Primary Ciliary Dyskinesia with normal Ciliary Ultrastructure. *Thorax* (2012) 67:433–41. doi:10.1136/thoraxjnl-2011-200301
13. Papon J-F, Bassinet L, Cariou-Patron G, Zerah-Lancner F, Vojtek A-M, Blanchon S, et al. Quantitative Analysis of Ciliary Beating in Primary Ciliary Dyskinesia: a Pilot Study. *Orphanet J Rare Dis* (2012) 7:78. doi:10.1186/1750-1172-7-78
14. Thomas B, Rutman A, O'Callaghan C. Disrupted Ciliated Epithelium Shows Slower Ciliary Beat Frequency and Increased Dyskinesia. *Eur Respir J* (2009) 34:401–4. doi:10.1183/09031936.00153308
15. Ringers C, Olstad EW, Jurisch-Yaksi N. The Role of Motile Cilia in the Development and Physiology of the Nervous System. *Phil Trans R Soc B* (2019) 375:20190156. doi:10.1098/rstb.2019.0156
16. Sanchez T, Welch D, Nicastro D, Dogic Z. Cilia-like Beating of Active Microtubule Bundles. *Science* (2001) 333(6041):456–9. doi:10.1126/science.1203963
17. Sanchez T, Chen DTN, DeCamp SJ, Heymann M, Dogic Z. Spontaneous Motion in Hierarchically Assembled Active Matter. *Nature* (2012) 491(7424):431–4. doi:10.1038/nature11591
18. Fily Y, Subramanian P, Schneider TM, Chelakkot R, Gopinath A. Buckling Instabilities and Spatio-Temporal Dynamics of Active Elastic Filaments. *J R Soc Interf* (2020) 17(165):20190794. doi:10.1098/rsif.2019.0794
19. Vilfan A, Frey E. Oscillations in Molecular Motor Assemblies. *J Phys Condens Matter* (2005) 17(47):S3901–S3911. doi:10.1088/0953-8984/17/47/018
20. Nguyen KD, Sharma N, Venkadesan M. Active Viscoelasticity of Sarcomeres. *Front Robot AI* (2018) 5:69. doi:10.3389/frobt.2018.00069
21. Vilfan A, Duke T. Synchronization of Active Mechanical Oscillators by an Inertial Load. *Phys Rev Lett* (2003) 91:114101. doi:10.1103/physrevlett.91.114101
22. Endow SA, Higuchi H. A Mutant of the Motor Protein Kinesin that Moves in Both Directions on Microtubules. *Nature* (2000) 406:913–6. doi:10.1038/35022617
23. Badoual M, Jülicher F, Prost J. Bidirectional Cooperative Motion of Molecular Motors. *Proc Natl Acad Sci U.S.A* (2002) 99:6696–701. doi:10.1073/pnas.102692399
24. Grill SW, Gönczy P, Stelzer EHK, Hyman AA. Polarity Controls Forces Governing Asymmetric Spindle Positioning in the *Caenorhabditis elegans* Embryo. *Nature* (2001) 409:630–3. doi:10.1038/35054572
25. Colombo K, Grill SW, Kimple RJ, Willard FS, Siderovski DP, Gönczy P. Translation of Polarity Cues into Asymmetric Spindle Positioning in *Caenorhabditis elegans* Embryos. *Science* (2003) 300:1957–61. doi:10.1126/science.1084146
26. Grill SW, Howard J, Schäffer E, Stelzer EHK, Hyman AA. The Distribution of Active Force Generators Controls Mitotic Spindle Position. *Science* (2003) 301:518–21. doi:10.1126/science.1086560
27. Li C, Qin B, Gopinath A, Arratia PE, Thomases B, Guy RD. Flagellar Swimming in Viscoelastic Fluids: Role of Fluid Elastic Stress Revealed by Simulations Based on Experimental Data. *J R Soc Interf* (2017) 14(135):20170289. doi:10.1098/rsif.2017.0289
28. Gopinath A, Chelakkot R, Mahadevan L. Filament Extensibility and Shear Stiffening Control Persistence of Strain and Loss of Coherence in Cross-Linked Motor-Filament Assemblies. *bioRxiv* (2020). doi:10.1101/423582
29. Camalet S, Jülicher F. Generic Aspects of Axonemal Beating. *New J Phys* (2000) 2:24.1–24.23. doi:10.1088/1367-2630/2/1/324
30. Patteson AE, Gopinath A, Goulian M, Arratia PE. Running and Tumbling with *E. coli* in Polymeric Solutions. *Sci Rep* (2015) 5(1):15761–11. doi:10.1038/srep15761
31. Hamilton E, Pellicciotta N, Feriani L, Cicuta P. Motile Cilia Hydrodynamics: Entrainment versus Synchronization when Coupling through Flow. *Phil Trans R Soc B* (2019) 375:20190152. doi:10.1098/rstb.2019.0152
32. Sangani A, Gopinath A. Elastohydrodynamical Instabilities of Active Filaments, Arrays and Carpets Analyzed Using Slender Body Theory. *Phys. Rev. Fluids* (2020). 5(8):083101.
33. Fatehiboroujeni S, Gopinath A, Goyal S. Nonlinear Oscillations Induced by Follower Forces in Prestressed Clamped Rods Subjected to Drag. *J Comp Non Dyn* (2018) 13(12):121005. doi:10.1115/1.4041681
34. Fatehiboroujeni S, Gopinath A, Goyal S. Follower Forces in Pre-stressed Fixed-Fixed Rods to Mimic Oscillatory Beating of Active Filaments. In: Proceedings of the ASME 2018 International Design Engineering Technical Conferences and Computers and Information in Engineering Conference. Volume 6: 14th International Conference on Multibody Systems, Nonlinear Dynamics, and Control; August 26–29, 2018; Quebec City, Quebec, Canada (2018). ASME DETC2018-85449, V006T09A033. doi:10.1115/detc2018-85449
35. Chelakkot R, Gopinath A, Mahadevan L, Hagan MF. Flagellar Dynamics of a Connected Chain of Active, Polar, Brownian Particles. *J R Soc Interf* (2014) 11(92):20130884. doi:10.1098/rsif.2013.0884
36. Chakrabarti B, Saintillan D. Spontaneous Oscillations, Beating Patterns, and Hydrodynamics of Active Microfilaments. *Phys Rev Fluids* (2019) 4:043102. doi:10.1103/physrevfluids.4.043102
37. Strogatz SH. *Nonlinear Dynamics and Chaos: With Applications to Physics, Biology, Chemistry, and Engineering*. Reading, Mass: Addison-Wesley (1994).
38. Anderson IA, Gisby TA, McKay TG, O'Brien BM, Calius EP. Multi-functional Dielectric Elastomer Artificial Muscles for Soft and Smart Machines. *J Appl Phys* (2012) 112:041101. doi:10.1063/1.4740023
39. Buerger SP, Hogan N. Complementary Stability and Loop Shaping for Improved Human-Robot Interaction. *IEEE Trans Robot* (2007) 23:232–44. doi:10.1109/TRO.2007.892229
40. George NT, Irving TC, Williams CD, Daniel TL. The Cross-Bridge Spring: Can Cool Muscles Store Elastic Energy? *Science* (2013) 340:1217–20. doi:10.1126/science.1229573
41. Hines L, Petersen K, Lum GZ, Sitti M. Soft Actuators for Small-Scale Robotics. *Adv Mater* (2017) 29:1603483–43. doi:10.1002/adma.201603483
42. Sharma P, Ghosh S, Bhattacharya S. Microrheology of a Sticking Transition. *Nat Phys* (2008) 4:960–6. doi:10.1038/nphys1105
43. Mani M, Gopinath A, Mahadevan L. How Things Get Stuck: Kinetics, Elastohydrodynamics, and Soft Adhesion. *Phys Rev Lett* (2012) 108(22):226104. doi:10.1103/physrevlett.108.226104

Conflict of Interest: The authors declare that the research was conducted in the absence of any commercial or financial relationships that could be construed as a potential conflict of interest.

frontiers | Frontiers in Physics

ORIGINAL RESEARCH
published: 30 June 2022
doi: 10.3389/fphy.2022.910882

Transport of *Pseudomonas aeruginosa* in Polymer Solutions

Giovanni Savorana[1], Steffen Geisel[2], Tianyu Cen[1], Yuya Ling[1], Roman Stocker[1], Roberto Rusconi[3,4] and Eleonora Secchi[1]*

[1]Institute of Environmental Engineering, Department of Civil, Environmental and Geomatic Engineering, ETH Zurich, Zurich, Switzerland, [2]Laboratory for Soft Materials, Department of Materials, ETH Zurich, Zurich, Switzerland, [3]Department of Biomedical Sciences, Humanitas University, Pieve Emanuele, Italy, [4]IRCCS Humanitas Research Hospital, Rozzano, Italy

Bacteria often live surrounded by polymer solutions, such as in animal respiratory, gastrointestinal, and reproductive tracts. In these systems, polymer solutions are often exposed to fluid flow, and their complex rheology can affect the transport of chemical compounds and microorganisms. Recent studies have focused on the effect of polymer solutions on the motility of bacteria in the absence of fluid flow. However, flow can be a game-changer on bacterial transport, as demonstrated by the depletion of motile bacteria from the low-shear regions and trapping in the high-shear regions in simple fluids, even for flows as simple as the Poiseuille one. Despite the relevance of polymer solutions in many bacterial habitats, the effect of their complex rheology on shear-induced trapping and bacterial transport in flow has remained unexplored. Using microfluidic experiments and numerical modeling, we studied how the shear rate and the rheological behavior of Newtonian and non-Newtonian polymer solutions affect the transport of motile, wild-type *Pseudomonas aeruginosa* in a Poiseuille flow. Our results show that, in Newtonian solutions, an increase in viscosity reduces bacterial depletion in the low-shear regions at the microchannel center, due to a reduction in the bacterial swimming velocity. Conversely, in the non-Newtonian solution, we observed a depletion comparable to the buffer case, despite its zero-shear viscosity being two orders of magnitude higher. In both cases, bacterial swimming and polymer fluid rheology control the magnitude of bacterial depletion and its shear-rate dependence. Our observations underscore the importance of the rheological behavior of the carrier fluid in controlling bacterial transport, in particular, close to surfaces giving rise to velocity gradients, with potential consequences on surface colonization and biofilm formation in many naturally relevant microbial habitats.

Keywords: bacterial motility, poiseuille flow, polymer solution, microfluidics, rheology, *Pseudomonas aeruginosa*

Edited by:
Xiang Cheng,
University of Minnesota Twin Cities,
United States

Reviewed by:
Bin Liu,
University of California, Merced,
United States
Harold Auradou,
Fluides, Automatique et Systèmes
Thermiques (FAST), France

***Correspondence:**
Eleonora Secchi
esecchi@ethz.ch

Specialty section:
This article was submitted to
Biophysics,
a section of the journal
Frontiers in Physics

Received: *01 April 2022*
Accepted: *31 May 2022*
Published: *30 June 2022*

Citation:
Savorana G, Geisel S, Cen T, Ling Y, Stocker R, Rusconi R and Secchi E (2022) Transport of Pseudomonas aeruginosa in Polymer Solutions. Front. Phys. 10:910882. doi: 10.3389/fphy.2022.910882

INTRODUCTION

Polymer fluids are found in the natural habitat of bacteria, as in organs covered in mucus [1], or in technological settings, like groundwater remediation and enhanced oil recovery [2]. In these systems, polymer fluids are often in flow, and their polymeric nature determines their complex rheology, which in turn affects the transport of chemicals, particles and microorganisms. Complex rheological behaviors include viscoelasticity, shear-thinning, and shear-thickening, where viscosity gradients can arise in the presence of shear rate gradients [3].

In no-flow conditions, polymer solutions affect bacterial swimming because of their complex rheology. Pioneering work of the 70' reported that a moderate increase in the viscosity of the suspending medium causes an increase in the swimming velocity of several species of flagellated bacteria, whereas a further increase in viscosity reduces it [4–7]. This observation was first explained in terms of gain in propulsive efficiency of the flagellum at moderate viscosities [4, 8]. Lately, the characteristics of the polymer network were also evaluated: experimental observation and a mathematical model have shown that the hydrodynamic forces exerted by the polymer network on the swimming cell body are responsible for the change in the bacterial swimming [5, 9]. This explained the observed dependence of the swimming velocity not only on the viscosity, but also on the type of polymer. Recent research studies further described how the local shear-thinning [10, 11], the elastic properties of the polymer solution [11–14] and the hydrodynamic interaction between individual bacteria and the colloidal component of complex fluids [15] are responsible for the change in swimming pattern and velocity of bacteria. Additionally, the influence of the details of the bacterial swimming behavior is currently under investigation [16–19]. The complexity of polymer rheology, the diversity of the bacterial propulsion strategies, and their interplay hindered the development of a unified description of swimming in polymer solutions. However, the key ingredients at play when the fluid is at rest have been identified.

Conversely, bacterial transport by flowing polymer solutions remains understudied. Water flow has been shown to affect bacterial transport and distribution, as described in several studies [20–22]. In a straight microfluidic channel, motile bacteria become trapped close to flat surfaces, causing their accumulation in the proximity of the channel walls and depletion from the central region of the channel [23]. This trapping is a hydrodynamic phenomenon determined by the action of fluid shear on motile, elongated bacteria [23–26], driving bacterial accumulation behind obstacles [27–29] and in the wake of sinking spheres [30]. These results were obtained in water, while, to date, the effect of flow of the polymer solutions has not been explored yet. In a polymer solution in flow, two elements could affect bacterial transport: the complex rheology of the fluid, potentially leading to the creation of viscosity gradients, and its effect on bacterial motility. The interplay between these two effects could completely change the observations compared to the case of water, with practical implications for the medical and industrial sectors.

In this work, we show that polymer fluids affect the transport of bacteria in a Poiseuille flow in a different way compared to the water case. By using both a Newtonian—polyvinylpyrrolidone (PVP)—and a non-Newtonian—xanthan gum—polymer solution as suspending fluids, we studied the transport of motile *Pseudomonas aeruginosa* PA14 wild-type cells in a serpentine microfluidic channel. First, we characterize the motility of the bacterial cells in the two polymer solutions at different concentrations in the absence of flow. Then, by coupling experiments and a mathematical model, in the Newtonian case, we show that increasing the polymer concentration both delays and reduces bacterial depletion from the channel center, as a result of the reduction of the bacterial swimming velocity. In the non-Newtonian case, we show that bacterial depletion is not significantly reduced compared to the buffer case as the high zero-shear viscosity in the Newtonian case would suggest. This result is due to the high values of the swimming velocity V in the xanthan gum solution and to the non-Newtonian shear rate profile across the channel width. Taken together, these results suggest that the complex rheology of polymer solutions has a crucial impact on bacterial transport.

MATERIALS AND METHODS

Polymer solutions. Polyvinylpyrrolidone (PVP) 360 (Sigma Aldrich) powder was suspended in phosphate-buffered saline (PBS) to a concentration of 15 w/v% and stirred overnight on a magnetic stirrer at ambient temperature. The polymer solution was then diluted to the final concentrations of 2.5 w/v%, 5 w/v%, and 10 w/v% by adding PBS and a fixed volume of bacterial suspensions. Xanthan gum powder from Xanthomonas campestris (Sigma Aldrich) was suspended in 85 mM NaCl solution to a concentration of 0.2 w/v% and stirred for 48 h on a heated magnetic stirrer at 65°C. The xanthan gum solution was then diluted with the bacterial suspension to a final concentration of 0.1 w/v%.

Rheological characterization of the polymer solutions. The viscosity of the polymer solutions was measured using a modular compact rheometer (MCR-302, Anton Paar). We used both cone plate (CP50-2) and double gap (DG26.7) geometries to obtain the flow curve of the polymer solution at each concentration. For each measurement, the shear rate was increased from $0.1\ s^{-1}$ to $500\ s^{-1}$ and then decreased from $500\ s^{-1}$ to $0.1\ s^{-1}$ while 5 logarithmically spaced measurement points per decade were recorded for 15 s each point.

Bacterial cultures. Experiments were performed using *P. aeruginosa* strain PA14 wild type. *P. aeruginosa* suspensions were prepared by inoculating 3 ml of Tryptone Broth (TB, 10 g L-1 tryptone) with cells from a frozen stock and incubating overnight at 37°C while shaking at 200 rpm. Approximately 30 µl of solution were then resuspended in 3 ml of the same medium and incubated under the same conditions for 5 h (OD_{600} = 1). To ensure a high percentage of motile bacteria in the experiments, non-motile and dead cells were gently removed from bacterial suspensions using sterile cell culture inserts incorporating a 3-µm-pore-size membrane, following the procedure described in [23, 29]. The filtered bacterial suspension was then mixed with the polymer solutions to the final desired polymer concentration and immediately used in the experiments. For the polymer-free control, the filtered bacterial suspension was resuspended in phosphate-buffered saline (PBS). Growth curves were acquired by measuring the OD_{600} of the bacterial suspensions in PVP 360 (2.5 w/v %, 5 w/v %, and 10 w/v %) and in xanthan gum (0.1 w/v %) solutions while incubated for 5 h at 37°C and shaking at 200 rpm. The growth curves did not show any differences from the PBS buffer case, suggesting that the bacteria did not metabolize the chosen polymers.

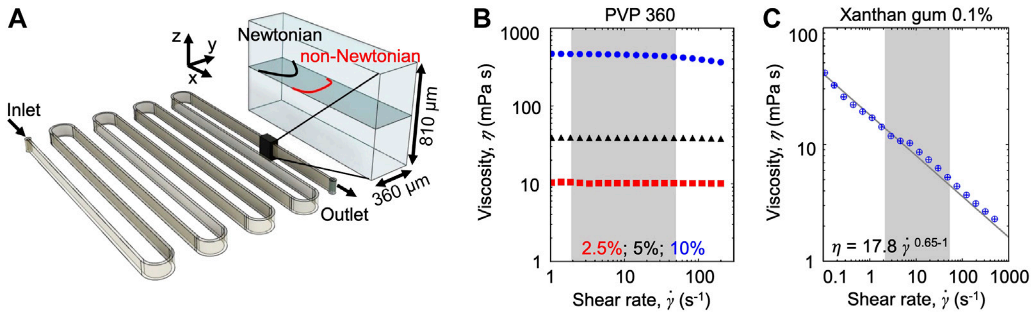

FIGURE 1 | (A) Schematic of the serpentine microchannel used for the experiments (left) and perspective view (right) showing the imaging plane (gray), the parabolic Newtonian flow profile (black), and a representative non-Newtonian profile (red). **(B,C)** Viscosity as a function of the shear rate for the Newtonian PVP 360 solutions at 2.5 w/v% (red), 5 w/v% (black), and 10 w/v% (blue) **(B)** and for the 0.1 w/v% xanthan gum solution **(C)**. The shaded areas highlight the shear rate $\dot{\gamma}$ range explored in the current study. The grey line in **(C)** represents the power-law fit which describes the non-Newtonian constitutive relation (blue circles).

Microfluidic assays. We fabricated a poly-dimethyl-siloxane (PDMS) [31] microfluidic device with a single 50 cm-long serpentine channel (**Figure 1A**). The serpentine channel is composed of 13 parallel straight sections, connected by curves with an inner radius R = 500 µm. Each straight section is 4 cm long. To ensure that the dominant velocity gradients occurred on the observation plane, we designed the microchannel with aspect ratio $H/W = 2.25$ (height $H = 810$ µm; width $W = 360$ µm). Flow was driven by a syringe pump (neMESYS 290N, CETONI, Germany), at constant flow rates in the range $Q = 4.5$–180 µl min^{-1}. At such flow rates, the mean of the absolute value of the shear rate $|\dot{\boldsymbol{\gamma}}(\boldsymbol{y})|$ on the horizontal midplane of the channel, defined as $S \equiv \frac{1}{W}\int_{-W/2}^{W/2}|\dot{\gamma}(y)|dy$, varied in the range 2.5–100 s^{-1}. Prior to use, all the microfluidic channels were washed with 2 ml of medium. Then, a diluted suspension of PA14 cells ($OD_{600} <$ 0.01; cell concentration $< 10^6$ cells ml^{-1}) was flown for the time required to replace the medium in the entire length of the channel (30 s–1 min, depending on the flow rate Q). The suspension was left at rest until the bacterial concentration was homogeneous. Finally, the flow was started and images were acquired at a distance of 50 cm from the inlet after a time required for the homogeneous suspension to travel 50 cm (30 s–1 min, depending on the flow rate Q). To characterize bacterial motility in polymer solutions, the same samples used for the transport experiments were loaded in 1 cm-long, 100 µm -high and 3 mm-wide PDMS chambers. The chambers were sealed to avoid drifts during the imaging. All the experiments were performed at room temperature.

Cell imaging and tracking. All imaging was performed on an inverted microscope (Ti-Eclipse, Nikon, Japan) using a digital camera (ORCA-Flash4.0 V3 Digital CMOS camera, Hamamatsu Photonics, Japan). Bacterial trajectories for motility characterization (**Figure 2A**) were extracted from time-lapse dark-field acquisitions (15× magnification; 87 frames per second (fps) in buffer, 20 fps in PVP 360 2.5 w/v% solution, 10 fps in PVP 360 5 w/v% solution, 5 fps in PVP 360 10 w/v% solution); 1,300 images were acquired in each polymer solution. To quantify bacterial transport in polymer solutions, images were acquired with phase-contrast microscopy (30× magnification, 25 fps); 3,000 images were acquired in every experimental condition. We experimentally measured the bacterial concentration B by counting bacterial cells in the laminar flow at a distance of 50 cm from the channel inlet. The concentration B was normalized by the initial homogeneous concentration and averaged over the imaging region, as in [23]. All image analysis was performed in Matlab (The Mathworks) using in-house cell tracking algorithms. The experiments were repeated three times with consistent results, but the data shown are from a single realization.

Numerical simulations. The mathematical model, adapted from [23], describes the transport of individual swimming bacteria by the two-dimensional (2D) velocity field inside the microchannel, for the same velocity and flow conditions used in the experiments. The equations of motion of an ellipsoidal swimmer in a 2D flow directed along the x axis are:

$$\begin{aligned}\dot{x} &= V\cos(\phi) + u(y)\\ \dot{y} &= V\sin(\phi)\\ \dot{\phi} &= -\frac{1}{2}\frac{\partial u(y)}{\partial y}\left(1 + \frac{1-q^2}{1+q^2}\cos(2\phi)\right) + \xi_R(t)\end{aligned} \tag{1}$$

where V is the bacterial swimming velocity, directed along the cell major axis, $u(y)$ is the flow speed inside the channel, ϕ is the angle between the major axis of the cell and the direction of flow, and $\xi_R(t)$ describes the angular deviations due to thermal noise and the specific bacterial swimming pattern. Here, *P. aeruginosa* cells were modeled as prolate ellipsoids with an effective aspect ratio $q = 9.4$ [29] and the swimming velocity V was set according to the values measured in our motility assays. We numerically integrated the equations of motion for 10^5 cells with a fourth-order Runge-Kutta scheme implemented in Matlab (The MathWorks) with time step $\Delta t = 4$ ms. In order to take into account the run-reverse-pause motility of *P. aeruginosa*, we integrated the equations of motion for a number of time steps equal to $t_{\mathrm{run}}/\Delta t$ by modeling $\xi_R(t)$ as the thermal rotational noise described by a Gaussian-distributed angular velocity with zero mean and variance $2D_{\mathrm{rot}}/\Delta t$, where $D_{\mathrm{rot}} = 0.0014$ rad^2/s is the Brownian rotational diffusion coefficient of a cell with aspect ratio $q = 9.4$ and a width of 1 µm. After every $t_{\mathrm{run}}/\Delta t$ steps, we modeled the reverse-pause events by adding a random angular deviation $\Delta\phi$ drawn by the angular distributions measured experimentally. The results did not change significantly when considering the

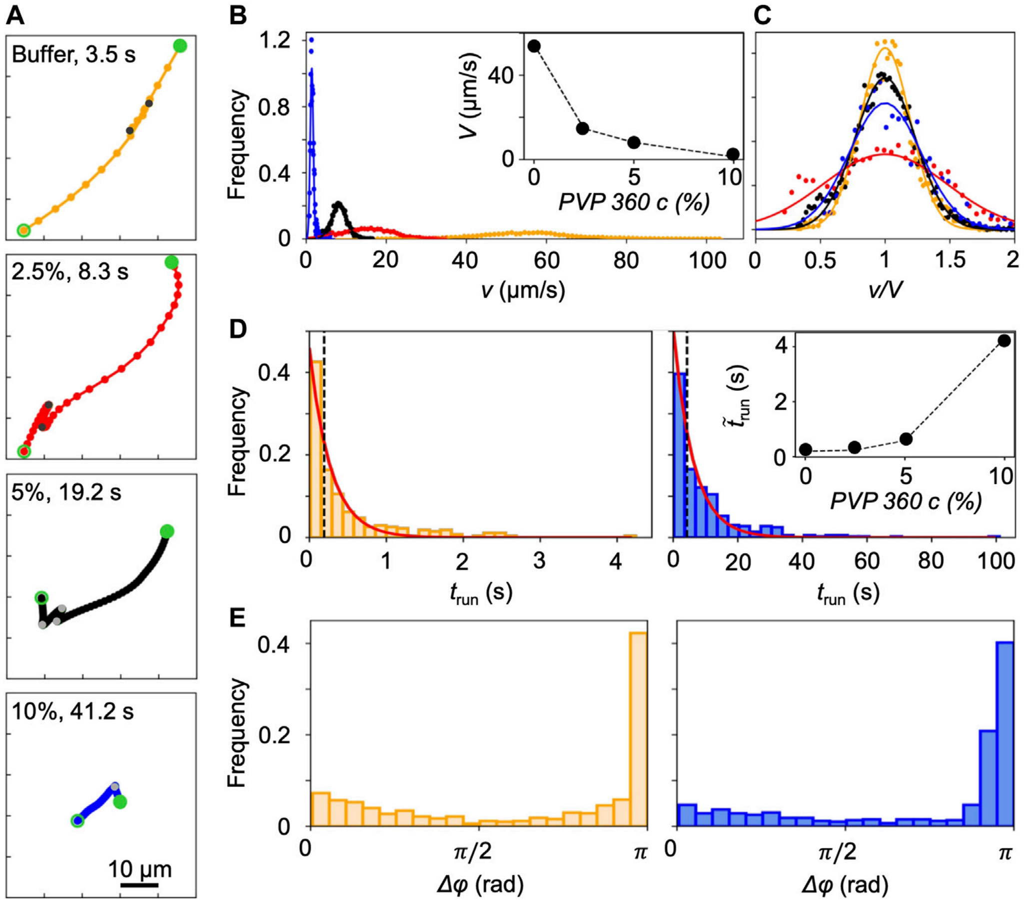

FIGURE 2 | (A) Typical trajectories of *P. aeruginosa* cells swimming in buffer (yellow) and in PVP 360 solutions at 2.5 w/v% (red), 5 w/v% (black), and 10 w/v% (blue) without flow. The trajectories begin at open green circles and end at filled green circles. Grey filled points mark the end of a run. The time interval between dots is equal to 0.2 s. **(B)** Distribution of swimming velocities, *v*, measured by tracking individual cells in a population of *P. aeruginosa* swimming in buffer (yellow), PVP 360 solutions at 2.5 w/v% (red), 5 w/v% (black), and 10 w/v% (blue) in no-flow conditions. The continuous curves are Gaussian fits with the mean velocities *V* reported in the inset. **(C)** Distribution of swimming velocities reported in panel **(B)** as a function of the normalized velocity *v/V*. **(D)** Distribution of the transit times t_{run} measured by tracking individual cells in a population of *P. aeruginosa* swimming in buffer (left panel) and in PVP 360 10 w/v% (right panel). The red curves are the exponential fits of the distributions. In the inset, the median values of t_{run} as a function of PVP 360 w/v concentration are reported. **(E)** Distribution of the angular changes $\Delta\varphi$ associated with reverse and pause events, measured by tracking individual cells in a population of *P. aeruginosa* swimming in buffer (left panel) and in PVP 360 10 w/v% (right panel).

Brownian rotational diffusion coefficient of a cell without taking the flagellum into account (aspect ratio $q = 2$, $D_{\mathrm{rot}} \approx 0.05\ \mathrm{rad}^2/\mathrm{s}$).

In the case of Newtonian fluids flowing in a straight channel, we considered a parabolic velocity profile $u(y) = U[1\text{-}4(y/W)^2]$, where U is the maximum flow speed, and a shear rate profile $\dot{\gamma}(y) = \partial u(y)/\partial y = -8Uy/W^2$. To simulate the Newtonian flow in a serpentine channel as the one used in the experiments, we first characterized the three-dimensional (3D) flow in the channel curves with computational fluid dynamics (CFD) simulations (COMSOL Multiphysics). Then, we numerically integrated **Eq. 1** by alternating sections with the velocity and shear rate profiles of the 4 cm-long straight sections and sections mimicking the curves to the left or to the right, according to the channel geometry. The length of the sections mimicking the curves was set to $(R + W/2)\pi$ and the corresponding velocity and shear rate profiles were assumed to be equal to those computed on the channel midplane at the center of a curve.

In the non-Newtonian case, we first characterized the 3D flow of the 0.1 w/v% xanthan gum solution inside the microchannel with CFD simulations. We then used the resulting 2D velocity and shear rate profiles on the midplane to integrate the equations of motion in **Eq. 1**. To simulate the rheological behavior of the xanthan gum solution, we set the fluid consistency index to $m = 17.8\ \mathrm{mPa\,s}$ and the flow behavior index to $n = 0.65$, according to our rheological measurements (**Figure 1C**). We set the lower shear rate limit to $\dot{\gamma}_{min} = 0.00188\ s^{-1}$. According to the shear-thinning behavior of xanthan gum solutions, channel flow gives rise to viscosity gradients. In our modelling, we do not explicitly account for any shear-thinning effect taking place at the microscale under the action of flagellar motion. In the following, we refer to the viscosity $\eta = \eta(y)$ determined only by channel flow as ambient viscosity. In no-flow conditions, ambient viscosity coincides with the zero-shear viscosity η_0.

Given that ambient viscosity is not homogeneous across the channel width, we investigated a possible dependence of bacterial swimming velocity on position. To do so, in the equations of motion for the non-Newtonian case, we considered that the swimming velocity $V = V(y)$ can vary across the channel width W, due to local changes in η. In order to find a relation between V and η, we used the following approach. We measured the swimming velocity V as a function of the xanthan gum concentration in the range $c = 0$ (buffer)—0.5 w/v%. In this concentration range, the relation between V and c is linear:

$$V = ac + d \tag{2}$$

where $a = -4.7\ 10^{-9}$ (m/s) (L/mg), $d = 33.9\ 10^{-6}$ m/s and c is expressed in ppm units (**Figure 6A**). According to [32], we established the following relation between c and the zero-shear viscosity η_0 for xanthan gum solutions in NaCl at 50 mM:

$$\eta_0(c) = \begin{cases} \dfrac{0.04}{500^2} c^2 = X_1 c^2 \ \text{ for } \ c \le c_\mathrm{e} \\ \dfrac{4}{2000^{4.67}} c^{4.67} = X_2 c^{4.67} \ \text{ for } \ c > c_e \end{cases} \tag{3}$$

where $c_e = 1000$ ppm is the entanglement concentration. Using this relation, we expressed V as a function of η_0 as:

$$V(\eta_0) = \begin{cases} a\left(\dfrac{\eta_0}{X_1}\right)^{1/2} + d \ \text{ for } \ \eta_0 \le \eta(c_\mathrm{e}) \\ a\left(\dfrac{\eta_0}{X_2}\right)^{1/4.67} + d \ \text{ for } \ \eta_0 > \eta(c_e) \end{cases} \tag{4}$$

where $\eta(c_e) = 160$ mPa s. Under the assumption that V in flowing xanthan gum solutions varies only due to the change in η, and that the dependence of V on η is the same as the one on η_0, we calculated V as a function of η by combining **Eqs 3**, **4**. Since the concentration of our sample was equal to c_e and xanthan gum solutions behave as shear-thinning fluids, the viscosity of the flowing sample is $\eta \le \eta(c_\mathrm{e})$. According to **Eq. 4**, $V(\eta_0)$ was calculated in the regime $\eta \le \eta(c_\mathrm{e})$. By combining **Eq. 4** with the power law relating η to $\dot{\gamma}$ (**Figure 1C**) and the numerical results for $\dot{\gamma}(y)$, we found the following expression for $V(y)$:

$$V(y) = \begin{cases} a^{\star}c + d \ \ for \ \ y: \ \dot{\gamma}(y) \le \dot{\gamma}^* \\ a\left(\dfrac{17.8 \cdot 10^{-3} \cdot (y)^{(0.65-1)}}{X_1}\right)^{1/2} + d \ \ for \ \ y: \ \dot{\gamma}(\mathrm{y}) > \gamma^* \end{cases} \tag{5}$$

where $\dot{\gamma}^* = 1.88 \cdot 10^{-3}\ \mathrm{s}^{-1}$ is defined as $\eta(\dot{\gamma}^*) = \eta_0(c_e)$ and the behavior for $\dot{\gamma}(y) \le \dot{\gamma}^*$ is fixed under the assumption that the swimming velocity cannot become smaller than the one measured in the no-flow case, where $\dot{\gamma} = 0$. As reported above, the lower shear rate limit used in the COMSOL simulations was set to $\dot{\gamma}^*$, since, under the aforementioned assumptions, variations of $\dot{\gamma}$ below this value did not affect the bacterial swimming velocity.

According to [23], we quantified the shear-induced depletion of both the experimental and numerical concentration profiles B with the depletion index I_D, defined as the fraction of bacteria depleted from the central half-width of the channel:

$$I_D = 2\left(\frac{1}{2} - \int_{-0.25}^{0.25} B(\tilde{y})\,d\tilde{y}\right) \tag{6}$$

Where $\tilde{y} = y/W \in [-0.5, 0.5]$ is the spanwise coordinate normalized by the channel width W.

RESULTS

Coupling Microfluidics and a Mathematical Model to Investigate *P. aeruginosa* Transport in Polymer Solutions

The effect of the polymeric nature of the fluid on bacterial transport was explored by combining microfluidic experiments with a mathematical model. During the experiments, we used optical microscopy to image the bacterial cells transported by the flow generated in a serpentine microfluidic channel (**Figure 1A**). The similarity of the geometry with the one presented in [23] allowed to easily compare the results. The aspect ratio of the channel $H/W > 1$ (height $H = 810$ µm; width $W = 360$ µm) ensures that the dominant velocity gradient occurred in the horizontal observation plane at the channel mid-depth. In this plane, for a Newtonian fluid—as culture media and the PVP 360 solutions—the flow profile is parabolic (**Figures 1A,B**), while for a non-Newtonian shear-thinning fluid—as the xanthan gum solution—the flow profile is flatter in the middle and decays faster towards the walls (**Figures 1A,C**). Motile *P. aeruginosa* cells were transported by the flow and imaged using video microscopy in phase-contrast mode to quantify their distribution across the width of the channel at 50 cm from the channel inlet (i.e., the entire length of the channel). Due to the low image quality close to the lateral channel walls, the cell distribution B, was quantified in a 220 µm-wide region centered at the centerline of the channel ($y/W \in [-0.3, 0.3]$).

We investigated the role of fluid rheology by comparing the results obtained with three different carrier fluids: PBS buffer, PVP 360 at different concentrations, and a 0.1 w/v% xanthan gum solution. PBS buffer had the same viscosity as water and was used as a reference fluid, as in [23]. PVP 360 solutions at different polymer concentrations were used as the prototype of the polymeric Newtonian fluid and allowed exploring the effect of a homogeneous increasing viscosity on bacterial transport (**Figure 1B**). The xanthan gum solution is a non-Newtonian fluid with a zero-shear viscosity $\eta_0 = 160$ mPa s, between those of PVP 360 5 w/v% and 10 w/v% and a marked shear-thinning behavior in the shear rate range explored in this study (**Figure 1C**). The shear-thinning behavior implies that η depends both on the flow rate and on the position y across the channel, and the shear rate profiles deviate from the linear ones observed in the Poiseuille flow of Newtonian fluids. The

Newtonian and non-Newtonian cases will be presented and analyzed individually in the following.

We observed that the polymeric nature of the carrier fluid modifies the shape of the cell distribution *B* and the magnitude of the depletion from the center of the channel and the accumulation towards the channel walls with respect to the buffer case. To interpret these observations, we adapted the mathematical model of cell motility in flow presented in [23, 29]. *P. aeruginosa* cells were modeled as prolate ellipsoids with aspect ratio $q = 9.4$ and swimming velocity V directed along their major axes [29]. In the Newtonian cases (buffer and PVP 360), we described the flow with a parabolic profile. In the non-Newtonian case, we characterized the flow field on the midplane of the channel with CFD simulations. The corresponding velocity and shear rate profiles were then used to compute single-cell trajectories. In both cases, the bacterial swimming direction was determined by a torque balance that accounts for the flow shear and the fluctuations in the bacterial orientation. Since the model accounts for the bacterial swimming strategy, which has been reported to change in polymeric fluids [10, 12], we characterized *P. aeruginosa* motility by tracking individual cells in the absence of flow and inserted the parameters into the model, as described in the following sub-section.

Newtonian PVP 360 Affects *P. aeruginosa* Motility in Quiescent Conditions

P. aeruginosa swims in a 3-step pattern of run-reverse-pause in buffer and PVP 360 polymer solutions at all the tested concentrations. Swimming in buffer has been described in [33, 34], in agreement with our observations. We imaged free-swimming cells on the midplane of a 100-μm high microfluidic channel, where cell motion was not affected by hydrodynamic interactions with the top and bottom walls. *P. aeruginosa* propels forward when its single polar flagellum rotates clockwise and backward when it rotates counterclockwise. Forward and backward runs are nearly straight [35] and are interrupted by pauses, sudden decreases in swimming velocity associated with small angular changes $\Delta\varphi$ in the swimming direction, or reverses, associated with angular changes $\Delta\varphi$ of about π [33] (yellow trajectory in **Figure 2A**). The same swimming pattern was observed in PVP 360 polymer solutions: the trajectories displayed straight runs, pauses and reverses at all the concentrations, as shown by the representative trajectories reported in **Figure 2A**. This observation indicated that the addition of PVP360 did not affect the swimming pattern of *P. aeruginosa*.

Conversely, the concentration of PVP 360 affected the distribution of swimming velocities v, measured by tracking individual *P. aeruginosa* cells. An increase in the polymer concentration led to a shift of the distribution towards lower values of v (**Figure 2B**). The distributions were fitted with Gaussian curves to estimate the mean swimming velocities V (**Figure 2B**, inset). Furthermore, the distributions of v normalized by the corresponding values of V, showed that the addition of PVP 360 caused a slight widening of the distributions, but did not affect their Gaussian shape. The widening was more pronounced at the lowest polymer concentration (2.5 w/v%) (**Figure 2C**).

The concentration of PVP 360 also affected the distribution of transit times t_{run} (**Figure 2D**), defined as the time elapsed between two consecutive changes in direction (marked by grey points in **Figure 2A**). As in [33], t_{run} followed exponential distributions both in the buffer and in the PVP 360 solutions (red curves in **Figure 2D**). However, the median value of t_{run} increased with increasing polymer concentration (**Figure 2D**, inset). Conversely, the distribution of angular changes $\Delta\varphi$ associated with pauses and reverses was not affected by PVP 360, and showed a peak at π at all the concentrations that we investigated (**Figure 2E**).

Newtonian PVP 360 Affects *P. aeruginosa* Transport in Flow

The bacterial population flowing in the channel was depleted from the center, where the shear rate $\dot{\gamma}$ was low, and accumulated in the lateral regions, where $\dot{\gamma}$ was higher, both in the buffer and in the PVP 360 polymer solutions. However, the distribution of bacterial cells across the channel width and the magnitude of the depletion effect depended on PVP 360 concentration. In the mathematical model, the bacterial motility at the different concentrations was described using the average swimming velocities V and the median values of t_{run}, reported in the insets of **Figures 2B,D**, and the distribution of $\Delta\varphi$ measured in buffer (left panel in **Figure 2E**). The model allowed comparing the effect of the propagation for 50 cm in a straight channel (continuous lines in **Figure 3**) and in a serpentine channel as the one we used in the experiments (dashed lines in **Figure 3**). In buffer, our observations are consistent with [23]: for average shear rates S in the range 2.5–100 s^{-1}, the depletion increases until $S \approx 20\ \mathrm{s}^{-1}$, and then decreases for larger shear rates.

The bacterial concentration profiles B obtained from the experiments (**Figure 3A**, symbols) were in good agreement with the ones simulated according to the mathematical model (lines) at all the tested values of S, especially when the curves in the serpentine geometry were taken into account (dashed lines). According to our simulations, the overall impact of the curves connecting the straight sections is to slightly widen the depleted region with respect to the straight channel case (dashed lines in **Figure 3**). The minimum of $|\dot{\gamma}|$ in the curves is not on the centerline, but is slightly shifted towards the center of curvature ($y > 0$ when turning to the left and $y < 0$ when turning to the right). As a consequence, when flowing in a curve, bacterial cells are more efficiently depleted in regions at the side of the centerline, causing a slight widening of the depleted region.

We quantified the shear-induced depletion with the depletion index I_{D} **Eq. 6**. The values of I_{D} confirm the agreement between experiments and simulations (**Figure 3B**). In the PVP 360 polymer solutions at 2.5 w/v% and 5 w/v%, the good agreement between numerical and experimental B profiles was remarkable at low S (lower than $S \approx 20\ \mathrm{s}^{-1}$) and becomes less precise for higher values of S (**Figures 3C,E**), as confirmed by I_{D} (**Figures 3D,F**). Interestingly, the maximum of I_{D} shifted to a lower shear rate for increasing polymer concentrations ($S \approx 10\ \mathrm{s}^{-1}$

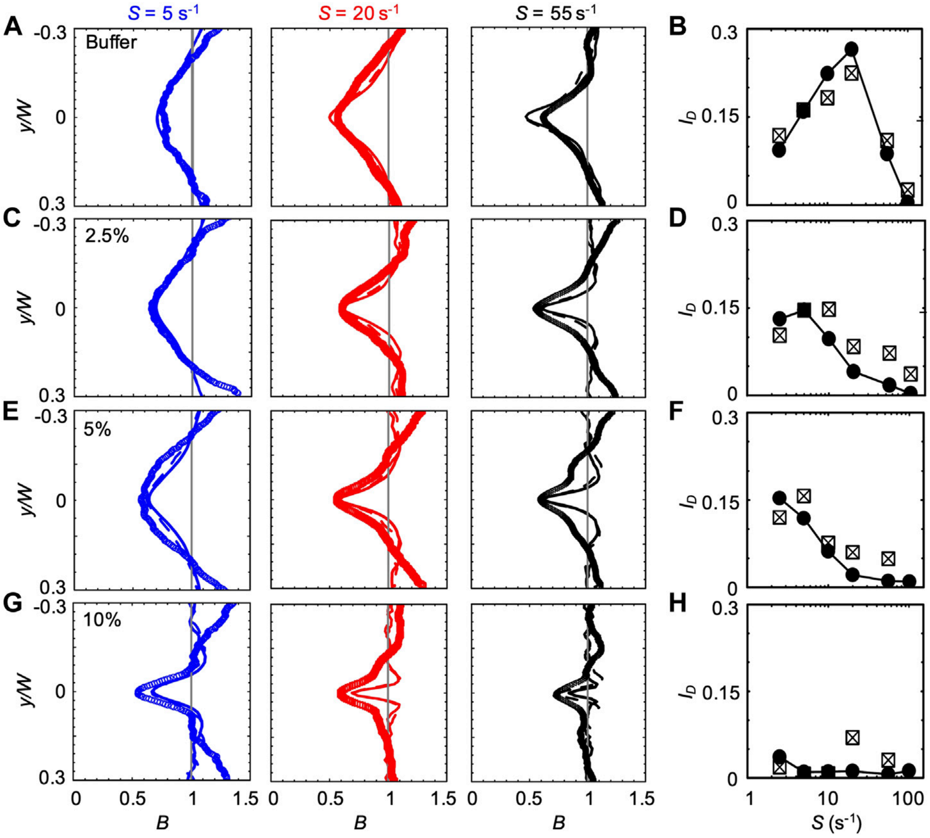

FIGURE 3 | (A,C,E,G) Bacterial concentration profiles *B* of *P. aeruginosa* obtained from the experiments (symbols) and from the mathematical model (lines) for mean shear rates $S = 5\ s^{-1}$ (blue), $S = 20\ s^{-1}$ (red), and $S = 55\ s^{-1}$ (black) in buffer **(A)** and in PVP 360 solutions at 2.5 w/v % **(C)**, 5 w/v % **(E)** and 10 w/v % **(G)**. All the profiles were measured or computed at a distance *D* = 50 cm from the inlet and normalized by the mean bacterial concentration in the no-flow case. The numerical concentration profiles were obtained by modelling bacterial transport in a straight 50 cm-long channel (continuous line) and in a 50 cm-long serpentine channel (dashed line). **(B,D,F,H)** The depletion index I_D as a function of the mean shear rate *S* in buffer **(B)** and in PVP 360 solutions at 2.5 w/v% **(D)**, 5 w/v% **(F)** and 10 w/v% **(H)**. The reported values were calculated for both the experimental (squares) and numerical (filled circles) bacterial concentration profiles. The numerical values were calculated from the profiles simulated in the straight 50 cm-long channel configuration.

and $S \approx 2.5\ s^{-1}$ at PVP 360 2.5 w/v% and 5 w/v%, respectively) (**Figures 3D,F**). The peak value of I_D was comparable at these two concentrations ($I_D \approx 0.146$ and $I_D \approx 0.153$ at PVP 360 2.5 w/v% and 5 w/v%, respectively), and was about 20% lower than the peak value of I_D in the buffer ($I_D \approx 0.19$). At the highest polymer concentration that we tested (PVP 360 10 w/v%), the agreement between the numerical and the experimental *B* profiles was good only for $S \leq 5\ s^{-1}$ (blue curves in **Figure 3G**), while for higher values of *S* the depletion from the center of the channel was larger in the experiments than in the model (red and black curves in **Figure 3G**). Additionally, I_D showed a drop in the depletion at PVP 360 10 w/v% compared to the lower polymer concentrations and the buffer case ($0.006 < I_D < 0.012$) (**Figure 3H**). Despite its low value, I_D decreased with increasing *S*, confirming the shift of the peak value of I_D to lower *S* values observed in PVP 360 2.5 w/v% and 5 w/v%. The transport experiments performed with dead cells (fixed by adding formaldehyde to a final concentration of 0.2%) did not show depletion at any of the PVP 360 concentrations and values of *S* we tested. Overall, we observed that PVP 360 caused a decrease of the shear-induced bacterial depletion compared to the buffer case and that the decrease was higher at larger PVP 360 concentrations.

B and I_D reach steady-state values once the cells have had time to swim towards high shear regions while being transported by the flow. Thus, the time required to reach the steady state increases when the swimming velocity *V* decreases. Accordingly, when *V* decreases, the steady state distribution will be observed at larger distances from the channel inlet. Consequently, increasing the concentration of PVP 360 increased the distance required to reach the steady-state, as shown by using the mathematical model to calculate I_D as a function of the distance *D* from the inlet for the different solutions at $S \approx 10\ s^{-1}$ (**Figure 4**). In buffer, *P. aeruginosa* cells swam at *V* = 54.7 μm/s and reached the steady-state distributions in less than 50 cm; thus, a longer traveling distance did not change *B* and I_D (**Figures 4A,B**). In PVP 360 solutions, *B* computed at a distance *D* = 50 cm (blue curves

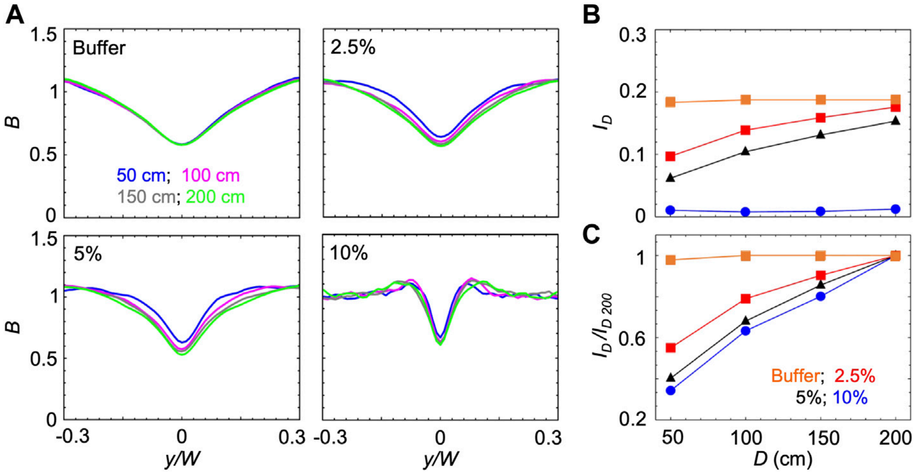

FIGURE 4 | (A) Bacterial concentration profiles *B* numerically calculated according to the mathematical model for mean shear rate $S = 10\ s^{-1}$ in buffer (upper left) and in PVP 360 solutions at 2.5 w/v% (upper right), 5 w/v% (lower left) and 10 w/v% (lower right). For each fluid, the profiles were computed at a distance *D* of 50 cm (blue), 100 cm (pink), 150 cm (grey) and 200 cm (green) from the inlet. **(B)** The depletion index I_D as a function of the distance from the inlet *D* in buffer (orange) and in PVP 360 solutions at 2.5 w/v% (red), 5 w/v % (blue) and 10 w/v% (black) measured from the numerical bacterial concentration profiles shown in **(A)**. **(C)** Depletion index normalized by the depletion index at *D* = 200 cm, $I_D/I_{D\ 200}$, as a function of the distance from the inlet *D*, calculated from the curves shown in **(B)**

in **Figure 4A**) had not reached the steady state yet, and the minima decreased when simulated at larger distances (pink and grey curves in **Figure 4A**). *B* reached the steady-state after 200 cm at all the tested concentrations (green curves in **Figure 4A**). The increase in the depletion with the traveling distance *D* was also visible from the trend of I_D (**Figure 4B**). To ease the comparison between different concentrations, we normalized I_D by its value at 200 cm, $I_D/I_{D\ 200}$. The normalized curves for $I_D/I_{D\ 200}$ showed that at higher PVP 360 concentrations the traveling distance required to reach the steady state is larger (**Figure 4C**). Consequently, we point out that in **Figure 3** we were not comparing the steady-state values for all the conditions, but the depletion reached by the bacterial suspension after flowing for 50 cm in the same channel.

The changes in the concentration profiles *B* and in the magnitude of the depletion observed in the PVP 360 solutions are attributable to changes in average swimming velocity *V* and median values of the transit time t_{run}, as shown by the good agreement between experimental and numerical results. Interestingly, if t_{tun} remained constant with increasing polymer concentration, we would not observe any depletion in the 10 w/v% solution at *D* = 50 cm. These observations suggest that an accurate description of the bacterial swimming is fundamental to accurately predict the shear-induced depletion. Consequently, in the results presented so far, we modeled the *P. aeruginosa* run-reverse-pause swimming pattern (Materials and Methods). When compared to the run-tumble pattern used to describe the motility of *B. subtilis* in [23], the run-reverse-pause motility in buffer had the same peak values, but different shapes of the depletion profile *B* at high shear rates (**Figure 5A**). In PVP 360 5 w/v% flowing at low *S*, also the peak values were different (**Figure 5C**). In the case of the buffer, a greater similarity between the *B* profiles simulated with run-reverse-pause and run-tumble motility was found at the lower *S*, while in the case of PVP 360 5 w/v% a greater similarity was found at higher values of *S*. Conversely, 10% variations in the swimming velocity would not affect the depletion at any shear rate, both in the buffer and in PVP 360 (**Figures 5B,D**).

Non-Newtonian Xanthan Gum Solution Affects *P. aeruginosa* Motility and Transport

In the non-Newtonian case, the complexity of the bacterial transport is increased by the complex rheological behavior of the carrier fluid. First, due to the shear-thinning behavior of xanthan gum, the shear rate $\dot{\gamma}$ is not linear across the channel width, as shown by CFD simulations (**Figure 7A**). Second, the ambient viscosity η varies across the channel as a function of $\dot{\gamma}$ (**Figures 1C, 7B**). Consequently, when transported by the ambient flow, bacteria swim through regions with different values of η. In this case, a dependence of *V* on the viscosity ($V = V(\eta)$) would imply a dependence of *V* also on the position *y* across the channel ($V = V(y)$). In addition, the shear-thinning action of the rotating flagella can also give rise to changes in η at the cell length scale.

We characterized the bacterial swimming in xanthan gum solutions at different concentrations, in no-flow conditions. By imaging free-swimming *P. aeruginosa* cells on the midplane of a 100 µm-high microfluidic channel, we observed that the non-Newtonian nature of the chosen polymer fluid did not affect the run-reverse-pause swimming pattern. As in the case of PVP 360, the average swimming velocity *V* decreases at increasing polymer concentration (**Figure 6A**), while the distributions of the swimming velocities *v* maintain a Gaussian shape (**Figure 6B**). In the case of xanthan gum, we found a linear

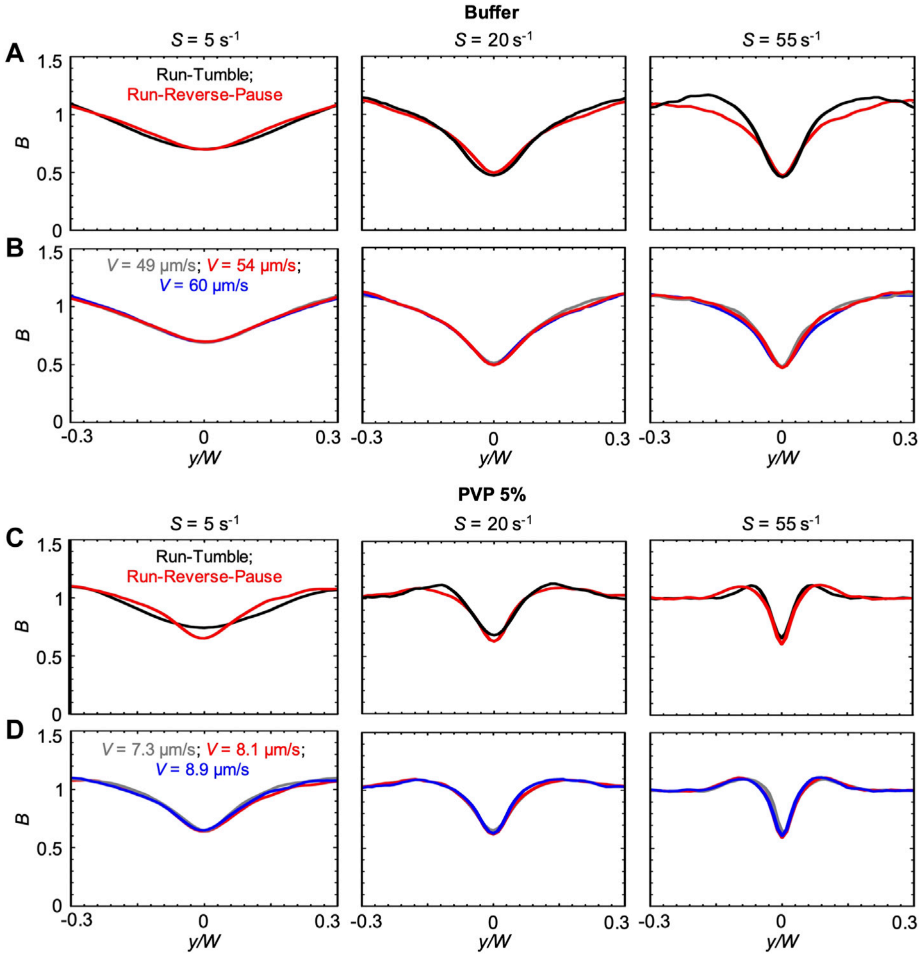

FIGURE 5 | (A) Bacterial concentration profiles B numerically calculated according to the mathematical model for mean shear rates $S = 5\ \mathrm{s}^{-1}$ (left), $S = 20\ \mathrm{s}^{-1}$ (center) and $S = 55\ \mathrm{s}^{-1}$ (right) in buffer, at a distance $D = 50$ cm for swimmers with run-tumble (black) and run-reverse-pause (red) patterns. For the run-tumble swimmers we used $q = 9.4$, $V = 54.17$, $\mu\mathrm{ms}^{-1}$, and $D_{\mathrm{R}} = 1.4\ \mathrm{rad}^2\ \mathrm{s}^{-1}$ as in [29], while the run-reverse-pause swimmers were simulated as described in the Materials and Methods. **(B)** Bacterial concentration profiles B calculated according to the mathematical model for mean shear rates $S = 5\ \mathrm{s}^{-1}$ (left), $S = 20\ \mathrm{s}^{-1}$ (center) and $S = 55\ \mathrm{s}^{-1}$ (right) in buffer for run-reverse-pause swimmers with a swimming velocity of $V = 49\ \mu\mathrm{ms}^{-1}$(grey), $54.17\ \mu\mathrm{ms}^{-1}$ (red) and $60\ \mu\mathrm{ms}^{-1}$ (blue). **(C)** Bacterial concentration profiles B numerically calculated according to the mathematical model for mean shear rates $S = 5\ \mathrm{s}^{-1}$ (left), $S = 20\ \mathrm{s}^{-1}$ (center) and $S = 55\ \mathrm{s}^{-1}$ (right) in PVP 360 5 w/v %, at a distance $D = 50$ cm from the inlet for swimmers with run-tumble (black) and run-reverse-pause (red) patterns. For the run-tumble swimmers we used $q = 9.4$, $V = 8.1$, $\mu\mathrm{ms}^{-1}$, and $D_{\mathrm{R}} = 1.4\ \mathrm{rad}^2\ \mathrm{s}^{-1}$ as in [29], while the run-reverse-pause swimmers were simulated as described in the Materials and Methods. **(D)** Bacterial concentration profiles B calculated according to the mathematical model for mean shear rates $S = 5\ \mathrm{s}^{-1}$ (left), $S = 20\ \mathrm{s}^{-1}$ (center) and $S = 55\ \mathrm{s}^{-1}$ (right) in PVP 360 5 w/v% for run-reverse-pause swimmers with a swimming velocity of $V = 7.3\ \mu\mathrm{ms}^{-1}$(grey), $8.1\ \mu\mathrm{ms}^{-1}$ (red) and $8.9\ \mu\mathrm{ms}^{-1}$ (blue).

relation between V and the polymer concentration c (Materials and Methods). The transit time distribution at 0.1 w/v% xanthan gum concentration followed an exponential curve as in the case of PVP 360, with a median transit time $t_{\mathrm{run}} = 0.6$ s. The distribution of angular changes $\Delta\varphi$ showed a peak at π (**Figure 6D**), as in the case of PVP 360.

The characterization of the bacterial swimming in no-flow conditions was aimed at establishing a link between the bacterial swimming parameters for the numerical model and the ambient viscosity in the channel. Ideally, it would have been advisable to characterize the swimming in a polymer solution in flow. However, this would not be possible in the presented experimental configuration. For this reason, we compared the numerical results obtained with three possible models of the bacterial swimming in the non-Newtonian fluid in flow. In the first case, we considered a constant swimming velocity $V{=}V_{0.1\%}$ equal to the one measured in xanthan gum 0.1 w/v% in no-flow conditions; in the second case, we considered a dependence of the swimming velocity on the local ambient viscosity $V{=}V(y)$; in the third case, we considered a swimming velocity dependent on the average ambient viscosity, $V{=}\ V(\eta_{\mathrm{S}})$. Our model did not explicitly account for the flagella-induced shear thinning (Materials and methods). However, by simulating the bacterial swimming with the parameters determined from the motility assays in xanthan gum solutions, the shear-thinning enhancement of motility in no-flow conditions is implicitly accounted for.

For the first model, we assumed that the bacterial swimming is not affected by the changes in the ambient viscosity of the carrier

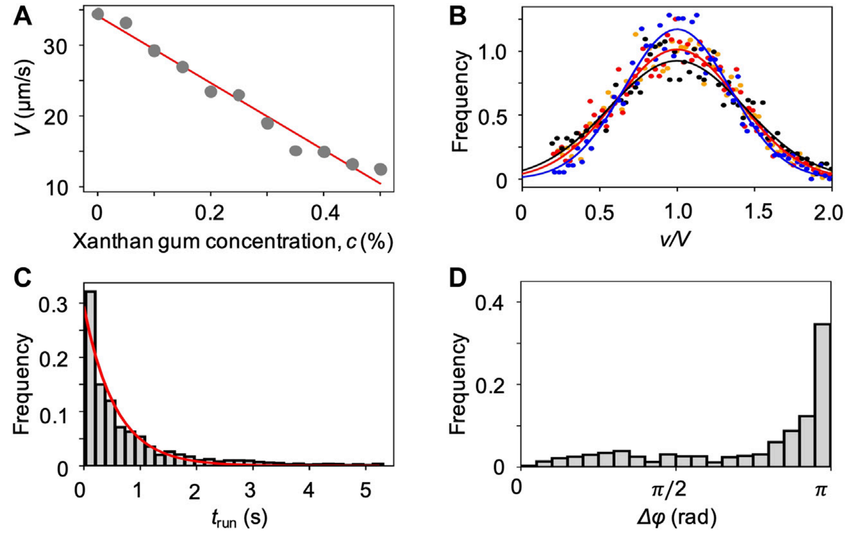

FIGURE 6 | (A) Mean swimming velocities V measured by tracking individual cells in a population of *P. aeruginosa* swimming in xanthan gum solutions at different concentrations in no-flow conditions. The red curve is the linear fit of the experimental data **(Eq. 2)**. **(B)** Distribution of swimming velocities as a function of the normalized velocity v/V, in buffer (yellow), and in xanthan gum solutions at 0.05 w/v% (red), 0.1 w/v% (black), and 0.2 w/v% (blue) in no-flow conditions. The continuous curves are Gaussian fits with the mean velocities V reported in **(A)**. **(C)** Distribution of the transit times t_{run} measured by tracking individual cells in a population of *P. aeruginosa* swimming in the 0.1 w/v% xanthan gum solution. The red curve is the exponential fit of the distribution. **(D)** Distribution of the angular changes $\Delta\varphi$ associated with reverse and pause events, measured by tracking individual cells in a population of *P. aeruginosa* swimming in the 0.1 w/v% xanthan gum solution.

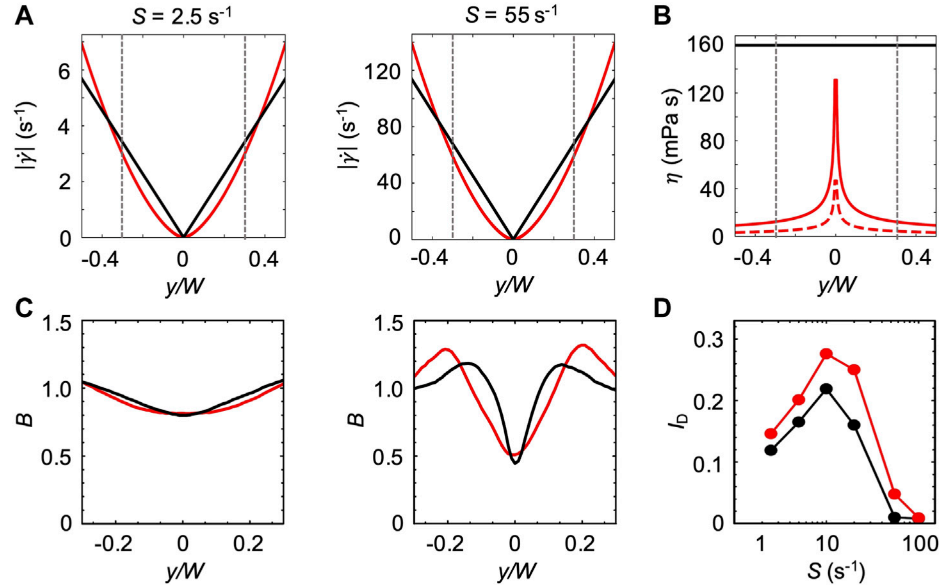

FIGURE 7 | (A) Absolute values of the shear rate $|\dot{\gamma}|$ in the channel in a Newtonian (black) and non-Newtonian (red) fluid at mean shear rates $S = 2.5\ s^{-1}$ (left panel) and $S = 55\ s^{-1}$ (right panel). The Newtonian profiles were calculated as $S = -8yU/W^2$. The non-Newtonian profiles were calculated with CFD simulations modeling the rheological behavior of xanthan gum 0.1 w/v%, as described in the Materials and Methods. **(B)** No-flow ambient viscosity η_0 of xanthan gum 0.1 w/v% (solid black line) and ambient viscosity profiles calculated with CFD simulations for $S = 2.5\ s^{-1}$ (solid red line) and $S = 55\ s^{-1}$ (dashed red line). **(C)** Concentration profiles B obtained from the mathematical model with the Newtonian (black) and non-Newtonian (red) shear rate profiles reported in panel A at mean shear rates $S = 2.5\ s^{-1}$ (left panel) and $S = 55\ s^{-1}$ (right panel). The numerical concentration profiles were obtained by modeling bacterial transport in a straight 50 cm-long channel, with bacterial swimming velocity $V=V_{0.1\%}$. **(D)** The depletion index I_D as a function of the mean shear rate S, measured from the numerical bacterial concentration calculated in the conditions described in **(C)**

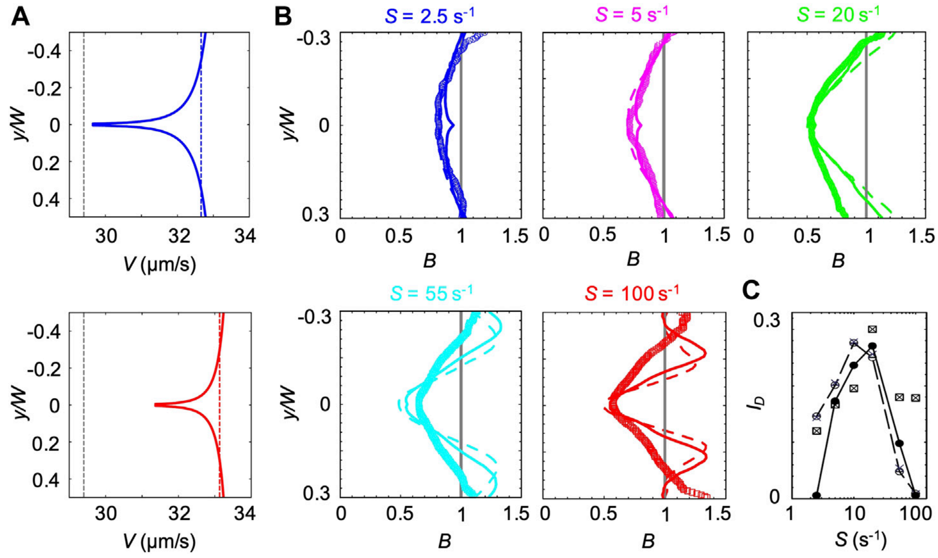

FIGURE 8 | (A) Bacterial swimming velocities *V(y)* (blue and red curve), $V(\eta_S)$ (blue and red dashed lines) and $V_{0.1\%}$ measured in a xanthan gum solution at 0.1 w/v% (grey dashed lines). The velocities are reported for mean shear rates *S* = 2.5 s^{-1} (upper panel) and *S* = 55 s^{-1} (lower panel). **(B)** Concentration profiles *B* of *P. aeruginosa* from experiments (symbols) and from the mathematical model (*V(y)* solid lines and $V_{0.1\%}$ dashed lines) for mean shear rates *S* = 2.5 (blue), 5 s^{-1} (pink), *S* = 20 s^{-1} (green), *S* = 55 s^{-1} (light blue) and 100 s^{-1} (red) in a xanthan gum solution at 0.1 w/v%. All the profiles were measured or computed at a distance *D* = 50 cm from the inlet and normalized by the mean bacterial concentration in the no-flow case. The numerical concentration profiles were obtained by modeling bacterial transport in a straight 50 cm-long channel using two different descriptions for the bacterial swimming velocity (*V(y)* and $V_{0.1\%}$). **(C)** The depletion index I_D as a function of the mean shear rate *S*, measured from the experimental (squares) and numerical (*V(y)*, filled circles; $V(\eta_S)$, crosses; $V_{0.1\%}$ empty circles) bacterial concentration profiles reported in **(B)**

fluid. We thus used the bacterial swimming parameters measured in xanthan gum 0.1 w/v% at rest to simulate swimming bacteria in the channel flow (**Figure 6**). In this case, the effect of the non-Newtonian behavior of xanthan gum in flow was accounted for by the shear rate profile $\dot{\gamma}$, while bacterial swimming velocity $V_{0.1\%}$ = 29.4 μm/s, transit time t_{run} and distribution of $\Delta\phi$ were kept constant at the values measured in xanthan gum 0.1 w/v% (**Figures 7A,B**). The comparison of the concentration profiles *B* corresponding to the Newtonian and non-Newtonian $\dot{\gamma}$ profiles showed that cells are depleted from a wider region at the center of the channel in the non-Newtonian case, both at *S* = 2.5 s^{-1} and *S* = 55 s^{-1} (**Figure 7C**). This effect is well captured by I_D, whose peak value is 25% higher in the non-Newtonian case (**Figure 7D**). This observation indicates that the non-Newtonian shear-thinning bulk behavior of the fluid promotes cell depletion, even when its effect on the bacterial swimming behavior is not accounted for.

Since $\eta(y)$ is dependent on the position across the channel width and affects bacterial swimming (**Figures 2**, **6**), in the second model, we investigated the effect of $\eta(y)$ on bacterial swimming by including a dependence of *V* on position. To do so, we assumed that the dependence of *V(y)* on $\eta(y)$ is the same as the one between *V* and η_0 of xanthan gum solutions at different concentrations in no-flow conditions (Materials and Methods). Based on this assumption, we used the relation between *V* and concentration *c* as determined in no-flow conditions (**Figure 6**; **Eq. 2**), and combined it with the relation between *c* and η_0 (**Eq. 3**). This allowed us to express *V* as a function of η_0 (**Eq. 4**). According to our assumption, by assuming that $V(\eta_0)$ and $V(\eta)$ have the same functional form, we combined **Eq. 4** with the power law describing η as a function of $\dot{\gamma}$ and obtained an expression for $V(\dot{\gamma})$. Finally, by numerically computing $\dot{\gamma}(y)$, we obtained a relation for $V(y)$ (**Eq. 5**) (blue and red solid lines in **Figure 8A**).

The third model is intermediate between the previous ones. In this case, we used the results from CFD simulations to calculate η_S, defined as the average value of $\eta(y)$ across the channel at the average shear rate *S*. Next, we used **Eq. 4** to compute the corresponding bacterial swimming velocity $V(\eta_S)$. $V(\eta_S)$ is constant across the channel but varies with *S* (blue and red dashed lines in **Figure 8A**). We then simulated the bacterial swimming using $V(\eta_S)$, and the median value of t_{run} and the distribution of $\Delta\phi$ measured in xanthan gum 0.1 w/v% in no-flow conditions.

The position-dependent swimming velocity $V(y)$ displayed a minimum at the channel centerline (red and blue solid lines in **Figure 8A**), where $|\dot{\gamma}|$ is minimum and $\eta(y)$ is maximum (**Figure 7B**). Overall, the variation of $V(y)$ across the channel width is no more than 10% of $V_{0.1\%}$. Similarly, $V(\eta_S)$ was in the range 32.5–33.2 μm/s, less than 13% higher than $V_{0.1\%}$. However, the numerical results showed that the position-dependence of the bacterial swimming velocity induced a small increase in *B* at the centerline of the channel at *S* < 55 s^{-1} (blue, pink, and green solid lines in **Figure 8B**). This feature was not observed in the numerical simulations with constant bacterial swimming velocities $V_{0.1\%}$ and $V(\eta_S)$. Besides the increase at the centerline, the overall shape of *B* with $V(y)$ did not display any significant differences compared to the cases at $V_{0.1\%}$ and $V(\eta_S)$ (solid and dashed line in **Figure 8B**). The values of I_D obtained for the $V(y)$, $V_{0.1\%}$ and $V(\eta_S)$ cases are similar, while the

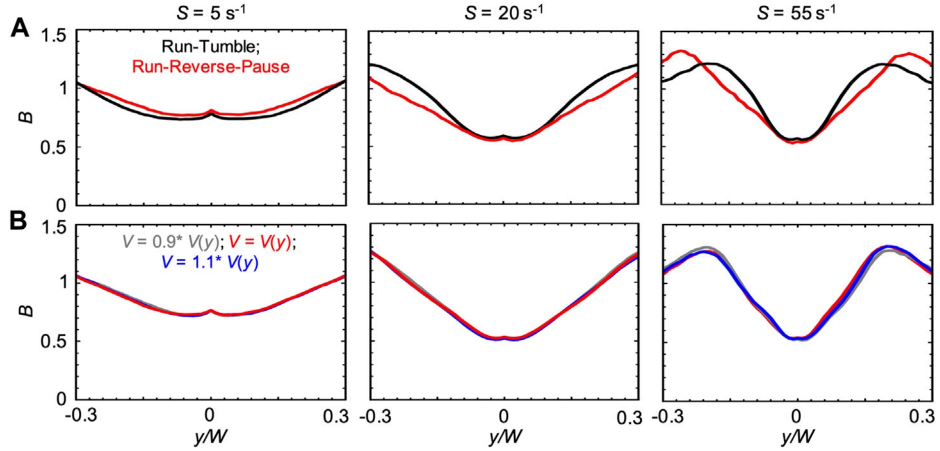

FIGURE 9 | (A) Bacterial concentration profiles B numerically calculated according to the mathematical model for mean shear rates $S = 5\ s^{-1}$ (left), $S = 20\ s^{-1}$ (center) and $S = 55\ s^{-1}$ (right) in xanthan gum 0.1 w/v %, at a distance $D = 50$ cm for swimmers with run-tumble (black) and run-reverse-pause (red) patterns. For the run-tumble swimmers we used $q = 9.4$, $V = 29.4$, μms^{-1}, and $D_R = 1.4\ rad^2\ s^{-1}$ as in [29], while the run-reverse-pause swimmers were simulated with swimming velocity $V(y)$, as described in the Materials and Methods. **(B)** Bacterial concentration profiles B calculated according to the mathematical model for mean shear rates $S = 5\ s^{-1}$ (left), $S = 20\ s^{-1}$ (center) and $S = 55\ s^{-1}$ (right) in xanthan gum at 0.1 w/v %, for run-reverse-pause swimmers with swimming velocities of $V(y)$, calculated according to **Eq. 5** (red), $V = 0.9\ V(y)$ (grey) and $V = 1.1V(y)$ (blue).

I_D peak is shifted towards lower S in the case of constant bacterial swimming velocities $V_{0.1\%}$ and $V(\eta_S)$ (**Figure 8C**).

The experimental B did not display the slight increase in B at the centerline of the channel generated by the spatial dependence of $V(y)$ and showed a better agreement with the profiles obtained at constant swimming velocity (**Figure 8B**). However, the overall agreement between the experimental and numerical results was satisfactory at shear rates $S < 55\ s^{-1}$, as shown by B and I_D (**Figures 8B,C**). In this case, I_D showed a maximum at $S \approx 20\ s^{-1}$, resembling the buffer case both in the trend and the magnitude (**Figure 3B**).

We also compared the run-reverse-pause and run-tumble swimming patterns for the case $V(y)$. In agreement with the Newtonian case, we observed that, for run-reverse-pause swimmers, B had the same peak values but different shapes at high values of S (**Figure 9A**). As already suggested by the negligible differences observed in the numerical results obtained with $V_{0.1\%}$ and $V(\eta_S)$, a 10% difference in the bacterial swimming velocity did not affect B (**Figure 9B**). This observation is consistent with the Newtonian cases reported in **Figure 6B**.

DISCUSSION

How complex fluids may affect the motility of microorganisms has been the subject of several experimental [4, 10–12] and numerical [8, 11, 19] studies. On the other hand, the effect of fluid flow on bacterial transport has been investigated only in simple fluids, where a mechanistic explanation of the interplay between cell motility and hydrodynamic shear resulting in the shear-trapping of bacteria has been given [23–26, 29]. However, the influence of a polymer fluid flow on bacterial transport remained an understudied topic. Here, we focused on bacterial transport in Newtonian and non-Newtonian polymer solutions and showed three major differences from the case of transport in water. First, the reduction of the bacterial swimming velocity V in Newtonian polymer solutions reduces bacterial depletion from the center of the channel. Second, it increases the distance D required to reach the steady-state distribution across the channel. Third, in the case of a non-Newtonian polymer solution in flow, bacterial depletion from the center of the channel is not reduced, even if the zero-shear viscosity of the fluid is much higher than the one of water. In this case, our mathematical model only captured the overall behavior of the bacterial transport. However, due to the approximations made in the model, the proposed investigation did not intend to be exhaustive. Instead, it aims at proposing a possible simplified procedure to macroscopically describe this complex problem.

The polymeric nature of the fluid plays a fundamental role in determining the motility of bacteria in no-flow conditions. In the case of *P. aeruginosa* swimming in Newtonian PVP 360 and non-Newtonian xanthan gum solutions, the swimming pattern did not change and could be described as run-reverse-pause in all the tested fluids. Similarly, the shape of the distribution of swimming velocities v and transit times t_{run} remained the same. In contrast, the mean swimming velocities V and the median of t_{run} showed significant changes, the extent of which depended on the type of polymer and its concentration in solution. In our case, the investigation in no-flow conditions was instrumental to determine the parameters describing bacterial motility to be used in the mathematical model of bacterial transport in flow.

In our study, V decreased at increasing polymer concentration, both in the Newtonian and non-Newtonian cases. Our results are consistent with recent work on *Vibrio cholerae* in PVP 360 with concentrations ranging from 0.9 to 6.7 w/w% and 1.2 w/w% mucin [7]. Conversely, previous studies performed with

Escherichia coli [10] and *P. aeruginosa* [4] in PVP 360 showed an increase in the velocity of the order of 10% at concentrations in the range between 1—2 w/v %. Considering our modelling results, a possible 10% variation in the mean swimming velocity would not affect the transport properties in all the investigated polymer fluids (**Figures 5B**, **9**). Conversely, shear-induced depletion was affected by the significant decrease of V in the PVP 360 concentration range we tested, where our results on motility are consistent with previous findings. Despite the drastic reduction of cell motility with increasing concentration of PVP360, we observe that the increase in transit time t_{run} still makes it possible to experimentally observe depletion at a distance D = 50 cm from the inlet of the channel even for the 10 w/v% solution. In the non-Newtonian case, the xanthan gum solution used in our study did not induce an enhancement of the swimming velocity observed, for example, for *E. coli* in Methocel [11] and in carboxy-methyl cellulose [12], but not for *V. cholerae* in mucin [7]. Given the complex interplay between flagellar motility and rheology of polymer fluids [11, 19], the differences in the observations could be attributed to the particular bacterium and polymer we chose.

The mathematical model accounts for the change in viscosity and bacterial motility of the different solutions. However, it does not account for the microscopic structure of the polymeric fluids, the possible structural changes caused by the shear flow, and the consequent impact they would have on bacterial motility. The discrepancies between the concentration profiles B obtained with the experiments and the numerical simulations at high shear rates and high concentrations in PVP 360 and at high shear rates in the xanthan gum solution could be explained in light of the shear-induced structural rearrangements of the suspending fluid at the microscale. In these cases, the bulk rheological behavior may not be sufficient to fully capture the complex interplay between bacterial motility and the polymeric fluid structure described in [11, 19]. However, our simplified model was able to describe the overall trend of the shear-induced depletion, indicating that the rheology of the fluid and a realistic description of the bacterial swimming pattern are the most important factors driving bacterial transport in flow.

Interestingly, although the viscosity of PVP 360 5 w/v% (η = 38 mPa s, **Figure 1B**) is significantly lower than the zero-shear viscosity of the xanthan gum solution (η_0 = 160 mPa s, **Figure 1C**), the shear-induced depletion was consistently lower in the Newtonian PVP 360 case. In the non-Newtonian case, the similarity between the experimental and the numerical B profiles obtained at constant bacterial swimming velocity ($V_{0.1\%}$ and $V(\eta_S)$) suggests that two main factors contribute to the strong depletion observed in the non-Newtonian case: the high value of the bacterial swimming velocity V (**Figure 6A**) and the non-Newtonian shear rate profile $\dot{\gamma}$ (**Figure 7**). In xanthan gum 0.1 w/v% solution, $V_{0.1\%}$ is reduced by only 15% with respect to the buffer, while in PVP 360 5 w/v%, the reduction is of about 80%, even if the η_0 of xanthan gum 0.1 w/v% is 4 times higher than the viscosity of PVP 360 5 w/v%. The high value of V in the xanthan gum solution could be attributed to the local shear-thinning performed by the bacterial flagella. Moreover, since the concentration profiles B obtained by simulations at constant V are in good agreement with the experiments, at least at low average shear rates S, we hypothesize that the local shear-thinning induced by the bacterial swimming is not deeply affected by the local flow conditions. The slight increase in B at the centerline of the channel—resulting from the numerical simulation at $V(y)$—is not observed in the experiments. Since the variation of $\eta(y)$ in the channel is appreciable over few tens of microns, this length scale may be too similar to the length of a bacterium (including the flagellum) to appreciably affect the bacterial swimming speed. At higher shear rates, more complex interactions between flagella and the fluid or changes in the fluid structure [11] may lead to the observed discrepancies.

Given the impact of shear-induced depletion on surface colonization [23, 29] and bacterial chemotaxis [23, 26], our findings could have substantial medical and technological implications. For example, the respiratory, gastrointestinal, and reproductive tracts of animals are covered in mucus [1], a complex polymer fluid which is continuously stirred by ciliary motion. In these systems, a realistic description of bacterial transport and surface colonization would require to take into account the interplay between shear rate, cell motility and fluid rheology. By describing two prototypical cases, we hope to raise the interest of the community and foster further investigation in more complex scenarios, contributing to the creation of a more accurate description of bacterial transport in polymer solutions.

DATA AVAILABILITY STATEMENT

The original contributions presented in the study are included in the article/Supplementary Material, further inquiries can be directed to the corresponding author.

AUTHOR CONTRIBUTIONS

ES, RR, and RS designed research. GS, ES, TC, and YL performed the experiments. GS and ES analysed all the data. SG performed the rheological characterization of the polymer solutions. GS, ES, and RR designed and built the mathematical model. GS and ES wrote the manuscript and all authors edited and commented on the manuscript.

FUNDING

The authors acknowledge support from SNSF PRIMA grant 179834 (to ES), from a Symbiosis in Aquatic Systems Investigator Award from the Gordon and Betty Moore Foundation (GBMF9197; https://doi.org/10.37807/GBMF9197) (to RS), and from Simons Foundation Grant 542395 (to RS) as part of the Principles of Microbial Ecosystems Collaborative (PriME).

ACKNOWLEDGMENTS

The authors acknowledge Dr. Sam Charlton and Ursin Eberhard for the insightful discussions; Ela Burmeister for the technical support.

REFERENCES

1. Lai SK, Wang Y-Y, Wirtz D, Hanes J. Micro- and Macrorheology of Mucus. *Adv Drug Deliv Rev* (2009) 61:86–100. doi:10.1016/j.addr.2008.09.012
2. Morgan SE, McCormick CL. Water-soluble Polymers in Enhanced Oil Recovery. *Prog Polym Sci* (1990) 15:103–45. doi:10.1016/0079-6700(90)90017-U
3. Sunthar P. Polymer Rheology. In: JM Krishnan, AP Deshpande, PBS Kumar, editors. *Rheology of Complex Fluids*. New York, NY: Springer (2010). p. 171–91. doi:10.1007/978-1-4419-6494-6_8
4. Schneider WR, Doetsch RN. Effect of Viscosity on Bacterial Motility. *J Bacteriol* (1974) 117:696–701. doi:10.1128/jb.117.2.696-701.1974
5. Berg HC, Turner L. Movement of Microorganisms in Viscous Environments. *Nature* (1979) 278:349–51. doi:10.1038/278349a0
6. Kaiser GE, Doetsch RN. Enhanced Translational Motion of *Leptospira* in Viscous Environments. *Nature* (1975) 255:656–7. doi:10.1038/255656a0
7. Grognot M, Mittal A, Taute KM. *Vibrio cholerae* Motility in Aquatic and Mucus-Mimicking. *Appl Environ Microbiol* (2021) 87:e01293–21. doi:10.1128/aem.01293-21
8. Keller JB. Effect of Viscosity on Swimming Velocity of Bacteria. *Proc Natl Acad Sci U.S.A* (1974) 71:3253–4. doi:10.1073/pnas.71.8.3253
9. Magariyama Y, Kudo S. A Mathematical Explanation of an Increase in Bacterial Swimming Speed with Viscosity in Linear-Polymer Solutions. *Biophysical J* (2002) 83:733–9. doi:10.1016/S0006-3495(02)75204-1
10. Martinez VA, Schwarz-Linek J, Reufer M, Wilson LG, Morozov AN, Poon WCK. Flagellated Bacterial Motility in Polymer Solutions. *Proc Natl Acad Sci U.S.A* (2014) 111:17771–6. doi:10.1073/pnas.1415460111
11. Qu Z, Breuer KS. Effects of Shear-Thinning Viscosity and Viscoelastic Stresses on Flagellated Bacteria Motility. *Phys Rev Fluids* (2020) 5:1–14. doi:10.1103/PhysRevFluids.5.073103
12. Patteson AE, Gopinath A, Goulian M, Arratia PE. Running and Tumbling with *E. coli* in Polymeric Solutions. *Sci Rep* (2015) 5:1–11. doi:10.1038/srep15761
13. Li C, Qin B, Gopinath A, Arratia PE, Thomases B, Guy RD. Flagellar Swimming in Viscoelastic Fluids: Role of Fluid Elastic Stress Revealed by Simulations Based on Experimental Data. *J R Soc Interf* (2017) 14:20170289. doi:10.1098/rsif.2017.0289
14. Qin B, Gopinath A, Yang J, Gollub JP, Arratia PE. Flagellar Kinematics and Swimming of Algal Cells in Viscoelastic Fluids. *Sci Rep* (2015) 5:9190. doi:10.1038/srep09190
15. Kamdar S, Shin S, Leishangthem P, Francis LF, Xu X, Cheng X. The Colloidal Nature of Complex Fluids Enhances Bacterial Motility. *Nature* (2022) 603:819–23. doi:10.1038/s41586-022-04509-3
16. Liu B, Powers TR, Breuer KS. Force-free Swimming of a Model Helical Flagellum in Viscoelastic Fluids. *Proc Natl Acad Sci U.S.A* (2011) 108:19516–20. doi:10.1073/pnas.1113082108
17. Spagnolie SE, Liu B, Powers TR. Locomotion of Helical Bodies in Viscoelastic Fluids: Enhanced Swimming at Large Helical Amplitudes. *Phys Rev Lett* (2013) 111:1–5. doi:10.1103/PhysRevLett.111.068101
18. Qu Z, Temel FZ, Henderikx R, Breuer KS. Changes in the Flagellar Bundling Time Account for Variations in Swimming Behavior of Flagellated Bacteria in Viscous media. *Proc Natl Acad Sci U.S.A* (2018) 115:1707–12. doi:10.1073/pnas.1714187115
19. Zöttl A, Yeomans JM. Enhanced Bacterial Swimming Speeds in Macromolecular Polymer Solutions. *Nat Phys* (2019) 15:554–8. doi:10.1038/s41567-019-0454-3
20. Wheeler JD, Secchi E, Rusconi R, Stocker R. Not just Going with the Flow: The Effects of Fluid Flow on Bacteria and Plankton. *Annu Rev Cel Dev. Biol.* (2019) 35:213–37. doi:10.1146/annurev-cellbio-100818-125119
21. Rusconi R, Stocker R. Microbes in Flow. *Curr Opin Microbiol* (2015) 25:1–8. doi:10.1016/j.mib.2015.03.003
22. Son K, Brumley DR, Stocker R. Live from under the Lens: Exploring Microbial Motility with Dynamic Imaging and Microfluidics. *Nat Rev Microbiol* (2015) 13:761–75. doi:10.1038/nrmicro3567
23. Rusconi R, Guasto JS, Stocker R. Bacterial Transport Suppressed by Fluid Shear. *Nat Phys* (2014) 10:212–7. doi:10.1038/NPHYS2883
24. Ezhilan B, Saintillan D. Transport of a Dilute Active Suspension in Pressure-Driven Channel Flow. *J Fluid Mech* (2015) 777:482–522. doi:10.1017/jfm.2015.372
25. Stark H. Swimming in External fields. *Eur Phys J Spec Top* (2016) 225:2369–87. doi:10.1140/epjst/e2016-60060-2
26. Bearon RN, Hazel AL. The Trapping in High-Shear Regions of Slender Bacteria Undergoing Chemotaxis in a Channel. *J Fluid Mech* (2015) 771:1–13. doi:10.1017/jfm.2015.198
27. Miño GL, Baabour M, Chertcoff R, Gutkind G, Clément E, Auradou H, et al. *E. coli* Accumulation behind an Obstacle. *AiM* (2018) 08:451–64. doi:10.4236/aim.2018.86030
28. Altshuler E, Miño G, Pérez-Penichet C, Río Ld., Lindner A, Rousselet A, et al. Flow-controlled Densification and Anomalous Dispersion of *E. coli* through a Constriction. *Soft Matter* (2013) 9:1864–70. doi:10.1039/c2sm26460a
29. Secchi E, Vitale A, Miño GL, Kantsler V, Eberl L, Rusconi R, et al. The Effect of Flow on Swimming Bacteria Controls the Initial Colonization of Curved Surfaces. *Nat Commun* (2020) 11:2851. doi:10.1038/s41467-020-16620-y
30. Słomka J, Alcolombri U, Secchi E, Stocker R, Fernandez VI. Encounter Rates between Bacteria and Small Sinking Particles. *New J Phys* (2020) 22:043016. doi:10.1088/1367-2630/ab73c9
31. Mcdonald JC, Duffy DC, Anderson JR, Chiu DT, Wu H, Schueller OJA, et al. Fabrication of Microfluidic Systems in Poly(dimethylsiloxane). *Electrophoresis* (2000) 21:27–40. doi:10.1002/(sici)1522-2683(20000101)21:1<27::aid-elps27>3.0.co;2-c
32. Wyatt NB, Liberatore MW. Rheology and Viscosity Scaling of the Polyelectrolyte Xanthan Gum. *J Appl Polym Sci* (2009) 114:4076–84. doi:10.1002/app.31093
33. Cai Q, Li Z, Ouyang Q, Luo C, Gordon VD. Singly Flagellated *Pseudomonas aeruginosa* Chemotaxes Efficiently by Unbiased Motor Regulation. *MBio* (2016) 7:7. doi:10.1128/mBio.00013-16
34. Qian C, Wong CC, Swarup S, Chiam K-H. Bacterial Tethering Analysis Reveals a "Run-Reverse-Turn" Mechanism for Pseudomonas Species Motility. *Appl Environ Microbiol* (2013) 79:4734–43. doi:10.1128/AEM.01027-13
35. Taylor BL, Koshland DE. Reversal of Flagellar Rotation in Monotrichous and Peritrichous Bacteria: Generation of Changes in Direction. *J Bacteriol* (1974) 119:640–2. doi:10.1128/jb.119.2.640-642.1974

Conflict of Interest: The authors declare that the research was conducted in the absence of any commercial or financial relationships that could be construed as a potential conflict of interest.

frontiers | Frontiers in Physics

ORIGINAL RESEARCH
published: 01 July 2022
doi: 10.3389/fphy.2022.904836

Biolocomotion and Premelting in Ice

Jérémy Vachier [1] and John S. Wettlaufer [1,2]**

[1]Nordita, KTH Royal Institute of Technology and Stockholm University, Stockholm, Sweden, [2]Departments of Earth and Planetary Sciences, Mathematics and Physics, Yale University, New Haven, CT, United States

Biota are found in glaciers, ice sheets and permafrost. Ice bound micro-organisms evolve in a complex mobile environment facilitated or hindered by a range of bulk and surface interactions. When a particle is embedded in a host solid near its bulk melting temperature, a melted film forms at the surface of the particle in a process known as interfacial premelting. Under a temperature gradient, the particle is driven by a thermomolecular pressure gradient toward regions of higher temperatures in a process called thermal regelation. When the host solid is ice and the particles are biota, thriving in their environment requires the development of strategies, such as producing exopolymeric substances (EPS) and antifreeze glycoproteins (AFP) that enhance the interfacial water. Therefore, thermal regelation is enhanced and modified by a process we term *bio-enhanced premelting*. Additionally, the motion of bioparticles is influenced by chemical gradients influenced by nutrients within the icy host body. We show how the overall trajectory of bioparticles is controlled by a competition between thermal regelation and directed biolocomotion. By re-casting this class of regelation phenomena in the stochastic framework of active Ornstein-Uhlenbeck dynamics, and using multiple scales analysis, we find that for an attractive (repulsive) nutrient source, that thermal regelation is enhanced (suppressed) by biolocomotion. This phenomena is important in astrobiology, the biosignatures of extremophiles and in terrestrial paleoclimatology.

Keywords: bioparticles, premelting, biolocomotion, active matter, Ornstein-Uhlenbeck process, extremophiles

OPEN ACCESS

Edited by:
Sujit Datta,
Princeton University, United States

Reviewed by:
Jay Nadeau,
Portland State University,
United States
Yuan-Nan Young,
New Jersey Institute of Technology,
United States

****Correspondence:***
Jérémy Vachier
jeremy.vachier@su.se,
John S. Wettlaufer
john.wettlaufer@yale.edu

Specialty section:
This article was submitted to
Biophysics,
a section of the journal
Frontiers in Physics

Received: *25 March 2022*
Accepted: *03 June 2022*
Published: *01 July 2022*

Citation:
Vachier J and Wettlaufer JS (2022)
Biolocomotion and Premelting in Ice.
Front. Phys. 10:904836.
doi: 10.3389/fphy.2022.904836

INTRODUCTION

Ice sheets are an essential reservoir of information on past climate and they contain an important record of micro-organisms on Earth, recording ice microbes and their viruses over long periods [1, 2]. In these extreme environments, the abundance of virus is well correlated with bacterial abundance, but is 10–100 times lower than in temperate aquatic ecosystems [3]. Even in these harsh conditions, the virus infection rate is relatively high [4], leading to the expectation of low long-term survival rates. However, recent studies have shown that some viruses develop survival strategies to maintain a long-term relationship with their hosts [4, 5], possibly up to thousands of years [6]. For example, viruses such as bacteriophages can switch to a lysogenic life strategy enabling them to replicate and maintain themselves in the bacterial population without lysis over multiple generations [4]. Moreover, among these viruses some can provide immunity to their hosts against other viruses [4, 7], or manipulate their metabolism to facilitate nutrient acquisition by affecting motility genes [6]. Indeed, motile biota are found to be active in ice for substantial periods. For example, recently a 30,000 year old giant virus *Pithovirus sibericum* was found in permafrost along with microbes and nematodes, and viable bacteria have been found in 750,000 year old glacial ice. Basal ice often contains subglacial debris and sediment, which serve as a source of nutrients and organic matter, providing a habitat for micro-organisms adapted to subfreezing conditions [8, 9]. Additionally, the microbiomes of sediment rich basal ices are distinct from those found in glacial ice and are equivalent to those found in permafrost [8], expanding the nature of subfreezing habitats.

Ice cores provide the highest resolution records of past climate states [10–15]. Of particular relevance to our study is their role as a refuge for micro-organisms, from the recent past [16, 17] to millennia [18–20]. Ice microbes are taxonomically diverse and have a wide range of taxonomic relatives [9, 19, 21–23]. Common algae taxa are centric and pennate diatoms, dinoflagellates and flagellates [24–26], whereas common bacterial taxa are pseudomonadota, actinobacteria, firmicutes and bacteroidetes [6, 27]. Many of these microbes have different motility mechanisms [28, 29] from swimming (e.g., *Chlamydomonas nivalis* [30] or *Methylobacterium* [6, 31, 32]) to gliding (e.g., *diatoms* [33, 34] *or Bacillus subtilis* [19, 35]), which can be used to assess their locomotion. Examples of biological proxies include diatoms [36] and bacteria colonies [37, 38], reflecting a unique range of physical-biological interactions in the climate system. Therefore, understanding the relationship between the evolution of ice bound micro-organisms and proxy dating methods is a key aspect of understanding the covariation of life and climate.

Finally, such understanding is essential for the study of extraterrestrial life. In our own solar system, despite the debate regarding the existence of bulk water on Mars [39], thin water films, such as those studied here, hold the most potential for harboring life under extreme conditions. Indeed, lipids, nucleic acids, and amino acids influenced by active motility may serve as biosignatures of extra terrestial life. Combining measurements of diffusivity-characterized-motility [40, 41] with bioparticle distribution observed on Earth, provides crucial information for development of new instrumentation to detect the presence of extra terrestrial life [41, 42]. Indeed, recently micro-organisms trapped in primary fluid inclusions in halite for millions of years have been discovered [43], providing promise for both terrestrial and extraterrestrial biosignature detection.

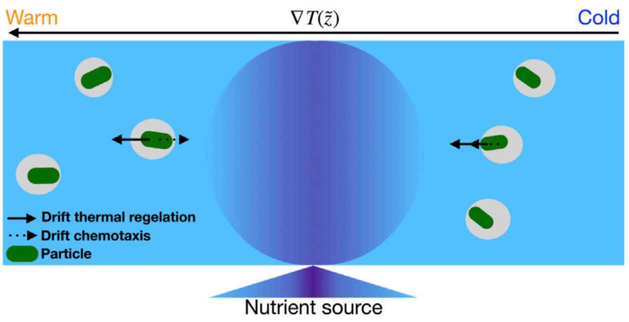

FIGURE 1 | Schematic of few active particles embedded in ice under an external temperature gradient ∇T along the $\tilde{z}$-axis. The nutrient source is shown by the purple gradient. The external temperature gradient induces a drift velocity, and particles move toward regions of higher temperature, in a process known as thermal regelation (black arrow). An additional drift velocity is associated with particle motion towards higher concentration of nutrients (black dotted arrow). Thus, depending on a particle's position, and the background temperature and nutrient gradients, these two drift effects can compete or amplify each other.

When a particle is embedded in ice near the bulk melting temperature, the ice may melt at the particle-ice surface in a process known as *interfacial premelting* [44]. The thickness of the melt film depends on the temperature, impurities, material properties and geometry. A temperature gradient is accompanied by a thermomolecular pressure gradient that drives the interfacial liquid from high to low temperatures, and hence the particle migrates from low to high temperatures in a process called *thermal regelation* [44–48]. Thermal regelation of inert particles plays a major role in the redistribution of material inside of ice, which has important environmental and composite materials implications [44–48]. Moreover, surface properties are central to the fact that extremophile organisms in Earth's cryosphere–glaciers, sea ice and permafrost–develop strategies to persist in challenging environments. Indeed, many biological organisms secrete exopolymeric substance (EPS) [49] or harness antifreeze glycoproteins (AFP) [50, 51] to maintain interfacial liquidity. For example, sea ice houses an array of algae and bacteria, some of which produce EPS to protect them at low temperature and high salinity [52, 53]. Additionally, the enhanced liquidity associated with high concentrations of EPS alters the physical properties of sea ice and thereby play a role in climate change [54, 55].

In bulk solution, active particles act as simple microscopic models for living systems and are particularly accurate at mimicking the propulsion of bacteria or algae [56–60]. By converting energy to motion using biological, chemical, or physical processes, they exhibit rich collective emergent motion from ostensibly simple rules [61, 62]. Algae and bacteria operate in complex geometries and translate environmental conditions into microscopic information that guides their behavior. Examples of such information include quorum sensing (e.g., particle population density), used by bacteria to regulate biofilm formation, defense against competitors and adapt to changing environments [63–65]; chemotaxis (e.g., concentration gradients of nutrients), used by algae/bacteria to direct their motion toward higher concentrations of beneficial, or lower concentrations of toxic, chemicals [66–70]. It is important to emphasize that factors such as surface adhesion, salinity, the segregation of impurities of all types from the ice lattice, among other factors [67, 69, 71, 72], make our treatment of chemotaxis a simplified starting point. However, field samples and laboratory experiments have shown that cell motility is influenced by chemotaxis at low temperature [40, 73, 74]. Thus, although there are many complicated interactions that provide scope for future work, the basic role of chemotaxis in the distribution of biota in ice must start with a self-consistent framework, which is the focus of our work.

The confluence of thermal regelation, bio-enhanced premelting and intrinsic mobility underlie our study. Indeed, intrinsic mobility and chemotaxis may compete with thermal regelation, which constitutes a new area of research–ice bound active particles in premelting ice, as illustrated in **Figure 1**. Moreover, including micro-organism protection mechanisms that enhance interfacial liquidity, such as the secretion of EPS, constitute a unique class of regelation phenomena. Finally, treating this corpus of processes quantitatively is particularly relevant for climatology and the global carbon cycle [75, 76].

Our framework is the active Ornstein-Uhlenbeck particle (AOUP) [77–83]. The active force is governed by an Ornstein-Uhlenbeck process with magnitude $\tilde{D}_a$, which is the active diffusivity. This force can be compared to a colored noise process [79, 84]. In addition to the active diffusivity, the AOUP is characterized by a time τ_a, which defines the noise persistence, from which the system switches from a ballistic to a diffusive regime. The active diffusivity $\tilde{D}_a$ and characteristic time τ_a can be measured experimentally [85–87]. The AOUP has been shown to provide accurate predictions for a range of complex phenomena [78, 80, 81, 88], and is theoretically advantageous due to its Gaussian nature [79]. These issues motivate our use of the AOUP model framework to describe the motion of active particles in ice under an external temperature gradient with a nutrient source. We analyze these particles in three dimensions using a multiple scale expansion to derive the associated Fokker-Planck equation.

The paper is organized as follows. In order to make our treatment reasonably self-contained we note that we are generalizing our previous approach [48, 89], which we recover in the appropriate limit. Thus, in §2 we introduce the active Ornstein-Uhlenbeck model for bio-premelted particles and in §3 we derive the associated Fokker-Planck equation using a multiple scale expansion. We then compare our analytic and numerical solutions after which, in §4, we draw conclusions.

METHODS

Thermal regelation is understood as a consequence of the premelted film around a particle, originally treated as *inert*, that 1) executes diffusive motion in the ice column with diffusivity $\tilde{D}(\tilde{z})\mathbb{I}$, where $\mathbb{I}$ is the identity matrix, and 2) experiences a drift velocity $\tilde{v}(\tilde{z}) = U(\tilde{z})\hat{\tilde{z}}$ parallel to the temperature gradient [48]. Therefore, regelation biases the motion of an *active particle* by the drift velocity $U(\tilde{z})\hat{\tilde{z}}$.

For inert particles with a sufficiently large number of moles of electrolyte impurities per unit area of surface, N_i, the premelted film thickness $d \propto N_i$ [48, 90]. However, the production of EPS/AFP enhances liquidity at the ice surface by increasing the impurity concentration [9, 54, 72, 91], which we treat here using an enhancement factor as $N = nN_i$, which gives

$$d = \frac{R_g T_m^2 \, N}{\rho_l q_m \Delta T}, \tag{1}$$

where the universal gas constant is R_g, the latent heat of fusion per mole of the solid is q_m, the molar density of the liquid is ρ_l, the undercooling is $\Delta T = T_m - T$ with $T_m = 273.15$K the pure bulk melting temperature and T the temperature of ice.

The velocity and premelting-controlled diffusivity are given by

$$U(\tilde{z}) = -\frac{A_3}{A_2^3}\frac{1}{\tilde{z}^3} \qquad \text{and} \tag{2}$$

$$\tilde{D}(\tilde{z}) = \frac{\left(R_g T_m N\right)^3}{8\pi\nu R^4 A_2^3}\frac{k_B T_m}{\tilde{z}^3}, \tag{3}$$

respectively, where $A_2 = \rho_l q_m \frac{|\nabla T|}{T_m}$ and $A_3 = \rho_s q_m |\nabla T| \frac{(R_g T_m N)^3}{6\nu R T_m}$, with $|\nabla T|$ the external temperature gradient. The viscosity of the fluid is ν, the particle radius is R and k_B is the Boltzmann constant. Here, $\rho_s q_m \sim 334 \times 10^6$ J m^{-3} [48]. The evolution of the particle position $\tilde{\boldsymbol{r}} = (\tilde{r}_1, \tilde{r}_2, \tilde{r}_3) = (\tilde{x}, \tilde{y}, \tilde{z})$ and its activity are described by two overdamped Langevin equations.

$$\frac{d}{d\tilde{t}}\tilde{\boldsymbol{r}}(\tilde{t}) = \beta_D \nabla_{\tilde{r}} \tilde{C}(\tilde{\boldsymbol{r}}, \tilde{t}) + \sqrt{2\tilde{D}_a}\tilde{\boldsymbol{\eta}} + \tilde{v}(\tilde{z}) + \sqrt{2\tilde{D}(\tilde{z})}\boldsymbol{\xi}_p(\tilde{t}) \qquad \text{and} \tag{4}$$

$$\frac{d}{d\tilde{t}}\tilde{\boldsymbol{\eta}}(\tilde{t}) = -\frac{1}{\tau_a}\tilde{\boldsymbol{\eta}}(\tilde{t}) + \frac{1}{\tau_a}\boldsymbol{\xi}_a(\tilde{t}). \tag{5}$$

The first term on the right-hand side of **Eq. 4** treats the chemotaxis response, representing the effect of the nutrient source of concentration $\tilde{C}$ on the particle dynamics, where β_D is the chemotactic strength [92–95], which we treat as a constant determined by the parameters in our system. We note, however, that the transport properties of sea- and glacial-ice depend on their unique phase fraction evolution [96–99], which would clearly influence the effective–porosity dependent β_D. In the ideal case, wherein the nutrient source is isotropic and purely diffusive, we have

$$\frac{\partial}{\partial\tilde{t}}\tilde{C}(\tilde{\boldsymbol{r}}, \tilde{t}) = \tilde{D}_{ch}\nabla_{\tilde{r}}^2 \tilde{C}(\tilde{\boldsymbol{r}}, \tilde{t}), \tag{6}$$

where $\tilde{D}_{ch}$ is the nutrient diffusivity. The activity, or self-propulsion, is given by the term $\sqrt{2\tilde{D}_a}\tilde{\boldsymbol{\eta}}$ in **Eq. 4**, with $\tilde{D}_a$ the active diffusivity. The latter represents the active fluctuations of the system, such as those originating in particular processes described in Refs. [100–103]. Nutrient sources, such as dissolved silica, oxygen, nitrogen and methane, play a vital role in the life of ice-bound micro-organisms, such as algae and bacteria [104–109]. Here we assume that $\tilde{D}_{ch} > \tilde{D}_a$, consistent with [110–112], and $\tilde{D}_{ch} > \tilde{D}(\tilde{z})$. The function $\tilde{\boldsymbol{\eta}} = (\tilde{\eta}_1, \tilde{\eta}_2, \tilde{\eta}_3)$ is described by an Ornstein-Uhlenbeck process, with correlations given by

$$\langle \tilde{\eta}_i(\tilde{t}')\tilde{\eta}_j(\tilde{t})\rangle = \frac{\delta_{ij}}{2\tau_a} e^{-\frac{|\tilde{t}'-\tilde{t}|}{\tau_a}}, \tag{7}$$

where τ_a is the noise persistence as noted above. In the small τ_a limit, $\tilde{\boldsymbol{\eta}}$ reduces to Gaussian white noise with correlations $\langle \tilde{\eta}_i(t')\tilde{\eta}_j(t)\rangle = \delta_{ij}\delta(\tilde{t}' - \tilde{t})$. In contrast, $\tilde{\boldsymbol{\eta}}$ does not reduce to Gaussian white noise when τ_a is finite, and **Eq. 4** does not reach equilibrium. Hence, τ_a controls the non-equilibrium properties of the dynamics [79, 80]. Finally, the random fluctuations in **Eqs 4**, **5** are given by zero mean Gaussian white noise processes $\langle \xi_{p_i}(\tilde{t}')\xi_{p_j}(\tilde{t})\rangle = \delta_{ij}\delta(\tilde{t}' - \tilde{t})$ and $\langle \xi_{a_i}(\tilde{t}')\xi_{a_j}(\tilde{t})\rangle = \delta_{ij}\delta(\tilde{t}' - \tilde{t})$.

The Langevin **Eqs 4**, **5**, allow us to express the probability of finding a particle at the position $\tilde{\boldsymbol{r}} = (\tilde{r}_1, \tilde{r}_2, \tilde{r}_3) = (\tilde{x}, \tilde{y}, \tilde{z})$ at a given time $\tilde{t}$ through the Fokker-Planck equation, which describes the evolution of the probability density function $P(\tilde{\boldsymbol{r}}, \tilde{\boldsymbol{\eta}}, \tilde{t} | \tilde{\boldsymbol{r}}_0, \tilde{\boldsymbol{\eta}}_0, \tilde{t}_0)$, with the initial condition $P(\tilde{\boldsymbol{r}}, \tilde{\boldsymbol{\eta}}, \tilde{t} = \tilde{t}_0 | \tilde{\boldsymbol{r}}_0, \tilde{\boldsymbol{\eta}}_0, \tilde{t}_0) = \delta(\tilde{\boldsymbol{r}} - \tilde{\boldsymbol{r}}_0)\delta(\tilde{\boldsymbol{\eta}} - \tilde{\boldsymbol{\eta}}_0)$. To simplify the notation, we write the conditional probability as

$P(\tilde{\boldsymbol{r}},\tilde{\boldsymbol{\eta}},\tilde{t}|\tilde{\boldsymbol{r}}_0,\tilde{\boldsymbol{\eta}}_0,\tilde{t}_0) \equiv P(\tilde{\boldsymbol{r}},\tilde{\boldsymbol{\eta}},\tilde{t})$ and eventually arrive at the following system of coupled equations

$$\begin{aligned}\frac{\partial}{\partial \tilde{t}}P(\tilde{\boldsymbol{r}},\tilde{\boldsymbol{\eta}},\tilde{t}) = -\beta_D\nabla_{\tilde{\boldsymbol{r}}}\cdot\left[P(\tilde{\boldsymbol{r}},\tilde{\boldsymbol{\eta}},\tilde{t})\nabla_{\tilde{\boldsymbol{r}}}\tilde{\mathcal{C}}(\tilde{\boldsymbol{r}},\tilde{t})\right] \\ -\frac{\partial}{\partial \tilde{r}_3}\left[\tilde{v}(\tilde{r}_3)P(\tilde{\boldsymbol{r}},\tilde{\boldsymbol{\eta}},\tilde{t})\right] - \sqrt{2\tilde{D}_a}\tilde{\boldsymbol{\eta}}\cdot\nabla_{\tilde{\boldsymbol{r}}}P(\tilde{\boldsymbol{r}},\tilde{\boldsymbol{\eta}},\tilde{t}) \\ +\nabla^2_{\tilde{\boldsymbol{r}}}\left[\tilde{D}(\tilde{r}_3)P(\tilde{\boldsymbol{r}},\tilde{\boldsymbol{\eta}},\tilde{t})\right] \\ +\frac{1}{\tau_a}\nabla_{\tilde{\boldsymbol{\eta}}}\cdot\left[\tilde{\boldsymbol{\eta}}P(\tilde{\boldsymbol{r}},\tilde{\boldsymbol{\eta}},\tilde{t})\right] + \frac{1}{2\tau_a^2}\nabla^2_{\tilde{\boldsymbol{\eta}}}P(\tilde{\boldsymbol{r}},\tilde{\boldsymbol{\eta}},\tilde{t}) \quad \text{and}\end{aligned} \tag{8}$$

$$\frac{\partial}{\partial \tilde{t}}\tilde{\mathcal{C}}(\tilde{\boldsymbol{r}},\tilde{t}) = \tilde{D}_{ch}\nabla^2_{\tilde{\boldsymbol{r}}}\tilde{\mathcal{C}}(\tilde{\boldsymbol{r}},\tilde{t}). \tag{9}$$

Equations 8, **9** describe the space-time evolution of the probability of finding a particle and the concentration of nutrients respectively, akin to those of [77, 79, 94], but including the effects of thermal regelation discussed above. Both equations contain microscopic and macroscopic scales. The regime of interest is the long time behavior, computed by deriving the effective macroscopic dynamics as described next.

RESULTS

Method of Multiple Scales

The macroscopic length characterizing the heat flux is

$$L = \frac{T_m}{|\nabla T|}. \tag{10}$$

The particle scale l is such that $l \ll L$, and hence their ratio defines a small parameter ϵ

$$\epsilon = \frac{l}{L}. \tag{11}$$

We use the microscopic length l and a characteristic time τ, determined *a posteriori*, and introduce the following dimensionless variables

$$\boldsymbol{\eta} = \sqrt{\tau_a}\tilde{\boldsymbol{\eta}}, \boldsymbol{r} = \frac{\tilde{\boldsymbol{r}}}{l}, t = \frac{\tilde{t}}{\tau}, v = \frac{\tilde{v}}{u}, v_a = \frac{\tilde{v}_a}{v_{ac}}, D = \frac{\tilde{D}}{D_c}, \\ D_{ch} = \frac{\tilde{D}_{ch}}{D_n} \text{ and } \mathcal{C} = \frac{\tilde{\mathcal{C}}}{c_h}, \tag{12}$$

where $\tilde{v}_a = \sqrt{\frac{2\tilde{D}_a}{\tau_a}}$ [113, 114], v_{ac} is the characteristic active velocity, u and D_c are the characteristic values of the regelation velocity and the premelting enhanced diffusivity respectively, and D_n and c_h are the characteristic values of the diffusivity and nutrient concentration respectively. With these scalings, **Eqs 8**, **9**, become

$$\begin{aligned}P_l\frac{\partial}{\partial t}P = -\beta_D\frac{c_h}{D_c}\nabla_{\boldsymbol{r}}\cdot[P\nabla_{\boldsymbol{r}}\mathcal{C}] - P_e\frac{\partial}{\partial r_3}[vP] - P_a v_a\boldsymbol{\eta}\cdot\nabla_{\boldsymbol{r}}P \\ +\nabla^2_{\boldsymbol{r}}[DP] + P_A\nabla_{\boldsymbol{\eta}}\cdot[\boldsymbol{\eta}P] + \frac{1}{2}P_A\nabla^2_{\boldsymbol{\eta}}P\end{aligned} \tag{13}$$

and (14)

$$P_{ch}\frac{\partial}{\partial t}\mathcal{C} = D_{ch}\nabla^2_{r}\mathcal{C}, \tag{15}$$

in which we have the following dimensionless numbers,

$$P_e = \frac{ul}{D_c}, P_a = \frac{v_{ac}l}{D_c}, P_l = \frac{l^2}{D_c\tau}, P_A = \frac{l^2}{D_c\tau_a} \text{ and } P_{ch} = \frac{l^2}{D_n\tau}. \tag{16}$$

We identify four characteristic time scales: $t_l^{\text{diff}} = l^2/D_c$, $t_l^{\text{adv}} = l/u$, $t_L^{\text{diff}} = L^2/D_c$ and $t_L^{\text{adv}} = L/u$, associated with "microscopic" diffusion and advection on the particle scale, l, and "macroscopic" diffusion and advection over the thermal length scale, L. Nutrient and premelting enhanced diffusivity are taken to operate on the same time scale; $t_{l,L}^{\text{diff}_n} \sim t_{l,L}^{\text{diff}}$. The Péclet number represents the ratio of the characteristic time for diffusion to that of advection, and those associated with regelation and activity are P_e and P_a respectively, and can be defined over both length scales,

$$P_e = \frac{t_l^{\text{diff}}}{t_l^{\text{adv}}} \quad \text{and} \quad P_e^L = \frac{t_L^{\text{diff}}}{t_L^{\text{adv}}}. \tag{17}$$

The temperature gradient across the entire system drives thermal regelation and hence advection dominates on the macroscopic scale, so that $P_e^L = \mathcal{O}(1/\epsilon)$, or equivalently, $t_L^{\text{adv}} = \epsilon t_L^{\text{diff}} \sim \epsilon t_L^{\text{diff}_n}$. Whence, $P_e = \mathcal{O}(1)$, or equivalently, $t_l^{\text{adv}} = t_l^{\text{diff}} \sim t_l^{\text{diff}_n}$. On the macroscopic scale P_e^L becomes large, as ϵ tends to zero, and thus we use the macroscopic advection time $\tau = t_L^{adv}$ as our characteristic time, so that Péclet numbers based on L are $\mathcal{O}(1/\epsilon)$ and those based on l are $\mathcal{O}(\epsilon)$. In consequence, **Eqs 13**, **15** become leading to $P_L = \mathcal{O}(1/\epsilon)$ and $P_l = \mathcal{O}(\epsilon)$, as well as $P_L^{ch} = \mathcal{O}(1/\epsilon)$ and $P_l^{ch} = \mathcal{O}(\epsilon)$. The system of Fokker-Planck equations, **Eqs 13–15**, becomes

$$\begin{aligned}\epsilon\frac{\partial}{\partial t}P = -\beta_D\frac{c_h}{D_c}\nabla_{\boldsymbol{r}}\cdot[P\nabla_{\boldsymbol{r}}c] - \frac{\partial}{\partial r_3}[vP] - P_a v_a\boldsymbol{\eta}\cdot\nabla_{\boldsymbol{r}}P \\ +\nabla^2_{\boldsymbol{r}}[DP] + P_A\nabla_{\boldsymbol{\eta}}\cdot[\boldsymbol{\eta}P] + \frac{1}{2}P_A\nabla^2_{\boldsymbol{\eta}}P \quad \text{and}\end{aligned} \tag{18}$$

$$\epsilon\frac{\partial}{\partial t}\mathcal{C} = D_{ch}\nabla^2_{\boldsymbol{r}}\mathcal{C}. \tag{19}$$

Now, we let $\boldsymbol{R} = \tilde{\boldsymbol{r}}/L$ describe the macroscopic length scale, and $T = \tilde{t}/t_l^{adv}$ describe the microscopic time scale, leading to the following stretching of the microscopic scales;

$$\boldsymbol{r} = \frac{1}{\epsilon}\boldsymbol{R} \quad \text{and} \quad T = \frac{1}{\epsilon}t. \tag{20}$$

Next, we use a power series ansatz for the state variables,

$$P = P^0 + \epsilon P^1 + \epsilon^2 P^2 + \text{h.o.t.} \quad \text{and} \tag{21}$$

$$\mathcal{C} = \mathcal{C}^0 + \epsilon\mathcal{C}^1 + \epsilon^2\mathcal{C} + \text{h.o.t.}, \tag{22}$$

to derive a system of equations at each order in ϵ [115], which for the concentration of nutrients, **Eq. 19**, are

$$\mathcal{O}(\epsilon^0)\colon D_{ch}\nabla^2_{\boldsymbol{r}}\mathcal{C}^0 = 0, \tag{23}$$

$$\mathcal{O}(\epsilon^1)\colon D_{ch}\nabla^2_{\boldsymbol{r}}\mathcal{C}^1 = \frac{\partial}{\partial T}\mathcal{C}^0 - 2D_{ch}\nabla_{\boldsymbol{r}}\cdot\nabla_{\boldsymbol{R}}\mathcal{C}^0 \quad \text{and} \tag{24}$$

$$\mathcal{O}(\epsilon^2)\colon\ D_{ch}\nabla_r^2 C^2 = \frac{\partial}{\partial T}C^1 + \frac{\partial}{\partial t}C^0 - 2D_{ch}\nabla_{\boldsymbol{r}}\cdot\nabla_{\boldsymbol{R}}C^1 - D_{ch}\nabla_{\boldsymbol{R}}^2 C^0, \tag{25}$$

shown to second order. We take the approach described in [116, 117] to solve **Eqs 23–25**. We integrate by parts over the microscale variables $\boldsymbol{r}$ and use the periodic boundary conditions to obtain the so-called weak formulation [118] of the leading order **Eq. 23**, the solution of which relies on the following product ansatz

$$C^0(\boldsymbol{r},\boldsymbol{R},T,t) = \zeta(\boldsymbol{r})c^0(\boldsymbol{R},T,t). \tag{26}$$

The existence and uniqueness of C^0 is ensured using the Lax-Milgram theorem [118], also known as the solvability condition or the Fredholm alternative [116]. Thus, C^0 is constant over $C^0(\boldsymbol{r},\boldsymbol{R},T,t) = C^0(\boldsymbol{R},T,t)$. The solvability condition for the equation at $\mathcal{O}(\epsilon)$ is

$$\int d\boldsymbol{r}\left(\zeta\frac{\partial}{\partial T}c^0\right) = 0, \tag{27}$$

from which we find that c^0 is stationary over T, leading to $C^0(\boldsymbol{R},T,t) = C^0(\boldsymbol{R},t)$ and $C^1(\boldsymbol{R},T,t) = C^1(\boldsymbol{R},t)$. Substituting C^1 into the $\mathcal{O}(\epsilon^2)$ **Eq. 25** and using the solvability condition, gives nutrient diffusion on the macroscale as

$$\frac{\partial}{\partial t}c^0 = D_{ch}\nabla_{\boldsymbol{R}}^2 c^0, \tag{28}$$

showing that, as expected, the homogenization procedure is consistent with the well-known self-similar behavior of diffusion [119]. The order by order equations for the probability density function described by **Eq. 18** are simplified by the observation that C^0 and C^1 do not depend on $\boldsymbol{r}$, and C^0 only contributes at order $\mathcal{O}(\epsilon^2)$, and hence we obtain

$$\mathcal{O}(\epsilon^0)\colon\ \mathcal{L}P^0 = 0, \tag{29}$$

$$\begin{aligned}\mathcal{O}(\epsilon^1)\colon\ \mathcal{L}P^1 = {}& \frac{\partial}{\partial T}P^0 + \beta_D\frac{c_h}{D_c}\nabla_{\boldsymbol{r}}\cdot\left[P^0\nabla_{\boldsymbol{R}}C^0\right] + \frac{\partial}{\partial R_3}\left[\nu P^0\right] + P_a v_a\boldsymbol{\eta}\cdot\nabla_{\boldsymbol{R}}P^0\\ & -2\nabla_{\boldsymbol{r}}\cdot\nabla_{\boldsymbol{R}}\left[DP^0\right], \qquad \text{and}\end{aligned} \tag{30}$$

$$\begin{aligned}\mathcal{O}(\epsilon^2)\colon\ \mathcal{L}P^2 = {}& \frac{\partial}{\partial T}P^1 + \frac{\partial}{\partial t}P^0 + \beta_D\frac{c_h}{D_c}\left\{\nabla_{\boldsymbol{r}}\cdot\left[P^1\nabla_{\boldsymbol{R}}C^1\right] + \nabla_{\boldsymbol{r}}\cdot\left[P^0\nabla_{\boldsymbol{R}}C^0\right] + \nabla_{\boldsymbol{R}}\cdot\left[P^0\nabla_{\boldsymbol{R}}C^0\right]\right\}\\ & + \frac{\partial}{\partial R_3}\left[\nu P^1\right] + P_a v_a\boldsymbol{\eta}\cdot\nabla_{\boldsymbol{R}}P^1 - 2\nabla_{\boldsymbol{r}}\cdot\nabla_{\boldsymbol{R}}\left[DP^1\right] - \nabla_{\boldsymbol{R}}^2\left[DP^0\right],\end{aligned} \tag{31}$$

where $\mathcal{L} = \mathcal{M} + \mathcal{Q}$, with $\mathcal{M} = -\frac{\partial}{\partial r_3}\nu - P_a v_a\boldsymbol{\eta}\cdot\nabla_{\boldsymbol{r}} + \nabla_{\boldsymbol{r}}^2 D$, and $\mathcal{Q} = P_A\nabla_{\boldsymbol{\eta}}\cdot\boldsymbol{\eta} + \frac{P_A}{2}\nabla_{\boldsymbol{\eta}}^2$.

Finally, as shown in **Supplementary Material Section S1**, upon substitution of P^1 into **Eq. 31** and using the solvability condition, we obtain the effective macroscopic dynamics as

$$\frac{\partial}{\partial\tilde{t}}\rho = -\beta_D\nabla_{\tilde{\boldsymbol{r}}}\cdot\left[\rho\nabla_{\tilde{\boldsymbol{r}}}\tilde{c}\right] - \frac{\partial}{\partial\tilde{z}}\left[\tilde{\nu}\rho\right] + \nabla_{\tilde{\boldsymbol{r}}}^2\left[\left(\tilde{D}_a + \tilde{D}\right)\rho\right] \qquad \text{and} \tag{32}$$

$$\frac{\partial}{\partial\tilde{t}}\tilde{c} = \tilde{D}_{ch}\nabla_{\tilde{\boldsymbol{r}}}^2\tilde{c}, \tag{33}$$

which are the dimensional forms of **Eqs 31**, **28** respectively. These capture the long time behavior wherein the active force is treated through the effective diffusivity, which is enhanced by thermal regelation, consistent with our previous work [89] and that in active matter systems generally [57, 78, 85].

Equations 32, **33** can be mapped onto the well-known Keller–Segel equations for chemotaxis [93–95, 120], where ρ is the cell density and the sign of β_D determines whether a cell is attracted or repelled by the nutrient. Finally, when nutrients are neglected, $\beta_D = 0$, we recover our previous results [48, 89].Although **Eq. 32** has an analytical solution in the large Péclet number limit, which previously allowed us to study the effect of the activity ([48, 89] or **Supplementary Material Section S2**), here we fix the activity and focus on the competition between thermal regelation and bio-locomotion that require solving **Eqs 32**, **33** numerically. We show dimensional results because of our specific interest in these processes in ice.

In the absence of nutrients, $\beta_D = 0$, **Figure 2** shows how the distribution of bio-particles parallel to the temperature gradient (the $\tilde{z}$-axis) is influenced by EPS/AFP production, which is modeled as a surface colligative effect. Namely, with $N_i = 50\mu\text{M m}^{-2}$ and four biological enhancement factors $n \in \{1, 2, 3, 4\}$. The active diffusivity is $\tilde{D}_a = 100\tilde{D}$ and the particle radius is $R = 9.0, \times, 10^{-6}$ m.

Figure 3 shows the evolution of the nutrient concentration along the $\tilde{z}$-axis computed from **Eq. 33**, at $\tilde{x} = \tilde{y} = 0$. The nutrients are centered at $\tilde{z}_0 = 55$m at $\tilde{t} = 0$ and we use a nutrient diffusivity of $\tilde{D}_{ch} = 10^{-10}\text{m}^2\text{s}^{-1}$ [121–124].

In order to study the effect of nutrients on bio-locomotion, we fix the interfacial concentration of impurities and vary the chemotaxis strength β_D, where nutrients either attract ($\beta_D > 0$)

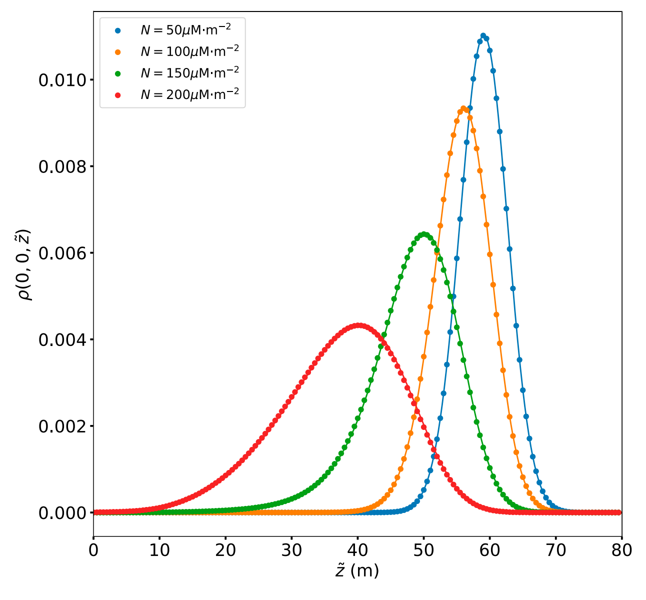

FIGURE 2 | Consequences of bio-enhanced premelting in the absence of nutrients ($\beta_D = 0$). The evolution of the probability density along the $\tilde{z}$-axis, computed from **Eq. 32** with $N_i = 50\mu\text{M m}^{-2}$ and four biological enhancement factors $n \in \{1, 2, 3, 4\}$, where $N = nN_i$. The probability density is shown at $\tilde{x} = \tilde{y} = 0$ and at time $\tilde{t} = 300$ years. The analytic solution (solid lines), (see **Supplementary Material Section S2**), is compared with the numerical solution (dots) of **Eq. 32**. The particle radius is $R = 9.0, \times, 10^{-6}$ m.

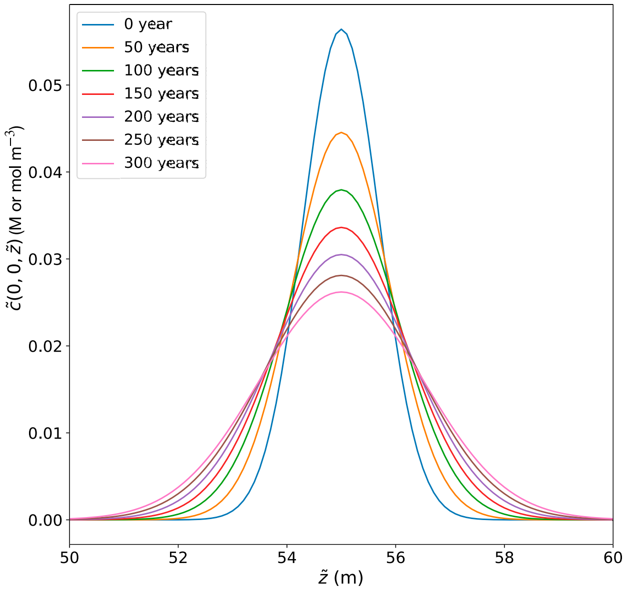

FIGURE 3 | Evolution of the nutrient concentration (in units of M, or mol m^{-3}) along the $\tilde z$-axis, computed from **Eq. 33**, at $\tilde x = \tilde y = 0$. At $\tilde t = 0$, the nutrient concentration is centered at $\tilde z_0 = 55$m and the nutrient diffusivity is $\tilde D_{ch} = 10^{-10}$m^{2}s^{-1}.

or repel ($\beta_D < 0$) the bio-particles. Because we are interested in the situation wherein the effects of chemotaxis compete with regelation, this constrains the magnitude of β_D as follows. We ask for what order of magnitude of β_D are the typical chemotactic speeds approximately the same as the regelation velocity in **Eq. 4**.

Figure 3 shows the Gaussian solution of the concentration field, with a flux that becomes arbitrarily small at long times, dominated by the algebraic contribution to $\nabla_{\tilde{\mathbf{r}}}\tilde C(\tilde{\mathbf{r}}, \tilde t) \propto x t^{-3/2} \exp(-\frac{x^2}{t}) \sim x t^{-3/2}$. For the parameters studied here, the regelation speeds are $10^{-12} - 10^{-10}$m s^{-1} [48, 89], and hence we capture this same range in $\beta_D \nabla_{\tilde{\mathbf{r}}}\tilde C(\tilde{\mathbf{r}}, \tilde t)$, with $|\beta_D| = 10^{-10}$ m^{2}M^{-1}s^{-1}, which is realized across a large time span wherein $\nabla_{\tilde{\mathbf{r}}}\tilde C(\tilde{\mathbf{r}}, \tilde t)$ varies by several orders of magnitude. This is also reflected in the dimensionless ratio $\beta_D\frac{c_h}{D_c}$ in **Eq. 13**. Namely, for micron to nm scale premelted films surrounding micron sized particles D_c ranges from about $10^{-14} - 10^{-13}$ m^{2}s^{-1}, and the nutrient concentration over relevant time scales has mean values ranging over $10^{-3} - 10^{-2}$ M. Therefore, $\beta_D\frac{c_h}{D_c}$ ranges from 1 to 100 and hence chemotaxis is on a similar footing to regelation under these circumstances. For all cases considered here we use $\beta_D = \pm 10^{-10}$ m^{2}M^{-1}s^{-1} for attractive/repulsive chemotaxis.

For attractive chemotaxis ($\beta_D > 0$), we show in **Figure 4A** the dependence of $\rho(\tilde{\mathbf{r}}, \tilde t)$ along the $\tilde z$-axis parallel to the temperature gradient and at $\tilde x = \tilde y = 0$, with the concentration of nutrients centered at $\tilde z = 55$m. For the same conditions in the absence of chemotaxis, the net displacement from low to high temperatures due to regelation is approximately 10 m [89]. We see here the chemo-attractive modulation of $\rho(\tilde{\mathbf{r}}, \tilde t)$ during this displacement, which "pulls up" the high temperature (low $\tilde z$) tail towards the lower temperature (large $\tilde z$) but higher concentration regions centered at $\tilde z = 55$m. The associated asymmetry depletes/attracts the low temperature regions at larger $\tilde z$ and concentrates the high temperature regions at smaller $\tilde z$, and is reflected in the evolution towards a sigmoidal region transecting the source at $\tilde z = 55$m. As the maximum of $\rho(\tilde{\mathbf{r}}, \tilde t)$ advects through the source region it first sharpens, due to the chemo-attraction from the source "behind" it

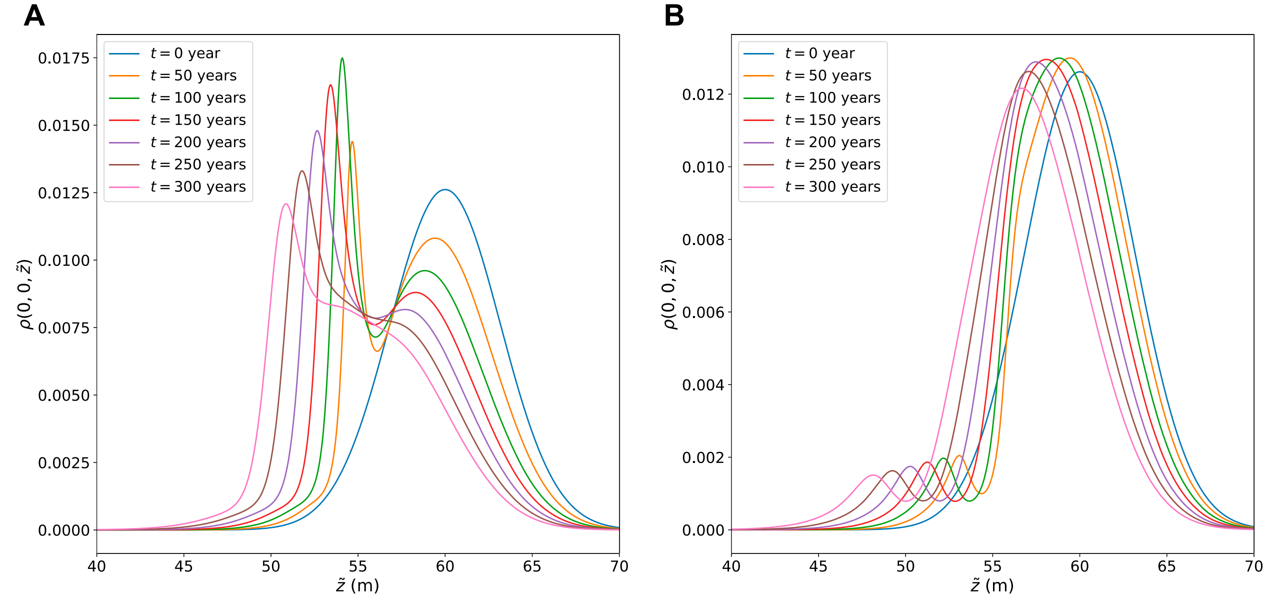

FIGURE 4 | Effect of nutrients on the particle dynamics. Evolution of the probability density function along the $\tilde z$-axis, at $\tilde x = \tilde y = 0$, for two values of the chemotaxis strength β_D **(A)** $\beta_D = 10^{-10}$ m^{2}M^{-1}s$^{-1} > 0$ (attractive) and **(B)** $\beta_D = -10^{-10}$ m^{2}M^{-1}s$^{-1} < 0$ (repulsive). At $\tilde t = 0$ the distribution is centered at $\tilde z_0 = 60$m. The solution of **Eq. 32** is computed using a finite difference method. The particle radius is $R = 10^{-6}$ m, the concentration of impurities is $N = 100\mu$M m^{-2}, the temperature gradient is $|\nabla T| = 0.1$K m^{-1} and the active diffusivity is $\tilde D_a = 100\tilde D$.

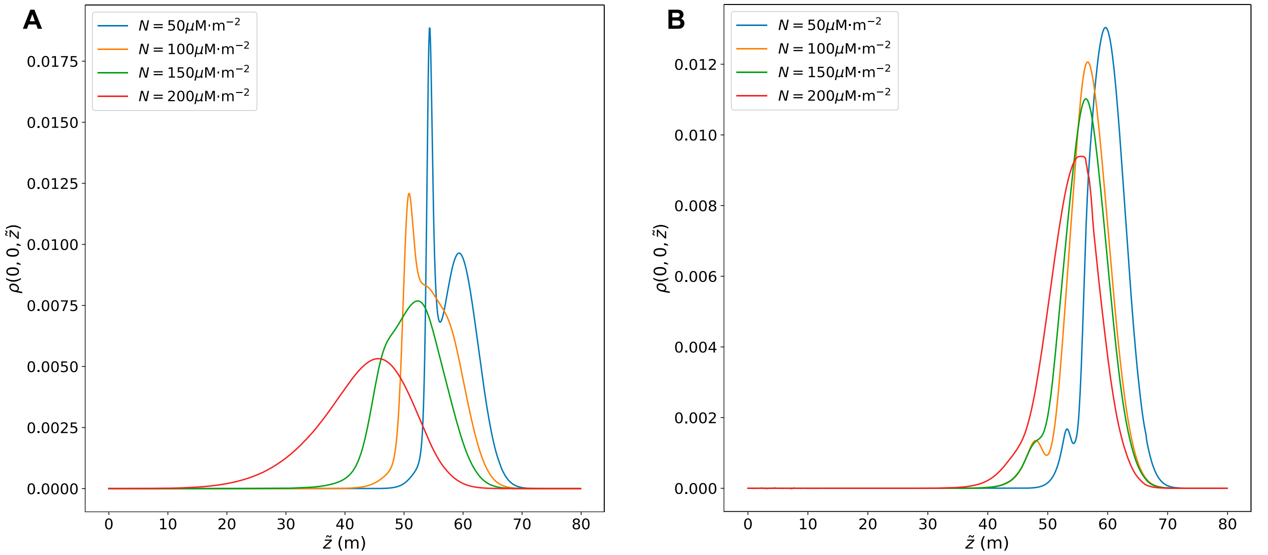

FIGURE 5 | The combined effects of the surface concentration of impurities and nutrients. The probability density function along the $\tilde{z}$-axis, at $\tilde{x} = \tilde{y} = 0$ and at $\tilde{t} = 300$years, for **(A)** attractive ($\beta_D = 10^{-10}$ m^{2}M^{-1}s^{-1}) and **(B)** repulsive ($\beta_D = -10^{-10}$ m^{2}M^{-1}s^{-1}) chemotaxis, for different surface concentration of impurities N, computed from **Eqs 32**, **33** using a finite difference method. The particle radius is $R = 10^{-6}$ m, the temperature gradient is $|\nabla T| = 0.1$K m^{-1} and the active diffusivity is $\tilde{D}_a = 100\tilde{D}$. The nutrient source is centered at $\tilde{z} = 55$ m.

at $\tilde{z} = 55$m, and then begins to spread out again because of the decay in the chemotactic gradient in time as seen in **Figure 3** and discussed above.

For repulsive chemotaxis ($\beta_D < 0$), we see in **Figure 4B** the broad sharpening of the initial distribution in the lower temperature (large $\tilde{z}$) regions as it regelates/advects into the diffuse repulsive tail of nutrient field to the right of the source region centered at $\tilde{z} = 55$m. However, because the initial high temperature (small $\tilde{z}$) tail of $\rho(\tilde{\boldsymbol{r}}, \tilde{t})$ interacts with the nutrient source region at $\tilde{z} = 55$m, chemo-repulsion quickly drives particles towards high temperature (small $\tilde{z}$) regions, and is clearly reflected in the creation of a local maximum. This maximum advects towards high temperature with a decaying amplitude and width due to the decay in the chemotactic gradient in time as seen in **Figure 3**.

In **Figure 5**, we show the combined effects of EPS/AFP surface enhancement of impurities in the absence of chemotaxis ($\beta_D = 0$), as shown in **Figure 2**, and the influence of chemotaxis on particle dynamics for fixed surface impurities, as shown in **Figure 4**. As we vary the surface concentration of impurities we observe the same basic features as described in **Figures 2**, **4** and hence the same physical description applies in their interpretation. Namely, regardless of whether chemo-attraction or chemo-repulsion is operative, if the interfacial concentration of impurities N is sufficiently large then the interfacial film thicknesses are sufficiently thick that thermal regelation dominates the evolution of $\rho(\tilde{\boldsymbol{r}}, \tilde{t})$. As the interfacial concentration of impurities N decreases chemotaxis exerts more control on the distribution, and the basic dynamics are the same as described in **Figure 4**. Because the magnitude of β_D is fixed, and the characteristic concentration c_h is 10^{-2} M, this N-dependence is simply assessed as discussed above, in terms of the dimensionless ratio $\beta_D \frac{c_h}{D_c}$ in **Eq. 13**. Namely, the numerator is fixed, but as N increases so too is the film thickness d through **Eq. 1**, and since $D_c \propto d^3$ [47], then $\beta_D \frac{c_h}{D_c}$ decreases as N^{-3}, and the balance between chemotaxis control of the distribution gives way to regelation control. The corpus of effects studied here are reflected in this basic balance and shown in **Figures 2**, **4**, **5**.

CONCLUSION

Micro-organisms in ice exhibit complex processes to persist and evolve in their harsh environments. They have developed different survival strategies, such as producing exopolymeric substances or antifreeze glycoproteins, and directing their motion toward nutrients or away from waste [34, 69, 125, 126]. We have modeled such micro-organisms using active Ornstein-Uhlenbeck particles subject to thermal regelation and biolocomotion in three dimensions. Firstly, we used a multi-scale expansion to derive the relevant coupled Fokker-Planck and diffusion **Eqs 32**, **33**. Secondly, when nutrients are neglected, and the chemotactic strength $\beta_D = 0$, we model the bio-production of surface chemicals, such as exopolymeric substances or antifreeze glycoproteins, as a surface colligative effect, and find that the associated bio-enhanced thermal regelation can dominate the distribution of particles in ice. Consistent with previous results [89], in a large Péclet number limit analytical solutions for the particle distributions are possible, and are consistent with the numerical solutions as shown in **Figure 2**. Thirdly, we studied the competition between thermal regelation and biolocomotion, as function of the chemotaxis strength β_D, the interplay between which is shown in **Figures 4**, **5**. The relative importance of chemo-attraction and chemo-repulsion to thermal regelation is captured by the dimensionless ratio $\beta_D \frac{c_h}{D_c}$. When this ratio is large we find a complex modulation of regelation by chemotaxis, and when small, due to increased surface impurity concentration, leads to regelation dominated redistribution of particles. We note, however, that we have not treated the process wherein nutrients themselves have a colligative effect, which would introduce a particularly complex spatio-temporal dynamics.

Finally, we describe settings to which our analysis is applicable. It is of general interest to understand how particles in ice migrate in response to environmental forcing, as they are used as proxy to infer past climate [14, 127, 128]. Moreover, bioparticles in ice migrate in response to environmental forcing, and microorganisms play an important role in climate change [129–131]. For example, an increase in temperature activates algae/bacteria trapped in ice, producing chemicals that increase their mobility [131]. Indeed, an increase in algae/bacteria decreases the albedo of the ice [132–134], thereby enhancing melting. Finally, understanding the distribution and viability of bioparticles in partially frozen media on Earth [135, 136] is essential in astrobiology [41, 42, 137].

DATA AVAILABILITY STATEMENT

The original contribution presented in the study are included in the article/**Supplementary Material**, further inquiries can be directed to the authors.

AUTHOR CONTRIBUTIONS

JW conceived the project. JV implemented the theory and performed simulations. JW and JV interpreted the data and wrote the paper. All authors contributed to the discussions and the final version of the manuscript.

FUNDING

This work was supported by the Swedish Research Council grant no. 638-2013-9243. Nordita is partially supported by Nordforsk.

ACKNOWLEDGMENTS

We thank Matthias Geilhufe, Navaneeth Marath and István Mátá Szécsényi for helpful conversations.

SUPPLEMENTARY MATERIAL

The Supplementary Material for this article can be found online at: https://www.frontiersin.org/articles/10.3389/fphy.2022.904836/full#supplementary-material

REFERENCES

1. Karl DM, Bird DF, Björkman K, Houlihan T, Shackelford R, Tupas L. Microorganisms in the Accreted Ice of Lake Vostok, Antarctica. *Science* (1999) 286:2144–7. doi:10.1126/science.286.5447.2144
2. Christner BC, Mosley-Thompson E, Thompson LG, Reeve JN. Isolation of Bacteria and 16s rDNAs from Lake Vostok Accretion Ice. *Environ Microbiol* (2001) 3:570–7. doi:10.1046/j.1462-2920.2001.00226.x
3. Anesio AM, Mindl B, Laybourn-Parry J, Hodson AJ, Sattler B. Viral Dynamics in Cryoconite Holes on a High Arctic Glacier (Svalbard). *J Geophys Res Biogeo* (2007) 112:1–10. doi:10.1029/2006jg000350
4. Bellas CM, Anesio AM, Barker G. Analysis of Virus Genomes from Glacial Environments Reveals Novel Virus Groups with Unusual Host Interactions. *Front Microbiol* (2015) 6:656. doi:10.3389/fmicb.2015.00656
5. Heilmann S, Sneppen K, Krishna S. Coexistence of Phage and Bacteria on the Boundary of Self-Organized Refuges. *Proc Natl Acad Sci U.S.A* (2012) 109:12828–33. doi:10.1073/pnas.1200771109
6. Zhong ZP, Tian F, Roux S, Gazitúa MC, Solonenko NE, Li YF, et al.Glacier Ice Archives Nearly 15,000-Year-Old Microbes and Phages. *Microbiome* (2021) 9:160–23. doi:10.1186/s40168-021-01106-w
7. Yau S, Lauro FM, DeMaere MZ, Brown MV, Thomas T, Raftery MJ, et al.Virophage Control of Antarctic Algal Host-Virus Dynamics. *Proc Natl Acad Sci U.S.A* (2011) 108:6163–8. doi:10.1073/pnas.1018221108
8. Doyle SM, Christner BC. Variation in Bacterial Composition, Diversity, and Activity Across Different Subglacial Basal Ice Types. *The Cryosphere Discussions* (2022) 2022:1–29. doi:10.5194/tc-2022-68
9. Anesio AM, Lutz S, Chrismas NAM, Benning LG. The Microbiome of Glaciers and Ice Sheets. *NPJ Biofilms Microbiomes* (2017) 3:10–1. doi:10.1038/s41522-017-0019-0
10. Royer A, De Angelis M, Petit JRA. A 30000 Year Record of Physical and Optical Properties of Microparticles from an East Antarctic Ice Core and Implications for Paleoclimate Reconstruction Models. *Climatic Change* (1983) 5:381–412. doi:10.1007/BF00140802
11. Legrand M, Mayewski P. Glaciochemistry of Polar Ice Cores: A Review. *Rev Geophys* (1997) 35:219–43. doi:10.1029/96rg03527
12. Stauffer B, Flückiger J, Wolff E, Barnes P. The EPICA Deep Ice Cores: First Results and Perspectives. *Ann Glaciol* (2004) 39:93–100. doi:10.3189/172756404781814500
13. Alley RB. Reliability of Ice-Core Science: Historical Insights. *J Glaciol* (2010) 56:1095–103. doi:10.3189/002214311796406130
14. Thomas C, Ionescu D, Ariztegui D, Team DS. Impact of Paleoclimate on the Distribution of Microbial Communities in the Subsurface Sediment of the Dead Sea. *Geobiology* (2015) 13:546–61. doi:10.1111/gbi.12151
15. Tetzner D, Thomas ER, Allen CS, Wolff EW. A Refined Method to Analyze Insoluble Particulate Matter in Ice Cores, and its Application to Diatom Sampling in the Antarctic Peninsula. *Front Earth Sci* (2021) 9:20. doi:10.3389/feart.2021.617043
16. Papina T, Blyakharchuk T, Eichler A, Malygina N, Mitrofanova E, Schwikowski M. Biological Proxies Recorded in a Belukha Ice Core, Russian Altai. *Clim Past* (2013) 9:2399–411. doi:10.5194/cp-9-2399-2013
17. Mao G, Ji M, Xu B, Liu Y, Jiao N. Variation of High (HNA) and Low (LNA) Nucleic Acid-Content Bacteria in Tibetan Ice Cores and Their Relationship to Black Carbon. *Front Microbiol* (2022) 299. doi:10.3389/fmicb.2022.844432
18. Achberger AM, Brox TI, Skidmore ML, Christner BC. Expression and Partial Characterization of an Ice Binding Protein from a Bacterium Isolated at a Depth of 3,519 Meters in the Vostok Ice Core, Antarctica. *Front Microbiol* (2011) 2:255. doi:10.3389/fmicb.2011.00255
19. Knowlton C, Veerapaneni R, D'Elia T, Rogers S. Microbial Analyses of Ancient Ice Core Sections from Greenland and Antarctica. *Biology* (2013) 2:206–32. doi:10.3390/biology2010206
20. Garcia-Lopez E, Moreno A, Bartolomé M, Leunda M, Sancho C, Cid C. Glacial Ice Age Shapes Microbiome Composition in a Receding Southern European Glacier. *Front Microbiol* (2021) 12:714537. doi:10.3389/fmicb.2021.714537
21. Wilhelm L, Singer GA, Fasching C, Battin TJ, Besemer K. Microbial Biodiversity in Glacier-Fed Streams. *ISME J* (2013) 7:1651–60. doi:10.1038/ismej.2013.44

22. Garcia-Lopez E, Moreno A, Bartolomé M, Leunda Esnaola M, Sancho C, Cid C. Glacial Ice Age Shapes Microbiome Composition in a Receding Southern European Glacier. *Front Mar Sci* (2021) 12. doi:10.3389/fmicb.2021.714537
23. Stibal M, Schostag M, Cameron KA, Hansen LH, Chandler DM, Wadham JL, et al. Different Bulk and Active Bacterial Communities in Cryoconite from the Margin and interior of the Greenland Ice Sheet. *Environ Microbiol Rep* (2015) 7:293–300. doi:10.1111/1758-2229.12246
24. Hop H, Vihtakari M, Bluhm BA, Assmy P, Poulin M, Gradinger R, et al. Changes in Sea-Ice Protist Diversity with Declining Sea Ice in the Arctic Ocean from the 1980s to 2010s. *Front Mar Sci* (2020) 7:243. doi:10.3389/fmars.2020.00243
25. Kauko HM, Olsen LM, Duarte P, Peeken I, Granskog MA, Johnsen G, et al. Algal Colonization of Young Arctic Sea Ice in spring. *Front Mar Sci* (2018) 5:199. doi:10.3389/fmars.2018.00199
26. Spilling K, Olli K, Lehtoranta J, Kremp A, Tedesco L, Tamelander T, et al.Shifting Diatom-Dinoflagellate Dominance during Spring Bloom in the Baltic Sea and its Potential Effects on Biogeochemical Cycling. *Front Mar Sci* (2018) 5:327. doi:10.3389/fmars.2018.00327
27. Itcus C, Pascu MD, Lavin P, Perşoiu A, Iancu L, Purcarea C. Bacterial and Archaeal Community Structures in Perennial Cave Ice. *Sci Rep* (2018) 8:15671–14. doi:10.1038/s41598-018-34106-2
28. Miyata M, Robinson RC, Uyeda TQP, Fukumori Y, Fukushima Si., Haruta S, et al. Tree of Motility - A Proposed History of Motility Systems in the Tree of Life. *Genes Cells* (2020) 25:6–21. doi:10.1111/gtc.12737
29. Hahnke RL, Meier-Kolthoff JP, García-López M, Mukherjee S, Huntemann M, Ivanova NN, et al. Genome-based Taxonomic Classification of Bacteroidetes. *Front Microbiol* (2016) 7:2003. doi:10.3389/fmicb.2016.02003
30. Hill NA, Häder D-P. A Biased Random Walk Model for the Trajectories of Swimming Micro-organisms. *J Theor Biol* (1997) 186:503–26. doi:10.1006/jtbi.1997.0421
31. Tsagkari E, Sloan W. The Role of the Motility of Methylobacterium in Bacterial Interactions in Drinking Water. *Water* (2018) 10:1386. doi:10.3390/w10101386
32. Doerges L, Kutschera U. Assembly and Loss of the Polar Flagellum in Plant-Associated Methylobacteria. *Naturwissenschaften* (2014) 101:339–46. doi:10.1007/s00114-014-1162-6
33. Svensson F, Norberg J, Snoeijs P. Diatom Cell Size, Coloniality and Motility: Trade-Offs between Temperature, Salinity and Nutrient Supply with Climate Change. *PloS One* (2014) 9:e109993. doi:10.1371/journal.pone.0109993
34. Aumack CF, Juhl AR, Krembs C. Diatom Vertical Migration within Land-Fast Arctic Sea Ice. *J Mar Syst* (2014) 139:496–504. doi:10.1016/j.jmarsys.2014.08.013
35. Christner B, Mosley-Thompson E, Thompson LG, Zagorodnov V, Sandman K, Reeve JN. Recovery and Identification of Viable Bacteria Immured in Glacial Ice. *Icarus* (2000) 144:479–85. doi:10.1006/icar.1999.6288
36. Biswas RK, Choudhury AK. Diatoms: Miniscule Biological Entities with Immense Importance in Synthesis of Targeted Novel Bioparticles and Biomonitoring. *J Biosci* (2021) 46:1–14. doi:10.1007/s12038-021-00222-x
37. Dong H, Jiang H, Yu B, Liu X, Zhang C, Chan M. Impacts of Environmental Change and Human Activity on Microbial Ecosystems on the Tibetan Plateau, NW China. *GSAT* (2010) 20:4–10. doi:10.1130/gsatg75a.1
38. Delgado-Baquerizo M, Bissett A, Eldridge DJ, Maestre FT, He J-Z, Wang J-T, et al.Palaeoclimate Explains a Unique Proportion of the Global Variation in Soil Bacterial Communities. *Nat Ecol Evol* (2017) 1:1339–47. doi:10.1038/s41559-017-0259-7
39. Benningfield D. The Bumpy Search for Liquid Water at the South Pole of Mars. *EOS* (2022) 103:1–6. doi:10.1029/2022EO220126
40. Lindensmith CA, Rider S, Bedrossian M, Wallace JK, Serabyn E, Showalter GM, et al. A Submersible, off-axis Holographic Microscope for Detection of Microbial Motility and Morphology in Aqueous and Icy Environments. *PloS one* (2016) 11:e0147700. doi:10.1371/journal.pone.0147700
41. Nadeau J, Lindensmith C, Deming JW, Fernandez VI, Stocker R. Microbial Morphology and Motility as Biosignatures for Outer Planet Missions. *Astrobiology* (2016) 16:755–74. doi:10.1089/ast.2015.1376
42. Jones RM, Goordial JM, Orcutt BN. Low Energy Subsurface Environments as Extraterrestrial Analogs. *Front Microbiol* (2018) 9:1605. doi:10.3389/fmicb.2018.01605
43. Schreder-Gomes SI, Benison KC, Bernau JA. 830-million-year-old Microorganisms in Primary Fluid Inclusions in Halite. *Geology* (2022). (in press). doi:10.1130/G49957.1
44. Dash JG, Rempel AW, Wettlaufer JS. The Physics of Premelted Ice and its Geophysical Consequences. *Rev Mod Phys* (2006) 78:695. doi:10.1103/RevModPhys.78.695
45. Rempel AW, Wettlaufer JS, Worster MG. Interfacial Premelting and the Thermomolecular Force: Thermodynamic Buoyancy. *Phys Rev Lett* (2001) 87:088501. doi:10.1103/PhysRevLett.87.088501
46. Wettlaufer JS, Worster MG. Premelting Dynamics. *Annu Rev Fluid Mech* (2006) 38:427–52. doi:10.1146/annurev.fluid.37.061903.175758
47. Peppin SSL, Spannuth MJ, Wettlaufer JS. Onsager Reciprocity in Premelting Solids. *J Stat Phys* (2009) 134:701–8. doi:10.1007/s10955-009-9699-z
48. Marath NK, Wettlaufer JS. Impurity Effects in thermal Regelation. *Soft Matter* (2020) 16:5886–91. doi:10.1039/d0sm00558d
49. Wingender J, Neu TR, Flemming H-C. What Are Bacterial Extracellular Polymeric Substances? In: *Microbial Extracellular Polymeric Substances*. Berlin, Heidelberg: Springer (1999). p. 1–19. doi:10.1007/978-3-642-60147-7_1
50. Bang JK, Lee JH, Murugan RN, Lee SG, Do H, Koh HY, et al. Antifreeze Peptides and Glycopeptides, and Their Derivatives: Potential Uses in Biotechnology. *Mar Drugs* (2013) 11:2013–41. doi:10.3390/md11062013
51. Eskandari A, Leow TC, Rahman MBA, Oslan SN. Antifreeze Proteins and Their Practical Utilization in Industry, Medicine, and Agriculture. *Biomolecules* (2020) 10:1649. doi:10.3390/biom10121649
52. Ewert M, Deming JW. Bacterial Responses to Fluctuations and Extremes in Temperature and Brine Salinity at the Surface of Arctic winter Sea Ice. *FEMS Microbiol Ecol* (2014) 89:476–89. doi:10.1111/1574-6941.12363
53. Ewert M, Deming JW. Sea Ice Microorganisms: Environmental Constraints and Extracellular Responses. *Biology (Basel)* (2013) 2:603–28. doi:10.3390/biology2020603
54. Krembs C, Eicken H, Deming JW. Exopolymer Alteration of Physical Properties of Sea Ice and Implications for Ice Habitability and Biogeochemistry in a Warmer Arctic. *Proc Natl Acad Sci U.S.A* (2011) 108:3653–8. doi:10.1073/pnas.1100701108
55. Decho AW, Gutierrez T. Microbial Extracellular Polymeric Substances (EPSs) in Ocean Systems. *Front Microbiol* (2017) 8:922. doi:10.3389/fmicb.2017.00922
56. Cates ME. Diffusive Transport without Detailed Balance in Motile Bacteria: Does Microbiology Need Statistical Physics? *Rep Prog Phys* (2012) 75:042601. doi:10.1088/0034-4885/75/4/042601
57. Bechinger C, Di Leonardo R, Löwen H, Reichhardt C, Volpe G, Volpe G. Active Particles in Complex and Crowded Environments. *Rev Mod Phys* (2016) 88:045006. doi:10.1103/revmodphys.88.045006
58. Ghosh A, Fischer P. Controlled Propulsion of Artificial Magnetic Nanostructured Propellers. *Nano Lett* (2009) 9:2243–5. doi:10.1021/nl900186w
59. Kim S, Qiu F, Kim S, Ghanbari A, Moon C, Zhang L, et al.Fabrication and Characterization of Magnetic Microrobots for Three-Dimensional Cell Culture and Targeted Transportation. *Adv Mater* (2013) 25:5863–8. doi:10.1002/adma.201301484
60. Jin C, Vachier J, Bandyopadhyay S, Macharashvili T, Maass CC. Fine Balance of Chemotactic and Hydrodynamic Torques: When Microswimmers Orbit a Pillar Just once. *Phys Rev E* (2019) 100:040601. doi:10.1103/PhysRevE.100.040601
61. Elgeti J, Winkler RG, Gompper G. Physics of Microswimmers-Single Particle Motion and Collective Behavior: A Review. *Rep Prog Phys* (2015) 78:056601. doi:10.1088/0034-4885/78/5/056601
62. Romanczuk P, Bär M, Ebeling W, Lindner B, Schimansky-Geier L. Active Brownian Particles. *Eur Phys J Spec Top* (2012) 202:1–162. doi:10.1140/epjst/e2012-01529-y
63. Li Y-H, Tian X. Quorum sensing and Bacterial Social Interactions in Biofilms. *Sensors* (2012) 12:2519–38. doi:10.3390/s120302519

64. Yan S, Wu G. Can Biofilm Be Reversed through Quorum Sensing in *Pseudomonas aeruginosa*? *Front Microbiol* (2019) 10:1582. doi:10.3389/fmicb.2019.01582
65. Lee CK, Vachier J, de Anda J, Zhao K, Baker AE, Bennett RR, et al. Social Cooperativity of Bacteria during Reversible Surface Attachment in Young Biofilms: A Quantitative Comparison of *Pseudomonas aeruginosa* PA14 and PAO1. *MBio* (2020) 11:e02644–19. doi:10.1128/mBio.02644-19
66. Wadhams GH, Armitage JP. Making Sense of it All: Bacterial Chemotaxis. *Nat Rev Mol Cel Biol* (2004) 5:1024–37. doi:10.1038/nrm1524
67. Showalter GM, Deming JW. Low-temperature Chemotaxis, Halotaxis and Chemohalotaxis by the Psychrophilic marine Bacterium Colwellia Psychrerythraea 34h. *Environ Microbiol Rep* (2018) 10:92–101. doi:10.1111/1758-2229.12610
68. Cremer J, Honda T, Tang Y, Wong-Ng J, Vergassola M, Hwa T. Chemotaxis as a Navigation Strategy to Boost Range Expansion. *Nature* (2019) 575: 658–63. doi:10.1038/s41586-019-1733-y
69. Bar Dolev M, Bernheim R, Guo S, Davies PL, Braslavsky I. Putting Life on Ice: Bacteria that Bind to Frozen Water. *J R Soc Interf* (2016) 13:20160210. doi:10.1098/rsif.2016.0210
70. Mattingly H, Kamino K, Machta B, Emonet T. *Escherichia coli* Chemotaxis is Information Limited. *Nat Phys* (2021) 17:1–6. doi:10.1038/s41567-021-01380-3
71. Bar-Dolev M, Celik Y, Wettlaufer JS, Davies PL, Braslavsky I. New Insights into Ice Growth and Melting Modifications by Antifreeze Proteins. *J R Soc Interf* (2012) 9:3249–59. doi:10.1098/rsif.2012.0388
72. Hansen-Goos H, Thomson ES, Wettlaufer JS. On the Edge of Habitability and the Extremes of Liquidity. *Planet Space Sci* (2014) 98:169–81. doi:10.1016/j.pss.2013.04.010
73. Junge K, Eicken H, Deming JW. Motility of Colwellia Psychrerythraea Strain 34H at Subzero Temperatures. *Appl Environ Microbiol* (2003) 69:4282–4. doi:10.1128/aem.69.7.4282-4284.2003
74. Mudge MC, Nunn BL, Firth E, Ewert M, Hales K, Fondrie WE, et al. Subzero, saline Incubations of Colwellia Psychrerythraea Reveal Strategies and Biomarkers for Sustained Life in Extreme Icy Environments. *Environ Microbiol* (2021) 23:3840–66. doi:10.1111/1462-2920.15485
75. Wadham JL, Hawkings JR, Tarasov L, Gregoire LJ, Spencer RGM, Gutjahr M, et al. Ice Sheets Matter for the Global Carbon Cycle. *Nat Commun* (2019) 10: 3567–17. doi:10.1038/s41467-019-11394-4
76. Holland AT, Williamson CJ, Sgouridis F, Tedstone AJ, McCutcheon J, Cook JM, et al. Dissolved Organic Nutrients Dominate Melting Surface Ice of the Dark Zone (Greenland Ice Sheet). *Biogeosciences* (2019) 16:3283–96. doi:10.5194/bg-16-3283-2019
77. Fodor É, Nardini C, Cates ME, Tailleur J, Visco P, van Wijland F. How Far from Equilibrium is Active Matter? *Phys Rev Lett* (2016) 117:038103. doi:10.1103/PhysRevLett.117.038103
78. Caprini L, Marini Bettolo Marconi U. Active Particles under Confinement and Effective Force Generation Among Surfaces. *Soft Matter* (2018) 14: 9044–54. doi:10.1039/c8sm01840e
79. Martin D, O'Byrne J, Cates ME, Fodor É, Nardini C, Tailleur J, et al. Statistical Mechanics of Active Ornstein-Uhlenbeck Particles. *Phys Rev E* (2021) 103: 032607. doi:10.1103/PhysRevE.103.032607
80. Dabelow L, Eichhorn R. Irreversibility in Active Matter: General Framework for Active Ornstein-Uhlenbeck Particles. *Front Phys* (2021) 8:516. doi:10.3389/fphy.2020.582992
81. Caprini L, Marini Bettolo Marconi U, Puglisi A. Activity Induced Delocalization and Freezing in Self-Propelled Systems. *Sci Rep* (2019) 9: 1386–9. doi:10.1038/s41598-018-36824-z
82. Bonilla LL. Active Ornstein-Uhlenbeck Particles. *Phys Rev E* (2019) 100: 022601. doi:10.1103/PhysRevE.100.022601
83. Dabelow L, Bo S, Eichhorn R. Irreversibility in Active Matter Systems: Fluctuation Theorem and Mutual Information. *Phys Rev X* (2019) 9: 021009. doi:10.1103/physrevx.9.021009
84. Sevilla FJ, Rodríguez RF, Gomez-Solano JR. Generalized Ornstein-Uhlenbeck Model for Active Motion. *Phys Rev E* (2019) 100:032123. doi:10.1103/PhysRevE.100.032123
85. Maggi C, Paoluzzi M, Pellicciotta N, Lepore A, Angelani L, Di Leonardo R. Generalized Energy Equipartition in Harmonic Oscillators Driven by Active Baths. *Phys Rev Lett* (2014) 113:238303. doi:10.1103/physrevlett.113.238303
86. Maggi C, Paoluzzi M, Angelani L, Di Leonardo R. Memory-less Response and Violation of the Fluctuation-Dissipation Theorem in Colloids Suspended in an Active bath. *Sci Rep* (2017) 7:17588–7. doi:10.1038/s41598-017-17900-2
87. Donado F, Moctezuma RE, López-Flores L, Medina-Noyola M, Arauz-Lara JL. Brownian Motion in Non-equilibrium Systems and the Ornstein-Uhlenbeck Stochastic Process. *Sci Rep* (2017) 7:12614–7. doi:10.1038/s41598-017-12737-1
88. Marini Bettolo Marconi U, Maggi C, Melchionna S. Pressure and Surface Tension of an Active Simple Liquid: A Comparison between Kinetic, Mechanical and Free-Energy Based Approaches. *Soft Matter* (2016) 12: 5727–38. doi:10.1039/c6sm00667a
89. Vachier J, Wettlaufer JS. Premelting Controlled Active Matter in Ice. *Phys Rev E* (2022) 105:024601. doi:10.1103/PhysRevE.105.024601
90. Wettlaufer JS. Impurity Effects in the Premelting of Ice. *Phys Rev Lett* (1999) 82:2516–9. doi:10.1103/physrevlett.82.2516
91. Ewert M, Deming J. Sea Ice Microorganisms: Environmental Constraints and Extracellular Responses. *Biology* (2013) 2:603–28. doi:10.3390/biology2020603
92. Keller EF, Segel LA. Model for Chemotaxis. *J Theor Biol* (1971) 30:225–34. doi:10.1016/0022-5193(71)90050-6
93. Saha S, Golestanian R, Ramaswamy S. Clusters, Asters, and Collective Oscillations in Chemotactic Colloids. *Phys Rev E Stat Nonlin Soft Matter Phys* (2014) 89:062316. doi:10.1103/PhysRevE.89.062316
94. Liebchen B, Löwen H. Synthetic Chemotaxis and Collective Behavior in Active Matter. *Acc Chem Res* (2018) 51:2982–90. doi:10.1021/acs.accounts.8b00215
95. Pohl O, Stark H. Dynamic Clustering and Chemotactic Collapse of Self-Phoretic Active Particles. *Phys Rev Lett* (2014) 112:238303. doi:10.1103/physrevlett.112.238303
96. Wettlaufer JS, Worster MG, Huppert HE. Natural Convection during Solidification of an alloy from above with Application to the Evolution of Sea Ice. *J Fluid Mech* (1997) 344:291–316. doi:10.1017/s0022112097006022
97. Rempel AW, Waddington ED, Wettlaufer JS, Worster MG. Possible Displacement of the Climate Signal in Ancient Ice by Premelting and Anomalous Diffusion. *Nature* (2001) 411:568–71. doi:10.1038/35079043
98. Rempel AW, Wettlaufer JS, Waddington ED. Anomalous Diffusion of Multiple Impurity Species: Predicted Implications for the Ice Core Climate Records. *J Geophys Res Solid Earth* (2002) 107:ECV 3–1–ECV 3–12. doi:10.1029/2002jb001857
99. Wells AJ, Wettlaufer JS, Orszag SA. Maximal Potential Energy Transport: A Variational Principle for Solidification Problems. *Phys Rev Lett* (2010) 105: 254502. doi:10.1103/physrevlett.105.254502
100. Joanny J-F, Jülicher F, Prost J. Motion of an Adhesive Gel in a Swelling Gradient: A Mechanism for Cell Locomotion. *Phys Rev Lett* (2003) 90:168102. doi:10.1103/physrevlett.90.168102
101. Peruani F, Morelli LG. Self-propelled Particles with Fluctuating Speed and Direction of Motion in Two Dimensions. *Phys Rev Lett* (2007) 99:010602. doi:10.1103/PhysRevLett.99.010602
102. Romanczuk P, Schimansky-Geier L. Brownian Motion with Active Fluctuations. *Phys Rev Lett* (2011) 106:230601. doi:10.1103/physrevlett.106.230601
103. Vandebroek H, Vanderzande C. The Effect of Active Fluctuations on the Dynamics of Particles, Motors and DNA-Hairpins. *Soft Matter* (2017) 13: 2181–91. doi:10.1039/c6sm02568d
104. Price PB. A Habitat for Psychrophiles in Deep Antarctic Ice. *Proc Natl Acad Sci U.S.A* (2000) 97:1247–51. doi:10.1073/pnas.97.3.1247
105. Campen RK, Sowers T, Alley RB. Evidence of Microbial Consortia Metabolizing within a Low-Latitude Mountain Glacier. *Geol* (2003) 31: 231–4. doi:10.1130/0091-7613(2003)031<0231:eomcmw>2.0.co;2
106. Tung HC, Price PB, Bramall NE, Vrdoljak G. Microorganisms Metabolizing on clay Grains in 3-Km-Deep Greenland Basal Ice. *Astrobiology* (2006) 6: 69–86. doi:10.1089/ast.2006.6.69
107. Mader HM, Pettitt ME, Wadham JL, Wolff EW, Parkes RJ. Subsurface Ice as a Microbial Habitat. *Geol* (2006) 34:169–72. doi:10.1130/g22096.1
108. Rohde RA, Price PB. Diffusion-controlled Metabolism for Long-Term Survival of Single Isolated Microorganisms Trapped within Ice Crystals.

Proc Natl Acad Sci U.S.A (2007) 104:16592–7. doi:10.1073/pnas.0708183104

109. Vancoppenolle M, Goosse H, De Montety A, Fichefet T, Tremblay B, Tison JL. Modeling Brine and Nutrient Dynamics in Antarctic Sea Ice: The Case of Dissolved Silica. *J Geophys Res Oceans* (2010) 115:1–18. doi:10.1029/2009jc005369
110. Wu M, Roberts JW, Kim S, Koch DL, DeLisa MP. Collective Bacterial Dynamics Revealed Using a Three-Dimensional Population-Scale Defocused Particle Tracking Technique. *Appl Environ Microbiol* (2006) 72:4987–94. doi:10.1128/aem.00158-06
111. Ben Amar M. Collective Chemotaxis and Segregation of Active Bacterial Colonies. *Sci Rep* (2016) 6:21269–9. doi:10.1038/srep21269
112. Wåhlin J, Klein-Paste A. The Effect of Mass Diffusion on the Rate of Chemical Ice Melting Using Aqueous Solutions. *Cold Regions Sci Techn* (2017) 139:11–21. doi:10.1016/j.coldregions.2017.04.001
113. Dabelow L, Bo S, Eichhorn R. How Irreversible Are Steady-State Trajectories of a Trapped Active Particle? *J Stat Mech Theor E.* (2021) 2021:033216. doi:10.1088/1742-5468/abe6fd
114. Caprini L, Marconi UMB, Wittmann R, Löwen H. Dynamics of Active Particles with Space-dependent Swim Velocity. *Soft Matter* (2022) 18: 1412–22. doi:10.1039/d1sm01648b
115. Bender CM, Orszag SA. *Advanced Mathematical Methods for Scientists and Engineers: Asymptotic Methods and Perturbation Theory*. New York, NY: Springer (2013).
116. Pavliotis G, Stuart A. *Multiscale Methods: Averaging and Homogenization*. New York, NY: Springer (2008).
117. Aurell E, Bo S, Dias M, Eichhorn R, Marino R. Diffusion of a Brownian Ellipsoid in a Force Field. *EPL* (2016) 114:30005. doi:10.1209/0295-5075/114/30005
118. Chipot M. Weak Formulation of Elliptic Problems. In: *Elliptic Equations: An Introductory Course*. Basel: Birkhäuser, Basel (2009). p. 35–42. doi:10.1007/978-3-7643-9982-5_3
119. Barenblatt GI. *Scaling, Self-Similarity, and Intermediate Asymptotics*. Cambridge, UK: Cambridge University Press (1996).
120. Liebchen B, Löwen H. Modeling Chemotaxis of Microswimmers: From Individual to Collective Behavior. In: *Chemical Kinetics: Beyond the Textbook*. New Jersey: World Scientific (2020). p. 493–516.
121. Theurkauff I, Cottin-Bizonne C, Palacci J, Ybert C, Bocquet L. Dynamic Clustering in Active Colloidal Suspensions with Chemical Signaling. *Phys Rev Lett* (2012) 108:268303. doi:10.1103/physrevlett.108.268303
122. Jin C, Krüger C, Maass CC. Chemotaxis and Autochemotaxis of Self-Propelling Droplet Swimmers. *Proc Natl Acad Sci U.S.A* (2017) 114: 5089–94. doi:10.1073/pnas.1619783114
123. Salek MM, Carrara F, Fernandez V, Guasto JS, Stocker R. Bacterial Chemotaxis in a Microfluidic T-Maze Reveals strong Phenotypic Heterogeneity in Chemotactic Sensitivity. *Nat Commun* (2019) 10: 1877–11. doi:10.1038/s41467-019-09521-2
124. Hokmabad BV, Agudo-Canalejo J, Saha S, Golestanian R, Maass CC. Chemotactic Self-Caging in Active Emulsions (2022) 119 (24): e2122269119. doi:10.1073/pnas.2122269119
125. Price PB. Microbial Life in Glacial Ice and Implications for a Cold Origin of Life. *FEMS Microbiol Ecol* (2007) 59:217–31. doi:10.1111/j.1574-6941.2006.00234.x
126. Stocker R, Seymour JR. Ecology and Physics of Bacterial Chemotaxis in the Ocean. *Microbiol Mol Biol Rev* (2012) 76:792–812. doi:10.1128/mmbr.00029-12
127. Miteva V. Bacteria in Snow and Glacier Ice. In: *Psychrophiles: From Biodiversity to Biotechnology*. Berlin, Heidelberg: Springer (2008). p. 31–50. doi:10.1007/978-3-540-74335-4_3
128. Han D, Nam SI, Kim JH, Stein R, Niessen F, Joe YJ, et al. Inference on Paleoclimate Change Using Microbial Habitat Preference in Arctic Holocene Sediments. *Sci Rep* (2017) 7:9652–11. doi:10.1038/s41598-017-08757-6
129. Mitchell JG, Kogure K. Bacterial Motility: Links to the Environment and a Driving Force for Microbial Physics. *FEMS Microbiol Ecol* (2006) 55:3–16. doi:10.1111/j.1574-6941.2005.00003.x
130. Dutta H, Dutta A. The Microbial Aspect of Climate Change. *Energ Ecol Environ* (2016) 1:209–32. doi:10.1007/s40974-016-0034-7
131. Cavicchioli R, Ripple WJ, Timmis KN, Azam F, Bakken LR, Baylis M, et al. Scientists' Warning to Humanity: Microorganisms and Climate Change. *Nat Rev Microbiol* (2019) 17:569–86. doi:10.1038/s41579-019-0222-5
132. Ryan JC, Hubbard A, Stibal M, Irvine-Fynn TD, Cook J, Smith LC, et al. Dark Zone of the Greenland Ice Sheet Controlled by Distributed Biologically-Active Impurities. *Nat Commun* (2018) 9:1065–10. doi:10.1038/s41467-018-03353-2
133. Perini L, Gostinčar C, Anesio AM, Williamson C, Tranter M, Gunde-Cimerman N. Darkening of the Greenland Ice Sheet: Fungal Abundance and Diversity Are Associated with Algal Bloom. *Front Microbiol* (2019) 10: 557. doi:10.3389/fmicb.2019.00557
134. Williamson CJ, Cook J, Tedstone A, Yallop M, McCutcheon J, Poniecka E, et al. Algal Photophysiology Drives Darkening and Melt of the Greenland Ice Sheet. *Proc Natl Acad Sci U.S.A* (2020) 117:5694–705. doi:10.1073/pnas.1918412117
135. Van Leeuwe MA, Tedesco L, Arrigo KR, Assmy P, Campbell K, Meiners KM, et al. Microalgal Community Structure and Primary Production in Arctic and Antarctic Sea Ice: A Synthesis. *Element Sci Anthropocene* (2018) 6:1–25. doi:10.1525/elementa.267
136. Cimoli E, Lucieer V, Meiners KM, Chennu A, Castrisios K, Ryan KG, et al. Mapping the *In Situ* Microspatial Distribution of Ice Algal Biomass through Hyperspectral Imaging of Sea-Ice Cores. *Sci Rep* (2020) 10:21848–17. doi:10.1038/s41598-020-79084-6
137. Wettlaufer JS. Sea Ice and Astrobiology. In: D Thomas G Dieckmann, editors. *Sea Ice*. 2nd ed. Oxford: Wiley-Blackwell (2010). p. 579–94. chap. 15.
138. Risken H. Fokker-Planck Equation. In: *The Fokker-Planck Equation*. Berlin, Heidelberg: Springer (1996). p. 63–95. doi:10.1007/978-3-642-61544-3_4
139. Celani A, Vergassola M. Bacterial Strategies for Chemotaxis Response. *Proc Natl Acad Sci U.S.A* (2010) 107:1391–6. doi:10.1073/pnas.0909673107
140. Kheifets S. *Application of the Green's Function Method to Some Nonlinear Problems of an Electron Storage Ring: Part 1, the Green's Function for the Fokker-Planck Equation*. Technical Report. Menlo Park, CA (USA): Stanford Linear Accelerator Center (1982).

Conflict of Interest: The authors declare that the research was conducted in the absence of any commercial or financial relationships that could be construed as a potential conflict of interest.

frontiers | Frontiers in Physics

REVIEW
published: 11 July 2022
doi: 10.3389/fphy.2022.890845

Soft Ionics: Governing Physics and State of Technologies

Max Tepermeister[1], Nikola Bosnjak[1], Jinyue Dai[1], Xinyue Zhang[2], Samuel M. Kielar[2], Zhongtong Wang[1], Zhiting Tian[1], Jin Suntivich[2] and Meredith N. Silberstein[1]*

[1]Sibley School of Mechanical and Aerospace Engineering, Cornell University, Ithaca, NY, United States, [2]Department of Materials Science and Engineering, Cornell University, Ithaca, NY, United States

Soft ionic materials combine charged mobile species and tailored polymer structures in a manner that enables a wide array of functional devices. Traditional metal and silicon electronics are limited to two charge carriers: electrons and holes. Ionic devices hold the promise of using the wide range of chemical and molecular properties of mobile ions and polymer functional groups to enable flexible conductors, chemically specific sensors, biocompatible interfaces, and deformable digital or analog signal processors. Stand alone ionic devices would need to have five key capabilities: signal transmission, energy conversion/harvesting, sensing, actuation, and signal processing. With the great promise of ionically-conducting materials and ionic devices, there are several fields working independently on pieces of the puzzle. These fields range from waste-water treatment research to soft robotics and bio-interface research. In this review, we first present the underlying physical principles that govern the behavior of soft ionic materials and devices. We then discuss the progress that has been made on each of the potential device components, bringing together findings from a range of research fields, and conclude with discussion of opportunities for future research.

Keywords: polyelectrolyte, ionomer, ionotronics, soft robotics, electrochemistry, polymer, circuits

Edited by:
Liheng Cai,
University of Virginia, United States

Reviewed by:
Shaoting Lin,
Massachusetts Institute of Technology, United States
Michael Dickey,
North Carolina State University, United States
Quan Chen,
Changchun Institute of Applied Chemistry (CAS), China

***Correspondence:**
Meredith N. Silberstein
meredith.silberstein@cornell.edu

Specialty section:
This article was submitted to Soft Matter Physics, a section of the journal Frontiers in Physics

Received: *06 March 2022*
Accepted: *29 April 2022*
Published: *11 July 2022*

Citation:
Tepermeister M, Bosnjak N, Dai J, Zhang X, Kielar SM, Wang Z, Tian Z, Suntivich J and Silberstein MN (2022) Soft Ionics: Governing Physics and State of Technologies. Front. Phys. 10:890845. doi: 10.3389/fphy.2022.890845

1 INTRODUCTION

Recent advances in soft ionic materials that incorporate mobile ions within flexible polymer matrices provide alternatives to traditional rigid inorganic materials, allowing devices to be deformable and have good performance [1]. Polymers have extensive tailorability due to the ease of changing their composition and sequence to tune physical/chemical properties. Furthermore, polymer-based materials often have advantages including low cost, ease of fabrication, biocompatibility, and operatability in complex environments [2]. As the palette of multifunctional polymers continues to grow, researchers have begun imagining how they could be used to create an entirely new class of functional devices. The past 100 years have been marked by the dramatic development and proliferation of electronics. However, electrical conductors are generally limited to electrons (and sometimes holes) as their current carrying particles, and are typically rigid. Ionic conductors can take advantage of the wide array of ions. A single wire could carry many ion signals simultaneously, or interact directly with the ionic signalling found throughout nature. Ionic materials promise to usher in a new era of ionic devices that are more biocompatible, biointerfacing, flexible, and low-power than electronics. The developments necessary to realize fully ionic devices are occurring in many fields simultaneously, while the building blocks share similar fundamental science. We aim to bring an ionic device lens to the varied ways that potential ionic device components are discussed, described, conceptualized, and formalized across these different fields (**Figure 1**).

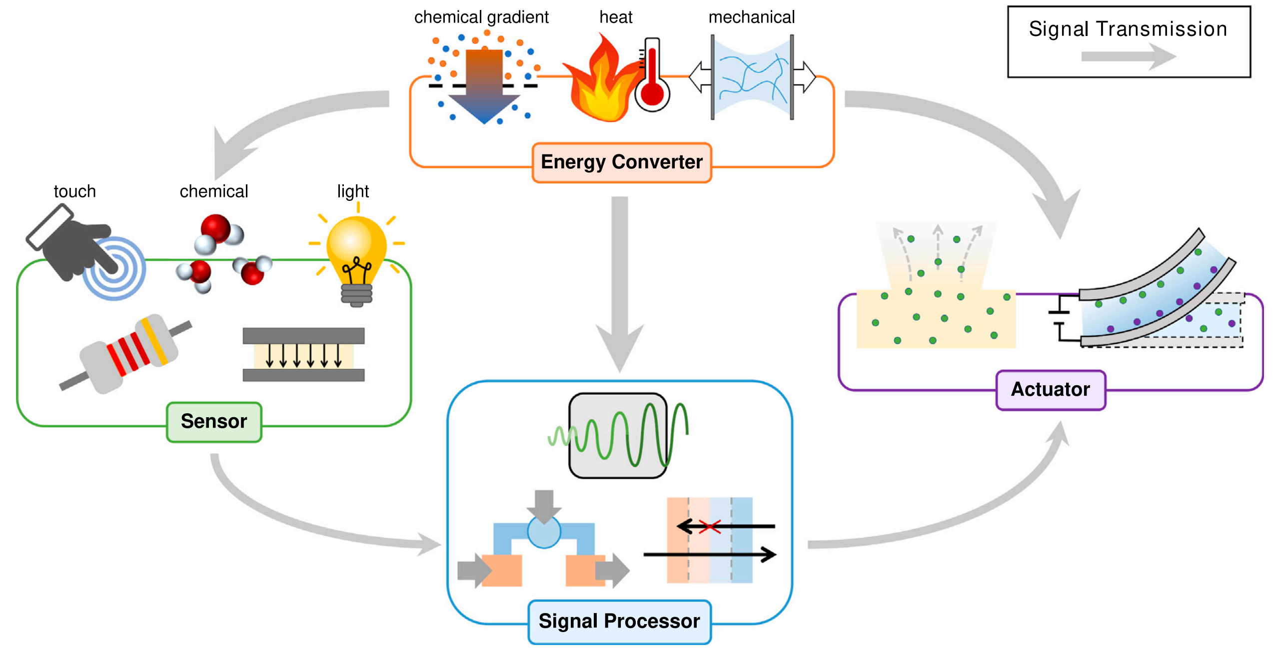

FIGURE 1 | Overview of functions commonly needed for a freestanding ionic device, how they interact with each other, and example ways the device would interact with the external world.

One essential function within a device is to move information from point A to point B. In ionic devices, this information takes the form of electric fields and chemical concentrations. In **Section 3.1**, we discuss the fundamental mechanisms for ion movement, and then talk about how researchers are improving the electrical, mechanical, and chemical properties of these ion signal carriers by tailoring the chemical composition, modifying the processing, and swelling the networks with different solvents and ions.

The next thing an ionic device must usually do is interact with its environment, bringing ion signals into and out of the device. These interactions with inputs and realizations of outputs take the form of sensors and actuators respectively. In **Section 3.2** we discuss the basic mechanisms of mechanical–ion coupling and then detail how researchers have used this coupling to create mechanical sensors and actuators. We then explore how tailored chemical functionalization is able to couple ionic polymers to other aspects of the environment like light, heat, and humidity.

After generating an ionic signal and transmitting it across the device, devices must process the incoming signal. In **Section 3.3** we discuss recent work creating ionic counterparts of electrical components like capacitors and transistors. We also discuss where the unique properties of polymers and ions enable device architectures not possible with traditional electronics, provide a categorization for diodes, and showcase state of the art ionic transistors.

Finally, ionic devices must follow the laws of thermodynamics, and thus moving information around and interacting with the outside world requires energy. There is simultaneously a deep literature on ionic power sources and little focus on powering ionic circuits. In **Section 3.4** we discuss energy storage and conversion technologies we believe are promising for soft ionic devices.

We then conclude with our thoughts on opportunities for future device development and where our understanding of the underlying mechanisms remains both thin and critical.

2 GOVERNING PHYSICS

2.1 Constituent Materials

Ionic devices are built from four main material types: electrical conductors, neutral gels, polyelectrolytes, and dielectric elastomers (see **Figure 2** for polymer naming convention). Each type is used for a variety of purposes, but shares a set of governing physics and common assumptions. For example, conductors can serve as both surface electrodes and internal conductive structures. This section details each material type, typical properties, and assumptions commonly made about each in the context of ionic devices.

2.1.1 Electrical Conductors

Electrical conductors are materials that allow electrons to flow freely inside them. They are able to accept and donate electrons of any energy level. The vast majority of conductors are metals. Some organic conjugated polymers like PEDOT:PSS (poly(3,4-ethylenedioxythiophene) polystyrene sulfonate) can also be conductors. Conductors generally follow Ohm's law, a linear relationship between the electric field across a conductor and the electric current that flows inside it. In physics this is generally written as in **Eq. 1**. Throughout this text, vectors are written with

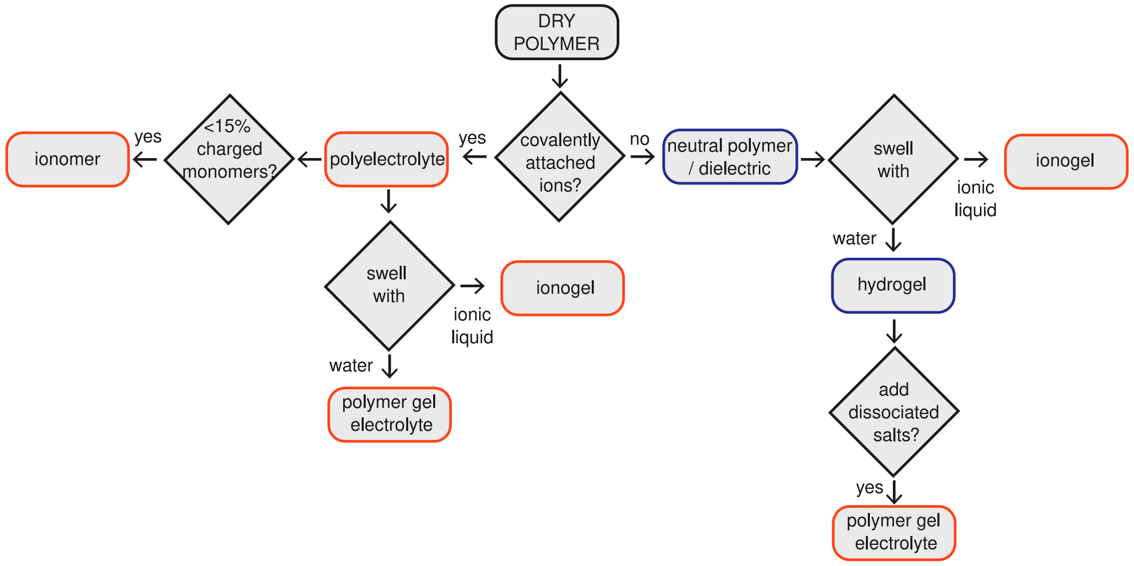

FIGURE 2 | Polymer naming convention used in this paper. Blue outlines indicate that the polymers are not ionically conductive, whereas the orange outlines indicate that the polymers are ionically conductive.

a single underbar and second order tensors are written with a double underbar.

$$\underline{J} = \underline{\underline{\sigma}}\,\underline{E} \tag{1}$$

where $\underline{E}$ is the local electric field, $\underline{J}$ is the current density, and $\underline{\underline{\sigma}}$ is the conductivity tensor. In electrical engineering, components are typically lumped into discrete elements. As such, the local vector fields in physics are replaced with net currents and potentials. The electric field $\underline{E}$ is integrated over the device length and becomes a voltage, V. The current density is integrated over the device area and becomes the total current, I. Finally, the conductivity is assumed isotropic, flattened to one dimension, and inverted to give a resistance, R. Taken together, these replacements give the engineering formulation of Ohm's law:

$$V = IR \tag{2}$$

When electrical conductors are used in ionic devices, their conductivity is typically orders of magnitude higher than the conductance of any other part of the system. This implies that the electric fields within conductors are smaller than in other parts of the system, and thus charge imbalances are only present at the boundaries. Therefore, they can carry large currents without large voltage drops. Electrical conductors in ionic devices are thus often assumed to contain no internal electric field and be at uniform voltage.

The most common use of conductors within ionic devices is as electrodes. These electrodes are often extremely thin films, and are thus assumed not to contribute to the mechanical properties of the device. Electrode design must still take into consideration the expected mechanical deformation of the device so as not to rupture or delaminate.

2.1.2 Neutral Gels

Neutral gels are crosslinked polymers that do not contain ionizable groups and are swollen in solvents. Most neutral gels used in ionic devices contain electrolytes with mobile ionic species. An electrolyte has mobile positive and negative ions. If swollen with water, they are generally referred to as hydrogels; the solvent content once swollen can exceed 99% by volume. If swollen with ionic liquids, they are referred to as ionogels. Ionogels tend to have greater stability and durability in air than hydrogels because they are not subject to water evaporation [3]. Neutral gels generally enable high mobility for a wide range of chemical species, which allows them to form the core of many ionic devices. They are to ions what electrical conductors are to electrons, and often act as ion carrying "wires". They additionally provide mechanical stability.

At smaller degrees of swelling, the porosity, connectivity, and chemical identity of the gel microstructure influence how easily mobile species move through it. They also determine how much and what type of solvent the gel can be swollen with [4]. Additionally, some gels have chemical functionality that allows them to change their properties in response to a stimulus. These stimuli can be light, chemical species, etc. as discussed in **Section 3.2** [5, 6]. The governing equations of gels can be broken up into mechanical, electrical, thermal, and diffusive parts, which can then be coupled together. For example, deformation can affect transport, and electric fields can induce stress.

There is a wealth of literature detailing the modelling of the mechanics of gels [7–9]. For most ionic devices, large-deformation isotropic incompressible elasticity captures the relevant features. This elasticity is typically given by the Neo-Hookean model for small to moderate deformation and the Gent or Arruda-Boyce models if stretches approaching failure are expected [10]. Expressions for the true stress under uniaxial tension for the Neo-Hookean and Gent models are given by **Eqs. 3** and **4** respectively.

$$\Sigma = G\left(\lambda^2 - \frac{1}{\lambda}\right) \tag{3}$$

$$\Sigma = G\frac{\lambda^2 - \lambda^{-1}}{1 - \left(\lambda^2 + 2/\lambda - 3\right)/I_m} \tag{4}$$

where Σ is the true stress in the direction of applied tension, λ is the stretch (ratio of final to initial length) in the direction of applied tension, G is the shear modulus that depends on the solvent content by $G \propto (V_{dry}/V_s)^{1/3}$ where V_s is the swollen gel volume and V_{dry} is the dry gel volume, and I_m is a material property that sets the stretch at which dramatic strain hardening will occur and will generally decrease with increasing solvent content. Most of the modelling complexity in gels for ionic devices comes from the interaction of their electric field, concentrations gradients, and mobile species. Electrochemical relations are covered in **Section 2.2**; mechano-electro-chemical-thermal coupling is discussed as technology relevant in **Section 3**.

Because gels provide the mechanical structure for most ionic devices, it is important that they can survive the stretching and deformation these devices undergo during operation. There has been significant work to improve the toughness and strength of gels. While covering this research in depth is out of scope of this paper, we direct readers to these papers on mechanical durability of hydrogels and ionogels [11–15].

2.1.3 Polyelectrolytes

The defining characteristic of polyelectrolytes is that they are polymers carrying ionizable moieties, which can dissociate in polar solvents, leaving charged groups covalently linked to polymer chains. These charged sites are balanced either by oppositely charged sites also fixed to polymer chains or by mobile charges. Polyelectrolytes with positive fixed charges are known as polycations, whereas polyelectrolytes with negative fixed charges are known as polyanions. Ionomers are a subclass of polyelectrolytes that have less than 15% of the monomers charged and for which these charged sites are typically phase segregated, forming a physical crosslink [16]. This fixed charge leads to one of the key behaviors of polyelectrolytes in ionic devices, which is referred to as Donnan exclusion: polycations tend to exclude mobile cations from their interior and polyanions tend to exclude mobile anions. Donnan exclusion, combined with the electrically insulating properties led to an alternative nomenclature for these materials when used as films: ion exchange membrane (IEM), cation exchange membrane (CEM), and anion exchange membrane (AEM) [17, 18].

Unlike gels, polyelectrolytes do not always contain additional solvent. The polyelectrolyte structure itself is sometimes sufficient for small ionic molecules to diffuse through it. Ionomers in particular tend to have reasonable ionic conductivity with relatively low solvent content because of the channels resulting from their phase segregated morphology [19], and therefore also tend to be stiffer and stronger than a hydrogel. Like gels, the mechanical properties of many polyelectrolytes can be well captured using the Neo-Hookean or Gent models (**Eqs. 3** and **4**). Many ionomers and other lower solvent content polyelectrolytes are compressible and have viscoplasticity as a limit on device range of operation [20, 21].

2.1.4 Dielectric Elastomers

Dielectric elastomers are stretchable polymers that are neither ionically nor electrically conductive and thus lack long range charge mobility. They do have polymer bond dipoles that give rise to a dielectric constant (see **Section 2.2**) and so retain a linear internal electric field. In the context of ionic devices the main properties of interest are shear modulus, bulk modulus, and dielectric permittivity [22, 23].

2.2 Mobile Species Transport

The electrochemical performance of both polyelectrolytes and neutral gels in ionic devices is largely determined by the behavior of their mobile species. While modelling electric fields in materials, we assume that the speed of light is instantaneous compared to the rearrangement timescale of mobile charges. Therefore, we do not consider the propagation delay of electromagnetic fields, and thus use the electrostatic form of Maxwell's equations as given in **Eqs. 5** and **6**. **Equation 5** is the local form of Gauss's law and describes the relationship between the divergence of the electric field and the charge density. **Equation 6** states that the electric field is conservative.

$$\nabla \cdot \underline{E} = \frac{\rho}{\epsilon_0} \tag{5}$$

$$\nabla \times \underline{E} = 0 \tag{6}$$

where ρ is the charge density, ϵ_0 is the permittivity of free space, $\nabla\cdot$ is the divergence and $\nabla\times$ is the curl. **Equations 5** and **6** enable computation of the electric field everywhere given the charge distribution of the device under study. In a polyelectrolyte or gel there are three main forms of charges to be considered. First, there are the mobile charges; these take the form of ions like Na^+ or Cl^-, or mobile electrons. Second, there are the bound and balanced electrons and protons within the solvent or in the polymer chains. Third, there are charges bound within the polymer chains but uncompensated by bound opposite charges. We assume that bound charges quickly and locally rearrange themselves in response to external fields. This rearrangement occurs much faster (on the order of ns) than the ms timescale of many ionic devices, so we assume that these rearrangements happen instantly [24]. They do however affect the electric field within the material. The charge rearrangement gives rise to an additional material dielectric constant, ϵ_r, that represents how much polarization the quasi-neutral polymer chains and solvent undergo. An absolute permittivity, ϵ, is defined according to **Eq. 7**. Typical values for ϵ are approximately 3 for dielectric elastomers, 10 for ionogels, and 80 for hydrogels.

$$\epsilon = \epsilon_0 \epsilon_r \tag{7}$$

Plugging **Eq. 7** back into **Eq. 5** and defining $\rho*$ as the charge density of mobile charges and uncompensated polymer chain charges, we get a modified form of Gauss's law (**Eq. 8**)

$$\nabla \cdot \underline{E} = \frac{\rho^*}{\epsilon} \tag{8}$$

Finally, diffusive relations govern the flux of mobile species, including solvent, through the gel. See Narayan et al. for a detailed derivation [25]. The procedure at a high level is as follows: We define an electrochemical potential energy for each species that describes the energy cost associated with increasing the local concentration of that species. Systems tend to minimize their free energy, and thus tend to minimize their electrochemical potential. Separate species are often assumed to obey ideal solution mixing, where their interactions with other species are identical to their self-interactions. The gradient of this electrochemical potential is taken as a force driving the system to electrochemical equilibrium. An isotropic linear relationship is assumed between the gradient of the electrochemical potential and the flux of a particular mobile species. This process gives the Nernst-Planck equation shown in **Eq. 9** where $\underline{J}^{(i)}$ is the flux, $z^{(i)}$ is the charge number, $C^{(i)}$ is the concentration, F is Faraday's constant, R is the universal gas constant, T is the temperature, and $u^{(i)}$ is the mobility of the i-th species.

$$\underline{J}^{(i)} = -u^{(i)}\left(RT\nabla C^{(i)} + C^{(i)}z^{(i)}F\nabla V\right) \tag{9}$$

Equation 9 describes the behavior of both neutral and charged species. For neutral species, the electric field does not contribute to their electrochemical potential because their charge number, $z^{(i)}$, is zero. For many gels and for the constituent solvent especially, ideal solution mixing is not a good assumption, since the solvent interacts differently with the polymer chains than it does with itself. Additionally, because the gel polymer matrix is able to exert mechanical forces it can exert a pressure on the solvent, which modifies the free energy. Consequently, the governing equations for the solvent are often described separately from the dilute mobile species.

The Nernst-Planck equation (**Eq. 9**) and Gauss's law (**Eq. 8**) lead to some fundamental device behaviors that are the main takeaways from this section. First, for mm scale devices, they ensure quasi-electrical neutrality throughout the vast majority of the device. Any electric dipole must either be limited to a small magnitude or a small length. The characteristic length scale over which electroneutrality is disobeyed is known as the Debye-Hückel length (λ_D).

$$\lambda_D = \sqrt{\frac{\epsilon RT}{2F^2 \sum_i \left((z^{(i)})^2 C_0^{(i)} \right)}} \tag{10}$$

where $C_0^{(i)}$ is the initial concentration in mol m^{-3} of species i. λ_D decreases as concentration increases. For many polymer systems λ_D is on the order of 1–100 nm. These small length scales with large electric fields tend to occur at the polymer boundaries. In fact, the requirement to minimize free energy ensures that large changes in species concentration can only occur at similarly large discontinuities. This happens at boundaries with conductors, free space, other polymers, etc. Second, the current response of a particular region of space to a given electric field strongly depends non-linearly on the concentration of mobile charged species in that region. This second feature is at the core of how many ionic devices amplify, change, and gate signals, and will be discussed in detail in **Section 3.3**. It is important to note that the equations discussed so far all rely on a statistical mechanical mean field assumption. That is, the space considered is large enough to allow the statistical average to dominate.

3 TECHNOLOGIES

In this section, we walk through the different ionic component functions that are commonly needed for independent soft ionic devices: signal transmission, sensing and actuating, signal transmuting (including memory), and energy/power sources.

3.1 Signal Transmission

Movement of mobile ions in response to an external stimuli allows for signal transmission across a soft ionic polymer. AC is a common way to achieve signal transmission through ionic conductors, especially when connected to an external electronic circuit. AC transmission is often preferable to DC because local ion concentration is maintained without concern for boundary conditions. DC transmission requires that ions are able to flow though an entire circuit without the impediment of non-ion-conducting materials and boundaries. Both transmission methods rely on the same ion transport mechanisms in the ionically conductive material (**Figure 3A**). The mechanisms shown in **Figure 3A** are the physics that underpin the magnitude of the ion mobility coefficient discussed in **Eq. 9**. This one coefficient includes combined contributions from each mechanism present in a given polymer.

One standard setup for AC ionic signal transmission is to place an ionically conductive material between two electrodes and apply a sinusoidal electric field. This causes the mobile ions to oscillate between the charged electrodes. Details of the transmission depend on frequency. At low frequencies, an electrical double layer (EDL) at the polymer electrode interface screens the charge by slowly charging and discharging in response to the alternating signal at the electrode surface (**Figure 3B**). The ionic current is out-of-phase with the input signal, observed as a phase angle approaches −90°, and the response of the material is governed by the interfacial properties, i.e., the capacitance of EDL. With an increase in frequency, the ionic signal becomes more in-phase with the applied signal, as the overall bulk properties become more dominant, leading to a resistor-like response, with the phase angle ≈0°. At high enough frequencies, very small time scales are insufficient for the EDL to fully charge/discharge. The rapid charge reorientation within the material leads to a response similar to that of a dielectric capacitor, and the phase angle approaches −90° again. The specific frequencies at which the device undergoes these transitions between in-phase and out-of-phase response are related to the Debye length, ionic mobility, and the distance between electrodes, and can be easily experimentally characterized by impedance spectroscopy so that it can be taken into account in device design.

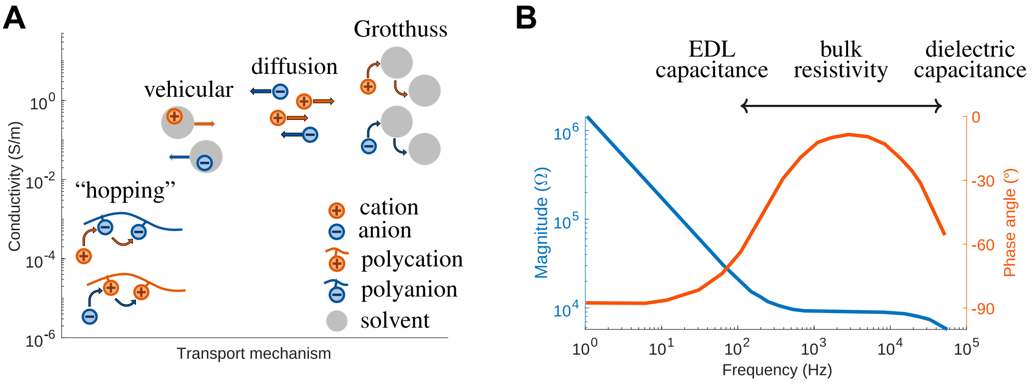

FIGURE 3 | (A) Conductivity achieved by different ion transport mechanisms. **(B)** Typical Bode plot for a polyelectrolyte system, denoting regions where signal transmission is dominated by: EDL capacitance, bulk resistivity, and dielectric capacitance. Experimental data is obtained by impedence spectroscopy on PSS [26].

Polyelectrolytes are candidates for ionic signal transmission because they can achieve relatively high conductivity. In hydrated CEMs, this high conductivity is primarily due to the Grotthuss mechanism—a transport mode involving rapid association and dissociation of protons to neighboring water molecules [27–29] (**Figure 3A**). The Grotthuss mechanism is also found in AEMs, where OH- can be transported in a similar manner [30–32]. Another mechanism, found in hydrated polyelectrolytes, and also in hydrogels and ionogels, is *en masse* or vehicular transport. Here, charges are associated to solvent or water molecules, using them as "vehicles" for transport. Conductivity for this mode of transport is reported to be up to 1 S m^{-1} [33]. In (nearly) dry IEMs, ions are transported by hopping along oppositely charged backbone sites. This results in a significantly lower conductivity. For example, experimental studies showed an increase in conductivity from ~10^{-5} S m^{-1} to ~10^{1} S m^{-1} with an increase in relative humidity for Nafion membranes [33–36].

Commercial IEMs, such as Nafion and Neosepta, were initially designed for use in fuel cells; see Berezina et al. for a comprehensive list of commercial IEMs, along with their electrochemical features [37]. Their high conductivity and ion selective transport is also utilized in devices ranging from energy conversion and storage [38] to bioelectronics [39]. However, one of the main issues encountered in many such polyelectrolyte conductors is chemical and mechanical degradation due to repeated swelling and deswelling [40–42]. In addition, these materials are designed for applications where large deformation is unlikely to occur, and typically lack the necessary stretchability and toughness for use in deformable technologies. To overcome these issues, one recent approach in developing IEMs involves layer-by-layer fabrication of composite polyelectrolytes [43–45]. The layer-by-layer method enables nanoscale composites of otherwise challenging to combine materials.

Hydrogels and ionogels can also be good ionic conductors. Conductivity in these systems can be on the order of 1 S m^{-1} [46], but generally decreases with increasing crosslink density [47], resulting in a tradeoff between mechanical and ionic transport properties. In one of the seminal publications on signal transmission employing hydrogels, Keplinger et al. reported on activation of a dielectric elastomer actuator (DEA) using controlled ionic signal [1]. Flow of Na$^+$ and Cl$^-$ through a polyacrylamide hydrogel network was used to deliver charge and activate VHB (very high bond tape, 3 M), a material widely used in DEA. The ionic signal was transmitted at frequencies exceeding 10 kHz and voltages above 10 kV, inducing rapid deformation of the DEA, sufficient for operating a loudspeaker. Building upon this seminal work, Yang et al. designed an ionic cable for signal transmission across significantly larger distance (45 cm), and at frequencies as high as 100 MHz [48]. Such performance was achieved by sandwiching a dielectric as an insulator between two parallel polyacrylamide conductors. The dielectric layer blocks charge transport between the parallel conductors, and each small segment of the cable behaves as a capacitor, charging and discharging in response to an AC signal. Chen et al. synthesized an ionogel capable of powering DEA in humidity ranging from 10% to 54% [49]. Such performance is achieved by infusing poly(acrylic acid) (PAA) with an ionic liquid. A similar concept of using ionogels to control DEA through ionic signals was also reported by Ming et al. [50]. More recently, Shi et al. reported ionic signal transmission in harsh environments by synthesizing an ionogel conductor using poly(ethyl acrylate) as the underlying polymer network [51]. This ionic conductor is capable of powering LEDs by ionic current at temperatures from −75°C to 75°C.

Self-healing is a desirable attribute for highly deformable ionic conductors, and in many cases arises naturally from the polymer structure. Cao et el. proposed an approach based on a polar polymer cross-linked by ion-dipole interactions and infused with ionic liquid [52]. Once healed, the material system proved capable of transmitting ionic current. More recently, Li et al. identified an elastomeric copolymer providing both self-healing properties and ionic conductivity, using it to power LEDs after healing [53]. Similarly, Zhao et al. demonstrated conductivity restoration upon self healing of PAA hydrogels with dissociated salt [54].

Ion selective transport, or ion exclusion, in charged polymeric backbones is another highly desirable feature which can be enhanced through layer-by-layer deposition. In contrast to filtering particles based on size, ion exclusion in polyelectrolytes typically arises due to electrostatic interaction

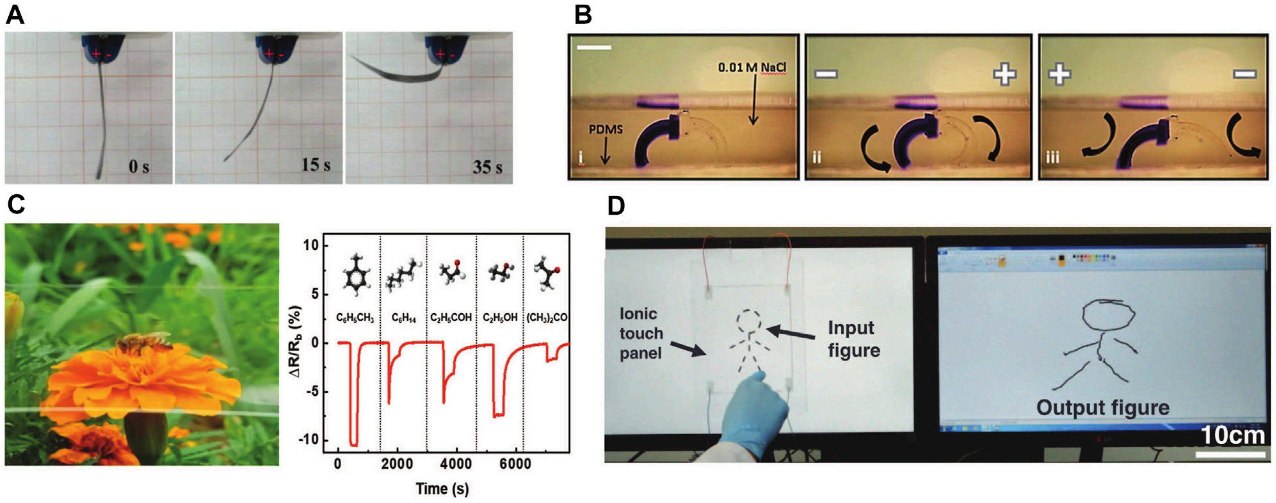

FIGURE 4 | Examples of ionic sensors and actuators. **(A)** An IPMC bending under applied voltage. Reproduced from [61] with permission from The Royal Society of Chemistry **(B)** Electro-actuated hydrogel walkers with dual responsive legs in an electrolyte solution. Reproduced from [62] with permission from The Royal Society of Chemistry **(C)** A transparent resistance-based chemical sensor of volatile organic chemicals ©2018 WILEY-VCH Verlag GmbH and Co. KGaA, Weinheim [63] **(D)** A transparent capacitor-based touch sensor. Reprinted with permission from AAAS [64].

between the mobile ions and charged polymer backbone [55–57]. The multilayer structure, such as the one reported by Cheng et al. [58], allows for enhanced selectivity by excluding divalent ions. To complement the design of novel ion exchange materials and structures, development of computational tools for predicting this mechanism has gained significant attention in recent years [59, 60].

3.2 Sensing and Actuating

Over the last few decades, soft sensors and actuators have advanced substantially [65]. Here we focus on ionically conducting polymers only, excluding other electroactive polymers such as: intrinsically conducting (conjugated) polymers, dielectric elastomers, and liquid crystal elastomers, for which comprehensive reviews exist [66–73]. We divide the discussion below into swelling/deswelling driven actuators and sensors, resistive sensors, capacitive sensors, and ion release actuators.

3.2.1 Swelling Sensors and Actuators

Many soft actuators and sensors are based on swelling/deswelling processes. When driven by electric fields, these processes are typically related to flow of mobile ions that may also bring solvent with them, and add/subtract specific volume to/from the polymer. A second, less direct, pathway is that electrochemical reactions drive pH changes in the actuator/sensor environment that change the ionization state of the polymer and therefore its equilibrium swelling in solvent (osmotic pressure). These types of soft actuators and sensors are typically designed for either in-air or in-fluid operation, with different design considerations for each. In-air devices have flexible electrodes attached to their surfaces. In-fluid devices can have both, one, or no electrodes attached. We will start by discussing the both electrodes attached case—a device commonly known as an ionic polymer metal composite (IPMC)—and then move on to the other cases, which operate only in a fluid environment.

IPMCs are bending mode actuators and sensors composed of a partially hydrated ionomer or polyelectrolyte-gel core, coated on each side with thin noble metal electrodes. The polymer is typically negatively charged, with mobile cation counter ions, but the reverse is possible. This bias towards polyanions is in large part due to their higher commercial availability and stability as compared to polycations [74]. As discovered simultaneously by Oguro et al. 1992, Shahinpoor et al. 1992, and Sadeghipour et al. 1992 [75–77], an applied voltage actuates bending (**Figure 4A**). A primary advantage of IPMCs, and ionic-based actuators more generally, is that they operate at relatively low voltages, typically in the range of 1V to 3V [66, 78]. The voltage drives cations to the cathode following the Nernst-Planck equations. These cations typically have a hydration shell that moves with them. The combined motion of the cations and solvent molecules causes expansion on the cathode side along with contraction on the anode side, that in concert lead to a bending motion. One downside of IPMC actuators is that they relax over time and eventually even bend in the opposite direction [78].

As sensors, IPMC respond to a bending type deformation, such as transverse tip deflection, since bending will drive motion of the ions and solvent. Sensing can be performed actively or passively through voltage, current, charge, impedance, or capacitance [78–82]. The passive approaches tend to be better for static deformation sensing and the active approaches tend to be better for dynamic deformation sensing. Each approach comes with trade-offs in terms of signal-to-noise, appropriate frequency range, environmental sensitivity, and device complexity. A primary deficiency of IPMCs as sensors is that the mechanical to electrical coupling is orders of magnitude weaker than the electrical to mechanical coupling [83].

Ionomer selection, ionomer processing, cation selection, and device geometry all critically influence IPMC performance. The most common ionomer used in IPMC is Nafion. Other common choices are Aciplex, Flemion, and PSS [61]. Each of these materials combines sufficiently high ion conductance and mechanical stiffness. The conductance, and to a lesser extent the mechanical properties, depend on the film processing and choice of cation. Ionogels and polymer electrolyte hydrogels can also be used as the polymer component of IPMC. The performance of hydrogel-based IPMC tend to suffer from drying out effects, but are promising from an ease of fabrication and bio-compatibility perspective [84]. Ionogel-based IPMC do not suffer from drying out and are less susceptible to back relaxation than ionomers in IPMC, but do tend to be less stiff and strong than ionomers [85–89]. Ion exchange of H^+ for Li^+, Na^+, K^+, TMA^+, etc. is also a common step in IPMC preparation since these other cations will have larger associated swelling strain [72]. The area of the electrode/polymer interface is also important because it sets the device capacitance. A wide range of approaches are used to create a large-area interaction between the ionomer and the noble-metal particulate electrode [74, 78, 90]. Finally, time scale and blocking force of the actuator are set by the mobility of the combined cations and hydration sphere and the thickness of the ionomer membrane. Relatively thin membranes are typically used (~ 200 μm), keeping the timescale of response in the seconds or faster range and blocking forces in the mn range [72]. Device thickness can be increased to increase actuator blocking force, but it comes with a trade-off in actuator displacement and response time [78, 91, 92]. Blocking forces for IPMC are typically in the 1–100 mN regime [78, 93].

Extensive work over the last 2 decades has gone into modeling of IPMCs in both the actuator and sensor context [78, 83, 94, 95]; these models can be used to design devices such as grippers and assess their expected performance. Continuum modeling approaches work well for describing actuation but typically require some fitting parameters and still struggle with back relaxation [25, 83, 96–100]. Equivalent circuit modeling works well for IPMC sensors as this is a fast, low computational cost approach to modeling that facilitates integration of IPMC into more complex devices, including for self-sensing purposes [79, 101–104].

In solution, polyelectrolytes can be actuated through additional mechanisms to that described for IPMC above. These mechanisms arise because ions can move through the solution and into/out of the polymer. As nicely described by Glazer et al. [105], the two primary additional mechanisms of swelling driven actuation available in solution are: 1) pH changes resulting from electrolysis at the electrodes change the polyelectrolyte protonation and therefore its equilibrium dimensions in solution, 2) ions distribute unevenly across the gel/electrolyte interfaces because of Donnan exclusion and this local ionic strength variation drives local expansion or contraction changes by osmotic swelling (aka dynamic enrichment/depletion by [106]); this swelling will be different on the gel sides facing the anode and cathode. Relevance of the pH mechanism heavily depends on timescale of the device actuation, the size of the electrodes, and distance from the electrodes to the specimen: electrolysis produced ions must first be produced at significant concentration and then diffuse into the polymer. The dynamic enrichment mechanism is more widely relevant. Either mechanism can drive bending or overall volumetric contraction given appropriate specimen geometry. In many devices, both mechanisms contribute to actuation in a manner not simple to differentiate. The deformation of an acidic copolymer gel electrolyte in solution under an applied non-contact electric field was first observed by [107]. In 1992, Osada et. al. demonstrated bending of a polymer gel made of weakly crosslinked acidic copolymer immersed in a surfactant solution, when 20V was applied to electrodes 20 mm apart, that are parallel to each other and to the gel [108]. Much experimental [62, 109–116] and modeling [117–120] work has been done since then to develop these concepts into actuators, usually for soft robotics-type applications, and usually using bending mode deformation [62, 121–127]. One particularly exciting example is that of Morales et. al., who demonstrated a walker that works within an electrolyte solution (0.01 M NaCl) with one leg composed of an anionic gel and one leg composed of an cationic gel (**Figure 4B**) [62].

3.2.2 Resistive Sensors

Resistive sensing relies on a change in resistance in the device in response to the input that is being sensed. Within a sensor, this resistance change can result from geometric changes and/or ionic conductivity changes. Drilling down one step further, ionic conductivity changes can result from changes in either ion diffusivity or ion concentration.

Gels with mobile ionic components work directly as resistive strain sensors because their internal conduction path changes when uniaxial tension is applied. For a nearly incompressible material like a gel, the concentration of conductive ions will remain nearly constant under deformation, and therefore the conductance of the material will remain nearly constant as well. The conductive path length however, will increase by the tensile stretch λ, and the cross-sectional area will decrease by a factor of $1/\lambda$ (**Figure 5A**): the resistance therefore increases by a factor of λ^2. For example, Cao et. al. synthesized a transparent, mechanically robust, and highly stable ionogel sensor using the poly(ethyl acrylate)-based elastomers and ionic liquids. The ionic liquid anions interact with the poly(ethyl acrylate) matrix via hydrogen bonding and increase the compatibility [128]. Much of the design concerns for these resistive strain sensors centers around enabling large reversible strain (e.g., by using a double network with dynamic and covalent bonds) and preventing loss of fluid from the gel (e.g., by using glycerol instead of water as the solvent) [129–133].

Ion concentration changes that result in resistance changes have been used to sense environmental humidity and have potential to sense light (**Figure 5B**). For many polyelectrolytes, ion dissociation commonly happens upon water absorption, making them natural humidity sensors [134–137]. For example, Yang et. al. demonstrated sulfonic acid doped poly(propargyl alcohol) as a humidity sensor: the presence of water facilitates the ionization of sulfonic acid as well as increases

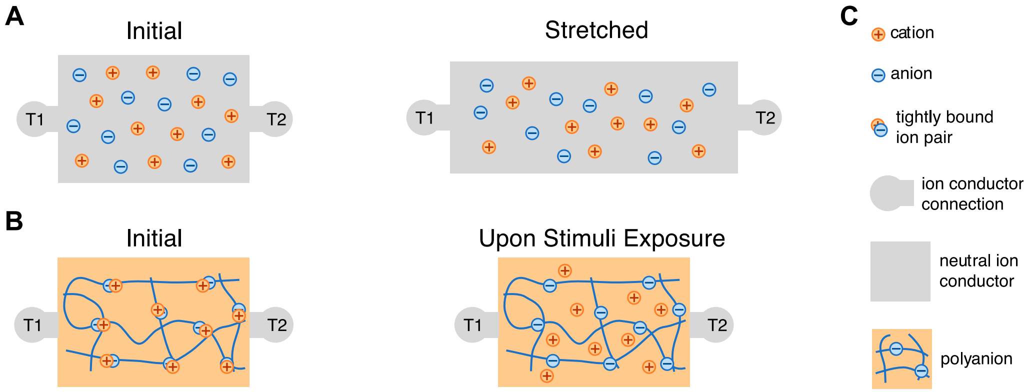

FIGURE 5 | Schematics of two concepts for resistive senors. **(A)** Direct resistive sensing via shape change of the stretchable resistor during mechanical deformation that results in a longer ionic conduction path and reduced cross-sectional area/ions per cross-section, and consequently an increase in resistance. **(B)** Resistive sensing of stimuli via change in the concentration of mobile ions. Depicted here is an increase in the concentration of mobile ions, which would correspond to a decrease in resistance. **(C)** Legend for both schematics.

the ion mobility. Thus the conductivity of the material increases as a function of the water vapor content [134]. Light has also recently been demonstrated as a method of modulating the ionic conductivity of polymer electrolytes, paving the way for these materials to be used as light sensors. This conductivity change in response to particular wavelengths was achieved by incorporating molecules that have photoswitchable binding of ions. Nie et. al. designed a copolymer with imidazolium-containing diarylethene (DAE) groups that bind to divalent nickel cations [138]. The DAE group is driven to a weaker metal binding ring open state by ultravioloet (UV) light and reverted to a stronger metal binding ring closed state by visible light. UV light therefore results in metal cations that move more freely through the material and overall a higher ionic conductivity material.

Finally, ionic mobility changes can be used for resistive sensors [63, 139, 140]. For example, Jin et. al. reported an ionic chemiresistor skin which can detect volatile organic compounds (VOCs). The core of the device is a highly stretchable ionogel film made of thermoplastic polyurethane matrix infused with ionic liquids. The sensor changes resistance when exposed to volatile organic compounds (VOCs) (**Figure 4C**). The ionic liquid viscosity decreases as the VOC concentration increases, and the viscosity decrease in turn increases ionic liquid diffusivity [63]. Similarly, a thermoplastic polyurethane-based ionogel was shown to detect temperature through temperature-dependent ionic mobility changes within the ionogel [140].

3.2.3 Capacitive Sensors

Changes in capacitance can be used for a variety of deformable sensor applications including stretch, touch, temperature, and humidity. Sun et. al. in 2014 introduced a configuration of two polymer electrolyte hydrogels sandwiching a soft dielectric for capacitive sensing [141]. The ionic hydrogels act as stretchable conductors, enabling measurement of changes in capacitance of the dielectric elastomer resulting from deformation (shape changes). The authors were able to demonstrate reversible sensing of uniaxial tensile deformation, equibiaxial deformation, finger bending, and pressure sensing under touch. Lai et. al. was able to perform capacitive stretch sensing using a similar configuration, but with ionogels in place of polymer electrolyte hydrogels, leading to greater stability in air [131]. Kim et. al. utilized a bilayer of ionogels with opposite fixed charges and ionic liquid counterions, coated with carbon nanotube electrodes on opposite sides, to form a sensor that changes capacitance under in-plane tensile deformation. This capacitance change arises primarily across the interface of the two ionogels [142]. Kim et. al. took a distinct approach to achieve touch sensing using a polyelectrolyte hydrogel: they applied uniform voltage across a strip of the hydrogel that the touch disturbed (acting as a capacitor to a ground point), thereby driving an ionic current that could be measured (**Figure 4D**) [64]. Sawar et. al. took a third tact in using polymer gel electrolytes for sensing touch independent of sensor deformation. They created arrays of parallel architected polymer gel electrolytes separated by a dielectric layer. When a voltage is applied across the two polymer gel electrolyte electrodes, there is a projected electric field that interacts capacitively with a finger as it approaches. The finger location is determined by sweeping the sensor array [143]. Subsequent papers have extended these three sensing concepts in terms of material formulation and sensor geometry [131, 144–146].

Beyond these essentially mechanical sensors, IPMCs can also be made into capacitive-type humidity sensors [147, 148]. For example, Esmaeli et. al. built a IPMC-based humidity sensor based on Cr/Au or Ti/Au electrodes sandwiching a Nafion sheet. The dielectric constant of the IPMC changes when water molecules occupy the nano-channels inside Nafion, resulting in higher capacitance [147, 149]. Recently, Wang et. al. demonstrated that changes in the diffuse layer capacitance of

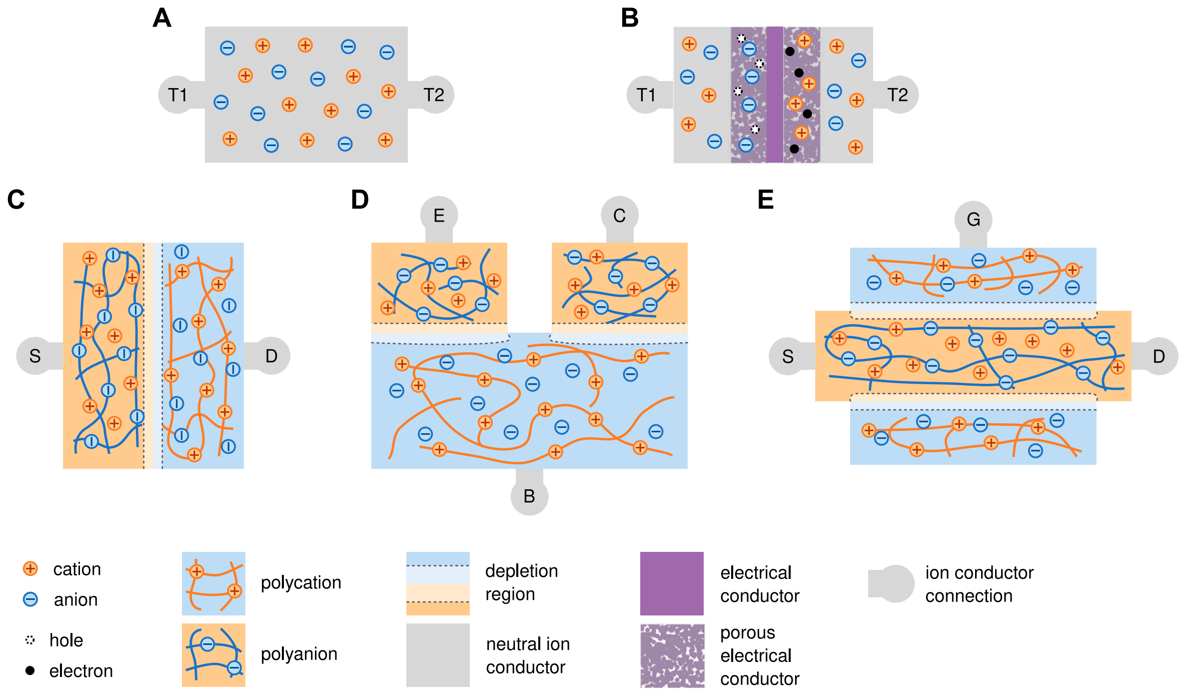

FIGURE 6 | Schematics of ionic signal transmutation approaches. Video animations of the operation of devices B, D, and E are included in the SI and on YouTube. **(A)** Polyelectrolyte resistor from a generic ion conductor with symmetric terminals T1 and T2. **(B)** Inverted supercapacitor in a charged state with T1 at a lower voltage than T2 **(C)** Type III PN Polyelectrolyte diode with source (S) and drain (D) ionic connections. Current can flow from left to right, but not from right to left. **(D)** PNP Bipolar Junction Transistor (BJT) with emitter (E), collector (C), and base (B). The current through the gate controls the current flowing from source to drain. **(E)** P-channel Junction Field Effect Transistor (JFET) with source (S), drain (D), and gate (G). Increasing reverse bias of the base-to-channel junction reduces the current from source to drain. **(F)** Legend for all schematics.

ion-conductor interfaces can be used to sense temperature [150]. They made a sandwich of hydrogel, dielectric elastomer, and a sensing electrode. As temperature increases, the Debye length increases, which lengthens the diffuse layer of the electrode double layer. This decreases the capacitance, which increases the voltage across the interface. The dielectric stops potential faradaic electrode reactions.

3.2.4 Ion Release Actuators

Ionic devices open the door to sensing and releasing biological signals, a feature highly utilized in many bioelectronic technologies, including controlled substance delivery actuators and neural recording sensors. In therapeutics, ion selectivity of PSS to conduct protons has been employed by [151] for targeted delivery of H^+ in response to an electric signal, while blocking the transport of Cl^-. Sjöström et al and Gabrielsson et al. both demonstrated different PSS-based actuators capable of releasing the neurotransmitter acetylcholine. Sjöström et al. focused on miniaturization and speed, achieving release times on the order of ms, while Gabrielssonn achieved large continuous currents of neurotransmitter with longer time scales [152, 153]. There are also ion actuators known as organic electronic ion pumps. These use the oxidation of conjugated polymers (usually PEDOT:PSS) to drive the continuous migration of an ion from a source reservoir to a target reservoir [154, 155]. Lastly, while largely outside the scope of this review, there has been significant work using polyelectrolytes and hydrogels in electrical biointerfaces and bioelectronics that read and influence the electrical and ion environment of the body [156–158].

3.3 Transmuting the Signals

In electrical circuits, the basic linear elements are resistors, capacitors, and inductors. In addition to these linear elements, analog circuits often take advantage of nonlinear elements. The most common of these are the transistor and the diode. Memory could also be realized through nonlinear history-dependent resistors known as memristors [159–164], but to the authors' knowledge polymer or gel ionic memristors do not yet exist. Almost any analog circuit can be produced by a combination of these five elements. There has been significant work in the literature to create these elements using ions instead of electrons. The simplest of the above is the ionic resistor. This is an element that has a linear relationship between the electrochemical potential difference between two places and the ion current that flows between those two places. As discussed in prior sections (and **Eq. 9**), almost all ionically conducting polymers can act as a resistor (**Figure 6A**). Thus, we focus in the following sections on the other circuit elements (**Figure 6**, **Supplementary Videos S1–S4**).

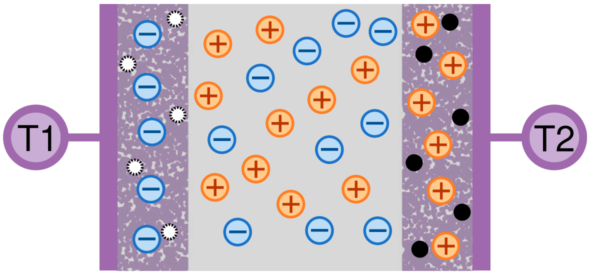

FIGURE 7 | The structure of a traditional electronic supercapacitor. Shown in a charged state with electrical terminal T1 at higher voltage and terminal T2 at lower voltage.

3.3.1 Capacitor

The second circuit element that has been recreated with ionics is the capacitor. Capacitors store energy in the form of electric fields. Generally they have a linear relationship between the stored charge and the voltage across them. One way to make an ionic capacitor is to sandwich a dielectric elastomer between two polymer electrolytes. Mobile ions in the electrolytes can then build up on opposite sides of the separating membrane and store energy in the resulting electric field. This is analogous to thin film solid state electrical capacitors. These devices tend to have low specific capacitances that are limited by the thickness of the separation layer but posses fast switching and charging times. They are also generally symmetric and thus can be charged in both polarities. Yang et al. created a capacitor of this type with two hydrogels separated by half a mm of VHB. Their device had an area of 2 cm^2 and a capacitance of 850 pF. This closely matches the theoretical parallel plate capacitance of 840 pF [48].

Ionic capacitors can also be made by inverting the structure of an electrolytic or super capacitor (**Figure 7**). In this setup, two electrolytes are separated by a thin electrically-conducting film. As the capacitor charges, ions build up on the two conductor faces. This build up induces a rearrangement of the charge inside the conductor, which leads the formation of two double layers of charge, one at either side of the conductor (**Figure 6B**, **Supplementary Video S1**). The capacitance of these devices scales with the surface area of the ion–conductor interface. The larger this interface, the more ions can be stored at it for a given voltage. Janson et al. achieved a high specific capacitance by using PEDOT:PSS as the interface between a carbon conductor [165]. The size of this interface was about 4 mm^2. The PEDOT:PSS is both an ionic conductor and an electrical conductor, and thus allows a very large number of ions to accumulate in its microstructure. As the device charges, electrons pass from one PSS interface to the other. This movement of charge changes the doping level in the PEDOT:PSS, oxidizing one side of the capacitor and reducing the other side. They reported a volumetric capacitance of 14.5F cm^{-3} which is at least six orders of magnitude larger than the basic parallel plate capacitor. However, unlike the parallel capacitor, the PEDOT:PSS electrodes were limited to about 1V before redox reactions like water splitting grew to dominate the charge transfer. The time constant of the capacitor charging was about 250 ms. Martin et al. took a similar approach with different materials, making an inside out capacitor from reduced graphene oxide and a central PDMS ion barrier. Similar to Jansen et al., most of the volume of the device had both high ionic and electrical conductivity, while a small barrier region was only electrically conductive. This maximized the surface area available to create an ion double layer. They reported a volumetric capacitance of 4.31F cm^{-3} with a time constant of approximately 5 s [167].

3.3.2 Diodes

Diodes are key nonlinear circuit elements. A polycation, with mobile counter anions, behaves similarly to an n-doped semiconductor, which has mobile negatively charged electrons. A polyanion, with mobile counter cations, behaves similarly to a p-doped semiconductor. When a polycation and polyanion are touched to each other, they form a bipolar membrane, which is a junction that behaves like a diode (**Figure 6C**, **Supplementary Video S2**). The specifics of how these devices function depends on the chemical identity of the mobile carriers in each polymer, as well as the mode of transport dominant in each polymer. Three diode classes are described below. To facilitate this description, we define some terminology and conventions. Device voltage is voltage at the mobile cation side minus voltage at the mobile anion side. For type II devices, device voltage is defined using with the initial locations of the non-interacting ion pair. Positive junction current is when positive charges flow from the mobile cation side to the mobile anion side or negative charges flow in the reverse direction. Open circuit voltage (OCV) is the device voltage when no current is flowing and the system is in electrochemical equilibrium. Applying voltages more positive than the open circuit voltage is called forward biasing; the converse is reverse biasing. Minority carriers are ions with the same charge and in the same region as fixed polyelectrolyte charges [167–169].

Type I diode: Annihilating ions with significant Donnan exclusion. This diode type is commonly created when bipolar membranes are placed between aqueous acid and base solutions. The membranes typically have high density of fixed charges and are selective to H^+ and OH^-. Under forward bias, H^+ and OH^- migrate toward the junction and combine to form water, which then diffuses away from the junction (similar to electron/hole annihilation in a traditional semiconductor PN junction). Under reverse bias, the mobile ions migrate away from the junction, leaving a region without charge carriers. This creates a large electric field that opposes the applied voltage and thus very little current flows in the device. If the reverse bias junction electric field is large enough, and there is a neutral species present in the junction made from the mobile ions (like H_2O), then this field can rip that neutral species apart into separate mobile charges and current will flow. This reverse bias breakdown can be intentionally used or suppressed, as discussed later.

Type II diode: Annihilating ions without significant Donnan exclusion. These diodes can be made from a hydrogel polyelectrolyte or a neutral gel, which does not exclude neutral salts. The rectification direction depends on the relative concentration of ionic charge carriers in baths bordering either side of the gel. Under forward bias, migration of the non-annihilating counterions dominates. Under reverse bias, the current is lower because chemical recombination of the annihilating ions creates a region of neutral species right at the bath/polymer junction that is higher in resistance than the bulk polymer. If the gel is neutral, this device is called an electrolytic diode.

Type III diode: Non-annihilating ions with Donnan exclusion. This describes junctions between most polyelectrolytes. Under forward bias, the concentration of mobile carriers increases until it is sufficient to drive minority carriers into the opposing region. Therefore, forward bias current must be carried by minority carriers. Reverse operation is similar to type I, but if non-hydrogel polyelectrolytes are used, can sustain larger reverse voltages without breakdown.

With these categories in mind, there are four main metrics used to evaluate the performance of an ionic diode: rectification ratio, forward bias current, (reverse) breakdown voltage, and switching time. Rectification ratio is the ratio of the current flowing through a diode under forward bias to the current in reverse bias. Note that for the small voltages often used for polyelectrolyte diodes, it is important whether the voltages used to bias the diode are centered around the open circuit voltage, or instead around 0 V. The current under forward bias is determined by the applied voltage and conductivity at the transition from an exponential growth to an ohmic I-V curve with increasing forward bias voltage. The breakdown voltage refers to the voltage where the current begins to increase dramatically under reverse bias of the junction. Finally, the switching time refers to how long the diode takes to reach a steady state current after a transition from reverse to forward bias or vice versa.

The simplest polymer diode is a type II electrolytic diode with only one material layer that separates baths with different concentrations of ionic charge carriers [169]. Because their function depends on the annihilation of charge carriers, these are generally made using acids and bases that react to form water [169]. Zhao et al. devised an enhanced type II diode by using ions that react to form an insoluble precipitate instead of water. When these ions are driven into the junction (under reverse bias), they rapidly form an impermeable salt barrier that prevents further ion migration [170]. Under forward bias, the large fields induced across the precipitate barrier rip it back apart into its constituent ions. The non-interacting counterions to the reactive ions are then free to cross the junction and sustain an ionic current.

Recently, type III diodes have been constructed from aqueous polyelectrolytes. One popular choice is to use PSS and PDAC as the polyanion and polycation respectively, with platinum foil as the electrode [171–173]. Carye et al. and Zhang et al. used these polymers directly while Wang et al. embedded them in a double network. The direct use of the polymers led to a much higher rectification ratio, but limited the device stretchability, while the double network diode retained performance up to a stretch of 4. One disadvantage of these water based systems was that the breakdown voltages were low. At around −2 V, the currents began to increase dramatically as water was dissociated at the junction. Because the electrodes in these devices were made from platinum or silver and thus semipolarizable, the measured response of the diode was a function of the electrode interface in addition to the polyelectrolyte junction. For example, while the open circuit voltage of the system was likely in the hundreds of mV range [173], the device only conducted well in forward bias above 2 V when the platinum electrodes were able to split water efficiently [168]. Han et al made a similar type III diode with non-polarizable electrodes and demonstrated a turn on voltage near 0 V [174].

There are two ways researchers have solved this low breakdown voltage. First, water dissociation can be avoided by eliminating water from the system. Kim et al. demonstrated a diode junction made from acrylate polymers swelled with ionic liquids [142]. Second, the water splitting reaction can be suppressed by reducing the local electric field or removing a base catalyst by changing the chemistry [175, 176]. Gabrielsson et al. demonstrated both suppression approaches. By placing a neutral gel between the polycationic and polyanionic layers of the junction, the junction electric field spreads over a much larger distance and water splitting was eliminated. Unfortunately, it dramatically harms another key diode metric, the switching time. The forward-to-reverse-bias switching time of this neutral layer device is on the order of hundreds of seconds, since all the ions must be extracted from the neutral layer before current stops flowing. By instead replacing the polyammonium group on their polycation with a polyphosphonium, they removed the weak base catalyst that speeds up water dissociation. With this polycation, they were able to reverse bias the junction up to −40 V without water splitting, and still retain the fast (~4 s) switching time of direct contact junctions [175].

Gabrielsson et al. also demonstrated that the neutral gel approach can be improved by changing to a type I diode. By using hydroxide and hydrogen ions as the mobile species, ions do not accumulate in the neutral region during forward bias, and so there is nothing to extract in reverse bias. To create a source of these mobile ions, Gabrielsson et al. additionally proposed using two other direct contact type I junctions oppositely biased to the main junction to generate mobile hydroxide and hydrogen on the fly [177].

3.3.3 Transistors

Transistors are three terminal devices where the current or voltage at one terminal controls the current between the other two terminals. Transistors are widely used in both digital and analog circuitry as the foundation for logic gates and amplifiers respectively. Ionic transistors would enable a wide variety of ionic circuits. There has been much research into creating transistors with nano-pores and microfluidic channels [178, 179], but relatively little progress in solid state bulk transistors that do not require nano-structuring. As far as the authors are aware, there are only five such transistors documented in the literature; three are Bipolar Junction Transistors (BJTs), while two are a Junction Field Effect Transistors (JFETs). One of these JFETs has only been proposed but not experimentally realized.

3.3.3.1 Bipolar Junction Transistors

BJTs consist of two junctions in series with opposite polarity. The three terminals spanning these two junctions are the emitter, base, and collector (**Figure 6D**, **Supplementary Video S3**). The ionic version of the BJT is simpler than the semiconductor equivalent in two ways [1]: these transistors do not rely on quantum mechanics or different energy bands to function [2]; the selective mobility in each polymer is created chemically rather than electronically. In a polymer BJT with a polycation base and a polyanion emitter and collector, the ionic current flowing from the emitter to the collector is controlled by the current flowing through the base. This is analogous to a PNP semiconductor BJT. If the materials and currents are reversed, then a device analogous to an NPN transistor is created. BJTs rely on movement of minority carriers for their operation. Key metrics for ionic BJTs are switching time, amplification gain, and side reactions.

For PNP devices, each junction acts like a type III diode. Forward biasing the emitter–base junction ($V_B < V_E$) injects a large number of mobile minority cations into the base. Some of the minority mobile ions that enter the base, flow out of the base terminal, comprising the emitter-base current. The base–collector junction is reverse biased ($V_B > V_C$), such that a large electric field is created across this junction. This field creates a depletion region of majority carriers (anions) in the base at the base-collector junction. The injected minority cations however, feel this field and migrate across the base–collector junction where they become majority carriers again and carry the source–drain current.

Tybrant et al. made a transistor using overoxidized PSS as the CEM and a commercial Fumatech membrane as the AEM with neutral PEG in the middle. PEG decreased the magnitude of the electric field between the polyelectrolyte membranes. This allowed for reverse bias voltages greater than 1.5 V on each of the junctions without water splitting. The junctions were on the order of 25 μm by 200 μm. They achieved a current amplification of about 10, and a switching time on the order of 10s. They used this transistor to deliver neurotransmitter to some cells [180, 181].

Gabrielsson et al. took their polyphosphonium material previously used to create a diode and used it to create a BJT. Their material contains no water, enabling them to remove the neutral gel separator that Tybrant et al. used. Polyphosphonium was patterned over an over-oxidized PEDOT:PSS base. PEDOT:PSS was additionally used as the electrodes. They report a gain of up to 43.9, with a switching time of under 2 s. They attribute this fast switching time to the small (2 μm) distance between collector and emitter and high voltages that are enabled by not having water splitting [182].

Kim et al. created a water-free BJT from an ionic liquid and acrylate polyelectrolytes. These are the same materials they used to create their diode described in **Section 3.3.2**. Their device had a switching time comparable to Gabrielsson et al., but suffered from a low gain of only slightly greater than one.

3.3.3.2 Field Effect Transistors

The second type of ionic transistor being researched is the Field Effect Transistor, which is quite different from the BJT (**Figure 6E**, **Supplementary Video S4**). By analogy with traditional semiconductors FETs, in an N-channel Junction FET (JFET), there would be a continuous polycation connecting the source to the drain terminals. This polycationic channel is then surrounded by a polyanion, which is connected to the gate terminal. When the gate is disconnected or at high voltage, anions can flow freely through the polycationic channel. When the gate is at a low potential, the gate–channel junction is driven into a stronger reverse bias. This bias increases the size of the depletion regions at the edge of the channels by forcing cations out, thereby reducing the current flowing through the device. With sufficient reverse bias, the depletion regions completely close off the channel, stopping the current flowing from source to drain. Boon et al. modeled how a fully ionic P-channel FET might be created [183]. The main challenge in creating ionic FETs is the small size of the depletion regions in ionic junctions due to their high carrier concentration and thus small Debye length. The polycation channel must have a diameter on the order of 10s of nanometers. Boon et al. proposed creating these channels by using an electrically conductive nano-porous carbon matrix. Instead of a continuous polyionic channel, a solvent filled nano-porous membrane would be capped by two polycationic membranes. This means that the junction is formed between a metal and an anion filled channel, rather than a polycation and a polyanion directly, but the operational mechanism is similar. Their model predicts an amplification factor of up to 6, with a switching time of better than 10 ms. They simulated these transistors in three configurations and demonstrated good functionality in all three cases. Zhong et al. [184] made a nanoscale FET using a Maleic–chitosan channel controlled by a silicon gate. Their device controls 2.5 nA of current from source to drain with a gate voltage swing of 30 V.

3.4 Energy Sources

Ionic devices need power sources in order to perform most of their functions. While a myriad of energy sources exist for powering traditional electronic circuits, the natural form of power for ionic devices is in the form of ions. In other words, the devices we have discussed will be run off of concentration gradients and electric fields. In fact, because the mobile species are often charged, concentration gradients lead to electrochemical potential gradients. Thus, in order to power our devices, we need something that is soft, polymeric, and able to set up an electrochemical potential gradient. This section explores four technologies that promise to do so: batteries, reverse-electrodialysis, mechanical harvesters, and thermoelectrics (**Figure 8**, **Supplementary Videos S5–S7**). The capacitors from **Section 3.3.1** have the potential to be used as energy storage devices, but are included there because of how they are used in existing literature.

3.4.1 Flexible Batteries

In traditional robotics, batteries are a ubiquitous source of power. They also work internally with ions, and so appear naturally adaptable for powering ionic circuits and devices. Wang et al. demonstrated how this might be done in their 2017 paper on inverted batteries [185]. By inverting the construction of a traditional lithium ion battery, the previously internal ion

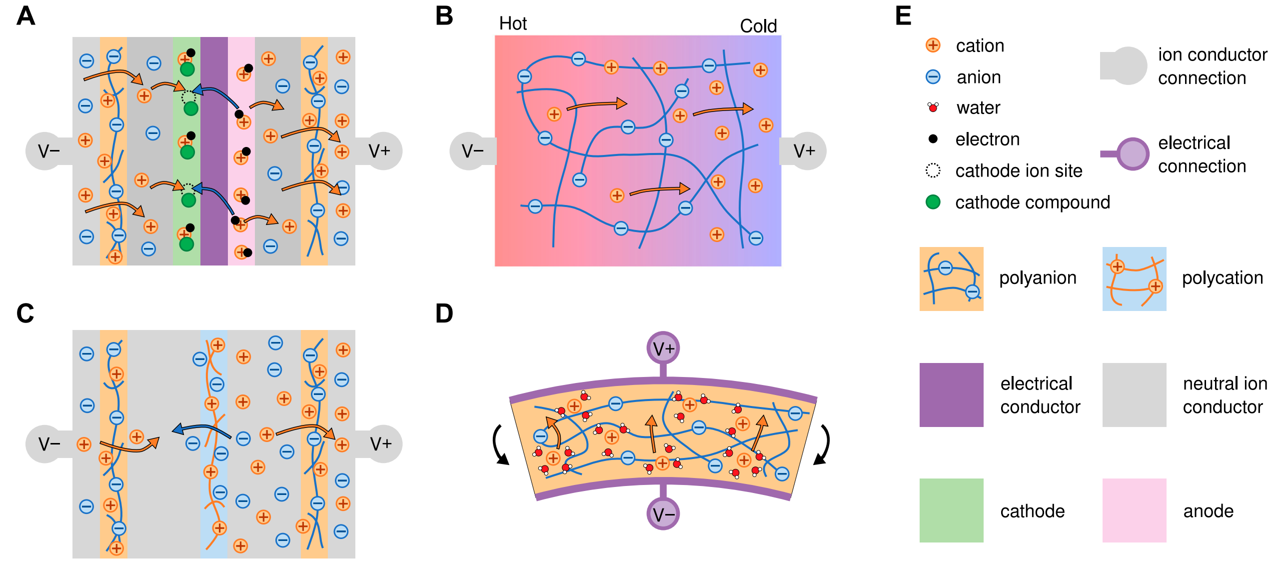

FIGURE 8 | Schematics of selected energy conversion approaches Video animations of parts A, C, and D are included in the **Supplementary Materials** for ease of visualization and on YouTube. **(A)** inverted battery with two ionic connections. Positive ions enter the device at the left and leave at the right. They are driven by the energy difference between the anode and cathode material. **(B)** Ionic Thermoelectric. A heat gradient from hot on the left to cold at the right causes mobile positive ions to travel towards the colder side of the device, increasing the electrochemical potential at the $V+$ connection and decreasing it at the $V-$ connection. **(C)** Reverse electrodialysis. The concentration difference between the right (initially salty) chamber and the left (initially salt-free) chamber drives mobile cations out the right $V+$ connection, increasing the electrochemical potential there and decreasing it at the left $V-$ connection. **(D)** Mechanical transducer (IPMC). The strain in the IPMC increases the pressure at the bottom of the device. This causes solvent to migrate upward, and the binding between solvent and ions carries positive mobile ions with it. Like the other energy devices, this increases the electrochemical potential at the $V+$ connection. Unlike the other devices, this change in potential is usually captured by an electrical connection instead of an ionic one. **(E)** Legend for all schematics.

transport now drives power through an external circuit. This inverted configuration is shown in **Figure 8A** and **Supplementary Video S5**. Electrons flow inside the battery and are compensated by ions flowing through the external terminals. One challenge is that lithium metal used as an anode is incompatible with water. In order to use a water-free battery electrolyte at the same time as a water based external circuitry, they used water impermeable cation exchange membranes near each battery terminal to provide a barrier between the internal and external electrolytes. This concept promises to allow the significant advancements in soft battery technology to relatively directly carry over to ionic circuitry [185].

There are still, however, obstacles to realizing fully soft polymeric batteries. There are two main challenges: creating effective polymer electrolytes and creating flexible, high density electrodes. Approaches to both of these problems can additionally be broken down into two camps. The first approach is to integrate thin films or small particles of conventional electrochemical materials into soft substrates. In this direction ("structural design"), the emphasis is to provide flexibility to materials that already have the desired chemical functionalities but are otherwise inflexible. In a second approach, one can start with soft materials, then impart the desired electrochemical properties ("materials design"). Either approach has led to successful energy conversion and storage devices. However, improving the performance and stability to match those of traditional electrochemical components remains a challenge.

Soft-ionic electrolytes have been extensively studied as gels, polymers, or composites [186–194], promising to replace the existing norms of hard solid-state electrolytes and liquid electrolyte/porous separator combinations. To meet this ambitious goal, soft-ionic electrolytes must fulfill the requirements of solid-state electrolytes, which include high ionic conductivity, mechanical and electrochemical stability, ease of processing, and low interfacial resistance [195]. These are similar to the requirements for good ionic conductors as discussed in **Section 3.1**, but with additional restrictions unique to batteries: electrochemical stability and low interfacial resistance. For example, many battery chemistries like lithium are incompatible with water, and so cannot use the variety of water based polyelectrolytes. Fulfilling these requirements, however, has required trade-offs. For example, the free volume in polymers can benefit the ion's motion but has a negative effect on the mechanical stability [196, 197]. Similarly, hydrocarbon polymers have low cost, good chemical stability, and easy integration with manufacturing; however, their low dielectric constants restrict the ion-pair dissociation required for high conductivity [195, 198]. Gel-based electrolytes using an inert polymer matrix (polyvinylidene fluoride, "PVdF") with battery salts (LiPF6) and solvents (mixture of carbonates) offer high energy density and ease of packaging [199]; however, the limited electrolyte fraction, interaction between ions and polymers, and poor interfacial contacts restrict the conductivity of gel-based battery systems [200, 201].

At present, these electrolyte membranes need to be combined with non-polymeric flexible electrodes to achieve flexible batteries. Because batteries with high gravimetric and volumetric energy densities require dense, well-packed electrodes and electrolytes, structural design and ease of processing are a critical consideration for the soft-ionic-materials integration [202]. This is especially true for electrodes containing inorganic oxides, which must be sufficiently thick to provide reasonable capacity, but not too thick such that the rigidity compromises the device mechanics. In addition to this trade-off, the interface between electrode and current collector must be able to handle bending stress. These challenges highlight the need to understand the electronic and ionic connectivity at the interface within and between electrodes, electrolytes, and current collectors. We point the readers to several excellent reviews on the structural design of flexible electrodes [203–205].

Electrodes are also tackled from a “materials design” approach. One example is to functionalize carbon nanomaterials, which are conductive and intrinsically flexible. The functionalized groups can be molecular or nanoparticles [206–210]. The goal is to increase the energy density and stability to match the performance of conventional batteries. To enable this improvement, one can increase the voltage windows by engineering the electronic structure of the redox center and their density [211–213]. With these advances, carbon-based electrodes with >1000 mA h g^{-1} capacities can now be obtained [212, 213]. However, these organic compounds were developed for energy density and thus their mechanical properties have yet to be evaluated. The next steps are to further improve the volumetric energy density and stability of these organic materials, and study more extensive combinations of batteries and ionic devices.

3.4.2 Reverse Electrodialysis

Reverse electrodialysis (RED) is a promising technology that generates electric power from a salinity gradient. In RED, an alternating series of AEMs and CEMs separate compartments of concentrated salt solution and less concentrated solution. These high and low salinity regions can take the form of fluids or gels. Salt wants to flow from high concentration to low concentration, but the specific configuration of ion exchange membranes means that one ion can only flow inside the RED device, while the counterion can only flow through the terminals and external circuit. This constraint on ion paths turns a salt flow into an electrochemical power source. The magnitude of power generated is primarily determined by the salinity gradient and the number of chambers in the RED device [214, 215] (**Figure 8C**, **Supplementary Video S6**). RED devices in literature are often characterized while connected to external electrical circuits with electrodes, but this is not required when using them with other ionic components. RED device performance and membrane stack design has been analyzed using multiphysics models similar to those discussed previously but with additional fluid motion terms (Navier-Stokes) [216–219].

Baek et al. reported using a miniaturized RED patch made from commercial IEMs to power a electro-chemiluminescent bio-sensing microchip [220]. An eight-layered patch was capable of generating 1.9 V while a ten-layered RED patch produced 2.5 V. The electrode-less RED patch was also used as an ionic power source for active transdermal drug delivery [221]. Shroeder et al. made a RED system that used hydrogels instead of liquid solutions for the salt chamber [222]. The maximum power density per unit cell was 27 mW cm^{-2} while the open-circuit voltage reached up to 110 V by stacking gels in series. It was also demonstrated that power density can be increased by reducing the thickness of hydrogel films to as thin as a few hundred nanometers [223]. Based on these results, exploration into ultrathin membranes with improved permselectivity and conductivity based on advanced materials opens up novel possibilities for robust energy harvesting with RED [224–230].

One challenge with most existing RED systems is that they need a mechanical pump or regular injection of saline solution into every compartment to maintain power levels. This makes traditional RED impractical for stand-alone ionic devices. To overcome this limitation, Baek et al. developed a RED device that uses precipitation and dissolution to maintain the ion concentrations in the high and low salinity chambers [231]. In this device, two different salts are placed into alternating high concentration chambers. These salts are chosen such that they are individually soluble, but both metathesis products are insoluble. Ions entering the low concentration chambers thus precipitate, maintaining that low concentration. The maximum power of a 20-stack precipitation assisted RED was $\sim 100\ \mu W$ while the open circuit potential maintained 90% of the maximum after $\sim 5hrs$. One potential challenge with this approach is the precipitate clogging the ion exchange membranes after extended periods of use.

3.4.3 Mechanical Ion Transducers

Energy harvesting from mechanical motion or vibration is a sustainable power source for various wearable devices and ionic gradient generation. Efforts have been dedicated to several types of mechanical transducers, such as electromagnetics, electrostatics, electrokinetics, piezoelectrics or triboelectrics [232–238]. However, these energy generators are efficient in collecting mechanical/vibrational energy at a relatively high frequency (>20 Hz) while dramatically compromising their energy harvesting performance with reduced operating frequency (<1 Hz), where most unused natural mechanical energy or human motion takes place. Ionic transducers can be soft and provide durable energy as well as sensitive in low frequencies, where electricity generation is based on ionic transport and conduction.

We mentioned ionic polymer metal composites (IPMCs) as sensors in **Section 3.1**, but with mechano-electric characteristics, high compliance and wet environment compatibility, they are also frequently applied to energy harvesting in underwater applications. Therefore, IPMCs have been used to harvest energy from base excitation [239], the flutter induced vibration of a heavy flag [240], hydroelastic impact under impulsive loading [241], fluid-induced mechanical buckling [242], hydrodynamic coupling between arrays of IPMC strip [243], fluid-structure interactions from a miniaturized turbine [244], and vibration of a biomimetic tail [245]. The harvested power ranged from 10^{-2} W to 10^{-9} W for centimeter-scale systems while the performance was heavily determined by the energy exchange between the coherent fluid structure, like vortex rings and pairs, and IPMCs [246]. This is shown in **Figure 8D** and **Supplementary Video S1**.

Other types of mechanical energy harvesters operative in a low frequency regime utilize different materials and mechanisms. Kim et al. [247] utilized electrochemically active materials to realize stress-composition coupling, where lithium ions migrating across an electrolyte membrane (microporous polypropylene monolayer soaked with electrolyte) under a bending-induced pressure difference drive electron flow in the outer circuit. Energy can also be harvested by cyclically changing the surface area and capacitance of ionic interfaces. Harvesting energy from electrode–ionic-conductor interfaces has been demonstrated [248, 249]. By using a polycation-polyanion interface instead, one can take advantage of the rectification behavior of the interface, creating DC currents from AC mechanical inputs [143, 250]. Hou et al. [250] proposed a flexible ionic diode that is an organic p-n junction with asymmetric ionic liquid/ionomer and multi-walled carbon nanotube incorporated into the matrix. The equilibrium of the p-n junction can be disrupted upon mechanical stimuli, producing a power density of 2 μWcm^{-3} at a frequency of 0.1 Hz.

Ionic triboelectric nanogenerators (TENG) harvest energy based on contact electrification and electrostatic induction [251–253]. Pu et al. created a skin-like TENG with PAAm-LiCl hydrogel as ionic conductor, realizing high stretchability and transparency as well as a maximum power density of 3.5 μWcm^{-2} [252]. Hwang et al. developed an ion-pump based TENG (iTENG), where the capacitance of the device changed with increasing number of free ions under pressure [253, 254]. The maximum power density achieved by a single iTENG is 2.2 Wcm^{-2}. Although the mechanisms governing ionic TENG are still somewhat debated, they are typically understood and modeled in terms of ion transfer from differential surface affinity of unbound anions and cations, assymetrical separation of water, and mechanochemical generation of ions and radicals [255–260]. Density functional theory is a particularly powerful approach for computationally investigating these mechanisms. The output performances of ionic TENGs could be further enhanced by maximizing the surface area, therefore maximizing the surface electrostatic charge density through surface treatments and modifications, or by increasing the dielectric permittivity through material optimization combining polymers with graphene sheets, graphite particles, and high-dielectric nanoparticles.

3.4.4 Ionic Thermoelectrics

Thermoelectric (TE) devices generate current from an applied temperature gradient, allowing for the re-conversion of waste heat to usable energy. Fundamental to these devices is the Seebeck effect, where a voltage is generated given a temperature gradient. The maximum efficiency of a TE material is determined by its figure of merit ZT:

$$ZT = \frac{S^2\sigma}{\kappa}T, \tag{11}$$

where κ is the thermal conductivity in W/mK, S is the Seebeck coefficient in V/K, σ is the electrical conductivity in S/m, and T is the temperature in Kelvin. The Seebeck effect is caused by the thermal diffusion of charge carriers. In traditional TE materials, the charge carriers are electrons or holes. Recently, ionic TE materials have gained interest, in which ions serve as a significant charge carrier. The ionic contribution to the Seebeck coefficient can be quantified via $S_{ionic} = \frac{F}{\sigma T} z^{(i)} C^{(i)} D_T$, where D_T is the Soret thermal diffusion coefficient of the ions in m^{2}s^{-1}K^{-1} [261]. In a conventional ionic TE, the Soret effect [262] creates a voltage on top of the electronic contribution. The large Seebeck coefficients in ionic TEGs could originate from temperature-dependent dissociation of ions [263]. Unlike electrons, ions cannot pass the interface between the TE material and external electrodes. Thus, one way to utilize the Soret effect is via ionic thermoelectric supercapacitors (ITESCs) [264]. These devices could be used, for example, to harness solar energy, in which the ITESC charges via the Sun's heat during the day and discharges at night [265]. ITESCs were also found to generate a voltage from a small temperature difference, making them appealing for wearables and other low-grade heat recovery [266].

To leverage the high conductivity of electrons and high Seebeck coefficient of ions, research has been conducted on mixed ionic and electronic conductors. For example, PEDOT: PSS is known for achieving a high ZT value of 0.42 in the organic TE field [267]. The addition of sodium ions further improved ionic conductivity and Seebeck coefficients [268]. Higher humidity is beneficial because water molecules weaken electrostatic potential traps created by anions [268]. Ionics and electronic conductivities could be simultaneously enhanced by altering oxygen positions on polymer side chains [269]. Additionally, the Seebeck coefficient was improved in various ways, including type II cellulose ionic conductors associated with high Na + selectivity [270], a gelatin matrix modified with added ion providers and redox couple species [271], an ionogel composed of ionic liquids and PVDF-HFP [272], and a low-cost ambipolar ionic polymer gel [273].

Despite recent work, a gap persists with respect to understanding the thermodynamics governing ionic thermodiffusion, making predictions of material performance difficult [265]. Furthermore, it is challenging to operate a purely ionic TEG in continuous mode.

4 DISCUSSION

Ionic devices and components have seen significant progress in the past 10 years. Here we discuss what they can enable and where we see opportunities for improvement.

Ideally, ionic devices should not be limited by a requirement to interface with traditional electronics. Much existing research involves tethering ionic devices to computers and power supplies that provide power and analyze the signals. While this approach is sufficient for characterizing single component performance in the lab, it has two problems in the context of ionic devices: 1) the devices are not tested with the boundary conditions they will experience when combined, and 2) it restricts the application of the devices to those where external computer connections are possible. As such, more development is needed to develop testing techniques that impose boundary conditions that components would experience within larger ionic circuits.

Some researchers have approached this challenge by using one ionic component to test the performance of another, while others seek to verify that performance in the context of a larger system. In that first category, Han et al combined a reverse electrodialysis energy source with hydrogel wires and a type III polyelectrolyte diode to make a complete circuit. This allowed them to characterize the diode behavior under DC ion current, in contrast with the AC methods popular with electrode boundary conditions [274]. In the second category we have logic gates. They are similar in architecture to traditional semiconductor diode based logic gates. Logic devices of up to three components have been experimentally realized in a few different architectures [171, 174, 177, 275].

Ionic devices are often conceptualized by analogy with traditional semiconductors. While this works well for many designs, there are a couple of key differences between ionic and electronic devices that will only become more relevant as more complicated circuits are created. First there are differences in scale. Ionics have conductivities on par with doped semiconductors, but even the best ionic conductors are many orders of magnitude higher resistance than metal wires (10 vs. 10^6 $\mathrm{Sm^{-1}}$). The carrier concentrations required to reach these modest conductivities result in characteristic length scales for ionics that are much smaller than their semiconductor equivalents. As mentioned in **Section 2.2**, the Debye-Hückel length for these systems is on the order of nano-meters while for semiconductors it is on the order of microns. This places strong limits on the behavior of junction-based devices like JFETs. These differences in scale are supplemented by differences in kind. For example, ionic devices are capable of simultaneously containing multiple charge carriers. This, combined with the fact that most charge carriers used are non-annihilating, means that the design space for ionic devices is both different and broader than traditional semiconductors. This benefit also has consequences for how ionic devices can be combined together. Many devices rely on specific ions in order to function well. This means that many components cannot be directly connected with one another. If that was tried, then the function of the components would change over time as the individual ions mixed together. In general, the long term functioning of a device is jeopardized if the thermodynamic equilibrium of each component is not the same as the operating condition of the device. For example, type I diodes that rely on the mixing of an acid and a base solution are difficult to integrate into a larger device both because they require something to regenerate that acid and base solution, and because the extreme pHs constrain the other connected ionic components.

The field also currently lacks, as far as we are aware, standardized metrics for comparing ionic devices against each other. This leads to a wide variety of device analyses, with little directly comparable performance. Selection of centralized metrics would be aided by more research and analysis of what are currently the critical bottlenecks in performance. These may be significantly different from those present when the ionic devices are used as part of a larger electronic system. For example, thermoionic power systems and diodes are limited by the interfacial capacitance when connected to electrical conductors [142, 261], but this bottleneck might disappear when they are used in ionic circuits because there is no electrode to saturate.

Further, we need better modelling and design methods if we are to invent more complex ionic circuits. Current approaches rely heavily on finite element solutions to the full continuum equations of state. This works well for individual components, but will likely have trouble scaling to simulate larger circuits that involve of many junctions. Computational approaches in general, while not the focus of this review paper, have proved rather difficult because of the large spread in length and time scales of the various effects at play in an ionic device.

5 CONCLUSION

This review paper discussed the current state and potential of soft ionic materials in the context of stretchable fully ionic devices. Soft ionics are poised to play a key role in a new era of biocompatible medical devices, fully soft robots, and novel signal processing systems. Many of the elements needed for these devices have already been developed—energy converters/harvesters, sensors, actuators, signal transmitters, capacitors, diodes, and transistors—but have not been designed for interacting with other ionic elements. Designing elements with device integration in mind, standardization of performance metrics, and expansion of system level modeling approaches will enable these devices to reach their potential.

AUTHOR CONTRIBUTIONS

MT, NB, and MS contributed to conceptualization. MT, NB, XZ, SK, and MS contributed to visualization. All authors contributed to writing - original draft and writing - review and editing. MS and ZT were responsible for funding acquisition.

FUNDING

The authors acknowledge the support through Defense Advanced Research Project Agency Young Faculty Award (DARPA YFA; HR00112010004). SK and ZT acknowledge the Academic Venture Fund from Cornell Atkinson Center for Sustainability.

SUPPLEMENTARY MATERIAL

The Supplementary Material for this article can be found online at: https://www.frontiersin.org/articles/10.3389/fphy.2022.890845/full#supplementary-material

REFERENCES

1. Keplinger C, Sun J-Y, Foo CC, Rothemund P, Whitesides GM, Suo Z. Stretchable, Transparent, Ionic Conductors. *Science* (2013) 341:984–7. doi:10.1126/science.1240228
2. El-Atab N, Mishra RB, Al-Modaf F, Joharji L, Alsharif AA, Alamoudi H, et al. Soft Actuators for Soft Robotic Applications: A Review. *Adv Intell Syst* (2020) 2:2000128. doi:10.1002/aisy.202000128
3. Zhao G, Lv B, Wang H, Yang B, Li Z, Junfang R, et al. Ionogel-based Flexible Stress and Strain Sensors. *Int J Smart Nano Mater* (2021) 12:307–36. doi:10.1080/19475411.2021.1958085
4. Flory PJ. *Principles of Polymer Chemistry*. Cornell University Press (1953). Google-Books-ID: CQ0EbEkT5R0C.
5. Buenger D, Topuz F, Groll J. Hydrogels in Sensing Applications. *Prog Polym Sci* (2012) 37:1678–719. doi:10.1016/j.progpolymsci.2012.09.001
6. Liu X, Liu J, Lin S, Zhao X. Hydrogel Machines. *Mater Today* (2020) 36:102–24. doi:10.1016/j.mattod.2019.12.026
7. Chester SA, Anand L. A Coupled Theory of Fluid Permeation and Large Deformations for Elastomeric Materials. *J Mech Phys Sol* (2010) 58:1879–906. doi:10.1016/j.jmps.2010.07.020
8. Liu Z, Toh W, Ng TY. Advances in Mechanics of Soft Materials: A Review of Large Deformation Behavior of Hydrogels. *Int J Appl Mech* (2015) 07:1530001. doi:10.1142/S1758825115300011
9. Lei J, Li Z, Xu S, Liu Z. Recent Advances of Hydrogel Network Models for Studies on Mechanical Behaviors. *Acta Mech Sin* (2021) 37:367–86. doi:10.1007/s10409-021-01058-2
10. Boyce MC. Direct Comparison of the Gent and the Arruda-Boyce Constitutive Models of Rubber Elasticity. *Rubber Chem Tech* (1996) 69:781–5. doi:10.5254/1.3538401
11. Wang M, Zhang P, Shamsi M, Thelen JL, Qian W, Truong VK, et al. Tough and Stretchable Ionogels by *In Situ* Phase Separation. *Nat Mater* (2022) 21:359–65. doi:10.1038/s41563-022-01195-4
12. Sun J-Y, Zhao X, Illeperuma WRK, Chaudhuri O, Oh KH, Mooney DJ, et al. Highly Stretchable and Tough Hydrogels. *Nature* (2012) 489:133–6. doi:10.1038/nature11409
13. Gong JP. Why Are Double Network Hydrogels So Tough? *Soft Matter* (2010) 6:2583–90. doi:10.1039/B924290B
14. Liu Y, He W, Zhang Z, Lee B. Recent Developments in Tough Hydrogels for Biomedical Applications. *Gels* (2018) 4:46. doi:10.3390/gels4020046
15. Chen Q, Chen H, Zhu L, Zheng J. Engineering of Tough Double Network Hydrogels. *Macromol Chem Phys* (2016) 217:1022–36. doi:10.1002/macp.201600038
16. Zhang L, Brostowitz NR, Cavicchi KA, Weiss RA. Perspective: Ionomer Research and Applications. *Macromol React Eng* (2014) 8:81–99. doi:10.1002/mren.201300181
17. Sarkar S, SenGupta AK, Prakash P. The Donnan Membrane Principle: Opportunities for Sustainable Engineered Processes and Materials. *Environ Sci Technol* (2010) 44:1161–6. doi:10.1021/es9024029
18. Donnan FG. Theory of Membrane Equilibria and Membrane Potentials in the Presence of Non-dialysing Electrolytes. A Contribution to Physical-Chemical Physiology. *J Membr Sci* (1995) 100:45–55. doi:10.1016/0376-7388(94)00297-c
19. Duncan AJ, Akle BJ, Long TE, Leo DJ. Ionomer Design for Augmented Charge Transport in Novel Ionic Polymer Transducers. *Smart Mater Struct* (2009) 18:104005. doi:10.1088/0964-1726/18/10/104005
20. Hong W, Zhao X, Suo Z. Large Deformation and Electrochemistry of Polyelectrolyte Gels. *J Mech Phys Sol* (2010) 58:558–77. doi:10.1016/j.jmps.2010.01.005
21. Wallmersperger T, Kröplin B, Gülch RW. Coupled Chemo-Electro-Mechanical Formulation for Ionic Polymer Gels-Nnumerical and Experimental Investigations. *Mech Mater* (2004) 36:411–20. doi:10.1016/s0167-6636(03)00068-1
22. Suo Z. Theory of Dielectric Elastomers. *Acta Mechanica Solida Sinica* (2010) 23:549–78. doi:10.1016/s0894-9166(11)60004-9
23. Henann DL, Chester SA, Bertoldi K. Modeling of Dielectric Elastomers: Design of Actuators and Energy Harvesting Devices. *J Mech Phys Sol* (2013) 61:2047–66. doi:10.1016/j.jmps.2013.05.003
24. *Basics of Measuring the Dielectric Properties of Materials* (Keysight Technologies). *Keysight Application Note 5989-2589* (2020).
25. Narayan S, Stewart EM, Anand L. Coupled Electro-Chemo-Elasticity: Application to Modeling the Actuation Response of Ionic Polymer-Metal Composites. *J Mech Phys Sol* (2021) 152:104394. doi:10.1016/j.jmps.2021.104394
26. Poghossian A, Abouzar MH, Schöning MJ. Capacitance-voltage and Impedance Characteristics of Field-Effect EIS Sensors Functionalised with Polyelectrolyte Multilayers. *IRBM* (2008) 29:149–54. doi:10.1016/j.rbmret.2007.11.018
27. Agmon N. The Grotthuss Mechanism. *Chem Phys Lett* (1995) 244:456–62. doi:10.1016/0009-2614(95)00905-J
28. Kreuer K-D. Proton Conductivity: Materials and Applications. *Chem Mater* (1996) 8:610–41. doi:10.1021/cm950192a
29. Cukierman S. Et Tu, Grotthuss! and Other Unfinished Stories. *Biochim Biophys Acta (Bba) - Bioenerg* (2006) 1757:876–85. doi:10.1016/j.bbabio.2005.12.001
30. Riccardi D, König P, Prat-Resina X, Yu H, Elstner M, Frauenheim T, et al. "Proton Holes" in Long-Range Proton Transfer Reactions in Solution and Enzymes: A Theoretical Analysis. *J Am Chem Soc* (2006) 128:16302–11. doi:10.1021/ja065451j
31. Deng Y, Josberger E, Jin J, Roudsari AF, Helms BA, Zhong C, et al. H+-type and OH−type Biological Protonic Semiconductors and Complementary Devices. *Sci Rep* (2013) 3:2481. doi:10.1038/srep02481
32. Miyake T, Rolandi M. Grotthuss Mechanisms: from Proton Transport in Proton Wires to Bioprotonic Devices. *J Phys Condens Matter* (2016) 28:023001. doi:10.1088/0953-8984/28/2/023001
33. Choi P, Jalani NH, Datta R. Thermodynamics and Proton Transport in Nafion. *J Electrochem Soc* (2005) 152:E123. doi:10.1149/1.1859814
34. Sanders EH, McGrady KA, Wnek GE, Edmondson CA, Mueller JM, Fontanella JJ, et al. Characterization of Electrosprayed Nafion Films. *J Power Sourc* (2004) 129:55–61. doi:10.1016/j.jpowsour.2003.11.020
35. Ochi S, Kamishima O, Mizusaki J, Kawamura J. Investigation of Proton Diffusion in Nafion117 Membrane by Electrical Conductivity and NMR. *Solid State Ionics* (2009) 180:580–4. doi:10.1016/j.ssi.2008.12.035
36. Sone Y, Ekdunge P, Simonsson D. Proton Conductivity of Nafion 117 as Measured by a Four-Electrode AC Impedance Method. *J Electrochem Soc* (1996) 143:1254–9. doi:10.1149/1.1836625
37. Berezina NP, Kononenko NA, Dyomina OA, Gnusin NP. Characterization of Ion-Exchange Membrane Materials: Properties vs Structure. *Adv Colloid Interf Sci* (2008) 139:3–28. doi:10.1016/j.cis.2008.01.002
38. Long L, Wang S, Xiao M, Meng Y. Polymer Electrolytes for Lithium Polymer Batteries. *J Mater Chem A* (2016) 4:10038–69. doi:10.1039/C6TA02621D
39. Iost RM, Crespilho FN. Layer-by-layer Self-Assembly and Electrochemistry: Applications in Biosensing and Bioelectronics. *Biosens Bioelectron* (2012) 31:1–10. doi:10.1016/j.bios.2011.10.040
40. Wu J, Yuan XZ, Martin JJ, Wang H, Zhang J, Shen J, et al. A Review of PEM Fuel Cell Durability: Degradation Mechanisms and Mitigation Strategies. *J Power Sourc* (2008) 184:104–19. doi:10.1016/j.jpowsour.2008.06.006
41. Inaba M, Kinumoto T, Kiriake M, Umebayashi R, Tasaka A, Ogumi Z. Gas Crossover and Membrane Degradation in Polymer Electrolyte Fuel Cells. *Electrochimica Acta* (2006) 51:5746–53. doi:10.1016/j.electacta.2006.03.008
42. Silberstein MN, Boyce MC. Hygro-thermal Mechanical Behavior of Nafion during Constrained Swelling. *J Power Sourc* (2011) 196:3452–60. doi:10.1016/j.jpowsour.2010.11.116
43. Farhat TR, Hammond PT. Designing a New Generation of Proton-Exchange Membranes Using Layer-By-Layer Deposition of Polyelectrolytes. *Adv Funct Mater* (2005) 15:945–54. doi:10.1002/adfm.200400318
44. Argun AA, Ashcraft JN, Hammond PT. Highly Conductive, Methanol Resistant Polyelectrolyte Multilayers. *Adv Mater* (2008) 20:1539–43. doi:10.1002/adma.200703205
45. Liu DS, Ashcraft JN, Mannarino MM, Silberstein MN, Argun AA, Rutledge GC, et al. Spray Layer-By-Layer Electrospun Composite Proton Exchange Membranes. *Adv Funct Mater* (2013) 23:3087–95. doi:10.1002/adfm.201202892
46. Ding Y, Zhang J, Chang L, Zhang X, Liu H, Jiang L. Preparation of High-Performance Ionogels with Excellent Transparency, Good Mechanical

Strength, and High Conductivity. *Adv Mater* (2017) 29:1704253. doi:10.1002/adma.201704253

47. Wu Y, Joseph S, Aluru NR. Effect of Cross-Linking on the Diffusion of Water, Ions, and Small Molecules in Hydrogels. *J Phys Chem B* (2009) 113:3512–20. doi:10.1021/jp808145x
48. Yang CH, Chen B, Lu JJ, Yang JH, Zhou J, Chen YM, et al. Ionic cable. *Extreme Mech Lett* (2015) 3:59–65. doi:10.1016/j.eml.2015.03.001
49. Chen B, Lu JJ, Yang CH, Yang JH, Zhou J, Chen YM, et al. Highly Stretchable and Transparent Ionogels as Nonvolatile Conductors for Dielectric Elastomer Transducers. *ACS Appl Mater Inter* (2014) 6:7840–5. doi:10.1021/am501130t
50. Ming X, Zhang C, Cai J, Zhu H, Zhang Q, Zhu S. Highly Transparent, Stretchable, and Conducting Ionoelastomers Based on Poly(ionic Liquid)s. *ACS Appl Mater Inter* (2021) 13:31102–10. doi:10.1021/acsami.1c05833
51. Shi L, Jia K, Gao Y, Yang H, Ma Y, Lu S, et al. Highly Stretchable and Transparent Ionic Conductor with Novel Hydrophobicity and Extreme-Temperature Tolerance. *Research* (2020) 2020:1–10. doi:10.34133/2020/2505619
52. Cao Y, Morrissey TG, Acome E, Allec SI, Wong BM, Keplinger C, et al. A Transparent, Self-Healing, Highly Stretchable Ionic Conductor. *Adv Mater* (2017) 29:1605099. doi:10.1002/adma.201605099
53. Li Ra., Fan T, Chen G, Zhang K, Su B, Tian J, et al. Autonomous Self-Healing, Antifreezing, and Transparent Conductive Elastomers. *Chem Mater* (2020) 32:874–81. doi:10.1021/acs.chemmater.9b04592
54. Zhao J, Gong J, Wang G, Zhu K, Ye K, Yan J, et al. A Self-Healing Hydrogel Electrolyte for Flexible Solid-State Supercapacitors. *Chem Eng J* (2020) 401:125456. doi:10.1016/j.cej.2020.125456
55. Lieleg O, Ribbeck K. Biological Hydrogels as Selective Diffusion Barriers. *Trends Cel Biol* (2011) 21:543–51. doi:10.1016/j.tcb.2011.06.002
56. Cheng C, Yaroshchuk A, Bruening ML. Fundamentals of Selective Ion Transport through Multilayer Polyelectrolyte Membranes. *Langmuir* (2013) 29:1885–92. doi:10.1021/la304574e
57. Farhat TR, Schlenoff JB. Ion Transport and Equilibria in Polyelectrolyte Multilayers. *Langmuir* (2001) 17:1184–92. doi:10.1021/la001298+
58. Cheng W, Liu C, Tong T, Epsztein R, Sun M, Verduzco R, et al. Selective Removal of Divalent Cations by Polyelectrolyte Multilayer Nanofiltration Membrane: Role of Polyelectrolyte Charge, Ion Size, and Ionic Strength. *J Membr Sci* (2018) 559:98–106. doi:10.1016/j.memsci.2018.04.052
59. Femmer R, Mani A, Wessling M. Ion Transport through Electrolyte/polyelectrolyte Multi-Layers. *Sci Rep* (2015) 5:11583. doi:10.1038/srep11583
60. Dykstra JE, Biesheuvel PM, Bruning H, Ter Heijne A. Theory of Ion Transport with Fast Acid-Base Equilibrations in Bioelectrochemical Systems. *Phys Rev E* (2014) 90:013302. doi:10.1103/PhysRevE.90.013302
61. Tang Y, Chen C, Ye YS, Xue Z, Zhou X, Xie X. The Enhanced Actuation Response of an Ionic Polymer-Metal Composite Actuator Based on Sulfonated Polyphenylsulfone. *Polym Chem* (2014) 5:6097–107. doi:10.1039/C4PY00663A
62. Morales D, Palleau E, Dickey MD, Velev OD. Electro-actuated Hydrogel Walkers with Dual Responsive Legs. *Soft Matter* (2014) 10:1337–48. doi:10.1039/C3SM51921J
63. Jin ML, Park S, Kim J-S, Kwon SH, Zhang S, Yoo MS, et al. An Ultrastable Ionic Chemiresistor Skin with an Intrinsically Stretchable Polymer Electrolyte. *Adv Mater* (2018) 30:1706851. doi:10.1002/adma.201706851
64. Kim CC, Lee HH, Oh KH, Sun JY. Highly Stretchable, Transparent Ionic Touch Panel. *Science* (2016) 353:682. doi:10.1126/science.aaf8810
65. Lee H-R, Kim C-C, Sun J-Y. Stretchable Ionics - A Promising Candidate for Upcoming Wearable Devices. *Adv Mater* (2018) 30:1704403. doi:10.1002/adma.201704403
66. Bar-Cohen Y, Anderson IA. Electroactive Polymer (EAP) Actuators-Background Review. *Mech Soft Mater* (2019) 1:5. doi:10.1007/s42558-019-0005-1
67. Melling D, Martinez JG, Jager EWH. Conjugated Polymer Actuators and Devices: Progress and Opportunities. *Adv Mater* (2019) 31:1808210. doi:10.1002/adma.201808210
68. Majidi C. Soft-Matter Engineering for Soft Robotics. *Adv Mater Tech* (2019) 4:1800477. doi:10.1002/admt.201800477
69. Kim J, Kim JW, Kim HC, Zhai L, Ko H-U, Muthoka RM. Review of Soft Actuator Materials. *Int J Precis Eng Manuf* (2019) 20:2221–41. doi:10.1007/s12541-019-00255-1
70. Hajiesmaili E, Clarke DR. Dielectric Elastomer Actuators. *J Appl Phys* (2021) 129:151102. doi:10.1063/5.0043959
71. Guo Y, Liu L, Liu Y, Leng J. Review of Dielectric Elastomer Actuators and Their Applications in Soft Robots. *Adv Intell Syst* (2021) 3:2000282. doi:10.1002/aisy.202000282
72. Feng C, Hemantha Rajapaksha CP, Jákli A. Ionic Elastomers for Electric Actuators and Sensors. *Engineering* (2021) 7:581–602. doi:10.1016/j.eng.2021.02.014
73. Zou M, Li S, Hu X, Leng X, Wang R, Zhou X, et al. Progresses in Tensile, Torsional, and Multifunctional Soft Actuators. *Adv Funct Mater* (2021) 31:2007437. doi:10.1002/adfm.202007437
74. Kim KJ, Shahinpoor M. Ionic Polymer Metal Composites: II. Manufacturing Techniques. *Smart Mater Struct* (2003) 12:65–79. doi:10.1088/0964-1726/12/1/308
75. Oguro K. Bending of an Ion-Conducting Polymer Film-Electrode Composite by an Electric Stimulus at Low Voltage. *J Micromachine Soc* (1992) 5:27–30.
76. Shahinpoor M. Conceptual Design, Kinematics and Dynamics of Swimming Robotic Structures Using Ionic Polymeric Gel Muscles. *Smart Mater Struct* (1992) 1:91–4. doi:10.1088/0964-1726/1/1/014
77. Sadeghipour K, Salomon R, Neogi S. Development of a Novel Electrochemically Active Membrane and 'smart' Material Based Vibration Sensor/damper. *Smart Mater Struct* (1992) 1:172–9. doi:10.1088/0964-1726/1/2/012
78. Hao M, Wang Y, Zhu Z, He Q, Zhu D, Luo M. A Compact Review of IPMC as Soft Actuator and Sensor: Current Trends, Challenges, and Potential Solutions from Our Recent Work. *Front Robot AI* (2019) 6:129. doi:10.3389/frobt.2019.00129
79. MohdIsa W, Hunt A, HosseinNia SH. Sensing and Self-Sensing Actuation Methods for Ionic Polymer-Metal Composite (IPMC): A Review. *Sensors* (2019) 19:3967. doi:10.3390/s19183967
80. Shahinpoor M, Bar-Cohen Y, Xue T, Harrison JS, Smith JG. *Some Experimental Results on Ionic Polymer-Metal Composites (IPMC) as Biomimetic Sensors and Actuators*. San Diego, CA (1998). p. 251. doi:10.1117/12.316870
81. Konyo M, Konishi Y, Tadokoro S, Kishima T. *Development of Velocity Sensor Using Ionic Polymer-Metal Composites*. San Diego, CA (2004). p. 307. doi:10.1117/12.540266
82. Wang J, Wang Y, Zhu Z, Wang J, He Q, Luo M. The Effects of Dimensions on the Deformation Sensing Performance of Ionic Polymer-Metal Composites. *Sensors* (2019) 19:2104. doi:10.3390/s19092104
83. Nemat-Nasser S, Li JY. Electromechanical Response of Ionic Polymer-Metal Composites. *J Appl Phys* (2000) 87:3321–31. doi:10.1063/1.372343
84. López-Díaz A, Martín-Pacheco A, Rodríguez AM, Herrero MA, Vázquez AS, Vázquez E. Concentration Gradient-Based Soft Robotics: Hydrogels Out of Water. *Adv Funct Mater* (2020) 30:2004417. doi:10.1002/adfm.202004417
85. White BT, Long TE. Advances in Polymeric Materials for Electromechanical Devices. *Macromol Rapid Commun* (2019) 40:1800521. doi:10.1002/marc.201800521
86. Liu X, He B, Wang Z, Tang H, Su T, Wang Q. Tough Nanocomposite Ionogel-Based Actuator Exhibits Robust Performance. *Sci Rep* (2014) 4:6673. doi:10.1038/srep06673
87. Kim O, Kim SY, Park B, Hwang W, Park MJ. Factors Affecting Electromechanical Properties of Ionic Polymer Actuators Based on Ionic Liquid-Containing Sulfonated Block Copolymers. *Macromolecules* (2014) 47:4357–68. doi:10.1021/ma500869h
88. Albehaijan HA, Piedrahita CR, Cao J, Soliman M, Mitra S, Kyu T. Mechanoelectrical Transduction of Polymer Electrolyte Membranes: Effect of Branched Networks. *ACS Appl Mater Inter* (2020) 12:7518–28. doi:10.1021/acsami.9b15599
89. Piedrahita CR, Yue P, Cao J, Lee H, Rajapaksha CP, Feng C, et al. Flexoelectricity in Flexoionic Polymer Electrolyte Membranes: Effect of Thiosiloxane Modification on Poly(ethylene Glycol) Diacrylate and Ionic Liquid Electrolyte Composites. *ACS Appl Mater Inter* (2020) 12:16978–86. doi:10.1021/acsami.0c02328
90. Wang Y, Zhu Z, Liu J, Chang L, Chen H. Effects of Surface Roughening of Nafion 117 on the Mechanical and Physicochemical Properties of Ionic Polymer-Metal Composite (IPMC) Actuators. *Smart Mater Struct* (2016) 25:085012. doi:10.1088/0964-1726/25/8/085012

91. He Q, Yu M, Song L, Ding H, Zhang X, Dai Z. Experimental Study and Model Analysis of the Performance of IPMC Membranes with Various Thickness. *J Bionic Eng* (2011) 8:77–85. doi:10.1016/S1672-6529(11)60001-2
92. Kim K, Shahinpoor M. A Novel Method of Manufacturing Three-Dimensional Ionic Polymer-Metal Composites (IPMCs) Biomimetic Sensors, Actuators and Artificial Muscles. *Polymer* (2002) 43:797–802. doi:10.1016/S0032-3861(01)00648-6
93. Bahramzadeh Y, Shahinpoor M. A Review of Ionic Polymeric Soft Actuators and Sensors. *Soft Robotics* (2014) 1:38–52. doi:10.1089/soro.2013.0006
94. Buechler MA, Leo DJ. Characterization and Variational Modeling of Ionic Polymer Transducers. *J Vibration Acoust* (2007) 129:113–20. doi:10.1115/1.2424973
95. Aureli M, Porfiri M. Nonlinear Sensing of Ionic Polymer Metal Composites. *Continuum Mech Thermodyn* (2013) 25:273–310. doi:10.1007/s00161-012-0253-x
96. Nardinocchi P, Pezzulla M, Placidi L. Thermodynamically Based Multiphysic Modeling of Ionic Polymer Metal Composites. *J Intell Mater Syst Structures* (2011) 22:1887–97. doi:10.1177/1045389X11417195
97. Wallmersperger T, Horstmann A, Kroplin B, Leo DJ. Thermodynamical Modeling of the Electromechanical Behavior of Ionic Polymer Metal Composites. *J Intell Mater Syst Structures* (2009) 20:741–50. doi:10.1177/1045389X08096356
98. Nemat-Nasser S. Micromechanics of Actuation of Ionic Polymer-Metal Composites. *J Appl Phys* (2002) 92:2899–915. doi:10.1063/1.1495888
99. Cha Y, Porfiri M. Mechanics and Electrochemistry of Ionic Polymer Metal Composites. *J Mech Phys Sol* (2014) 71:156–78. doi:10.1016/j.jmps.2014.07.006
100. Galante S, Lucantonio A, Nardinocchi P. The Multiplicative Decomposition of the Deformation Gradient in the Multiphysics Modeling of Ionic Polymers. *Int J Non-Linear Mech* (2013) 51:112–20. doi:10.1016/j.ijnonlinmec.2013.01.005
101. Newbury KM, Leo DJ. Electromechanical Modeling and Characterization of Ionic Polymer Benders. *J Intell Mater Syst Structures* (2002) 13:51–60. doi:10.1177/1045389X02013001978
102. Newbury KM, Leo DJ. Linear Electromechanical Model of Ionic Polymer Transducers -Part I: Model Development. *J Intell Mater Syst Structures* (2003) 14:333–42. doi:10.1177/1045389X03034976
103. Park K, Lee H-K. Evaluation of Circuit Models for an IPMC (Ionic Polymer-Metal Composite) Sensor Using a Parameter Estimate Method. *J Korean Phys Soc* (2012) 60:821–9. doi:10.3938/jkps.60.821
104. Qaviandam Z, Naghavi N, Safaie J. A New Approach to Improve IPMC Performance for Sensing Dynamic Deflection: Sensor Biasing. *IEEE Sensors J* (2020) 20:8614–22. doi:10.1109/JSEN.2020.2986091
105. Glazer PJ, van Erp M, Embrechts A, Lemay SG, Mendes E. Role of pH Gradients in the Actuation of Electro-Responsive Polyelectrolyte Gels. *Soft Matter* (2012) 8:4421–6. doi:10.1039/C2SM07435D
106. Doi M, Matsumoto M, Hirose Y. Deformation of Ionic Polymer Gels by Electric fields. *Macromolecules* (1992) 25:5504–11. doi:10.1021/ma00046a058
107. Hamlen RP, Kent CE, Shafer SN. Electrolytically Activated Contractile Polymer. *Nature* (1965) 206:1149–50. doi:10.1038/2061149b0
108. Osada Y, Okuzaki H, Hori H. A Polymer Gel with Electrically Driven Motility. *Nature* (1992) 355:242–4. doi:10.1038/355242a0
109. Tanaka T, Nishio I, Sun ST, Ueno-Nishio S. Collapse of Gels in an Electric Field. *Science* (1982) 218:467. doi:10.1126/science.218.4571.467
110. Shiga T, Kurauchi T. Bneding of Polyacrylic Acid Gel in Elec-Tnc Fields. *Polym Preprints Jpn* (1985) 34:509.
111. Shiga T. Deformation and Viscoelastic Behavior of Polymer Gels in Electric fields. *Adv Polym Sci* (1997) 134:133. doi:10.1007/3-540-68449-2_2
112. Osada Y, Gong J-P. Soft and Wet Materials: Polymer Gels. *Adv Mater* (1998) 10:827–37. doi:10.1002/(sici)1521-4095(199808)10:11<827::aid-adma827>3.0.co;2-l
113. Kim SJ, Kim HI, Park SJ, Kim IY, Lee SH, Lee TS, et al. Behavior in Electric fields of Smart Hydrogels with Potential Application as Bio-Inspired Actuators. *Smart Mater Struct* (2005) 14:511–4. doi:10.1088/0964-1726/14/4/008
114. Safronov AP, Shakhnovich M, Kalganov A, Kamalov IA, Shklyar TF, Blyakhman FA, et al. DC Electric fields Produce Periodic Bending of Polyelectrolyte Gels. *Polymer* (2011) 52:2430–6. doi:10.1016/j.polymer.2011.03.048
115. Jabbari E, Tavakoli J, Sarvestani AS. Swelling Characteristics of Acrylic Acid Polyelectrolyte Hydrogel in a Dc Electric Field. *Smart Mater Struct* (2007) 16:1614–20. doi:10.1088/0964-1726/16/5/015
116. Jackson N, Stam F. Optimization of Electrical Stimulation Parameters for Electro-Responsive Hydrogels for Biomedical Applications. *J Appl Polym Sci* (2015) 132. doi:10.1002/app.41687
117. Segalman DJ, Witkowski WR, Adolf DB, Shahinpoor M. Theory and Application of Electrically Controlled Polymeric Gels. *Smart Mater Struct* (1992) 1:95–100. doi:10.1088/0964-1726/1/1/015
118. Attaran A, Brummund J, Wallmersperger T. Modeling and Simulation of the Bending Behavior of Electrically-Stimulated Cantilevered Hydrogels. *Smart Mater Struct* (2015) 24:035021. doi:10.1088/0964-1726/24/3/035021
119. Attaran A, Keller K, Wallmersperger T. Modeling and Simulation of Hydrogels for the Application as finger Grippers. *J Intell Mater Syst Structures* (2018) 29:371–87. doi:10.1177/1045389X17708040
120. Leichsenring P, Wallmersperger T. Time-dependent Chemo-Electro-Mechanical Behavior of Hydrogel-Based Structures. In: HE Naguib, editor. *Behavior and Mechanics of Multifunctional Materials and Composites XII*. Denver, United States: SPIE (2018). p. 55. doi:10.1117/12.2297693
121. Migliorini L, Santaniello T, Yan Y, Lenardi C, Milani P. Low-voltage Electrically Driven Homeostatic Hydrogel-Based Actuators for Underwater Soft Robotics. *Sensors Actuators B: Chem* (2016) 228:758–66. doi:10.1016/j.snb.2016.01.110
122. Engel L, Berkh O, Adesanya K, Shklovsky J, Vanderleyden E, Dubruel P, et al. Actuation of a Novel Pluronic-Based Hydrogel: Electromechanical Response and the Role of Applied Current. *Sensors Actuators B: Chem* (2014) 191:650–8. doi:10.1016/j.snb.2013.10.031
123. Liu Q, Dong Z, Ding Z, Hu Z, Yu D, Hu Y, et al. Electroresponsive Homogeneous Polyelectrolyte Complex Hydrogels from Naturally Derived Polysaccharides. *ACS Sust Chem. Eng.* (2018) 6:7052–63. doi:10.1021/acssuschemeng.8b00921
124. Yang S, Liu G, Cheng Y, Zheng Y. Electroresponsive Behavior of Sodium Alginate-G-Poly (Acrylic Acid) Hydrogel under DC Electric Field. *J Macromolecular Sci A* (2009) 46:1078–82. doi:10.1080/10601320903245433
125. Yang S, Liu G, Wang X, Song J. Electroresponsive Behavior of a Sulfonated Poly(vinyl Alcohol) Hydrogel and its Application to Electrodriven Artificial Fish. *J Appl Polym Sci* (2010) 117:2346–53. doi:10.1002/app.32069
126. Yang S, Liu G, Xu F. Electroresponsive Behavior of Sulfonated Benzal Poly(vinyl Alcohol) Hydrogel under Direct-Current Electric Field. *J Macromolecular Sci Part A* (2011) 48:198–203. doi:10.1080/10601325.2011.544629
127. Han D, Farino C, Yang C, Scott T, Browe D, Choi W, et al. Soft Robotic Manipulation and Locomotion with a 3D Printed Electroactive Hydrogel. *ACS Appl Mater Inter* (2018) 10:17512–8. doi:10.1021/acsami.8b04250
128. Cao Z, Liu H, Jiang L. Transparent, Mechanically Robust, and Ultrastable Ionogels Enabled by Hydrogen Bonding between Elastomers and Ionic Liquids. *Mater Horiz* (2020) 7:912–8. doi:10.1039/C9MH01699F
129. Liu S, Li L. Ultrastretchable and Self-Healing Double-Network Hydrogel for 3D Printing and Strain Sensor. *ACS Appl Mater Inter* (2017) 9:26429–37. doi:10.1021/acsami.7b07445
130. Qiao H, Qi P, Zhang X, Wang L, Tan Y, Luan Z, et al. Multiple Weak H-Bonds Lead to Highly Sensitive, Stretchable, Self-Adhesive, and Self-Healing Ionic Sensors. *ACS Appl Mater Inter* (2019) 11:7755–63. doi:10.1021/acsami.8b20380
131. Lai J, Zhou H, Jin Z, Li S, Liu H, Jin X, et al. Highly Stretchable, Fatigue-Resistant, Electrically Conductive, and Temperature-Tolerant Ionogels for High-Performance Flexible Sensors. *ACS Appl Mater Inter* (2019) 11:26412–20. doi:10.1021/acsami.9b10146
132. Wang S, Sun Z, Zhao Y, Zuo L. A Highly Stretchable Hydrogel Sensor for Soft Robot Multi-Modal Perception. *Sensors Actuators A: Phys* (2021) 331:113006. doi:10.1016/j.sna.2021.113006
133. Zhang X, Sheng N, Wang L, Tan Y, Liu C, Xia Y, et al. Supramolecular Nanofibrillar Hydrogels as Highly Stretchable, Elastic and Sensitive Ionic Sensors. *Mater Horiz* (2019) 6:326–33. doi:10.1039/C8MH01188E
134. Yang MJ, Sun HM, Casalbore-Miceli G, Camaioni N, Mari C-M. Poly(propargyl Alcohol) Doped with Sulfuric Acid, a New Proton Conductor Usable for Humidity Sensor Construction. *Synth Met* (1996) 81:65–9. doi:10.1016/0379-6779(96)80230-x

135. Park S-H, Park J-S, Lee C-W, Gong M-S. Humidity Sensor Using Gel Polyelectrolyte Prepared from Mutually Reactive Copolymers. *Sensors Actuators B: Chem* (2002) 86:68–74. doi:10.1016/S0925-4005(02)00149-1
136. Lee C, Joo S, Gong M. Polymeric Humidity Sensor Using Polyelectrolytes Derived from Alkoxysilane Cross-Linker. *Sensors Actuators B: Chem* (2005) 105:150–8. doi:10.1016/S0925-4005(04)00397-1
137. Lv X, Li Y, Li P, Yang M. A Resistive-type Humidity Sensor Based on Crosslinked Polyelectrolyte Prepared by UV Irradiation. *Sensors Actuators B: Chem* (2009) 135:581–6. doi:10.1016/j.snb.2008.10.008
138. Nie H, Schauser NS, Self JL, Tabassum T, Oh S, Geng Z, et al. Light-Switchable and Self-Healable Polymer Electrolytes Based on Dynamic Diarylethene and Metal-Ion Coordination. *J Am Chem Soc* (2021) 143: 1562–9. doi:10.1021/jacs.0c11894
139. Gil-González N, Benito-Lopez F, Castaño E, Morant-Miñana MC. Imidazole-based Ionogel as Room Temperature Benzene and Formaldehyde Sensor. *Microchim Acta* (2020) 187:638. doi:10.1007/s00604-020-04625-9
140. Jiang N, Chang X, Hu D, Chen L, Wang Y, Chen J, et al. Flexible, Transparent, and Antibacterial Ionogels toward Highly Sensitive Strain and Temperature Sensors. *Chem Eng J* (2021) 424:130418. doi:10.1016/j.cej.2021.130418
141. Sun J-Y, Keplinger C, Whitesides GM, Suo Z. Ionic Skin. *Adv Mater* (2014) 26:7608–14. doi:10.1002/adma.201403441
142. Kim HJ, Chen B, Suo Z, Hayward RC. Ionoelastomer Junctions between Polymer Networks of Fixed Anions and Cations. *Science* (2020) 367:773–6. doi:10.1126/science.aay8467
143. Sarwar MS, Dobashi Y, Preston C, Wyss JKM, Mirabbasi S, Madden JDW. Bend, Stretch, and Touch: Locating a finger on an Actively Deformed Transparent Sensor Array. *Sci Adv* (2017) 3. doi:10.1126/sciadv.1602200
144. Lei Z, Wang Q, Sun S, Zhu W, Wu P. A Bioinspired Mineral Hydrogel as a Self-Healable, Mechanically Adaptable Ionic Skin for Highly Sensitive Pressure Sensing. *Adv Mater* (2017) 29:1700321. doi:10.1002/adma.201700321
145. He B, Zhou Y, Wang Z, Wang Q, Shen R, Wu S. A Multi-Layered Touch-Pressure Sensing Ionogel Material Suitable for Sensing Integrated Actuations of Soft Robots. *Sensors Actuators A: Phys* (2018) 272:341–8. doi:10.1016/j.sna.2018.01.035
146. Shen Z, Zhu X, Majidi C, Gu G. Cutaneous Ionogel Mechanoreceptors for Soft Machines, Physiological Sensing, and Amputee Prostheses. *Adv Mater* (2021) 33:2102069. doi:10.1002/adma.202102069
147. Esmaeli E, Ganjian M, Rastegar H, Kolahdouz M, Kolahdouz Z, Zhang GQ. Humidity Sensor Based on the Ionic Polymer Metal Composite. *Sensors Actuators B: Chem* (2017) 247:498–504. doi:10.1016/j.snb.2017.03.018
148. Wang Y, Tang G, Zhao C, Wang K, Wang J, Ru J, et al. Experimental Investigation on the Physical Parameters of Ionic Polymer Metal Composites Sensors for Humidity Perception. *Sensors Actuators B: Chem* (2021) 345: 130421. doi:10.1016/j.snb.2021.130421
149. Lei H, Lim C, Tan X. Humidity-dependence of IPMC Sensing Dynamics: Characterization and Modeling from a Physical Perspective. *Meccanica* (2015) 50:2663–73. doi:10.1007/s11012-015-0164-6
150. Wang Y, Jia K, Zhang S, Kim HJ, Bai Y, Hayward RC, et al. Temperature Sensing Using Junctions between mobile Ions and mobile Electrons. *Proc Natl Acad Sci* (2022) 119:e2117962119. doi:10.1073/pnas.2117962119
151. Jonsson A, Song Z, Nilsson D, Meyerson BA, Simon DT, Linderoth B, et al. Therapy Using Implanted Organic Bioelectronics. *Sci Adv* (2015) 1. doi:10.1126/sciadv.1500039
152. Sjöström TA, Jonsson A, Gabrielsson EO, Berggren M, Simon DT, Tybrandt K. Miniaturized Ionic Polarization Diodes for Neurotransmitter Release at Synaptic Speeds. *Adv Mater Technol* (2020) 5:1900750. doi:10.1002/admt.201900750
153. Gabrielsson EO, Janson P, Tybrandt K, Simon DT, Berggren M. A Four-Diode Full-Wave Ionic Current Rectifier Based on Bipolar Membranes: Overcoming the Limit of Electrode Capacity. *Adv Mater* (2014) 26: 5143–7. doi:10.1002/adma.201401258
154. Larsson KC, Kjäll P, Richter-Dahlfors A. Organic Bioelectronics for Electronic-To-Chemical Translation in Modulation of Neuronal Signaling and Machine-To-Brain Interfacing. *Biochim Biophys Acta (Bba) - Gen Subjects* (2013) 1830:4334–44. doi:10.1016/j.bbagen.2012.11.024
155. Isaksson J, Kjäll P, Nilsson D, Robinson N, Berggren M, Richter-Dahlfors A. Electronic Control of Ca2+ Signalling in Neuronal Cells Using an Organic Electronic Ion Pump. *Nat Mater* (2007) 6:673–9. doi:10.1038/nmat1963
156. Yuk H, Lu B, Zhao X. Hydrogel Bioelectronics. *Chem Soc Rev* (2019) 48: 1642–67. doi:10.1039/c8cs00595h
157. Carli S, Di Lauro M, Bianchi M, Murgia M, De Salvo A, Prato M, et al. Water-Based PEDOT:Nafion Dispersion for Organic Bioelectronics. *ACS Appl Mater Inter* (2020) 12:29807–17. doi:10.1021/acsami.0c06538
158. Vreeland RF, Atcherley CW, Russell WS, Xie JY, Lu D, Laude ND, et al. Biocompatible PEDOT:Nafion Composite Electrode Coatings for Selective Detection of Neurotransmitters *In Vivo*. *Anal Chem* (2015) 87:2600–7. doi:10.1021/ac502165f
159. Najem JS, Taylor GJ, Weiss RJ, Hasan MS, Rose G, Schuman CD, et al. Memristive Ion Channel-Doped Biomembranes as Synaptic Mimics. *ACS Nano* (2018) 12:4702–11. doi:10.1021/acsnano.8b01282
160. Zhang P, Xia M, Zhuge F, Zhou Y, Wang Z, Dong B, et al. Nanochannel-Based Transport in an Interfacial Memristor Can Emulate the Analog Weight Modulation of Synapses. *Nano Lett* (2019) 19:4279–86. doi:10.1021/acs.nanolett.9b00525
161. Liao K, Lei P, Tu M, Luo S, Jiang T, Jie W, et al. Memristor Based on Inorganic and Organic Two-Dimensional Materials: Mechanisms, Performance, and Synaptic Applications. *ACS Appl Mater Inter* (2021) 13:32606–23. doi:10.1021/acsami.1c07665
162. Koo H-J, So J-H, Dickey MD, Velev OD. Towards All-Soft Matter Circuits: Prototypes of Quasi-Liquid Devices with Memristor Characteristics. *Adv Mater* (2011) 23:3559–64. doi:10.1002/adma.201101257
163. Kim SJ, Kim S, Jang HW. Competing Memristors for Brain-Inspired Computing. *iScience* (2021) 24:101889. doi:10.1016/j.isci.2020.101889
164. Li C, Xiong T, Yu P, Fei J, Mao L. Synaptic Iontronic Devices for Brain-Mimicking Functions: Fundamentals and Applications. *ACS Appl Bio Mater* (2021) 4:71–84. doi:10.1021/acsabm.0c00806
165. Janson P, Gabrielsson EO, Lee KJ, Berggren M, Simon DT. An Ionic Capacitor for Integrated Iontronic Circuits. *Adv Mater Technol* (2019) 4: 1800494. doi:10.1002/admt.201800494
166. Martin ST, Akbari A, Chakraborty Banerjee P, Neild A, Majumder M. The Inside-Out Supercapacitor: Induced Charge Storage in Reduced Graphene Oxide. *Phys Chem Chem Phys* (2016) 18:32185–91. doi:10.1039/C6CP06463A
167. Yamamoto T, Doi M. Electrochemical Mechanism of Ion Current Rectification of Polyelectrolyte Gel Diodes. *Nat Commun* (2014) 5:4162. doi:10.1038/ncomms5162
168. Nyamayaro K, Triandafilidi V, Keyvani P, Rottler J, Mehrkhodavandi P, Hatzikiriakos SG. The Rectification Mechanism in Polyelectrolyte Gel Diodes. *Phys Fluids* (2021) 33:032010. doi:10.1063/5.0040838
169. Iván K, Simon PL, Wittmann M, Noszticzius Z. Electrolyte Diodes with Weak Acids and Bases. I. Theory and an Approximate Analytical Solution. *J Chem Phys* (2005) 123:164509. doi:10.1063/1.2085047
170. Zhao R, He G, Deng Y. Non-water Ionic Diode Based on Bias-dependent Precipitation. *Electrochemistry Commun* (2012) 23:106–9. doi:10.1016/j.elecom.2012.07.019
171. Wang Y, Wang Z, Su Z, Cai S. Stretchable and Transparent Ionic Diode and Logic gates. *Extreme Mech Lett* (2019) 28:81–6. doi:10.1016/j.eml.2019.03.001
172. Cayre OJ, Chang ST, Velev OD. Polyelectrolyte Diode: Nonlinear Current Response of a junction between Aqueous Ionic Gels. *J Am Chem Soc* (2007) 129:10801–6. doi:10.1021/ja072449z
173. Zhang Y, Jeong CK, Wang J, Chen X, Choi KH, Chen LQ, et al. Hydrogel Ionic Diodes toward Harvesting Ultralow-Frequency Mechanical Energy. *Adv Mater* (2021) 33:2103056. doi:10.1002/adma.202103056
174. Han J-H, Kim KB, Kim HC, Chung TD. Ionic Circuits Based on Polyelectrolyte Diodes on a Microchip. *Angew Chem Int Ed* (2009) 48:3830–3. doi:10.1002/anie.200900045
175. Gabrielsson EO, Berggren M. Polyphosphonium-based Bipolar Membranes for Rectification of Ionic Currents. *Biomicrofluidics* (2013) 7:064117. doi:10.1063/1.4850795
176. Simons R. The Origin and Elimination of Water Splitting in Ion Exchange Membranes during Water Demineralisation by Electrodialysis. *Desalination* (1979) 28:41–2. doi:10.1016/S0011-9164(00)88125-4
177. Gabrielsson EO, Tybrandt K, Berggren M. Ion Diode Logics for pH Control. *Lab Chip* (2012) 12:2507–13. doi:10.1039/C2LC40093F
178. Lucas RA, Lin C-Y, Baker LA, Siwy ZS. Ionic Amplifying Circuits Inspired by Electronics and Biology. *Nat Commun* (2020) 11:1568. doi:10.1038/s41467-020-15398-3
179. Sun G, Senapati S, Chang H-C. High-flux Ionic Diodes, Ionic Transistors and Ionic Amplifiers Based on External Ion Concentration Polarization by an Ion

Exchange Membrane: a New Scalable Ionic Circuit Platform. *Lab Chip* (2016) 16:1171–7. doi:10.1039/C6LC00026F

180. Tybrandt K, Larsson KC, Richter-Dahlfors A, Berggren M. Ion Bipolar junction Transistors. *Proc Natl Acad Sci U.S.A* (2010) 107:9929–32. doi:10.1073/pnas.0913911107
181. Tybrandt K, Gabrielsson EO, Berggren M. Toward Complementary Ionic Circuits: The Npn Ion Bipolar Junction Transistor. *J Am Chem Soc* (2011) 133:10141–5. doi:10.1021/ja200492c
182. Gabrielsson EO, Tybrandt K, Berggren M. Polyphosphonium-based Ion Bipolar junction Transistors. *Biomicrofluidics* (2014) 8:064116. doi:10.1063/1.4902909
183. Boon N, Olvera de la Cruz M. 'Soft' Amplifier Circuits Based on Field-Effect Ionic Transistors. *Soft Matter* (2015) 11:4793–8. doi:10.1039/C5SM00573F
184. Zhong C, Deng Y, Roudsari A, Kapetanovic A, Anantram MP, Rolandi M A Polysaccharide Bioprotonic Field-Effect Transistor. *Nat Commun* (2011) 2: 476. doi:10.1038/ncomms1489
185. Wang C, Fu K, Dai J, Lacey SD, Yao Y, Pastel G, et al. Inverted Battery Design as Ion Generator for Interfacing with Biosystems. *Nat Commun* (2017) 8: 15609. doi:10.1038/ncomms15609
186. Chen J, Henderson WA, Pan H, Perdue BR, Cao R, Hu JZ, et al. Improving Lithium-Sulfur Battery Performance under Lean Electrolyte through Nanoscale Confinement in Soft Swellable Gels. *Nano Lett* (2017) 17: 3061–7. doi:10.1021/acs.nanolett.7b00417
187. Fan W, Zhang X, Li C, Zhao S, Wang J. UV-initiated Soft-Tough Multifunctional Gel Polymer Electrolyte Achieves Stable-Cycling Li-Metal Battery. *ACS Appl Energ Mater.* (2019) 2:4513–20. doi:10.1021/acsaem.9b00766
188. Li Q, Ardebili H. Flexible Thin-Film Battery Based on Solid-like Ionic Liquid-Polymer Electrolyte. *J Power Sourc* (2016) 303:17–21. doi:10.1016/j.jpowsour.2015.10.099
189. Saunier J, Alloin F, Sanchez JY, Caillon G. Thin and Flexible Lithium-Ion Batteries: Investigation of Polymer Electrolytes. *J Power Sourc* (2003) 119-121:454–9. doi:10.1016/S0378-7753(03)00197-6
190. Wan J, Xie J, Kong X, Liu Z, Liu K, Shi F, et al. Ultrathin, Flexible, Solid Polymer Composite Electrolyte Enabled with Aligned Nanoporous Host for Lithium Batteries. *Nat Nanotechnol* (2019) 14:705–11. doi:10.1038/s41565-019-0465-3
191. Gorecki W, Jeannin M, Belorizky E, Roux C, Armand M. Physical Properties of Solid Polymer Electrolyte PEO(LiTFSI) Complexes. *J Phys Condens Matter* (1995) 7:6823–32. doi:10.1088/0953-8984/7/34/007
192. Kim J-K, Lim YJ, Kim H, Cho G-B, Kim Y. A Hybrid Solid Electrolyte for Flexible Solid-State Sodium Batteries. *Energy Environ. Sci.* (2015) 8:3589–96. doi:10.1039/C5EE01941A
193. Xie D, Zhang M, Wu Y, Xiang L, Tang Y. A Flexible Dual-Ion Battery Based on Sodium-Ion Quasi-Solid-State Electrolyte with Long Cycling Life. *Adv Funct Mater* (2020) 30:1906770. doi:10.1002/adfm.201906770
194. Chen L, Li Y, Li S-P, Fan L-Z, Nan C-W, Goodenough JB. PEO/garnet Composite Electrolytes for Solid-State Lithium Batteries: From "Ceramic-In-Polymer" to "Polymer-In-Ceramic". *Nano Energy* (2018) 46:176–84. doi:10.1016/j.nanoen.2017.12.037
195. Zhao Q, Stalin S, Zhao C-Z, Archer LA. Designing Solid-State Electrolytes for Safe, Energy-Dense Batteries. *Nat Rev Mater* (2020) 5:229–52. doi:10.1038/s41578-019-0165-5
196. Fan L-Z, Hu Y-S, Bhattacharyya AJ, Maier J. Succinonitrile as a Versatile Additive for Polymer Electrolytes. *Adv Funct Mater* (2007) 17:2800–7. doi:10.1002/adfm.200601070
197. Lu Y, Cai Y, Zhang Q, Liu L, Niu Z, Chen J. A Compatible Anode/succinonitrile-Based Electrolyte Interface in All-Solid-State Na-CO2 Batteries. *Chem Sci* (2019) 10:4306–12. doi:10.1039/C8SC05178J
198. Xu K. Electrolytes and Interphases in Li-Ion Batteries and beyond. *Chem Rev* (2014) 114:11503–618. doi:10.1021/cr500003w
199. Boudin F, Andrieu X, Jehoulet C, Olsen II. Microporous PVdF Gel for Lithium-Ion Batteries. *J Power Sourc* (1999) 81-82:804–7. doi:10.1016/S0378-7753(99)00154-8
200. Saikia D, Kumar A. Ionic Conduction in P(VDF-HFP)/PVDF-(PC + DEC)-LiClO 4 Polymer Gel Electrolytes. *Electrochimica Acta* (2004) 49:2581–9. doi:10.1016/j.electacta.2004.01.029
201. Cheng X, Pan J, Zhao Y, Liao M, Peng H. Gel Polymer Electrolytes for Electrochemical Energy Storage. *Adv Energ Mater.* (2018) 8:1702184. doi:10.1002/aenm.201702184
202. Chang J, Huang Q, Zheng Z. A Figure of Merit for Flexible Batteries. *Joule* (2020) 4:1346–9. doi:10.1016/j.joule.2020.05.015
203. Qian G, Liao X, Zhu Y, Pan F, Chen X, Yang Y. Designing Flexible Lithium-Ion Batteries by Structural Engineering. *ACS Energ Lett.* (2019) 4:690–701. doi:10.1021/acsenergylett.8b02496
204. Zhou G, Li F, Cheng H-M. Progress in Flexible Lithium Batteries and Future Prospects. *Energ Environ. Sci.* (2014) 7:1307–38. doi:10.1039/C3EE43182G
205. Fu KK, Cheng J, Li T, Hu L. Flexible Batteries: From Mechanics to Devices. *ACS Energ Lett.* (2016) 1:1065–79. doi:10.1021/acsenergylett.6b00401
206. Li Q, Li D, Wang H, Wang H-g., Li Y, Si Z, et al. Conjugated Carbonyl Polymer-Based Flexible Cathode for Superior Lithium-Organic Batteries. *ACS Appl Mater Inter* (2019) 11:28801–8. doi:10.1021/acsami.9b06437
207. Zhou M, Li W, Gu T, Wang K, Cheng S, Jiang K. A Sulfonated Polyaniline with High Density and High Rate Na-Storage Performances as a Flexible Organic Cathode for Sodium Ion Batteries. *Chem Commun* (2015) 51: 14354–6. doi:10.1039/C5CC05654C
208. Lee SW, Yabuuchi N, Gallant BM, Chen S, Kim B-S, Hammond PT, et al. High-power Lithium Batteries from Functionalized Carbon-Nanotube Electrodes. *Nat Nanotech* (2010) 5:531–7. doi:10.1038/nnano.2010.116
209. Wu H, Shevlin SA, Meng Q, Guo W, Meng Y, Lu K, et al. Flexible and Binder-free Organic Cathode for High-Performance Lithium-Ion Batteries. *Adv Mater* (2014) 26:3338–43. doi:10.1002/adma.201305452
210. Chen H, Armand M, Demailly G, Dolhem F, Poizot P, Tarascon J-M. From Biomass to a Renewable LiXC6O6 Organic Electrode for Sustainable Li-Ion Batteries. *ChemSusChem* (2008) 1:348–55. doi:10.1002/cssc.200700161
211. Wu X, Jin S, Zhang Z, Jiang L, Mu L, Hu Y-S, et al. Unraveling the Storage Mechanism in Organic Carbonyl Electrodes for Sodium-Ion Batteries. *Sci Adv* (2015) 1:e1500330. doi:10.1126/sciadv.1500330
212. Peng C, Ning G-H, Su J, Zhong G, Tang W, Tian B, et al. Reversible Multi-Electron Redox Chemistry of π-conjugated N-Containing Heteroaromatic Molecule-Based Organic Cathodes. *Nat Energ* (2017) 2:17074. doi:10.1038/nenergy.2017.74
213. Lei Z, Yang Q, Xu Y, Guo S, Sun W, Liu H, et al. Boosting Lithium Storage in Covalent Organic Framework via Activation of 14-electron Redox Chemistry. *Nat Commun* (2018) 9:576. doi:10.1038/s41467-018-02889-7
214. Lacey RE. Energy by Reverse Electrodialysis. *Ocean Eng* (1980) 7:1–47. doi:10.1016/0029-8018(80)90030-X
215. Campione A, Gurreri L, Ciofalo M, Micale G, Tamburini A, Cipollina A. Electrodialysis for Water Desalination: A Critical Assessment of Recent Developments on Process Fundamentals, Models and Applications. *Desalination* (2018) 434:121–60. doi:10.1016/j.desal.2017.12.044
216. Tedesco M, Hamelers HVM, Biesheuvel PM. Nernst-Planck Transport Theory for (Reverse) Electrodialysis: I. Effect of Co-ion Transport through the Membranes. *J Membr Sci* (2016) 510:370–81. doi:10.1016/j.memsci.2016.03.012
217. Gurreri L, Battaglia G, Tamburini A, Cipollina A, Micale G, Ciofalo M. Multi-physical Modelling of Reverse Electrodialysis. *Desalination* (2017) 423:52–64. doi:10.1016/j.desal.2017.09.006
218. Moya AA. A Nernst-Planck Analysis on the Contributions of the Ionic Transport in Permeable Ion-Exchange Membranes to the Open Circuit Voltage and the Membrane Resistance in Reverse Electrodialysis Stacks. *Electrochimica Acta* (2017) 238:134–41. doi:10.1016/j.electacta.2017.04.022
219. Jin D, Xi R, Xu S, Wang P, Wu X. Numerical Simulation of Salinity Gradient Power Generation Using Reverse Electrodialysis. *Desalination* (2021) 512: 115132. doi:10.1016/j.desal.2021.115132
220. Baek S, Kwon S-R, Yeon SY, Yoon S-H, Kang CM, Han SH, et al. Miniaturized Reverse Electrodialysis-Powered Biosensor Using Electrochemiluminescence on Bipolar Electrode. *Anal Chem* (2018) 90: 4749–55. doi:10.1021/acs.analchem.7b05425
221. Kwon S-R, Nam SH, Park CY, Baek S, Jang J, Che X, et al. Electrodeless Reverse Electrodialysis Patches as an Ionic Power Source for Active Transdermal Drug Delivery. *Adv Funct Mater* (2018) 28:1705952. doi:10.1002/adfm.201705952
222. Schroeder TBH, Guha A, Lamoureux A, VanRenterghem G, Sept D, Shtein M, et al. An Electric-Eel-Inspired Soft Power Source from Stacked Hydrogels. *Nature* (2017) 552:214–8. doi:10.1038/nature24670
223. Ide T, Takeuchi Y, Yanagida T. Development of an Experimental Apparatus for Simultaneous Observation of Optical and Electrical Signals from Single Ion Channels. *Single Mol* (2002) 3:33–42. doi:10.1002/1438-5171(200204)3:1<33::aid-simo33>3.0.co;2-u

224. Sint K, Wang B, Král P. Selective Ion Passage through Functionalized Graphene Nanopores. *J Am Chem Soc* (2008) 130:16448–9. doi:10.1021/ja804409f
225. Siria A, Poncharal P, Biance A-L, Fulcrand R, Blase X, Purcell ST, et al. Giant Osmotic Energy Conversion Measured in a Single Transmembrane boron Nitride Nanotube. *Nature* (2013) 494:455–8. doi:10.1038/nature11876
226. Angelova P, Vieker H, Weber N-E, Matei D, Reimer O, Meier I, et al. A Universal Scheme to Convert Aromatic Molecular Monolayers into Functional Carbon Nanomembranes. *ACS Nano* (2013) 7:6489–97. doi:10.1021/nn402652f
227. Feng J, Graf M, Liu K, Ovchinnikov D, Dumcenco D, Heiranian M, et al. Single-layer MoS2 Nanopores as Nanopower Generators. *Nature* (2016) 536:197–200. doi:10.1038/nature18593
228. Moreno C, Vilas-Varela M, Kretz B, Garcia-Lekue A, Costache MV, Paradinas M, et al. Bottom-up Synthesis of Multifunctional Nanoporous Graphene. *Science* (2018) 360:199–203. doi:10.1126/science.aar2009
229. Yang Y, Yang X, Liang L, Gao Y, Cheng H, Li X, et al. Large-area Graphene-Nanomesh/carbon-Nanotube Hybrid Membranes for Ionic and Molecular Nanofiltration. *Science* (2019) 364:1057–62. doi:10.1126/science.aau5321
230. Liu X, He M, Calvani D, Qi H, Gupta KBSS, de Groot HJM, et al. Power Generation by Reverse Electrodialysis in a Single-Layer Nanoporous Membrane Made from Core-Rim Polycyclic Aromatic Hydrocarbons. *Nat Nanotechnol* (2020) 15:307–12. doi:10.1038/s41565-020-0641-5
231. Yeon SY, Yun J, Yoon S-h., Lee D, Jang W, Han SH, et al. A Miniaturized Solid Salt Reverse Electrodialysis Battery: a Durable and Fully Ionic Power Source. *Chem Sci* (2018) 9:8071–6. doi:10.1039/C8SC02954G
232. Maamer B, Boughamoura A, Fath El-Bab AMR, Francis LA, Tounsi F. A Review on Design Improvements and Techniques for Mechanical Energy Harvesting Using Piezoelectric and Electromagnetic Schemes. *Energ Convers Manag* (2019) 199:111973. doi:10.1016/j.enconman.2019.111973
233. Wei C, Jing X. A Comprehensive Review on Vibration Energy Harvesting: Modelling and Realization. *Renew Sust Energ Rev* (2017) 74:1–18. doi:10.1016/j.rser.2017.01.073
234. Vidal JV, Slabov V, Kholkin AL, dos Santos MPS. Hybrid Triboelectric-Electromagnetic Nanogenerators for Mechanical Energy Harvesting: A Review. *Nano-micro Lett* (2021) 13:199. doi:10.1007/s40820-021-00713-4
235. Safaei M, Sodano HA, Anton SR. A Review of Energy Harvesting Using Piezoelectric Materials: State-Of-The-Art a Decade Later (2008-2018). *Smart Mater Struct* (2019) 28:113001. doi:10.1088/1361-665X/ab36e4
236. Zou H-X, Zhao L-C, Gao Q-H, Zuo L, Liu F-R, Tan T, et al. Mechanical Modulations for Enhancing Energy Harvesting: Principles, Methods and Applications. *Appl Energ* (2019) 255:113871. doi:10.1016/j.apenergy.2019.113871
237. Gao Q, Cheng T, Wang ZL. Triboelectric Mechanical Sensors-Progress and Prospects. *Extreme Mech Lett* (2021) 42:101100. doi:10.1016/j.eml.2020.101100
238. Fan FR, Tang W, Wang ZL. Flexible Nanogenerators for Energy Harvesting and Self-Powered Electronics. *Adv Mater* (2016) 28:4283–305. doi:10.1002/adma.201504299
239. Aureli M, Prince C, Porfiri M, Peterson SD. Energy Harvesting from Base Excitation of Ionic Polymer Metal Composites in Fluid Environments. *Smart Mater Struct* (2009) 19:015003. doi:10.1088/0964-1726/19/1/015003
240. Giacomello A, Porfiri M. Underwater Energy Harvesting from a Heavy Flag Hosting Ionic Polymer Metal Composites. *J Appl Phys* (2011) 109:084903. doi:10.1063/1.3569738
241. Cha Y, Phan CN, Porfiri M. Energy Exchange during Slamming Impact of an Ionic Polymer Metal Composite. *Appl Phys Lett* (2012) 101:094103. doi:10.1063/1.4748577
242. Cellini F, Cha Y, Porfiri M. Energy Harvesting from Fluid-Induced Buckling of Ionic Polymer Metal Composites. *J Intell Mater Syst Structures* (2014) 25:1496–510. doi:10.1177/1045389X13508333
243. Cellini F, Intartaglia C, Soria L, Porfiri M. Effect of Hydrodynamic Interaction on Energy Harvesting in Arrays of Ionic Polymer Metal Composites Vibrating in a Viscous Fluid. *Smart Mater Struct* (2014) 23:045015. doi:10.1088/0964-1726/23/4/045015
244. Cellini F, Pounds J, Peterson SD, Porfiri M. Underwater Energy Harvesting from a Turbine Hosting Ionic Polymer Metal Composites. *Smart Mater Struct* (2014) 23:085023. doi:10.1088/0964-1726/23/8/085023
245. Cha Y, Verotti M, Walcott H, Peterson SD, Porfiri M. Energy Harvesting from the Tail Beating of a Carangiform Swimmer Using Ionic Polymer-Metal Composites. *Bioinspir Biomim* (2013) 8:036003. doi:10.1088/1748-3182/8/3/036003
246. Peterson SD, Porfiri M. Chapter 14. Energy Exchange between Coherent Fluid Structures and Ionic Polymer Metal Composites, toward Flow Sensing and Energy Harvesting. In: *Ionic Polymer Metal Composites (IPMCs)*. Cambridge, United Kingdom: RSC (2015). p. 1–18. doi:10.1039/9781782627234-00001
247. Kim S, Choi SJ, Zhao K, Yang H, Gobbi G, Zhang S, et al. Electrochemically Driven Mechanical Energy Harvesting. *Nat Commun* (2016) 7:10146. doi:10.1038/ncomms10146
248. Moon JK, Jeong J, Lee D, Pak HK. Electrical Power Generation by Mechanically Modulating Electrical Double Layers. *Nat Commun* (2013) 4:1487. doi:10.1038/ncomms2485
249. Vallem V, Roosa E, Ledinh T, Jung W, Kim Ti., Rashid-Nadimi S, et al. A Soft Variable-Area Electrical-Double-Layer Energy Harvester. *Adv Mater* (2021) 33:2103142. doi:10.1002/adma.202103142
250. Hou Y, Zhou Y, Yang L, Li Q, Zhang Y, Zhu L, et al. Flexible Ionic Diodes for Low-Frequency Mechanical Energy Harvesting. *Adv Energ Mater.* (2017) 7:1601983. doi:10.1002/aenm.201601983
251. Parida K, Kumar V, Jiangxin W, Bhavanasi V, Bendi R, Lee PS. Highly Transparent, Stretchable, and Self-Healing Ionic-Skin Triboelectric Nanogenerators for Energy Harvesting and Touch Applications. *Adv Mater* (2017) 29:1702181. doi:10.1002/adma.201702181
252. Pu X, Liu M, Chen X, Sun J, Du C, Zhang Y, et al. Ultrastretchable, Transparent Triboelectric Nanogenerator as Electronic Skin for Biomechanical Energy Harvesting and Tactile Sensing. *Sci Adv* (2017) 9:1700015. doi:10.1126/sciadv.1700015
253. Hwang HJ, Kim JS, Kim W, Park H, Bhatia D, Jee E, et al. An Ultra-Mechanosensitive Visco-Poroelastic Polymer Ion Pump for Continuous Self-Powering Kinematic Triboelectric Nanogenerators. *Adv Energ Mater.* (2019) 9:1803786. doi:10.1002/aenm.201803786
254. Jin ML, Park S, Lee Y, Lee JH, Chung J, Kim JS, et al. An Ultrasensitive, Visco-Poroelastic Artificial Mechanotransducer Skin Inspired by Piezo2 Protein in Mammalian Merkel Cells. *Adv Mater* (2017) 29:1605973. doi:10.1002/adma.201605973
255. McCarty LS, Whitesides GM. Electrostatic Charging Due to Separation of Ions at Interfaces: Contact Electrification of Ionic Electrets. *Angew Chem Int Ed* (2008) 47:2188–207. doi:10.1002/anie.200701812
256. Kim W-G, Kim D-W, Tcho I-W, Kim J-K, Kim M-S, Choi Y-K. Triboelectric Nanogenerator: Structure, Mechanism, and Applications. *ACS Nano* (2021) 15:258–87. doi:10.1021/acsnano.0c09803
257. Pence S, Novotny VJ, Diaz AF. Effect of Surface Moisture on Contact Charge of Polymers Containing Ions. *Langmuir* (1994) 10:592–6. doi:10.1021/la00014a042
258. Diaz AF, Felix-Navarro RM. A Semi-quantitative Tribo-Electric Series for Polymeric Materials: the Influence of Chemical Structure and Properties. *J Electrostatics* (2004) 62:277–90. doi:10.1016/j.elstat.2004.05.005
259. Baytekin HT, Baytekin B, Soh S, Grzybowski BA. Is Water Necessary for Contact Electrification? *Angew Chem* (2011) 123:6898–902. doi:10.1002/ange.201008051
260. Pan S, Zhang Z. Fundamental Theories and Basic Principles of Triboelectric Effect: A Review. *Friction* (2019) 7:2–17. doi:10.1007/s40544-018-0217-7
261. Yang B, Portale G. Ionic Thermoelectric Materials for Waste Heat Harvesting. *Colloid Polym Sci* (2021) 299:465–79. doi:10.1007/s00396-020-04792-4
262. Zhao D, Würger A, Crispin X. Ionic Thermoelectric Materials and Devices. *J Energ Chem* (2021) 61:88–103. doi:10.1016/j.jechem.2021.02.022
263. Kim SL, Hsu J-H, Yu C. Thermoelectric Effects in Solid-State Polyelectrolytes. *Org Elect* (2018) 54:231–6. doi:10.1016/j.orgel.2017.12.021
264. Wang H, Zhao D, Khan ZU, Puzinas S, Jonsson MP, Berggren M, et al. Ionic Thermoelectric Figure of Merit for Charging of Supercapacitors. *Adv Electron Mater* (2017) 3:1700013. doi:10.1002/aelm.201700013
265. Zhao D, Wang H, Khan ZU, Chen JC, Gabrielsson R, Jonsson MP, et al. Ionic Thermoelectric Supercapacitors. *Energ Environ. Sci.* (2016) 9:1450–7. doi:10.1039/C6EE00121A
266. Kim SL, Lin HT, Yu C. Thermally Chargeable Solid-State Supercapacitor. *Adv Energ Mater.* (2016) 6:1600546. doi:10.1002/aenm.201600546

267. Kim G-H, Shao L, Zhang K, Pipe KP. Engineered Doping of Organic Semiconductors for Enhanced Thermoelectric Efficiency. *Nat Mater* (2013) 12:719–23. doi:10.1038/nmat3635
268. Wang H, Ail U, Gabrielsson R, Berggren M, Crispin X. Ionic Seebeck Effect in Conducting Polymers. *Adv Energ Mater*. (2015) 5:1500044. doi:10.1002/aenm.201500044
269. Onorato JW, Wang Z, Sun Y, Nowak C, Flagg LQ, Li R, et al. Side Chain Engineering Control of Mixed Conduction in Oligoethylene Glycol-Substituted Polythiophenes. *J Mater Chem A* (2021) 9:21410–23. doi:10.1039/d1ta05379e
270. Li T, Zhang X, Lacey SD, Mi R, Zhao X, Jiang F, et al. Cellulose Ionic Conductors with High Differential thermal Voltage for Low-Grade Heat Harvesting. *Nat Mater* (2019) 18:608–13. doi:10.1038/s41563-019-0315-6
271. Han C-G, Qian X, Li Q, Deng B, Zhu Y, Han Z, et al. Giant Thermopower of Ionic Gelatin Near Room Temperature. *Science* (2020) 368:1091–8. doi:10.1126/science.aaz5045
272. Cheng H, He X, Fan Z, Ouyang J. Flexible Quasi-Solid State Ionogels with Remarkable Seebeck Coefficient and High Thermoelectric Properties. *Adv Energ Mater*. (2019) 9:1901085. doi:10.1002/aenm.201901085
273. Zhao D, Martinelli A, Willfahrt A, Fischer T, Bernin D, Khan ZU, et al. Polymer Gels with Tunable Ionic Seebeck Coefficient for Ultra-sensitive Printed Thermopiles. *Nat Commun* (2019) 10:1093. doi:10.1038/s41467-019-08930-7
274. Han SH, Kwon S-R, Baek S, Chung T-D. Ionic Circuits Powered by Reverse Electrodialysis for an Ultimate Iontronic System. *Sci Rep* (2017) 7:14068. doi:10.1038/s41598-017-14390-0
275. Tybrandt K, Forchheimer R, Berggren M. Logic gates Based on Ion Transistors. *Nat Commun* (2012) 3:871. doi:10.1038/ncomms1869

Conflict of Interest: The authors declare that the research was conducted in the absence of any commercial or financial relationships that could be construed as a potential conflict of interest.

frontiers | Frontiers in Physics

ORIGINAL RESEARCH
published: 22 July 2022
doi: 10.3389/fphy.2022.926609

Simulating Microswimmers Under Confinement With Dissipative Particle (Hydro) Dynamics

C. Miguel Barriuso Gutiérrez[1], José Martín-Roca[1,2], Valentino Bianco[2], Ignacio Pagonabarraga[3,4,5] and Chantal Valeriani[1,6]**

[1]Departamento de Estructura de la Materia, Física Térmica y Electrónica, Universidad Complutense de Madrid, Madrid, Spain, [2]Departamento de Química Física, Facultad de Química, Universidad Complutense de Madrid, Madrid, Spain, [3]Departament de Física de la Matèria Condesada, Facultat de Física, Universitat de Barcelona, Barcelona, Spain, [4]Universitat de Barcelona Institute of Complex Systems, Barcelona, Spain, [5]Centre Européen de Calcul Atomique et Moléculaire (CECAM), Ecole Polytechnique Fédérale de Lausanne (EPFL), Lausanne, Switzerland, [6]GISC—Grupo Interdisciplinar de Sistemas Complejos, Madrid, Spain

Edited by:
Sujit Datta,
Princeton University, United States

Reviewed by:
Suvendu Mandal,
Darmstadt University of Technology, Germany
Marco G. Mazza,
Loughborough University, United Kingdom

***Correspondence:**
C. Miguel Barriuso Gutiérrez
carbarri@ucm.es
Chantal Valeriani
cvaleriani@ucm.es

Specialty section:
This article was submitted to Soft Matter Physics, a section of the journal Frontiers in Physics

Received: *22 April 2022*
Accepted: *14 June 2022*
Published: *22 July 2022*

Citation:
Barriuso Gutiérrez CM, Martín-Roca J, Bianco V, Pagonabarraga I and Valeriani C (2022) Simulating Microswimmers Under Confinement With Dissipative Particle (Hydro) Dynamics. Front. Phys. 10:926609. doi: 10.3389/fphy.2022.926609

In this work we study microwimmers, whether colloids or polymers, embedded in bulk or in confinement. We explicitly consider hydrodynamic interactions and simulate the swimmers via an implementation inspired by the squirmer model. Concerning the surrounding fluid, we employ a Dissipative Particle Dynamics scheme. Differently from the Lattice-Boltzmann technique, on the one side this approach allows us to properly deal not only with hydrodynamics but also with thermal fluctuations. On the other side, this approach enables us to study microwimmers with complex shapes, ranging from spherical colloids to polymers. To start with, we study a simple spherical colloid. We analyze the features of the velocity fields of the surrounding solvent, when the colloid is a pusher, a puller or a neutral swimmer either in bulk or confined in a cylindrical channel. Next, we characterise its dynamical behaviour by computing the mean square displacement and the long time diffusion when the active colloid is in bulk or in a channel (varying its radius) and analyze the orientation autocorrelation function in the latter case. While the three studied squirmer types are characterised by the same bulk diffusion, the cylindrical confinement considerably modulates the diffusion and the orientation autocorrelation function. Finally, we focus our attention on a more complex shape: an active polymer. We first characterise the structural features computing its radius of gyration when in bulk or in cylindrical confinement, and compare to known results obtained without hydrodynamics. Next, we characterise the dynamical behaviour of the active polymer by computing its mean square displacement and the long time diffusion. On the one hand, both diffusion and radius of gyration decrease due to the hydrodynamic interaction when the system is in bulk. On the other hand, the effect of confinement is to decrease the radius of gyration, disturbing the motion of the polymer and thus reducing its diffusion.

Keywords: active matter, swimmers, squirmers, Dissipative Particle Dynamics (DPD), bulk, confinement and solvent effect, numerical simulations

1 INTRODUCTION

Active Matter is a branch of Physics that focuses on the study of intrinsically out-of-equilibrium systems due to energy being constantly supplied, converted into directed motion and dissipated by individual constituents. Active Matter is a field that has raised a lot of interest in the last decade, since it captures complex collective behaviours, often exclusively associated to living matter, and might enable a wide range of technological applications [1]. One of the paradigmatic systems of Active Matter consists of a suspension of active particles. Active particles can be living (such as bacteria) or synthetic (such as active colloids). Active colloids are micron-size particles which self-propel through a medium by converting energy extracted from their environment into directed motion [2, 3], with potential medical and technological applications [4–10]. The collective behaviour of systems constituted by a large number of these particles is rich and complex as shown by a series of recent numerical [11–17] and experimental [18] works, and in many cases cannot be ascribed solely to the particles motion since hydrodynamics due to the surrounding solvent might need to be taken into account [19]. This is the case for *microswimmers* [20], whose motion is an essential aspect of life.

Microswimmers are usually ciliated and/or flagellated microorganisms that achieve propulsion thanks to the movement of their cilia located on their outer surface: for this reason one can consider them as self-propelled microorganisms. In the last few years microswimmers have been intensively studied, being of interest in several interdisciplinary sciences. Examples of living microswimmers are *Escherichia coli* bacterium, *Paramecium* or sperm cells, or algae (such as *Chlamidomonas* or *Volvox*). Whereas examples of synthetic microswimmers are Janus colloidal particles. When considering the effect of hydrodynamic interactions, numerical studies of a two dimensional suspension of self-propelled repulsive swimmers have demonstrated that hydrodynamics affects, not only the phase behaviour of a dense suspension [21], as suggested by Ishikawa [22] in an early work, but also the dynamics of transient clusters at lower densities [23]. Moreover, other theoretical, numerical and experimental results have also revealed the importance of hydrodynamics in these systems [24–27].

To model microswimmers, Blake and Lighthill proposed the so called *squirmer* model [28, 29]. The squirmer model reproduces the induced hydrodynamic flow around a spherical swimmer while preserving the main features of the active stresses generated by it [30]. The spherical squirmer particle mimics the effect of the cilia on the fluid as a prescribed slip velocity tangential to the surface. The described mechanism is the one that leads to the swimmer's propulsion. A squirmer is characterized by two modes accounting for its swimming velocity and its active stress. Depending on the active stress, it is possible to classify squirmers as pushers (e.g., *E. coli*, sperm), pullers (e.g., *Chlamydomonas*) and neutral (e.g., *Paramecium*) swimmers [31, 32]. The squirmer model has been expanded for complex swimmers, such as non-spherical swimmers [32] and explicitly ciliated microorganisms [31].

Besides mimicking the swimmer's behaviour, it is important to choose a model to mimic the features of the surrounding fluid. The applicability of atomistic algorithms (Molecular Dynamics-like) to simulate the fluid is limited, since they only allow to study short time and length scales (few hundreds of nanoseconds and few tens of nanometers). To explore longer length/time scales, more relevant for living swimmers, atomistic methods become computationally inefficient. Thus, one might consider mesoscopic methods, that bridge the gap between the microscopic and the macroscopic continuum scale [33]. These methods span longer length and time scales: from several nanometers to micrometers and from nanoseconds to microseconds. The most renown mesocopic numerical models used to simulate fluids that fully consider hydrodynamic interactions are Lattice-Boltzmann [34], Multiparticle Collision Dynamics [35–37] and Dissipative Particle Dynamics [38]. The Lattice Boltzmann (LB) approach consists in describing the solvent in terms of the density of particles with a given velocity at a node of a given lattice. The discretized velocities join the nodes and prescribe the lattice connectivity [39]. The LB model reproduces the dynamics of a Newtonian liquid of a given shear viscosity η. Relevant hydrodynamic variables are recovered as moments of the one-particle velocity distribution functions. The total force and torque the fluid exerts on a particle embedded in it are obtained by imposing that the total momentum exchange between the particle and the fluid nodes vanishes. Since a Lattice Boltzmann code is computationally expensive, from a practical point of view it is possible to parallelize it using Message Passage Interface to exploit the excellent scalability of LB on supercomputing facilities [40]. In the Multiparticle Collision Dynamics (MPCD) approach [35–37] a fluid is represented by N point particles with continuous positions and velocities. The particle dynamics proceeds in two steps: streaming and collision. During the streaming step, particles move ballistically. Whereas in the collision step particles interact locally via an instantaneous stochastic process, that could be based on stochastic rotation dynamics with angular momentum conservation [32]. For this purpose, the simulation box is partitioned into cubic collision cells. Within MPCD Galilean invariance is ensured, together with thermal fluctuations. The algorithm conserves mass, linear, and angular momentum on the collision cell level, which gives rise to hydrodynamics on large length and long time scales. Dissipative particle dynamics (DPD) is one of the most efficient mesoscale coarse-grained approaches for modeling soft matter systems. DPD was originally proposed by Hoogerbrugge and Koelmann [38] as an off-lattice, momentum conserving, Galilean invariant mesoscopic method, the coarse-grained dynamics of which obeys the Navier-Stokes equations and preserve hydrodynamics. Later on, Espanol and Warren [41] reformulated the DPD model in terms of stochastic differential equations. DPD consists in modified Langevin equations that operate between pairs of particles interacting via three different forces: conservative, dissipative and random (thermal) forces. The DPD model has already been used to model complex colloidal suspensions, such as proteins [42] or red globules in blood [43].

Along with hydrodynamics, confinement also plays a major impact on the dynamics of microswimmers. Their interaction with bounding walls is different depending on the type of microswimmer we are dealing with and can lead to different transport and aggregation phenomena. As of today, this facts have been studied theoretically [44–46], numerically [47–49] and experimentally [31, 50]. While in these works the study focuses mainly in the interaction of microswimmers with plane boundaries, other types of confinement also display relevant features, for instance the effect of porous media in bacterial suspensions has also been reported [51]. Finally, of course it is worth noting that the effect of confinement is not only limited to active matter systems but also plays a role in a wide range of systems, such as passive hard spheres [52].

In the present work we propose to model suspensions of microwimmers with DPD hydrodynamics inspired by the squirmer model. When the agent is a sphere we choose a *raspberry*-like structure [53–55] and we will directly consider the squirmer model. Whereas when the agent is a polymer, we will build the polymer as a chain of monomers, and treat each monomer similarly, but not rigorously, as a squirmer. To properly deal with hydrodynamics, we will mimic the surrounding fluid via DPD interactions, using an in-house extension of the LAMMPS [56] open source package implementing appropriate reaction forces on the swimmer's particles that balance the forces exerted on the fluid and enable its propulsion [57, 58]. Our choice is motivated by the fact that differently from LB [34], DPD easily allows to take into account thermal fluctuations and to simulate colloids with complex shapes (not only spherical). Moreover, it is also easier to control compressibility and Schmidt number in DPD than MCPD. Hence, in DPD it is easier to control the appropriate dynamic regime that couples the solvent and solute dynamics. Although this is not the focus of his paper, DPD also allows for a more thorough control of the phase diagram of the solvent and how to deal with fluid phase coexistence. Firstly we study the dynamical behaviour of either microwimmer in bulk. In the case of active colloids, we establish the flow fields surrounding the particle and compute their diffusion, comparing pushers, pullers and neutral swimmers. In the case of active polymers, besides the dynamics we also study its conformational features. Next, we confine either microwimmer in a cylindrical channel, and unravel the effect of hydrodynamics as compare to the equivalent systems where hydrodynamics is not present. For each system we explore different Reynolds and Péclet numbers. The Reynolds number [59] is the ratio of inertial to viscous forces within a fluid subjected to relative internal motion: this number measures the amount of turbulence of the solvent in the system. The Péclet number [11, 60] is defined as the ratio of the rate of advection of a physical quantity by the flow to the rate of diffusion of the same quantity. This number quantifies the degree of activity of microwimmers.

The manuscript is organised as follows. In **Section 2** we describe the relevant physical quantities and the technical details of the implementation. We first describe the DPD method to simulate the solvent (**Section 2.1**), implemented within the LAMMPS open source numerical package [56]. Next, we present the two microwimmers under study: the active colloid (**Section 3.1**) and the active polymer (**Section 3.2**). In **Section 3.1**, we introduce the *raspberry*-like active colloid (**Figure 1A**) in bulk and when interacting with a cylindrical surface (**Figure 1C**). In **Section 3.2**, we report the active polymer (**Figure 1B**), as in ref. [11], in bulk and under cylindrical confinement (**Figure 1D**). The way we implemented hydrodynamics is reported in **Section 2.4**, being the same for both active objects embedded in a DPD solvent. In the same section we characterize the physical quantities of a fluid such as the kinematic viscosity (ν) and the solvent diffusion coefficient (D_{sol}), and parameters to quantify the activity of the colloid/polymer embedded in a fluid, such as the Reynolds number and the Péclet number. Finally, in **Section 2.5** we report the analysis tools used to study the microwimmers in bulk or under confinement. In **Section 3** we present the results obtained, first for the colloid (**Section 3.1**) and then for the polymer (**Section 3.2**). In **Section 4** we discuss the results and comment on future avenues.

2 MATERIALS AND METHODS

In this work we study an active colloid and an active polymer embedded in a fluid solvent either in bulk or confined inside a cylindrical channel. We simulate the active colloid as a spherically-shaped collection of particles merged together by rigid interactions. Whereas the active polymer is built as a chain of monomers glued together by harmonic interactions that enable their relative movement. The rest of the interactions are the DPD-like interactions between any two particles, the hydrodynamic force-field that enables the agents' propulsion and, in the case of the confined polymer, a repulsive (WCA-like) potential between channel (particles) and polymer/solvent particles.

2.1 Modeling the Solvent With Dissipative Particle Dynamics

Our system consists of microwimmers embedded in a solvent, where hydrodynamics is explicitly taken into account. The fluid surrounding the microwimmer is simulated as a collection of individual particles interacting via Dissipative Particle Dynamics [38]. According to DPD, below a given cutoff r_c, the force acting on the i-th solvent particle consists of three contributions,

$$\vec{F}_i = \sum_j \left(\vec{F}_{ij}^C + \vec{F}_{ij}^D + \vec{F}_{ij}^R \right) \hat{r}_{ij} \qquad \text{if} \quad r < r_c, \tag{1}$$

being $\hat{r}_{ij} = (\vec{r}_i - \vec{r}_j)/r_{ij}$ the inter-particle unitary direction between the i-th and j-th particles. The conservative term is $\vec{F}_{ij}^C = A\, w(r_{ij})$, where A is the amplitude and $w(r_{ij}) = 1 - r_{ij}/r_c$ a weighting factor varying between 0 and 1 as in ref. [33]. The dissipative contribution reads $\vec{F}_{ij}^D = -\gamma w^2(r_{ij})\, (\hat{r}_{ij} \cdot \vec{v}_{ij})$ with friction coefficient γ. Finally, the thermal contribution $\vec{F}_{ij}^R = \sigma \alpha w(r_{ij}) / \sqrt{\Delta t}$ is a random force, where α, is a Gaussian random number with zero mean and unit variance, Δt the chosen time-step for the time integration and $\sigma = \sqrt{2 k_B T \gamma}$ is related to the mean of the random force via fluctuation-dissipation, being T the temperature of the system.

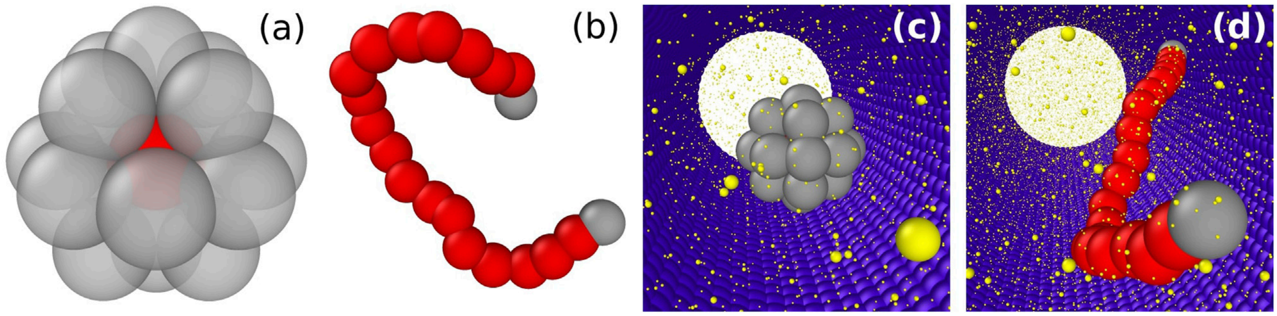

FIGURE 1 | (A): A *raspberry*-like active colloid composed of 18 *filler* particles and one *thruster* particles at the center. Note that in these figures the filler particle radius is scaled down to 1 for better visibility, but in all simulations we use $r_c^{sf} = 2$ as the solvent-filler DPD cutoff in order to obtain a more spherical colloid and to prevent the solvent particles from stepping into the colloid. **(B)**: An active polymer composed of 20 beads. **(C)**: An active colloids in a cylindrical confinement. **(D)**: An active polymer in a cylindrical confinement. Red: *thruster* particles. Gray: *filler* particles. Blue: wall particles composing the confining channel. Yellow: solvent particles.

TABLE 1 | DPD parameters used to study a spherical colloidal squirmer for (*COL*) embedded in a solvent (*SOL*), in bulk or in a cylindrical confinement (*CYL*). All parameters are in reduced DPD units.

	SOL-SOL	*SOL-COL*	*SOL-CYL*	*COL -COL*	*COL -CYL*
A	25.0	25.0	100.0	25.0	25.0
γ	4.5	4.5	4.5	4.5	4.5
r_c	1.0	2.0	1.0	2.0	2.0

TABLE 2 | DPD parameters used to study an active polymer (*POL*) embedded in a solvent (*SOL*), in bulk or in a cylindrical confinement (*CYL*). All parameters are in reduced DPD units.

	SOL-SOL	*SOL-POL*	*SOL-CYL*	*POL-POL*	*POL-CYL*
A	25.0	25.0	25.0	25.0	0.0
γ	4.5	4.5	4.5	4.5	0.0
r_c	1.0	1.0	1.0	1.0	0.0
ϵ	0.0	0.0	0.0	0.0	1.0

In the current work, we implement the DPD solvent via the LAMMPS open source package [56], setting the time step to $\Delta t/\tau = 10^{-2}$ for the simulations of the active colloid and $\Delta t/\tau = 5 \cdot 10^{-3}$ for the simulations of the active polymer. In both systems, we choose an equilibration time of ~ 10^4 steps, while the production run is of the order of 10^6 steps. The number of solvent particles for the system contaning the active colloid in bulk is $N = 10{,}125$, distributed in a cubic simulation box of $L = 15$. In cylindrical confinement, depending on the channel radius $R_{\text{cyl}} = \{3.5, 4.5, 5.5, 6.5\}$ the number of solvent particles is $N_{sol} = \{3464, 5726, 8553, 11{,}946\}$, respectively, and the channel length is fixed to $L_{\text{cyl}} = 30$. The number of solvent particles for the polymer system in bulk is around $N_{sol} = 24{,}000$ distributed in a cubic simulation box of $L = 20$. In the polymer confined case, with channel radius $R_{\text{cyl}} = 6$ and length $L = 50$, the number of solvent particles is around $N_{sol} = 17{,}000$. For all simulations, the mass of the solvent particles is fixed to $m = 1$ and the numerical density to $\rho_{\text{sol}} = 3$. The characteristic length scale for all our simulations is the DPD cutoff distance between solvent particles $r_c \equiv r_c^{ss} = 1$, the mass scale is fixed by the mass of one solvent particle $m = 1$, and for the time scale we fix $\tau = 1$. Following ref. [33], the DPD interaction parameters between solvent-solvent particles are set to $A^{ss} = 25.0$, $\gamma^{ss} = 4.5$ and $r_c^{ss} = 1.0$ (see **Tables 1**, **2** in the following subsections). The physical properties of a DPD fluid depend on its viscosity [33] that can be computed from the Green-Kubo relation [61] for the stress autocorrelation function (zero-shear viscosity). Later on we will discuss our choice for the fluid's viscosity. Whereas the DPD parameters used for each microwimmer are reported in their corresponding sections.

It is worth noting that when confining the DPD fluid in a cylinder we observed concentric ring-shaped density fluctuations in the vicinity of the wall at $T = 0.1$. These fluctuation have been previously observed and can lead to undesirable effects [62]. For this reason we chose $T = 1$ for all our confined simulations in which these fluctuations were not observed.

2.2 Colloids in Bulk and in Confinement

To study a spherical squirmer, we build a *raspberry*-like [53–55] colloid made of 19 particles rigidly bonded. In **Figure 1A**, we represent the active colloids, consisting of one particle (the *thruster* particle) located at the center of the sphere and the remaining 18 (*filler* particles) evenly distributed on the surface of a sphere of radius R_{col} around the center particle. The reason for choosing this structure has been guided by simplicity, balancing the number of particles and sphericity, and is inspired by previously proposed models for complex colloids [53–55]. The reason to consider only one thruster particle is because such an approach is enough to generate activity with a minimal disturbance on the geometrical properties of the swimmer. The shell of passive particles is necessary to control the dimension and shape of the colloid, rendering it an extended body that has an orientation. The propulsion mechanism of the thruster particle will be explained in the next section, when detailing the implementation of the hydrodynamic interactions.

The orientation of the colloid is defined by the "active axis" identified by three chosen co-linear particles. This axis is also the symmetry axis of the force field we will apply to the solvent, and thus will define the colloid's direction of propulsion. All particles belonging to each colloid interact via DPD: 1) with the solvent, 2) with particles belonging to other colloids and 3) with particles building the channel. However, particles belonging to each colloid do not interact between them (so their overlap does not cause any trouble), except for the rigid interactions that keep them glued together. In **Table 1** we report the chosen DPD parameters for all interactions between particles: solvent-solvent, solvent-colloid, solvent-cylinder, colloid-colloid, colloid-cylinder.

In **Section 2.4** we will describe different squirmer models, such as pushers, pullers and neutral swimmers, each one characterised by a different velocity field in the surrounding fluid. In order to check whether the *raspberry*-like colloid reproduces the features of the different squirmers, we compute the velocity fields and compared them to those reported for the different squirmers in ref. [49].

Having studied the active colloid in bulk, we study its physical behaviour when confined in cylindrical environments of different radii. The cylinder is composed of DPD overlapping particles, properly aligned along the x axis at given angles. Overlapped DPD particles are left out of the time integration and their DPD interactions are switched off thus they can be used to model a wall. Particles are first evenly distributed along a circumference in the yz-plane and then this circumference is repeated through the x-axis. The separation of the particles is chosen so that the roughness of the inner surface of the cylinder is the same along the angular and longitudinal directions. Periodic boundary condition (PBC) are applied along the longitudinal direction (x axis). Particles' interaction parameters are reported in **table 1**. Choosing DPD interactions for modelling the collisions with the channel allows us to maintain a large time step $\Delta t = 10^{-2}$. Due to the softness of the DPD interactions, we have appropriately set the DPD parameters for the channel particles to avoid leaking of solvent particles through the channel wall. Moreover, DPD enables adding a friction between the solvent and the channel wall. In our case, we have tested that for high enough values of γ we are able to simulate Poiseuille flow. However, for our study we have decided to explore low values of γ, which correspond to the implementation of slip boundary conditions at the channel's surface.

2.3 Polymers in Bulk and in Confinement

Following ref. [11], we model the active polymer as a chain of active monomers. As shown in **Figure 1B**, each of the N_b monomers is composed by a single *thruster* DPD particle, except the head and tail monomer. Since the first (last) particle of the polymer does not have previous (posterior) neighbors, no force is applied on them. Alternatively, one could consider that the activity direction is extrapolated from the neighbor monomer in the chain. However, this alternative approach will not affect the main results and features described in the manuscript. Previously proposed models for active polymers have also taken this approach [11]. Monomers are held together to their first neighbours via a harmonic potential $V_{\text{harmonic}}(r) = K(r - r_0)^2$, acting between *thruster* particles of the connected beads separated by a distance r, with $K = 30 k_B T / r_c^2$, being $r_0 \equiv 1.5\ r_c$. Since all interaction between particles are soft (DPD-like), we can choose $dt = 10^{-2}$ as the time step to integrate the equations of motion. As in ref. [11], we assume that all monomers are active apart from the first and the last (in grey in **Figure 1**). An active force $\mathbf{F}_{a,i}$ acts on each *thruster* monomer at $\mathbf{r}_i$. The force is characterised by a constant magnitude F_a and a direction of $\mathbf{r}_{i+1} - \mathbf{r}_{i-1}$ parallel to the polymer backbone tangent, being $\mathbf{r}_{i+1}$ and $\mathbf{r}_{i-1}$ the position vectors of the *thruster* particles first neighboring monomers.

To characterise the bulk properties of an active polymer, we study a dilute system of 4 active polymers in a box with edge $L = 20$ at a solvent density of $\rho = 3$. Care must be taken if the volume fraction of polymers is not low enough, since polymers might interact between each other via hydrodynamics. In our case we avoid this by working with a polymer volume fraction that is always lower than 5%.

To study the effects of confinement we embed the active polymer and the solvent in a cylindrical channel with periodic boundary conditions along the axial axis. The cylinder consists of $N_c = 24{,}415$ frozen WCA-like particles that interact with the DPD particles (solvent and polymers) via a WCA-like potential

$$V_{\text{LJ}}(r) = \begin{cases} 4\epsilon\left[\left(\frac{\sigma}{r}\right)^{12} - \left(\frac{\sigma}{r}\right)^{6}\right] + \epsilon; & \text{for } r < 2^{1/6}\,\sigma, \\ 0; & \text{for } r \geq 2^{1/6}\,\sigma, \end{cases} \tag{2}$$

where ϵ is the unit of energy and σ represent the channel's particle diameter set to $\sigma = r_c = 1$. In all simulations we set $k_B T = 1.0$ (Lennard-Jones units). Cylinder particles are located close enough to avoid DPD solvent particles to cross the cylinder's wall.

The chosen values for the DPD parameters are reported in **Table 2** for all interactions between particles: solvent-solvent, solvent-polymer, solvent-cylinder, polymer-polymer, polymer-cylinder.

We should stress the fact that when dealing with active colloids or active polymers we have chosen to simulate the cylindrical channel in a different way. In the former case, the channel has been simulated by means of particles interacting via DPD, as explained earlier. Whereas in the latter case, the channel has been built using particles interacting via a repulsive WCA potential, to compare with ref. [11].

2.4 Swimming Induced by Hydrodynamics

In order to numerically consider full hydrodynamic interactions between the microwimmers and the surrounding solvent, we prescribe a force field for the solvent particles surrounding the thruster particles (the red particles in **Figure 1**).

When dealing with a spherical squirmer, the usual approach consists in prescribing tangential velocities to the solvent particles at the swimmers surface [28]. Note that we have not followed the usual squirmer approach. In our case, tangential solvent forces, instead of velocities, are prescribed over a hydrodynamic active volume Γ_H around the colloid, instead of just at the colloid's surface. This approach is more general since it enables the possibility of studying different agent shapes and inertial effects, which are present in many active systems [63].

In this study we only consider axisymmetric force fields (**Eq. 3**). We choose the hydrodynamic region Γ_H as a spherical shell around the thruster particles of inner and outer radii R_c and R_H, respectively. The expressions of the force fields considered for the

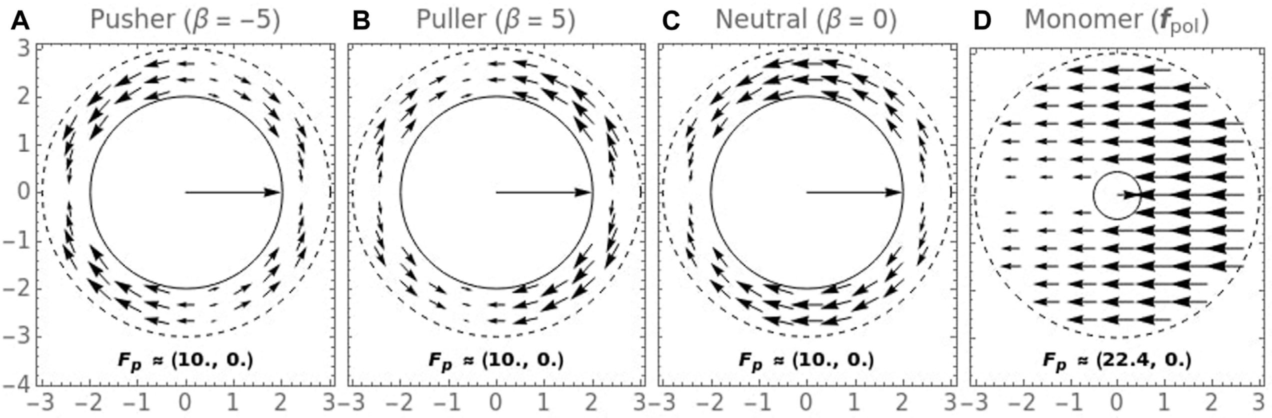

FIGURE 2 | Examples of 2D hydrodynamic redistribution force fields for all the studied cases: a pusher **(A)** with $\beta = -5$, a puller **(B)** with $\beta = 5$, a neutral squirmer **(C)** with $\beta = 0$ and a monomer of the active polymer **(D)**. These correspond to a section of the 3D field passing through the equator of the redistribution sphere. The arrow inside the central colloid indicates the direction of the propulsion force F_p, with magnitude indicated in each panel. Here, the hydrodynamic region Γ_H would be the area contained between the solid and dashed circles.

colloid and the polymer are reported in what follows (see the **Supplementary Appendix** for more details). The general expression for an axisymmetric force field that vanishes everywhere except inside the aforementioned spherical shell is given by,

$$\boldsymbol{f}(r,\theta) = \left[f_r(r,\theta)\hat{\boldsymbol{e}}_r + f_\theta(r,\theta)\hat{\boldsymbol{e}}_\theta\right] P_{R_c,R_H}(r) \tag{3}$$

where r is the distance from the thruster to the solvent particle, θ the angle between the colloid's orientation vector $\hat{\boldsymbol{e}}$ and the solvent position vector, $\hat{\boldsymbol{e}}_r$ and $\hat{\boldsymbol{e}}_\theta$ are the radial and tangential unitary vectors with respect to the colloid frame of reference and $P_{R_c,R_H}(r) = \Theta(r - R_c)\Theta(R_H - r)$ is a pulse function in the radial dimension which defines the spherical shell.

In order to have more control over the propelling force, we normalize the force field over the hydrodynamic region Γ_H, and multiply by a factor F_p. F_p is the input parameter for the magnitude of the self-propelling force. Thus the hydrodynamic force field that will be applied to the solvent reads,

$$\boldsymbol{f}_H(r,\theta) = F_p\frac{\boldsymbol{f}(r,\theta)}{N}, \quad \text{where} \quad N = \left|\int_{\Gamma_H}\boldsymbol{f}(r,\theta)\,\mathrm{d}V\right|. \tag{4}$$

Since in our case we are dealing with a discrete fluid (made of solvent particles), the i-th solvent particle will feel a force,

$$\boldsymbol{f}_H^i = F_p\frac{\boldsymbol{f}(r_i,\theta_i)}{N}, \quad \text{where} \quad N = \left|\sum_{j\in\Gamma_H}\boldsymbol{f}\left(r_j,\theta_j\right)\Delta V\right| \tag{5}$$

where the sum is taken over all the solvent particles that are inside Γ_H and $\Delta V = r_c^3 = 1$. Similarly to the squirmer model, here we only consider the two first surface modes of the polar component, $f_\theta(r,\theta)$, while the radial component is neglected $f_r(r,\theta) = 0$ (see **Supplementary Appendix Section 5.1** for the details). Thus, the force field becomes,

$$\boldsymbol{f}(r,\theta) = (B_1\sin\theta + B_2\sin\theta\cos\theta)P_{R_c,R_H}(r)\hat{\boldsymbol{e}}_\theta \equiv \boldsymbol{f}_{\text{col}}, \tag{6}$$

for which $N = (R_H^3 - R_c^3)B_1\pi^2/4$. In this way, the total propulsion force (which is precisely the integral appearing in **Eq. 4**) experimented by the colloid is just F_p. B_2 controls the force dipole contribution to the force field and thus wether we are dealing with pushers ($B_2 < 0$), neutrals ($B_2 = 0$) or pullers ($B_2 > 0$). Because of this formulation, B_1 plays no role and will be fixed to 1.0 from here on. As in the squirmer model, we define $\beta = B_2/B_1$ as the active stress parameter that controls the type of squirmer (see **Figure 2**). Under the assumption of Stokes flow (low Reynolds number), it is reasonable to think that the velocity field of the solvent particles will resemble that of the squirmer model[1] [28, 49].

Now we need to deal with the reaction force that is exerted on the colloid which will result in its thrust. Moreover, since an active colloid is an extended rigid object we would like to preserve the torque that may arise due to density fluctuations or interactions with other objects. The reaction thrust force, $\boldsymbol{f}_T$, is applied on the nearest colloid particle (thruster or not) to each of the solvent particles and it is equal and opposite to the redistributed force on that solvent particle:

$$\boldsymbol{f}_T^k(r,\theta) = -\boldsymbol{f}_H^{i(k)}(r,\theta) \tag{7}$$

where $i(k)$ represents the nearest solvent particle to the k-th colloid particle.

At each step, we implement the following algorithm:

1. Starting from a reference microswimmer, we identify the neighboring solvent particles around the swimmer's thruster particles located between the swimmer's radius

---

[1] Under the same Stokes flow assumption, the colloid's propulsion velocity v_p can be computed from the self-propulsion force F_p via the Stokes law $F_p = 6\pi\eta R_c v_p$. However, this assumption may not hold in some cases that are also worth studying. For these cases, we "measure" v_p as the time averaged projection of the colloids velocity v_{col} over its orientation axis $v_p = \langle \boldsymbol{v}_{\text{col}} \cdot \hat{\boldsymbol{e}}\rangle_t$ as will be explained later on.

(R_{col} for the colloid; r_c for the polymer) and the "hydrodynamic" radius R_H.

2. We compute the force field $\boldsymbol{f}_H$ in **Eq. 4** at each of the neighbors positions, consistently with the swimmer's orientation. The norm of the total distributed force is also computed.
3. For each neighbor:
    3.1 We apply the corresponding normalized force.
    3.2 We find the nearest agent particle and apply the same and opposite force.

In this way self-propulsion is achieved, while linear and angular momenta are locally conserved at each step. This procedure enables physically realistic modeling of the propulsion mechanism of a wide range of self-propelled systems, both living and artificial.

In case of the active polymer, we have considered a constant field modulated by $\cos(\theta/2)$ for each thruster monomer,

$$\boldsymbol{f}(r,\theta) = -\cos\left(\frac{\theta}{2}\right) P_{R_c,R_H}(r)\,\hat{\boldsymbol{e}} \equiv \boldsymbol{f}_{\mathrm{pol}}, \tag{8}$$

where $\hat{\boldsymbol{e}} = \cos\theta\,\hat{\boldsymbol{e}}_r - \sin\theta\,\hat{\boldsymbol{e}}_\theta$ is the self-propulsion direction of the thruster particle. In this case, a reaction force that provides thrust to the agent is applied on each thruster particle. This force is equal and opposite to the total force distributed among the solvent particles in each step. Since in this case we are dealing with a flexible object that has many thruster particles, we need not to worry about finding the nearest agent particle, since this is already taken care of, as the force that each thruster particle redistributes is equal and opposite to the one that is exerted on it.

In **Figure 2** we can see the hydrodynamic force fields, $\boldsymbol{f}$, we have used in this work. The continuous and dashed circumferences represent the inner (R_c), and outer (R_H) radius respectively and define the region Γ_H where redistribution occurs. As an example, in this figure the propulsion force is computed as the surface integral of the vector field inside this region, $\boldsymbol{F}_p = -\int_{\Gamma_H} \boldsymbol{f}_H(r,\theta)\,d\boldsymbol{S}$, in this case computed in 2D. Since the force field is asymmetric there exists a net propulsion force that provides thrust to the agent. In the case of the polymer (d), each polymer bead (or monomer) acts as a small colloid with its own redistribution field, so in this case $R_c = r_c$ would represent the beads radius, i.e. the thickness of the polymer.

To conclude, the total force experienced by an agent particle consists of the following contributions

$$\boldsymbol{F} = \boldsymbol{F}_C + \boldsymbol{F}_D + \boldsymbol{F}_R + \boldsymbol{F}_T \tag{9}$$

where $\boldsymbol{F}_T$ is the total thrust force, computed as the sum of all the reaction forces on each colloid's particle $\boldsymbol{F}_T = \sum_k \boldsymbol{f}_T^k$.

It is worth noting that while in this study we have restricted ourselves to axisymmetric force fields, the code implementation is made for general force fields, allowing for example azimuthal flows, like those of the Volvox algae [64].

2.4.1 Quantifying Activity

To characterise a microwimmer in the solvent, we will define dimensionless numbers such as the Reynolds number and the Péclet number. For this, we will need to establish the viscosity η of the fluid. η can be numerically computed in a DPD fluid, as recently shown in ref. [65], or estimated via a mean field, as in Warren and Groot [33]. In our work, we follow the second approach, according to which the DPD solvent kinematic viscosity ν, defined as $\frac{\eta}{\rho}$, can be computed as

$$\nu = \frac{\eta}{\rho} = \frac{D_{sol}}{2} + \frac{2\pi\gamma\rho r_c^5}{1575} \tag{10}$$

where the diffusion coefficient D_{sol} is

$$D_{sol} = \frac{45 k_B T}{2\pi\gamma\rho r_c^3}. \tag{11}$$

For more details, see Warren and Groot [33]. Note that in MPCD the viscosity can be computed as $\eta = 16.05\,\sqrt{m_0 k_B T}/a_0^2$, where m_0 and a_0 are the mass and the size of the cell used in MPCD algorithm. See [60, 66–68] for more details.

Once we know the viscosity, we compute the Reynolds number and the Péclet number. The Reynolds number quantifies the amount of inertial versus viscous forces acting on an object that moves in a fluid,

$$\mathrm{Re} = \frac{v_p r_c}{\nu} \tag{12}$$

where $r_c = 1$ is the solvent characteristic length and v_p is the microwimmer's propulsion velocity. For both the active colloids and the active polymer, the velocity is the one of the center of mass.

The Péclet number is an adimensional number used to quantify the measure of the activity. It is directly proportional to the self-propulsion speed and to the reorientation time [69]. The Péclet number has been used in bulk suspensions of Active Brownian Particles [70, 71] to quantify particles' activity. Differently from ABP, when dealing with swimmers (as in our case) the rotational dynamics of the colloid arises from interaction with the fluid and it is not prescribed (such as in ABP). Therefore we introduce a Péclet number based on the propulsion velocity, v_p. In this way one should expect that, for a given set of parameters, the reorientation time increases with the propulsion velocity and thus with the Péclet. In other words, the Péclet number is defined to describe the degree of activity in the system as the ratio between the self-propulsion of the microwimmer and a diffusion scale $\mathrm{Pe} = v_p\ \tau_r/\sigma$. However, different works have shown different definitions for this number. We define the Péclet number for the colloid following ref. [60] as,

$$\mathrm{Pe}_{col} = \frac{v_p R_{\mathrm{col}}}{D_{col}} \tag{13}$$

here $D_{col} = k_B T/6\pi\eta R_{col}$ is the estimated diffusion coefficient of the colloid and R_{col} is the colloid radius that is fixed to 2 for all our simulations (with the exception of the flow fields shown in **Figure 3** in which $R_{\mathrm{col}} = 3$ was chosen for better visibility). We have studied the following ranges $F_p \in [0, 50]$, $v_p \in [0, 1.25]$, $\mathrm{Pe} \in [0, 156]$ and $\mathrm{Re} \in [0, 12]$. As mentioned earlier, for some parameters we cannot assume that we are in Stokes flow conditions, so we should not use the relation $v_p = F_p/6\pi\eta R_c$

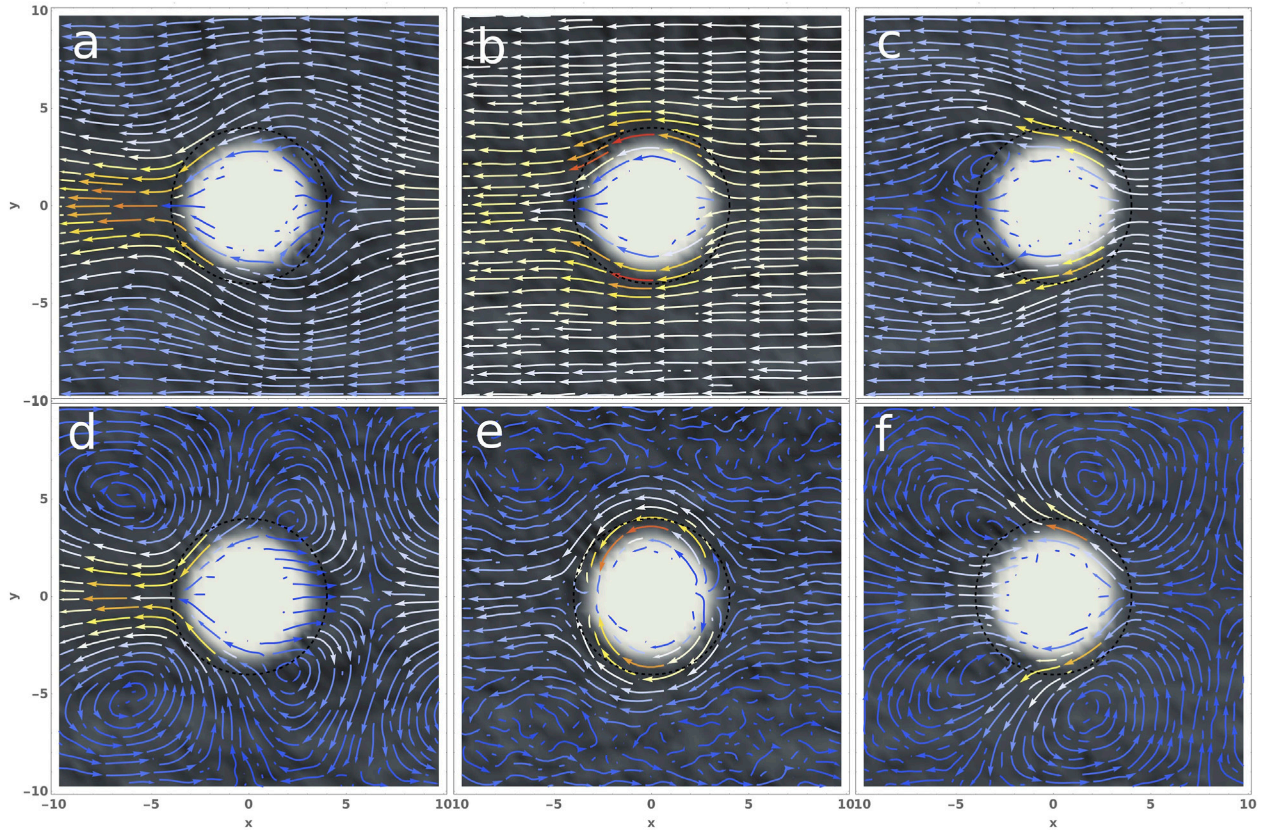

FIGURE 3 | Sections of the velocity fields in the lab frame (bottom row) and moving with the colloid (top row), for the pusher **(A,D)**, neutral **(B,E)** and puller **(C,F)** squirmer. surrounded by ~ 10^4 fluid particles and swimming to the right. The colour of the background is the averaged density of fluid particles, the colour of the arrows shows the fields magnitude. Here the colloid radius is $R_c = 3$ and $F_p = 100$ in order to obtain a clearer flow field. These values produce Pe ≈ {818, 655, 573} and Re ≈ {25, 20, 17} for the pusher, neutral and puller squirmers respectively.

for computing the colloids propulsion velocity, this is why we "measure" it as $v_p = \langle \boldsymbol{v}_{\mathrm{col}} \cdot \hat{\boldsymbol{e}} \rangle_t$. The values obtained are shown in **Figure 1** of the **Supplementary Material**. Note that it was found that the propulsion velocity of the colloid, and thus the Pe and Re, are not always linear with the propulsion force F_p. Moreover, they change whether we are dealing with pusher, neutral or puller squirmers. In **Figure 1** of the **Supplementary Material** we show the different propulsion velocities found (and their corresponding Pe and Re) for each type of squirmer. However, in all simulations presented, we remain in the range $F_p \in [0, 50]$ where the separation between the v_p values for different squirmer types is not so dramatic and the behaviour does not depart too much from linearity.

For the polymer we follow the ref. [11] and define the Péclet number as

$$\mathrm{Pe}_{pol} = \frac{F_p \, r_c}{k_B T} \tag{14}$$

where $r_c = 1$ represents the characteristic length of the monomers. The polymer's lengths, N_b, studied lay in a range between 40 and 100. For this particular cases we have explored values Pe = {0.01, 0.1, 1.0} that correspond with Reynolds numbers in the laminar regimen, around Re≈ 0.3.

2.5 Analysis Tools

In order to characterise our systems, we compute both structural and dynamical features. Concerning the active colloid, we first establish the velocity field of the solvent surrounding the swimmer to characterise the nature of each spherical squirmer (whether pusher, puller or neutral). Next, we study its dynamics by computing the mean square displacement, and estimate the effective diffusion coefficient from its long time behaviour. When dealing with the colloid in confinement we also analyze the orientation autocorrelation function (OACF) that supplies information about the reorientation time of the colloid. Concerning the active polymer, we first characterise how activity affects its structural features by computing the radius of gyration. Next, we study its dynamics by computing the mean square displacement of the center of mass and again estimate the effective diffusion coefficient from its long time behaviour.

2.5.1 Velocity Fields

For computing the solvent velocity fields around the colloid we run simulations of a fixed colloid in the center of the box pointing to the positive x-axis. Then, we perform a binning of the simulation box and average the velocities of the solvent particles inside each bin, finally we also take ensemble and time averages in the stationary state. The velocity fields shown in **Figure 3** correspond to a slab that has the same height as the colloid (D_{col}). The arrows represent the *xy*-projection of the full 3D velocities.

2.5.2 MSD

Concerning dynamical features, we compute the mean square displacement

$$\mathrm{MSD}(t) = \langle [\mathbf{r}_{\mathrm{cm}}(t) - \mathbf{r}_{\mathrm{cm}}(0)]^2 \rangle \tag{15}$$

Where $\mathbf{r}_{\mathrm{cm}}$ indicates the position of the center of mass of the colloid/polymer. The average is taken over several colloids/polymers. The long time behaviour of the MSD, corresponds to the diffusion coefficient D, $\mathrm{MSD}(t) = 6Dt$. It is worth noting that when confinement takes place in a cylinder with a small radius, it might be better to consider the system as one dimensional, thus $\mathrm{MSD}(t) = 2Dt$. However, this is not our case since we consider that the agents have sufficient space to diffuse in the transverse directions. This leads to a more straightforward comparison between the different systems.

2.5.3 OACF

The orientation autocorrelation function is computed for the colloid in confinement to asses the impact of the confinement in the rotational diffusion (or equivalently, the reorientation time) of the colloid.

$$\mathrm{OACF}(\Delta t) = \frac{1}{N_{\Delta t}} \sum_{i=0}^{N_{\Delta t}} \hat{\boldsymbol{e}}(t_i) \cdot \hat{\boldsymbol{e}}(t_i + \Delta t) \tag{16}$$

Here $\Delta t = n\ dt$ where dt is our base time step. The scalar product of the orientation at a given time $\hat{\boldsymbol{e}}(t_i)$ with itself at a delayed time $\hat{\boldsymbol{e}}(t_i + \Delta t)$ is averaged over the intervals of length Δt, starting at all the possible t_i's, that fit into the total simulation time $T_{\mathrm{sim}} = N_{\mathrm{tot}} dt$. So there would be $N_{\Delta t} = N_{\mathrm{tot}} - n + 1$ intervals of the same length in the full simulation interval for a given n.

2.5.4 RoG

The radius of gyration R_g for the active polymer is computed according to the relation,

$$R_g^2 = \frac{1}{N} \sum_{k=1}^{N} (\boldsymbol{r}_k - \boldsymbol{r}_{\mathrm{cm}})^2, \tag{17}$$

where $\boldsymbol{r}_{\mathrm{cm}}$ is the position of the center of mass of the polymer, $\boldsymbol{r}_k$ is position of the *k thruster* particle and N is the number of bead of the polymer.

3 RESULTS

In what follows we present the results obtained for both microwimmers, either in bulk or in cylindrical confinement. We start with the simplest object: the spherical squirmer (**Section 3.1**) characterising its hydrodynamic features (**Section 3.1.1**) and its dynamical properties (**Section 3.1.2**). When confined in a cylindrical channel, we also compute its orientation autocorrelation function (**Section 3.1.3**). Next, we study the more complex-shape active polymer (**Section 3.2**), characterizing its structural (**Section 3.2.1**) and dynamical (**Section 3.2.2**) properties, compare our results with the passive and Brownian counterpart.

3.1 Active Colloids

3.1.1 Flow Fields

To start with, we present our results for a spherical squirmer and study the velocity fields for the pusher, the puller, and the neutral swimmer.

Figure 3 displays the velocity flow fields for this three squirmers computed as explained in the previous section: pusher (a, d), neutral (b, e) and puller (c, f) squirmer. Comparing our results with the typical flow fields expected for squirmers (e.g. ref. [49]) the flow fields reported in **Figure 3** are not so symmetrical, in the case of the puller and pusher lab frames (**Figures 3D,F**). The four characteristic vortices of the flow field when periodic boundary conditions are present [48] seem to be shifted to the negative *x*-direction, compressing the two at the front and stretching the two at the back. In the same way, in the relative frame, we can see smaller swirls than usual at the front of the pusher (**Figure 3A**) and somewhat elongated ones at the back of the puller (**Figure 3C**). In the case of the neutral swimmer, the characteristic source dipole of the lab frame (**Figure 3E**) is completely compressed against the swimmers surface, and some turbulent flow is appreciated at the edges of the *y*-dimension of the section. All these deviations from the usual flow fields are ascribed to inertial effects of the fluid stemming from the high Reynolds number present in our simulations [59]. In **Supplementary Material** we show the flow fields for a different set of parameters (lower Reynolds number, at Re ≈ 0.1) for which we find a more typical squirmer flow field [48, 49]. In ref. [48] the authors also comment on an analytical solution and state that it is indistinguishable from the one found in their simulations. An analytical solution for the flow field without PBCs in terms of a source dipole, a force dipole and a source quadrupole is also provided in ref. [46] following a different approach but compatible with the usual derivation by Blake followed by [48]. Ref. [59] studies in detail how the Reynolds number affects the flow fields around squirmers.

Confining the colloid inside a cylindrical channel has a drastic impact in the solvent flow fields (**Figure 4**), since the channel walls change the boundary conditions of the fluid.

For the pusher and the puller in the absolute frame (**Figures 4A,D**) we observe that the two vortices at the back and front respectively have disappeared, while the other two (at the front of the pusher and at the back of the puller) seem to have retracted to a closer position directly in front of the pusher and behind the puller. A similar damping of vorticity has already been reported in ref. [72] and may be attributed to the suppression of the fluid's long-wavelength modes due to the confinement [73]. In the relative frame of reference, the swirls have also contracted further, and it is now difficult to distinguish them from just turbulent flow. In the case of the neutral swimmer (**Figures 4B,E**) the flow fields do not differ that much with respect to the ones

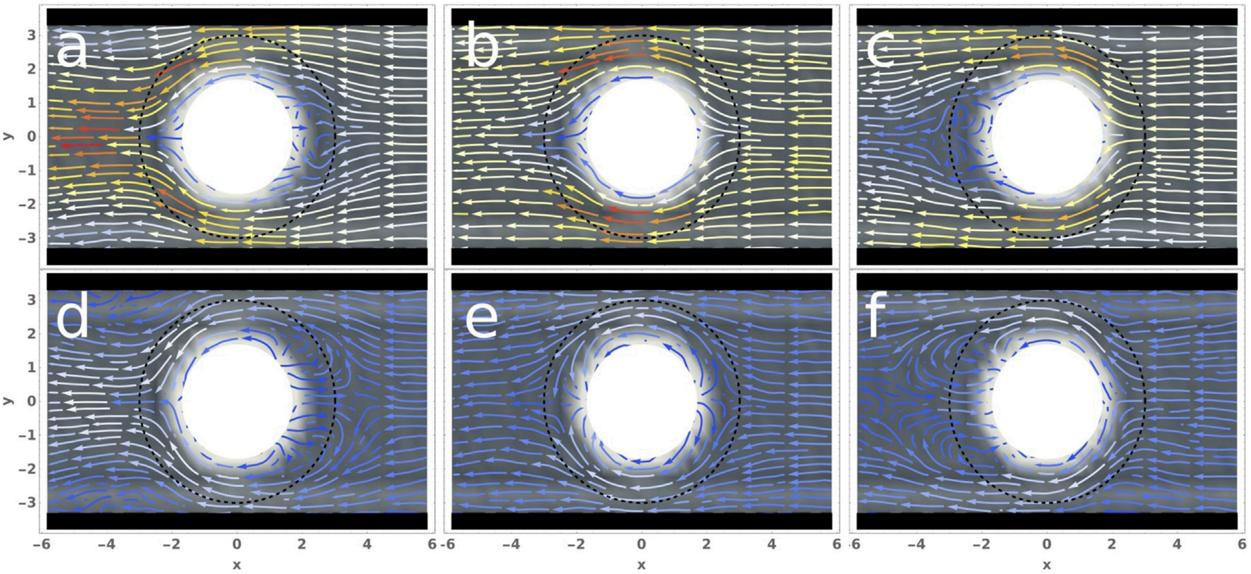

FIGURE 4 | Solvent flow fields of the colloid confined in an cylindrical channel ($R_{\mathrm{cyl}} = 3.5$) in the lab frame (bottom row) and moving with the colloid (top row), for the pusher **(A,D)**, neutral **(B,E)**, and puller **(C,F)** squirmer. Here the colloid radius is $R_c = 2$ and $F_p = 50$. These values produce Pe ≈ {90, 76, 61} and Re ≈ {3.9, 3.3, 2.7} for the pusher, neutral and puller squirmer respectively.

encountered in bulk, with the exception that now there are no turbulent regions at the edges of the flow field.

3.1.2 Diffusion

When dealing with a colloidal squirmer in bulk, we study its dynamical features by estimating the long time diffusion coefficient normalised by the diffusion of a passive colloid in bulk via the center of mass mean square displacement, as explained in **Section 2.5.**, for the three types of squirmers (**Figures 5A–C**).

The top row of panels in **Figure 5** represent the MSD for a bulk dilute suspension of pushers (a), neutrals (b) and pullers (c). Their long time behaviour corresponds to the diffusion coefficient reported in **Figure 6A** From the results presented, it is reasonable to conclude that the three types of squirmer diffuse almost the same for the ranges of Péclet numbers studied. As expected, the diffusion of the three of them increases when increasing their thrust force and thus their Péclet number.

In **Figure 6A** it is worth noting that as we increase the thrust force and thus the Péclet and Reynolds numbers, the diffusion behavior changes significantly. When we are in the range of Re ≪ 1 the diffusion increases significantly while we increase the Pe. When we approach Re ≈ 1 the increase in diffusion is dampened reaching what seems to be a saturation as Re ≫ 1.

The middle and bottom row of panels in **Figure 5** represent the MSD for a confined dilute suspension of pushers (a), neutrals (b) and pullers (c). The middle panels study the dynamics of swimmers in a channel with the smallest radius, while varying the Peclet number for pushers (d), neutrals (e) and pullers (f). The bottom panels study the dynamics of swimmers at the highest Peclet in a channel with varying radius for pushers (g), neutrals (h) and pullers (i). When we confine the active colloid inside a cylindrical channel the symmetry between pushers and pullers is lost. Pushers will tend to reorient parallel to the wall, while pullers will do so perpendicularly. In this way, mobility of pushers should be increased while pullers should be more prone of getting "stuck" at the wall, which is reflected in the MSD curves in **Figures 5D–F**. This is a well known behavior for the interaction of squirmers with walls [45, 49], that has been used to explain the accumulation of certain microorganisms at surfaces [50]. The coupling between a microswimmer close to the wall and the solvent is affected because a portion of its hydrodynamics region (see **Figure 2**) lies outside the cylinder, where no solvent particles are present. Although this effect can contribute an additional torque, the volume of this excluded region is small compared with the rest of the hydrodynamic region, and it is not seen to affect the qualitative features of the hydrodynamic coupling between the microswimmer and the confining wall. Moreover, when studying the diffusion for different channel radii (**Figure 6C**), if this effect had a relevant contribution, we would expect to see a clear modulation of the diffusion varying radius for all types of squirmers, since the greater the radius, the smaller the excluded portion of the hydrodynamic region.

The same information can be recovered when plotting the OACF for each system (as will be shown in **Figures 7E–G**) curves).

As shown in the MSD curves (**Figures 5D–F**), for the pusher we detect a slight increase at large times, while for the puller the curves collapse showing a significant decrease in its motility at large times for all studied Péclet numbers. This is due to the wall-facing effect described previously, which is consistent not only with the decrease of motility, but also with the apparent independence of the diffusion with the Péclet number. The shape of the MSDs curves for the neutral

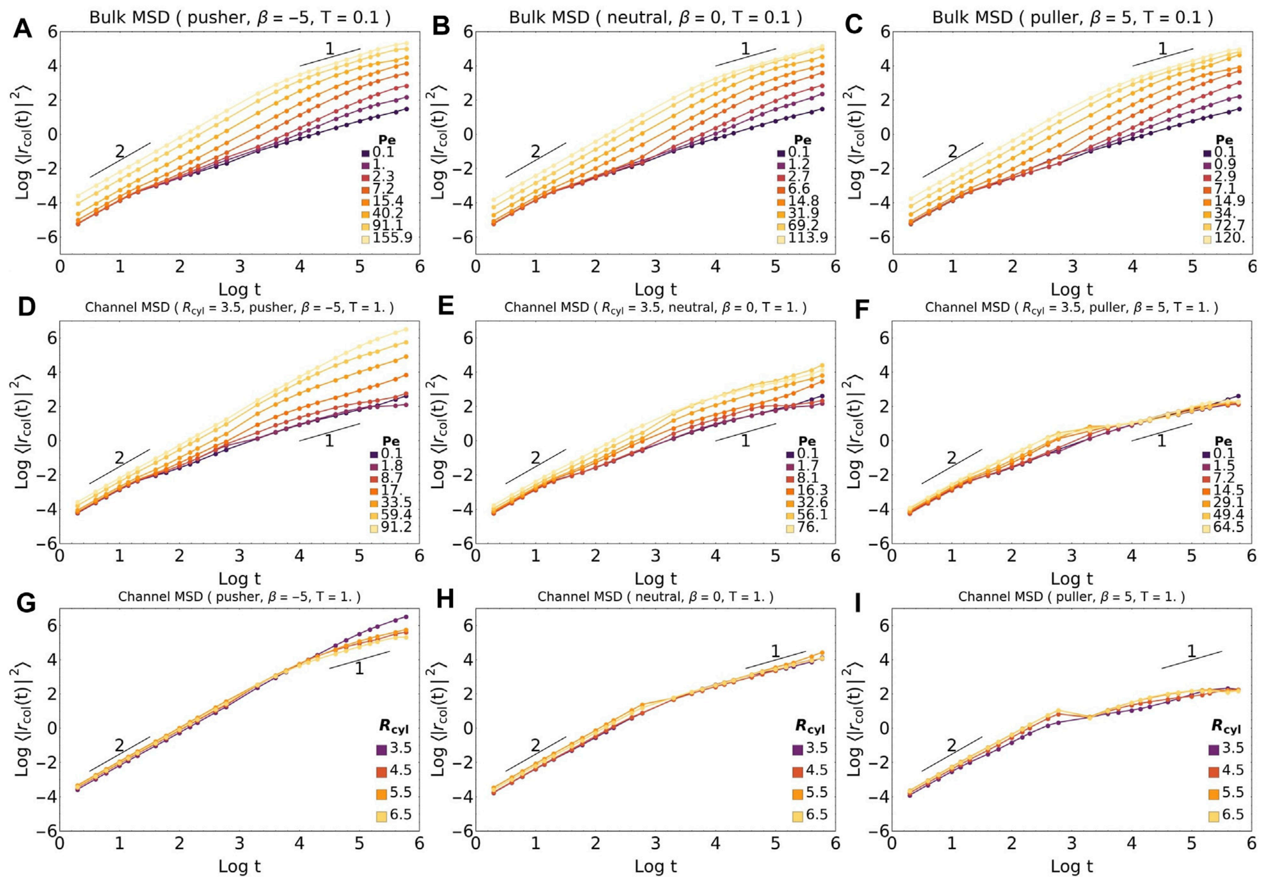

FIGURE 5 | MSDs for the three squirmer types studied. Left column: pusher [panels **(A, D,** and **G)]**. Center column: neutral [panels **(B, E,** and **H)**]. Right column: puller [panels (**C, F,** and **I)**]. Top row: bulk [panels **(A, B,** and **C)**]. Center row: in cylindrical confinement for different Pe's for the smallest channel radius $R_{\mathrm{cyl}} = 3.5$ [panels **(D, E,** and **F)**]. Bottom row: for different channel radii for the highest Péclet numbers available corresponding to the highest thrust force $F_p = 50$ [panels **(G, H,** and **I)**].

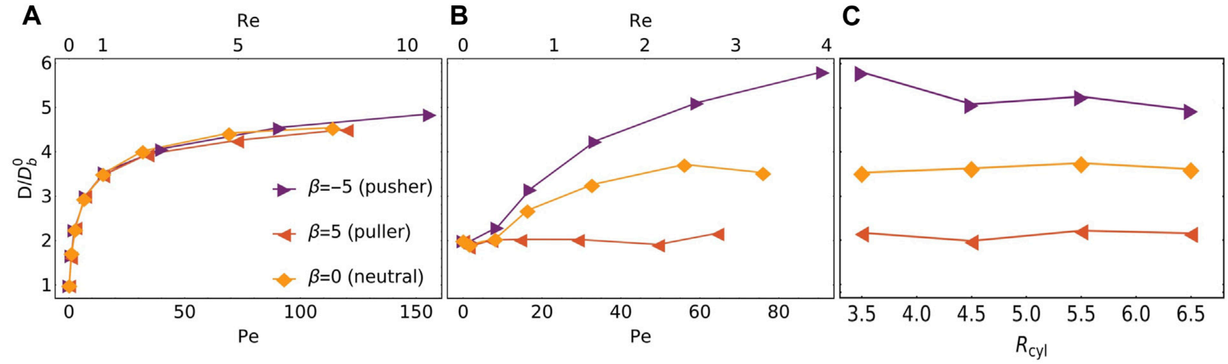

FIGURE 6 | Measured diffusion as a function of the Péclet number for the active colloid in bulk **(A)**, in confinement for the narrowest channel $R_{\mathrm{cyl}} = 3.5$ **(B)** and as a function of the cylinder radius for the highest Péclets **(C)** for the three squirmer types studied. We normalize by the diffusion of a passive colloid in bulk $D_b^0 = 0.032179$. In the two first plots a secondary horizontal axis shows the corresponding Reynols number.

swimmer (**Figure 5E**) also follow from this argument. The neutral squirmer gains its thrust force symmetricaly between its front and back. Therefore, it propels on its front more than the pusher but less than the puller, and propels on its back more than the puller but less than the pusher. The fact that this system is between the two is confirmed by the MSDs curves. The diffusion curves (**Figures 6A–C**) show more clearly what we have just addressed.

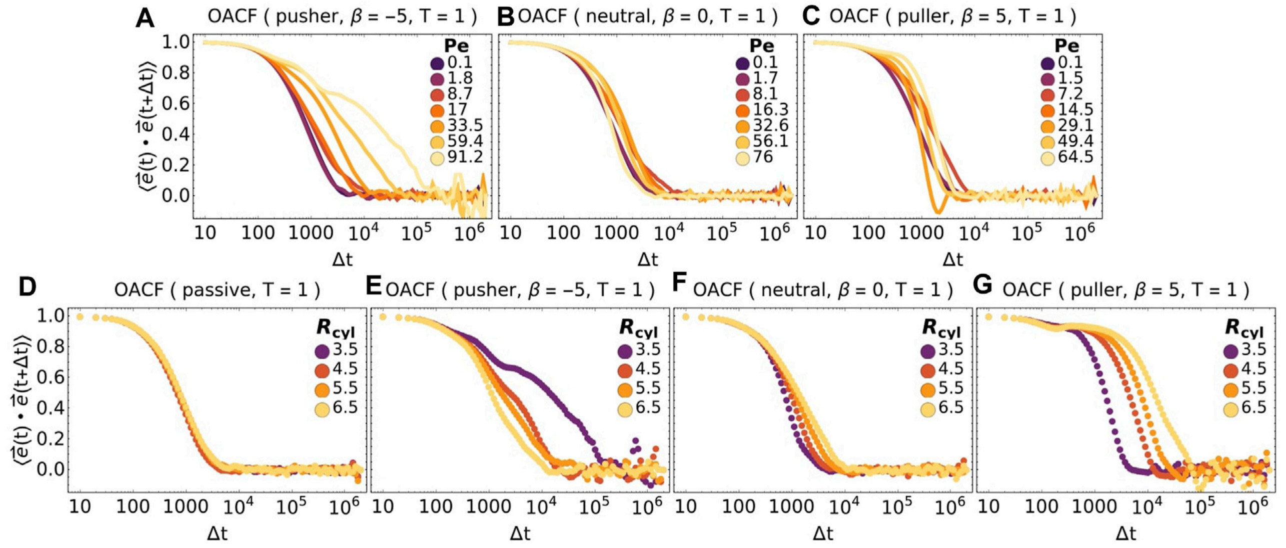

FIGURE 7 | Auto-correlation function for the colloids orientation vector. Top: for the smallest cylinder radius $R_{cyl} = 3.5$ and all the Péclet numbers studied for pusher **(A)**, neutral **(B)** and puller **(C)**. Bottom: for all the studied cylinder radii for a passive colloid **(D)** for which $F_p = 0$, Pe = 0.1 ≈ 0 and the highest Péclet numbers available (all corresponding to $F_p = 50$) for the three types of squirmers: pusher **(E)**, puller **(F)**, and neutral **(G)**.

In **Figure 6C** we report the normalized diffusion for the highest Péclet number of the three types of squirmers in confinement as a function of the channel radius. The major effect of varying the channel radius occurs for the pusher, while the puller and neutral squirmer's diffusion seems to remain unaffected by it (in the studied range). This is coherent with the wall-facing argument previously described. The diffusion is a long time property, while for the studied radii the colloid reaches the channel wall at much shorter time scales. Therefore once the colloid has reached the wall, it might get stuck due to the wall-facing effect regardless of the channels radius.

3.1.3 Orientation Aturocorrelation Function

Finally, we compute the orientation auto-correlation function (OACF) when active colloids are confined in a cylindrical channel, as depicted in **Figure 7**. The OACF measures the rotational diffusion (or equivalently, the reorientation time) of a colloid, i.e., for how long the colloid retains its swimming direction before it is randomized by fluctuations.

The top row of **Figure 7** represents the OACF for the system confined in the smallest cylinder, when varying the Péclet number. Whereas the bottom row represents the OACF for an active colloid propelling at the highest Péclet number and confined in cylinders with different radii. In the case of a pusher (**Figure 7A**) we detect a clear increase of the reorientation time with increasing Pe. This is expected for any non-chiral active particle which increases its Pe by increasing its propulsion force [69]. Moreover, due to the wall-rebound argument discussed previously, this effect could be amplified. When dealing with the neutral (**Figure 7B**) and the puller (**Figure 7C**) squirmers, the interpretation is less clear. It seems that in both cases starting from the lowest Pe the reorientation time increases until it reaches a point where the behaviours for both squirmers is different. For the neutral squirmer, as we keep increasing Pe the reorientation time decreases, reaching a minimum for the highest Pe. Whereas for the puller, at Pe = 14.5 there is a sharp decrease and then, as we keep increasing Pe, a slight recovery. Anyhow it is hard to draw solid conclusions in both cases. One reason could also be due to not enough statistics.

Figures 7D–G offers a much clearer interpretation. In these panels we show how the OACF changes as we vary the channel radius keeping in all cases the maximum Pe available, corresponding to the highest thrust force $F_p = 50$. As expected for a passive colloid (**Figure 7D**) the OACF is the same regardless of the channel radius. Moving now to the pusher (**Figure 7E**) we notice an increase of the reorientation time as we decrease the channel radius, consistent with the wall-rebound argument. For the puller (**Figure 7G**) we encounter the opposite behaviour, the reorientation time increases with increasing radius: this can be explained with the wall-facing argument plus the fact that when the puller is swimming against the wall it is in an unstable state, similar to when a pencil is left standing at its tip, so it will change its orientation. Some times this reorientation will lead him back to the center of the channel, but the narrower the channel, the sooner it will encounter again the wall and reorient again. For the neutral squirmer (**Figure 7F**) we are again in between pushers and pullers but since neutrals propel in their front side, as pullers, the behaviour observed is more similar to pullers than to pushers.

3.2 Active Polymer

In this section we present our results on structural and dynamical features of the active polymer in an explicit solvent. In particular, we focus on the radius of gyration R_g, and on the diffusion coefficient D, computed via the long-time behaviour of the mean square displacement of the polymer's center of mass. We consider the active polymer first in bulk and then confined in a cylindrical

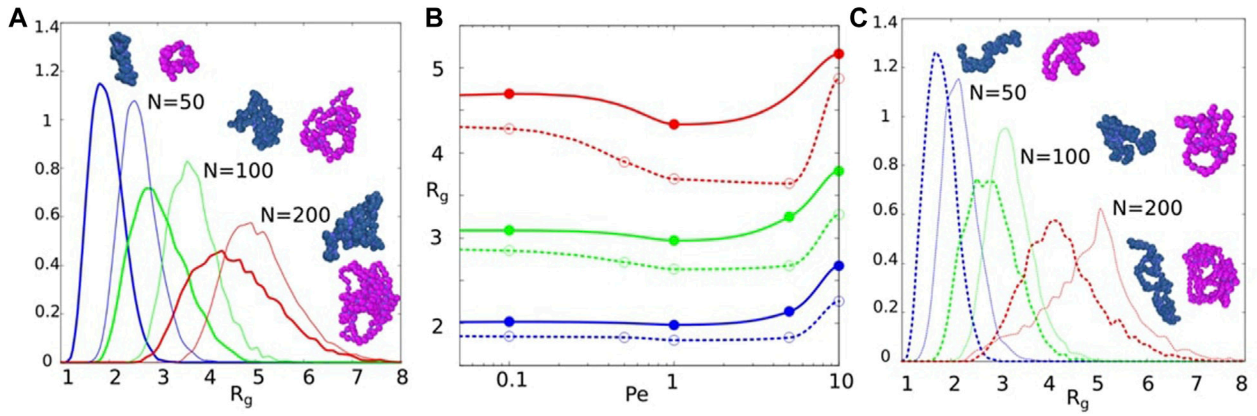

FIGURE 8 | Probability distribution of the radius of gyration for passive (Pe = 0, thick line) and active (Pe = 10, thin line) polymers of N = 50 (blue), N = 100 (green), N = 200 (red) monomers in bulk **(A)** and in confinement **(C)**. The snapshots illustrate typical conformations for the passive (blue) or active (magenta) polymers. **(B)** Average value of R_g as function of Pe for different polymer sizes. Continuous lines are for the polymer in bulk and dashed lines for the polymer under confinement.

channel, underlying the effect of the activity in comparison with the passive polymer behaviour in the same conditions. When in bulk, we unravel the effect of hydrodynamics comparing our results to the results obtained in ref. [11] for Active Brownian polymers (without hydrodynamics).

3.2.1 Radius of Gyration

Figures 8A,C shows the probability distribution function of the radius of gyration for the polymer in bulk (panel A, continuous lines) and confined in a channel (panel C, dashed lines), comparing the passive (thick lines) to the active (thin lines) case. We also sketch snapshots representing typical conformations observed in each case, both for the passive case (in blue) and for the active one (in magenta). Panel B represents the average radious of gyration as a function of the Péclet number for polymer length of N = 50 (blue), N = 100 (green) and N = 200 (red) in bulk (continous line) and in a channel (dashed line).

When studying a passive polymer in bulk (thick lines in **Figure 8A**), our model recovers the expected increase of the radius of gyration with the polymer size. This behaviour is observed also in the presence of active forces as shown by the thin lines in **Figure 8A**. In order to underline the relevance of hydrodynamics it would be interesting to compare the results obtained for the active polymer with those for the Active Brownian Polymer reported in ref. [11]. However, a direct comparison is not possible, due to the different features of the chosen polymer's model. In ref. [11] the authors used a bead-spring self-avoiding polymer, whereas in our study we have used an ideal polymer.

When studying the average of the radius of gyration as a function of the Péclet number (**Figure 8B**) we detect a non-monotonic behaviour.

For short polymers (N = 50), R_g remains constant at low activities (until Pe = 5): the same behaviour has been detected in ref. [11] for Active Brownian polymers, sign that hydrodynamics is not relevant for low activities.For relatively short polymers (N = 50 and 100) the radius of gyrations is almost constant when activity is low, and increases at high activity. This behaviour corresponds to what one would expect if the polymer behaved like a flexible polymer [17]. The collapse is a consequence of the time scale separation of the thermal and active contributions. The subsequent increase of the radius of gyration is due to the reduced influence of hydrodynamic interactions for larger values of Peclet number.However, when activity increases, the presence of hydrodynamics affects the polymer conformation since R_g increases. On the other side, without hydrodynamics, R_g decreases. For larger polymers (N > 50) R_g reaches a minimum value before increasing again. The same behaviour has been already reported in ref. [17] for active fully flexible Brownian self-avoiding polymer.

Larger polymers (N > 200) behave like a semi-flexible polymer [17], characterised by an initial decrease of R_g (more compact shape) for small values of the Péclet number, leading to an increase of R_g with the activity (more open shape). This non-monotonic behaviour resembles the behaviour observed for the end-to-end distance of active polymers in the presence of hydrodynamics [13, 14].

Even when an active polymer is confined in a cylindrical channel (**Figure 8C**), activity plays the same role on the probability distribution of the radius of gyration. The radius of gyration increases with the number of monomers N when hydrodynamics is taken into account. This is expected, as we increase the mass of a polymer. Moreover, comparing the active (thin) to the passive (thick) polymer, the increase is more stretched in the active than in the passive case. Interestingly, the confinement does not seem to affect R_g since same size active polymers (50, ≤ ,N ≤ 200) are characterised by the same radius of gyration when in bulk or in a channel. Probably, the reason for this is that we have chosen to study a channel whose diameter is relatively large, thus not differing too much from the bulk system.

3.2.2 Diffusion

In order to understand the dynamical features of an active polymer in bulk and in confinement, we compute the MSD of the active polymer's center of mass.

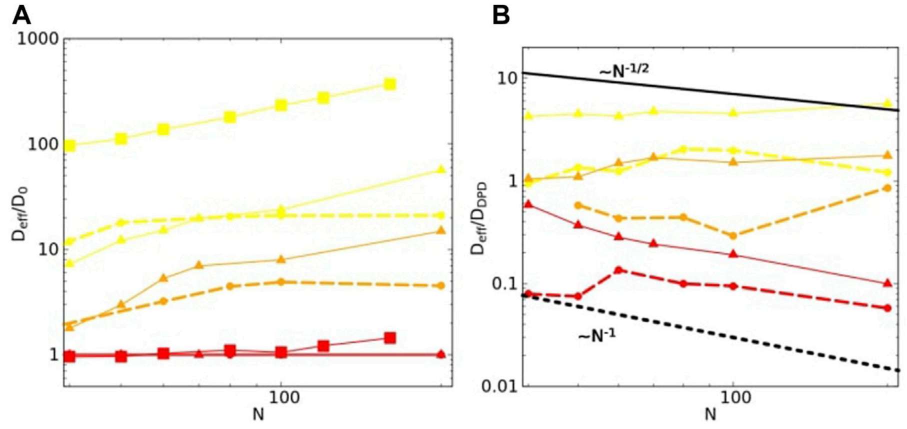

FIGURE 9 | Diffusion coefficient of the polymer center of mass D_{eff} as a function of the polymer length for three different Pe values 0 (red), 0.1 (orange) and 1 (yellow). **(A)** Normalised by the diffusion coefficient of the passive polymer (D_0); **(B)** normalised by the mean field diffusion of a DPD solvent particle **Eq. 11**. Square dots are results from ref. [11] triangles are results for the system in bulk and circles for system in confinement.

As in ref. [11] for the system without hydrodynamics and like the squirmers studied in the previous section, the MSDs present at short time a ballistic regime ($MSD \propto t^2$), a diffusive dependence at long time ($MSD \propto t$) and for intermediate times there is a crossover typical of a super-diffusive regime ($MSD \propto t^{\nu}$, with $1 < \nu < 2$). From the MSD long time dependence, we estimate the diffusion coefficient. **Figure 9** represents the diffusion coefficient D_{eff} of the polymer's center of mass as a function of the polymer size, when varying the Péclet number. While in panel A we have normalised the diffusion coefficient by the diffusion coefficient of the passive polymer (D_0), in panel B we have normalised the diffusion coefficient by the mean field diffusion of a DPD solvent particle (D_{sol} in Eq. 22).

In **Figure 9A**. we show the results for the effective diffusion normalized by the diffusion coefficient of the passive case (D_0) as a function of the polymer size. We study values of activity ranging from the passive case (in red) to Pe = 1 (yellow case) and observe that activity increases the effective polymer diffusion. Meanwhile, if we compare the Brownian diffusion [11] (yellow square) for the same activity Pe = 1.0 with our results (yellow triangles) we detect the same dependence with N but approximately 10 times smaller. The effect of hydrodynamics is to slow down the polymers' motion, as expected. Finally, if we compare the results obtained for the bulk system with the ones for the channel we observe how confinement does not seem to affect the small polymers ($N < 50$), but turns out to be relevant when the length of the polymer is increased. For longer polymers ($N > 70$) the confinement affects the polymer's motion and the diffusion decreases when the polymer is too long.

On the other hand, in **Figure 9B**. the effective diffusion has been normalized by the mean-field diffusion given by **Eq. (11)**. The idea to represent the data in this way was to be able to establish a power law dependence of the diffusion coefficient with the polymer size and compare it with the prediction expected for the diffusion by the Rouse and Zimm [74] theory of Gaussian chains. Within this theory, the chain center of mass diffusion $D_{Rouse} \propto N^{-1}$ and $D_{Zimm} \propto N^{-1/2}$. As shown in **Figure 9B**, when the polymer is passive (red line), the power law resembles that predicted by the Zimm model, which takes into account the hydrodynamic interactions between the beads of the polymer. While when the activity is relatively high (yellow line) the behavior is not similar to that expected in this model, since other effects appear due to the activity of the system.

In order to understand this behaviour, we compute the Schmidt number, defined as $Sc = \nu/D_{sol}$, being $\nu = 1.25$ the kinematic viscosity of the DPD fluid and D_{sol} the diffusion of the solvent particles. Estimating the kinematic viscosity via the mean field model of Groot and Warren's [33], and measuring D_{sol}, we estimate Sc = 2.35 for the solvent in all simulations. Whenever the Schmidt number is larger than one, the momentum diffusion dominates and hydrodynamics is relevant. However, since in our case the Schmidt number is around one, we conclude that the hydrodynamic coupling is not too strong. Therefore, we observe both scaling regimes, Rouse and Zimm.

4 DISCUSSION

In many paradigmatic examples of active matter such as biological microswimmers or synthetic active colloids, these are typically immersed in a solvent and the hydrodynamic interactions produced by the movement of the particles are relevant. Usually the introduction of these hydrodynamic interactions in active systems has been carried out through lattice models such as LB, that consider hydrodynamic effects but neglect thermal fluctuations, or MPCD that allow for the study of systems at low Reynolds number [75]. In this work we develop a new framework for the introduction of hydrodynamic interactions in mesoscopic molecular dynamics simulations. To do so, we have used the well known DPD model that has been showed to be a simple and well behaved coarse-grain model (for a specific set of parameters) for the implementation of hydrodynamics interactions in passive systems.

One of the main advantages of this new implementation is the possibility of easily taking into account thermal fluctuations for swimmers of complex shapes. Moreover, our implementation has been developed as an extension of the LAMMPSs open source package and will be sent to the LAMMPS developers (constantly maintaing the code), making our numerical approach readily available to everyone.

In active systems there are a plethora of different mechanisms that produce the propulsion of the microwimmers, such as beating of flagella or chemical reactions. In our approach, we focus on the fact that in all these cases, the agents exert a force on the solvent in which they are immersed in order to achieve thrust. Depending on the type of propulsion mechanism employed, the exerted force has its own distinct features but it always respects the conservation laws of the different physical quantities. The model and its implementation is described in details, mainly based on momentum conservation: this corresponds to the fact that the force experienced by the microwimmer in its propulsion must be compensated by the stresses induced in the solvent.

To verify the validity of our model, we study two particular cases whose phenomenology has been well characterised by other numerical methods. The first of these cases are spherical squirmers, which represent the simplest model of a microwimmer in which the hydrodynamics of the system is taken into account. The second example studied is an active polymer, which is nothing more than a first approximation to a slightly more complex structure: a chain of swimmers. In this case, our proposed method is applied in the same way for each of the monomers (swimmers) that form the polymer. As shown in the Results section, the proposed method leads to a phenomenology, such as flow fields, dynamical and structural features, consistent with the results obtained for the same systems studied with different numerical models.

Concerning the active colloid, we have been able to reproduce the solvent flow fields for the different types of swimmers (**Figure 3**), observing a characteristic deformation of the solvent flow fields due to the inertial effects present in the fluid at moderate Reynolds numbers Re ~ 20. We have been able to asses the impact of these inertial effects on the dynamics and hydrodynamics of the swimmer and to conclude that pushers are the most efficient swimmers (in the sense that they develop a larger propulsion velocity for the same propulsion force, **Figure 1** of the **Supplementary Material**), followed by neutrals and pullers when the Reynolds number is increased enough. For the ranges studied in the majority of our work, we showed that when swimming in bulk, diffusion is hardly affected by the choice of squirmer type (**Figure 6A**), and begins to saturate as we venture into higher Reynolds numbers. When the swimmer is confined inside a cylindrical channel, the flow fields changed dramatically in order for the fluid to adapt to the new boundary conditions (**Figure 4**). The confined geometry breaks this symmetry in the diffusion between the squirmer types (**Figure 6B**), as the behaviour of each swimmer near the channel wall is completely different: while pushers tend to rebound, aligning parallel to the wall and thus increasing their diffusion, pullers tend to get stuck, aligning perpendicularly with the wall and thus drastically decreasing their diffusion. Neutral squirmers lay in between both behaviours, but closer to pullers, as they slightly rely on the solvent ahead of them for achieving thrust. When varying the radius of the confining channel, diffusion of neutrals and pullers was hardly affected, while pushers enhanced their diffusion with decreasing channel radius (**Figure 6C**). Finally, we discussed the effect of the confinement in the reorientation time of the swimmers (**Figure 7**). We showed that pushers have slower reorientation dynamics the larger the Péclet number, but could not conclude anything too clear for neutrals and pullers. Although when the Péclet is the highest and we increase the channel radius, the reorientation behaviour of pushers and pullers is clearly opposite: pushers increase their reorientation time while pullers decrease it. Again, neutrals lay in-between both behaviours although a little closer to pullers than to pushers.

In the active polymer case, we have compared the radius of gyration R_g and diffusion to the system without hydrodynamics (Active Brownian Polymer). Concerning the radius of gyration R_g, the behavior of the polymer has been characterised as a function of both the polymer length and the Péclet number. Even though the radius of gyration monotonically increases with the polymer length (**Figure 8**), the dependence with the activity is not so straightforward. For short polymers R_g always increases with activity, whereas for long polymers it reaches a minimum value. This behaviour has been already detected in active fully flexible Brownian self-avoiding polymers. On the other hand, confinement always decreases R_g with respect to the system in bulk. When studying the dynamics of the polymer, we have compared our results with the analytical results for the Rouse and Zimm models, and concluded that our model (for the set of parameters used) is compatible with the prediction of the Rouse model at low Peclet (when hydrodynamics does not seem to play a relevant role), and is compatible to the Zimm model at higher Peclet number, when the monomers of the polymer chain can interact with each others due to hydrodynamics.

As in Ref. 76, having characterised the behaviour of individual swimmers in a solvent, we plan to use our numerical tool to study more dense suspensions of active colloids or active polymers. This will allow us to study their collective behaviour, their aggregation (if present) and the interplay played by hydrodynamics and activity, with the idea of comparing our numerical results to experiments on active synthetic colloids or active living swimmers (such as algae or bacteria), where hydrodynamics is relevant.

DATA AVAILABILITY STATEMENT

The raw data supporting the conclusions of this article will be made available by the authors, without undue reservation.

AUTHOR CONTRIBUTIONS

All authors listed have made a substantial, direct, and intellectual contribution to the work and approved it for publication.

FUNDING

CV acknowledges fundings from MINECO PID2019-105343GB-I00 and EUR2021-122001. I. Pagonabarraga acknowledges support from Ministerio de Ciencia, Innovación y Universidades MCIU/AEI/FEDER for financial support under grant agreement PGC2018-098373-B-100 AEI/FEDER-EU, from Generalitat de Catalunya under project 2017SGR-884, Swiss National Science Foundation Project No. 200021-175719 and the EU Horizon 2020 program through 766972-FET-OPEN NANOPHLOW.

SUPPLEMENTARY MATERIAL

The Supplementary Material for this article can be found online at: https://www.frontiersin.org/articles/10.3389/fphy.2022.926609/full#supplementary-material

REFERENCES

1. Gompper G, Winkler RG, Speck T, Solon A, Nardini C, Peruani F, et al. The 2020 Motile Active Matter Roadmap. *J Phys Condens Matter* (2020) 32(19): 193001. doi:10.1088/1361-648x/ab6348
2. Aranson IS. Active Colloids. *Phys.-Usp.* (2013) 56(1):79–92. doi:10.3367/ufne.0183.201301e.0087
3. Zöttl A, Stark H. Emergent Behavior in Active Colloids. *J Phys Condens Matter* (2016) 28(25):253001. doi:10.1088/0953-8984/28/25/253001
4. De Corato M, Arqué X, Patiño T, Arroyo M, Sánchez S, Pagonabarraga I. Self-propulsion of Active Colloids via Ion Release: Theory and Experiments. *Phys Rev Lett* (2020) 124(10):108001. doi:10.1103/physrevlett.124.108001
5. Lucia A, Guzmán E. Emulsions Containing Essential Oils, Their Components or Volatile Semiochemicals as Promising Tools for Insect Pest and Pathogen Management. *Adv Colloid Interf Sci* (2021) 287:102330. doi:10.1016/j.cis.2020.102330
6. Ebbens SJ. Active Colloids: Progress and Challenges towards Realising Autonomous Applications. *Curr Opin Colloid Interf Sci* (2016) 21:14–23. doi:10.1016/j.cocis.2015.10.003
7. Hortelão AC, Patiño T, Perez-Jiménez A, Blanco À, Sánchez S. Enzyme-powered Nanobots Enhance Anticancer Drug Delivery. *Adv Funct Mater* (2018) 28(25):1705086. doi:10.1002/adfm.201705086
8. Li J, Thamphiwatana S, Liu W, Esteban-Fernández de Ávila B, Angsantikul P, Sandraz E, et al. Enteric Micromotor Can Selectively Position and Spontaneously Propel in the Gastrointestinal Tract. *ACS nano* (2016) 10(10):9536–42. doi:10.1021/acsnano.6b04795
9. Qian J, Kai G. Application of Micro/nanomaterials in Adsorption and Sensing of Active Ingredients in Traditional Chinese Medicine. *J Pharm Biomed Anal* (2020) 190:113548. doi:10.1016/j.jpba.2020.113548
10. Palacci J, Sacanna S, Vatchinsky A, Chaikin PM, Pine DJ. Photoactivated Colloidal Dockers for Cargo Transportation. *J Am Chem Soc* (2013) 135(43): 15978–81. doi:10.1021/ja406090s
11. Bianco V, Locatelli E, Malgaretti P. Globulelike Conformation and Enhanced Diffusion of Active Polymers. *Phys Rev Lett* (2018) 121(21):217802. doi:10.1103/physrevlett.121.217802
12. Isele-Holder RE, Elgeti J, Gompper G. Self-propelled Worm-like Filaments: Spontaneous Spiral Formation, Structure, and Dynamics. *Soft matter* (2015) 11(36):7181–90. doi:10.1039/c5sm01683e
13. Eisenstecken T, Gompper G, Winkler R. Conformational Properties of Active Semiflexible Polymers. *Polymers* (2016) 8(8):304. doi:10.3390/polym8080304
14. Winkler RG, Gompper G. The Physics of Active Polymers and Filaments. *J Chem Phys* (2020) 153(4):040901. doi:10.1063/5.0011466
15. Michieletto D. Non-equilibrium Living Polymers. *Entropy* (2020) 22(10):1130. doi:10.3390/e22101130
16. Locatelli E, Bianco V, Malgaretti P. Activity-induced Collapse and Arrest of Active Polymer Rings. *Phys Rev Lett* (2021) 126(9):097801. doi:10.1103/physrevlett.126.097801
17. Das S, Kennedy N, Cacciuto A. The Coil-Globule Transition in Self-Avoiding Active Polymers. *Soft Matter* (2021) 17(1):160–4. doi:10.1039/d0sm01526a
18. Deblais A, Woutersen S, Bonn D. Rheology of Entangled Active Polymer-like T. Tubifex Worms. *Phys Rev Lett* (2020) 124(18):188002. doi:10.1103/physrevlett.124.188002
19. Martín-Gómez A, Eisenstecken T, Gompper G, Winkler RG. Active Brownian Filaments with Hydrodynamic Interactions: Conformations and Dynamics. *Soft Matter* (2019) 15(19):3957–69. doi:10.1039/c9sm00391f
20. Elgeti J, Winkler RG, Gompper G. Physics of Microswimmers-Single Particle Motion and Collective Behavior: a Review. *Rep Prog Phys* (2015) 78(5):056601. doi:10.1088/0034-4885/78/5/056601
21. Matas-Navarro R, Golestanian R, Liverpool TB, Fielding SM. Hydrodynamic Suppression of Phase Separation in Active Suspensions. *Phys Rev E Stat Nonlin Soft Matter Phys* (2014) 90(3):032304. doi:10.1103/PhysRevE.90.032304
22. Ishikawa T, Pedley TJ. Coherent Structures in Monolayers of Swimming Particles. *Phys Rev Lett* (2008) 100(8):088103. doi:10.1103/PhysRevLett.100.088103
23. Llopis I, Pagonabarraga I. Dynamic Regimes of Hydrodynamically Coupled Self-Propelling Particles. *Europhys Lett* (2006) 75(6):999–1005. doi:10.1209/epl/i2006-10201-y
24. Schwarzendahl FJ, Mazza MG. Maximum in Density Heterogeneities of Active Swimmers. *Soft Matter* (2018) 14:4666–78. doi:10.1039/c7sm02301d
25. Schwarzendahl FJ, Mazza MG. Hydrodynamic Interactions Dominate the Structure of Active Swimmers' Pair Distribution Functions. *J Chem Phys* (2019) 150(18):184902. doi:10.1063/1.5085755
26. Stenhammar J, Nardini C, Nash RW, Marenduzzo D, Morozov A. Role of Correlations in the Collective Behavior of Microswimmer Suspensions. *Phys Rev Lett* (2017) 119:028005. doi:10.1103/PhysRevLett.119.028005
27. Liu Z, Zeng W, Ma X, Cheng X. Density Fluctuations and Energy Spectra of 3d Bacterial Suspensions. *Soft Matter* (2021) 17:10806–17. doi:10.1039/d1sm01183a
28. Lighthill MJ. On the Squirming Motion of Nearly Spherical Deformable Bodies through Liquids at Very Small reynolds Numbers. *Comm Pure Appl Math* (1952) 5(2):109–18. doi:10.1002/cpa.3160050201
29. Blake JR. A Spherical Envelope Approach to Ciliary Propulsion. *J Fluid Mech* (1971) 46(1):199–208. doi:10.1017/s002211207100048x
30. Ramachandran S, Sunil Kumar PB, Pagonabarraga I. A Lattice-Boltzmann Model for Suspensions of Self-Propelling Colloidal Particles. *Eur Phys J E* (2006) 20(2):151–8. doi:10.1140/epje/i2006-10009-1
31. Lauga E, Powers TR. The Hydrodynamics of Swimming Microorganisms. *Rep Prog Phys* (2009) 72(9):096601. doi:10.1088/0034-4885/72/9/096601
32. Theers M, Westphal E, Gompper G, Winkler RG. Modeling a Spheroidal Microswimmer and Cooperative Swimming in a Narrow Slit. *Soft Matter* (2016) 12(35):7372–85. doi:10.1039/c6sm01424k
33. Groot RD, Warren PB. Dissipative Particle Dynamics: Bridging the gap between Atomistic and Mesoscopic Simulation. *J Chem Phys* (1997) 107(11):4423–35. doi:10.1063/1.474784
34. Succi S. *The Lattice Boltzmann Equation: For Fluid Dynamics and beyond*. Oxford University Press (2001).
35. Malevanets A, Kapral R. Mesoscopic Model for Solvent Dynamics. *J Chem Phys* (1999) 110(17):8605–13. doi:10.1063/1.478857
36. Kapral R. Multiparticle Collision Dynamics: Simulation of Complex Systems on Mesoscales. *Adv Chem Phys* (2008) 140:89–146. doi:10.1002/9780470371572.ch2
37. Kroll DM, Winkler RG, Gompper G, Ihle T. Multi-particle Collision Dynamics: A Particle-Based Mesoscale Simulation Approach to the Hydrodynamics of Complex Fluids. In: *Advanced Computer Simulation Approaches for Soft Matter Sciences III* (2009). p. 1–87.

38. Hoogerbrugge PJ, Koelman JMVA. Simulating Microscopic Hydrodynamic Phenomena with Dissipative Particle Dynamics. *Europhys Lett* (1992) 19(3): 155–60. doi:10.1209/0295-5075/19/3/001
39. Cates ME, Stratford K, Adhikari R, Stansell P, Desplat J-C, Pagonabarraga I, et al. Simulating Colloid Hydrodynamics with Lattice Boltzmann Methods. *J Phys Condens Matter* (2004) 16(38):S3903–S3915. doi:10.1088/0953-8984/16/38/009
40. Stratford K, Pagonabarraga I. Parallel Simulation of Particle Suspensions with the Lattice Boltzmann Method. *Comput Mathematics Appl* (2008) 55(7): 1585–93. doi:10.1016/j.camwa.2007.08.018
41. Español P, Warren P. Statistical Mechanics of Dissipative Particle Dynamics. *Europhys Lett* (1995) 30(4):191–6. doi:10.1209/0295-5075/30/4/001
42. Wei J, Liu Y, Song F. Coarse-grained Simulation of the Translational and Rotational Diffusion of Globular Proteins by Dissipative Particle Dynamics. *J Chem Phys* (2020) 153(23):234902. doi:10.1063/5.0025620
43. Fedosov DA, Pan W, Caswell B, Gompper G, Karniadakis GE. Predicting Human Blood Viscosity In Silico. *Proc Natl Acad Sci U.S.A* (2011) 108(29): 11772–7. doi:10.1073/pnas.1101210108
44. Blake JR. A Note on the Image System for a Stokeslet in a No-Slip Boundary. *Math Proc Camb Phil Soc* (1971) 70(2):303–10. doi:10.1017/s0305004100049902
45. Spagnolie SE, Lauga E. Hydrodynamics of Self-Propulsion Near a Boundary: Predictions and Accuracy of Far-Field Approximations. *J Fluid Mech* (2012) 700:105–47. doi:10.1017/jfm.2012.101
46. Pak OS, Lauga E. Chapter 4 Theoretical Models of low-reynolds-number Locomotion. In: *Fluid-Structure Interactions in Low-Reynolds-Number Flows*. London: Soft Matter Series (2016). p. 100–67.
47. Zhu L, Lauga E, Brandt L. Low-reynolds-number Swimming in a Capillary Tube. *J Fluid Mech* (2013) 726:285–311. doi:10.1017/jfm.2013.225
48. Kuron M, Stärk P, Burkard C, De Graaf J, Holm C. A Lattice Boltzmann Model for Squirmers. *J Chem Phys* (2019) 150(14):144110. doi:10.1063/1.5085765
49. Zöttl A, Stark H. Simulating Squirmers with Multiparticle Collision Dynamics. *Eur Phys J E Soft Matter* (2018) 41(5):61–11. doi:10.1140/epje/i2018-11670-3
50. Berke AP, Turner L, Berg HC, Lauga E. Hydrodynamic Attraction of Swimming Microorganisms by Surfaces. *Phys Rev Lett* (2008) 101:038102. doi:10.1103/PhysRevLett.101.038102
51. Kurzthaler C, Mandal S, Bhattacharjee T, Löwen H, Datta SS, Stone HA. A Geometric Criterion for the Optimal Spreading of Active Polymers in Porous media. *Nat Commun* (2021) 12(1):7088. doi:10.1038/s41467-021-26942-0
52. Mandal S, Lang S, Gross M, Oettel M, Raabe D, Franosch T, et al. Multiple Reentrant Glass Transitions in Confined Hard-Sphere Glasses. *Nat Commun* (2014) 5(1):4435. doi:10.1038/ncomms5435
53. Lobaskin V, Dünweg B. A New Model for Simulating Colloidal Dynamics. *New J Phys* (2004) 6:54. doi:10.1088/1367-2630/6/1/054
54. de Graaf J, Peter T, Fischer LP, Holm C. The Raspberry Model for Hydrodynamic Interactions Revisited. Ii. The Effect of Confinement. *J Chem Phys* (2015) 143(8):084108. doi:10.1063/1.4928503
55. de Graaf J, Menke H, Mathijssen AJTM, Fabritius M, Holm C, Shendruk TN. Lattice-boltzmann Hydrodynamics of Anisotropic Active Matter. *J Chem Phys* (2016) 144(13):134106. doi:10.1063/1.4944962
56. Plimpton S. Fast Parallel Algorithms for Short-Range Molecular Dynamics. *J Comput Phys* (1995) 117(1):1–19. doi:10.1006/jcph.1995.1039
57. Nash RW, Adhikari R, Tailleur J, Cates ME. Run-and-tumble Particles with Hydrodynamics: Sedimentation, Trapping, and Upstream Swimming. *Phys Rev Lett* (2010) 104:258101. doi:10.1103/PhysRevLett.104.258101
58. Menzel AM, Saha A, Hoell C, Löwen H. Dynamical Density Functional Theory for Microswimmers. *J Chem Phys* (2016) 144(2):024115. doi:10.1063/1.4939630
59. Chisholm NG, Legendre D, Lauga E, Khair AS. A Squirmer across reynolds Numbers. *J Fluid Mech* (2016) 796:233–56. doi:10.1017/jfm.2016.239
60. Kuhr J-T, Blaschke J, Rühle F, Stark H. Collective Sedimentation of Squirmers under Gravity. *Soft Matter* (2017) 13(41):7548–55. doi:10.1039/c7sm01180f
61. Kubo R. Statistical-mechanical Theory of Irreversible Processes. I. General Theory and Simple Applications to Magnetic and Conduction Problems. *J Phys Soc Jpn* (1957) 12(6):570–86. doi:10.1143/jpsj.12.570
62. Pivkin IV, Karniadakis GE. Controlling Density Fluctuations in wall-bounded Dissipative Particle Dynamics Systems. *Phys Rev Lett* (2006) 96:206001. doi:10.1103/PhysRevLett.96.206001
63. Löwen H. Inertial Effects of Self-Propelled Particles: From Active Brownian to Active Langevin Motion. *J Chem Phys* (2020) 152(4):040901. doi:10.1063/1.5134455
64. Drescher K, Leptos KC, Tuval I, Ishikawa T, Pedley TJ, Goldstein RE. DancingVolvox: Hydrodynamic Bound States of Swimming Algae. *Phys Rev Lett* (2009) 102(16):168101. doi:10.1103/physrevlett.102.168101
65. Panoukidou M, Wand CR, Carbone P. Comparison of Equilibrium Techniques for the Viscosity Calculation from Dpd Simulations. *Soft Matter* (2021) 17(36):8343–53. doi:10.1039/d1sm00891a
66. Noguchi H, Gompper G. Dynamics of Fluid Vesicles in Shear Flow: Effect of Membrane Viscosity and thermal Fluctuations. *Phys Rev E Stat Nonlin Soft Matter Phys* (2005) 72(1):011901. doi:10.1103/PhysRevE.72.011901
67. Kikuchi N, Pooley CM, Ryder JF, Yeomans JM. Transport Coefficients of a Mesoscopic Fluid Dynamics Model. *J Chem Phys* (2003) 119(12):6388–95. doi:10.1063/1.1603721
68. Tüzel E, Strauss M, Ihle T, Kroll DM. Transport Coefficients for Stochastic Rotation Dynamics in Three Dimensions. *Phys Rev E Stat Nonlin Soft Matter Phys* (2003) 68(3):036701. doi:10.1103/PhysRevE.68.036701
69. Martin-Roca J, Martinez R, Alexander LC, Diez AL, Aarts DGAL, Alarcon F, et al. Characterization of Mips in a Suspension of Repulsive Active Brownian Particles through Dynamical Features. *J Chem Phys* (2021) 154(16):164901. doi:10.1063/5.0040141
70. Stenhammar J, Marenduzzo D, Allen RJ, Cates ME. Phase Behaviour of Active Brownian Particles: the Role of Dimensionality. *Soft Matter* (2014) 10: 1489–99. doi:10.1039/c3sm52813h
71. Fang L, Li LL, Guo JS, Liu YW, Huang XR. Time Scale of Directional Change of Active Brownian Particles. *Phys Lett A* (2022) 427:127934. doi:10.1016/j.physleta.2022.127934
72. Pagonabarraga I, Hagen MHJ, Lowe CP, Frenkel D. Short-time Dynamics of Colloidal Suspensions in Confined Geometries. *Phys Rev E* (1999) 59:4458–69. doi:10.1103/physreve.59.4458
73. Bocquet L, Barrat J-L. Hydrodynamic Properties of Confined Fluids. *J Phys Condens Matter* (1996) 8:9297–300. doi:10.1088/0953-8984/8/47/019
74. Zimm BH. Dynamics of Polymer Molecules in Dilute Solution: Viscoelasticity, Flow Birefringence and Dielectric Loss. *J Chem Phys* (1956) 24(2):269–78. doi:10.1063/1.1742462
75. Michael PH, Arash N, Jeremy CP. Modeling Hydrodynamic Interactions in Soft Materials With Multiparticle Collision Dynamics. *Curr Opin Chem Eng* (2019) 23:34–43. doi:10.1016/j.coche.2019.02.007
76. Qi K, Westphal E, Gompper G, Winkler RG. Emergence of Active Turbulence in Microswimmer Suspensions due to Active Hydrodynamic Stress and Volume Exclusion. *Communications Physics* (2022) 5:1–12.

Conflict of Interest: The authors declare that the research was conducted in the absence of any commercial or financial relationships that could be construed as a potential conflict of interest.

frontiers | Frontiers in Physics

TYPE Original Research
PUBLISHED 26 July 2022
DOI 10.3389/fphy.2022.948415

OPEN ACCESS

EDITED BY
Sujit Datta,
Princeton University, United States

REVIEWED BY
Ali Najafi,
Institute for Advanced Studies in Basic Sciences (IASBS), Iran
Ricard Alert,
Max Planck Institute for the Physics of Complex Systems, Germany

*CORRESPONDENCE
Paarth Gulati,
paarthgulati@physics.ucsb.edu

SPECIALTY SECTION
This article was submitted to Soft Matter Physics,
a section of the journal
Frontiers in Physics

RECEIVED 19 May 2022
ACCEPTED 28 June 2022
PUBLISHED 26 July 2022

CITATION
Gulati P, Shankar S and Marchetti MC (2022), Boundaries control active channel flows.
Front. Phys. 10:948415.
doi: 10.3389/fphy.2022.948415

Boundaries control active channel flows

Paarth Gulati[1]*, Suraj Shankar[2] and M. Cristina Marchetti[1]

[1]Physics Department, University of California, Santa Barbara, Santa Barbara, CA, United States, [2]Physics Department, Harvard University, Cambridge, MA, United States

Boundary conditions dictate how fluids, including liquid crystals, flow when pumped through a channel. Can boundary conditions also be used to control internally driven *active* fluids that generate flows spontaneously? By using numerical simulations and stability analysis we explore how parallel surface anchoring of active agents at the boundaries and substrate drag can be used to rectify coherent flow of an active polar fluid in a 2D channel. Upon increasing activity, a succession of dynamical states is obtained, from laminar flow to vortex arrays to eventual turbulence, that are controlled by the interplay between the hydrodynamic screening length and the extrapolation length quantifying the anchoring strength of the orientational order parameter. We highlight the key role of symmetry in both flow and order and show that coherent laminar flow with net throughput is only possible for weak anchoring and intermediate activity. Our work demonstrates the possibility of controlling the nature and properties of active flows in a channel simply by patterning the confining boundaries.

KEYWORDS

active matter, polar fluid, confined channels, boundary anchoring, coherent flow

1 Introduction

Active fluids are composed of active entities, such as bacteria [1, 2], biofilaments driven by motor proteins [3, 4] or self-propelled colloids [5, 6], that consume energy to generate their own motion. Such active particles exert dipolar forces on their surroundings, driving self-sustained active flows. The elongated nature of the active units endows the fluid with liquid crystalline degrees of freedom, allowing for the onset of orientational order, with either polar or nematic symmetry [7].

The orientationally ordered state of bulk active fluids is generically unstable at all activities due to the feedback between deformations and flow [8], resulting in spatiotemporal chaotic dynamics at zero Reynolds number that has been referred to as bacterial or active turbulence [9]. Several strategies have been proposed to stabilize laminar flows in active fluids such as the inclusion of substrate friction [10–13] or spatial confinement [14–20], but a systematic treatment unifying these various results has remained elusive.

The dynamics of confined two-dimensional (2D) active fluids also depends on the symmetry of local order, though some features are common. Polar active fluids, such as dense suspensions of swimming bacteria, transition from laminar to undulating and periodic travelling flows upon increasing the channel width, eventually giving place to turbulent dynamics [21–24]. In active nematics, both numerical studies [25–28] and experiments with microtubule-kinesin suspensions [29] with strong anchoring to the channel walls have revealed a transition from laminar to oscillatory flows to a lattice of counter-rotating flow vortices with associated order of disclinations in the nematic texture. Similar flow states and transitions are also reported in other geometries, such as in circular confinement [15, 19, 30]. Recent work has also begun exploring the influence of varying and conflicting anchoring boundary conditions in active nematics in channels [24, 31]. In general the interplay of the geometry of confinement and boundary conditions yields a rich variety of flow states, but coherent flow with a finite throughput in the channel is only achieved by finely tuning activity and other system parameters. Hence, quantifying the conditions that yield specific flow patterns, and especially identifying states of finite throughput is important for controlling bacterial flow through channels and for microfluidic applications of active flows [32–36].

Motivated by the sensitivity of liquid crystals to surface effects and anchoring on the boundary [37], in this paper, we suggest a simple strategy to control channel flows of active fluids by tuning boundary conditions. We consider an incompressible polar active fluid confined to a two-dimensional (2D) channel with friction, and examine the role of parallel surface anchoring in selecting the spontaneously flowing states of the fluid. The model may be appropriate, for instance, to describe the spontaneous flow of a bacterial suspension in a channel. We show that the selection of the flow patterns is controlled by the interplay of two length scales: 1) the hydrodynamic screening length $\ell_\eta = \sqrt{\eta/\Gamma}$ that quantifies the scale beyond which dissipation by substrate friction (Γ) dominates over dissipation from internal shear viscosity (η), and 2) the extrapolation length, $\ell_\kappa = K/E_a$ governing the length scale over which elastic torques controlled by the stiffness K of the polar fluid balance the wall anchoring energy E_a of the orientational degrees of freedom. The hydrodynamic length screens flows and controls the penetration of the boundary conditions on the flow field $\mathbf{v}$ into the bulk of the channel. The extrapolation length controls the relative strength between nematic elasticity and surface anchoring. Strong wall anchoring corresponds to a short ℓ_κ, while weak anchoring corresponds to large ℓ_κ [37].

We find that coherent active flows with finite throughput are only possible when the orientational order parameter is weakly anchored to the channel walls, corresponding to large ℓ_κ compared to the width W of the channel. In the opposite limit of strong anchoring, the spontaneous flow transition leads instead to a single file of flow vortices evenly spaced along the length of the channel that we refer to as flow vortex lattice. These vortices appear in counter-rotating pairs and their number is determined by the aspect ratio of the channel and the activity. The succession of flow states obtained when activity is increased above the spontaneous flow instability on the way to turbulence are summarized schematically in Figure 1 for both weak and strong homogeneous anchoring. For weak anchoring, the spontaneous flow transition leads to coherent laminar flow and associated splay deformation of the polarization field. At higher activity the system settles into a state of shear banded flow, with bend deformations of the polarization field across the channel. For strong anchoring, in contrast, the spontaneous flow instability first results in a lattice of flow vortices lined up along the channel, with longitudinal bend deformations of the polarization. At higher activity this gives way to the shear banded flow as for weak anchoring, albeit with stronger amplitude of polarization deformations. For all anchoring strengths, the flow eventually becomes chaotic at larger activity (not shown). By considering variable boundary conditions, we unify previous results in a comprehensive phase diagram that crucially combines the well-known active length scale $\ell_\alpha = \sqrt{K/|\alpha_0|}$ (α_0 measuring the strength of the active stress) [38, 39] controlling patterns in the bulk of the fluid along with boundary related length scales in both flow (ℓ_η) and order (ℓ_κ).

In the rest of the paper, we first introduce the hydrodynamic model and the boundary conditions used in the channel geometry. In section 3 we report results from numerical solutions of the continuum equations and describe the various spontaneous flow states observed with increasing activity. We define and evaluate the mean normalized throughput through the channel to distinguish between coherent and non-coherent flows. In section 4 we present a linear stability analysis of the hydrodynamic model for a rectangular periodic box that qualitatively accounts for the transitions between the various flow states. The results are summarized in a comprehensive phase diagram in terms of activity, hydrodynamic screening and anchoring strength. In Section 5 we discuss the effect of a polar propulsive force in the momentum equation which breaks flow symmetry and destroys the non-flowing ordered state. Finally, we conclude with a discussion of potential experimental realisations and possible extensions of our work.

2 Hydrodynamic model

We consider a two-dimensional active polar fluid on a frictional substrate, as appropriate, for instance, to describe a thin film of a bacterial suspension [40]. At high bacterial concentration, we assume both the suspension density and the bacterial concentration to be constant and describe the dynamics in terms of two fields, the bacterial polarization $\mathbf{p}$ that characterizes the local direction of bacterial motility and the flow velocity $\mathbf{v}$ of the fluid.

The dynamics of the polarization is governed by

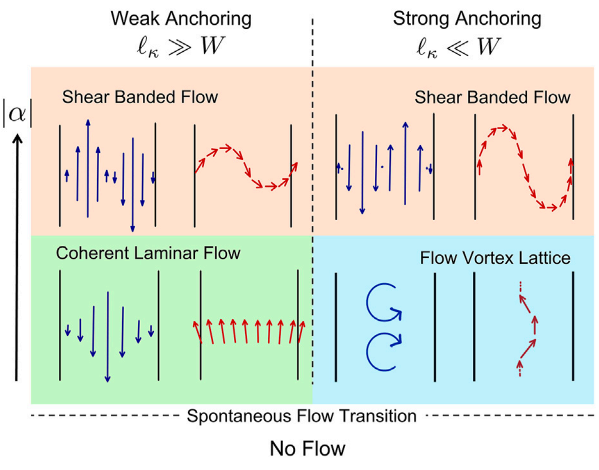

FIGURE 1
Schematic showing the effect of wall anchoring of the polarization on the steady flow states of a polar active fluid in a channel of width W. The blue arrows depict the flow field, **v**, and the red arrows represent the polarization, **p**. The extended arrow on the left indicates the direction of increasing activity $|\alpha|$.

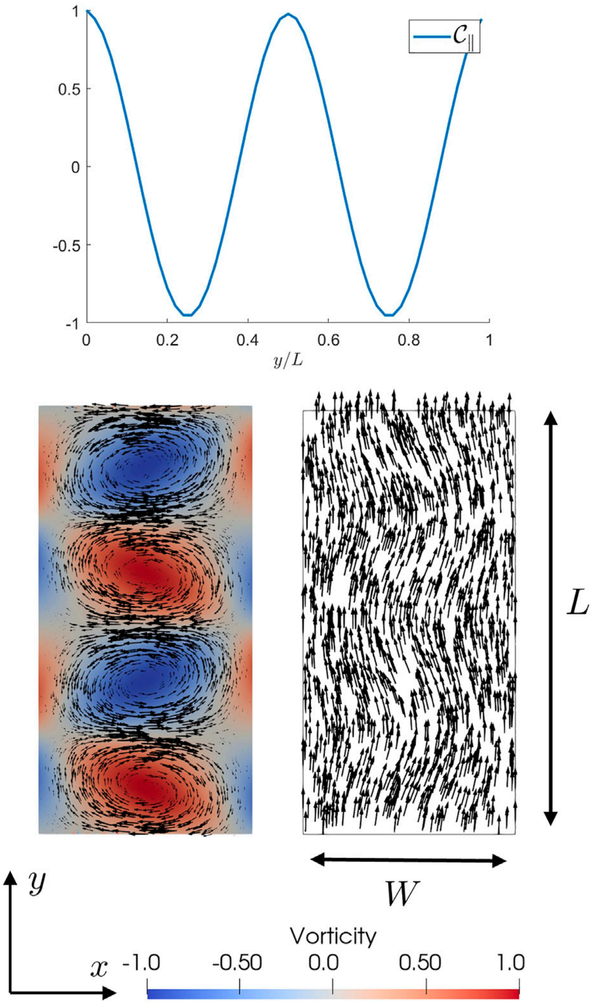

FIGURE 2
The velocity correlation function along the channel, $C_{\|}$, for the vortex lattice state ($\ell_\eta = 0.30$, $\alpha = -2.00$) with strong anchoring ($\ell_\kappa = 0.01$). The flow profile **v** (bottom left) and polarization **p** (bottom right) in the vortex lattice state are plotted at the bottom.

$$D_t\mathbf{p} = \lambda\mathbf{S}\cdot\mathbf{p} + \frac{1}{\gamma}\mathbf{h}, \tag{1}$$

where $D_t\mathbf{p} = \partial_t\mathbf{p} + \mathbf{v}\cdot\nabla\mathbf{p} + \mathbf{\Omega}\cdot\mathbf{p}$ is the material derivative that embodies advection and rotation of polarization by flow, with $\mathbf{\Omega} = (\nabla\mathbf{v} - \nabla\mathbf{v}^T)/2$ the vorticity tensor. The first term on the right-hand side of Eq. 1 describes flow alignment, with $\mathbf{S} = (\nabla\mathbf{v} + \nabla\mathbf{v}^T)/2$ the strain rate tensor and λ a microscopic parameter that depends on the shape of the active entities ($\lambda > 1$ for elongated swimmers). The second term is the molecular field that drives relaxation with a rate set by the rotational viscosity γ. It is determined by a Landau free energy as $\mathbf{h} = -\delta F/\delta\mathbf{p}$, with

$$F = \frac{1}{2}\int_{\mathbf{r}}\left\{K\left(\partial_i p_j\right)^2 - a\left(\frac{c}{c_0} - 1\right)\mathbf{p}^2 + \frac{b}{2}\mathbf{p}^4\right\}, \tag{2}$$

where $a, b > 0$ and the bacterial concentration c controls the transition to polar order. Here, we have assumed that a single elastic constant K controls the stiffness to both bend and splay distortions. For simplicity we neglect in Eq. 1 flow alignment terms proportional to **v** which arise through a lubrication approximation [40]. We have verified that these terms do not qualitatively change our results.

At low Reynolds number the flow is governed by force balance through the Stokes equation,

$$\Gamma\mathbf{v} = -\nabla\Pi + \eta\nabla^2\mathbf{v} + \nabla\cdot\left(\boldsymbol{\sigma}^{\mathrm{a}} + \boldsymbol{\sigma}^{\mathrm{lc}}\right), \tag{3}$$

where the pressure Π is determined by the condition of incompressibility, $\nabla\cdot\mathbf{v} = 0$. Here, Γ is the friction with the substrate. Dissipation is controlled by the interplay of friction and viscosity η, with $\ell_\eta = \sqrt{\eta/\Gamma}$ the viscous screening length that controls the penetration of the no-slip boundary conditions into the channel. The passive liquid-crystalline stress, $\boldsymbol{\sigma}^{\mathrm{lc}}$, describes the elastic stresses due to distortions of the polarization field and is given by

$$\boldsymbol{\sigma}^{\mathrm{lc}} = -\frac{\lambda+1}{2}\mathbf{ph} - \frac{\lambda-1}{2}\mathbf{hp} + K\nabla p_i\nabla p_i. \tag{4}$$

Finally, the dipolar forces exerted by the swimmers on the fluid yield an active stress $\boldsymbol{\sigma}^{\mathrm{a}}$ [7],

$$\boldsymbol{\sigma}^{\mathrm{a}} = \alpha_0\left(\mathbf{pp} - \frac{|\mathbf{p}|^2}{2}\mathbf{I}\right), \tag{5}$$

where the activity α_0 provides a measure of the strength of active forces, depending, for instance, on bacterial concentration and swimming speed. Its sign depends on whether such forces are extensile ($\alpha_0 < 0$ as for pushers) or contractile ($\alpha_0 > 0$ as for pullers). Here we focus on extensile active forces which are relevant to most bacteria. Note that, other sources of activity such as self-advection are neglected here for simplicity, and their effects are briefly discussed later in Section 5.

We assume that the fluid is confined to a channel of width W and length L, in the geometry shown in Figure 2, with periodic boundary conditions along the y direction. Below we focus on the dynamics of the ordered state with $c > c_0$ and $\mathbf{p} = \sqrt{a/b}\,\hat{\mathbf{y}}$. We normalize the polarization so that $|\mathbf{p}| = 1$ in the aligned state.

The hydrodynamic equations are solved with the boundary conditions.

$$\mathbf{v}|_{x=0,W} = 0, \tag{6}$$

$$\left[E_a(\mathbf{p} - \hat{\mathbf{y}}) + K(\hat{\mathbf{n}} \cdot \nabla \mathbf{p})\right]_{x=0,W} = 0, \tag{7}$$

Where $\hat{\mathbf{n}}$ is a unit normal pointing outward from the walls. The boundary condition on the polarization expresses the balance between a torque $E_a p_x$ that penalizes misalignment with the boundary, with E_a an anchoring energy per unit length, and the nematic torque $K\partial_x p_x$ that penalizes deviations from the aligned state. The ratio $\ell_\kappa = K/E_a$ defines the extrapolation length [37], with the following limiting cases

$$\begin{array}{lll} \ell_\kappa \to 0: & [\mathbf{p}]_{x=0,W} = \hat{\mathbf{y}} & \text{strong anchoring} \\ \ell_\kappa \to \infty: & [\partial_x \mathbf{p}]_{x=0,W} = \mathbf{0} & \text{weak anchoring} \end{array}$$

The hydrodynamic equations for our model have nematic symmetry, as they are invariant for $\mathbf{p} \to -\mathbf{p}$. The boundary conditions, however, break the symmetry in polarization by aligning $\mathbf{p}$ with the channel walls in $\hat{\mathbf{y}}$ direction. As we will discuss later in Section 5, this still allows for symmetry in the flow direction, which can by broken by introducing an active self propulsion term in Eq. 3.

3 Numerical simulations

The hydrodynamic equations are solved numerically using the finite element platform FEniCs [41, 42]. We use the width of the channel, W, as unit of length, the nematic relaxation time, $\tau_n = \gamma/a$, as unit of time and the condensation energy a in the polar free energy as a unit of stress. With this choice, the dimensionless activity $\alpha = |\alpha_0|/a = (\ell_\alpha/\xi)^2$ is simply the square of the ratio between the active length $\ell_\alpha = \sqrt{K/|\alpha_0|}$ and the nematic correlation length $\xi = \sqrt{K/a}$. Unless specified otherwise, the results are shown for channel dimensions with $L = 2W$, flow alignment parameter $\lambda = 2$, and nematic correlation length $\xi = 0.1W$. To carry out the finite element simulations, the channel is triangulated into a rectangular mesh with grid size $dx \sim 0.01W$. The time step used in most simulations is $dt = \tau_n/10$ and we typically run simulations for a total time $T = 1000\tau_n$ or longer.

In bulk, an extensile active fluid ordered along y, is destabilized at any value of activity by the unbounded growth of bend fluctuations $\delta p_x(y,t)$ of the order parameter [8, 14]. Both substrate friction (Γ) and a finite system size (L along the y direction) generate a finite activity threshold for the onset of spontaneous flow given by [12, 43].

$$\alpha_c^b = \frac{2K\Gamma}{\gamma(\lambda+1)}\left[1 + \left(\frac{2\pi\ell_\eta}{L}\right)^2\right]. \tag{8}$$

For vanishing friction ($\Gamma \to 0$), the screening length diverges ($\ell_\eta \to \infty$) and we recover the viscous limit of the finite size activity threshold $\alpha_c^L = (2K\eta/\gamma(\lambda+1))(2\pi/L)^2$ [14].

As shown below, wall anchoring geometrically frustrates this bulk instability mode and alters the mechanisms and nature of the instability which is now controlled by an interplay of three length scales: the channel width W, the flow screening length ℓ_η and the extrapolation length ℓ_κ.

Upon increasing activity, the quiescent state in a channel is destabilized, driving the system through a succession of flowing states. To classify such dynamical states, we examine the velocity correlation function parallel to the channel, defined as

$$C_\parallel(y) = \langle \mathbf{v}(\mathbf{r}) \cdot \mathbf{v}(\mathbf{r} + y\hat{\mathbf{y}}) \rangle_{\mathbf{r}}, \tag{9}$$

where $\langle \cdot \rangle_{\mathbf{r}}$ denotes a spatial average over the entire channel domain. The number of oscillations in the correlation function is used to classify the nature of the flow; see Figure 2 for an example of a flow state (the vortex lattice) with the associated correlation function plotted.

While $C_\parallel$ captures vorticity in flow patterns, states with finite throughput are quantified by evaluating the normalized throughput

$$\phi = \left| \left\langle \frac{v_y}{|\mathbf{v}|} \right\rangle_{\mathbf{r}} \right|, \tag{10}$$

where $\langle |\mathbf{v}| \rangle_{\mathbf{r}}$ is the mean velocity.

3.1 Strong anchoring, $\ell_\kappa \ll W$

The flow states obtained for strong anchoring (here $\ell_\kappa/W = 0.01$) are summarized in the phase diagram of Figure 3B obtained by varying the activity α and the screening length ℓ_η. Upon increasing activity at fixed ℓ_η, we first observe a transition from a quiescent ordered state (grey region of Figure 3B) to a flowing state (blue region) with $\langle |\mathbf{v}| \rangle \neq 0$. Strong anchoring suppresses pure bend fluctuations. The instability is then controlled by a growing mode that necessarily has both splay and bend components, as discussed in Section 4. This is evident from the polarization profiles displayed in Figure 4B. The resulting flow is a lattice of counter-rotating flow vortices that span the channel width, with zero net throughput. We refer to this state as a “vortex lattice”.

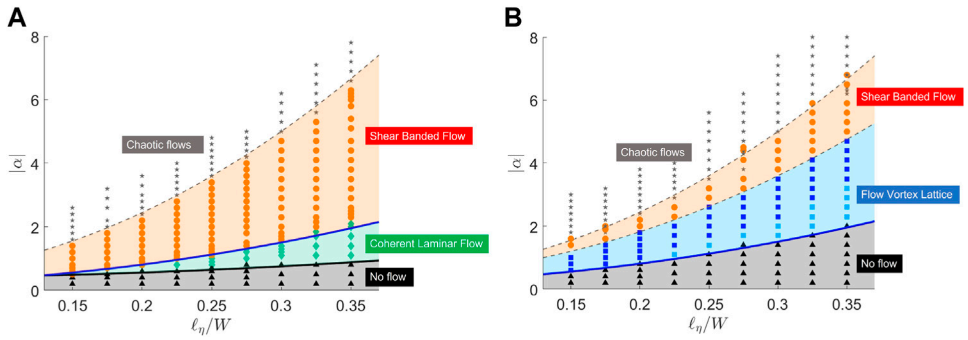

FIGURE 3
These phase diagrams show the various steady flow states in the channel as we change the screening length and the activity at a fixed anchoring strength. The dashed lines are fits to the observed phase boundaries whereas the solid lines correspond to the curves calculated using linear stability analysis in Section 4, with no fitting parameters. The solid blue line in both phase diagrams corresponds to the *mixed* bend-splay instability α^m and the solid black line in **(B)** corresponds to the *splay* instability with weak anchoring, $\alpha^{s,w}$ (Eq. 16). **(A)** Weak Anchoring, $\ell_\kappa/W = 100$. **(B)** Strong Anchoring, $\ell_\kappa/W = 0.01$.

The number n of counter-rotating vortex pairs in the vortex lattice is controlled by the aspect ratio L/W of the channel, together with the topological constraint that the net vorticity must be zero. This can be understood by comparing the energy cost of bend and splay deformations transverse and parallel to the long direction of the channel, with the number of pairs of vortices $n \sim (L/W)\ (A_s/A_v)$, where A_s and A_v are the amplitude of the polarization angle in the vortex-lattice and the shear banded flow states (Section 3.3). The minimum number of pairs of counter-rotating vortices is equal to the integer part of the aspect ratio and as we increase activity, additional vortices are added in pairs (light and dark blue points in Figure 3B).

Upon further increasing the activity, we note a transition (blue to orange in Figure 3B) from the ordered vortex lattice to a shear banded flow, with increasing number of shear bands at higher activities. This state is characterized by a bend about the short channel direction, transverse to the original orientation of the polarization field. Here, the flow and polarization are invariant along the channel. Interestingly, the flow transitions to a 'more ordered state' on increasing activity.

3.2 Weak anchoring, $\ell_\kappa \gg W$

For weak anchoring, and sufficiently large values of ℓ_η, the steady state corresponds to coherent laminar flow with finite throughput (green region in Figure 3A). But as we increase activity, an ordered vortex lattice similar to that in the strong anchoring limit forms transiently but then leads to a shear banded flow as the long time steady state (Figure 4A).

Notably, the laminar flowing state has non-zero *splay* but zero bend and can be seen only above a characteristic screening length ℓ_η^* (dependant on the extrapolation length ℓ_κ). From Figure 3A, this value $\ell_\eta^* \approx 0.2W$ for $\ell_\kappa/W = 100$. This absence of coherent laminar flow at short screening length is further discussed in Section 4.

Figure 5 shows a phase diagram as a function of activity and extrapolation length, at a fixed screening $\ell_\eta = 0.35 > \ell_\eta^*$. As ℓ_κ decreases the coherent flow region for the splay state vanishes and the ordered flow vortices become stable for larger activities. We find that the transition to the flow vortex lattice (transient in the weak anchoring limit) is largely unaffected by the anchoring strength. Also, we observe that the activity threshold for the onset of unsteady chaotic flows is not affected by the extrapolation length, generalizing previous results [19, 30].

3.3 Lattice of flow vortices

Upon transition from the quiescent to the vortex state, the flow organizes into a single pair of counter-rotating vortices spanning the channel length L and of size of order $L/2$ (when $L = 2W$), as illustrated in Figure 4B for $\alpha = -2$. This is observed in simulations for a large range of ℓ_η and ℓ_κ. Upon increasing activity, the number of vortex pairs increases, until eventually the system transitions to shear banded flow. The maximum number n of vortex pairs that can be accommodated in the channel depends of the channel's aspect ratio. To estimate this number, we examine the elastic energy of channel-spanning bend deformations of the polarization field, described by the angle θ, with $\cos\theta = \mathbf{p}\cdot\hat{\mathbf{x}}$, given by

$$E \approx K \int_\Omega d\mathbf{r}\ (\nabla\theta)^2. \tag{11}$$

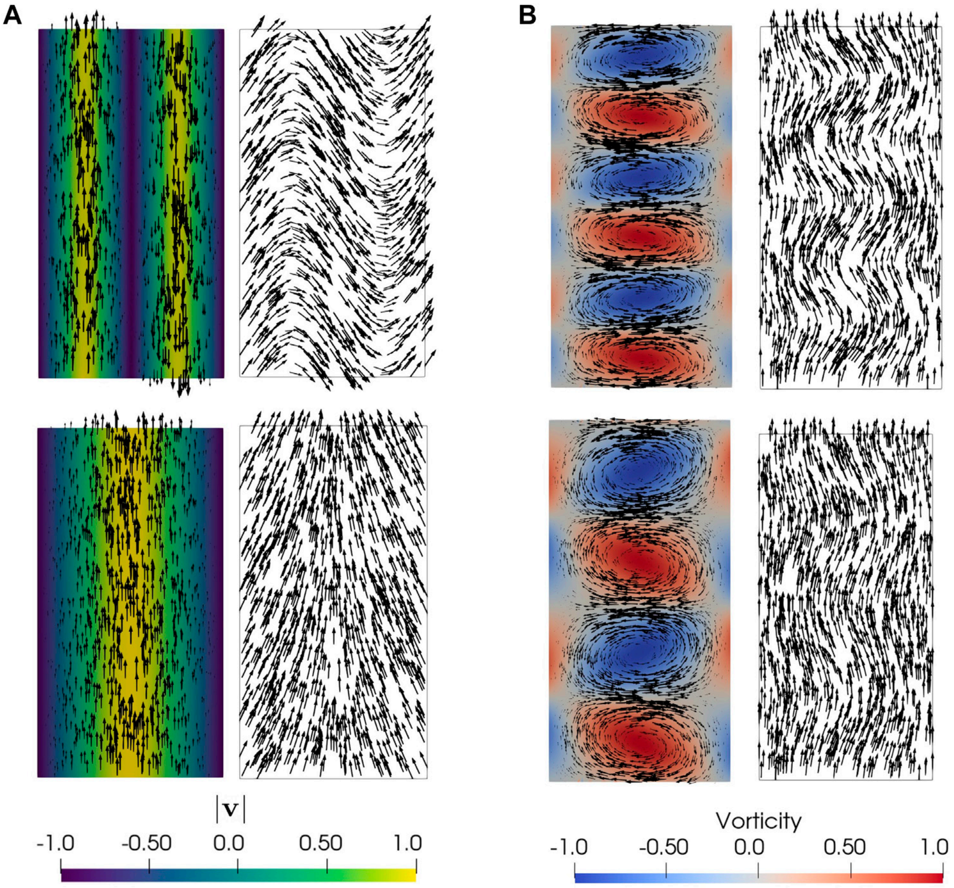

FIGURE 4
Some of the steady states observed in the phase diagrams (ℓ_η = 0.35) are shown in terms of the flow **v** (left in each frame) and the polarization **p** (right). The vorticity and the flow magnitude are colorized to show relative magnitudes and have been scaled by the corresponding maximum/ minimum. The arrows represent the vectors for **v** and **p** scaled by their magnitudes. ℓ_κ. **(A)** Steady States with weak anchoring, ℓ_κ W =100, and low activity (bottom, α-1.75) and high activity (top, α=-4.00). **(B)** Steady States with strong anchoring, ℓ_κ W =0.01, and low activity (bottom, α-2.00) and high activity (top, α =-3.00).

In the shear banded state, the bend deformation is primarily transverse to the channel direction (Figure 6A), corresponding to an angle profile of the form $\theta_s \sim A_s \sin(2\pi x/W)$. In the vortex lattice state, away from the walls, bend deformations are primarily along the length of the channel (Figure 6B), corresponding to an angle profile of the form $\theta_v \sim A_v \sin(2\pi n y/L)$, where n is the number of counter-rotating vortex pairs. Note that the amplitudes A_s and A_v of the two deformations depend on activity and on the strength of anchoring, and are generally different.

The corresponding deformation energies E_s and E_v for the shear banded and flow states are then immediately obtained by substituting the respective deformations into (11), with the result $E_s = KA_s^2 L/W$ and $E_v = Kn^2 A_v^2 W/L$. By setting $E_s \sim E_v$ we can estimate the number of vortex pairs in the channel as

$$n \sim (L/W)\left(A_s/A_v\right). \tag{12}$$

The scaling of the number of vortex pairs with the channel aspect ratio for the lattice of flow vortices is confirmed by numerical simulations in longer channels, as shown in Figure 7, supporting the idea that the channel geometry determines the number of flow vortices.

In the limit of weak anchoring, we observe transient vortex lattices, but the stable state is always shear banded. We can understand this because in this case the system can easily accommodate bend deformations across the channel, while bend deformations along the channel, which would be required for a vortex state, are energetically more costly.

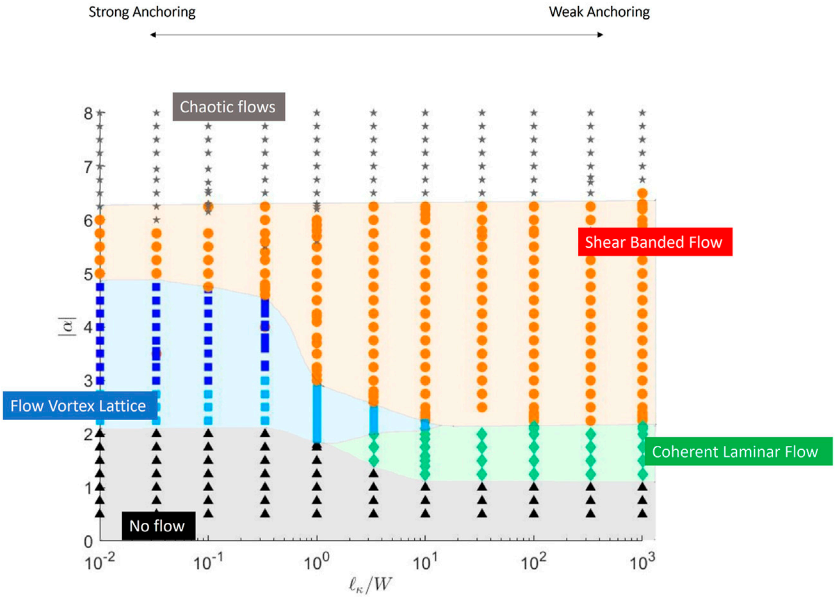

FIGURE 5
Phase diagram as we change the extrapolation length ℓ_κ at a fixed screening length ℓ_η = 0.35.

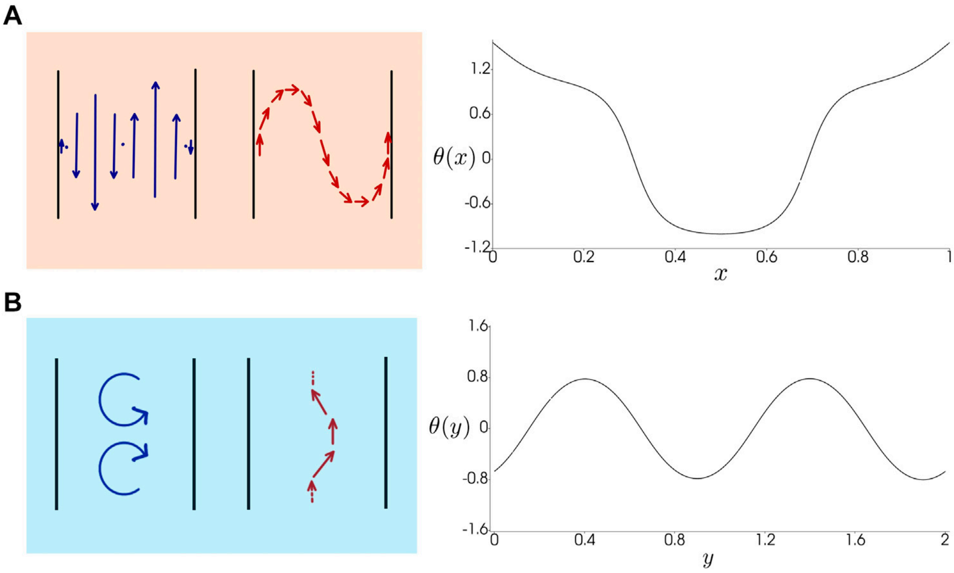

FIGURE 6
Schematic (L = W) for the shear banded and the vortex lattice flows. The line plot shows the angle θ along the polarization **p** for the two flow states from the numerical simulations (L = 2W) in the case of strong anchoring (ℓ_κ/W = 0.01, ℓ_η/W = 0.30). **(A)** Shear Banded Flow (angular profile is shown for α =-3.80). **(B)** Flow Vortex Lattice (angular profile is shown for α =-2.00).

4 Linear stability analysis

The steady state channel flows summarized in the previous section can be understood using a linear stability analysis of an initial uniformly aligned state with no flow.

First, let us consider the stability of an unconfined active fluid on a frictional substrate. For small activity, the uniform quiescent state with finite polarization $\mathbf{p} = \hat{\mathbf{y}}$ and zero flow is stable. In the absence of friction, this state is generically unstable for any activity [8, 14]. The presence of friction yields a finite activity

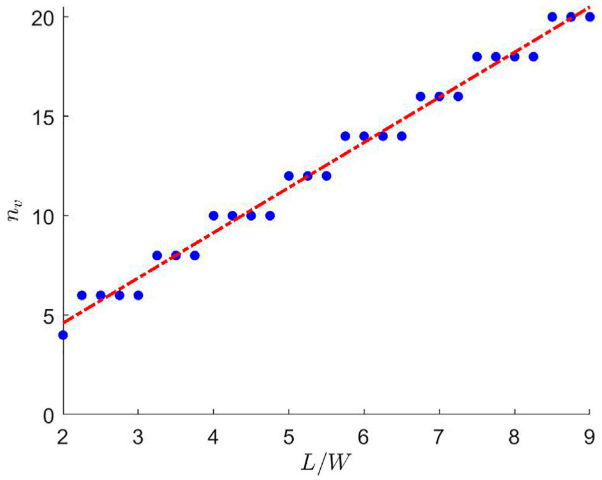

FIGURE 7
Scaling of the number of vortices, n_v, in the flow vortex lattice state for strong anchoring as a function of the channel aspect ratio L/W. The blue points correspond to n_v observed in numerical simulations ($\ell_\kappa = 0.01$, $\ell_\eta = 0.35$, $\alpha = -2.30$) by increasing L/W in steps of 0.25 from L/W = 2 to L/W = 9. The value of n_v increases in steps of 2, corresponding to the addition of a vortex/anti-vortex pair so as to maintain zero net vorticity. The growth is linear, as predicted by the simple scaling argument given in Section 3.3, but with a slope 2.270 ± 0.005 (dashed red line).

threshold for the onset of spontaneous flow [12]. A linear stability analysis of the uniformly polarized state shows that fluctuations in the Fourier amplitude of wavevector $\mathbf{q}$ of the transverse component of polarization δp_x evolve as $\delta p_x\,(\mathbf{q},\,t) \sim e^{\nu(\mathbf{q})t}$, with the growth rate

$$\nu(\mathbf{q}) = -\frac{K}{\gamma}q^2 + \frac{|\alpha_0|\left(q_x^2 - q_y^2\right)}{2\Gamma\left(1 + \ell_\eta^2 q^2\right)}\left[\lambda\left(\hat{q}_x^2 - \hat{q}_y^2\right) - 1\right] + \mathcal{O}\left(q^4\right), \quad (13)$$

where, $q = |\mathbf{q}|$, $\hat{q}_{x,y} = q_{x,y}/q$ and $\ell_\eta = \sqrt{\eta/\Gamma}$ is the viscous screening length.

4.1 Bulk

For extensile systems ($\alpha_0 < 0$) of elongated active units ($\lambda > 1$), the decay rate given in Eq. 13 can become positive, signalling the instability of the uniformly polarized state. It is known that in a bulk system, defined as one with periodic boundary conditions in all directions, the most unstable modes are bend deformations of the polarization field, corresponding to spatial variations along the direction of order, i.e., $q_x = 0$ and finite q_y. The hydrodynamic instability sets in at the longest wavelength, which in a periodic box of size L is $2\pi/L$, yielding an activity threshold α_c^b (Eq. 8). Note, here the threshold is defined by its absolute value. The bend modes of wavelength $2\pi/L$ become unstable as $\alpha_0 < -\alpha_c^b$ or $|\alpha_0| > \alpha_c^b$.

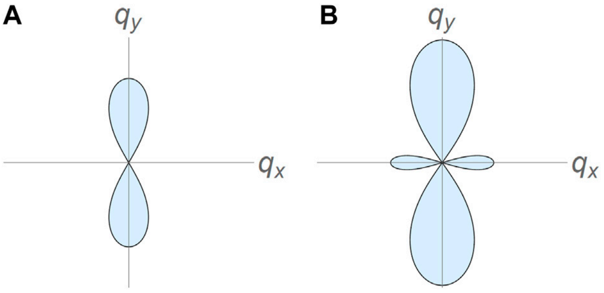

FIGURE 8
The shaded region in the q_x-q_y plane corresponds to unstable modes ($\nu > 0$) in an extensile active fluid. Beyond the critical activity α_c^b only the bend modes ($q_x = 0$) become unstable. Further increasing the activity beyond α_c^s, pure splay modes ($q_y = 0$) also become unstable. **(A)** $\alpha_b^c < \alpha_0 < \alpha_c^s$. **(B)** $\alpha_0 > \alpha_c^s$.

Viscous dissipation enters through the screening length ℓ_η and shifts the instability to higher values of activity whenever $\ell_\eta \sim L$. In other words, viscous dissipation stabilizes the uniform quiescent state. When $\ell_\eta \ll L$ one recovers the infinite system frictional threshold, $\alpha_c^\infty = 2K\Gamma/[\gamma(\lambda + 1)]$. The bulk result given in Eq. 8 fits very well with finite element simulations in a periodic box (not shown).

Upon further increasing activity, splay modes, corresponding to $q_y = 0$, also become unstable. This splay instability occurs above a threshold

$$\alpha_c^s = \frac{2K\Gamma}{\gamma(\lambda - 1)}\left[1 + \left(\frac{2\pi\ell_\eta}{W}\right)^2\right]. \quad (14)$$

Note the dependence on the width W of the channel rather than the length L. In a periodic square box ($L = W$), for elongated flow-aligning swimmers ($\lambda > 1$), $\alpha_c^s > \alpha_c^b$, i.e., the bend instability always precedes the splay instability in an extensile system [7]. The situation can, however, be reversed for large values of ℓ_η and suitable aspect ratios (W/L).

The angular dependence of the instability threshold is displayed in the polar plots of Figure 8, where the shaded region corresponds to unstable modes ($\nu(\mathbf{q}) > 0$) in the $q_x - q_y$ plane. It is evident that the fastest growing modes are always along the $q_x = 0$ direction and become unstable for $|\alpha_0| > \alpha_c^b$. Pure splay modes (corresponding to $q_y = 0$) are stable for $|\alpha_0| < \alpha_c^s$ (Figure 8A) and only become unstable for $|\alpha_0| > \alpha_c^s$, as evident by the emergence of the two additional lobes elongated along the q_x axis (Figure 8B).

4.2 Channel

In a channel geometry, boundary conditions can differentially frustrate bend and splay distortions [31, 44],

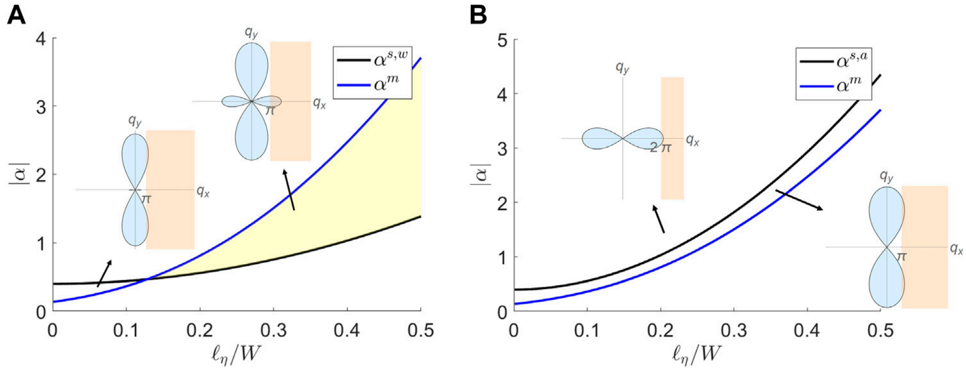

FIGURE 9
Linear instability for splay and the vortex-lattice state in the limits of weak and strong anchoring. In the insets, the orange regions delineate the values of wavector where the instability can occur, as discussed in Section 4.2. The yellow shaded region marks the range of parameters where $\alpha_c^{s,w} < \alpha_c^m$, allowing for a region of coherent flow. For the strong anchoring limit, α_c^m is always smaller than $\alpha_c^{s,a}$ and no coherent flow is possible. **(A)** Weak Anchoring ($\ell_\kappa \rightarrow \infty$). **(B)** Strong Anchoring (ℓ_κ =0).

allowing for distinct modes of spontaneous flow transitions to emerge. As in Ref. [12], we first consider a quasi-1D model that assumes only spatial variations along the direction x of the channel width. This is consistent with the observation that in the channel bend fluctuations ($q_y \neq 0$) are suppressed either by strong anchoring requiring $p_x = 0$ at the boundaries [12, 14] and/or by the condition of no-slip. The instability to spontaneous flow is then controlled by splay fluctuations ($q_x \neq 0$) and the threshold activity generally depends on the anchoring length, ℓ_κ. For strong anchoring ($\ell_\kappa \rightarrow 0$) the no-slip requirement on the velocity further excludes the possibility of a mode with wavelength $2W$. Hence the longest allowed wavelength corresponds to $q_x = 2\pi/W$ and the splay (s) instability threshold for the case of strong anchoring 1) can be estimated as

$$\alpha_c^{s,a} = \frac{2K\Gamma}{\gamma(\lambda-1)}\left[1+\left(\frac{2\pi\ell_\eta}{W}\right)^2\right], \qquad \ell_\kappa = 0. \tag{15}$$

For weak anchoring ($\ell_\kappa \rightarrow \infty$) conversely $\partial_x p_x = 0$ at the boundaries, allowing for a cosine wave of wavelength $2W$ instead that also satisfies no-slip. Hence the splay (s) instability threshold for the case of weak anchoring (w) is estimated as

$$\alpha_c^{s,w} = \frac{2K\Gamma}{\gamma(\lambda-1)}\left[1+\left(\frac{\pi\ell_\eta}{W}\right)^2\right]; \qquad \ell_\kappa \rightarrow \infty \tag{16}$$

In the case of weak anchoring, this simple argument provides a good estimate for the transition from the quiescent state to the coherent laminar flow. This is shown in Figure 3A by comparing the expression for $\alpha_c^{s,w}$ (Eq. 16, shown as a solid black line) to the spontaneous flow transition observed in numerical simulations. On the other hand, this one dimensional model fails to account for the onset of the vortex lattice with strong anchoring.

The transition to the vortex lattice can be described as arising from the instability of a mixed bend-splay mode where both q_x, q_y $\neq 0$. To capture this instability, we fix the transverse wave number as $q_x = q_x^\star$ and then determine the critical activity above which the eigenvalue $\nu(q_x = q_x^\star, q_y)$ becomes positive. Figure 5 indicates that the transition to the vortex lattice state depends only weakly on the strength of anchoring. For this reason we simply take $q_x^\star = \pi/W$, as suggested by the fact that vortices typically have the size of the channel width at onset. The resulting critical activity for the transition to the vortex lattice state (which we refer to as a mixed instability and denote by α_c^m) is compared in Figure 9 to the splay lines given by Eqs 15, 16 for the case of strong and weak anchoring, respectively. The critical activity α_c^m is computed numerically by using the dispersion relation (Eq. 13), and computing the smallest activity such that we have an unstable mode with $q_x = \pi/W$. For weak anchoring (Figure 3A), the splay instability line $\alpha^{s,w}$ (solid black line) falls *below* the mixed instability α_c^m (solid blue line) signaling the onset of banded flow, allowing for an intervening region of coherent laminar flow shown in green. For strong anchoring (Figure 3B), the splay instability line $\alpha_{s,w}$ is always *above* the mixed instability line α_c^m (solid blue line). The splay line is therefore not shown in the figure and the systems transitions directly from the quiescent state to the vortex lattice.

5 Role of self propulsion

Throughout the discussion we have described the bacterial fluid using a polar order parameter, **p** but the model considered has nematic symmetry. In this case the flow arises from spontaneous symmetry breaking of the quiescent state and is entirely determined by deformations of the polarization field.

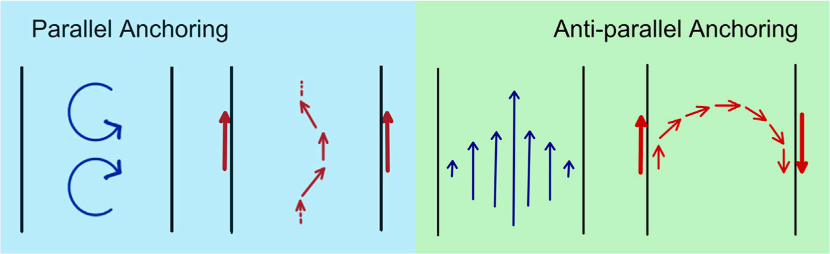

FIGURE 10
The symmetry of the boundary conditions for the polarization controls the steady flow states. Left frame: strong polar anchoring where the polarization is anchored in the same direction on both channel walls suppresses splay deformations and yields bend deformation along the wall with associated flow vortices. Right frame: strong apolar anchoring where the polarization is anchored in opposite directions on the two walls explicitly breaks the nematic symmetry even in the absence of polar self propulsion ($v_0 = 0$) and leads to coherent flow. Both flow states can occur if the boundary conditions are nematic, i.e., agnostic to the direction of the polarization vector.

The direction of flow is equally likely to be up or down the channel, with associated "splay-in" and "splay-out" configurations of polarization. In the simulations with finite anchoring this symmetry is broken externally by the boundary conditions on the polarization. The presence of a frictional substrate can, however, allow an additional propulsive force linear in **p** to be present in force balance [40, 45, 46] which takes the form

$$\Gamma\left(\mathbf{v} - v_0\mathbf{p}\right) = -\nabla\Pi + \eta\nabla^2\mathbf{v} + \nabla\cdot\left(\boldsymbol{\sigma}^{\mathrm{a}} + \boldsymbol{\sigma}^{\mathrm{lc}}\right). \tag{17}$$

This polar active force explicitly breaks the up-down symmetry of the flow. The homogeneous state in bulk is now a uniformly flowing state with $\mathbf{v} = v_0\mathbf{p}$. As a result, any finite self-propulsion v_0 then breaks the flow symmetry and selects the direction of the flowing state. A small self-propulsion provides therefore the minimal forcing required for creating sustained unidirectional channel flows. For small values of v_0, corresponding to $v_0 \ll |\alpha_0|/\Gamma\ell_\eta$, the dipolar active stress dominates over the propulsive force and the structure of the steady state flows is qualitatively unaffected. Above the critical activity for spontaneous flow, we recover coherent laminar flows arising from polarization splay for weak anchoring and flow vortex lattices for strong anchoring, as in the absence of polar self propulsion. The flow lattice, however, acquires a steady drift at speed proportional to v_0.

6 Discussion

Using a hydrodynamic model of extensile polar active matter, we have examined the role of confinement and boundary alignment in controlling the spatial and temporal organizations of active flows in a channel. We show that surface anchoring controls the flow structures by selectively frustrating bend or splay distortions in the polarization and that flows with finite throughput can only be obtained with weak surface anchoring. Strong surface anchoring leads to the formation of lattices of flow vortices, with the number of vortices determined by the aspect ratio of the channel, consistent with previous results [25, 26].

Our hydrodynamic model is inherently polar as the anchoring boundary conditions (Eq. 7) imposed at the channel walls break nematic symmetry even in the absence of any polar self propulsion (Section 5). As is evident, the symmetry of the boundary conditions plays a profound role on the selection of flow states. Strong polar anchoring, where the polarization is forced to point in the same direction on both sides of the channel, prevent splay deformation and facilitate bend along the channel walls, resulting in a state of flow vortices (Figure 10, left panel). Strong antipolar anchoring, where the polarization is forced to point in opposite directions on the two sides of the channel, allows bend deformation across the channel, resulting in finite-throughput laminar flow (Figure 10, right panel). We have also examined the case of nematic anchoring where the polarization is forced to orient with the channel wall, but with no preferred direction. This was enforced by requiring

$$\left[(\mathbf{p}\cdot\hat{\mathbf{n}})\hat{\mathbf{n}} + \ell_\kappa\left(\hat{\mathbf{n}}\cdot\nabla\mathbf{p}\right)\right]_{x=0,W} = 0. \tag{18}$$

In this case both flow states depicted in Figure 10 coexist in the phase diagram. Finally, we note that the lattice of flow vortices reported here is distinct from the state of dancing half-integer disclinations found earlier in active nematics confined to channels [47]. Here we consider a polar system, where defect in the polarization texture are +1 and −1 vortices. Such defects are indeed observed in the turbulent state at high activity. The lattice of flow vortices reported here is, however, a defect-free steady state.

Our work quantifies the role surface anchoring in controlling the spatio-temporal structure of confined active flows. This understanding can be useful for the design of active microfluidic devices where channel dimensions and boundary preparation can be independently tuned to control viscous screening and anchoring, respectively.

Recent experiments on microtubule suspensions in 3D and associated numerical studies have demonstrated that coherent flow is only possible for finely tuned geometries [17, 48–50]. Our work suggests that it would be interesting to additionally explore the role of anchoring in these 3D systems where antagonistic boundary conditions on the three walls could result in as of yet unexplored states.

Finally, it would also be interesting to explore the role of surface anchoring on temporal as well as spatial organization of active flows. Recent experiments in dense bacterial suspensions [51] have revealed that viscoelasticity of the suspending medium can drive a circular droplet to self-organize in time-periodic states of vortical flow, consisting of a system-spanning vortex that switches its chirality at a rate controlled by the solvent relaxation time. The vortex state of a circular drops corresponds to unidirectional laminar flow in a channel. As we have seen, the direction of the flow is directly determined by the splay-in or splay-out configuration of the polarization field, which in turn can be controlled with suitable anchoring. This suggest that anchoring may play an important role in controlling temporal as well as spatial organization and that it may be possible to control oscillations between flows of opposite chirality by tuning the boundary conditions. These questions are left for future studies.

Data availability statement

The raw data supporting the conclusion of this article will be made available by the authors, without undue reservation.

Author contributions

PG performed the numerical simulations and prepared the figures. All authors contributed to the formulation of the project, the analysis of the model and the writing of the paper.

Funding

This work was directly supported by NSF grant DMR-2041459. SS acknowledges support from the Harvard Society of Fellows. Use was made of computational facilities purchased with funds from the National Science Foundation (CNS-1725797) and administered by the Center for Scientific Computing (CSC). The CSC is supported by the California NanoSystems Institute and the Materials Research Science and Engineering Center (MRSEC; NSF DMR 1720256) at UC Santa Barbara.

Conflict of interest

The authors declare that the research was conducted in the absence of any commercial or financial relationships that could be construed as a potential conflict of interest.

Publisher's note

References

1. Wensink HH, Dunkel J, Heidenreich S, Drescher K, Goldstein RE, Löwen H, et al. Meso-scale turbulence in living fluids. *Proc Natl Acad Sci U S A* (2012) 109: 14308–13. doi:10.1073/pnas.1202032109

2. Zhou S, Sokolov A, Lavrentovich OD, Aranson IS. Living liquid crystals. *Proc Natl Acad Sci U S A* (2014) 111:1265–70. doi:10.1073/pnas.1321926111

3. Sanchez T, Chen DT, DeCamp SJ, Heymann M, Dogic Z. Spontaneous motion in hierarchically assembled active matter. *Nature* (2012) 491:431–4. doi:10.1038/nature11591

4. Schaller V, Weber C, Semmrich C, Frey E, Bausch AR. Polar patterns of driven filaments. *Nature* (2010) 467:73–7. doi:10.1038/nature09312

5. Palacci J, Sacanna S, Steinberg AP, Pine DJ, Chaikin PM. Living crystals of light-activated colloidal surfers. *Science* (2013) 339:936–40. doi:10.1126/science.1230020

6. Bricard A, Caussin JB, Desreumaux N, Dauchot O, Bartolo D. Emergence of macroscopic directed motion in populations of motile colloids. *Nature* (2013) 503: 95–8. doi:10.1038/nature12673

7. Marchetti MC, Joanny JF, Ramaswamy S, Liverpool TB, Prost J, Rao M, et al. Hydrodynamics of soft active matter. *Rev Mod Phys* (2013) 85:1143–89. doi:10.1103/revmodphys.85.1143

8. Simha RA, Ramaswamy S. Hydrodynamic fluctuations and instabilities in ordered suspensions of self-propelled particles. *Phys Rev Lett* (2002) 89:058101. doi:10.1103/physrevlett.89.058101

9. Alert R, Casademunt J, Joanny JF. Active turbulence. *Annu Rev Condens Matter Phys* (2021) 13:143–70. doi:10.1146/annurev-conmatphys-082321-035957

10. Duclos G, Garcia S, Yevick H, Silberzan P. Perfect nematic order in confined monolayers of spindle-shaped cells. *Soft matter* (2014) 10:2346–53. doi:10.1039/c3sm52323c

11. Doostmohammadi A, Adamer MF, Thampi SP, Yeomans JM. Stabilization of active matter by flow-vortex lattices and defect ordering. *Nat Commun* (2016) 7: 10557. doi:10.1038/ncomms10557

12. Duclos G, Blanch-Mercader C, Yashunsky V, Salbreux G, Joanny JF, Prost J, et al. Spontaneous shear flow in confined cellular nematics. *Nat Phys* (2018) 14: 728–32. doi:10.1038/s41567-018-0099-7

13. Thijssen K, Khaladj DA, Aghvami SA, Gharbi MA, Fraden S, Yeomans JM, et al. Submersed micropatterned structures control active nematic flow, topology, and concentration. *Proc Natl Acad Sci U S A* (2021) 118:e2106038118. doi:10.1073/pnas.2106038118

14. Voituriez R, Joanny JF, Prost J. Spontaneous flow transition in active polar gels. *Europhys Lett* (2005) 70:404–10. doi:10.1209/epl/i2004-10501-2

15. Wioland H, Woodhouse FG, Dunkel J, Kessler JO, Goldstein RE. Confinement stabilizes a bacterial suspension into a spiral vortex. *Phys Rev Lett* (2013) 110:268102. doi:10.1103/physrevlett.110.268102

16. Lushi E, Wioland H, Goldstein RE. Fluid flows created by swimming bacteria drive self-organization in confined suspensions. *Proc Natl Acad Sci U S A* (2014) 111:9733–8. doi:10.1073/pnas.1405698111

17. Wu KT, Hishamunda JB, Chen DT, DeCamp SJ, Chang YW, Fernández-Nieves A, et al. Transition from turbulent to coherent flows in confined three-dimensional active fluids. *Science* (2017) 355:eaal1979. doi:10.1126/science.aal1979

18. Chen S, Gao P, Gao T. Dynamics and structure of an apolar active suspension in an annulus. *J Fluid Mech* (2018) 835:393–405. doi:10.1017/jfm.2017.759

19. Opathalage A, Norton MM, Juniper MP, Langeslay B, Aghvami SA, Fraden S, et al. Self-organized dynamics and the transition to turbulence of confined active nematics. *Proc Natl Acad Sci U S A* (2019) 116:4788–97. doi:10.1073/pnas.1816733116

20. You Z, Pearce DJ, Giomi L. Confinement-induced self-organization in growing bacterial colonies. *Sci Adv* (2021) 7:eabc8685. doi:10.1126/sciadv.abc8685

21. Wioland H, Lushi E, Goldstein RE. Directed collective motion of bacteria under channel confinement. *New J Phys* (2016) 18:075002. doi:10.1088/1367-2630/18/7/075002

22. Tjhung E, Cates ME, Marenduzzo D. Nonequilibrium steady states in polar active fluids. *Soft Matter* (2011) 7:7453. doi:10.1039/c1sm05396e

23. Giomi L, Marchetti MC, Liverpool TB. Complex spontaneous flows and concentration banding in active polar films. *Phys Rev Lett* (2008) 101:198101. doi:10.1103/physrevlett.101.198101

24. Yang X, Wang Q. Role of the active viscosity and self-propelling speed in channel flows of active polar liquid crystals. *Soft Matter* (2016) 12:1262–78. doi:10.1039/c5sm02115d

25. Chandragiri S, Doostmohammadi A, Yeomans JM, Thampi SP. Active transport in a channel: Stabilisation by flow or thermodynamics. *Soft matter* (2019) 15:1597–604. doi:10.1039/c8sm02103a

26. Shendruk TN, Doostmohammadi A, Thijssen K, Yeomans JM. Dancing disclinations in confined active nematics. *Soft Matter* (2017) 13:3853–62. doi:10.1039/c6sm02310j

27. Samui A, Yeomans JM, Thampi SP. Flow transitions and length scales of a channel-confined active nematic. *Soft Matter* (2021) 17:10640–8. doi:10.1039/d1sm01434j

28. Wagner CG, Norton MM, Park JS, Grover P. Exact coherent structures and phase space geometry of preturbulent 2d active nematic channel flow. *Phys Rev Lett* (2022) 128:028003. doi:10.1103/physrevlett.128.028003

29. Hardoüin J, Hughes R, Doostmohammadi A, Laurent J, Lopez-Leon T, Yeomans JM, et al. Reconfigurable flows and defect landscape of confined active nematics. *Commun Phys* (2019) 2:121. doi:10.1038/s42005-019-0221-x

30. Norton MM, Baskaran A, Opathalage A, Langeslay B, Fraden S, Baskaran A, et al. Insensitivity of active nematic liquid crystal dynamics to topological constraints. *Phys Rev E* (2018) 97:012702. doi:10.1103/physreve.97.012702

31. Rorai C, Toschi F, Pagonabarraga I. Active nematic flows confined in a two-dimensional channel with hybrid alignment at the walls: A unified picture. *Phys Rev Fluids* (2021) 6:113302. doi:10.1103/physrevfluids.6.113302

32. Poujade M, Grasland-Mongrain E, Hertzog A, Jouanneau J, Chavrier P, Ladoux B, et al. Collective migration of an epithelial monolayer in response to a model wound. *Proc Natl Acad Sci U S A* (2007) 104:15988–93. doi:10.1073/pnas.0705062104

33. Conrad JC, Poling-Skutvik R. Confined flow: Consequences and implications for bacteria and biofilms. *Annu Rev Chem Biomol Eng* (2018) 9:175–200. doi:10.1146/annurev-chembioeng-060817-084006

34. Beebe DJ, Mensing GA, Walker GM. Physics and applications of microfluidics in biology. *Annu Rev Biomed Eng* (2002) 4:261–86. doi:10.1146/annurev.bioeng.4.112601.125916

35. Clark AG, Vignjevic DM. Modes of cancer cell invasion and the role of the microenvironment. *Curr Opin Cel Biol* (2015) 36:13–22. doi:10.1016/j.ceb.2015.06.004

36. Needleman D, Dogic Z. Active matter at the interface between materials science and cell biology. *Nat Rev Mater* (2017) 2:17048. doi:10.1038/natrevmats.2017.48

37. DeGennes P, Prost J. *Physics of liquid crystals*. Oxford: Clarendon (1994).

38. Giomi L. Geometry and topology of turbulence in active nematics. *Phys Rev X* (2015) 5:031003. doi:10.1103/physrevx.5.031003

39. Hemingway EJ, Mishra P, Marchetti MC, Fielding SM. Correlation lengths in hydrodynamic models of active nematics. *Soft Matter* (2016) 12:7943–52. doi:10.1039/c6sm00812g

40. Maitra A, Srivastava P, Marchetti MC, Ramaswamy S, Lenz M. Swimmer suspensions on substrates: Anomalous stability and long-range order. *Phys Rev Lett* (2020) 124:028002. doi:10.1103/physrevlett.124.028002

41. Alnæs M, Blechta J, Hake J, Johansson A, Kehlet B, Logg A, et al. The fenics project version 1.5. *Archive Numer Softw* (2015) 3.

42. Logg A, Mardal KA, Wells G. *Automated solution of differential equations by the finite element method: The FEniCS book, vol. 84*. Berlin, Germany: Springer Science & Business Media (2012).

43. Thampi SP, Golestanian R, Yeomans JM. Active nematic materials with substrate friction. *Phys Rev E* (2014) 90:062307. doi:10.1103/physreve.90.062307

44. Green R, Toner J, Vitelli V. Geometry of thresholdless active flow in nematic microfluidics. *Phys Rev Fluids* (2017) 2:104201. doi:10.1103/physrevfluids.2.104201

45. Brotto T, Caussin JB, Lauga E, Bartolo D. Hydrodynamics of confined active fluids. *Phys Rev Lett* (2013) 110:038101. doi:10.1103/physrevlett.110.038101

46. Kumar N, Soni H, Ramaswamy S, Sood A. Flocking at a distance in active granular matter. *Nat Commun* (2014) 5:4688. doi:10.1038/ncomms5688

47. Alert R, Joanny JF, Casademunt J. Universal scaling of active nematic turbulence. *Nat Phys* (2020) 16:682–8. doi:10.1038/s41567-020-0854-4

48. Chandragiri S, Doostmohammadi A, Yeomans JM, Thampi SP. Flow states and transitions of an active nematic in a three-dimensional channel. *Phys Rev Lett* (2020) 125:148002. doi:10.1103/physrevlett.125.148002

49. Chandrakar P, Varghese M, Aghvami SA, Baskaran A, Dogic Z, Duclos G, et al. Confinement controls the bend instability of three-dimensional active liquid crystals. *Phys Rev Lett* (2020) 125:257801. doi:10.1103/physrevlett.125.257801

50. Varghese M, Baskaran A, Hagan MF, Baskaran A. Confinement-induced self-pumping in 3d active fluids. *Phys Rev Lett* (2020) 125:268003. doi:10.1103/physrevlett.125.268003

51. Liu S, Shankar S, Marchetti MC, Wu Y. Viscoelastic control of spatiotemporal order in bacterial active matter. *Nature* (2021) 590:80–4. doi:10.1038/s41586-020-03168-6

Advantages of publishing in Frontiers

OPEN ACCESS
Articles are free to read for greatest visibility and readership

FAST PUBLICATION
Around 90 days from submission to decision

HIGH QUALITY PEER-REVIEW
Rigorous, collaborative, and constructive peer-review

TRANSPARENT PEER-REVIEW
Editors and reviewers acknowledged by name on published articles

Frontiers
Avenue du Tribunal-Fédéral 34
1005 Lausanne | Switzerland

Visit us: www.frontiersin.org
Contact us: frontiersin.org/about/contact

REPRODUCIBILITY OF RESEARCH
Support open data and methods to enhance research reproducibility

DIGITAL PUBLISHING
Articles designed for optimal readership across devices

FOLLOW US
@frontiersin

IMPACT METRICS
Advanced article metrics track visibility across digital media

EXTENSIVE PROMOTION
Marketing and promotion of impactful research

LOOP RESEARCH NETWORK
Our network increases your article's readership